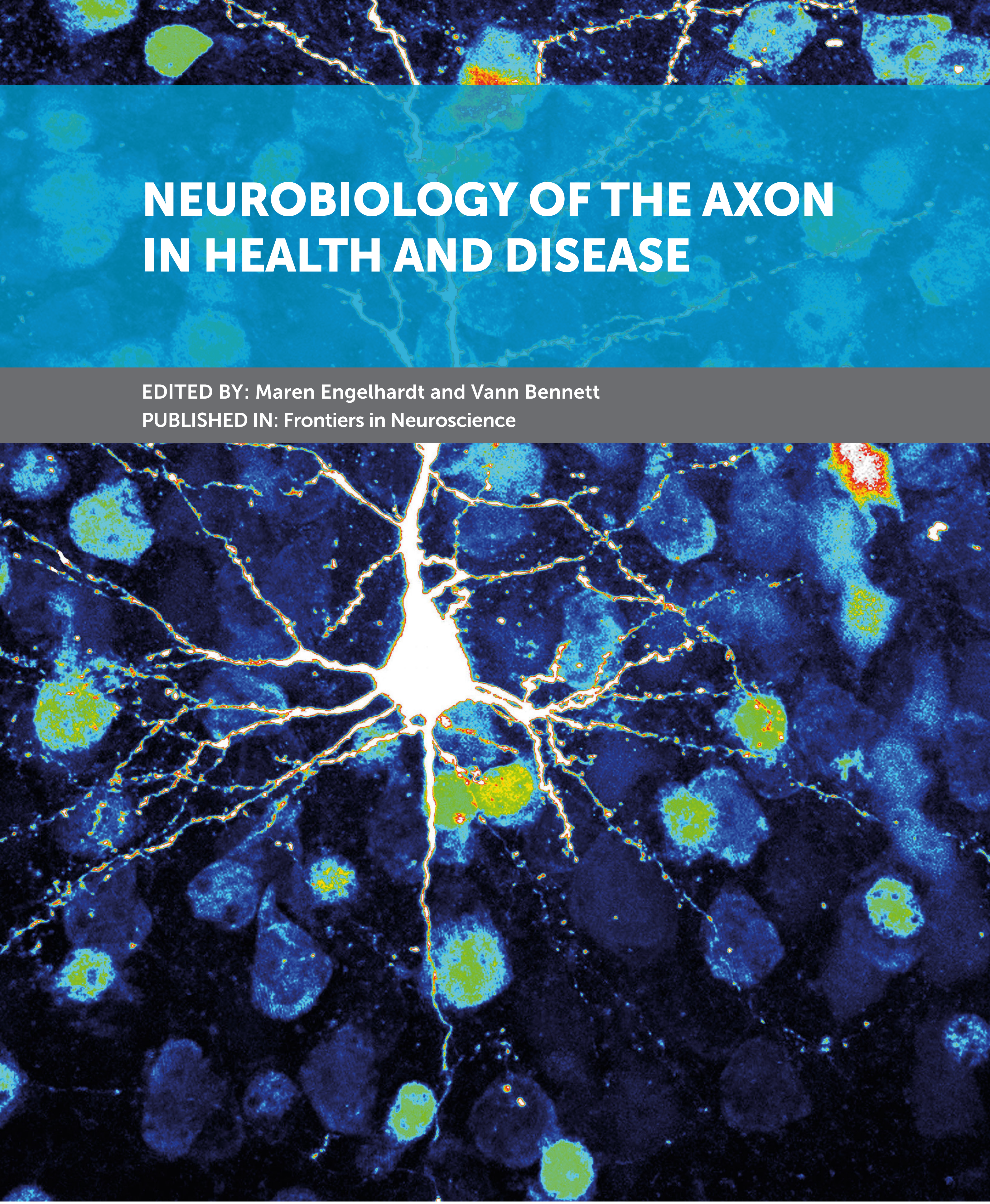

NEUROBIOLOGY OF THE AXON IN HEALTH AND DISEASE

EDITED BY: Maren Engelhardt and Vann Bennett
PUBLISHED IN: Frontiers in Neuroscience

frontiers Research Topics

ISSN 1664-8714
ISBN 978-2-88919-488-9
DOI 10.3389/978-2-88919-488-9

About Frontiers

Frontiers is more than just an open-access publisher of scholarly articles: it is a pioneering approach to the world of academia, radically improving the way scholarly research is managed. The grand vision of Frontiers is a world where all people have an equal opportunity to seek, share and generate knowledge. Frontiers provides immediate and permanent online open access to all its publications, but this alone is not enough to realize our grand goals.

Frontiers Journal Series

The Frontiers Journal Series is a multi-tier and interdisciplinary set of open-access, online journals, promising a paradigm shift from the current review, selection and dissemination processes in academic publishing. All Frontiers journals are driven by researchers for researchers; therefore, they constitute a service to the scholarly community. At the same time, the Frontiers Journal Series operates on a revolutionary invention, the tiered publishing system, initially addressing specific communities of scholars, and gradually climbing up to broader public understanding, thus serving the interests of the lay society, too.

Dedication to Quality

Each Frontiers article is a landmark of the highest quality, thanks to genuinely collaborative interactions between authors and review editors, who include some of the world's best academicians. Research must be certified by peers before entering a stream of knowledge that may eventually reach the public - and shape society; therefore, Frontiers only applies the most rigorous and unbiased reviews.
Frontiers revolutionizes research publishing by freely delivering the most outstanding research, evaluated with no bias from both the academic and social point of view.
By applying the most advanced information technologies, Frontiers is catapulting scholarly publishing into a new generation.

What are Frontiers Research Topics?

Frontiers Research Topics are very popular trademarks of the Frontiers Journals Series: they are collections of at least ten articles, all centered on a particular subject. With their unique mix of varied contributions from Original Research to Review Articles, Frontiers Research Topics unify the most influential researchers, the latest key findings and historical advances in a hot research area! Find out more on how to host your own Frontiers Research Topic or contribute to one as an author by contacting the Frontiers Editorial Office: researchtopics@frontiersin.org

NEUROBIOLOGY OF THE AXON IN HEALTH AND DISEASE

Topic Editors:
Maren Engelhardt, Medical Faculty Mannheim, Heidelberg University, Germany
Vann Bennett, Duke University, United States

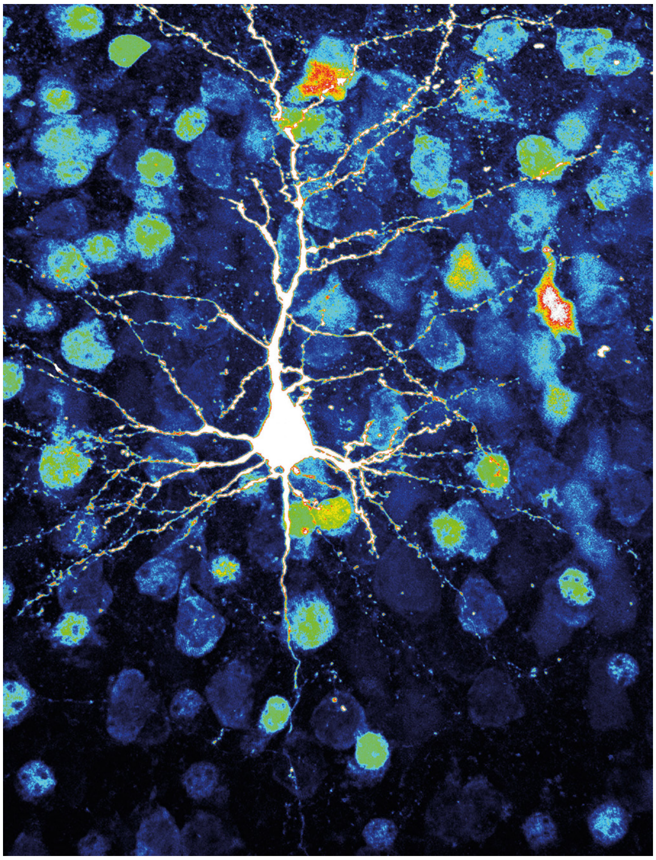

A single layer II/III pyramidal neuron from mouse primary somatosensory cortex barrel field, filled with biocytin (white) and surrounded by NeuN-positive neurons (blue/green). Image enhanced for brightness and contrast in Photoshop, LUT from Fiji (ImageJ).
Image: Nora Jamann & Maren Engelhardt.

Ever since Santiago Ramón y Cajal sketched his captivating panels of the microscopic structure of the brain with its vast diversity of neuronal morphology over a century ago, scientists have been drawn to this seemingly chaotic network of neurites and processes to uncover how structure relates to function. During the course of a century, we have moved from merely describing neuronal and glial morphology to furthering our understanding of such intricate processes as organelle and factor transport, cellular compartmentalization, neuronal polarity, cytoskeleton dynamics, neurite pathfinding, and the impact of pathophysiological insult on these structures and events. Yet to this day, and likely for the foreseeable future, much work remains to be done to fully grasp the exceptional role of neurites for the function of larger neuronal ensembles and networks. While the somatodendritic domain of neurons has been in the focus of attention for many years, mostly because of its great dynamic remodeling capacity during events of plasticity (e.g. learning), the axonal domain has somehow remained in the background despite the fact that especially recent comprehensive studies from various fields of research underline the axon's contribution to dynamic plasticity processes. Consequently, this Research Topic focuses on the many exciting aspects of axonal neurobiology – ranging from membrane composition and molecular determination during development to axonal domain specialization and physiology in health and disease.

In Chapter 1 "Axons in the PNS", Bombeiro et al. use immunodeficient mice to study the role of lymphocytes during the regeneration of peripheral nerves, showing that the modulation of immune responses after injury can be an efficient approach to enhance nerve regeneration in the PNS. Using a DRG model, Berbusse et al. identify the onset of damage to mitochondrial structure and dynamics as a key event during early axon degeneration and provide evidence that Nmnat1, a member of the family of nicotinamide-nucleotide adenylyltransferases, can have protective effects by preserving normal mitochondrial integrity and dynamics. In another study of PNS nerve regeneration, Law et al. use proteomics approaches via Mass Spectrometry to provide evidence that rosovitine, a synthetic purine nucleoside analog, can successfully promote PNS axon regeneration.

In Chapter 2 "Axonal development in the central nervous system", Yoshimura et al. analyze specialized axonal domains, namely the axon initial segment and nodes of Ranvier, with regards to their expression profiles of the major scaffolding protein ßIV-spectrin. Super resolution microscopy reveals a potential developmental switch of spectrin isoforms at both axonal domains. In a related study, also using super resolution microscopy, Leterrier et al. examine a potential reciprocal role of membrane partners in ankyrin-G targeting and stabilization at the axonal membrane during development. The authors demonstrate a tight and precocious association of ankyrin-G with its membrane partners. Höfflin et al. address the question of axon initial segment morphology across different cell classes in cortical organotypic slice cultures and find a surprising heterogeneity especially between pyramidal cells and interneurons in primary visual cortex. In a major step towards establishing a successful live label of the axon initial segment, Dumitrescu et al. report the development of a genetically-encoded construct consisting of a voltage-gated sodium channel intracellular domain fused to yellow fluorescent protein (YFP-NaVII-III). Nelson and Jenkins then provide a comprehensive Review article on the axon initial segment and nodes of Ranvier with a special focus on the various scaffolding protein isoforms and their role in human disease.

In Chapter 3 "Axonal physiology and plasticity", Nikitin et al. investigate fast onset dynamics of action potentials during neuronal development in vitro, showing that encoding of high frequencies improves upon culture maturation, accompanied by the development of passive electrophysiological properties and action potential generation. Using pharmacological and RNA interference approaches, Tapia et al. provide evidence that cannabinoid receptors and their ligands can modulate dendritic morphology and thus, indirectly, also affect ankyrin-G accumulation at the axon initial segment. A Mini Review by Zbili et al. discusses the potential impact of subthreshold changes in presynaptic membrane potential before action potential initiation on neurotransmitter release, and which significant impact such mechanisms could have on information processing in neuronal circuits. Yamada and Kuba close this chapter with a Mini Review on axon initial segment plasticity with a particular focus on ion channels and the biophysics of excitability.

In Chapter 4 "Axon degeneration and regeneration", Hamada et al. investigate the often overlooked question to which extent myelin loss affects action potential propagation along distal branch points and axon collaterals. Using the cuprizone demyelination model and optical voltage-sensitive dye imaging, the authors uncover functional consequences of demyelination that reach well beyond the main axon. In a model of mild traumatic brain injury, Vascak et al. demonstrate complex aspects of this injury type on neocortical circuit function, including changes in inhibitory perisomatic input and axon initial segment-driven output in affected layer V neurons. In a Mini Review, Grosch et al. discuss recent advances in the field of Parkinson's disease with a focus on early degeneration in dopaminergic and serotonergic neurons of the basal ganglia. The last two articles cover the topic of axonal regeneration. Li et al. investigate the role of activated astrocytes in spinal cord lesion and how their functional downregulation via an inhibitor of mitochondrial fission, Mdivi-1, could potentially have positive impact on lesion scar formation and axonal regeneration. In a final Review, Liu et al. highlight recent advances in the development of biomaterial scaffolds and cell transplantation strategies to combine two promising therapeutic approaches for spinal cord injury.

Citation: Engelhardt, M., Bennett, V., eds. (2019). Neurobiology of the Axon in Health and Disease. Lausanne: Frontiers Media. doi: 10.3389/978-2-88919-488-9

Table of Contents

CHAPTER 1

AXONS IN THE PERIPHERAL NERVOUS SYSTEM

CHAPTER 2

AXONAL DEVELOPMENT IN THE CENTRAL NERVOUS SYSTEM

SECTION

MOLECULAR AND CELLULAR MECHANISMS

CHAPTER 3
AXONAL PHYSIOLOGY AND PLASTICITY

CHAPTER 4
AXON DEGENERATION AND REGENERATION
SECTION
DEGENERATION

SECTION
REGENERATION

frontiers
in Cellular Neuroscience

ORIGINAL RESEARCH
published: 14 June 2016
doi: 10.3389/fncel.2016.00151

Enhanced Immune Response in Immunodeficient Mice Improves Peripheral Nerve Regeneration Following Axotomy

André L. Bombeiro, Júlio C. Santini, Rodolfo Thomé, Elisângela R. L. Ferreira, Sérgio L. O. Nunes, Bárbara M. Moreira, Ivan J. M. Bonet, Cesar R. Sartori, Liana Verinaud and Alexandre L. R. Oliveira*

Department of Structural and Functional Biology, Institute of Biology, University of Campinas, Campinas, Brazil

Injuries to peripheral nerves cause loss of motor and sensory function, greatly affecting life quality. Successful repair of the lesioned nerve requires efficient cell debris removal, followed by axon regeneration and reinnervation of target organs. Such process is orchestrated by several cellular and molecular events in which glial and immune cells actively participate. It is known that tissue clearance is largely improved by macrophages, which activation is potentiated by cells and molecules of the acquired immune system, such as T helper lymphocytes and antibodies, respectively. In the present work, we evaluated the contribution of lymphocytes in the regenerative process of crushed sciatic nerves of immunocompetent (wild-type, WT) and T and B-deficient (RAG-KO) mice. In Knockout animals, we found increased amount of macrophages under basal conditions and during the initial phase of the regenerative process, that was evaluated at 2, 4, and 8 weeks after lesion (wal). That parallels with faster axonal regeneration evidenced by the quantification of neurofilament and a growth associated protein immunolabeling. The motor function, evaluated by the sciatic function index, was fully recovered in both mouse strains within 4 wal, either in a progressive fashion, as observed for RAG-KO mice, or presenting a subtle regression, as seen in WT mice between 2 and 3 wal. Interestingly, boosting the immune response by early adoptive transference of activated WT lymphocytes at 3 days after lesion improved motor recovery in WT and RAG-KO mice, which was not ameliorated when cells were transferred at 2 wal. When monitoring lymphocytes by *in vivo* imaging, in both mouse strains, cells migrated to the lesion site shortly after transference, remaining in the injured limb up to its complete motor recovery. Moreover, a first peak of hyperalgesia, determined by von-Frey test, was coincident with increased lymphocyte infiltration in the damaged paw. Overall, the present results suggest that a wave of immune cell infiltration takes place during subacute phase of axonal regeneration, resulting in transient set back of motor recovery following peripheral axonal injury. Moreover, modulation of the immune response can be an efficient approach to speed up nerve regeneration.

Keywords: sciatic nerve, PNS, neuroimmunology, inflammation, axonal regeneration

Edited by:
Maren Engelhardt,
Heidelberg University, Germany

Reviewed by:
Alexander K. Murashov,
East Carolina University, USA
George Smith,
Temple University, USA

****Correspondence:***
Alexandre L. R. Oliveira
alroliv@unicamp.br

Received: *15 February 2016*
Accepted: *27 May 2016*
Published: *14 June 2016*

Citation:
Bombeiro AL, Santini JC, Thomé R, Ferreira ERL, Nunes SLO, Moreira BM, Bonet IJM, Sartori CR, Verinaud L and Oliveira ALR (2016) Enhanced Immune Response in Immunodeficient Mice Improves Peripheral Nerve Regeneration Following Axotomy. Front. Cell. Neurosci. 10:151. doi: 10.3389/fncel.2016.00151

INTRODUCTION

Peripheral nervous system (PNS) demyelinating diseases (Juarez and Palau, 2012; Ripellino et al., 2014; Winer, 2014) and trauma result in action potential impairments with loss of function (Siddique and Thakor, 2014). Successful repair of the lesioned nerve requires efficient cell debris removal, followed by axon regeneration and reinnervation of target organs, a process that is orchestrated by several cellular and molecular events in which glial and immune cells actively participate. After PNS injuries, damaged tissue undergoes clearance and remodeling, the so called Wallerian degeneration. In this process, axons from the distal stump degenerate and the myelin sheaths breakdown, the blood nerve barrier permeability increases and macrophage influx occurs (Vargas and Barres, 2007). Myelin fragments are removed and Schwann cells proliferate and migrate to the lesion site providing structural and physiological support to axon guided growth (Vargas and Barres, 2007; Rotshenker, 2011).

Both the innate and the acquired immune responses are activated after PNS trauma. In the first few days post-injury, Schwann cells remove myelin debris and release neurotrophic factors, cytokines, and chemokines that recruit phagocytes to the lesion site. Tissue clearance is improved by macrophages, which phagocytic capacity is potentiated by pro-inflammatory cytokines released by infiltrating CD4 T cells and opsonins, such as C3b proteins of the complement system (Bruck and Friede, 1990; Sarma and Ward, 2011) and antibodies produced by B lymphocytes. Such molecules are important for rapid myelin removal after nerve injury (Vargas et al., 2010). Tissue clearance is an important step for the regenerative process since axon growth inhibitory proteins, such as the myelin-associated glycoprotein (MAG), are present in the fragmented myelin (Fruttiger et al., 1995; Jessen and Mirsky, 2008). When cell fragments and myelin debris are cleared, the inflammatory response is suppressed by M2 macrophages and T helper (Th) 2 lymphocytes, creating a microenvironment prone to the neuroregenerative process (Gaudet et al., 2011). Although cytotoxic CD8 T cells are found in demyelinating and neurodegenerative diseases, such as multiple sclerosis and amyotrophic lateral sclerosis, their function in disease onset and progression is not fully understood. While some studies suggest a regulatory role of CD8 T lymphocytes on CD4 T cell activity (Zozulya and Wiendl, 2008) and dendritic cell activation (Kashi et al., 2014) during experimental autoimmune encephalomyelitis (EAE), other demonstrate that CD8 T cells aggravate CD4 T cell mediated EAE (Mars et al., 2007). Regarding the PNS regeneration after traumas, very few are known about the role of CD8 T lymphocytes during this process.

In view of the importance of the immune response for nerve regeneration, we evaluated regeneration and motor recovery after crushing the sciatic nerve of mice with distinct levels of acquired immune competency. In this way, we compared the regenerative performance of immunocompetent mice with those lacking mature T and B lymphocytes. Moreover, we analyzed motor function recovery and nociceptive threshold after increasing the immune response by adoptive transference of activated lymphocytes. In this regard, migration to the lesion site was monitored *in vivo* via live imaging analysis.

MATERIALS AND METHODS

Animals

For this study, we used C57BL/6 immunocompetent (wild type, WT) and C57BL/6 recombination activating gene 1 (RAG1)-knockout (KO) mice. During T-and B-cell development, antigen receptor genes undergo somatic recombination to generate a repertoire of cells with distinct antigen receptors, each cell being capable of recognizing one specific antigen. This process depends on the activity of proteins encoded by the RAG1 and the RAG2 genes. In the absence of any of those genes, immune cells do not complete their maturation process, dying by apoptosis before reaching secondary lymphoid organs in the periphery. In this sense, RAG1-KO mice do not produce mature B and T lymphocytes (Mombaerts et al., 1992). Six to eight week old male mice were bred in-house, at the Laboratory of Neural Regeneration, Institute of Biology, State University of Campinas. Mice were kept in appropriate micro-isolators, under a light-dark cycle of 12 h, with controlled temperature and humidity, receiving water and food *ad libitum*. All experiments concerning animal handling were approved by the Institutional Committee for Ethics in Animal Experimentation (Committee for Ethics in Animal Use – Institute of Biology – CEUA/IB/UNICAMP, protocol numbers 2524-1 and 3753-1) and were performed in accordance to the guidelines of the Brazilian College for Animal Experimentation.

Experimental Procedures

Experimental mice ($n = 18$ each strain) were anesthetized with ketamine (Fort Dodge, USA, 100 mg/kg) and xylazine (König, Argentina, 20 mg/kg) and the left sciatic nerve was crushed at the sciatic notch level, with a flat tip forceps (number 4), being applied a constant pressure during 30 s. Animals were submitted to a functional gait analysis, as described below and at 2, 4, and 8 weeks after lesion (wal), mice ($n = 6$ per time point, each strain) were deeply anesthetized (ketamine 200 mg/kg and xilasin 40 mg/kg) and euthanized by transcardial perfusion with ice cold phosphate buffer saline (PBS) 0.1 M, pH 7.4, followed by cold fixative solution (formaldehyde 10% in PB 0.1 M, pH 7.4). Crushed nerves were dissected out for immunohistochemistry procedures. As negative control, left sciatic nerve of mice that were not submitted to surgery ($n = 6$) were obtained as described above.

Tissue Preparation and Sampling for Histological Analysis

The two third distal portion of the sciatic nerve (distally to the crushing site) was post-fixed overnight at 4°C, rinsed 3× in PBS 0.1 M and then stored overnight sequentially in 10 and 20% (w/v) sucrose at 4°C. Cryoprotected samples were immersed in tissue freezing medium (Tissue-Tek, Sakura Finetek), frozen in liquid nitrogen cooled *n*-hexane at −35°C and cryostat sectioned (Microm, HM 525). Non-adjacent longitudinal sections (12 μm thick) were mounted in gelatin-coated glass slides, in such a manner that the interval between sections in each slide was

108 μm. In general, 2–3 sections were placed in each slide, depending on the size of the sample. Slides were kept at −20°C up to use (immunohistochemical procedures, H&E or Sudan Black staining).

Functional Analysis

For the motor function evaluation, we used the automated Cat Walk System (Noldus Inc., Netherlands) as previously described (Barbizan et al., 2013), and calculated the Sciatic Function Index (SFI). In brief, the animal walks on a glass platform that is illuminated in its thickness with green leds, what enhances the footprints, when the paws contact the glass surface. A high-speed camera underneath the walkway records the run and data are transferred to a host computer, where a software analyzes the paw prints. For adaptation, mice were allowed to freely walk in the system during 3 days, 5 min/day, before the real experiments. Control runs were registered before surgery. Data were collected on a daily basis. To calculate the SFI, we employed the following formula (de Medinaceli et al., 1982): $\mathrm{SFI} = 118.9((\mathrm{ETS} - \mathrm{NTS})/\mathrm{NTS}) - 51.2((\mathrm{EPL} - \mathrm{NPL})/\mathrm{NPL}) - 7.5$, where N, normal or non-operated side; E, experimental or crushed side; PL, print length and TS, total toe spread.

Mechanical Hyperalgesia

Mice were individually placed in wire grid floor-acrylic cages (10 × 10 × 20 cm high) with a tilted mirror below them, to provide a view of the hind paws. A gradual increasing pressure was applied in the central plantar area of the injured hind paw with a 0.5-mm^2 polypropylene tip coupled in a handheld force transducer (electronic anesthesiometer, EFF 301 by Insight, Ribeirão Preto, Brazil), evoking flexion reflex and thus the paw withdraw. Pressure intensity was automatically recorded three times for each animal, with an interval of approximately 10 min between each measurement. The baseline paw-withdrawal threshold was obtained before surgery, being 8 g the maximum pressure limit stablished. Mice were evaluated up to 35 days after surgery, as indicated in the results. Data are expressed as the mean of the pressure intensity minus the mean of the baseline pressure values.

Immunofluorescence and Protein Quantification

Sections were washed with PB 0.1 M and blocked with bovine serum albumin (BSA) 3% (w/v, diluted in PB 0.1 M) for 1 h, at room temperature. Then, samples were incubated overnight at 4°C, with one of the following primary antibodies: mouse anti-neurofilament protein (1:4000, Dako Cytomation, Cat. code: M0762), rabbit anti-growth associated protein 43 (GAP-43, 1:250, Santa Cruz, Cat. code: SC-10786) and rabbit anti-Iba-1 (1:700, Wako, Cat. code: 019-19741). After rinsing, sections were incubated for 45 min, at room temperature, with one of the secondary antibodies: Cy3-AffiniPure donkey anti-mouse IgG (1:500, Jackson ImmuneResearch, Cat. code: 715-165-150) and Cy3-AffiniPure donkey anti-rabbit IgG (1:500, Jackson ImmuneResearch, Cat. code: 715-165-152). Sections were rinsed in PBS and coverslips were mounted with anti-fading media (ProLong® Gold anti-fading reagent, Invitrogen, Cat. code: P36930). All antibodies were diluted in PB 0.1 M solution containing BSA 1% (w/v) and Triton X-100 0.2% (v/v). For detection of autoantibodies produced by WT mice used for the adoptive cell transfer (bellow), nerve sections from unlesioned RAG-KO mice were incubated with serum (1:30) obtained from unlesioned or sciatic nerve crushed WT mice (14 dal) overnight at 4°C, followed by CY3 anti-mouse IgG, as previously described. As internal control, sections were submitted to the same procedures, being incubated with PBS instead of serum. For protein quantification, sections were analyzed in a fluorescence microscopy (Nikon Eclipse TS100 microscope connected to a Nikon DXM1200F digital camera or Leica DM5500B microscope coupled with a Leica DFC345 FX camera). For each sample, distal to the lesion site, five equidistant representative pictures were obtained. The integrated density of pixels (IDP) was obtained with the ImageJ software (version 1.45s, National Institute of Health, USA), applying the enhance contrast and density slicing feature in a fixed area of each picture (490,000 pixels^2). The IDP mean values from each sample were considered as the raw data. Results are expressed as the ratio of the mean values of the operated groups by their respective controls (non-operated) when no difference in the IDP between the unlesioned groups was observed. If differences between the control groups were observed, data are shown as the raw IDP mean values.

Lymphocyte Adoptive Transfer

Unilateral sciatic nerve crushed WT mice ($n = 4$) were euthanized by halothane inhalation at 14 days after lesion (dal). Spleens were collected and dissociated in cold PBS with a 70 μm cell strainer. Lymphocytes were isolated by Percoll (Sigma–Aldrich, Cat. code: P1644) gradient according to the manufacturer instructions, labeled with carboxyfluorescein succinimidyl ester (CFSE, 1.25 μM, Sigma–Aldrich, USA) and intravenously injected by the retro-orbital route (1.5×10^6) in sciatic nerve-lesioned mice, under deep anesthesia (ketamine 25 mg/kg and xylazine 5 mg/kg). WT and RAG-KO mice were divided into two groups: one that received cells at 3 dal ($n = 5$) and another that received cells at 14 dal ($n = 5$). One day before crushing and from 3 to 28 dal, recipient mice were submitted to the CatWalk functional analysis evaluation, as described above. At 28 dal, all animals were euthanized and the damaged nerves were collected for immunohistochemistry evaluation, as previously described. A scheme summarizing this experiment is shown in **Figure 1**.

Flow Cytometry

After isolation by Percoll gradient for adoptive transfer (see above), sets of unlabeled lymphocytes were incubated (30 min, 4°C) with antibodies, as follows: (i) anti-mouse CD8a FITC (0.5 μg, eBioscience, Cat. code: 11-0081); (ii) anti-CD4 PerCP-Cy5.5 (0.5 μg, eBioscience, Cat. code: 45-0042-82); (iii) anti-TCRβ PE-Cy7 (0.5 μg, eBioscience, Cat. code: 25-5961-82), and (iv) anti-CD19 FITC (0.5μg, BD, Cat. code: 553785).

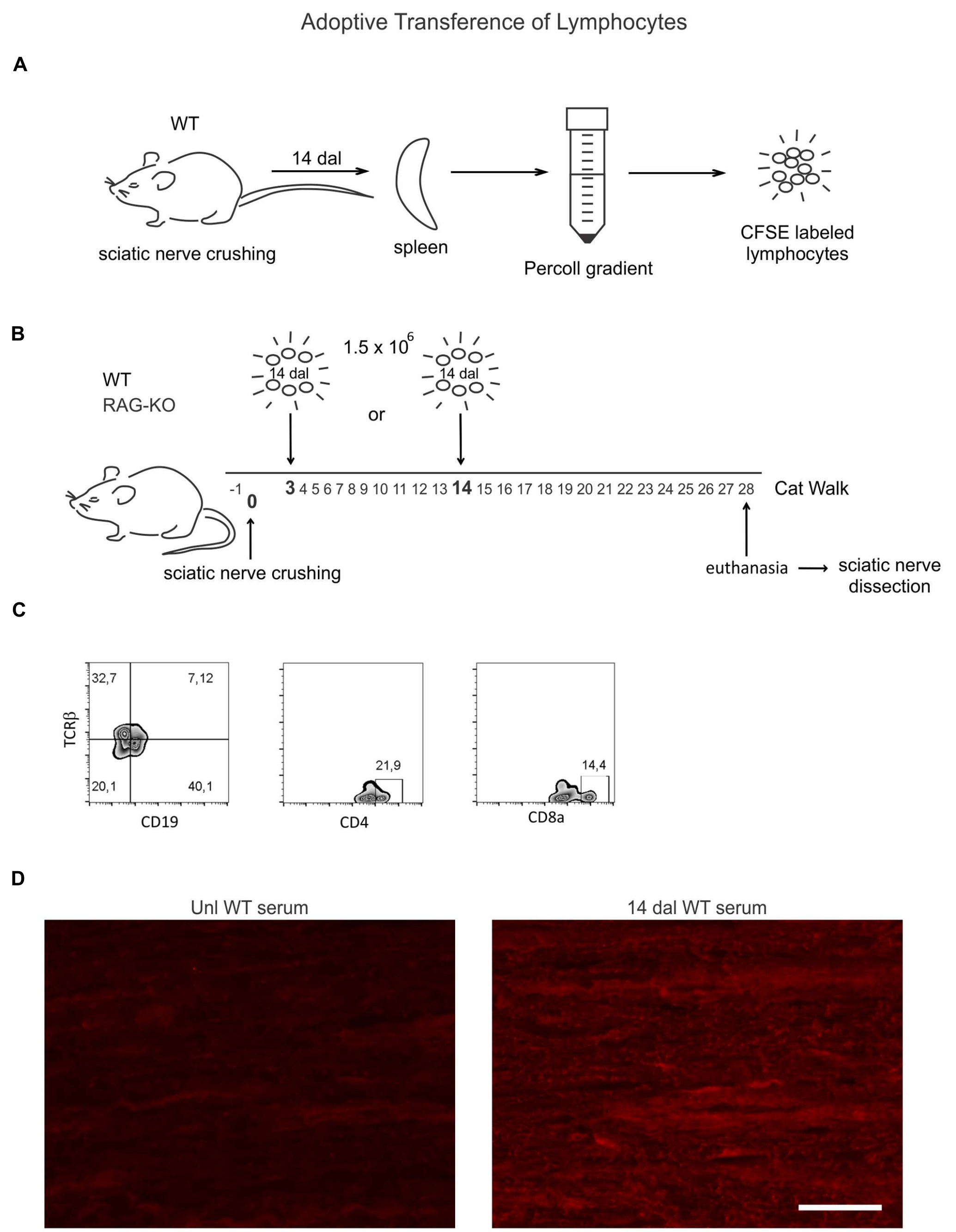

FIGURE 1 | Wild-type (WT) lymphocyte adoptive transfer procedures and cell phenotyping. (A) Spleen lymphocytes of WT mice at 14 days after sciatic nerve crushing ($n = 4$) were isolated by Percoll gradient and labeled with a fluorescent probes (CFSE). **(B)** 1.5×10^6 cells were injected via retro-orbital plexus in WT and RAG-knockout (KO) mouse groups at 3 ($n = 5$) or 14 ($n = 5$) days after nerve crushing. Recipient mice were submitted to the CatWalk test before (−1 dal) and after (3–28 dal) surgery, being euthanized at 28 dal and the sciatic nerve dissected out for immunostaining evaluation. **(C)** CFSE unlabeled isolated lymphocytes were phenotyped by flow cytometry, as indicated. **(D)** Unlesioned RAG-KO mouse nerve sections were incubated with serum from unlesioned or sciatic nerve crushed WT mice (14 dal), indicating the production of antibodies against components of the peripheral nerve by injured WT mice (right panel). Scale bar: 50 μm.

Cells were washed and 50,000 events were acquired from each sample in a cytometer (Gallios, Beckman Coulter) and analyzed with FlowJo 10.0.5 software (Tree Star Inc., Ashland, OR, USA).

In Vivo Imaging

Percoll isolated lymphocytes obtained as for the adoptive cell transfer (see above) were labeled with nanocrystals according to the manufactory's instructions (Qtracker 800 Cell Labeling Kit, Molecular Probes, Cat. code: Q25071MP). Sciatic nerve-crushed WT ($n = 3$) and RAG-KO ($n = 5$) mice were injected with labeled cells (1.5×10^6) via the retro-orbital route at 3 days after surgery. Groups of WT ($n = 5$) and RAG-KO mice ($n = 5$) that were submitted to all the surgical procedures without nerve crushing (Sham control) also received labeled lymphocytes. Cell migration to the site of injury was accompanied in different time points, as indicated in the results, using an *in vivo* imaging analyzer (*in vivo* FXBRO, Bruker, TX, USA). For that, fluorophore excitation and emission wavelengths were 710 and 790 nm, respectively, and the imaging time was 1.5 min. Additionally, mice were X-rayed for the anatomical localization of the labeling. During the imaging procedures, mice were kept under anesthesia (isoflurane 3%). To exclude possible unspecific labeling, a negative control mouse (operated, but without labeled lymphocytes) was imaged together with sham and cell-recipient mice. Special care was taken regarding the fur, that was completely removed from the interest area, as well as the skin, that was cleaned to avoid fluorescence interfering materials (food and cage substrate).

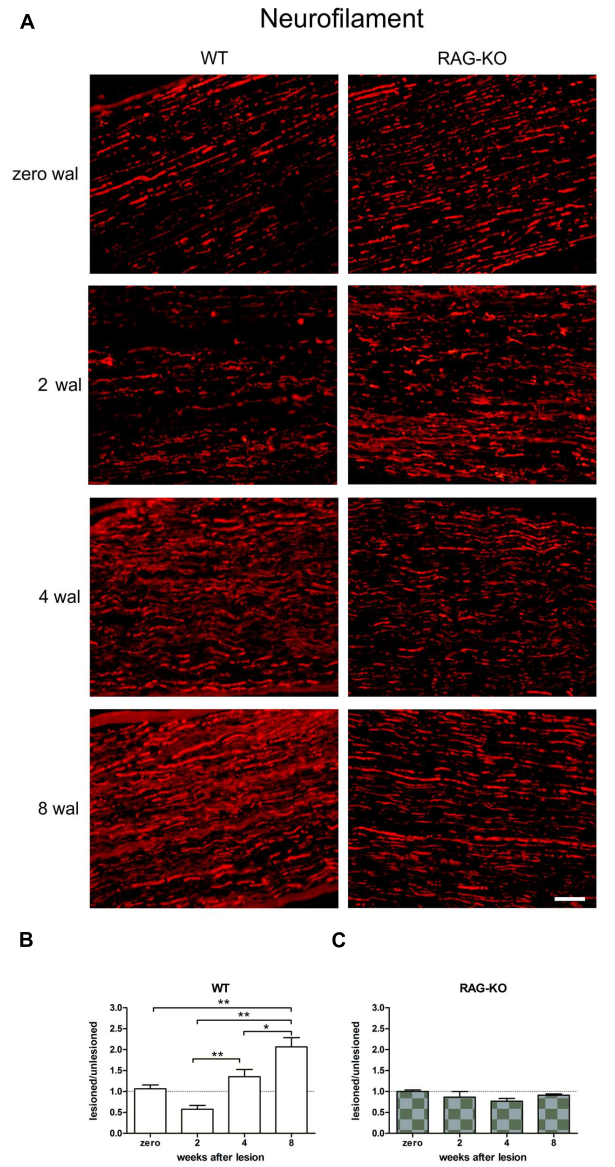

FIGURE 2 | Crushed sciatic nerve axonal regeneration. Crushed sciatic nerves from WT and RAG-KO mice were dissected out 2, 4, and 8 weeks after surgery and immunolabeled against neurofilaments (axonal cytoskeleton protein), which expression was quantified by the integrated density of pixels method. Unlesioned mice were used as control. **(A)** Representative images of the neurofilament labeling in mouse strains throughout the time course of the experiments. Zero represents unlesiond mice. wal, weeks after lesion. Scale bar: 50 μm. Ratio of the integrated density of pixels of the nerve crushed groups by each respective unlesioned control group for WT **(B)** and RAG-KO mice **(C)**. Data are presented as mean ± SEM. $n = 6$ in each time point for both strains. $^{*}p < 0.05$; $^{**}p < 0.01$ according to the one-way ANOVA, followed by Bonferroni post-test.

Statistical Analysis

Data were analyzed by the one-way analysis of variance (ANOVA) when comparing groups belonging to the same mouse strain through the experiment time course, or by the two-way ANOVA when comparing WT and RAG-KO groups among them along the time course of the experiment. In both ANOVA approaches, Bonferroni's multiple comparison tests were carried out as *post hoc* test. Data are expressed as mean ± standard error mean (SEM) and P values < 0.05 were considered significant. All statistical analyses were performed using GraphPad Prism (version 4.00, GraphPad Software, San Diego, CA, USA).

RESULTS

Axonal Regeneration

The immunolabeling evaluation revealed an upregulation of neurofilament expression during the regenerative process following sciatic nerve crushing in the WT samples, reaching the peak at 8 wal (**Figures 2A,B**; Supplementary Table S1). However, no change in the RAG-KO tissue was observed in the analyzed time points (**Figures 2A,C**; Supplementary Table S1). Comparison between mouse strains revealed that WT mice presented more neurofilaments than RAG-KO at 4 wal ($p < 0.01$; **Figures 2B,C**) and 8 wal ($p < 0.001$; **Figures 2B,C**). Of note, no difference in the labeling was seen between the mouse lineages under basal conditions.

Although the neurofilament baseline level recovery in RAG-KO nerves at 2 wal was suggestive of a faster regenerative process, it could also indicate a slower removal of axon debris. In order to address this question, we analyzed the expression of the growth associated protein 43 (GAP-43), which is expressed by regenerating axons, especially in growth cone membranes (Skene et al., 1986). In the WT, GAP-43 levels increased throughout the time course ($p < 0.05$, **Figures 3A,B**, Supplementary Table S2), while it peaked in RAG-KO at 2 wal, decreasing thereafter (**Figures 3A,C**; Supplementary Table S2). Differences in the integrated density of pixels between the strains were observed at 2 wal, when RAG-KO presented more GAP-43 than WT ($p < 0.001$; **Figures 3B,C**). Under basal conditions, GAP-43 expression was higher in RAG-KO than in WT mice ($p < 0.01$; **Figures 3B,C**). These data are suggestive of a faster axonal recovery in the immunodeficient mice.

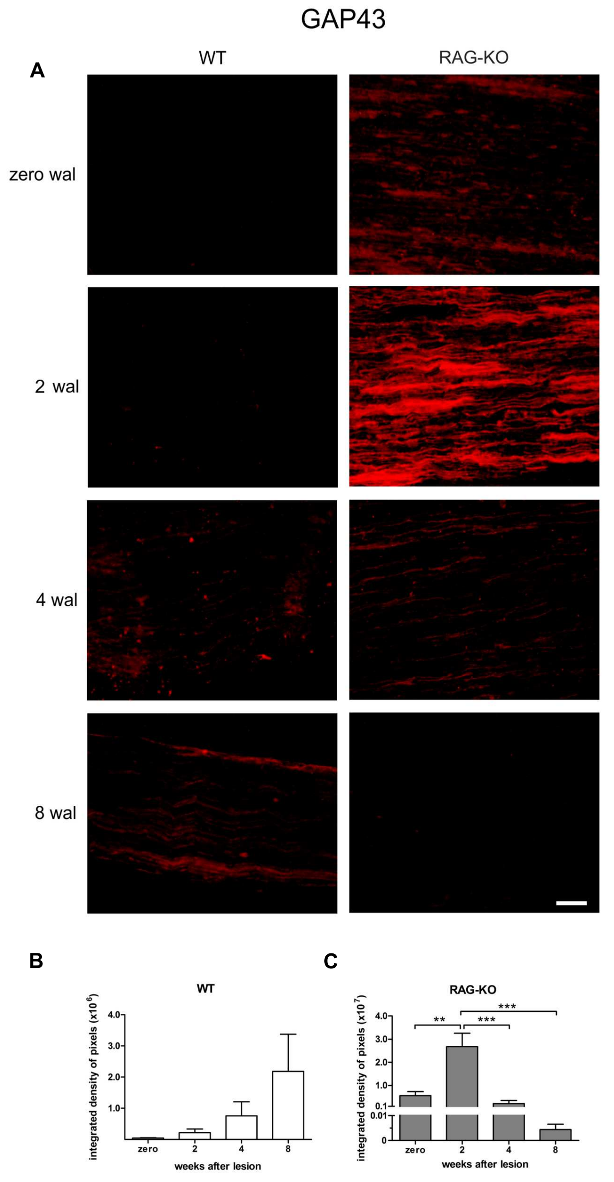

FIGURE 3 | Expression of growth-associated protein (GAP) 43 during the nerve regenerative process. (A) Representative images of GAP-43 labeling in WT and RAG-KO sciatic nerves at 2, 4 and 8 weeks after crushing. Zero represents nerve sections from non-operated mice. wal, weeks after lesion. Scale bar: 50 μm. Integrated density of pixels (arbitrary units) of GAP-43 immunolabeling in the sciatic nerve of WT **(B)** and RAG-KO mice **(C)**. Note the higher immunolabeling in the RAG-KO group under basal conditions (0 wal), compared to the WT group. Data are presented as mean ± SEM. $n = 6$ in each time point for both strains. $^{**}p < 0.01$; $^{***}p < 0.001$ according to the one-way ANOVA, followed by Bonferroni post-tests.

Myelin staining revealed low number of myelinated axons at 2 wal for both mouse strains (**Figure 4**), being this pattern reversed at 4 wal, when more myelinated axons were seen (**Figure 4**). Interestingly, at 2 wal more myelin fragments or cell debris were observed in the RAG-KO nerve as compared to the WT (**Figure 4**).

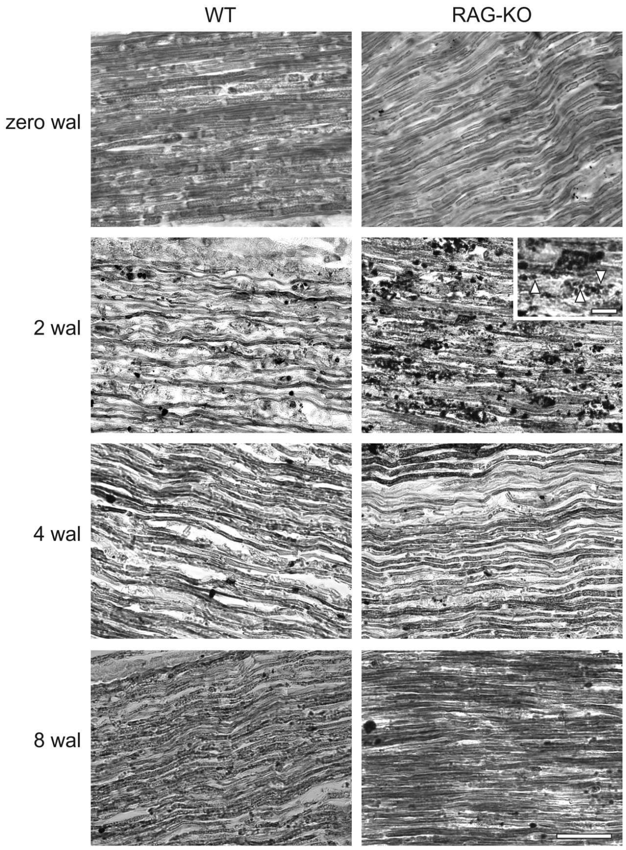

FIGURE 4 | Myelination after crushing of the sciatic nerve. Sudan black staining of uninjured and crushed sciatic nerves of WT and RAG-KO mice. Note the high amount of lipid fragments in the RAG-KO nerve at 2 wal (inset, arrowheads). Zero represents nerves from non-operated mice. wal, weeks after lesion. Scale bar: 50 μm; inset: 10 μm.

Peripheral Cell Infiltration in the Crushed Sciatic Nerve

After injury, the establishment of an inflammatory immune response is an essential step for the recovery of the tissue homeostatic state. As expected, we observed a high amount of infiltrating cells in the WT and RAG-KO nerves at 2 weeks after crushing, decreasing along the time, as regeneration occurred (**Figure 5**). When investigating the presence of macrophages in the injured nerve, we also observed an increased amount of cells at 2 wal in both mouse strains, decreasing thereafter (**Figures 6A–C**; Supplementary Table S3). However, comparison between strains revealed that, at the peak of macrophage infiltration, namely 2 wal, RAG-KO mice presented around 30% more Iba-1 immunolabeled cells than the WT animals ($p < 0.01$; **Figures 6B,C**). Interestingly, under basal conditions we observed 50-fold more Iba-1 immunoreactivity in RAG-KO nerve sections than in the WT tissue ($p < 0.001$; **Figures 6B,C**), suggesting a stronger innate immune response as a compensatory mechanism to the impaired adaptive immunity carried by the KO animals.

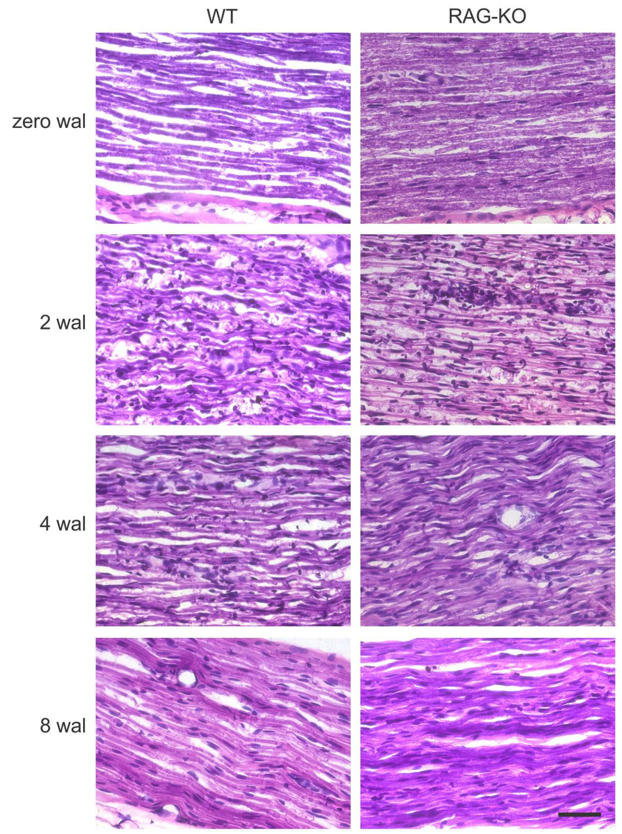

FIGURE 5 | Peripheral cell infiltration after crushing of the sciatic nerve. H&E staining of uninjured and crushed sciatic nerves of WT and RAG-KO mice. Note the high amount of infiltrating cell nuclei at 2 wal, which progressively decreased up to 8 wal. Zero represents nerves from non-operated mice. wal, weeks after lesion. Scale bar: 50 μm.

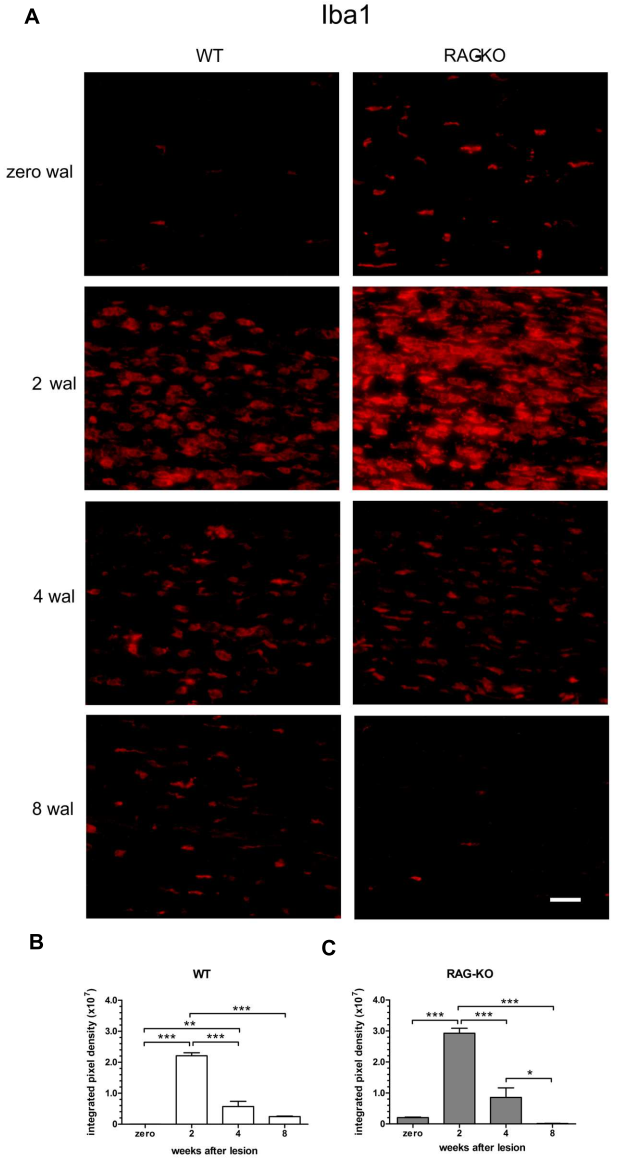

FIGURE 6 | Macrophage infiltration in the sciatic nerve after crushing. Intact or crushed sciatic nerves of WT and RAG-KO mice were imunolabeled against the macrophage marker Iba1 and submitted to the quantification method of the integrated density of pixels. **(A)** Representative images of Iba-1 labeled macrophages from both mouse strains through the time course of the study. Zero represents unlesiond mice. wal, weeks after lesion. Scale bar: 50 μm. Integrated density of pixels (arbitrary units) of Iba-1 immunolabeling in the sciatic nerve of WT **(B)** and RAG-KO mice **(C)**. Note that under basal conditions, KO mice have more macrophages than WT. Data are presented as mean ± SEM. $n = 6$ in each time point for both strains. *$p < 0.05$; **$p < 0.01$; ***$p < 0.001$ according to the one-way ANOVA, followed by Bonferroni post-test.

Functional Analysis

Besides the faster axonal regenerative response presented by the KO animals, we were interested in investigating the functional recovery, assessed by an automated walking track test system. The functional analysis demonstrated that WT and RAG-KO reestablished lesioned hind limb movements after 20 and 18 days post-injury, respectively (**Figures 7A,B**). Interesting, while KO animals recovered motor function in a progressive fashion (**Figure 7B**), WT mice relapsed from days 11 to 18 after crushing, successfully recovering thereafter (**Figure 7A**). Of note, 18 dal is the only time point in which WT group differs from RAG-KO mice ($p < 0.05$, according to the 2-way ANOVA). **Figure 7C** shows differences in the left hind limb footprint pattern of WT mice in different time points.

Adoptive Transference of Lymphocytes Interferes in the Motor Recovery Following Nerve Injury

Relapse of motor recovery in WT group at 18 days after nerve crushing indicates that the adaptive immune response is involved, since mutant mice recovered without subtle regression (**Figure 7**). To address if such finding could be reproduced in RAG-KO mice, we transferred lymphocytes from the spleen of crushed sciatic nerve WT mice to immuno-competent and deficient animals. After injuries, antigens are presented to lymphocytes in the peripheral lymphoid organs, such as the

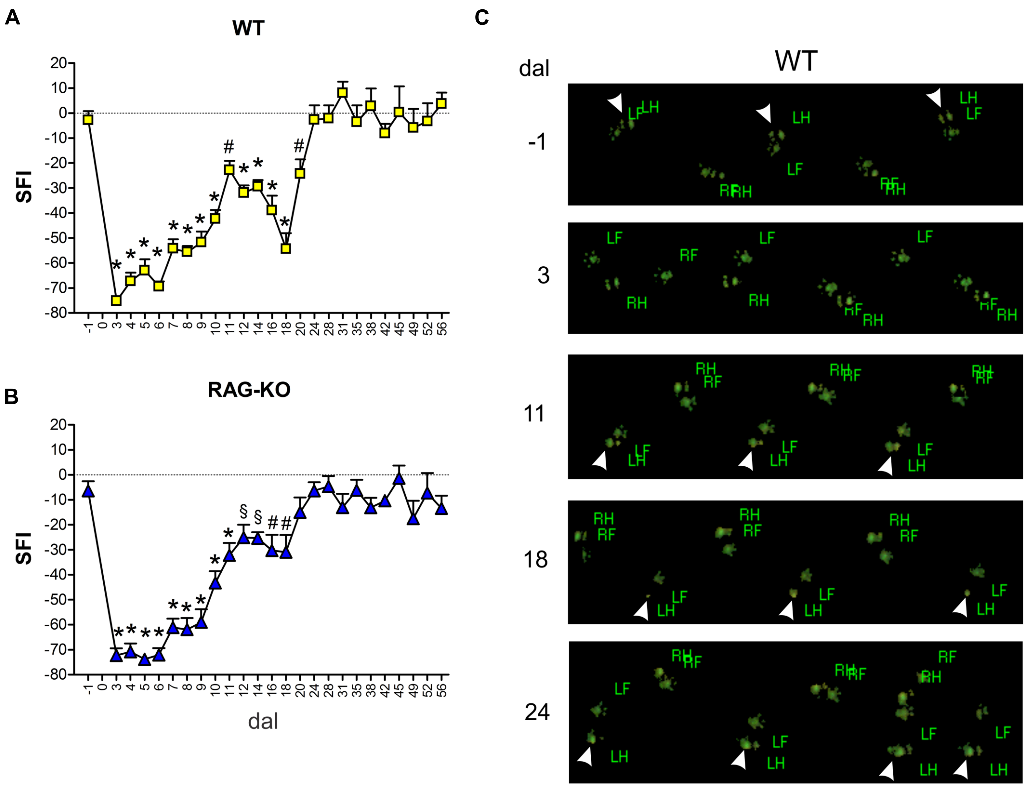

FIGURE 7 | Motor function evaluation. WT and RAG-KO mice were submitted to the automated walking track test before (−1 dal) and after (3–56 dal) the left sciatic nerve crushing. Sciatic function index (SFI) values (arbitrary units) of WT **(A)** and RAG-KO mice **(B)** along the time course. Data are presented as mean ± SEM. *n* = 18 (−1 to 14 dal), *n* = 12 (16–28 dal), *n* = 6 (31–56 dal). $^{\S}p < 0.05$; $^{\#}p < 0.01$; $^{*}p < 0.001$ in comparison to mice before surgery (−1 dal), according to the one-way ANOVA followed by Bonferroni post-test. **(C)** WT footprints before (−1 dal) and after (3–24 dal) the surgery. Arrowheads indicate left hind limb footprints. dal, days after lesion; RF, right front; RH, right hind; LF, left front; LH, left hind.

spleen and lymph nodes, where those cells undergo clonal expansion before migrating to the lesion site. In this way, the spleen is a good source of lymphocytes with specificity to the crushed nerve antigens. Since lymphocyte proliferation requires time, cells were obtained at 14 days after sciatic nerve crushing, a period coincident with a substantial influx of such cells into the damaged nerve (Gaudet et al., 2011). A phenotypic analysis of those splenic cells reveled that approximately 40% of them were B lymphocytes (CD19^{+}), while 22% were CD4 T cells and 14% were CD8 T cells (**Figure 1C**). In order to evidence the production of antibodies against components of the crushed nerve by the transferred B cells, we incubated RAG-KO intact nerve tissue with serum obtained from the lymphocyte donor WT mice, as well as from non-operated control WT animals. According to **Figure 1D**, the intact nerve was largely immunolabeled when incubated with serum from operated mice. Of note, natural antibodies were also found in the serum of unlesioned mice (**Figure 1D**). No immunolabeling was visualized when the tissue was incubated with PBS instead of serum, followed by CY3 anti-mouse IgGs (not shown).

Boosting the immune response by the adoptive transference of lymphocytes to WT animals at 3 dal did not worsen motor recovery, instead, it prevented motor loss relapse (**Figure 8A**). On the other hand, the late adoptive transference of lymphocytes did not cause the same effects. WT mice that received cells at 14 dal presented motor loss from 17 to 20 dal and impaired motor recovery up to 24 dal (**Figure 8A**). Regarding RAG-KO mice, cell transfer at 3 dal improved motor recovery, which SFI baseline values (−1 dal) were quickly reached at 8 dal (**Figure 8C**), while in the non-transferred control group it occurred more than 10 days later, i.e., longer than 18 dal (**Figure 7B**). Interesting, recipient RAG-KO group presented a subtle regression at 13 dal, fully recovering movements from day 14 on (**Figure 8C**). Transference of lymphocytes at 14 dal in RAG-KO mice had an opposite effect, impairing motor recovery up to 23 dal (**Figure 8C**), i.e., 5 days more than the control group (**Figure 7B**). When analyzing the crushed nerve at the end of the experimental period (28 dal), we observed that lymphocytes in fact migrated to the damaged tissue when injected at 3 or 14 dal, in both immune-competent and immune-deficient animals (**Figure 8C**).

Lymphocyte Migration to the Crushed Nerve and Paw Sensibility Following Adoptive Cell Transference

Better results on motor recovering were obtained when cells were transferred in the beginning of the degenerative process

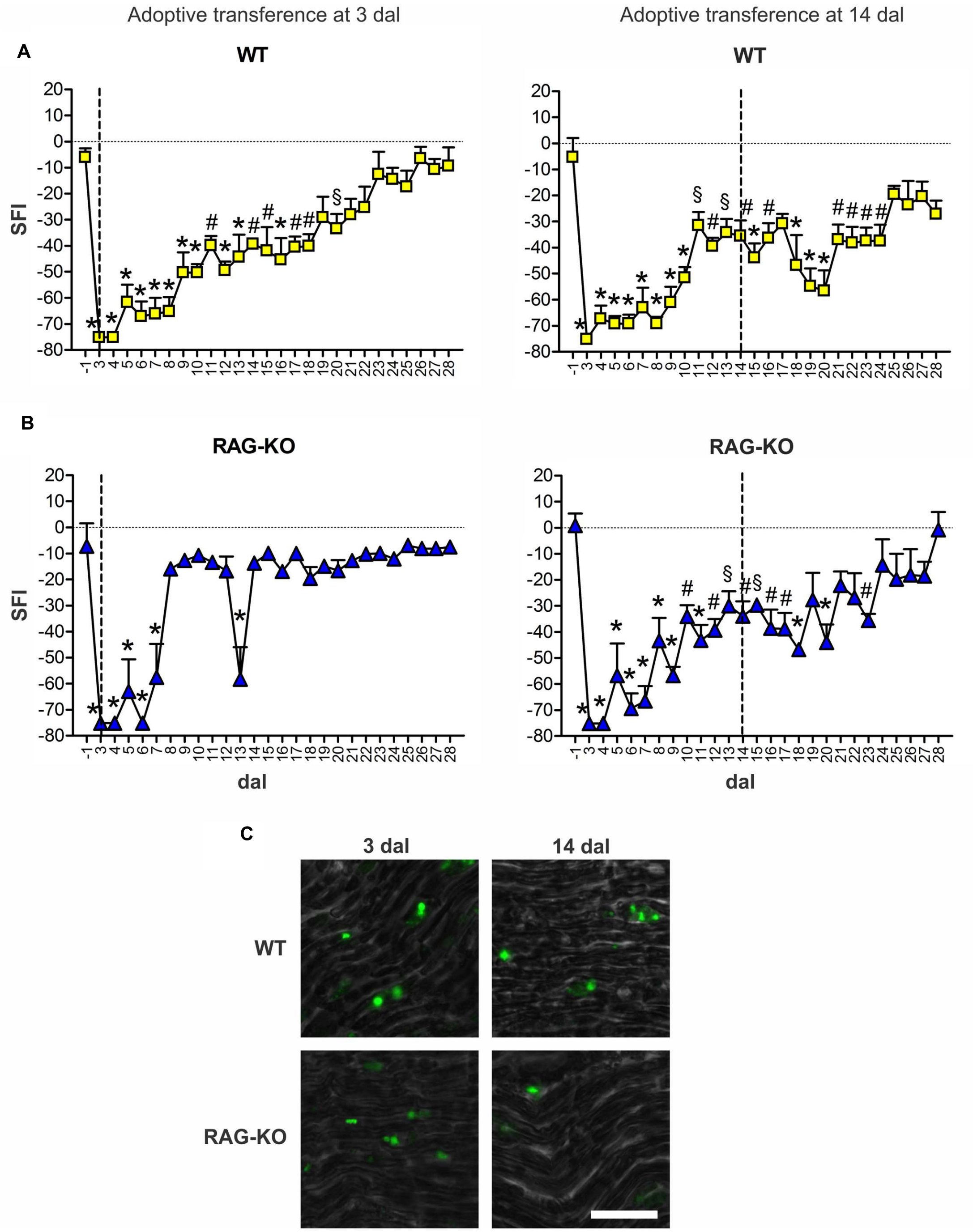

FIGURE 8 | Motor function interference by adoptive transference of WT lymphocytes. WT **(A)** and RAG-KO **(B)** mice that adoptively received WT lymphocytes at 3 or 14 days after sciatic nerve crushing were submitted to the automated walking track test before (−1 dal) and after the surgery (3–28 dal). At 28 dal, nerves were dissected out and the CSFE labeled lymphocytes were observed **(C)**. Data are presented as mean ± SEM. *n* = 5 for all cell recipient mouse groups. § $p < 0.05$; $^{\#}p < 0.01$; $^{*}p < 0.001$ in comparison to mice before surgery (−1 dal), according to the one-way ANOVA followed by Bonferroni post-test. SFI, sciatic function index; dal, days after lesion. Scale bar: 30 μm.

(**Figure 8**). To determine when lymphocytes migrated to the damaged tissue and the period they acted there, cells were labeled immediately before transference (at 3 dal) and tracked *in vivo* up to 35 dal, when motor function was fully reestablished. In WT and RAG-KO groups, lymphocytes were seen in the crushed nerve as soon as 3 h after transference, remaining in the tissue until the end of the experiment (**Figure 9A**). Up to 7 dal, cells were present in both the thigh and the paw, after this period,

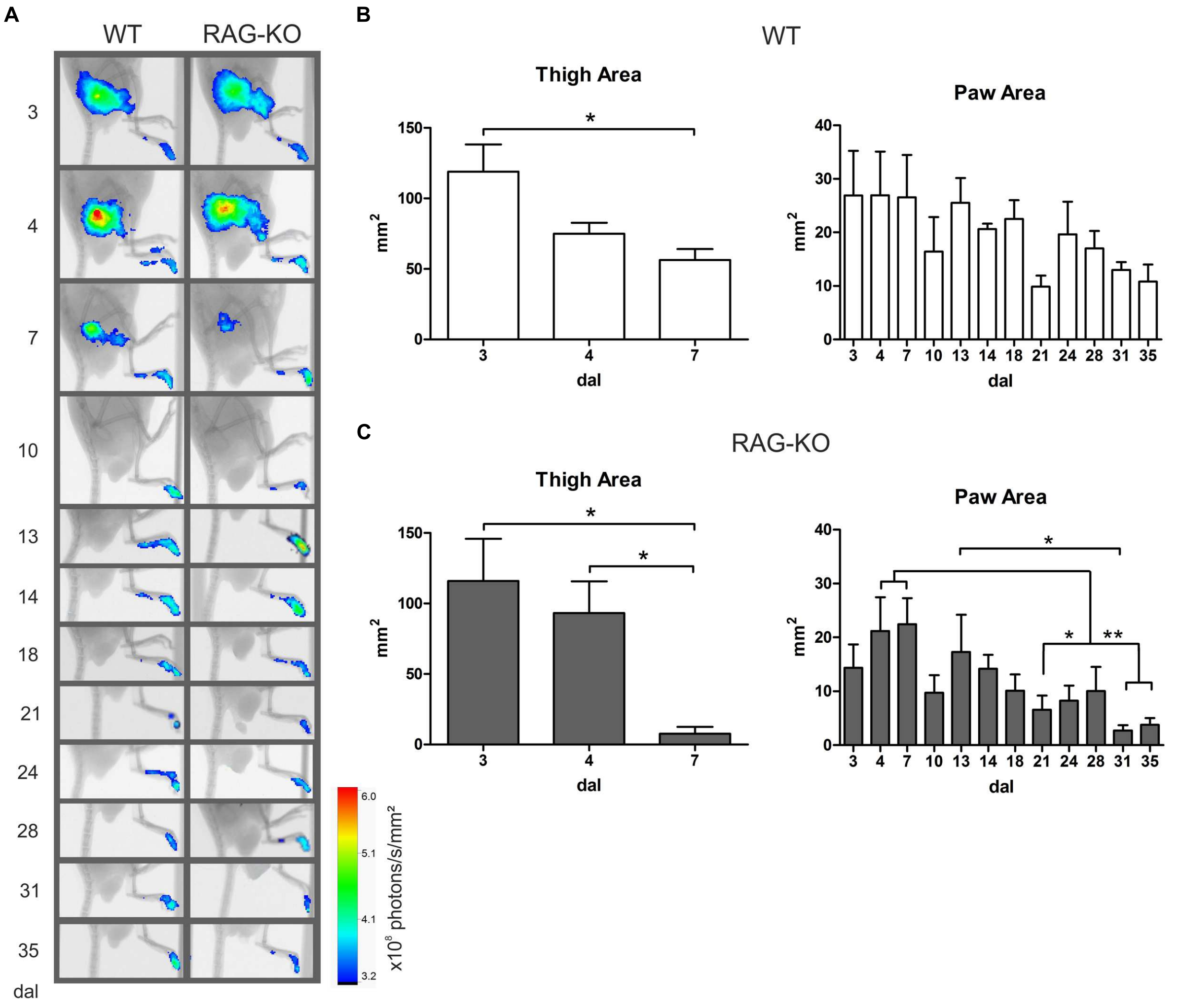

FIGURE 9 | Lymphocyte migration to the crushed nerve following cell adoptive transfer. WT and RAG-KO mice were submitted to sciatic nerve crushing and at 3 days after surgery, they received nano crystal-labeled lymphocytes. Cell migration was followed from 3 h after transference up to 35 days after lesion **(A)** and the labeling area in the thigh and paw was quantified in WT **(B)** and RAG-KO **(C)** groups. Data are presented as mean ± SEM. $^*p < 0.05$; $^{**}p < 0.01$, according to the one-way ANOVA followed by Bonferroni post-test. $n = 3$ for WT; $n = 5$ for RAG-KO. dal, days after lesion.

being visualized only in the paw (**Figure 9A**). Thigh labeled area measurements showed us that in the WT group there was a decrease from 119 to 56 mm^2 from day 3 to 7 after lesion ($p < 0.05$), while in the RAG-KO group, it was reduced from 116 to 8 mm^2 in the same period ($p < 0.05$). Of note, from day 4 to 7 no significant decrease in the labeling area was observed in the WT thigh, on the contrary of that seen in the RAG-KO group (**Figures 9B,C**; Supplementary Table S4), suggesting the need of lymphocytes for a prolonged period in the regenerative process of the WT nerve. Regarding the paw labeled areas, both the groups presented oscillations through the time course ($p < 0.01$ for WT and $p < 0.001$ for RAG-KO, according to the two-way ANOVA) and were different between then in a global analysis ($p < 0.001$, according to the two-way ANOVA). Both presented a similar kinetics in the labeling area that picked on day 7 after crushing (**Figures 9A–C**; Supplementary Table S5). Curiously, a second and a third wave of infiltrating lymphocytes were observed for both lineages between days 10 and 21, and 21 and 35 after crushing (**Figures 9B,C**; Supplementary Table S5). No difference in the labeling intensity was observed between the lineages for the analyzed parameters (data not shown).

When analyzing the paw sensibility, it was possible to observe that animals presented no sensibility at 3 dal (**Figure 10**), a period they were completely paralyzed (**Figure 8**). As expected, both groups recovered sensibility baseline levels throughout the time course (**Figure 10**). Interestingly, a first peak of hyperalgesia was observed at 13 dal for WT and RAG-KO mice (**Figure 10**), coincident with the second peak of infiltrating lymphocytes in the damaged paw (**Figures 9B,C**) and with the subtle regression of movements displayed by RAG-KO mice after cell transference (**Figure 8B**). A second peak of

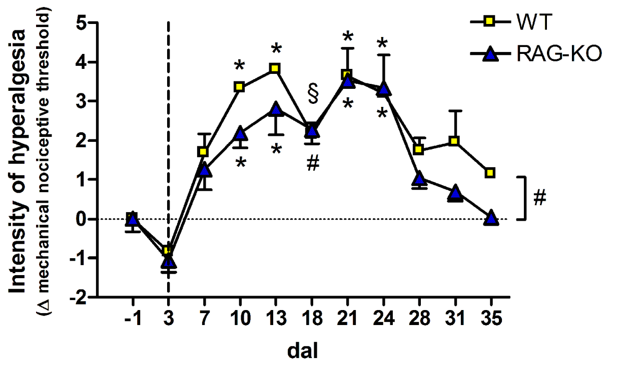

FIGURE 10 | Hyperalgesia of crushed-nerve mice following adoptive transfer of lymphocytes. Lymphocyte recipient WT and RAG-KO mice were submitted to the electronic Von Frey test to measure the paw sensibility before (−1 dal) and after sciatic nerve crushing, up to 35 dal. Values below zero indicate analgesia while above zero, hyperalgesia. The vertical dashed line signalizes the adoptive cell transfer day. Data are presented as mean ± SEM. $^{\S}p < 0.05$; $^{\#}p < 0.01$; $^{*}p < 0.001$ in comparison to mice before surgery (−1 dal), according to the one-way ANOVA followed by Bonferroni post-test. $n = 3$ for WT; $n = 5$ for RAG-KO dal, days after lesion.

hyperalgesia was observed at 21 days after crushing for both lineages (**Figure 10**), however, when nerve regeneration must be in an advanced stage and lymphocyte infiltration in the paw is reduced (**Figures 9B,C**).

DISCUSSION

Neuronal and glial responses to PNS damage have been addressed in many studies. Nevertheless, the cellular and molecular mechanisms behind the neuroregenerative process still are not fully understood. More recently, attention has been given to the possible overlap between immune and neural response to injury, so that many molecules have been shown to develop dual roles, participating in the classical immune response, but also in the interaction between neurons and surrounding glia. In this way, it has become more evident that the nervous and immune system interact and overlap mechanisms that in turn interfere in the success or failure of the regeneration process after neuronal injury (Gaudet et al., 2011; Rotshenker, 2011; Shastri et al., 2013; Xanthos and Sandkuhler, 2014).

An increasing number of studies show a neuroprotective role for T cells, in special CD4 T lymphocytes, after damage to the nervous system (Hendrix and Nitsch, 2007; Walsh et al., 2014). Following mouse facial nerve axotomy, Serpe et al. (2003) demonstrated that motorneuron survival is higher in WT mice than in CD4-KO and RAG-2-KO mice. However, neurons are rescued from death to the same level of WT animals when both KO groups were reconstituted with CD4 T lymphocytes. Besides that, the lack of CD8 T cells or B cells did not worsen neuronal survival, which was also not improved in RAG-2-KO mice reconstituted with either CD8 T cells or B lymphocytes (Serpe et al., 2003). Moreover, neuroprotection was mediated by autoreactive CD4 T cells independently of their ability to secret brain derived neurotrophic factor (BDNF) (Xin et al., 2012). In order to evaluate the involvement of the acquired immune-response after damage of the sciatic nerve, we employed T and B cell deficient mice, but contrarily to our expectations, no deficit in the regenerative process was observed in those animals, which presented even more neurofilaments and axon growth proteins in the initial phase of the regenerative process. Accordingly, improved motor recovery and enhanced axon regrowth and myelination were observed in RAG-2-KO animals submitted to either nerve transection followed by tubulization (Mehanna et al., 2014) or to spinal cord compression (Wu et al., 2012), both the cases at six weeks after surgery. In a mouse model of Charcot–Marie–Tooth disease, a demyelinating peripheral neuropathy, the lack of mature T and B lymphocytes was also beneficial, decreasing the percentage of demyelinated axons, supernumerary Schwann cells and periaxonal vacuoles in the PNS (Kobsar et al., 2003).

Additionally, the immunodeficient mice herein studied presented, under basal conditions, significantly more macrophages than the WT animals, as well as in the initial phase of the regenerative process. As largely known, macrophages and Schwann cells are important for myelin removal during Wallerian degeneration, a process that precedes the axonal regeneration when considering the presence of axon growth inhibitory proteins in the myelin debris. In the first few days post-injury, Schwann cells are responsible for myelin clearance of the distal stump and around 3 dal, phagocytosis is improved by monocyte-derived macrophages that enter the damaged nerve, peaking from 14 to 21 days post-injury (Vargas and Barres, 2007). Although Schwann cells may remove myelin in the absence of infiltrating macrophages (Perry et al., 1995), it has been shown that myelin clearance during Wallerian degeneration is delayed in mice with impaired macrophage infiltration due to the lack of chemotactic substances (Liefner et al., 2000; Sugiura et al., 2000). Moreover, myelin phagocytosis by macrophages is strongly dependent on the complement receptor-3 (CR-3) (Bruck and Friede, 1990) and antibodies against myelin compounds (Vargas and Barres, 2007), being the nullity of immunoglobulin in B cell deficient mice also responsible for impaired axon regeneration after sciatic nerve crushing (Vargas et al., 2010). Aside the phagocytic capacity, macrophages also produce neurotrophins, such as insulin-like growth factor (IGF) (Suh et al., 2013), BDNF, neurotrophin 3 (NT-3) (Barouch et al., 2001a) and nerve growth factor (NGF) (Barouch et al., 2001b) and also stimulate production of NGF by Schwann cells via interleukin-1 (Lindholm et al., 1987). More recently, it was reported that under hypoxia conditions, macrophages release the pro-angiogenic factor VEGF-A, stimulating polarized blood vessels formation in the damaged nerve (Cattin et al., 2015). Moreover, Schwann cells use those new vessels as tracks to guide their migration across the wound, taking the growing axons with them (Cattin et al., 2015). In view of the importance of macrophages in the neuronal regenerative process, it is reasonable to attribute part of the improved axonal regeneration displayed herein by the KO mice to the increased amount of macrophages in the acute period post-injury, rather than the lack of lymphocytes.

One interesting finding of the present work is the motor function loss relapse presented by WT, but not by the immune-deficient mice after two weeks following peripheral nerve injury. Although the most remarkable difference between those animals is the impaired adaptive immune response carried by the KO mice, our data also point to an enhanced innate immune response leading to a higher macrophage infiltration in the first two weeks after nerve crushing in RAG-KO animals. Although inflammation is necessary to reestablishing tissue homeostasis, it can be harmful when exacerbated due to the intensity and duration of the antigenic stimuli. Pro-inflammatory mediators and free radicals may cause damage to the nervous tissue, impairing axonal conductivity or even causing retrograde neuronal death (Hendriks et al., 2005; Brown, 2007). In this sense, the motor function loss relapse presented by WT mice seems to be linked to the effects of the adaptive immune response, possibly leading to transitory impairment of axonal conductivity or even pain that hampered functionality of the lesioned limb. When transferring activated lymphocytes to WT mice at 3 days after crushing, we anticipated the acquired immune response that should have potentiated the innate immunity, improving tissue clearance and thus resulting in a milder inflammation thereafter, causing no loss of movements at 18 days after crushing.

The benefits of the early cell transfer became more evident in RAG-KO mice, which recovered movements in a few days after cell injection, accompanied by an immediate lymphocyte migration to the lesion that should have stimulated phagocytic cell activation and improved tissue clearance. Additionally, lymphocytes could also have repopulated the secondary lymphoid organs, migrating to the damaged tissue when stimulated. In this way, we observed in RAG-KO mice a second set of lymphocytes that arrived in the injured paw near two weeks after nerve crushing, possibly enhancing local inflammatory response and causing hyperalgesia and transient loss of movements. One interesting finding was that at 21 days after crushing, when regeneration is advanced and the anti-inflammatory response is predominant (Mietto et al., 2015), a second peak of hyperalgesia was observed, without increased lymphocyte influx in the paw. Of note, during the same period the nerve is under an intense process of tissue remodeling, and the newly regenerated sensory fibers may have a low pain threshold (Zhang et al., 1997), responsible for the hyperalgesia. However, many surplus and non-functional axonal sprouts are still present in the regenerating nerve, and should be eliminated. Thus, a second wave of degeneration occurs in the nerve (Liuzzi and Tedeschi, 1991; Madison et al., 1996) and, apparently, the adaptive immunity acts in the tissue remodeling process, as evidenced by the third peak of lymphocyte infiltration in the paw between days 21 and 35 after injury. Finally, transference of lymphocytes 14 days after nerve crushing resulted in no further overall improvement in both mouse strains, possibly due to the completion of Wallerian degeneration at such moment, accompanied by a decreased inflammatory response.

Overall, the present data indicate that the modulation of the immune response is a key strategy for achieving better motor recovery following peripheral nerve injury. In line with this, suppression of immune activation by regulatory T cells is neuroprotective in a mouse model of Parkinson's disease (Reynolds et al., 2007) and acute experimental stroke (Liesz et al., 2009). Shifting the pro-inflammatory Th1 response to the anti-inflammatory Th2 can also promote neuroprotection. In this way, the administration of the Th2 inducer glatiramer acetate increased synapse stability during EAE (Scorisa et al., 2011) while simvastatin, another Th2 inducer, was shown to improve functional recovery of the crushed sciatic nerve in rats, as well as to decrease mononuclear cell infiltrate and edema areas in the damaged tissue (Xavier et al., 2012). Herein, mice with enhanced innate immune capacity presented improved axonal growth and no transient impairments in the motor recovery, which was further ameliorated by the transference of activated lymphocytes in the early stage of the Wallerian degeneration. Such findings may in turn provide the basis for a more effective immune response based therapy following peripheral injury in patients.

AUTHOR CONTRIBUTIONS

AB, JS and RT conceived and designed experiments, acquired, analyzed and interpreted data and wrote the manuscript. SN, BM, EF and IB contributed to acquiring, analyzing and interpreting data. CS and LV contributed to data comprehension and wrote the manuscript. AR conceived and designed experiments, interpreted data and wrote the manuscript. All authors read and approved the final manuscript.

FUNDING

Grants were provided by the following Brazilian agencies: FAPESP (2011/08712-4, 2012/20456-6; 2014/06892-3), CAPES, and CNPq (300553/2013-9).

SUPPLEMENTARY MATERIAL

The Supplementary Material for this article can be found online at: http://journal.frontiersin.org/article/10.3389/fncel.2016.00151

REFERENCES

Barbizan, R., Castro, M. V., Rodrigues, A. C., Barraviera, B., Ferreira, R. S., and Oliveira, A. L. (2013). Motor recovery and synaptic preservation after ventral root avulsion and repair with a fibrin sealant derived from snake venom. *PLoS ONE* 8:e63260. doi: 10.1371/journal.pone.0063260

Barouch, R., Appel, E., Kazimirsky, G., and Brodie, C. (2001a). Macrophages express neurotrophins and neurotrophin receptors. Regulation of nitric oxide production by NT-3. *J. Neuroimmunol.* 112, 72–77.

Barouch, R., Kazimirsky, G., Appel, E., and Brodie, C. (2001b). Nerve growth factor regulates TNF-alpha production in mouse macrophages via MAP kinase activation. *J. Leukoc. Biol.* 69, 1019–1026.

Brown, G. C. (2007). Mechanisms of inflammatory neurodegeneration: iNOS and NADPH oxidase. *Biochem. Soc. Trans.* 35, 1119–1121. doi: 10.1042/BST0351119

Bruck, W., and Friede, R. L. (1990). Anti-macrophage CR3 antibody blocks myelin phagocytosis by macrophages in vitro. *Acta Neuropathol.* 80, 415–418. doi: 10.1007/BF00307696

Cattin, A. L., Burden, J. J., Van Emmenis, L., Mackenzie, F. E., Hoving, J. J., Garcia Calavia, N., et al. (2015). Macrophage-induced blood vessels guide schwann cell-mediated regeneration of peripheral nerves. *Cell* 162, 1127–1139. doi: 10.1016/j.cell.2015.07.021

de Medinaceli, L., Freed, W. J., and Wyatt, R. J. (1982). An index of the functional condition of rat sciatic nerve based on measurements made from walking tracks. *Exp. Neurol.* 77, 634–643. doi: 10.1016/0014-4886(82)90234-5

Fruttiger, M., Montag, D., Schachner, M., and Martini, R. (1995). Crucial role for the myelin-associated glycoprotein in the maintenance of axon-myelin integrity. *Eur. J. Neurosci.* 7, 511–515. doi: 10.1111/j.1460-9568.1995.tb00347.x

Gaudet, A. D., Popovich, P. G., and Ramer, M. S. (2011). Wallerian degeneration: gaining perspective on inflammatory events after peripheral nerve injury. *J. Neuroinflammation* 8:110. doi: 10.1186/1742-2094-8-110

Hendriks, J. J., Teunissen, C. E., de Vries, H. E., and Dijkstra, C. D. (2005). Macrophages and neurodegeneration. *Brain Res. Brain Res. Rev.* 48, 185–195. doi: 10.1016/j.brainresrev.2004.12.008

Hendrix, S., and Nitsch, R. (2007). The role of T helper cells in neuroprotection and regeneration. *J. Neuroimmunol.* 184, 100–112. doi: 10.1016/j.jneuroim.2006.11.019

Jessen, K. R., and Mirsky, R. (2008). Negative regulation of myelination: relevance for development, injury, and demyelinating disease. *Glia* 56, 1552–1565. doi: 10.1002/glia.20761

Juarez, P., and Palau, F. (2012). Neural and molecular features on Charcot-Marie-Tooth disease plasticity and therapy. *Neural Plast.* 2012:171636. doi: 10.1155/2012/171636

Kashi, V. P., Ortega, S. B., and Karandikar, N. J. (2014). Neuroantigen-specific autoregulatory CD8+ T cells inhibit autoimmune demyelination through modulation of dendritic cell function. *PLoS ONE* 9:e105763. doi: 10.1371/journal.pone.0105763

Kobsar, I., Berghoff, M., Samsam, M., Wessig, C., Maurer, M., Toyka, K. V., et al. (2003). Preserved myelin integrity and reduced axonopathy in connexin32-deficient mice lacking the recombination activating gene-1. *Brain* 126, 804–813. doi: 10.1093/brain/awg072

Liefner, M., Siebert, H., Sachse, T., Michel, U., Kollias, G., and Bruck, W. (2000). The role of TNF-alpha during Wallerian degeneration. *J. Neuroimmunol.* 108, 147–152. doi: 10.1016/S0165-5728(00)00262-9

Liesz, A., Suri-Payer, E., Veltkamp, C., Doerr, H., Sommer, C., Rivest, S., et al. (2009). Regulatory T cells are key cerebroprotective immunomodulators in acute experimental stroke. *Nat. Med.* 15, 192–199. doi: 10.1038/nm.1927

Lindholm, D., Heumann, R., Meyer, M., and Thoenen, H. (1987). Interleukin-1 regulates synthesis of nerve growth factor in non-neuronal cells of rat sciatic nerve. *Nature* 330, 658–659. doi: 10.1038/330658a0

Liuzzi, F. J., and Tedeschi, B. (1991). Peripheral nerve regeneration. *Neurosurg. Clin. N. Am.* 2, 31–42.

Madison, R. D., Archibald, S. J., and Brushart, T. M. (1996). Reinnervation accuracy of the rat femoral nerve by motor and sensory neurons. *J. Neurosci.* 16, 5698–5703.

Mars, L. T., Bauer, J., Gross, D. A., Bucciarelli, F., Firat, H., Hudrisier, D., et al. (2007). CD8 T cell responses to myelin oligodendrocyte glycoprotein-derived peptides in humanized HLA-A*0201-transgenic mice. *J. Immunol.* 179, 5090–5098. doi: 10.4049/jimmunol.179.8.5090

Mehanna, A., Szpotowicz, E., Schachner, M., and Jakovcevski, I. (2014). Improved regeneration after femoral nerve injury in mice lacking functional T- and B-lymphocytes. *Exp. Neurol.* 261, 147–155. doi: 10.1016/j.expneurol.2014.06.012

Mietto, B. S., Mostacada, K., and Martinez, A. M. (2015). Neurotrauma and inflammation: CNS and PNS responses. *Mediators Inflamm.* 2015:251204. doi: 10.1155/2015/251204

Mombaerts, P., Iacomini, J., Johnson, R. S., Herrup, K., Tonegawa, S., and Papaioannou, V. E. (1992). RAG-1-deficient mice have no mature B and T lymphocytes. *Cell* 68, 869–877. doi: 10.1016/0092-8674(92)90030-G

Perry, V. H., Tsao, J. W., Fearn, S., and Brown, M. C. (1995). Radiation-induced reductions in macrophage recruitment have only slight effects on myelin degeneration in sectioned peripheral nerves of mice. *Eur. J. Neurosci.* 7, 271–280. doi: 10.1111/j.1460-9568.1995.tb01063.x

Reynolds, A. D., Banerjee, R., Liu, J., Gendelman, H. E., and Mosley, R. L. (2007). Neuroprotective activities of $CD4^+CD25^+$ regulatory T cells in an animal model of Parkinson's disease. *J. Leukoc. Biol.* 82, 1083–1094. doi: 10.1189/jlb.0507296

Ripellino, P., Fleetwood, T., Cantello, R., and Comi, C. (2014). Treatment of chronic inflammatory demyelinating polyneuropathy: from molecular bases to practical considerations. *Autoimmune Dis.* 2014:201657. doi: 10.1155/2014/201657

Rotshenker, S. (2011). Wallerian degeneration: the innate-immune response to traumatic nerve injury. *J. Neuroinflammation* 8:109. doi: 10.1186/1742-2094-8-109

Sarma, J. V., and Ward, P. A. (2011). The complement system. *Cell Tissue Res.* 343, 227–235. doi: 10.1007/s00441-010-1034-0

Scorisa, J. M., Freria, C. M., Victorio, S. C., Barbizan, R., Zanon, R. G., and Oliveira, A. L. (2011). Glatiramer acetate treatment increases stability of spinal synapses and down regulates MHC I during the course of EAE. *Int. J. Biol. Sci.* 7, 1188–1202. doi: 10.7150/ijbs.7.1188

Serpe, C. J., Coers, S., Sanders, V. M., and Jones, K. J. (2003). $CD4^+$ T, but not $CD8^+$ or B, lymphocytes mediate facial motoneuron survival after facial nerve transection. *Brain Behav. Immun.* 17, 393–402. doi: 10.1016/S0889-1591(03)00028-X

Shastri, A., Bonifati, D. M., and Kishore, U. (2013). Innate immunity and neuroinflammation. *Mediators Inflamm.* 2013:342931. doi: 10.1155/2013/342931

Siddique, R., and Thakor, N. (2014). Investigation of nerve injury through microfluidic devices. *J. R. Soc. Interface* 11:20130676. doi: 10.1098/rsif.2013.0676

Skene, J. H., Jacobson, R. D., Snipes, G. J., McGuire, C. B., Norden, J. J., and Freeman, J. A. (1986). A protein induced during nerve growth (GAP-43) is a major component of growth-cone membranes. *Science* 233, 783–786. doi: 10.1126/science.3738509

Sugiura, S., Lahav, R., Han, J., Kou, S. Y., Banner, L. R., de Pablo, F., et al. (2000). Leukaemia inhibitory factor is required for normal inflammatory responses to injury in the peripheral and central nervous systems in vivo and is chemotactic for macrophages in vitro. *Eur. J. Neurosci.* 12, 457–466. doi: 10.1046/j.1460-9568.2000.00922.x

Suh, H. S., Zhao, M. L., Derico, L., Choi, N., and Lee, S. C. (2013). Insulin-like growth factor 1 and 2 (IGF1, IGF2) expression in human microglia: differential regulation by inflammatory mediators. *J. Neuroinflammation* 10:37. doi: 10.1186/1742-2094-10–37

Vargas, M. E., and Barres, B. A. (2007). Why is Wallerian degeneration in the CNS so slow? *Annu. Rev. Neurosci.* 30, 153–179. doi: 10.1146/annurev.neuro.30.051606.094354

Vargas, M. E., Watanabe, J., Singh, S. J., Robinson, W. H., and Barres, B. A. (2010). Endogenous antibodies promote rapid myelin clearance and effective axon regeneration after nerve injury. *Proc. Natl. Acad. Sci. U.S.A.* 107, 11993–11998. doi: 10.1073/pnas.1001948107

Walsh, J. T., Watson, N., and Kipnis, J. (2014). T cells in the central nervous system: messengers of destruction or purveyors of protection? *Immunology* 141, 340–344. doi: 10.1111/imm.12187

Winer, J. B. (2014). An update in guillain-barre syndrome. *Autoimmune Dis.* 2014:793024. doi: 10.1155/2014/793024

Wu, B., Matic, D., Djogo, N., Szpotowicz, E., Schachner, M., and Jakovcevski, I. (2012). Improved regeneration after spinal cord injury in mice lacking functional T- and B-lymphocytes. *Exp. Neurol.* 237, 274–285. doi: 10.1016/j.expneurol.2012.07.016

Xanthos, D. N., and Sandkuhler, J. (2014). Neurogenic neuroinflammation: inflammatory CNS reactions in response to neuronal activity. *Nat. Rev. Neurosci.* 15, 43–53. doi: 10.1038/nrn3617

Xavier, A. M., Serafim, K. G., Higashi, D. T., Vanat, N., Flaiban, K. K., Siqueira, C. P., et al. (2012). Simvastatin improves morphological and functional recovery of sciatic nerve injury in Wistar rats. *Injury* 43, 284–289. doi: 10.1016/j.injury.2011.05.036

Xin, J., Mesnard, N. A., Beahrs, T., Wainwright, D. A., Serpe, C. J., Alexander, T. D., et al. (2012). CD4$^+$ T cell-mediated neuroprotection is independent of T cell-derived BDNF in a mouse facial nerve axotomy model. *Brain Behav. Immun.* 26, 886–890. doi: 10.1016/j.bbi.2012.02.011

Zhang, J. M., Donnelly, D. F., Song, X. J., and Lamotte, R. H. (1997). Axotomy increases the excitability of dorsal root ganglion cells with unmyelinated axons. *J. Neurophysiol.* 78, 2790–2794.

Zozulya, A. L., and Wiendl, H. (2008). The role of CD8 suppressors versus destructors in autoimmune central nervous system inflammation. *Hum. Immunol.* 69, 797–804. doi: 10.1016/j.humimm.2008.07.014

Conflict of Interest Statement: The authors declare that the research was conducted in the absence of any commercial or financial relationships that could be construed as a potential conflict of interest.

frontiers
in Cellular Neuroscience

ORIGINAL RESEARCH
published: 19 July 2016
doi: 10.3389/fncel.2016.00179

Mitochondrial Dynamics Decrease Prior to Axon Degeneration Induced by Vincristine and are Partially Rescued by Overexpressed cytNmnat1

Gregory W. Berbusse[1], *Laken C. Woods*[2], *Bhupinder P. S. Vohra*[3] *and Kari Naylor*[2]*

[1] *Department of Cellular Physiology and Molecular Biophysics, University of Arkansas for Medical Sciences, Little Rock, AR, USA,* [2] *Department of Biology, University of Central Arkansas, Conway, AR, USA,* [3] *Department of Neurology, Yale University School of Medicine, New Haven, CT, USA*

OPEN ACCESS

Edited by:
Maren Engelhardt,
Heidelberg University, Germany

Reviewed by:
Yen-Chung Chang,
National Tsing Hua University, Taiwan
Tatsuro Mutoh,
Fujita Health University School of Medicine, Japan

***Correspondence:**
Kari Naylor
kknaylor@uca.edu

Received: *19 May 2016*
Accepted: *04 July 2016*
Published: *19 July 2016*

Citation:
Berbusse GW, Woods LC, Vohra BPS and Naylor K (2016) Mitochondrial Dynamics Decrease Prior to Axon Degeneration Induced by Vincristine and are Partially Rescued by Overexpressed cytNmnat1. Front. Cell. Neurosci. 10:179. doi: 10.3389/fncel.2016.00179

Axon degeneration is a prominent feature of various neurodegenerative diseases, such as Parkinson's and Alzheimer's, and is often characterized by aberrant mitochondrial dynamics. Mitochondrial fission, fusion, and motility have been shown to be particularly important in progressive neurodegeneration. Thus we investigated these imperative dynamics, as well as mitochondrial fragmentation in vincristine induced axon degradation in cultured dorsal root ganglia (DRG) neurons. CytNmnat1 inhibits axon degeneration in various paradigms including vincristine toxicity. The mechanism of its protection is not yet fully understood; therefore, we also investigated the effect of cytNmnat1 on mitochondrial dynamics in vincristine treated neurons. We observed that vincristine treatment decreases the rate of mitochondrial fission, fusion and motility and induces mitochondrial fragmentation. These mitochondrial events precede visible axon degeneration. Overexpression of cytNmnat1 inhibits axon degeneration and preserves the normal mitochondrial dynamics and motility in vincristine treated neurons. We suggest the alterations in mitochondrial structure and dynamics are early events which lead to axon degeneration and cytNmnat1 blocks axon degeneration by halting the vincristine induced changes to mitochondrial structure and dynamics.

Keywords: neurodegeneration, mitochondria, Nmnat, fission, fusion, vincristine

INTRODUCTION

In addition to providing the largest sources of cellular ATP, mitochondria are intimately involved in the regulation of intracellular calcium levels and pH, they serve as oxygen sensors, and are the source of super-oxide radicals (Müller et al., 2005). Current views of mitochondrial dynamics have disproven the traditional notion of singular, randomly dispersed organelles and it is now accepted that mitochondria constitute a population of organelles that are actively transported through the cell, fuse, divide, and undergo regulated turnover (Nunnari et al., 1997; Dedov and Roufogalis, 1999; Chen and Chan, 2005, 2009). Because of these dynamic processes, mitochondria are able to respond to cellular demands, influence cytosolic communication and signaling cascades, be moved to critical subcellular compartments, and finally, assess and respond to mitochondrial fitness (Chen and Chan, 2009). Within the past decade, studies have highlighted the impetus of mitochondrial dynamics in maintaining integral cell and animal physiological processes, influencing function, differentiation, and ultimately affecting survival (Chen and Chan, 2005, 2009). More specifically mis-regulated dynamics-mitochondrial fission and fusion- have been shown to increase reactive oxygen species (ROS), decrease ATP production, as well as detrimentally alter apoptosis (Liesa et al., 2009; Martin, 2012) and mitophagy (Rambold et al., 2011; Shen et al., 2014). These deficits are also associated with numerous neurodegenerative disorders including Parkinson's, Alzheimer's, Charcot-Marie Tooth, Amyotrophic Lateral Sclerosis, and Huntington's diseases (Wang et al., 2005; Press and Milbrandt, 2008; Chen and Chan, 2009; Vohra et al., 2010; Wen et al., 2011; Martin, 2012; Alobuia et al., 2013; Korobova et al., 2013).

Typically preceding clinical symptoms, axonal degeneration is a prominent feature of peripheral neuropathies and neurodegenerative disorders. Wallerian degeneration, a self-destructive process at the distal portion of transected axons, has proven to be a useful model for studying the mechanism of axon degeneration (Wang et al., 2005). Having been shown to occur without activating the caspase family of cysteine proteases, Wallerian degeneration is described as being mechanistically different from neuronal apoptosis triggered by nerve growth factor (NGF) deprivation (Wang et al., 2005; Press and Milbrandt, 2008; Vohra et al., 2010; Wen et al., 2011). Insight into the mechanism of Wallerian degeneration came from a spontaneously occurring mutant mouse strain whose axons survived for weeks post-transection due to the overexpression of a fusion protein (Wld^S) containing full length nicotinamide mononucleotide adenylyl transferase1 (Nmnat1; Wang et al., 2005). Further investigation revealed that overexpression of Nmnat1, an enzyme required for nicotinamide adenine dinucleotide (NAD^+) biosynthesis, alone can prevent axon degeneration from physical and chemical triggers (Wang et al., 2005). Catalyzing a key step in NAD^+ synthesis, Nmnat1 plays an evolutionarily conserved role in neuronal maintenance (Sasaki et al., 2009). Although overexpression of Nmnat1 does not increase the level of NAD^+ in the neurons, it has been shown to reduce the loss of NAD^+ in transected axons (Wang et al., 2005; Sasaki et al., 2009). NAD^+ depletion in transected neurons is decreased in parallel with ATP levels supporting the notion that Nmnat1 acts through local bioenergetics pathways in transected axons (Wang et al., 2005; Press and Milbrandt, 2008; Vohra et al., 2010; Wen et al., 2011).

Mitochondria are implicated in neurodegeneration (Martin, 2012), for example mitochondrial depolarization induces axon degeneration that is independent of classical cell death pathways (Gerdts et al., 2013). Interestingly this form of degeneration can be prevented by depletion of Sarm1 (SARM, sterile α-motif-containing and armadillo-motif containing protein) (Araki et al., 2004; Gerdts et al., 2013; Summers et al., 2014). Additionally, Nmnat1 overexpression prevents axon degeneration induced by mitochondrial toxins (Press and Milbrandt, 2008). Recent work has demonstrated that loss of mitochondrial dynamics prevent mitophagy which is linked to neurodegeneration in mice (Twig et al., 2008; Chen et al., 2015). Finally it has been indicated that activation of the mitochondrial transition pore (mPTP) is a key regulator of axonal degeneration (Barrientos et al., 2011).

At this time the role of mitochondria in neurodegeneration is not completely understood especially the role mitochondrial dynamics may play. Thus we investigated the relationship of mitochondrial dynamics in vincristine induced axon degeneration and Nmnat1 mediated axonal protection. We analyzed mitochondrial dynamics in cultured dorsal root ganglia (DRG) neurons overexpressing cytNmnat1 and treated with vincristine. Vincristine, an anti-cancer drug, is a known stabilizer of microtubules and has been shown to cause peripheral neurotoxicity, likely through alteration of calcium and ATP levels (Canta et al., 2015). The effect of cytNmnat1 overexpression on the rates of mitochondrial fission, fusion, motility, and mitochondrial fragmentation was assessed utilizing confocal laser microscopy at time points associated with axon degeneration—as elucidated from previous studies (Press and Milbrandt, 2008; Vohra et al., 2010; Wen et al., 2011). Our results indicate that during the process of neuronal degeneration, induced by vincristine, fission, fusion and motility rates were decreased and the mitochondria fragmented. More importantly, we show that the neuroprotective protein, cytNmnat1 significantly prevented the alteration of mitochondrial fission, fusion and fragmentation. Most interesting is that our work suggests these alterations occur prior to significant deterioration of the axon.

MATERIALS AND METHODS

DRG Culture

This study was carried out in accordance with the recommendations of PHS Policy on Humane Care and Use of Laboratory Animals, the Guide for the Care and Use of Laboratory Animals, and the policies and procedures of the University of Central Arkansas. The protocol was approved by the UCA Animal Care and Use committee.

Mouse DRG were collected from embryonic day 12.5 (E12.5) CD1 mice embryos. The DRGs from 5 embryos (∼200 total DRGs) of CD1 mice were dissociated and resuspended in 50 μl of Neurobasal media (Invitrogen) containing 2% B27 (Invitrogen) and 50 ng/ml NGF (Harlan Bioproducts) per dissected embryo. Suspended DRG neurons were placed as a drop (2 μl) near one end of each well in Lab TekII 4-well chambered cover glass (Nalge Nunc International), which had been previously coated with poly-D-lysine (0.1 mg/ml) and laminin (2–5 ug/ml). The chambered cover glass was then incubated at 37°C at 5% CO_2 for 15 min before 500 μl of Neurobasal media containing 2% B27, 50 ng/ml NGF, 1 μm 5-fluro-2′-deoxyuridine (Sigma), and 1μm uridine (Sigma) was added to each well.

Vincristine (0.4 μM) was added to 14 days *in vitro* (DIV) cultures to induce axon degeneration.

Lentiviral Infection of DRG Neurons

Lentiviruses were generated as previously described (Araki et al., 2004). DRG neurons were infected with lentiviruses expressing Ds-Red Mito to track mitochondria and GFP-cytNmnat1 (10^5–10^6 infectious units in 1 DIV neurons) (Baloh et al., 2007; Vohra et al., 2010). Control cells were infected with lentivirus expressing Ds-Red Mito and EGFP-only vector. Virus-containing medium was replaced with fresh media at 2 DIV and gene expression was verified via fluorescent microscopy of the EGFP or Ds Red reporter.

Quantification of Mitochondrial Fission and Fusion in E12.5 CD-1 Mouse DRGs

A Zeiss laser scanning LSM Pascal confocal microscope with 40 × and 63 × objective lenses was used to visualize 0.50 μm thick optical slices of DRG axons with a single plane imaged every 2.97 s for 180 s or until bleaching occurred. Fluorescent images as well as bright field images were collected.

An organelle splitting into two separate entities and remaining that way for the next couple of frames was classified as a fission event. Fusion events were identified when two organelles approached each other, connected, and remained that way for the next couple of frames (Schimmel et al., 2012). To ensure accurate quantification, two approaching organelles, appearing to undergo fusion, which appeared in subsequent frames to have passed by each other—returning to a similar arrangement as in the preceding frames—were not counted as an event; similar precautions were taken when identifying fission events where an organelle that appeared to split into separate organelles only to return to its original conformation in the subsequent frames was not counted.

Rates of fission and fusion were calculated by taking the average number of events/min for each time point at each condition and presented as a mean ± the standard error. Statistical analysis was conducted utilizing Graph Pad Prism version 6.07 and analyzed via non-parametric Kruskal-Wallis with Dunn's *post hoc*. Statistics generated are from embryos from at least two independent litters, collected on at least two different occasions, except for 96 h, litters were only collected once (3–5 images were collected for each condition/litter), p-values less than 0.05 were considered statistically significant.

Quantifying Mitochondrial Fragmentation in E12.5 CD-1 Mouse DRGs

Zeiss LSM browser was utilized to take a single frame out of two movies from each time point. The lengths and widths of 30 mitochondria were measured under each condition. Fragmentation was determined by the average length to width assessment of the organelles.

Statistical analysis was conducted utilizing a non-parametric multiple comparisons Wilcoxon analysis by JMP statistical analysis software (SAS Institute, Inc.) to compare the measurements from each condition and time point with p-values less than 0.05 being considered statistically significant. Comparison of treatments to control at 96 h was carried out in Graph Pad Prism version 6.07 via 1-way ANOVA, Holm-Sidak's multiple comparisons test.

Quantifying Mitochondrial Motility in E12.5 CD-1 Mouse DRGs

Kymographs were generated using ImageJ from the single plane time lapse confocal images collected as described above. A region of interest (ROI) was selected in three different areas in the first image of each series, for a minimum of 15 kymographs (approximately 60 mitochondria) for each condition. The ROIs were approximately the same width and length in each instance. The ROIs were converted, stacked, and used to create kymographs, which depict mitochondrial movement specific to the selected ROI. To quantify motility, mitochondrial movement in the kymograph was traced with a line where the slope of the line represents velocity in pixels/time point. These velocities were converted to μm/s.

Statistical analysis was conducted by utilizing Graph Pad Prism version 6.07 to compare velocity measurements within each treatment and across time points with p-values less than 0.05 being considered statistically significant. Rates were analyzed via non-parametric Kruskal-Wallis with Dunn's *post hoc*.

Scoring Degeneration of Axons

Single frames from every video acquired, as described above, were analyzed for neurodegeneration. A minimum of 50 axons were quantified for all treatments except cytNmnat1 96 h treated axons which only had 32 distinguishable axons. Each axon was classified based on degeneration into five categories and assigned a value between 1 and 5 (adapted from Fang et al., 2014). Axons classified as 5 were fully intact with smooth membrane along the length of the axon (**Figure 4B** left column). Category 4 were intact axons that had 21–40% of its membrane beginning to bleb (**Figure 4B** vincristine 24 h frame). Axons that scored a 3 were 41–60% degenerated; these were still intact, had not begun fragmenting, but had extensive blebbing (**Figure 4B** vincristine 48 h frame). The fourth category, which was assigned a value of 2, were 61–80% degenerated; these axons had begun fragmenting in addition to extensive blebbing of the membranes (**Figure 4B** vincristine 48 h). Please note: vincristine 48 h treatment images consistently contained both category 2 and category 3 axons. The final category, valued as a 1, were 100% degenerated axons, in these images it was not possible to identify the original number of axons (**Figure 4B** bottom frame of middle column). Each image was given a score by multiplying the number of axons that fell into each category (i.e., 5 axons in category 5 so $5 \times 5 = 25$; 2 axons in category 1 so $2 \times 1 = 2$) followed by these values being added together (i.e., $25 + 2 = 27$). For each treatment the image scores were averaged and a two-way ANOVA with *post hoc* Tukey test in Graph Pad Prism version 6.07 was performed.

RESULTS

Overexpression of cytNmnat1 in DRGs Maintains Rates of Mitochondrial Fission and Fusion in the Presence of Vincristine, an Inducer of Neurodegeneration

To determine the effect of vincristine induced axon degeneration and cytNmnat1 on mitochondrial fission and fusion, axons

TABLE 1 | Rates of fission and fusion in axons treated with vincristine (events/min).

		24 h	48 h	96 h
cytNmnat1	Fission	1.202 ± 0.216	1.049 ± 0.215	0.750 ± 0.226
	Fusion	1.219 ± 0.286	1.136 ± 0.164	1.158 ± 0.413
Vincristine	Fission	0.497 ± 0.117	0.029 ± 0.029	0.000 ± 0.000
	Fusion	0.387 ± 0.111	0.115 ± 0.064	0.000 ± 0.000
cytNmnat1 + vincristine	Fission	0.557 ± 0.135	0.389 ± 0.151	0.509 ± 0.195
	Fusion	0.400 ± 0.136	0.286 ± 0.093	0.390 ± 0.119

were imaged at different time points and the rates of fission and fusion were quantified. Mitochondrial fission rates decreased in the axons of 24 h vincristine treated neurons by 59% compared to cytNmnat1 expressing cultures (**Table 1**). Similarly, mitochondrial fusion rates also decreased in the axons of vincristine treated neurons by 68% as compared to the cytNmnat1 expressing cells (**Table 1**). These events were undetectable after 96 h of vincristine treatment (**Figure 1**, **Table 1**).

To determine if cytNmnat1 will prevent the vincristine induced loss of fission and fusion, rates in vincristine treated axons were compared to rates of fission and fusion in axons overexpressing cytNmnat1 and exposed to vincristine. By 48 h of treatment, fission and fusion rates are recovering; the expression of cytNmnat1 increased these rates by 93% and 60%, respectively, as compared to the axons of vincristine treated neurons (**Table 1**). This trend shows significant protection by 96 h for both fission and fusion ($p < 0.05$, **Figure 1**, **Table 1**). In conclusion, the overexpression of cytNmnat1 recovered the fission and fusion processes in the axons inhibited by vincristine, maintaining the rates at cytNmnat1 expressing culture levels by 96 h.

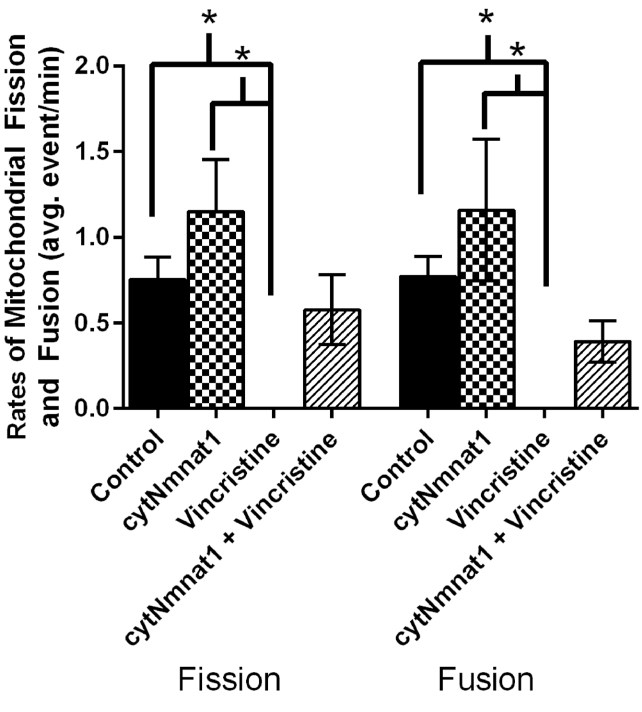

FIGURE 1 | The average rates of mitochondrial fission and fusion in axons of dorsal root ganglion neuronal cultures at 96 h. Cultures were either untreated, overexpressed the protective protein GFP-cytNmnat1, treated with 0.4 μM vincristine, or overexpressed GFP-cytNmnat1 and treated with vincristine. The overexpression of cytNmnat1 recovered the fission and fusion processes inhibited by vincristine ($p < 0.05$). * Indicate significance.

cytNmnat1 Overexpression Inhibits Mitochondrial Fragmentation

In order to assess cytNmnat1's effect on mitochondrial fragmentation the length and width of 30 mitochondria from each time point were measured in the axons of DRG neuronal cultures that were overexpressing cytNmnat1, incubated with vincristine alone, or overexpressing cytNmnat1 + vincristine.

As expected, vincristine treatment fragmented the mitochondria as measured by decreased length and increased width resulting in more circular or round mitochondria ($p < 0.05$, **Figure 2**). In axons overexpressing cytNmnat1, the total mitochondrial length and width were relatively stable over time, though they did get shorter ($p < 0.05$, **Figure 2**), indicating that the organelles remain filamentous overtime with cytNmnat1 overexpression. Finally, axons treated with overexpressed cytNmnat1 + vincristine were statistically similar to cells only overexpressing cytNmnat1, thus cytNmnat1 protects the cells from the vincristine induced mitochondrial fragmentation ($p < 0.05$, **Figure 2**). It is interesting to note that mitochondria are larger-both in length and width- in the untreated axons ($p < 0.05$, **Figure 2**).

Mitochondrial Motility is Partially Maintained when Neurodegeneration is Prevented by cytNmnat1

The final aspect of mitochondrial dynamics that we studied is velocity of organelle movement by analyzing kymographs from the three treatments. Treatment with vincristine shows a trend of decreasing mitochondrial movement from 0.132 ± 0.234 μm/s at 24 h vincristine treatment to no movement at all by 96 h (**Table 2**). We show that mitochondria move an average of 0.191 ± 0.088 μm/s when cytNmnat1 is overexpressed for 24 h, this rate is relatively stable out to 96 h (**Table 2**). Overexpression of cytNmnat1 does protect from the vincristine defect bringing velocities back up to 0.083 ± 0.015 μm/s by 96 h treatment, though not up to the level of cytNmnat1 expressing axons (**Figure 3**, **Table 2**).

In summary, vincristine treatment significantly alters all measured mitochondrial parameters and cytNmnat1 expression significantly counteracts fission, fusion, and fragmentation changes in the axons of vincristine treated neurons.

Vincristine Alters Mitochondrial Dynamics Prior to Visible Axon Degeneration

Thus far, we have shown that cytNmnat1 overexpression, which is known to protect axons from degeneration, significantly

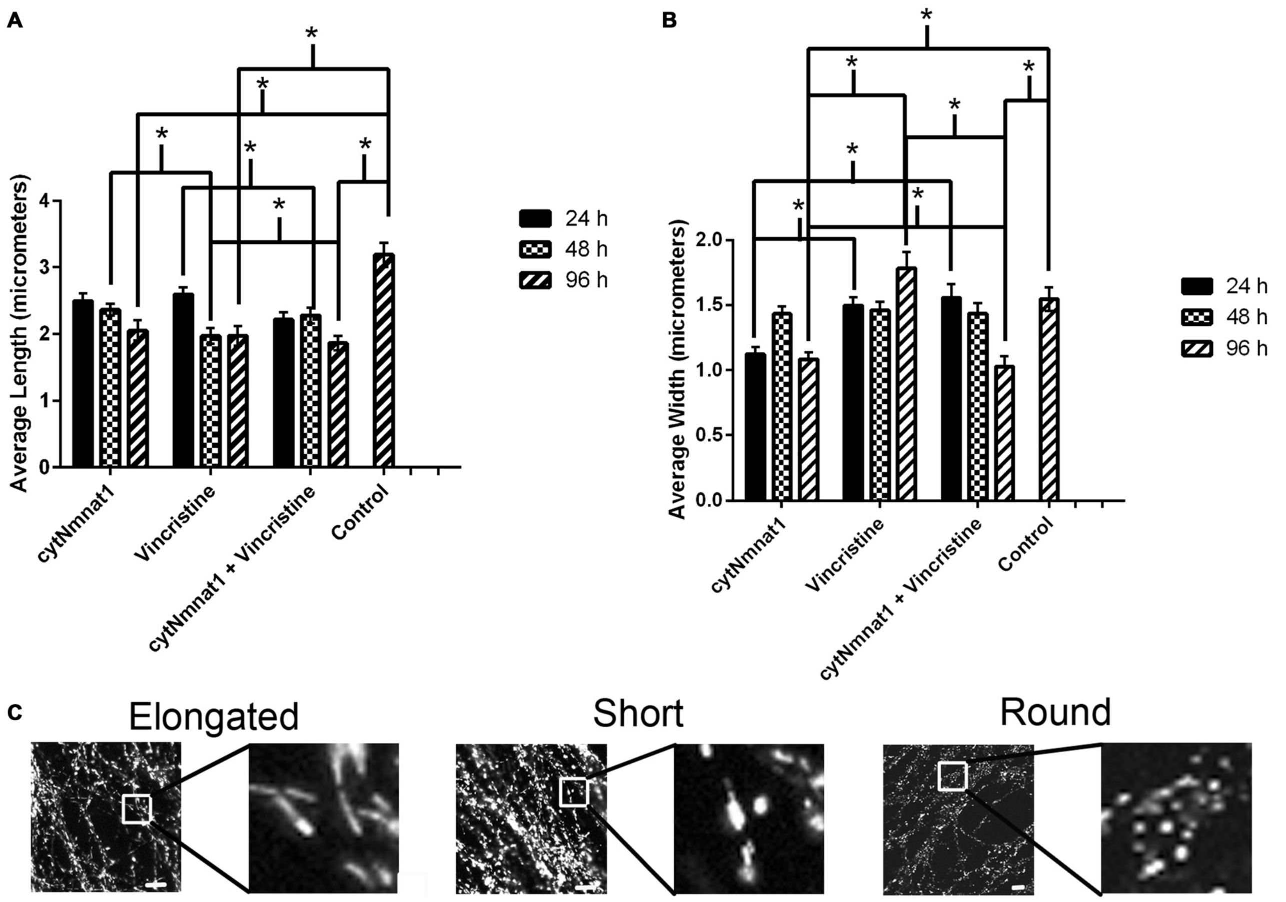

FIGURE 2 | The length and width of mitochondria for each treatment condition of dorsal root ganglion neuronal cultures over time. (A) Graph representing the average mitochondrial length for each treatment over time. **(B)** Graph representing the average mitochondrial width for each treatment over time. The mitochondrial length decreased in correlation with an increase in the mitochondrial width in vincristine only treated cells, indicating an increase in fragmentation. The data indicate that overexpression of cytNmnat1 preserves mitochondrial morphology when axon degeneration has been initiated by vincristine ($p < 0.05$). For simplicity only significance between treatments, not over time, is shown. **(C)** Representative mitochondrial images showing elongated, short, and round or fragmented organelles. In general mitochondria with overexpressed cytNmnat1 are elongated but do get shorter over time, while vincristine treated mitochondria become round and fragmented. Scale bar is equivalent to 10 μm. * Indicate significance.

prevents the alteration of mitochondrial dynamics as well. In an effort to understand more about the process of vincristine induced neurodegeneration, we assessed degeneration over time to determine which takes place first, the axonal morphological changes or the changes in mitochondrial dynamics. Our results indicate that degeneration of the axons induced by vincristine was detectible by 24 h but was not significantly different from cytNmnat1 or cytNmnat1 + vincristine treatments until 96 h ($F_{(2,75)} = 11.4$ $p < 0.0001$, **Figure 4**). As expected, throughout the time course there was no difference between the cytNmnat1 overexpressing axons and the cytNmnat1 overexpressing plus vincristine treatment.

Mitochondrial fission and fusion are significantly decreased by 24 h (Fission: $p < 0.0116$, Fusion: $p < 0.0123$, **Table 1**) while fragmentation in these degenerating neurons was apparent by 48 h when compared to cytNmnat1 overexpressed cells ($p < 0.0004$), (**Figure 2**). From these results we can conclude that vincristine treatment causes a decrease in fission and fusion, followed by mitochondrial fragmentation, then visible axon degeneration.

TABLE 2 | Velocity of mitochondria in axons treated with vincristine and cytNmnat1 (μm/s).

	24 h	48 h	96 h
cytNmnat1	0.191 ± 0.088	0.168 ± 0.118	0.179 ± 0.057
Vincristine	0.132 ± 0.234	0.011 ± 0.02	0
cytNmnat1 + vincristine	0.066 ± 0.033	0.108 ± 0.039	0.083 ± 0.015

DISCUSSION

Axon degeneration, a hallmark of many neurodegenerative diseases, has been found to occur prior to clinical manifestation of symptoms and has been linked to mitochondrial dysfunction in a number of instances (Press and Milbrandt, 2008;

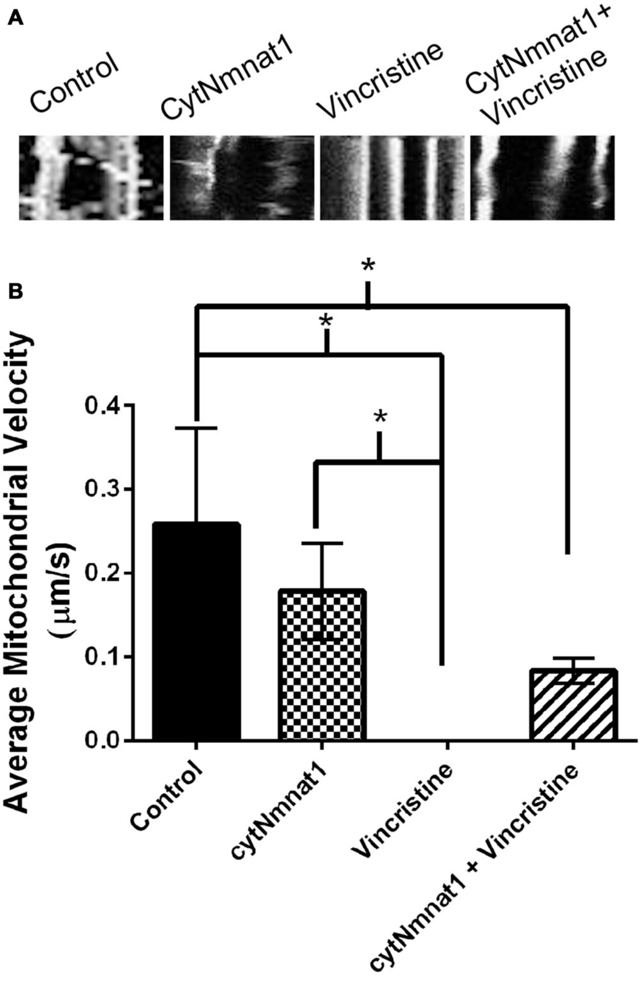

FIGURE 3 | Mitochondrial velocity for each treatment condition. **(A)** Representative kymographs of mitochondria under each treatment. **(B)** Graph representing the average mitochondrial velocity at 96 h post treatment. The overexpression of cytNmnat1 in vincristine treated cells allows the mitochondria to partially regain motility as compared to vincristine treatment alone. * Indicate significance.

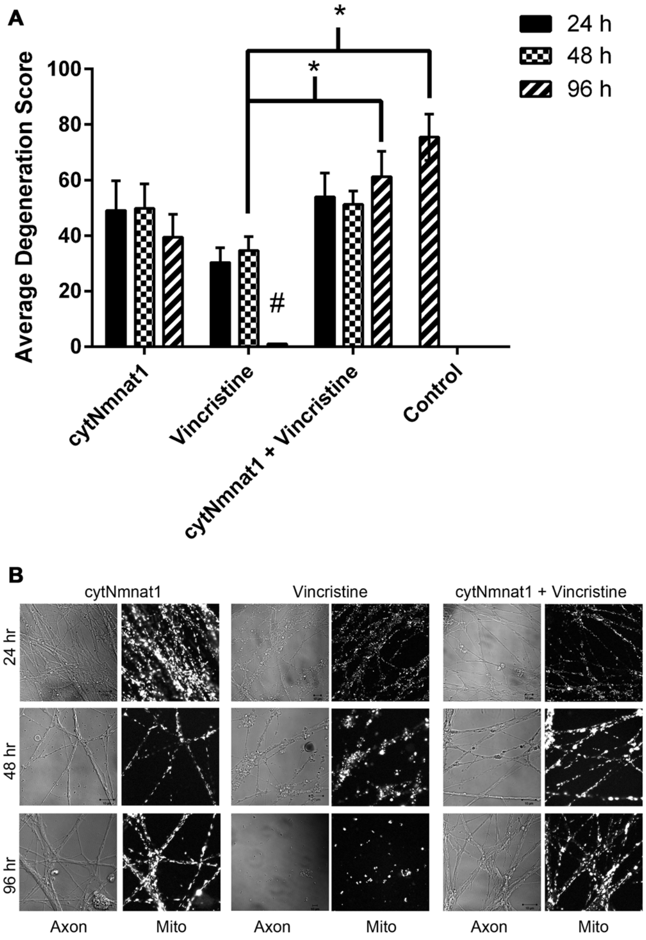

FIGURE 4 | Degeneration of axons over time. Axons were assigned a score (see "Materials and Methods" Section) based on their degeneration status. **(A)** Graph of degeneration for each treatment. Vincristine treated axons were degenerated by 96 h, which overexpression of cytNmnat1 prevented ($p < 0.0001$). $^{\#}$ A significant difference when compared to all means, * a significant difference between the paired columns. **(B)** Representative images for each treatment. Fully intact axons are found in all cytNmnat1 treatments. Vincristine treated axons for 24 h typically showed intact axons with blebbing beginning to occur. Extensive blebbing and axon fragmentation can be seen in 48 h vincristine treatments, whereas fully degenerated axons are found in 96 h vincristine treatment. More than 100 axons were analyzed for each treatment except for: 96 h cytNmnat1 overexpression and 96 h cytNmnat1 + vincristine, 30 and 50 axons respectively were quantified.

Vohra et al., 2010). Elucidating the mechanism of axon degeneration, especially as it relates to mitochondrial dysfunction in neurodegeneration, can lead to preventative and therapeutic measures against such debilitating afflictions. Recent work has indicated that axon degeneration is an active but apoptosis-independent mechanism (Vohra et al., 2010; Gerdts et al., 2013). However, mitochondrial involvement in the form of opening of mitochondrial permeability transition pores and mitochondrial Sarm1 is implicated in axon degeneration (Barrientos et al., 2011). Furthermore, abnormal mitochondrial dynamics and altered mitochondrial motility is implicated in synaptic degeneration in the mouse models of Alzheimer's disease (Calkins et al., 2011). In the present investigation we analyzed the relationship between mitochondria dynamics, morphology and neurodegeneration.

As expected, we show that vincristine fragments the mitochondria and decreases mitochondrial motility (Avery et al., 2012; Kitay et al., 2013). We also show that vincristine significantly disrupts mitochondrial fission and fusion. This is most likely because loss of microtubules -induced by vincristine- drastically reduces mitochondrial dynamics, most recently shown in Woods et al. (2016).

To try and understand the mechanism of neurodegeneration, we furthered our analysis by looking at the protective effect of cytNmnat1 on mitochondrial dynamics and morphology after vincristine induced neurodegeneration. Nmnat protects axons against various insults but its protective mechanism is still obscure. Nmnat protects axons in conditions of rotenone toxicity and blocks the ROS production in rotenone treated neurons (Press and Milbrandt, 2008). Nmnat overexpression also prevents the depletion of axonal NAD^+ and maintains the levels of ATP in the transected axons (Wang et al., 2005; Press and Milbrandt, 2008; Vohra et al., 2010; Wen et al., 2011), thus suggesting that mitochondrial function may be influenced by the overexpression of Nmnat. Here we demonstrate that cytNmnat1 can prevent the loss of fission and fusion due to vincristine. We and others also show that various forms of Nmnat recover mitochondrial motility after induction of neurodegeneration, though not always significantly (Avery et al., 2012). It has also been demonstrated that this mitochondrial transport is required for Nmnat's protective activity (Avery et al., 2012; Fang et al., 2014). Similar types of deficits in axonal mitochondrial motility have been observed in axon degeneration induced by: expression of the human mitofusion2 (Mfn2) mutant protein in the cultured DRG neurons (Baloh et al., 2007; Misko et al., 2010), hydrogen peroxide exposure and oxygen-glucose deprivation in primary hippocampal cultures (Fang et al., 2014). Cagalinec et al. (2013) also observed decreased motility, fission, and fusion in neurodegeneration disease models involving Huntingtin and Tau. Additionally, our work and that of Kitay et al. (2013) indicates that cytNmnat1 prevents mitochondrial fragmentation. The direct reason for mitochondrial fragmentation during neuron degeneration is unclear, but it is likely a result of the combined decrease in mitochondrial fission, fusion and motility.

Finally, the work presented here suggests that the decrease in fission, fusion, motility, and mitochondrial fragmentation occur prior to the axon's morphological changes when treated with vincristine. Barrientos et al. (2011) also showed that mitochondrial swelling precedes neurodegeneration, supporting our study.

Are mitochondrial dynamics directly involved in axon degeneration? It is well established that mitochondrial function is controlled by proper morphology and distribution (Nunnari and Suomalainen, 2012) and that morphology and distribution is maintained by mitochondrial dynamics (Nunnari et al., 1997; Bleazard et al., 1999; Karbowski and Youle, 2003; Twig and Shirihai, 2011; El Zawily et al., 2014). The literature demonstrates that mitochondrial dynamics are involved in the regulation of autophagy; more specifically mutations in PINK (which cause parkinsonism and mis-regulate autophagy) induce fragmentation of the mitochondria through a block in fusion. Additionally, work on the mitochondrial motility protein -Miro- has signified that it is a substrate of PINK/parkin thus autophagy will also prevent mitochondrial motility. Thus, the loss of fission, fusion, and motility may inhibit mitochondrial function, and stimulate mitophagy.

Additionally, Wallerian degeneration is induced by a calcium overload (Wang et al., 2012) that likely activates the mitochondrial permeability transition pore (Barrientos et al., 2011). Therefore, we suggest calcium overload decreases mitochondrial dynamics (fission, fusion, and motility), inducing fragmentation and subsequently, mitochondrial function, leading to mitophagy and neurodegeneration. Avery et al. (2012) also showed something similar, demonstrating that axotomy induces a calcium overload, while Wld^S prevents this overload, maintains permeability resistance and mitochondrial motility. Future experiments need to focus on mitochondrial dynamics under calcium overload conditions, and neurodegeneration measurements with Mdivi-1 treatment. Mdivi-1 is an inhibitor of DRPs the regulators of mitochondrial fission and fusion. It must also be stated that the work presented here only begins to look at the role of mitochondria in neurodegeneration-specifically studying mitochondrial dynamics. At this time cytochrome c release, change in membrane potential, and the induction of apoptosis were not determined, though these are important future experiments to definitively identify the role of mitochondria in degeneration.

In conclusion, we propose that vincristine induced axon degeneration is triggered/propagated by decreased mitochondrial dynamics and fragmentation, and that cytNmnat1 inhibits axonal degeneration by preserving normal mitochondrial integrity and dynamics.

AUTHOR CONTRIBUTIONS

BPSV designed the project. KN, GWB, LCW acquired, analyzed, and interpreted the work. KN, GWB, LCW, BPSV, were involved in writing, editing and final approval of the version to be published. KN, GWB, LCW, BPSV agree to be accountable for all aspects of the work.

ACKNOWLEDGMENTS

The project described was supported by grants from the National Center for Research Resources (5P20RR016460-11) and the National Institute of General Medical Sciences (8 P20 GM103429-11) from the National Institutes of Health. The Zeiss LSM Pascal confocal microscope used for image acquisition was funded by National Science Foundation (NSF) Award Number 0215847. The authors would also like to thank Nicholas West for his critical review of the manuscript.

REFERENCES

Alobuia, W. M., Xia, W., and Vohra, B. P. S. (2013). Axon degeneration is key component of neuronal death in amyloid-β toxicity. *Neurochem. Int.* 63, 782–789. doi: 10.1016/j.neuint.2013.08.013

Araki, T., Sasaki, Y., and Milbrandt, J. (2004). Increased nuclear NAD biosynthesis and SIRT1 activation prevent axonal degeneration. *Science* 305, 1010–1013. doi: 10.1126/science.1098014

Avery, M. A., Rooney, T. M., Pandya, J. D., Wishart, T. M., Gillingwater, T. H., Geddes, J. W., et al. (2012). Wld^S prevents axon degeneration through increased mitochondrial flux and enhanced mitochondrial Ca^{2+} buffering. *Curr. Biol.* 22, 596–600. doi: 10.1016/j.cub.2012.02.043

Baloh, R. H., Schmidt, R. E., Pestronk, A., and Milbrandt, J. (2007). Altered axonal mitochondrial transport in the pathogenesis of charcot-marie-tooth disease from mitofusin 2 mutations. *J. Neurosci.* 27, 422–430. doi: 10.1523/JNEUROSCI.4798-06.2007

Barrientos, S. A., Martinez, N. W., Yoo, S., Jara, J. S., Zamorano, S., Hetz, C., et al. (2011). Axonal degeneration is mediated by the mitochondrial permeability transition pore. *J. Neurosci.* 31, 966–978. doi: 10.1523/JNEUROSCI.4065-10.2011

Bleazard, W., McCaffery, J., King, E., Bale, S., Mozdy, A., Tieu, Q., et al. (1999). The dynamin-related GTPases, Dnm1, regulates mitochondrial fission in yeast. *Nat. Cell Biol.* 1, 298–304. doi: 10.1038/13014

Cagalinec, M., Safiulina, D., Liiv, M., Liiv, J., Choubey, V., Wareski, P., et al. (2013). Principles of the mitochondrial fusion and fission cycle in neurons. *J. Cell Sci.* 126, 2187–2197. doi: 10.1242/jcs.118844

Calkins, M. J., Manczak, M., Mao, P., Shirendeb, U., and Reddy, P. H. (2011). Impaired mitochondrial biogenesis, defective axonal transport of mitochondria, abnormal mitochondrial dynamics and synaptic degeneration in a mouse model of Alzheimer's disease. *Hum. Mol. Genet.* 20, 4515–4529. doi: 10.1093/hmg/ddr381

Canta, A., Pozzi, E., and Carozzi, V. (2015). Mitochondrial dysfunction in Chemotherapy-Induced Peripheral Neuropathy (CIPN). *Toxics* 3, 198–223.doi: 10.3390/toxics3020198

Chen, H., and Chan, D. C. (2005). Emerging functions of mammalian mitochondrial fusion and fission. *Hum. Mol. Genet.* 14, R283–R289. doi: 10.1093/hmg/ddi270

Chen, H., and Chan, D. C. (2009). Mitochondrial dynamics-fusion, fission, movement and mitophagy-in neurodegenerative diseases. *Hum. Mol. Genet.* 18, R169–R176. doi: 10.1093/hmg/ddp326

Chen, L., Xie, Z., Turkson, S., and Zhuang, X. (2015). A53T human α-synuclein overexpression in transgenic mice induces pervasive mitochondria macroautophagy defects preceding dopamine neuron degeneration. *J. Neurosci.* 35, 890–905. doi: 10.1523/JNEUROSCI.0089-14.2015

Dedov, V. N., and Roufogalis, B. D. (1999). Organisation of mitochondria in living sensory neurons. *FEBS Lett.* 456, 171–174. doi: 10.1016/s0014-5793(99)00951-5

El Zawily, A. M., Schwarzländer, M., Finkemeier, I., Johnston, I. G., Benamar, A., Cao, Y., et al. (2014). FRIENDLY regulates mitochondrial distribution, fusion and quality control in arabidopsis. *Plant Physiol.* 166, 808–828. doi: 10.1104/pp.114.243824

Fang, C., Decker, H., and Banker, G. (2014). Axonal transport plays a crucial role in mediating the axon-protective effects of NmNAT. *Neurobiol. Dis.* 68, 78–90. doi: 10.1016/j.nbd.2014.04.013

Gerdts, J., Summers, D. W., Sasaki, Y., DiAntonio, A., and Milbrandt, J. (2013). Sarm1-mediated axon degeneration requires Both SAM and TIR interactions. *J. Neurosci.* 33, 13569–13580. doi: 10.1523/JNEUROSCI.1197-13.2013

Karbowski, M., and Youle, R. (2003). Dynamics of mitochondrial morphology in healthy cells and during apoptosis. *Cell Death Differ.* 10, 870–880. doi: 10.1038/sj.cdd.4401260

Kitay, B. M., McCormack, R., Wang, Y., Tsoulfas, P., and Zhai, R. G. (2013). Mislocalization of neuronal mitochondria reveals regulation of Wallerian degeneration and NMNAT/WLDS-mediated axon protection independent of axonal mitochondria. *Hum. Mol. Genet.* 22, 1601–1614. doi: 10.1093/hmg/ddt009

Korobova, F., Ramabhadran, V., and Higgs, H. N. (2013). An actin-dependent step in mitochondrial fission mediated by the ER-associated formin INF2. *Science* 339, 464–467. doi: 10.1126/science.1228360

Liesa, M., Palacín, M., and Zorzano, A. (2009). Mitochondrial dynamics in mammalian health and disease. *Physiol. Rev.* 89, 799–845. doi: 10.1152/physrev.00030.2008

Martin, L. J. (2012). "Chapter 11–biology of mitochondria in neurodegenerative diseases," in *Progress in Molecular Biology and Translational Science*, ed. B. T. David (Cambridge, UK: Academic Press), 355–415.

Misko, A., Jiang, S., Wegorzewska, I., Milbrandt, J., and Baloh, R. H. (2010). Mitofusin 2 is necessary for transport of axonal mitochondria and interacts with the miro/milton complex. *J. Neurosci.* 30, 4232–4240. doi: 10.1523/JNEUROSCI.6248-09.2010

Müller, M., Mironov, S. L., Ivannikov, M. V., Schmidt, J., and Richter, D. W. (2005). Mitochondrial organization and motility probed by two-photon microscopy in cultured mouse brainstem neurons. *Exp. Cell Res.* 303, 114–127. doi: 10.1016/j.yexcr.2004.09.025

Nunnari, J., Marshall, W., Straight, A., Murray, A., Sedat, J., and Walter, P. (1997). Mitochondrial transmission during mating in S. cerevisiae is determined by mitochondrial fusion and fission and the intramitochondrial segregation of mtDNA. *Mol. Biol. Cell* 8, 1233–1242. doi: 10.1091/mbc.8.7.1233

Nunnari, J., and Suomalainen, A. (2012). Mitochondria: in sickness and in health. *Cell* 148, 1145–1159. doi: 10.1016/j.cell.2012.02.035

Press, C., and Milbrandt, J. (2008). Nmnat delays axonal degeneration caused by mitochondrial and oxidative stress. *J. Neurosci.* 28, 4861–4871. doi: 10.1523/JNEUROSCI.0525-08.2008

Rambold, A. S., Kostelecky, B., Elia, N., and Lippincott-Schwartz, J. (2011). Tubular network formation protects mitochondria from autophagosomal degradation during nutrient starvation. *Proc. Natl. Acad. Sci. U S A* 108, 10190–10195. doi: 10.1073/pnas.1107402108

Sasaki, Y., Vohra, B. P. S., Lund, F. E., and Milbrandt, J. (2009). Nicotinamide mononucleotide adenylyl transferase-mediated axonal protection requires enzymatic activity but not increased levels of neuronal nicotinamide adenine dinucleotide. *J. Neurosci.* 29, 5525–5535. doi: 10.1523/JNEUROSCI.5469-08.2009

Schimmel, B., Berbusse, G., and Naylor, K. (2012). Mitochondrial fission and fusion in Dictyostelium discoideum: a search for proteins involved in membrane dynamics. *BMC Res. Notes* 5:505. doi: 10.1186/1756-0500-5-505

Shen, Q., Yamano, K., Head, B. P., Kawajiri, S., Cheung, J. T. M., Wang, C., et al. (2014). Mutations in Fis1 disrupt orderly disposal of defective mitochondria. *Mol. Biol. Cell* 25, 145–159. doi: 10.1091/mbc.E13-09-0525

Summers, D. W., DiAntonio, A., and Milbrant, J. (2014). Mitochondrial dysfunction induces Sarm-1dependent cell death in sensory neurons. *J. Neurosci.* 34, 9338–9350. doi: 10.1523/JNEUROSCI.0877-14.2014

Twig, G., Elorza, A., Molina, A. J. A., Mohamed, H., Wikstrom, J. D., Walzer, G., et al. (2008). Fission and selective fusion govern mitochondrial segregation and elimination by autophagy. *EMBO J.* 27, 433–446. doi: 10.1038/sj.emboj.7601963

Twig, G., and Shirihai, O. S. (2011). The interplay between mitochondrial dynamics and mitophagy. *Antioxid. Redox Signal.* 14, 1939–1951. doi: 10.1089/ars.2010.3779

Vohra, B. P. S., Sasaki, Y., Miller, B. R., Chang, J., DiAntonio, A., and Milbrandt, J. (2010). Amyloid precursor protein cleavage-dependent and -independent axonal degeneration programs share a common nicotinamide mononucleotide adenylyltransferase 1-sensitive pathway. *J. Neurosci.* 30, 13729–13738. doi: 10.1523/JNEUROSCI.2939-10.2010

Wang, J. T., Medress, Z. A., and Barres, B. A. (2012). Axon degeneration: molecular mechanisms of a self-destruction pathway. *J. Cell Biol.* 196, 7–18. doi: 10.1083/jcb.201108111

Wang, J., Zhai, Q., Chen, Y., Lin, E., Gu, W., McBurney, M. W., et al. (2005). A local mechanism mediates NAD-dependent protection of axon degeneration. *J. Cell Biol.* 170, 349–355. doi: 10.1083/jcb.200504028

Wen, Y., Parrish, J. Z., He, R., Zhai, R. G., and Kim, M. D. (2011). Nmnat exerts neuroprotective effects in dendrites and axons. *Mol. Cell. Neurosci.* 48, 1–8. doi: 10.1016/j.mcn.2011.05.002

Woods, L. C., Berbusse, G. W., and Naylor, K. (2016). Microtubules are essential for mitochondrial dynamics-fission, fusion and motility-in dictyostelium discoideum. *Front. Cell Dev. Biol.* 4:19. doi: 10.3389/fcell.2016.00019

Conflict of Interest Statement: The authors declare that the research was conducted in the absence of any commercial or financial relationships that could be construed as a potential conflict of interest.

frontiers
in Cellular Neuroscience

ORIGINAL RESEARCH
published: 17 October 2016
doi: 10.3389/fncel.2016.00238

Enhancement of Peripheral Nerve Regrowth by the Purine Nucleoside Analog and Cell Cycle Inhibitor, Roscovitine

*Vincent Law[1], Sophie Dong[2], Jesusa L. Rosales[3], Myung-Yung Jeong[4], Douglas Zochodne[2] and Ki-Young Lee[1]**

[1] Department of Cell Biology and Anatomy, Arnie Charbonneau Cancer Institute, Hotchkiss Brain Institute, University of Calgary, Calgary, AB, Canada, [2] Department of Clinical Neurosciences, Hotchkiss Brain Institute, University of Calgary, Calgary, AB, Canada, [3] Department of Biochemistry and Molecular Biology, Snyder Institute for Chronic Diseases, University of Calgary, Calgary, AB, Canada, [4] Department of Cogno-Mechatronics Engineering, Pusan National University, Pusan, South Korea

Peripheral nerve regeneration is a slow process that can be associated with limited outcomes and thus a search for novel and effective therapy for peripheral nerve injury and disease is crucial. Here, we found that roscovitine, a synthetic purine nucleoside analog, enhances neurite outgrowth in neuronal-like PC12 cells. Furthermore, *ex vivo* analysis of pre-injured adult rat dorsal root ganglion (DRG) neurons showed that roscovitine enhances neurite regrowth in these cells. Likewise, *in vivo* transected sciatic nerves in rats locally perfused with roscovitine had augmented repopulation of new myelinated axons beyond the transection zone. By mass spectrometry, we found that roscovitine interacts with tubulin and actin. It interacts directly with tubulin and causes a dose-dependent induction of tubulin polymerization as well as enhances Guanosine-5'-triphosphate (GTP)-dependent tubulin polymerization. Conversely, roscovitine interacts indirectly with actin and counteracts the inhibitory effect of cyclin-dependent kinases 5 (Cdk5) on Actin-Related Proteins 2/3 (Arp2/3)-dependent actin polymerization, and thus, causes actin polymerization. Moreover, in the presence of neurotrophic factors such as nerve growth factor (NGF), roscovitine-enhanced neurite outgrowth is mediated by increased activation of the extracellular signal-regulated kinases 1/2 (ERK1/2) and p38 mitogen-activated protein kinase (MAPK) pathways. Since microtubule and F-actin dynamics are critical for axonal regrowth, the ability of roscovitine to activate the ERK1/2 and p38 MAPK pathways and support polymerization of tubulin and actin indicate a major role for this purine nucleoside analog in the promotion of axonal regeneration. Together, our findings demonstrate a therapeutic potential for the purine nucleoside analog, roscovitine, in peripheral nerve injury.

Keywords: peripheral nerve, injury, axon, regeneration, cytoskeleton

Edited by:
Vann Bennett,
Howard Hughes Medical Institute,
USA

Reviewed by:
Stefania Ceruti,
University of Milan, Italy
Yen-Chung Chang,
National Tsing Hua University, Taiwan

***Correspondence:**
Ki-Young Lee
kylee@ucalgary.ca

Received: *15 July 2016*
Accepted: *30 September 2016*
Published: *17 October 2016*

Citation:
Law V, Dong S, Rosales JL, Jeong M-Y, Zochodne D and Lee K-Y (2016) Enhancement of Peripheral Nerve Regrowth by the Purine Nucleoside Analog and Cell Cycle Inhibitor, Roscovitine. Front. Cell. Neurosci. 10:238. doi: 10.3389/fncel.2016.00238

INTRODUCTION

Unlike in the central nervous system, some degree of axonal regeneration and functional recovery is possible after injury in the peripheral nervous system. However, the process is slow and many times incomplete. Following injury, Wallerian-like degeneration (WLD) occurs in the denervated distal stump where myelin and myelin-associated glycoproteins are broken down to allow axonal regeneration (Stoll et al., 2002). This event correlates with upregulation of cytosolic and secreted forms of phospholipase A2 in Schwann cells (SC; De et al., 2003), which undergo dedifferentiation to promote a change in the damaged nerve environment to support neuron survival and axon regrowth (Jessen and Mirsky, 2008).

Axonal regrowth is one of the cellular processes that require modulation of actin and tubulin polymerization (Eng et al., 1999; Richardson et al., 2009). Indeed, during injured peripheral nerve recovery, the growth cone depends on the upregulation of tubulin subunits in its core and in the core of the trailing axon as well as actin, which forms the filopodia. Thus, tubulin and actin form the major cytoskeletal framework of elongating axons of the regenerating nerve (Chierzi et al., 2005; Vogelaar et al., 2009).

A multitude of endogenous and exogenous factors have been demonstrated to have an impact on the speed and direction of growth of regenerating axons. For example, the naturally occurring purine nucleoside, inosine, has been implicated in collateral axon growth in the corticospinal tract after focal traumatic brain injury and stroke (Dachir et al., 2014). In addition, the purine nucleosides, adenosine and guanosine, have been suggested to influence axonal degeneration after injury of dorsal root ganglia neurons (Press and Milbrandt, 2009). Furthermore, adenosine was found to aid axon preservation after injury (Press and Milbrandt, 2009). These observations suggest that purine nucleosides may have the ability to protect axon integrity.

A synthetic purine analog, R-roscovitine (also known as CYC202 and Seliciclib), interacts with a number of proteins, including cyclin-dependent kinases (Cdks), camodulin-dependent protein kinases (CaM kinases) and extracellular signal-regulated kinases (ERK; Bach et al., 2005), and has a varying inhibitory effect on these kinases (Meijer et al., 1997; Planchais et al., 1997). Roscovitine is particularly known as an inhibitor of Cdks, which are key regulators of cell cycle progression. Interestingly, inhibiting the cell cycle has been shown to cause decreased neuronal death as well as improved sensory motor recovery following spinal cord injury (Wu et al., 2011), and purine nucleosides have been demonstrated to protect axon integrity (Press and Milbrandt, 2009) and support axon growth (Dachir et al., 2014). However, there have also been studies showing that roscovitine inhibits neurite outgrowth (Harada et al., 2001; Lee and Kim, 2004; Carter et al., 2008). Thus, the role of roscovitine in neurite outgrowth remains to be elucidated.

Although roscovitine inhibits mitogen-activated protein kinase (MAPKs), it is a poor inhibitor of these kinases with IC_{50} values of 34 μM, 14 μM and >10 μM for ERK1, ERK2 and p38 MAPK, respectively, in *in vitro* purified enzyme assays (Meijer et al., 1997). The molecular mechanism by which roscovitine inhibits protein kinase activity involves competition for adenosine 5′-triphosphate (ATP)-binding pockets within the enzyme (De Azevedo et al., 1997; Gray et al., 1999). The binding of roscovitine is a reversible process, and based on pharmacokinetic studies using intravenous injections in mouse and rat models, it shows a high degree of dissemination and rapid metabolomic degradation (Vita et al., 2004; Nutley et al., 2005; Raynaud et al., 2005). Interestingly, roscovitine is currently being explored as a therapeutic agent for specific types of cancer such as non-small cell lung cancer (Hamilton et al., 2014) and nasopharyngeal cancer (Hui et al., 2009) as well as therapy for Cushing's disease (Liu et al., 2015).

Previously, roscovitine has been shown to rescue actin stress fibers formation in Rat-2 fibroblast cells that overexpress CKIγ2. It was thought that this was achieved through a Cdk-independent $p27^{KIP}$ pathway (Latreille et al., 2012). Roscovitine has also been correlated with microtubule formation in mitotic *S2 Drosophila* cells. It was believed that this correlation involved inactivation of Cdk1 (Moutinho-Pereira et al., 2010). In yet another study, roscovitine was associated with the formation of cytoskeletal aggregates in apoptotic bodies in human CHP212 neuroblastoma cells (van Engeland et al., 1997). Based on these findings, we came to the hypothesis that roscovitine may interact with cytoskeletal components, particularly actin and tubulin, and that it is possible that following peripheral nerve injury, exposure to roscovitine could result in the alteration of actin and tubulin dynamics and subsequently promote axonal regeneration.

Previous investigations on the signaling cascades that regulate neurite outgrowth and nerve regeneration following injury have demonstrated the involvement of ERK1/2 and p38 MAPK. While for example, it was found that the ERK and p38 MAPK inhibitors, PD98059 and SB203580, respectively, inhibited artemisinin-induced neurite outgrowth (Sarina et al., 2013). In separate studies of rat crushed sciatic nerves, it was also determined that ERK activity increased on days 3 and 7 post injury while AKT and p38 MAPK showed increasing activities from 3 to 28 days post injury (Yamazaki et al., 2009). These findings are consistent with the idea that activation of ERK, p38 MAPK and AKT are involved in neurite outgrowth and axon regeneration.

In this study, we provide new insight into the targeting of both actin and tubulin by roscovitine. We demonstrate the ability of roscovitine to interact with actin and tubulin, and induce actin and tubulin polymerization. We also demonstrate that in addition to enhancing actin- and tubulin-dependent neurite outgrowth, roscovitine augments axonal regrowth and nerve regeneration following injury. Furthermore, we show that enhanced activation of ERK and p38 MAPK is linked to roscovitine-induced neurite outgrowth.

MATERIALS AND METHODS

Animals and Preconditioning Lesion Experiments

Adult male Sprague-Dawley rats (Charles River Laboratory, Senneville, QC, Canada) with an initial weight of 300–500 g were used and all animal studies conformed to regulatory standards and were approved by the University of Calgary Health Sciences Animal Care Committee. For preconditioning, the sciatic nerve was cut at the mid-thigh region 3 days prior to harvesting dorsal root ganglia (DRG). A sham injury in separate animals was performed by exposing but not severing the sciatic nerve.

PC12 Cell Culture, R-roscovitine Treatment and Neurite Outgrowth Analysis

PC12 cells were seeded at 1.5×10^5 and 4.5×10^5 (for western blot analysis) into 35 mm and 60 mm tissue culture dishes, respectively, in high serum-containing RPMI (10% horse serum, 5% fetal bovine serum) with penicillin-streptomycin. After 24 h, cells were subjected to serum starvation in RPMI containing 0.2% horse serum and penicillin-streptomycin for 18 h. Cells were then treated with 10 ng/ml nerve growth factor (NGF; Invitrogen Life Technologies), and/or graded concentrations (0.2, 2, 5, 10, 20 and 40 μM) of R-roscovitine (Invitrogen Life Technologies) for 24 h. Neurite outgrowth was examined by light microscopy (Olympus IX71) and images were analyzed using the Image-Pro Express software (Media Cybernetics). The length of neurites was analyzed using the Image-J software. Three optical fields and 50 cells/field were evaluated for each condition. Cell viability was assessed by trypan blue assay. Measurements were taken from 50 cells in each treatment ($n = 3$).

Western Blot Analysis

For time-course assays, cells were exposed to 10 ng/ml NGF alone, 10 μM roscovitine alone, or both, and lysed at 0, 1, 3, 10, 30, 90 and 180 min post-treatment. Equal amounts of protein samples were then resolved in 12.5% sodium dodecyl sulfate-polyacrylamide gel electrophoresis (SDS-PAGE) and subjected to western blot analysis using total or phospho-antibodies against ERK1/2, p38 MAPK and AKT (Cell Signaling Technology, Inc.). Cdk5 and HRP-conjugated secondary antibodies were from Santa Cruz Biotechnology, Inc. and Invitrogen Life Technologies, respectively.

Primary DRG Sensory Neuron Culture

Dissociated adult sensory neuron culture protocols using rat DRG were as described previously (Christie et al., 2014). Briefly, rats were anesthetized with Isoflurane (Abbot Laboratories) and then killed 3 days following the conditioning lesion or sham surgery. L4–L6 DRGs were removed from the rats and placed into L15 (Invitrogen) medium. The DRGs were rinsed and then transferred to a tube containing 2 ml 0.1% collagenase (Invitrogen)/L15. Following incubation at 37°C, the DRGs were placed into single-cell suspension by triturating. The single-cell suspension was spun and washed three times in 2 ml L15. After the final spin, the cells were resuspended in L15 and passed through a 70 mm mesh (VWR International Co.) and then placed in 500 ml L15 enriched with 1:100 dilution of N2 supplement (Invitrogen) and 0.1% BSA (Sigma) and placed into a culture medium of Dulbecco's Modified Eagle Medium/F12 (DMEM/F12; Invitrogen) + 1:100 dilution N-2 supplement, 0.5–0.8% BSA and 0.2 ng/ml NGF (Cedarlane Labs) plus Penicillin 50 U/ml, Streptomycin 50 U/ml (Invitrogen) and plated on poly-L-lysine (Sigma-Aldrich) and 10 μg/ml mouse laminin (Invitrogen)-coated cover slips. Cells were grown for 24 h prior to roscovitine treatment (0.2, 2 or 10 μM) for 24 h.

Immunocytochemistry of Primary DRG Sensory Neurons

Roscovitine-treated and untreated neurons were washed with 1× Phosphate-buffered saline (PBS) and fixed with 4% paraformaldehyde (Invitrogen Life Technologies), stained with β-tubulin III antibody (1:200 dilution; Sigma-Aldrich Co.) in 1× PBS containing 10% goat serum and 0.3% Triton X-100 and Cy3-conjugated anti-mouse secondary antibody (1:200 dilution; Sigma-Aldrich Co.) in 1× PBS containing 10% goat serum and 0.3% Triton X-100. Images were captured under a Zeiss fluorescence microscope. Neurite length was analyzed by the MetaXpress software and by an observer blinded to their condition (Molecular Devices, Sunnyvale, CA, USA). Between 40 and 60 neurons were analyzed per condition. Three to four rats per condition were routinely used. Graph Pad Prism was used for statistical analysis. Student's *t*-tests were carried out with the statistical significance set at $p \leq 0.05$.

Mass Spectrometry

R-roscovitine bound proteins were eluted from agarose beads by SDS sample buffer and briefly subjected to SDS-PAGE. Coomassie stained protein bands were cut and analyzed by LC-MS/MS on a Micromass Q-ToF-2TM mass spectrometer coupled with a Waters CapLC capillary HPLC (SAMS Centre, University of Calgary). The peptide and protein false discovery rates were set at 1%. A total of 22 roscovitine-interacting proteins were identified, i.e., proteins identified and quantified from at least two unique peptides. Keratin contaminants were not counted. Significance values were determined by Perseus tool using significance B. Proteins with ratio greater than 1.9 and significance B lesser than 0.1 were considered significantly enriched. Eleven proteins listed in **Figure 4B** satisfied these criteria.

R-roscovitine Agarose Pull-Down Assay and Analysis of R-roscovitine Binding Proteins

Lysates of PC12 cells treated with 10 ng/ml NGF or 10 ng/ml NGF + 10 μM roscovitine for 24 h were pre-cleared with agarose beads for 20 min and subsequently incubated with R-roscovitine agarose beads (provided by Dr. L. Meijer, Station Biologique de Roscoff, CNRS UPR, France) for 40 min. Beads were washed with 50 mM Tris, pH 7.4, containing 5 mM NaF, 250 mM NaCl, 5 mM EDTA, 5 mM EGTA, 0.1% Triton X-100 and protease inhibitor cocktail. R-roscovitine-binding proteins were eluted from beads with 2× SDS-PAGE sample buffer and resolved by SDS-PAGE. Separated proteins were stained with Sypro-Ruby Red (Invitrogen Life Technologies) and detected using the BioDoc IT^{TM} Image System. To identify R-roscovitine-binding proteins, pulled-down samples were subjected to SDS-PAGE and ran into the 12.5% gel. Protein bands were cut and analyzed by LC-MS/MS (SAMS Centre for Proteomics, University of Calgary).

Nerve Regeneration Analysis

Axon regrowth was analyzed in transected rat sciatic nerve as described previously (Christie et al., 2010). An incision (3 cm) was made on the lateral region of the left thigh from the sciatic notch to the knee area. Another incision on the dorsal region superior to the scapulae and parallel to the vertebrae was performed to enable insertion of a microinjection port (MIP). Forceps were used to create a channel through the subdermal fascia between the incisions. Forceps were also used to pull the MIP catheter from the anterior site to the posterior incision. The MIP catheter was then attached to the T-chamber access tube. The left sciatic nerve was exposed and mobilized by blunt dissection, and transected at the mid-thigh region with a scalpel blade (11-0). The nerve stumps were attached to the nerve chamber with a nylon suture (Ethicon, 9-0) through the epineurium. A 3 mm gap was left between the proximal and distal stumps. Single sutures (Ethicon, 4-0) were used to attach the tube's T-intersection to the underlying muscle and to reattach the retracted gluteal muscle. A continuous suture (4-0) was performed to close the incisions. On days 2, 4 and 6 following nerve injury, 100 μl of 10 μM roscovitine was administered. At the experimental end points, both the proximal and distal nerve segments were cut a few millimeters away from the nerve chamber. The epineurial sutures were removed to free the nerve bridge (regenerate), which was harvested by pulling it through the chamber. Four of the nine rats were sacrificed to detect early regenerating fibers 7 days post-injury. The rest ($n = 5$) of the animals were analyzed for regenerating myelinated axons 21 days post-injury. Immunohistochemistry was performed on bridges spanning the sciatic nerve transections using mouse NF200 (1:800; Sigma) and rabbit glial fibrillary acid protein (GFAP; 1:250; Dako) antibodies. Transected bridges were fixed with modified Zamboni's solution overnight at 4°C then rinsed in PBS and suspended in PBS-20% sucrose solution overnight (4°C). Samples were then frozen in optimum cutting temperature (OCT; Tissue-Tek Sakura Finetek) and cryostat sections (12 μM) were placed on slides that were frozen at −80°C. For immunostaining, tissues were permeabilized with 0.3% Triton-X in 5% goat serum and 1% BSA for 1 h. Tissues were double labeled with NF-200 and GFAP, rinsed in PBS and incubated with secondary CY3 sheep anti-mouse (1:100, Sigma) and Alexa Fluor 488 goat anti-rabbit (1:500, Cedarlane) antibodies for 1 h. Tissues were then rinsed and mounted using Polyaquamount medium (Polysciences) and visualized using a Zeiss Axioscope with digital camera and Axiovision imaging software (Zeiss Axioskope, Axiovision, and Axiocam, Zeiss, North York, ON, Canada). Profiles of serial regions (every 270 mm) perpendicular to the direction of the bridge were examined and counted blindly.

Epon Embedding and Sectioning

Segments of nerve are fixed in 2.5% glutaraldehyde in 0.025 M cacodylate buffer, washed with cacodylate buffer (0.15 M), postfixed (2% osmium tetroxide in 0.12 M cacodylate buffer), then dehydrated through graded ethanol and propylene oxide. Next, the nerve segments undergo infiltration with a 50/50 EPON/propylene oxide mixture overnight and are thereafter embedded in EPON and baked for 3 days (45°C for first day and then 65°C for final 2 days). Central segments of the nerve bridge (i.e., 1.5 mm from the proximal stump) are then cut into ∼1 μM sections and stained with toluidine blue.

Tubulin Polymerization Assay

Tubulin polymerization assay was performed using a kit, and with slight modification of the manufacturer's (Cytokeleton Inc.) protocol. The recommendation for the *in vitro* tubulin polymerization assay kit is to use tubulin at 2 mg/ml in fluorescence buffer (80 mM PIPES pH 6.9, 2.0 mM $MgCl_2$, 0.5 mM EGTA, 10 μM fluorescent reporter) + 1 mM Guanosine-5′-triphosphate (GTP) in black 96-well plates. As R-roscovitine is a synthetic GTP analog, a comparable amount of R-roscovitine was used: 0.2 mM or 0.4 mM when used alone or 0.4 mM when used together with 0.5 mM GTP. For control, Dimethyl sulfoxide (DMSO) and ddH_2O were used instead of R-rsocovitine and GTP, respectively. The kinetics of tubulin polymerization was measured up to 60 min at 37°C using a spectrophotometer (SpectraMax M2, Molecular Devices; Softmax Pro software). Excitation and emission wavelengths were set at 355 nm and 460 nm, respectively.

Purification of Strep-WAVE1

Strep-WAVE1 DNA construct (pAAV-CBA-ST-WAVE1) was transfected into COS7 cells using Lipofectamine 2000 (Invitrogen Life Technologies). After 48 h, transfected cells were lysed and Strep-WAVE1 was purified using the Strep-Tactic Spin Column (BioTAGnology) as described by Kim et al. (2006). Purification of WAVE1 was assessed by SDS-PAGE and Coomassie brilliant blue staining.

Actin Polymerization Assay

Actin Polymerization assays were performed as described by the manufacturer (Cytokeleton Inc.). Pyrene-actin (40 μg) and non-muscle actin (20 μg) mixed in general actin buffer (0.2 mM ATP and 1 mM Dithiothreitol, DTT) were kept on ice for 1 h to allow depolymerization. For WAVE1 phosphorylation by Cdk5/p25, Strep-WAVE1 (36 nM), Actin-Related Proteins 2/3 (Arp2/3) protein complex (220 nM) were incubated with reconstituted Glutathione S-transferase (GST)-Cdk5/GST-p25 (16 μg) in 10 mM Tris-HCl buffer, pH 7.6, containing 50 μM ATP, 5 mM $MgCl_2$, 50 mM KCl and 5 mM EGTA, for 30 min in a 30^{o}C. To inhibit the activity of GST-Cdk5/p25, the strep-WAVE1 mixture was pre-incubated with 0.1 mM R-roscovitine before adding 50 μM ATP. An equal volume of DMSO was added to the control. For polymerization assays, pyrene-actin and non-muscle actin mix were aliquoted into black 96-well plates along with GST-Cdk5/GST-p25-phosphorylated WAVE1 (with or without 0.1 mM R-roscovitine) and Arp2/3 protein complex. Polymerization buffer (500 mM KCl, 20 mM $MgCl_2$ and 10 mM ATP) was added to initiate polymerization. The kinetics of actin polymerization was measured up to 30 min using the SpectraMax M2 spectrophotometer at excitation and emission wavelengths of 355 nm was 405 nm, respectively.

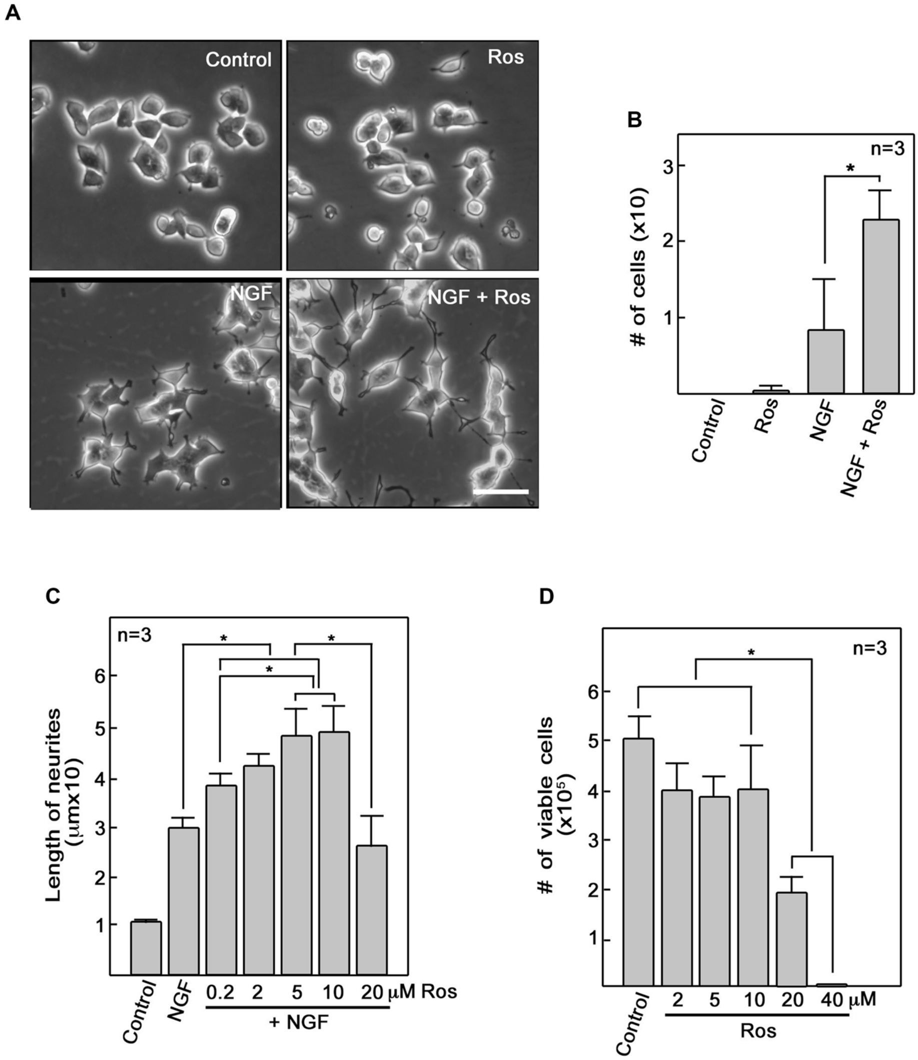

FIGURE 1 | Roscovitine enhances nerve growth factor (NGF)-mediated neurite outgrowth in PC12 cells. (A) PC12 cells were plated as described in "Materials and Methods" Section. After 18 h in low serum DM, cells were treated with roscovitine alone (10 μM, upper right panel), NGF alone (10 ng/ml NGF; lower left panel), or NGF and roscovitine simultaneously (lower right panel). The upper left panel shows cells that were not treated with either roscovitine or NGF. Photographs were taken 24 h after treatment. Scale bar = 50 μM. **(B)** Shows the number of cells with neurites longer than 20 μM. Measurements were taken from 50 cells in each treatment ($n = 3$). Statistical significance using student's *t*-test was set at $p < 0.05^*$. **(C)** Neurite lengths of differentiating PC12 cells were measured 24 h after treatment with NGF in the absence or presence of roscovitine at various concentrations. Untreated cells were used as control. Values are means ± SD of three ($n = 3$) independent experiments. Statistical significance using student's *t*-test was set at $p < 0.05^*$. **(D)** Viability of cells treated with various concentrations of roscovitine was assessed after 24 h by cell counting using a hemocytometer. Values are means ± SD of three ($n = 3$) independent experiments. Statistical significance using student's *t*-test was set at $p < 0.05^*$.

RESULTS

Roscovitine Enhances NGF-Mediated Neurite Outgrowth

To further investigate the role of roscovitine in neurite outgrowth, we initially used differentiating PC12 cells. We found that addition of roscovitine caused increased numbers of NGF-treated differentiating PC12 cells that exhibit longer neurites compared to those treated with NGF alone (**Figures 1A,B**). This is interesting but contradicts previous reports that roscovitine inhibits neurite outgrowth in PC12 cells (Harada et al., 2001; Lee and Kim, 2004; Carter et al., 2008). Since we used 10 μM roscovitine in our studies while others used 20–100 μM (Harada et al., 2001; Lee and Kim, 2004; Carter et al., 2008), we performed a roscovitine dose response analysis of NGF-treated differentiating PC12 cells. As shown in **Figure 1C**, it is clear that addition of roscovitine at 0.2–10 μM enhanced neurite lengths of NGF-treated cells ($p < 0.05$). Roscovitine at 0.2–10 μM caused a pattern of increasing neurite lengths, with 5 and 10 μM causing significantly ($p < 0.05$) greater length of neurites compared to that caused by 0.2 μM. However, a further increase in roscovitine concentration to 20 μM caused a drastic decrease ($p < 0.05$) in neurite length compared to treatment with 5 and 10 μM. Neurite length at 20 μM roscovitine is comparable to that of cells treated with NGF alone. While roscovitine has been shown to cause apoptosis (Gao et al., 2005; Zheng et al., 2007), we found that concentrations at which it can enhance neurite length (up to 10 μM) were insufficient to cause significant cell death (**Figure 1D**) but increasing the concentration to 20 and 40 μM caused loss of cell viability by ∼60% and almost 100%, respectively ($p < 0.05$). Thus, our findings demonstrate that at lower concentrations, i.e., at 0.2–10 μM, roscovitine enhances neurite length instead of neuronal apoptosis.

Roscovitine Enhances Axonal Regrowth

Repair of peripheral nerve injury normally requires axonal regrowth (Christie et al., 2014). Therefore, we examined the possibility that roscovitine can enhance axon regrowth in *ex vivo* adult primary neurons. For this experiment, adult male Sprague-Dawley rats were subjected to sciatic nerve transection at the mid-thigh region. After 3 days, L4 to L6 DRG were isolated from these rats, dissociated, and cultured to examine whether roscovitine will affect neurite outgrowth of these pre-injured primary sensory neurons. As with differentiating PC12 cells, we noted increased number and significantly ($p < 0.05$) longer neurites in cells treated with 0.2 μM roscovitine (**Figures 2A,B**). At this concentration, the average length of neurites was about twice those of neurons not treated with roscovitine. Interestingly, unlike in PC12 cells, increasing the concentration of roscovitine to 2 and 10 μM did not cause a pattern of increasing neurite length. DRG neuronal cell viability, upon addition of 2 and 10 μM roscovitine, trended toward a decline (data not shown). Although PC12 cells and primary neurons exhibit different sensitivities to roscovitine at 0.2–10 μM, it is clear that roscovitine can cause increased neurite length/axon regrowth in differentiating PC12 cells and preconditioned/pre-injured neurons.

Roscovitine Increases the Number of Myelinated Axons that Repopulate Regenerating Rat Sciatic Nerve

Given our *in vitro* and *ex vivo* findings, we wondered whether roscovitine would improve axon regrowth in an adult rat *in vivo* regenerative model following total peripheral nerve trunk transection. A 3–5 mm gap was created after sciatic nerve transection and subsequent nerve retraction of the proximal and distal stumps; a scenario that simulates human nerve injury (**Figure 3A**). Administration of roscovitine was performed using a silicone conduit as described previously (McDonald and Zochodne, 2003). Repeated injections of 100 μl of 10 μM roscovitine or Ringer's solution were performed on days 2, 4 and 6 ($n = 9$). Four of the nine rats were sacrificed for detection of early regenerating fibers on day 7 post-injury. The rest ($n = 5$) of the animals were analyzed for regenerating myelinated axons on day 21 post-injury. Since myelinated axons have not yet appeared on day 7 post-injury, we performed immunohistochemistry of longitudinal sections at this time point to obtain an index of early outgrowth when the earliest fibers begin to enter the regenerative stump. However, we found that roscovitine had no significant effect on early axon outgrowth in transected sciatic nerve 7 days after treatment (**Figures 3B,C**). On day 21 post-injury, immunohistochemistry imaging fields are crowded by a host of new fibers making discrete counting problematic. Thus, for day 21 post-injury samples, we analyzed EPON embedded semi-thin sections to appraise early and successful reconstitution of myelinated axons. Indeed, at 21 days following

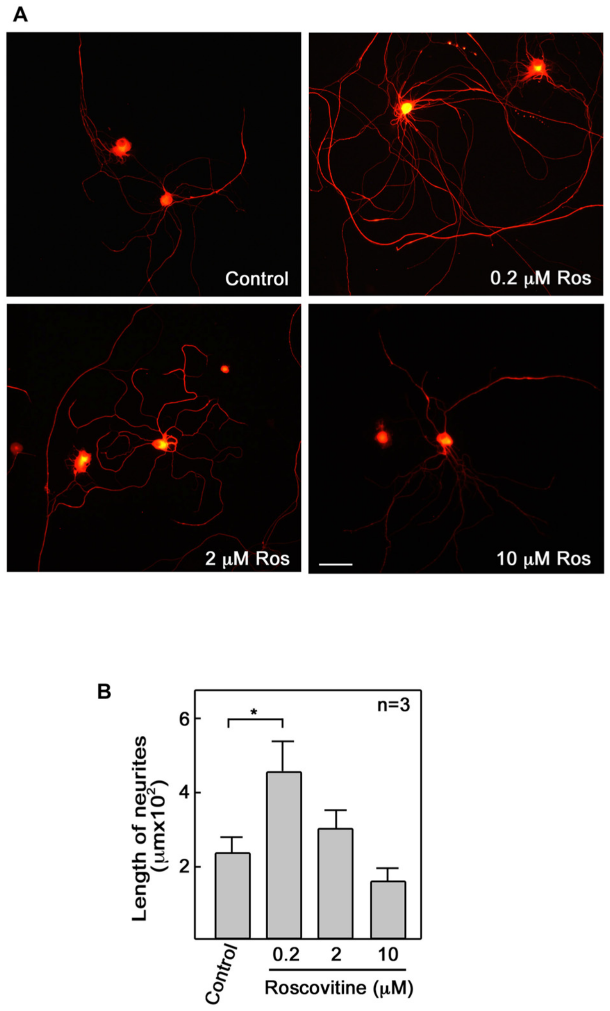

FIGURE 2 | Roscovitine enhances axonal regrowth of pre-injured rat primary dorsal root ganglia (DRG) sensory neurons. (A) Neurons isolated from rat L4–L6 DRGs 3 days after sciatic nerve transection were cultured on laminin and poly-L-lysine coated cover slips in primary neuron media, containing N-2 supplement, BSA and 0.2 ng/ml NGF, in the absence or presence of roscovitine (0.2, 2.0 or 10 μM). After 48 h, cells were fixed in 4% paraformaldehyde and immunostained with β-III tubulin antibody. Scale bar = 50 μM. **(B)** Axon lengths of DRG neurons exposed to different concentrations of roscovitine. Values are means ± SD of three independent experiments. Statistical significance using student's *t*-test was set at $p < 0.05$*.

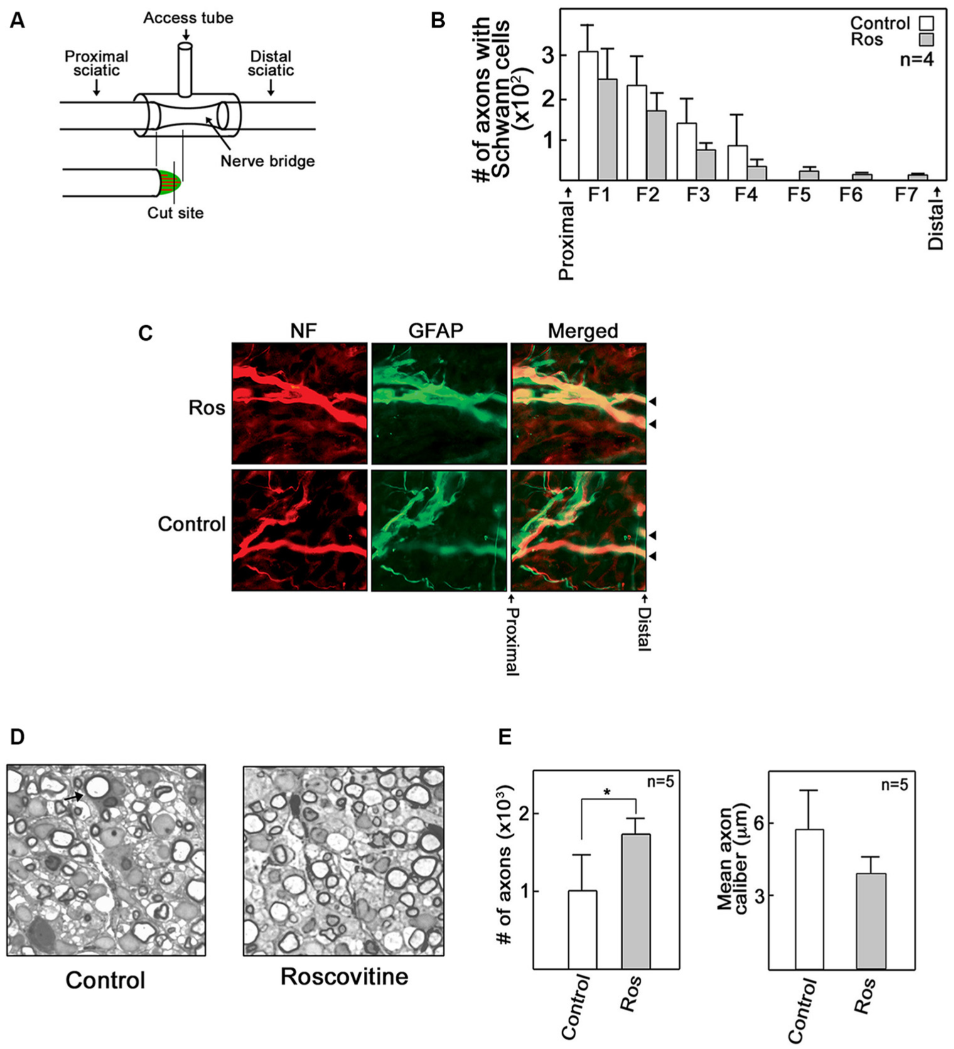

FIGURE 3 | Roscovitine increases the number of myelinated axons in regenerating rat sciatic nerve. Adult male SD rats were subjected to sciatic nerve transection as described in "Materials and Methods" Section. **(A)** A schematic diagram showing the sciatic nerve lesion, the regeneration chamber and cutting site of EPON embedded section that lies perpendicular to the direction of the bridge. **(B)** Analysis of the number of axons with Schwann cells (SC) in control and roscovitine-treated rats 7 days after sciatic nerve transection. Axonal outgrowth were measured by serial counts (fields 1–7) proximal to the distal stump of a cut sciatic nerve by co-immunohistochemical staining for neurofilament (for neurons) and glial fibrillary acid protein (GFAP; for SC). Values are means ± SD; $n = 4$. Changes in values did not reach to statistical significance using Student's *t*-test at $p \leq 0.05$. **(C)** Representative image of axons with SC (examined in **B**) in control and roscovitine-treated rats at 7 days. Arrowheads are directed at axons. **(D)** Twenty-one days post-transection, axonal regeneration was evaluated by morphometric analysis of toluidine blue-stained EPON embedded cross sections of sciatic nerve bridges treated with Ringer's solution (left panel) or 10 μM roscovitine (right panel). Arrow is directed at a myelinated axon. **(E)** Analysis of the number of myelinated axons (left panel) and axon caliber (right panel) in control (Ringer's solution-treated) and roscovitine-treated rats 21 days after sciatic nerve transection. Values are means ± SD; $n = 5$. Statistical significance using student's *t*-test was set at $p < 0.05$*.

sciatic nerve transection, morphometric analysis of sections from the central portions of the nerve bridges revealed significantly ($p < 0.05$) increased numbers of repopulating myelinated axons in the roscovitine-treated group compared to the control group (**Figures 3D,E** left panel). We also assessed axon caliber but found no significant difference between the roscovitine-treated nerves and the control group. Overall, these observations extend our *in vitro* and *ex vivo* findings, indicating that roscovitine can be translated into a significant *in vivo* paradigm, with an impact on myelinated fiber repopulation of regenerating nerves.

Roscovitine Interacts with Tubulin and Actin in Differentiating PC12 Cells

To understand the underlying molecular mechanism(s) behind roscovitine-induced increase in neurite outgrowth, axonal regrowth and peripheral nerve regeneration, we sought to identify the neuronal targets of roscovitine. To do so, lysates of differentiating PC12 cells treated with NGF and roscovitine were used for R-roscovitine-agarose pull-down assays. As shown in **Figure 4A**, after pre-clearing the cell lysates with agarose beads and mass spectrometry of the pulled down sample,

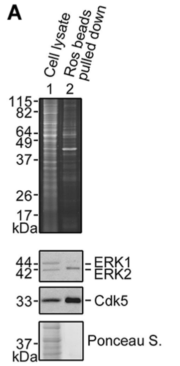

B

Roscovitine interacting proteins	MW (kDa)
γ-actin	75
CaM kinase 2β	72
CaM kinase 2δ	60
CaM kinase 2γ	58
Tubulin	56
CK1δ	49
ERK1	44
α1-actin precursor	42
ERK2	42
PDXK	34
Cdk5	33

FIGURE 4 | Identification of roscovitine interacting proteins in differentiating PC12 cells. (A) Neuronal differentiation of PC12 cells was induced using NGF. After pre-clearing with agarose beads, differentiating PC12 cell lysates were subjected to pull-down assay using roscovitine-agarose beads. The pulled-down proteins were analyzed by sodium dodecyl sulfate-polyacrylamide gel electrophoresis (SDS-PAGE) and stained with Sypro-Ruby Red (upper panel). A parallel SDSPAGE loaded with the same samples and analyzed by western blotting showed immunoreactivity to extracellular signal-regulated kinases 1/2 (ERK1/2) and Cdk5. **(B)** Pulled-down proteins were also analyzed by mass spectrometry. A list of roscovitine interacting proteins in differentiating PC12 cells treated with NGF and roscovitine is shown.

we determined that the R-roscovitine-agarose beads effectively bound the known roscovitine targets, Cdk5 and ERK1/2 (Bach et al., 2005). We also detected binding of nine other known roscovitine targets, including calmodulin (CaM)-dependent kinases, casein kinase 1 (CK1) and pyridoxal kinase (PDXK; Bach et al., 2005; **Figure 4B**). However, we also detected two additional roscovitine-interacting proteins, tubulin and actin. Since peripheral nerve regeneration is dependent upon rapid polymerization of microtubules and dynamics of actin filaments in the growth cone (Kalil and Dent, 2005), we proceeded to characterize the interaction of roscovitine with tubulin and actin.

Roscovitine Enhances Tubulin Polymerization

To characterize the interaction between tubulin and roscovitine, we initially performed R-roscovitine-agarose bead pull down assay of purified tubulin and mouse brain homogenates pre-incubated/-cleared with agarose beads. By western blotting (**Figure 5A**), we found that mouse brain homogenate tubulin (lane 1) and purified tubulin (lane 4) bound to the roscovitine beads while preincubation of purified tubulin with roscovitine prevents their interaction (lane 3), indicating that tubulin directly binds to roscovitine. We then examined whether roscovitine affects tubulin polymerization. To assess this possibility, we examined polymerization of tubulin in the presence and absence of roscovitine. As shown in **Figure 5B**, roscovitine by itself caused a dose-dependent increase in tubulin polymerization (○). Following normalization (subtraction of values at time 0), we detected more than 2-fold increase in tubulin polymerization upon addition of roscovitine alone. When added together with GTP, roscovitine caused earlier nucleation and enhanced rate (Δ) of GTP-dependent (●) tubulin polymerization. Indeed, the time needed to complete GTP-dependent polymerization was cut in half upon addition of roscovitine (15 min vs. 30 min).

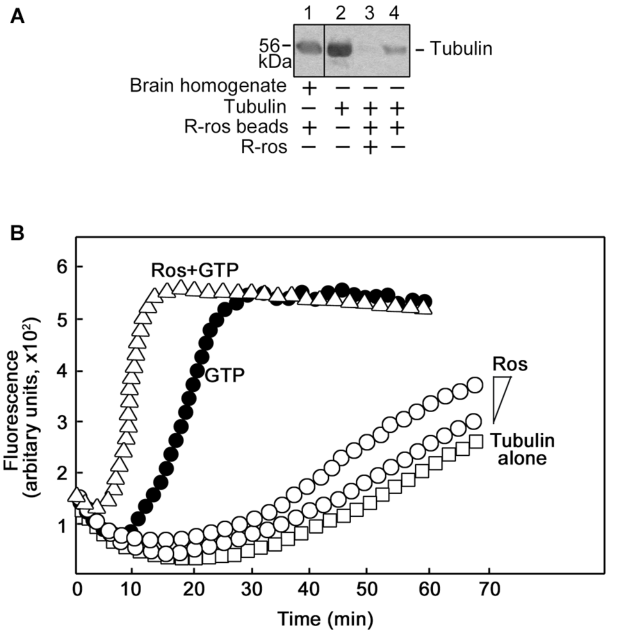

FIGURE 5 | Roscovitine interacts with tubulin directly, and enhances tubulin polymerization. (A) Mouse brain homogenate (lane 1) and purified tubulin (lanes 3 and 4) were pre-cleared/-incubated with agarose beads and subsequently incubated with roscovitine-agarose beads. Tubulin binding to roscovitine beads was analyzed by western blotting using a tubulin antibody. Purified tubulin served as positive control (lane 2). For negative control (lane 3), tubulin was pre-incubated with 0.2 mM roscovitine (ros) prior to incubation with roscovitine-agarose beads. Note that no agarose-tubulin binding was observed after a second pre-clearing of brain homogenates.
(B) Spectrophotometric tubulin polymerization assay was performed using a kit, and with slight modification of the manufacturer's (Cytokeleton Inc.) protocol. To obtain detectable levels of polymerization, the recommendation for the *in vitro* tubulin polymerization assay kit is to use tubulin at 2 mg/ml in fluorescence buffer (80 mM PIPES pH 6.9, 2.0 mM $MgCl_2$, 0.5 mM EGTA, 10 μM fluorescent reporter) + 1 mM Guanosine-5′-triphosphate (GTP). As R-roscovitine is a synthetic GTP analog, a comparable amount of R-roscovitine was used: 0.2 mM or 0.4 mM when used alone or 0.4 mM when used together with 0.5 mM GTP. Analysis of: polymerization of 4′,6-diamidino-2-phenylindole (DAPI)-tubulin alone (□) or (1) incubated with increasing concentrations of roscovitine (○; 0.2 mM or 0.4 mM); or (2) GTP (●, positive control; 0.5 mM), or GTP and roscovitine (Δ; 0.5 mM and 0.4 mM, respectively). Data from the two independent analyses with similar range of fluorescence values are shown together.

Roscovitine Enhances Arp2/3/Wave1-Mediated Actin Polymerization

Next, we examined actin interaction with roscovitine with a further pull-down assay and western blot analysis. As shown in **Figure 6A**, although actin in pre-cleared mouse brain homogenates (lane 1) bound to the roscovitine beads, purified actin (lane 4) did not, indicating that actin

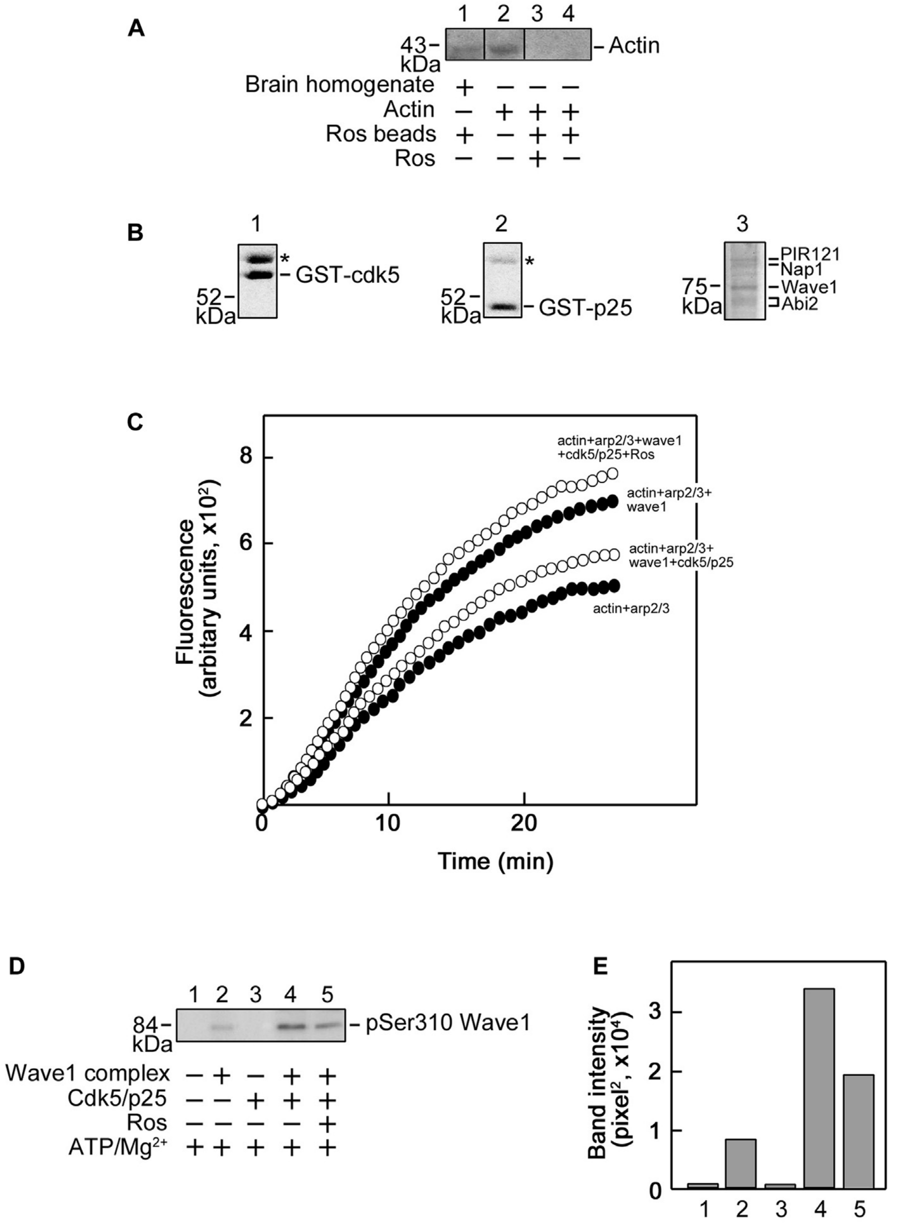

FIGURE 6 | Roscovitine interacts with actin indirectly, and enhances Actin-Related Proteins 2/3 (Arp2/3)/Wave1-mediated actin polymerization. **(A)** Mouse brain homogenate (lane 1) and purified actin (lanes 3 and 4) were pre-cleared/-incubated with agarose beads and subsequently incubated with roscovitine-agarose beads. Actin binding to roscovitine beads was analyzed by western blotting using an actin antibody. Purified actin served as positive control (lane 2). For negative control (lane 3), actin was pre-incubated with 0.2 mM roscovitine (ros) prior to incubation with roscovitine-agarose beads. The lack of actin immunoreactivity in lane 4 indicates that actin in the brain homogenate (lane 1) interacts with roscovitine indirectly. Note that no agarose-actin binding was observed after a second pre-clearing of brain homogenates. **(B)** SDS-PAGE and Coomassie brilliant blue staining of purified Glutathione S-transferase-cyclin-dependent kinases 5 (GST-Cdk5; left panel), GST-p25 (middle panel; Cdk5 activator) and Strep-Wave1 complex (right panel). Asterisks correspond to the heat shock chaperon protein that copurifies with GST-Cdk5 and GST-p25. **(C)** Polymerization curve of pyrene-actin incubated with Arp2/3 ± Wave1 complex ± Cdk5/p25 ± preincubation with roscovitine. Values shown are obtained following a preincubation time of 11 min and fluorescence was set to an arbitrary value of zero. For all treatments, fluorescence start to plateau at ~27 min. **(D)** Western blot for Wave1 phospho-Ser310 showing that Cdk5/p25 phosphorylates Wave1 at Ser310 and this phosphorylation is inhibited by roscovitine. **(E)** Densitometric analysis of the representative blot in **(D)** using the NIH Image-J 1.61 software.

(in brain homogenates) binds to roscovitine indirectly. Indeed, actin is known to bind to Cdk5 (Xu et al., 2011), a recognized direct target of roscovitine. Since Cdk5 has been shown to inhibit Arp2/3-dependent actin polymerization through phosphorylation of Wave1 (Kim et al., 2006), we examined whether roscovitine, a known Cdk5 inhibitor, could rescue actin polymerization. For this experiment, we used recombinant Cdk5 (**Figure 6B**, left panel), p25 (Cdk5 activator; **Figure 6B**, middle panel) and Wave1 (**Figure 6B**, right panel) that, as described previously (Kim et al., 2006), forms a complex and copurifies with endogenous PIR121, Nap1 and Abi2. We found that roscovitine, indeed, completely reversed the Cdk5/p25 inhibition of Arp2/3-Wave1-mediated actin polymerization (**Figure 6C**). Since under our experimental conditions, Cdk5/p25 clearly phosphorylates Wave1 (**Figures 6D,E**, lane 4 and bar 4, respectively), and roscovitine noticeably inhibits such phosphorylation (**Figures 6D,E**, lane 5 and bar 5, respectively), our results indicate that roscovitine-induced actin polymerization occurred through roscovitine interaction with Cdk5, which prevented Cdk5-mediated phosphorylation of Wave1 and subsequently, prevented Cdk5 inhibition of Arp2/3-Wave1-mediated actin polymerization.

Roscovitine Causes Enhanced Activation of ERK1/2 and p38 MAPK in NGF-Treated Differentiating PC12 Cells

ERK1/2, p38 MAPK and AKT have been implicated in neurite outgrowth and axonal regeneration (Agthong et al., 2009; Okada et al., 2011; Wang et al., 2011; Kato et al., 2013; Sarina et al., 2013; Mufti et al., 2014). Therefore, we wondered whether increased axon regrowth resulting from roscovitine treatment is due to synergistic activation of ERK1/2, p38 MAPK and/or AKT signaling pathways in addition to enhancement of tubulin and actin polymerization. For this experiment, we again used PC12 cells as a substantial number of injured rats would be required to obtain a sufficient number of DRG neurons for several western blots. Lysates of differentiating PC12 cells grown in the presence of NGF with or without roscovitine were examined for the phosphorylation levels of ERK1/2, p38 MAPK and AKT. As shown in **Figures 7A,B**, simultaneous treatment with NGF and roscovitine (middle panels) caused considerable activation of ERK1/2 and p38 MAPK at an earlier time point (1 min) compared to cells treated with NGF alone (3 min; left panels). In addition, we observed enhanced and prolonged activation of ERK1/2 in cells treated with NGF + roscovitine (90 min) compared to cells treated with roscovitine alone (30 min). While we also noted AKT activation following treatment with NGF, addition of roscovitine did not cause a change in activation of this kinase.

DISCUSSION

It is recognized that triggering the cell cycle plays a role in post-mitotic cell death. Interestingly, activation of the cell cycle has also been implicated in secondary damage following injury to the spinal cord (Byrnes et al., 2007). Consequently, blocking major cell cycle signaling molecules inhibits not only cell proliferation but also injury-related cell death. For example, in rodent spinal cord injury models, it was shown that inhibiting the cell cycle results in a reduction of both neuronal death and inflammation, and subsequently, improved sensory motor recovery (Wu et al., 2011). The synthetic purine analog, roscovitine, has been shown to regulate both the cell cycle and inflammatory process but a potential role in sensory motor neuron recovery has not yet been investigated.

Our current findings suggest that roscovitine, which inhibits cell cycle Cdks, has the ability to promote nerve regeneration. In this study, myelinated axons were chosen as an index of maturating fibers and to establish a correlation with functional outcome. While early measurements in a nerve conduit and *in vitro* are unmyelinated as we assessed by day 7, some are destined to grow in caliber and become myelinated. Thus, this population of fibers (early unmyelinated) does not necessarily predict later myelinated axon repopulation of a mature nerve. Unmyelinated counts can also be complex later since they are a mix of fibers destined to remain unmyelinated and axons that will be myelinated later. By focusing on myelinated axons, we believe we have a better index of the population that translates into functional recovery. As shown in our adult rat *in vivo* regenerative model system, treatment with low-dose roscovitine following total peripheral nerve trunk transection caused an increase in number of repopulating myelinated axons. Although we could not disregard the fact that roscovitine binds to several ATP-dependent protein targets, and principally, GTP- or NAD-dependent protein kinases (Bach et al., 2005), its ability to interact with tubulin and actin, may be a major mechanism in its ability to promote axonal regeneration. It is possible that inosine effect on collateral axon growth (Dachir et al., 2014) and adenosine and/or guanosine effects on axonal degeneration and axon preservation after injury (Press and Milbrandt, 2009) occur through a similar mechanism.

Indeed, we found that roscovitine binds to tubulin directly and such interaction causes tubulin polymerization that is independent of GTP. In the presence of GTP, roscovitine has the ability to induce earlier nucleation and enhance the rate of tubulin polymerization. This may be explained by roscovitine binding to the tubulin exchangeable nucleotide-binding site (E-site) with high affinity (De Azevedo et al., 1997; Gray et al., 1999). Consistent with this suggestion, it has been shown that an analog of GTP, guanylyl-(alpha, beta)-methylene-diphosphonate (GMPCPP), which is insensitive to hydrolyzation, favors polymerization by strongly promoting spontaneous nucleation of microtubules (Hyman et al., 1992) which is critical for the early stages of microtubule assembly (Wang et al., 2005).

On the other hand, roscovitine does not bind actin directly. Therefore, its ability to enhance actin polymerization is likely due to its interaction with other intermediate proteins. Indeed, Cdk5, a direct target of roscovitine (Bach et al., 2005), has the ability to bind actin (Xu et al., 2011). Previously, Kim et al. (2006) reported that WAVE1 phosphorylation by Cdk5 directly interferes with Arp2/3-dependent actin polymerization, which is known to be critical for growth cone formation. Since roscovitine is a potent inhibitor of Cdk5, roscovitine binding and inhibition of Cdk5 activity could account for the enhanced polymerization effect on actin by roscovitine.

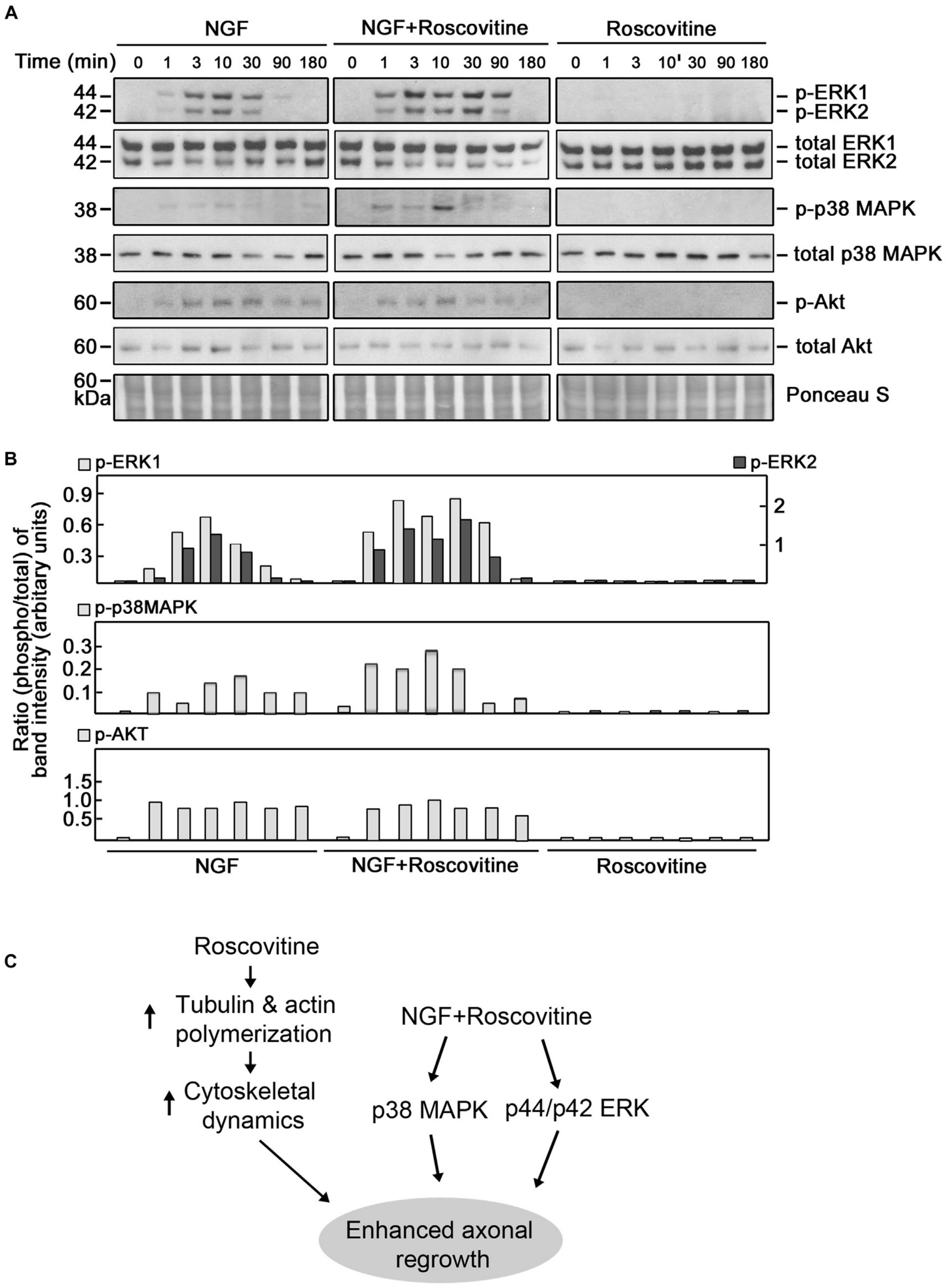

FIGURE 7 | Roscovitine enhances the activation of ERK1/2 and p38 mitogen-activated protein kinase (MAPK) in differentiating NGF-treated PC12 cells. (A) Representative set of blots (from three sets/independent experiments) of lysates of PC12 cells plated and treated as described in "Materials and Methods" Section. After serum starvation for 18 h, cells were treated with NGF alone (10 ng/ml; left panel), roscovitine alone (10 μM; right panel) or NGF+roscovitine simultaneously (middle panel), and lysed at 0, 1, 3, 10, 30, 90 and 180 min post-treatment. Equal amounts of protein samples were then resolved in 12.5% SDS-PAGE and subjected to

(*Continued*)

FIGURE 7 | Continued
western blot analysis using phospho-antibodies against ERK1/2, p38 MAPK and AKT. Additional test for loading equivalent amounts of protein was performed by Ponceau S staining. **(B)** The ratios of the band intensities [from the representative blots in **(A)**] of phospho-ERK1/2, phospho-p38 MAPK and phospho-Akt vs. total ERK, total p38 MAPK and total Akt, respectively, were determined following densitometric scanning of bands using the NIH Image-J 1.61 software. Note the different Y-axis scales for p-ERK1/total ERK (left) and p-ERK2/total ERK (right). Analysis of the ratios of the band intensities of phospho-AKT vs. total AKT did not show any considerable changes at different time points in the three treatment groups. **(C)** Proposed molecular mechanisms by which roscovitine enhances NGF-induced axonal regrowth. Roscovitine promotes axonal regrowth by inducing tubulin and actin polymerization (left panel). In the presence of NGF, roscovitine enhances axonal regrowth through activation of the ERK1/2 and p38 MAPK pathways.

Incidentally, this further supports the notion that Cdk5 serves as an inhibitor of actin polymerization (Kim et al., 2006). Thus, our findings suggest that roscovitine promotes not only tubulin-dependent neuronal functions but also actin-dependent functions. These roscovitine roles may, indeed, occur during roscovitine-induced neurite outgrowth, *ex vivo* axon regrowth and regeneration of injured sciatic nerve in rats.

It is interesting that, although PC12 cells exhibit a dose-dependent increase in neurite outgrowth from 0.2 to 5 μM roscovitine, primary DRG sensory neurons isolated following sciatic nerve transection showed a more enhanced axon regrowth at a lower roscovitine concentration. In other words, axonal regeneration in pre-injured primary DRG sensory neurons is greater at 0.2 μM than at 2 μM roscovitine, and 2 μM elicited greater axon regrowth than 10 μM. This appears to suggest that primary DRG sensory neurons have greater uptake ability for roscovitine compared to differentiating PC12 cells, or that the primary DRG sensory neurons have better representation of neural properties. It is also possible that increased sensitivity of DRG neurons to roscovitine is due to the difference in the required culture conditions to induce neurite outgrowth. While PC12 cells were cultured in the presence of 10 ng/ml NGF to induce differentiation, DRG primary neurons are maintained in media containing 0.2 ng/ml NGF. Thus, it appears that with the higher amount of NGF in PC12 cell cultures, which can already cause neurite outgrowth, a higher concentration of roscovitine is needed to see an enhanced effect on neurite outgrowth. Conversely, a relatively lower concentration of roscovitine is needed in DRG neuronal cultures, which are grown in low NGF media, to see an axon regrowth promoting effect. Nonetheless, our findings indicate that roscovitine has a parallel impact on neurite/axon regrowth in PC12 cells and in preconditioned/pre-injured neurons.

ERK1/2, p38 MAPK and AKT have all been implicated in neurite outgrowth and axonal regeneration (Agthong et al., 2009; Okada et al., 2011; Wang et al., 2011; Kato et al., 2013; Sarina et al., 2013). In this study, we also found that these kinases are activated in differentiating PC12 cells. However, we further found that roscovitine causes earlier activation of ERK1/2 and p38 MAPK as well as prolonged activation of ERK1/2. This is not surprising as roscovitine's IC50 values for ERK1, ERK2 and p38 MAPK are quite high as indicated above. Thus, while roscovitine may inhibit MAPKs at high concentrations (i.e., greater than their respective IC50 values) the low-dose roscovitine that we used (10 μM) has no inhibitory effect but instead, enhanced the activation of ERK1/2 and p38 MAPK. These findings suggest that both ERK1/2 and p38 MAPK are involved in roscovitine-induced neurite outgrowth and axonal regeneration. Indeed, there has been an earlier report that activation of ERK1/2 and p38 MAPK is linked to neurite outgrowth in PC12 cells (Sarina et al., 2013). Thus, consistent with our findings, we propose a model (**Figure 7C**) whereby roscovitine promotes axonal regrowth through induction of tubulin and actin polymerization. In the presence of neurotrophic factors, such as NGF, axonal regrowth is enhanced by roscovitine via increased activation of the p38 MAPK and ERK1/2 signaling pathways.

Interestingly, the ERK1/2 pathway has been associated with the promotion of dedifferentiation of myelinating SC (Jessen and Mirsky, 2008; Napoli et al., 2012), a process that supports axon regeneration. In addition, p38 MAPK activation induces denervated SC phenotype and negatively regulates SC differentiation and myelination (Yang et al., 2012). However, once axons have started to regenerate, SC redifferentiate and remyelinate. Thus, our finding that enhanced activation of ERK1/2 and p38 MAPK play important roles in neurite outgrowth in neuronal cultures complements previous suggestions that these kinases are key regulators of axonal regeneration.

Certainly, roscovitine-induced actin and tubulin polymerization may explain our *in vitro*, *ex vivo and in vivo* data, demonstrating enhancement of neurite outgrowth in neuronal-like PC12 cells, axonal regrowth in primary DRG sensory neurons and induction of regeneration of transected rat sciatic nerve, respectively. While it should be noted that depolymerization is at least as important as polymerization in mobilizing microtubular plasticity in the growth cone, our premise that the ability of roscovitine to enhance tubulin polymerization is linked to its ability to induce regeneration of injured rat sciatic nerve is consistent with recent reports. Indeed, the anti-cancer agents, paclitaxel (Hellal et al., 2011) and epothilone B (Ruschel et al., 2015), both of which stabilize microtubules, promote axon regrowth. Furthermore, the ability of epothilone B to induce axon regrowth was shown to cause restoration of locomotive function in a rat spinal cord injury model (Ruschel et al., 2015). Interestingly, roscovitine is currently under phase II clinical trial in combination with standard chemotherapy regimens for advanced breast cancer and stage IIIB/IV non-small cell lung cancer (Aldoss et al., 2009; Nair et al., 2011). It appears that the microtubule-mediated mechanisms of roscovitine- and epothilone B-induced nerve repair are similar.

Taken together, our findings point to a therapeutic potential of roscovitine for peripheral nerve injury. Therefore, the next step is to assess this potential by initial functional recovery tests in animals and, if promising, subsequently in human clinical testing. If, indeed, promising, much remains to be explored on the potential use of roscovitine as therapy for peripheral nerve injury, aside from appropriate route of administration, toxicity profile and maximum tolerated dose. Given its role in axon protection and regrowth, and potential for cancer therapy, roscovitine may simultaneously offer some protection against chemotherapy-induced neuropathy, a possibility that is worth exploring.

AUTHOR CONTRIBUTIONS

VL performed most of the experiments and wrote a draft of the manuscript. SD performed the experiments in **Figure 2**. JLR, DZ and K-YL conceived the idea for the project and contributed to writing the final manuscript. M-YJ contributed to the design of an experiment and discussion about the project.

FUNDING

This work was supported in part by grants from the Canadian Institutes of Health Research (MOP-123400), Natural Sciences and Engineering Research Council of Canada (NSERC) (RGPIN/312985-2011) and the Korean Ministry of Education, Science and Technology to K-YL; NSERC (RGPIN/356448-2008) to JLR; the WCU program (R31-20004) through the NRFK funded by the Korean Ministry of Education, Science and Technology to M-YJ.

ACKNOWLEDGMENTS

We thank Drs. Paul Greengard at the Rockefeller University and Laurent Meijer at the Centre National de la Recherche Scientifique, France, for providing us Strep-WAVE1 construct and roscovitine agarose beads, respectively.

REFERENCES

Agthong, S., Koonam, J., Kaewsema, A., and Chentanez, V. (2009). Inhibition of MAPK ERK impairs axonal regeneration without an effect on neuronal loss after nerve injury. *Neurol. Res.* 31, 1068–1074. doi: 10.1179/174313209X380883

Aldoss, I. T., Tashi, T., and Ganti, A. K. (2009). Seliciclib in malignancies. *Expert Opin. Investig. Drugs* 18, 1957–1965. doi: 10.1517/13543780903418445

Bach, S., Knockaert, M., Reinhardt, J., Lozach, O., Schmitt, S., Baratte, B., et al. (2005). Roscovitine targets, protein kinases and pyridoxal kinase. *J. Biol. Chem.* 280, 31208–31219. doi: 10.1074/jbc.M500806200

Byrnes, K. R., Stoica, B. A., Fricke, S., Di Giovanni, S., and Faden, A. I. (2007). Cell cycle activation contributes to post-mitotic cell death and secondary damage after spinal cord injury. *Brain* 130, 2977–2992. doi: 10.1093/brain/awm179

Carter, J. M., Demizieux, L., Campenot, R. B., Vance, D. E., and Vance, J. E. (2008). Phosphatidylcholine biosynthesis via CTP: phosphocholine cytidylyltransferase 2 facilitates neurite outgrowth and branching. *J. Biol. Chem.* 283, 202–212. doi: 10.1074/jbc.M706531200

Chierzi, S., Ratto, G. M., Verma, P., and Fawcett, J. W. (2005). The ability of axons to regenerate their growth cones depends on axonal type and age and is regulated by calcium, cAMP and ERK. *Eur. J. Neurosci.* 21, 2051–2062. doi: 10.1111/j.1460-9568.2005.04066.x

Christie, K. J., Krishnan, A., Martinez, J. A., Purdy, K., Singh, B., Eaton, S., et al. (2014). Enhancing adult nerve regeneration through the knockdown of retinoblastoma protein. *Nat. Commun.* 5:3670. doi: 10.1038/ncomms4670

Christie, K. J., Webber, C. A., Martinez, J. A., Singh, B., and Zochodne, D. W. (2010). PTEN inhibition to facilitate intrinsic regenerative outgrowth of adult peripheral axons. *J. Neurosci.* 30, 9306–9315. doi: 10.1523/JNEUROSCI.6271-09.2010

Dachir, S., Shabashov, D., Trembovler, V., Alexandrovich, A. G., Benowitz, L. I., and Shohami, E. (2014). Inosine improves functional recovery after experimental traumatic brain injury. *Brain Res.* 1555, 78–88. doi: 10.1016/j.brainres.2014.01.044

De Azevedo, W. F., Leclerc, S., Meijer, L., Havlicek, L., Strnad, M., and Kim, S. H. (1997). Inhibition of cyclin-dependent kinases by purine analogues: crystal structure of human cdk2 complexed with roscovitine. *Eur. J. Biochem.* 243, 518–526. doi: 10.1111/j.1432-1033.1997.0518a.x

De, S., Trigueros, M. A., Kalyvas, A., and David, S. (2003). Phospholipase A2 plays an important role in myelin breakdown and phagocytosis during wallerian degeneration. *Mol. Cell. Neurosci.* 24, 753–765. doi: 10.1016/s1044-7431(03)00241-0

Eng, H., Lund, K., and Campenot, R. B. (1999). Synthesis of β-tubulin, actin and other proteins in axons of sympathetic neurons in compartmented cultures. *J. Neurosci.* 19, 1–9.

Gao, J. X., Zhou, Y. Q., Zhang, R. H., Ma, X. L., and Liu, K. J. (2005). Caspase-3 plays a required role in PC12 cell apoptotic death induced by roscovitine. *Sheng Li Xue Bao* 57, 755–760.

Gray, N., Detivaud, L., Doerig, C., and Meijer, L. (1999). ATP-site directed inhibitors of cyclin-dependent kinases. *Curr. Med. Chem.* 6, 859–875.

Hamilton, G., Klameth, L., Rath, B., and Thalhammer, T. (2014). Synergism of cyclin-dependent kinase inhibitors with camptothecin derivatives in small cell lung cancer cell lines. *Molecules* 19, 2077–2088. doi: 10.3390/molecules19022077

Harada, T., Morooka, T., Ogawa, S., and Nishida, E. (2001). ERK induces p35, a neuron-specific activator of Cdk5, through induction of Egr1. *Nat. Cell Biol.* 3, 453–459. doi: 10.1038/35074516

Hellal, F., Hurtado, A., Ruschel, J., Flynn, K. C., Laskowski, C. J., Umlauf, M., et al. (2011). Microtubule stabilization reduces scarring and causes axon regeneration after spinal cord injury. *Science* 331, 928–931. doi: 10.1126/science.1201148

Hui, A. B., Yue, S., Shi, W., Alajez, N. M., Ito, E., Green, S. R., et al. (2009). Therapeutic efficacy of seliciclib in combination with ionizing radiation for human nasopharyngeal carcinoma. *Clin. Cancer Res.* 15, 3716–3724. doi: 10.1158/1078-0432.CCR-08-2790

Hyman, A. A., Salser, S., Drechsel, D. N., Unwin, N., and Mitchison, T. J. (1992). Role of GTP hydrolysis in microtubule dynamics: information from a slowly hydrolyzable analogue, GMPCPP. *Mol. Biol. Cell* 3, 1155–1167. doi: 10.1091/mbc.3.10.1155

Jessen, K. R., and Mirsky, R. (2008). Negative regulation of myelination: relevance for development, injury and demyelinating disease. *Glia* 56, 1552–1565. doi: 10.1002/glia.20761

Kalil, K., and Dent, E. W. (2005). Touch and go: guidance cues signal to the growth cone cytoskeleton. *Curr. Opin. Neurobiol.* 15, 521–526. doi: 10.1016/j.conb.2005.08.005

Kato, N., Matsumoto, M., Kogawa, M., Atkins, G. J., Findlay, D. M., Fujikawa, T., et al. (2013). Critical role of p38 MAPK for regeneration of the sciatic nerve following crush injury *in vivo*. *J. Neuroinflammation* 10:1. doi: 10.1186/1742-2094-10-1

Kim, Y., Sung, J. Y., Ceglia, I., Lee, K. W., Ahn, J. H., Halford, J. M., et al. (2006). Phosphorylation of WAVE1 regulates actin polymerization and dendritic spine morphology. *Nature* 442, 814–817. doi: 10.1038/nature04976

Latreille, M., Abu-Thuraia, A., Oliva, R., Zuo, D., and Larose, L. (2012). Casein kinase igamma2 impairs fibroblasts actin stress fibers formation and delays cell cycle progression in g1. *Int. J. Cell Biol.* 2012:684684. doi: 10.1155/2012/684684

Lee, J. H., and Kim, K. T. (2004). Induction of cyclin-dependent kinase 5 and its activator p35 through the extracellular-signal-regulated kinase and protein kinase A pathways during retinoic-acid mediated neuronal differentiation in human neuroblastoma SK-N-BE(2)C cells. *J. Neurochem.* 91, 634–647. doi: 10.1111/j.1471-4159.2004.02770.x

Liu, N. A., Araki, T., Cuevas-Ramos, D., Hong, J., Ben-Shlomo, A., Tone, Y., et al. (2015). Cyclin E-mediated human proopiomelanocortin regulation as a therapeutic target for cushing disease. *J. Clin. Endocrinol. Metab.* 100, 2557–2564. doi: 10.1210/jc.2015-1606

McDonald, D. S., and Zochodne, D. W. (2003). An injectable nerve regeneration chamber for studies of unstable soluble growth factors. *J. Neurosci. Methods* 122, 171–178. doi: 10.1016/s0165-0270(02)00319-9

Meijer, L., Borgne, A., Mulner, O., Chong, J. P., Blow, J. J., Inagaki, N., et al. (1997). Biochemical and cellular effects of roscovitine, a potent and selective inhibitor of the cyclin-dependent kinases cdc2, cdk2 and cdk5. *Eur. J. Biochem.* 243, 527–536. doi: 10.1111/j.1432-1033.1997.t01-2-00527.x

Moutinho-Pereira, S., Matos, I., and Maiato, H. (2010). *Drosophila* S2 cells as a model system to investigate mitotic spindle dynamics, architecture and function. *Methods Cell Biol.* 97, 243–257. doi: 10.1016/S0091-679X(10)97014-3

Mufti, R. E., Sarker, K., Jin, Y., Fu, S., Rosales, J. L., and Lee, K. Y. (2014). Thrombin enhances NGF-mediated neurite extension via increased and sustained activation of p44/42 MAPK and p38 MAPK. *PLoS One* 9:e103530. doi: 10.1371/journal.pone.0103530

Nair, B. C., Vallabhaneni, S., Tekmal, R. R., and Vadlamudi, R. K. (2011). Roscovitine confers tumor suppressive effect on therapy-resistant breast tumor cells. *Breast Cancer Res.* 13:R80. doi: 10.1186/bcr2929

Napoli, I., Noon, L. A., Ribeiro, S., Kerai, A. P., Parrinello, S., Rosenberg, L. H., et al. (2012). A central role for the ERK-signaling pathway in controlling Schwann cell plasticity and peripheral nerve regeneration *in vivo*. *Neuron* 73, 729–742. doi: 10.1016/j.neuron.2011.11.031

Nutley, B. P., Raynaud, F. I., Wilson, S. C., Fischer, P. M., Hayes, A., Goddard, P. M., et al. (2005). Metabolism and pharmacokinetics of the cyclin-dependent kinase inhibitor R-roscovitine in the mouse. *Mol. Cancer Ther.* 4, 125–139.

Okada, K., Tanaka, H., Temporin, K., Okamoto, M., Kuroda, Y., Moritomo, H., et al. (2011). Akt/mammalian target of rapamycin signaling pathway regulates neurite outgrowth in cerebellar granule neurons stimulated by methylcobalamin. *Neurosci. Lett.* 495, 201–204. doi: 10.1016/j.neulet.2011.03.065

Planchais, S., Glab, N., Tréhin, C., Perennes, C., Bureau, J. M., Meijer, L., et al. (1997). Roscovitine, a novel cyclin-dependent kinase inhibitor, characterizes restriction point and G2/M transition in tobacco BY-2 cell suspension. *Plant J.* 12, 191–202. doi: 10.1046/j.1365-313x.1997.12010191.x

Press, C., and Milbrandt, J. (2009). The purine nucleosides adenosine and guanosine delay axonal degeneration *in vitro*. *J. Neurochem.* 109, 595–602. doi: 10.1111/j.1471-4159.2009.06002.x

Raynaud, F. I., Whittaker, S. R., Fischer, P. M., McClue, S., Walton, M. I., Barrie, S. E., et al. (2005). *In vitro* and *in vivo* pharmacokinetic-pharmacodynamic relationships for the trisubstituted aminopurine cyclin-dependent kinase inhibitors olomoucine, bohemine and CYC202. *Clin. Cancer Res.* 11, 4875–4887. doi: 10.1158/1078-0432.ccr-04-2264

Richardson, P. M., Miao, T., Wu, D., Zhang, Y., Yeh, J., and Bo, X. (2009). Responses of the nerve cell body to axotomy. *Neurosurgery* 65, A74–A79. doi: 10.1227/01.NEU.0000352378.26755.C3

Ruschel, J., Hellal, F., Flynn, K. C., Dupraz, S., Elliott, D. A., Tedeschi, A., et al. (2015). Axonal regeneration. Systemic administration of epothilone B promotes axon regeneration after spinal cord injury. *Science* 348, 347–352. doi: 10.1126/science.aaa2958

Sarina, Yagi, Y., Nakano, O., Hashimoto, T., Kimura, K., Asakawa, Y., et al. (2013). Induction of neurite outgrowth in PC12 cells by artemisinin through activation of ERK and p38 MAPK signaling pathways. *Brain Res.* 1490, 61–71. doi: 10.1016/j.brainres.2012.10.059

Stoll, G., Jander, S., and Myers, R. R. (2002). Degeneration and regeneration of the peripheral nervous system: from Augustus Waller's observations to neuroinflammation. *J. Peripher. Nerv. Syst.* 7, 13–27. doi: 10.1046/j.1529-8027.2002.02002.x

van Engeland, M., Kuijpers, H. J., Ramaekers, F. C., Reutelingsperger, C. P., and Schutte, B. (1997). Plasma membrane alterations and cytoskeletal changes in apoptosis. *Exp. Cell Res.* 235, 421–430. doi: 10.1006/excr.1997.3738

Vita, M., Meurling, L., Pettersson, T., Cruz-Sidén, M., Sidén, A., and Hassan, M. (2004). Analysis of roscovitine using novel high performance liquid chromatography and UV-detection method: pharmacokinetics of roscovitine in rat. *J. Pharm. Biomed. Anal.* 34, 425–431. doi: 10.1016/s0731-7085(03)00534-x

Vogelaar, C. F., Gervasi, N. M., Gumy, L. F., Story, D. J., Raha-Chowdhury, R., Leung, K. M., et al. (2009). Axonal mRNAs: characterisation and role in the growth and regeneration of dorsal root ganglion axons and growth cones. *Mol. Cell. Neurosci.* 42, 102–115. doi: 10.1016/j.mcn.2009.06.002

Wang, H. W., Long, S., Finley, K. R., and Nogales, E. (2005). Assembly of GMPCPP-bound tubulin into helical ribbons and tubes and effect of colchicine. *Cell Cycle* 4, 1157–1160. doi: 10.4161/cc.4.9.2042

Wang, X., Wang, Z., Yao, Y., Li, J., Zhang, X., Li, C., et al. (2011). Essential role of ERK activation in neurite outgrowth induced by alpha-lipoic acid. *Biochim. Biophys. Acta* 1813, 827–838. doi: 10.1016/j.bbamcr.2011.01.027

Wu, J., Stoica, B. A., and Faden, A. I. (2011). Cell cycle activation and spinal cord injury. *Neurotherapeutics* 8, 221–228. doi: 10.1007/s13311-011-0028-2

Xu, J., Tsutsumi, K., Tokuraku, K., Estes, K. A., Hisanaga, S., and Ikezu, T. (2011). Actin interaction and regulation of cyclin-dependent kinase 5/p35 complex activity. *J. Neurochem.* 116, 192–204. doi: 10.1111/j.1471-4159.2010.06824.x

Yamazaki, T., Sabit, H., Oya, T., Ishii, Y., Hamashima, T., Tokunaga, A., et al. (2009). Activation of MAP kinases, Akt and PDGF receptors in injured peripheral nerves. *J. Peripher. Nerv. Syst.* 14, 165–176. doi: 10.1111/j.1529-8027.2009.00228.x

Yang, D. P., Kim, J., Syed, N., Tung, Y. J., Bhaskaran, A., Mindos, T., et al. (2012). p38 MAPK activation promotes denervated Schwann cell phenotype and functions as a negative regulator of Schwann cell differentiation and myelination. *J. Neurosci.* 32, 7158–7168. doi: 10.1523/JNEUROSCI.5812-11.2012

Zheng, Y. L., Li, B. S., Kanungo, J., Kesavapany, S., Amin, N., Grant, P., et al. (2007). Cdk5 Modulation of mitogen-activated protein kinase signaling regulates neuronal survival. *Mol. Biol. Cell* 18, 404–413. doi: 10.1091/mbc.e06-09-0851

Conflict of Interest Statement: The authors declare that the research was conducted in the absence of any commercial or financial relationships that could be construed as a potential conflict of interest.

frontiers
in Cellular Neuroscience

ORIGINAL RESEARCH
published: 10 January 2017
doi: 10.3389/fncel.2016.00304

Developmental Changes in Expression of βIV Spectrin Splice Variants at Axon Initial Segments and Nodes of Ranvier

*Takeshi Yoshimura[1,2†‡], Sharon R. Stevens[1‡], Christophe Leterrier[3], Michael C. Stankewich[4] and Matthew N. Rasband[1]**

[1]*Department of Neuroscience, Baylor College of Medicine, Houston, TX, USA,* [2]*Division of Neurobiology and Bioinformatics, National Institute for Physiological Sciences, National Institutes of Natural Sciences, Okazaki, Japan,* [3]*CNRS, Center for Research in Neurobiology and Neurophysiology of Marseille (CRN2M) UMR 7286, Aix Marseille Université, Marseille, France,* [4]*Department of Pathology, Yale University, New Haven, CT, USA*

Axon initial segments (AIS) and nodes of Ranvier are highly specialized axonal membrane domains enriched in Na^+ channels. These Na^+ channel clusters play essential roles in action potential initiation and propagation. AIS and nodal Na^+ channel complexes are linked to the actin cytoskeleton through βIV spectrin. However, neuronal βIV spectrin exists as two main splice variants: a longer βIVΣ1 variant with canonical N-terminal actin and αII spectrin-binding domains, and a shorter βIVΣ6 variant lacking these domains. Here, we show that the predominant neuronal βIV spectrin splice variant detected in the developing brain switches from βIVΣ1 to βIVΣ6, and that this switch is correlated with expression changes in ankyrinG (ankG) splice variants. We show that βIVΣ1 is the predominant splice variant at nascent and developing AIS and nodes of Ranvier, but with increasing age and in adults βIVΣ6 becomes the main splice variant. Remarkably, super-resolution microscopy revealed that the spacing of spectrin tetramers between actin rings remains unchanged, but that shorter spectrin tetramers may also be present. Thus, during development βIV spectrin may undergo a switch in the splice variants found at AIS and nodes of Ranvier.

Keywords: cytoskeleton, spectrin, axon, node of Ranvier, axon initial segment, ankyrin

Edited by:
Maren Engelhardt,
Heidelberg University, Germany

Reviewed by:
Juan José Garrido,
Spanish National Research Council, Spain
Damaris N. Lorenzo,
University of North Carolina-Chapel Hill, USA

Correspondence:
Matthew N. Rasband
rasband@bcm.edu

*†**Present address:***
Takeshi Yoshimura,
Department of Child Development and Molecular Brain Science, United Graduate School of Child Development, Osaka University, Suita, Osaka, Japan

‡These authors have contributed equally to this work.

Received: *01 December 2016*
Accepted: *22 December 2016*
Published: *10 January 2017*

Citation:
Yoshimura T, Stevens SR, Leterrier C, Stankewich MC and Rasband MN (2017) Developmental Changes in Expression of βIV Spectrin Splice Variants at Axon Initial Segments and Nodes of Ranvier.
Front. Cell. Neurosci. 10:304.
doi: 10.3389/fncel.2016.00304

INTRODUCTION

Neurons are highly polarized cells comprised of two structurally and functionally distinct domains: the axon and dendrites (Craig and Banker, 1994). The polarization of neurons allows for the unidirectional flow of information from dendrites/soma to axons. The dendrites and soma receive the upstream synaptic inputs; these are integrated and the decision to fire an action potential is made at the axon initial segment (AIS; Yoshimura and Rasband, 2014). AIS are characterized by high densities of voltage-gated Na^+ and K^+ channels that function to initiate and modulate action potentials (Kole and Stuart, 2012). In myelinated axons of vertebrates, action potentials propagate through the opening of Na^+ channels at nodes of Ranvier.

The AIS and nodes of Ranvier have a common molecular organization; in addition to the clustering of Na^+ and K^+ channels, these two regions share an enrichment of adhesion molecules and molecular scaffolds (Chang and Rasband, 2013). AnkyrinG (ankG) and βIV spectrin are the main components of the cytoskeleton at the AIS and nodes of Ranvier in neurons

(Kordeli et al., 1995; Berghs et al., 2000). AnkG interacts with and clusters membrane proteins (e.g., Na+ channels) and βIV spectrin, while βIV spectrin is thought to link the ankG/Na+ channel membrane protein complex to the actin cytoskeleton (Yang et al., 2007; Ho et al., 2014). Loss of ankG disrupts AIS assembly and neuronal function (Zhou et al., 1998). In βIV spectrin deficient mice, ankG and Na$^+$ channel densities are reduced at the AIS, probably due to diminished stability of the complex (Komada and Soriano, 2002). Thus, both ankG and βIV spectrin are essential for proper AIS ion channel complexes and axon domain organization.

Alternative splicing generates six βIV spectrin splice variants (βIVΣ1–βIVΣ6; Berghs et al., 2000; Komada and Soriano, 2002). Two variants, βIVΣ1 and βIVΣ6, are thought to be at the AIS and nodes of Ranvier (Komada and Soriano, 2002; Lacas-Gervais et al., 2004). βIVΣ1 is the largest of the splice variants and consists of an N-terminal actin-binding domain, 17 spectrin repeats (SRs), a "specific" domain (SD) and a pleckstrin homology (PH) domain (**Figure 1A**). βIVΣ6 is an N-terminal truncation that lacks the actin-binding domain, SRs 1–9, and part of SR 10 (**Figure 1A**). Spectrins are thought to function as heterotetramers consisting of two α and two β spectrin subunits, with the minimal lateral interactions occurring between the first two triple-helical domains of β-spectrins and the last two triple helical domains of α-spectrins (Speicher et al., 1992). Thus, it is not clear how βIVΣ6 would function in a heterotetramer. Due to the poorly understood expression patterns of the βIV spectrin splice variants, their individual roles remain unclear. Although the ∼190 nm spacing of βIV spectrin as revealed by super-resolution microscopy suggests they function as tetramers in the AIS, no α spectrin has yet been reported at the AIS (Galiano et al., 2012; Xu et al., 2013; Leterrier et al., 2015).

Here, we examined the spatial and temporal expression patterns of βIVΣ1 and βIVΣ6 at the AIS and nodes of Ranvier. We used anti-βIV spectrin antibodies against the N-terminal region that detects βIVΣ1, and antibodies against the SD that detects both βIVΣ1 and βIVΣ6 (**Figure 1A**). We found in early development that βIVΣ1 is the dominant splice variant at the AIS and nodes of Ranvier. However, as development proceeded, this shifted and βIVΣ6 became the dominant isoform in adult mice. Finally, stochastic optical reconstruction microscopy (STORM) super-resolution microscopy revealed that the pattern of βIV spectrin immunoreactivity remained periodic despite the switch in expression of these two splice variants, although a more complicated periodic pattern suggests the existence of shorter spectrin tetramers that may include βIVΣ6. Together, these studies reveal the differential expression and localization of βIV spectrin splice variants at the AIS and nodes of Ranvier during development of the nervous system.

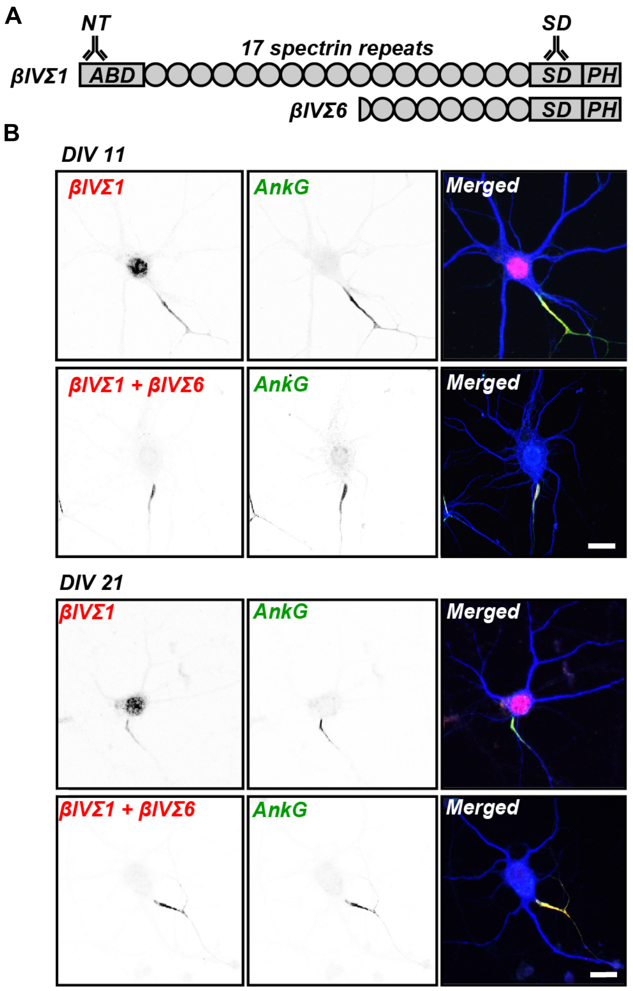

FIGURE 1 | βIV spectrin splice variants. (A) Two βIV spectrin splice variants, Σ1 and Σ6, are found at the axon initial segments (AIS) and nodes of Ranvier. These proteins have multiple spectrin repeats (SRs), βIVΣ1 has an actin binding domain (ABD), and both have specific domains (SD) and pleckstrin homology (PH) domains. Antibodies against the NT and SD domains can be used to detect these splice variants. **(B)** Immunostaining of cultured hippocampal neurons at days *in vitro* (DIV) 11 and 21 using NT (βIVΣ1) and SD (βIVΣ1 + βIVΣ6) antibodies labels AIS. AIS are defined by the immunostaining for AnkyrinG (ankG). MAP2, a somatodendritic marker, is shown in blue in the merged images. Scale bar = 20 μm.

MATERIALS AND METHODS

Animals

Sprague Dawley rats were obtained from Harlan Sprague Dawley (Indianapolis, IN, USA). C57BL/6 mice were from Charles River Laboratories (Wilmington, MA, USA). Both male and female mice were used in these studies. All experiments were performed in compliance with the National Institutes of Health Guide for the Care and Use of Laboratory Animals and were approved by the Baylor College of Medicine Institutional Animal Care and Use Committee.

Antibodies

Rabbit anti-βIV spectrin NT, and rabbit or chicken anti-βIV spectrin SD antibodies were previously described (Yang et al., 2004). The anti-βIV spectrin NT antibody was generated against a synthetic peptide corresponding to amino acids 15–38 of the βIVΣ1 splice variant. Anti-βIV spectrin SD antibody was generated against the SD (Berghs et al., 2000). The goat anti-ankG antibody for immunoblot analysis was generated against the C-terminal domain of ankG and was kindly provided by Dr. Vann Bennett (Duke University, Durham, NC, USA; Ho et al., 2014). The following other primary antibodies were used: mouse monoclonal anti-ankG for immunostaining (N106/36, UC Davis/NIH NeuroMab facility, Davis, CA, USA); rabbit anti-GAPDH (Sigma-Aldrich, St. Louis, MO, USA); mouse monoclonal anti-Caspr (K65/35, UC Davis/NIH NeuroMab facility); and chicken polyclonal anti-MAP2 (EnCor Biotechnology, Gainesville, FL, USA) antibodies. Secondary antibodies were purchased from Jackson ImmunoResearch Laboratories (West Grove, PA, USA) and Life Technologies (Thermo Fisher Scientific, Waltham, MA, USA).

Brain Lysate Preparation

Whole mouse brains were dissected and homogenized in ice-cold homogenization buffer (0.32M sucrose, 5 mM sodium phosphate, pH 7.4, 1 mM sodium fluoride and 1 mM sodium orthovanadate, containing 0.5 mM phenylmethylsulfonyl fluoride, 2 μg/ml aprotinin, 1 μg/ml leupeptin, 2 μg/ml antipain and 10 μg/ml benzamidine). Crude homogenates were then centrifuged at 600× g for 10 min to remove debris and nuclei. The resulting supernatant was centrifuged at 30,000× g for 90 min, then the pellet was re-suspended in ice-cold homogenization buffer. Protein concentrations were determined using the BCA method (Thermo Fisher Scientific, Waltham, MA, USA). After adding SDS sample buffer, the samples were subjected to SDS–PAGE and immunoblot analysis.

RT-qPCR

RNA was isolated from whole mouse brains in triplicate using Trizol (Invitrogen, Carlsbad, CA, USA) and converted to cDNA with Superscript (Invitrogen) using a combination of oligo(T)s and random hexamers. mRNA was quantified with a Nanodrop spectrophotometer to ensure equal starting amounts. Gene specific primers that bridged consecutive exons were used to ensure detection of mRNA. For qPCR, using Power SYBR® Green PCR Master Mix (Applied Biosystems), the signal from every reaction at the end of each 60°C annealing extension step of each cycle was recorded on a CFX96 Real Time System (BioRad). Data are normalized to GAPDH. Primers used are as follows: βIVΣ1 (forward) TGAGGGCCCAGCAGTGGATGC; βIVΣ6 (forward) GACGCTCCTCCAACGCCG; βIVΣ1/Σ6 (reverse) GGTGCCG GAGCCATCTCTTGT; 190 AnkG (forward) CTTTGCCTCCC TAGCTTTAC; 190 AnkG (reverse) TCTGTCCAACTAAGTCC CAG; 270 AnkG (forward) GCCATGTCTCCAGATGTTG; (reverse) TCTGTCCAACTAAGTCCCAG; 480 AnkG (forward) AGTAGGAGGACTGGTCCG; (reverse) AGTTGTGGCATTCT TTCCG.

Culture of Hippocampal Neurons

Brains from embryonic day 18 rat embryos were collected into ice-cold HBSS without calcium or magnesium (Invitrogen, Carlsbad, CA, USA). Embryonic hippocampi were dissected and collected in ice-cold HBSS. The collected tissue was incubated with 0.25% Trypsin in HBSS at 37°C for 15 min and washed with HBSS. After adding plating media (Neurobasal medium (Invitrogen) with 10% HyClone FetalClone III serum (Thermo Fisher Scientific, Waltham, MA, USA)), these hippocampi were mechanically dissociated using a fire-polished Pasteur pipette. The suspension was centrifuged for 5 min at 200× g. The pelleted cells were briefly washed and resuspended in plating media. Neurons were plated on glass coverslips coated with poly-D-lysine (Sigma-Aldrich) at low density for immunocytochemistry (120 cells/mm^2) and on plastic dishes with poly-D-lysine at high density for western blot (520 cells/mm^2). After neurons were incubated in a humidified 5% CO_2 incubator at 37°C for 3 h, the media was exchanged to maintaining media (Neurobasal medium with 2% B-27 supplement (Invitrogen) and 2 mM GlutaMAX (Invitrogen)). The cultures were maintained by exchanging half of the volume of media twice a week with new maintaining media. For immunoblotting, neurons were washed with PBS, and collected with SDS sample buffer. The samples were subjected to SDS–PAGE and immunoblot analysis.

Immunostaining and Imaging

Cultured neurons at 11 and 21 days *in vitro* (DIV) were fixed in 4% paraformaldehyde (PFA) in 0.1 M phosphate buffer (PB, pH 7.2) at 4°C for 30 min, followed by treatment with PBTGS (0.1M PB with 0.3% Triton X-100 (Sigma-Aldrich) and 10% goat serum (Invitrogen)) for 1 h at room temperature. For immunostaining of nervous system tissues, brains, optic and sciatic nerves were dissected at the indicated times, fixed in 4% PFA for 30 min for optic and sciatic nerves, or 1.5 h for brains; this was followed by immersion in 20% sucrose (w/v) in 0.1 M PB overnight at 4°C. The tissues were then frozen in Tissue-Tek OCT compound (Sakura Finetek, Tokyo, Japan) and sectioned using a Cryostat (CryoStar NX70, Thermo Fisher Scientific). Sections were collected and suspended in 0.1 M PB, then spread out on glass coverslips. The tissues were treated with PBTGS for 1 h at room temperature. The samples were incubated with primary antibodies diluted in PBTGS at room temperature overnight. Following this, samples were incubated with secondary antibodies for 1 h at room temperature. Immunofluorescence labeling was visualized, and images were collected on an AxioImager Z1 microscope (Carl Zeiss, Jena, Germany) fitted with an AxioCam digital camera (Carl Zeiss). AxioVision (Carl Zeiss) software was used for the collection and measurement of images. Images used for fluorescent signal quantification were collected using the same exposure settings across all animals and stages for the channels with βIV spectrin NT and βIV spectrin SD.

STORM Imaging

After 13–28 days in culture, neurons were fixed using 4% PFA for 10 min. After blocking, they were incubated with primary antibodies overnight at 4°C, then with secondary antibodies for 1 h at room temperature. STORM imaging was performed on an

N-STORM microscope (Nikon Instruments, Melville, NY, USA). Coverslips were imaged in STORM buffer: Tris 50 mM (pH 8); NaCl 10 mM; 10% glucose; 100 mM MEA; 3.5 U/ml pyranose oxidase; and 40 mg/ml catalase. The sample was continuously illuminated at 647 nm (full power) and 30,000–60,000 images were acquired at 67 Hz, with progressive reactivation by simultaneous 405-nm illumination (Leterrier et al., 2015).

Image Quantification

Images were analyzed using NIH ImageJ software. Mean fluorescent signal intensities of rabbit anti-βIV spectrin NT and chicken anti-βIV spectrin SD were quantified in raw images using a line scan along the length of the AIS or for a region of interest encompassing the area of the node of Ranvier. All visible AIS or nodes of Ranvier were measured in each image; these measurements were averaged for individual animals. Population means were calculated for all tissues and developmental stages. Measurements for the rabbit anti-βIV spectrin NT antibody showed expression of βIVΣ1; the difference of the fluorescence intensities for the two βIV spectrin antibodies gave the relative expression of βIVΣ6. Three animals were used at each time point analyzed. All statistical comparisons were performed using Student's *t*-test. The number of AIS measured: P1 (n = 96), P3 (n = 96), P9 (n = 96), 5-mo (n = 56). Number of nodes of Ranvier measured in optic nerves: P9 (n = 115), P15 (n = 80), P30 (n = 80), 5-mo (n = 80). Number of nodes of Ranvier measured in sciatic nerves: P1 (n = 120), P3 (n = 120), P9 (n = 118), 5-mo (n = 80). Number of nodes of Ranvier measured in cerebellum: P9 (n = 141), P15 (n = 90), P30 (n = 102), 5-mo (n = 114).

RESULTS

βIVΣ6 Is Highly Upregulated Following AIS Formation

Cultured hippocampal neurons are commonly used to study the development of neuronal polarity and assembly of unique domains (e.g., synapses, AIS, etc.; Galiano et al., 2012). To investigate the spatial expression patterns of βIV spectrin splice variants in neurons, we used two anti-βIV spectrin antibodies generated against the NT and SD domains (**Figure 1A**; Yang et al., 2004). The anti-βIV spectrin SD antibody recognizes both Σ1 and Σ6 variants, whereas the anti-βIV spectrin NT antibody recognizes only the Σ1 variant (**Figure 1A**). Immunostaining 11 and 21 DIV cultured hippocampal neurons with these antibodies showed both the SD and NT immunoreactivities colocalized with ankG at the AIS (**Figure 1B**). Since only the NT antibody showed any staining in the nucleus, but not the SD antibody that recognizes both splice variants, we conclude the nuclear NT immunoreactivity is nonspecific.

To determine the temporal expression profile of βIV spectrin splice variants, we performed immunoblotting using homogenates of cultured hippocampal neurons and developing brain (**Figures 2A,B**). Both in cultured neurons and in developing mouse brain the βIVΣ1 splice variant was the earliest splice variant observed. However, the expression levels of βIVΣ6 dramatically increased at later time points both in culture and in the brain, indicating the most abundant form of βIV spectrin in mature neurons is the shorter βIVΣ6 splice variant.

βIV spectrin is localized to the AIS through the binding of its 15th SR to ankG; unlike the actin-binding-domain, the ankG-binding domain is present in both βIVΣ1 and βIVΣ6 (**Figure 1A**; Yang et al., 2007). We examined the expression levels of ankG in cultured hippocampal neurons and in developing mouse brain (**Figures 2A,B**). The main ankG splice variants thought to be located at AIS and nodes of Ranvier are the 480 and 270 kDa isoforms (Kordeli et al., 1995). In cultured neurons all ankG splice variants increased with age (**Figure 1A**). In contrast, in the brain there was a dramatic increase in the ankG 190 kDa isoform, and an apparent reduction in 480 and 270 kDa splice variants. Although these same antibodies robustly label AIS in brain sections (data not shown), we speculate the apparent reduction in 480 and 270 kDa forms may reflect their extreme detergent insolubility and poor resolvability by SDS-PAGE.

To further define the differential expression of the βIV spectrin and ankG splice variants, we measured their transcript levels by reverse transcription-quantitative polymerase chain reaction (RT-qPCR; **Figures 2C,D**). Consistent with the immunoblotting results, the βIVΣ6 transcript levels from adult mice were significantly higher than those from newborn mice (**Figure 2C**). In contrast βIVΣ1 transcript levels from newborn mice were slightly higher when compared to adult mice. AnkG transcripts from adult mice showed that levels of ankG 190 and 270 kDa were increased relative to newborn mice, while the levels of ankG 480 transcripts were significantly lower than in newborn mice. These results indicate that transcript and protein expression levels of βIV spectrin and ankG splice variants reflect similar changes during mouse brain development. In particular, βIVΣ6 is dramatically increased during development, while 480 kDa ankG is reduced.

βIV Spectrin Splice Variants Change at the AIS and Nodes of Ranvier during Development

To determine if the change in βIV spectrin splice variant expression occurs specifically at AIS, we compared the expression levels of βIVΣ1 and βIVΣ6 at AIS in mouse cortex throughout development by double-immunolabeling with rabbit anti-NT (βIVΣ1) and chicken anti-SD (βIVΣ1 + Σ6) antibodies. The SD immunoreactivity was localized at the AIS in both P1 and 5 month-old mouse cortex (**Figure 3A**). The NT immunoreactivity also labeled AIS and colocalized with the SD staining (**Figure 3A**; except for the non-specific nuclear immunoreactivity). Keeping all imaging parameters constant for each time point measured, we then subtracted the measured NT fluorescence intensity (βIVΣ1) from the measured SD fluorescence intensity (βIVΣ1 + Σ6) which permitted us to estimate the relative contribution of Σ6 to the SD immunostaining. We found that during early AIS assembly, βIVΣ1 is the predominant splice variant at AIS, but that this gradually changes such that by 5 months

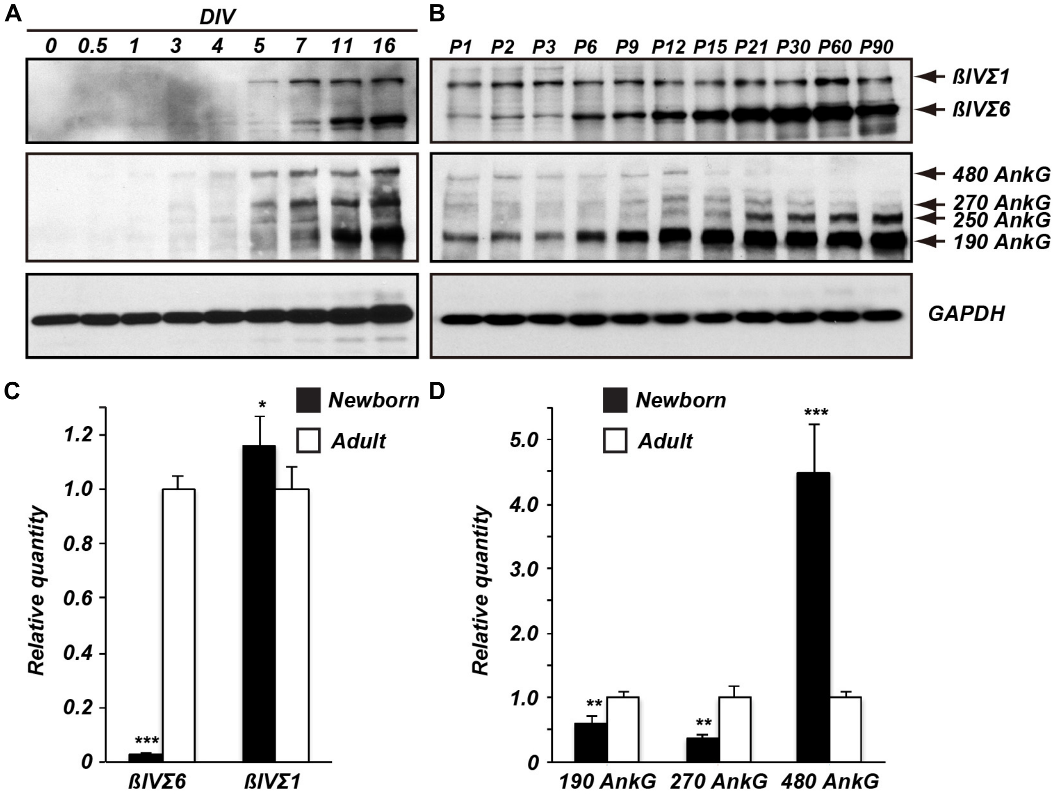

FIGURE 2 | Temporal expression of βIV spectrin and ankG splice variants. Immunoblots of βIV spectrin and ankG from cultured neurons **(A)** and from brain homogenates **(B).** Reverse transcription-quantitative polymerase chain reaction (RT-qPCR) of βIV spectrin **(C)** and ankG **(D)** splice variant transcripts detected in developing brain. Error bars ± SEM. *$p < 0.01$, **$p < 0.001$, ***$p < 0.0001$.

of age βIVΣ6 increases at the AIS relative to βIVΣ1 (**Figure 3B**).

Next, we performed a similar comparison of βIVΣ1 and βIVΣ6 immunostaining at nodes of Ranvier in sciatic nerve (**Figures 4A,B**), optic nerve (**Figure 4C**), and in cerebellum (**Figure 4D**). Remarkably, we found a similar shift at nodes from βIVΣ1 at new nodes of Ranvier to βIVΣ6 in older animals. These results suggest that while βIVΣ1 is the main βIV spectrin splice variant found at the AIS and nodes of Ranvier during early development, with increasing age βIVΣ1 may be replaced by the shorter βIVΣ6 splice variant. These observations are consistent with the results obtained by immunoblotting and RT-qPCR (**Figure 2**).

Super-Resolution Imaging of βIV Spectrin Distribution during Development

Recent experiments using STORM super-resolution microscopy revealed a periodic cytoskeleton at the AIS consisting of rings of actin spaced at ~190 nm intervals (Xu et al., 2013; Leterrier et al., 2015). Intriguingly, the spacing of these rings corresponds to the length of spectrin tetramers. Indeed, STORM imaging of βIV spectrin using our NT and SD antibodies revealed that the actin rings colocalized or alternate with the spectrin immunoreactivity, respectively (Xu et al., 2013; Leterrier et al., 2015). Although the spacing of AIS actin rings has not yet been shown to depend on βIV spectrin, the spacing of actin rings in the distal axon does depend on βII spectrin (Zhong et al., 2014). Since the lengths of βIVΣ1 and βIVΣ6 are quite different, we wondered if the spacing of actin rings might change during development with the increased abundance of the shorter splice variant at AIS. To test this possibility, we performed STORM imaging using SD antibodies on cultured hippocampal neurons at DIV 13, 16, 20 and 28 (**Figures 5A–D**). Despite the increased protein and expression of the shorter βIVΣ6 splice variant, we still observed that the major peak of SD immunoreactivity occurred at an interval of ~190 nm in older neurons, suggesting that the spacing continues to be determined primarily by the βIVΣ1 splice variant. Nevertheless, secondary peaks of lesser intensity could be detected on intensity profiles that were 55 ± 2.67 nm (SEM) to each side of the major peaks (see **Figure 5C**, asterisks). Importantly, these secondary peaks became more frequent and pronounced with increasing age.

DISCUSSION

βIV spectrin is highly enriched at the AIS and nodes of Ranvier and functions to link membrane proteins to the actin-based

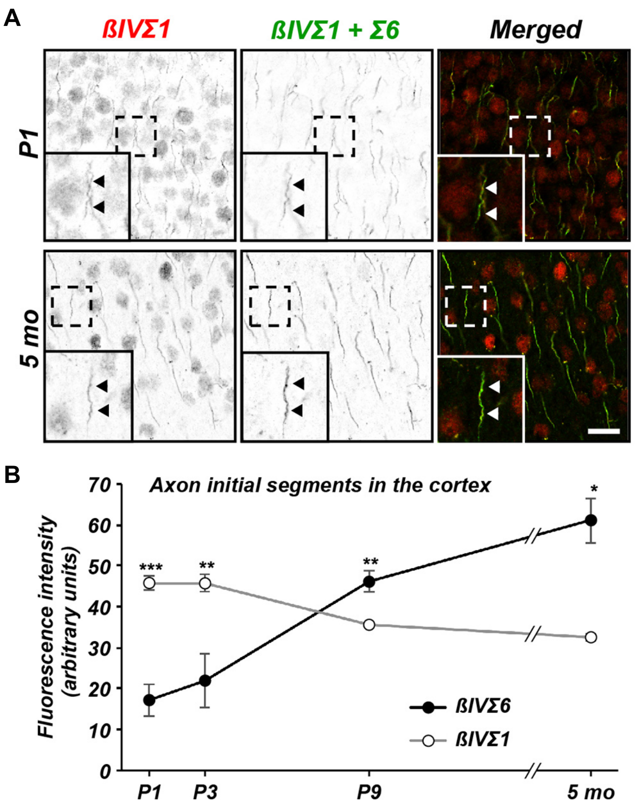

FIGURE 3 | Differential expression of βIV spectrin splice variants at cortical AIS. (A) Immunolabeling of cortical AIS using NT (βIVΣ1) and SD (βIVΣ1 + βIVΣ6) antibodies in P1 and 5 month-old brain. Scale bar = 10 μm. **(B)** Quantification of relative βIVΣ1 and βIVΣ6 expression at the AIS in sections of cortex as a function of age. Error bars ± SEM. $*p < 0.01$, $**p < 0.001$, $***p < 0.0001$.

cytoskeleton through ankG (Berghs et al., 2000; Komada and Soriano, 2002; Yang et al., 2007). Mouse mutants of βIV spectrin have a myriad of nervous system abnormalities including disrupted nodes and AIS, hearing loss, ataxia, and even axon degeneration (Parkinson et al., 2001; Yang et al., 2004). Here, we showed that a shift from βIVΣ1 to βIVΣ6 occurs at the AIS and nodes of Ranvier during development, with βIVΣ1 being dominant in early development, but βIVΣ6 being dominant in mature neurons.

Spectrin α and β subunits form antiparallel dimers that self-associate to form tetramers of ~190 nm in length, and that function as a submembranous scaffolding network anchored to actin filaments by β spectrins (Bennett and Healy, 2008). In axons, the spectrin-actin cytoskeleton forms a periodic network of circumferential actin rings along the inner cytoplasmic face of the axon membrane; these actin rings are evenly spaced along axonal shafts by spectrin tetramers. This network has been proposed to participate in both the polarization of the AIS membrane and to provide structural support to axons to withstand mechanical stresses (Xu et al., 2013). Despite the canonical view of spectrin tetramers, the composition of the AIS spectrin cytoskeleton remains an enigma since: (1) the

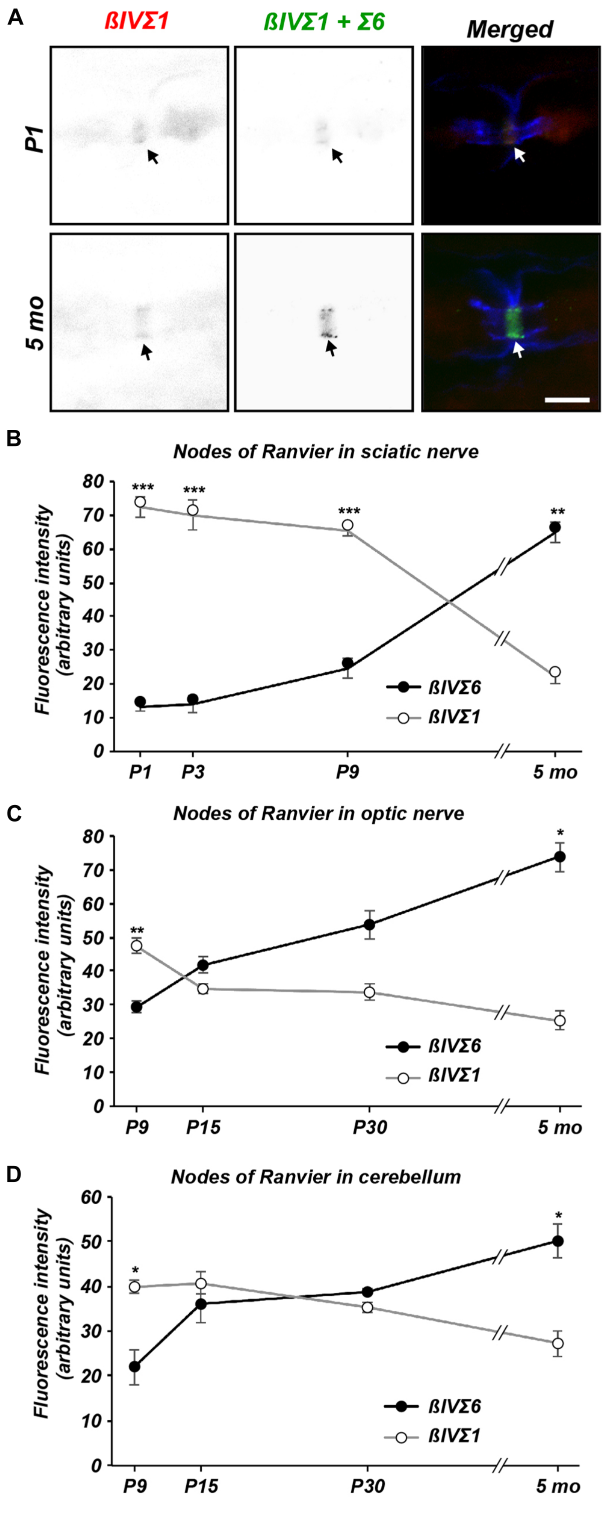

FIGURE 4 | Differential expression of βIV spectrin splice variants at nodes of Ranvier. (A) Immunolabeling of nodes of Ranvier using NT (βIVΣ1) and SD (βIVΣ1 + βIVΣ6) antibodies in P1 and 5 sciatic nerve. Caspr immunostaining is shown in blue. Scale bar = 5 μm. **(B–D)** Quantification of relative βIVΣ1 and βIVΣ6 expression in sciatic nerve **(B)**, optic nerve **(C)** and cerebellar nodes **(D)** as a function of age. Error bars ± SEM. $*p < 0.01$, $**p < 0.001$, $***p < 0.0001$.

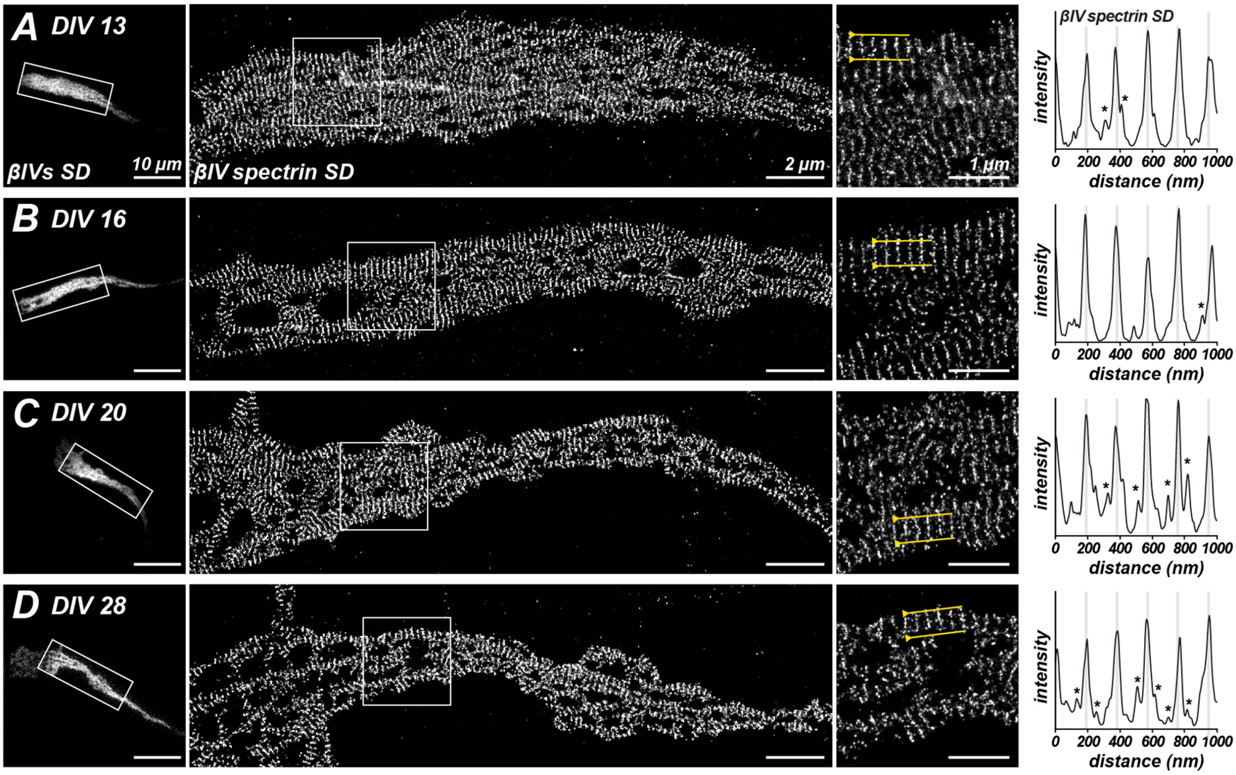

FIGURE 5 | Stochastic optical reconstruction microscopy (STORM) imaging of βIV SD localization at different ages in culture. (A–D) Immunostaining for βIV spectrin SD at the AIS of cultured hippocampal neurons at DIV 13, 16, 20 and 28. Boxed regions correspond to magnified images at the right. Intensity profiles at the far right of each panel and correspond to regions between the yellow lines in the magnified images at the right. Lower intensity peaks, possibly corresponding to βIVΣ6 splice variants, in line scans are indicated by an asterisk. Scale bars = 10 μm (left widefield images), 2 μm (STORM images), 1 μm (right magnified images).

α spectrin subunit that partners with βIV spectrin has not yet been reported; and (2) βIVΣ6 lacks both the actin and α spectrin-binding domains. Despite our observation that βIVΣ6 is the main splice variant in mature neurons, the length of spectrin tetramers, as measured using SD antibodies, remained constant at about 190 nm. In addition, intensity profiles along the AIS revealed secondary peaks in SD immunoreactivity that may correspond to spectrin tetramers that include a βIVΣ6 subunit. Thus, it is possible that a single AIS (or node) spectrin tetramer consists of both βIVΣ1 and βIVΣ6 subunits. While co-immunoprecipitation experiments using expression constructs in heterologous cells may be able to determine if these splice variants can function in the same tetramer, the extreme detergent insolubility of the AIS makes it difficult to confirm that these tetramers of mixed splice variants exist in the brain. It is possible that βIV spectrin splice variants can associate with α spectrins through previously unidentified interacting domains present in both βIVΣ1 and βIVΣ6. Future studies of mice lacking βIVΣ1 using STORM might provide key insights into how the periodic spectrin cytoskeleton forms and is maintained, and how βIVΣ6 interacts with the actin cytoskeleton. Furthermore, it will be important to determine if α spectrin functions at the AIS in concert with βIV spectrin splice variants.

Different Na^+ channels occupy distinct subdomains of the AIS. In cortical pyramidal neurons, Nav1.2 and Nav1.6 are found in the proximal and distal regions of the AIS, respectively (Hu et al., 2009). Furthermore, during development Nav1.2 is first found at nodes of Ranvier, but then as neurons mature, Nav1.6 replaces these channels. The switch in the type of nodal Na+ channels correlates with the onset of myelination and the sustained expression of Nav1.6 depends on myelination. Although the distributions of βIVΣ1 and βIVΣ6 are similar in the proximal and distal regions of the AIS, the switch in βIV spectrin splice variants was also coincident with the onset of myelination. However, since the switch in splicing also occurs in cultured hippocampal neurons that lack myelin, the change in splice variant expression does not depend on myelination. Furthermore, the switch from Nav1.2 to Nav1.6 is unlikely to depend on the change in βIV spectrin splice variant expression since Na^+ channel binding to ankG is both necessary and sufficient for their AIS and nodal localization (Garrido et al., 2003; Gasser et al., 2012).

Why is there an increase in the amount of βIVΣ6 expression at AIS and nodes with increasing age? Although our experiments cannot answer this, it is unlikely that replacing βIVΣ1 with βIVΣ6 reflects the recruitment of additional proteins to the AIS since all of the protein coding regions found in βIVΣ6 are also found in βIVΣ1. Instead, we speculate that a decrease in βIVΣ1 may reflect a maturation of the AIS and loss of some proteins that associated with the N-terminal half of βIVΣ1 during AIS assembly or establishment of the trafficking filter associated with the AIS.

In conclusion, using two kinds of anti-βIV spectrin antibodies, NT for βIVΣ1 and SD for both βIVΣ1 and βIVΣ6 splice variants, we found a switch in the expression levels and localization of these splice variants at the AIS and nodes of Ranvier during development. Additional experiments will be required to determine the role this switch has for nervous system function.

AUTHOR CONTRIBUTIONS

TY and SRS performed immunoblots, immunostaining and quantification of signals. CL performed STORM imaging. MCS performed RT-qPCR. MNR and MCS conceived and directed the project. All authors contributed to writing and revising of the final manuscript.

FUNDING

This work was supported by National Institutes of Health (NIH) grants NS044916 and the Dr. Miriam and Sheldon G. Adelson Medical Research Foundation. CL acknowledges B. Dargent for support, through grant ANR-2011-BSV4-001-1 by Agence Nationale de la Recherche.

REFERENCES

Bennett, V., and Healy, J. (2008). Organizing the fluid membrane bilayer: diseases linked to spectrin and ankyrin. *Trends Mol. Med.* 14, 28–36. doi: 10.1016/j.molmed.2007.11.005

Berghs, S., Aggujaro, D., Dirkx, R. Jr., Maksimova, E., Stabach, P., Hermel, J. M., et al. (2000). βIV spectrin, a new spectrin localized at axon initial segments and nodes of ranvier in the central and peripheral nervous system. *J. Cell Biol.* 151, 985–1002. doi: 10.1083/jcb.151.5.985

Chang, K. J., and Rasband, M. N. (2013). Excitable domains of myelinated nerves: axon initial segments and nodes of Ranvier. *Curr. Top. Membr.* 72, 159–192. doi: 10.1016/B978-0-12-417027-8.00005-2

Craig, A. M., and Banker, G. (1994). Neuronal polarity. *Annu. Rev. Neurosci.* 17, 267–310. doi: 10.1146/annurev.ne.17.030194.001411

Garrido, J. J., Giraud, P., Carlier, E., Fernandes, F., Moussif, A., Fache, M. P., et al. (2003). A targeting motif involved in sodium channel clustering at the axon initial segment. *Science* 300, 2091–2094. doi: 10.1126/science.1085167

Galiano, M. R., Jha, S., Ho, T. S., Zhang, C., Ogawa, Y., Chang, K. J., et al. (2012). A distal axonal cytoskeleton forms an intra-axonal boundary that controls axon initial segment assembly. *Cell* 149, 1125–1139. doi: 10.1016/j.cell.2012.03.039

Gasser, A., Ho, T. S., Cheng, X., Chang, K. J., Waxman, S. G., Rasband, M. N., et al. (2012). An ankyrinG-binding motif is necessary and sufficient for targeting Nav1.6 sodium channels to axon initial segments and nodes of Ranvier. *J. Neurosci.* 32, 7232–7243. doi: 10.1523/JNEUROSCI.5434-11.2012

Ho, T. S., Zollinger, D. R., Chang, K. J., Xu, M., Cooper, E. C., Stankewich, M. C., et al. (2014). A hierarchy of ankyrin-spectrin complexes clusters sodium channels at nodes of Ranvier. *Nat. Neurosci.* 17, 1664–1672. doi: 10.1038/nn.3859

Hu, W., Tian, C., Li, T., Yang, M., Hou, H., and Shu, Y. (2009). Distinct contributions of $Na_V1.6$ and $Na_V1.2$ in action potential initiation and backpropagation. *Nat. Neurosci.* 12, 996–1002. doi: 10.1038/nn.2359

Kole, M. H., and Stuart, G. J. (2012). Signal processing in the axon initial segment. *Neuron* 73, 235–247. doi: 10.1016/j.neuron.2012.01.007

Komada, M., and Soriano, P. (2002). βIV-spectrin regulates sodium channel clustering through ankyrin-G at axon initial segments and nodes of Ranvier. *J. Cell Biol.* 156, 337–348. doi: 10.1074/jbc.m609223200

Kordeli, E., Lambert, S., and Bennett, V. (1995). AnkyrinG. A new ankyrin gene with neural-specific isoforms localized at the axonal initial segment and node of Ranvier. *J. Biol. Chem.* 270, 2352–2359.

Lacas-Gervais, S., Guo, J., Strenzke, N., Scarfone, E., Kolpe, M., Jahkel, M., et al. (2004). βIVΣ1 spectrin stabilizes the nodes of Ranvier and axon initial segments. *J. Cell Biol.* 166, 983–990. doi: 10.1083/jcb.200110003

Leterrier, C., Potier, J., Caillol, G., Debarnot, C., Rueda Boroni, F., and Dargent, B. (2015). Nanoscale architecture of the axon initial segment reveals an organized and robust scaffold. *Cell Rep.* 13, 2781–2793. doi: 10.1016/j.celrep.2015.11.051

Parkinson, N. J., Olsson, C. L., Hallows, J. L., McKee-Johnson, J., Keogh, B. P., Noben-Trauth, K., et al. (2001). Mutant β-spectrin 4 causes auditory and motor neuropathies in quivering mice. *Nat. Genet.* 29, 61–65. doi: 10.1038/ng710

Speicher, D. W., Weglarz, L., and DeSilva, T. M. (1992). Properties of human red cell spectrin heterodimer (side-to-side) assembly and identification of an essential nucleation site. *J. Biol. Chem.* 267, 14775–14782.

Xu, K., Zhong, G., and Zhuang, X. (2013). Actin, spectrin and associated proteins form a periodic cytoskeletal structure in axons. *Science* 339, 452–456. doi: 10.1126/science.1232251

Yang, Y., Lacas-Gervais, S., Morest, D. K., Solimena, M., and Rasband, M. N. (2004). βIV spectrins are essential for membrane stability and the molecular organization of nodes of Ranvier. *J. Neurosci.* 24, 7230–7240. doi: 10.1523/JNEUROSCI.2125-04.2004

Yang, Y., Ogawa, Y., Hedstrom, K. L., and Rasband, M. N. (2007). βIV spectrin is recruited to axon initial segments and nodes of Ranvier by ankyrinG. *J. Cell Biol.* 176, 509–519. doi: 10.1083/jcb.200610128

Yoshimura, T., and Rasband, M. N. (2014). Axon initial segments: diverse and dynamic neuronal compartments. *Curr. Opin. Neurobiol.* 27, 96–102. doi: 10.1016/j.conb.2014.03.004

Zhong, G., He, J., Zhou, R., Lorenzo, D., Babcock, H. P., Bennett, V., et al. (2014). Developmental mechanism of the periodic membrane skeleton in axons. *Elife* 3:e04581. doi: 10.7554/eLife.04581

Zhou, D., Lambert, S., Malen, P. L., Carpenter, S., Boland, L. M., and Bennett, V. (1998). AnkyrinG is required for clustering of voltage-gated Na channels at axon initial segments and for normal action potential firing. *J. Cell Biol.* 143, 1295–1304. doi: 10.1083/jcb.143.5.1295

Conflict of Interest Statement: The authors declare that the research was conducted in the absence of any commercial or financial relationships that could be construed as a potential conflict of interest.

frontiers
in Cellular Neuroscience

ORIGINAL RESEARCH
published: 26 January 2017
doi: 10.3389/fncel.2017.00006

Ankyrin G Membrane Partners Drive the Establishment and Maintenance of the Axon Initial Segment

*Christophe Leterrier, Nadine Clerc[‡], Fanny Rueda-Boroni, Audrey Montersino, Bénédicte Dargent[†] and Francis Castets[†]**

CNRS, CRN2M, Aix Marseille University, Marseille, France

The axon initial segment (AIS) is a highly specialized neuronal compartment that plays a key role in neuronal development and excitability. It concentrates multiple membrane proteins such as ion channels and cell adhesion molecules (CAMs) that are recruited to the AIS by the scaffold protein ankyrin G (ankG). The crucial function of ankG in the anchoring of AIS membrane components is well established, but a reciprocal role of membrane partners in ankG targeting and stabilization remained elusive. In rat cultured hippocampal neurons and cortical organotypic slices, we found that shRNA-mediated knockdown of ankG membrane partners (voltage-gated sodium channels (Nav) or neurofascin-186) led to a decrease of ankG concentration and perturbed the AIS formation and maintenance. These effects were rescued by expressing a recombinant AIS-targeted Nav or by a minimal construct containing the ankyrin-binding domain of Nav1.2 and a membrane anchor (mABD). Moreover, overexpressing mABD in mature neurons led to ankG mislocalization. Altogether, these results demonstrate that a tight and precocious association of ankG with its membrane partners is a key step for the establishment and maintenance of the AIS.

Keywords: ankyrin G, axon initial segment, neurofascin-186, voltage gated sodium channel, organotypic slices, cultured hippocampal neurons

OPEN ACCESS

Edited by:
Maren Engelhardt,
Heidelberg University, Germany

Reviewed by:
Daniela Mauceri,
Heidelberg University, Germany
Vann Bennett,
Howard Hughes Medical Institute, USA

****Correspondence:***
Francis Castets
francis.castets@univ-amu.fr

[†] *These authors have contributed equally to this work.*

[‡] ***Present address:***
Nadine Clerc,
Aix Marseille University, CNRS, IBDM,
Marseille, France

Received: *09 December 2016*
Accepted: *12 January 2017*
Published: *26 January 2017*

Citation:
Leterrier C, Clerc N, Rueda-Boroni F, Montersino A, Dargent B and Castets F (2017) Ankyrin G Membrane Partners Drive the Establishment and Maintenance of the Axon Initial Segment. Front. Cell. Neurosci. 11:6. doi: 10.3389/fncel.2017.00006

INTRODUCTION

Neurons exhibit an axonal/dendritic polarity that allows the directional propagation of signals throughout the nervous system. A major player in the maintenance of this polarity is the axon initial segment (AIS), a specialized domain located within the first 50 μm of the axon. The AIS isolates the axon from the cell body and regulates protein exchange between the axonal and somatodendritic compartments (Rasband, 2010; Leterrier, 2016). Besides this important role in neuronal polarity, the AIS is also the site of generation of action potentials (Clark et al., 2009; Kole and Stuart, 2012). At the molecular level, the AIS is organized by ankyrin G (ankG), a specialized scaffolding protein that directly binds to the submembrane cytoskeletal lattice of ßIV-spectrin (ßIVsp) and actin. The amino-terminus of ankG, called the membrane-binding domain (MBD), is apposed to the inner face of the plasma membrane and directly interacts with transmembrane proteins such as voltage-gated sodium channels (Nav), potassium channels Kv7.2/3 (KCNQ2/KCNQ3), and the cell adhesion molecules (CAMs) NrCAM and Neurofascin-186 (Nfasc186; Xu et al., 2013; Leterrier et al., 2015). AnkG is also associated with the microtubule cytoskeleton by a direct interaction with End-Binding proteins (EB1 and EB3; Leterrier et al., 2011b; Fréal et al., 2016).

AnkG is considered to be the master organizer of the AIS (Rasband, 2010). It is the earliest component addressed to the AIS and is responsible for the subsequent recruitment of most AIS-enriched proteins (Jenkins and Bennett, 2001; Hedstrom et al., 2008; Galiano et al., 2012). AnkG depletion not only impairs the accumulation of other AIS components, but also causes a progressive loss of neuronal polarity (Hedstrom et al., 2007; Sobotzik et al., 2009). Precisely how and where ankG interacts with its membrane partners during AIS formation and maintenance is still elusive. The "diffusion and trapping" model proposes that an existing ankG scaffold immobilizes membrane proteins at the AIS (Brachet et al., 2010; Xu and Cooper, 2015). Alternatively, recent data suggest that a preformed complex of ankG and Nav is transported to the AIS (Barry et al., 2014) and that Nav can be directly inserted at the AIS (Akin et al., 2015). Moreover, several results suggest an interplay between ankG and its membrane partners: the establishment of the AIS is impaired in motor neurons depleted for Nav (Xu and Shrager, 2005) and Nfasc186 elimination in Purkinje cells of adult mice results in progressive AIS disassembly (Zonta et al., 2011). In addition, we have shown that perturbing the ankG/Nav interaction by inhibiting the protein kinase CK2 downregulates Nav accumulation at the AIS and subsequently decreases ankG concentration (Bréchet et al., 2008; Brachet et al., 2010). To reveal and characterize the interplay between ankG and its membrane partners, we have examined the role of AIS membrane proteins (Nav and Nfasc186) in AIS assembly and maintenance. We performed shRNA-mediated silencing of Nav and Nfasc186 in cultured neurons during and after the AIS formation as well as in organotypic slices. In all conditions, knockdown of Nav and Nfasc-186 resulted in a cumulative impairment of the AIS stability. Rescue experiments with a full-length Nav1.6 or a minimal construct combining the ankG binding domain of Nav and a membrane targeting motif showed that anchoring of ankG to the plasma membrane via its partners is necessary for its targeting and stable assembly at the AIS. Finally, overexpression of the membrane-anchored ankG-binding construct induced a mislocalization of ankG, suggesting that interaction of ankG with its membrane partners occurs before the insertion of ankG into the AIS.

MATERIALS AND METHODS

Antibodies and Plasmids

A rabbit anti-ßIV spectrin antibody (Eurogentec) was developed against amino acid residues 15–38 of the human sequence (XP 006723369). Mouse monoclonal antibodies to ankG (1:400, N106/36 NeuroMab), Nfasc186 (1:200, L11A/41 NeuroMab) and sodium channels (pan Nav; 1:100; Sigma-Aldrich), rabbit polyclonal antibodies to GFP (1:1000; A11122 ThermoFisher), and chicken polyclonal antibodies to map2 (1:10,000; Abcam) were used. Secondary goat antibodies conjugated to Alexa Fluor 488, 555, 647 (ThermoFisher) or DyLight 405 (Jackson ImmunoResearch Laboratories) were used at 1:400 dilutions.

The nucleotide sequences of rat Nav1.2 fragment coding from amino acid 1081–1203 (wild type [WT], mutated for E1111, mutated for S1112/1123/1124/1126 or mutated for both E and the four S) were obtained by PCR amplification (Expand High Fidelity Taq polymerase, Roche Molecular Biochemicals) on pKv2.1-Nav1.2 plasmids (Bréchet et al., 2008) and inserted into the pEGFP-F (Clontech) in the 5′ of EGFP sequence. The resulting sequence encodes a chimeric protein we called membranous Ankyrin Binding Domain (mABD; see **Figures 6A,B**). All constructs were verified by DNA sequencing (Beckman Coulter Genomics).

Animals, Cultured Hippocampal Neurons and Organotypic Slice Culture

All experiments were carried out in accordance to the guidelines established by the European Animal Care and Use Committee (86/609/EEC) and was approved by the ethic committee of Marseille N°14 (agreement D13-055-8 from French ESR Ministry). For primary neuronal cell culture, pregnant female Wistar rats (Janvier labs) were sacrificed by decapitation and E18 embryos brains were quickly removed. Hippocampal neurons were then prepared according to the Banker-type culture protocol (Kaech and Banker, 2006) and either nucleofected before plating using an Amaxa rat nucleofector kit (Lonza) according to the manufacturer's intrusions or transfected at 8 days *in vitro* (8 div) using Lipofectamine 2000 (ThermoFisher). Cortical slices (350 μm) were made from rat pups of 7 days sacrificed by decapitation. They were cultured for 7 days according to the protocol described by Stoppini et al. (1991) and received microinjections of lentivirus (0.1–0.2 μl; titer from 10^8 to 10^{10} pfu/ml) at the first day in culture.

Lentivus Vectors

The pFUGW plasmid (Lois et al., 2002) was modified to express farnesylated EGFP (from pEGFP-F, Clontech), tdTomato (from ptdTomato-N1, Clontech) or mABD (see above) rather than EGFP. On the 5′ of the ubiquitin-C promoter (PacI site) specific shRNA expression cassette (U6 promoter/T5/shRNA/T5/H1promoter from pFIV-H1/U6 siRNA vector, System Biosciences) was introduced by restriction. The sequence of shRNAs directed against ankG, Nav1 and Nfasc186 have been previously described (Hedstrom et al., 2007). Luciferase shRNA (shLuc 159 also known as SHC007 sigma) was validated as a control (Abad et al., 2010). Modified plasmids were used either directly by transfection of neuronal cells or to produce pseudotyped lentivirus according to Dull et al. (1998). Lentivirus liberated in cell culture medium was concentrated by ultracentrifugation, titrated and kept at −80° in PBS-1% glycerol. The lentivirus production was performed in the lentivector production facility/SFR BioSciences Gerland—Lyon Sud (UMS3444/US8).

Immunocyto- and Immunohistochemistry

Transfected cells were processed for immunofluorescence 6 or 7 days post transfection. They were fixed 10 min in 4%

paraformaldehyde, permeabilized and blocked with 0.1% of Triton X-100 and 0.22% gelatin in 0.1 M phosphate buffer for 30 min and then incubated for 1 h with primary antibodies in the blocking solution. Corresponding secondary antibodies conjugated to Alexa Fluor or DyLight fluorophores were incubated for 1 h. Coverslips were mounted in Fluor Save reagent (EMD). Free-floating organotypic slices kept on hydrophilized PTFE membranes (Millipore) were fixed for 30 min in 4% paraformaldehyde 7 days post infection. They were blocked and permeabilized overnight in PBS containing 0.5% of Triton X-100, 1% Normal Goat Serum (NGS) and 100 μg/ml of Bovine Serum Albumin (BSA). Then, slices were incubated for 4 h in PBS containing 0.25% of Triton X-100, 0.5% NGS and 50 μg/ml of BSA and for 1 h in the corresponding secondary antibodies conjugated to Alexa Fluor fluorophores. Finally, slices were counterstained for nuclei with Hoechst 33342 (1 μg/mL) and dry-mounted in ProLong Gold (Life Technologies).

Images Acquisition and Analysis

For organotypic slices, image acquisition was performed on a Zeiss LSM780 (Zeiss, Jena, Germany) confocal microscope equipped with a 63× 1.4 N.A. oil immersion objective. Three-dimensional *z*-stacks were collected automatically as frame by frame sequential image series (80–120 optical slices). For cultured hippocampal neurons, image acquisition was performed on a Zeiss Axio Imager Z2 equipped with a 40× 1.4 N.A. oil immersion objective. For illustration purposes, image editing was performed using ImageJ software[1] and was limited to Sigma Plus Filter, linear contrast enhancement and gamma adjustment. Quantification was performed using ImageJ. Regions of interest corresponding to proximal axons or dendrites were selected on ankG or GFP images using NeuronJ plugin. The AIS was automatically detected along the proximal axon tracing by a custom ImageJ script (Leterrier et al., 2015)[2], which determines the point of the maximum intensity of the ankG labeling. The beginning and the end of the AIS were determined from either sides at 33% of the maximum intensity along the tracing (Grubb and Burrone, 2010). The intensity of ankG labeling was then measured along the defined AIS segment with a 2 pixel (0.325 μm) width for each neuron. The mean intensity along the AIS of the transfected neurons was normalized by dividing it by the mean intensity along the AIS of untransfected surrounding neurons in the same image, allowing to circumvent variations related to the immunolabeling. All intensities were corrected for background signal (taken as the mode of the whole image histogram). To determine the intensity in channels other than ankG, the AIS segment region was detected on ankG labeling, then reported to the other channel and the intensity was measured as described above. Results are expressed as mean ± SEM. AIS/dendrite ratio is the mean labeling intensity of the proximal axon divided by the mean labeling intensity of three dendrites. The polarity index (for ankG quantification in organotypic slices) is the ratio of the mean labeling intensities: (AIS − soma) divided by (AIS + soma). The width was measured perpendicularly to the axon at the point of maximum intensity of ankG along the AIS. Statistical analyses were performed using Prism 5 (Graphpad Software, La Jolla, CA, USA). Significances were tested using two-tailed unpaired *t* tests (two conditions) or one-way ANOVA followed by Kruskal-Wallis post-test (three or more conditions). In all figures significance is coded as: $^{*}p < 0.05$; $^{**}p < 0.01$; $^{***}p < 0.001$.

Electrophysiology and Data Analysis

Seven or eight days post transduction, organotypic cortical slices were transferred into a recording/perfusion chamber placed on the fixed-stage of an upright microscope (BX51WI, Olympus; fitted with 4× air and 40× water-immersion objectives, a Photonics VX55 camera and a BX-FLA illumination system) and superfused at 1–3 ml/min with artificial cerebrospinal fluid (ACSF) maintained at room temperature and saturated with 95% O_2 and 5% CO_2. Voltage-clamp recordings were performed with patch pipettes pulled from borosilicate glass (World Precision Instruments) and having an electrode resistance of 1.5–2.5 MΩ. Selective recording of Na^+ currents was performed by using patch pipettes filled with an internal solution containing (in mM) 140 CsFl (to block K^+ and hyperpolarization-activated cation currents), 1 $MgCl_2$, 10 Hepes, 2 EGTA, 2 ATP, 0, 2 GTP (pH7, 4) and a modified ACSF solution (Na^+ current isolation solution) containing (in mM): 120 NaCl, 3 KCl, 26 $NaHCO_3$, 10 Glucose, 1 $MgCl_2$. This external solution did not contain $CaCl_2$ (to prevent Ca^{2+} currents) but was added with 10 mM tetraethyl-ammonium, 4 mM 4-Aminopyridine, 3 mM kynurenic acid (Sigma Aldrich) to attenuate K^+ currents and glutamate synaptic transmission. Separate recording sessions were also performed with 500 nM TTX (Tetrodotoxin, Ascent Scientific) added to the Na^+ current isolation solution in order to check that the recorded current was carried by Na^+ ions. Na^+ currents were evoked by voltage ramps reaching +40 mV from a holding potential of −90 mV and applied at a speed of 0.2 mV/ms.

All recordings were performed exclusively from GFP positive neurons using an Axopatch 200B (Molecular Devices). A computer interfaced to a 12-bit A/D converter (Digidata 1322A using Clampex 9.x; Molecular Devices LLC) controlled the voltage-clamp protocols and data acquisition. The signals were filtered at 5 KHz and digitized at 20 KHz. Uncompensated series resistance was 8 ± 0.5 MΩ. Analysis was conducted in Clampfit 10.3 (Molecular Devices) and SigmaPlot 12 (Systat Software Inc.). After off line linear leak subtraction, the following parameters were measured: threshold voltage for both Na^+ persistent current (INaP) and Na^+ transient currents (INaT), peak voltage for INaP and peak amplitudes for both INaP and INaT. Membrane potentials are uncorrected for the liquid junction potential (8.9 mV). Data are shown as mean ± SEM. Mann-Whitney rank sum test was used to test for statistical differences with a significance level of $p < 0.05$.

---

[1] http://rsb.info.nih.gov/ij/

[2] https://github.com/cleterrier/ProFeatFit

RESULTS

Nav1 Knockdown Reduces Na$^+$ Current in Organotypic Slices and Impairs AnkG Concentration

We and others have demonstrated that Nav1 clustering at the AIS requires a direct interaction between the ankyrin-binding-domain (ABD) of Nav channels and the MBD of ankG (Garrido et al., 2003; Gasser et al., 2012; Montersino et al., 2014). We wanted to know if the Nav-ankG interaction could conversely contribute to ankG concentration and AIS integrity. We first assessed the effect of Nav depletion on ankG concentration at the AIS in cultured organotypic slices (Stoppini et al., 1991). Cortical slices obtained from 7 day rats were transduced with a recombinant lentivirus expressing a previously validated shRNA directed against Nav1.1/Nav1.2/Nav1.3 (shNav; Xu and Shrager, 2005; Hedstrom et al., 2007; Hien et al., 2014) or against ankG (shAnkG; Hedstrom et al., 2007; Leterrier et al., 2011b). After 7 days, we evaluated the AIS integrity using immunostaining against Nav and ankG. The membrane-targeted GFP (mGFP) marker co-expressed with the shRNA allowed visualizing the full morphology of the transduced neurons (**Figure 1**). AnkG staining was readily observable in 86% of the neurons transduced with a control shRNA (**Figures 1A,D**) but was detected in only a small proportion of neurons expressing shAnkG (**Figures 1B,D**). In neurons transduced with shNav, ankG accumulation was observed in only 48% of the neurons (**Figures 1C,D**). As compared to control neurons, Nav1-depleted neurons had a significantly reduced ankG concentration at the AIS (ankG ratio—mean intensity of ankG labeling at the AIS and normalized to ankG labeling in surrounding non-infected neurons—down from 1.10 ± 0.06 in shCtrl neurons to 0.72 ± 0.05 in shNav neurons, **Figure 1E**). These results demonstrate that the depletion of Nav induces a significant decrease of ankG accumulation at the AIS.

To evaluate how Na$^+$ currents were affected by ankG or Nav silencing, we performed electrophysiological recording on cultured slices, 7–8 days after infection. In large neurons with fully developed processes, space clamp problems prevent adequate voltage clamp recording of rapidly inactivating, i.e., transient, Na$^+$ current (INaT). However, all the Nav types expressed in central nervous system neurons generate also a slowly inactivating, i.e., persistent, Na$^+$ current (INaP) that follows INaT (Mantegazza et al., 2005; Rush et al., 2005; Estacion and Waxman, 2013). Using depolarizing voltage ramps at adequate speed, we were able to record both correctly clamped INaP and unclamped INaT (Del Negro et al., 2002). The recorded currents were suppressed in the presence of TTX, showing that TTX-sensitive Nav channels generate these currents. In all the neurons transduced with the control shRNA, voltage ramps generated a large INaP that started to activate

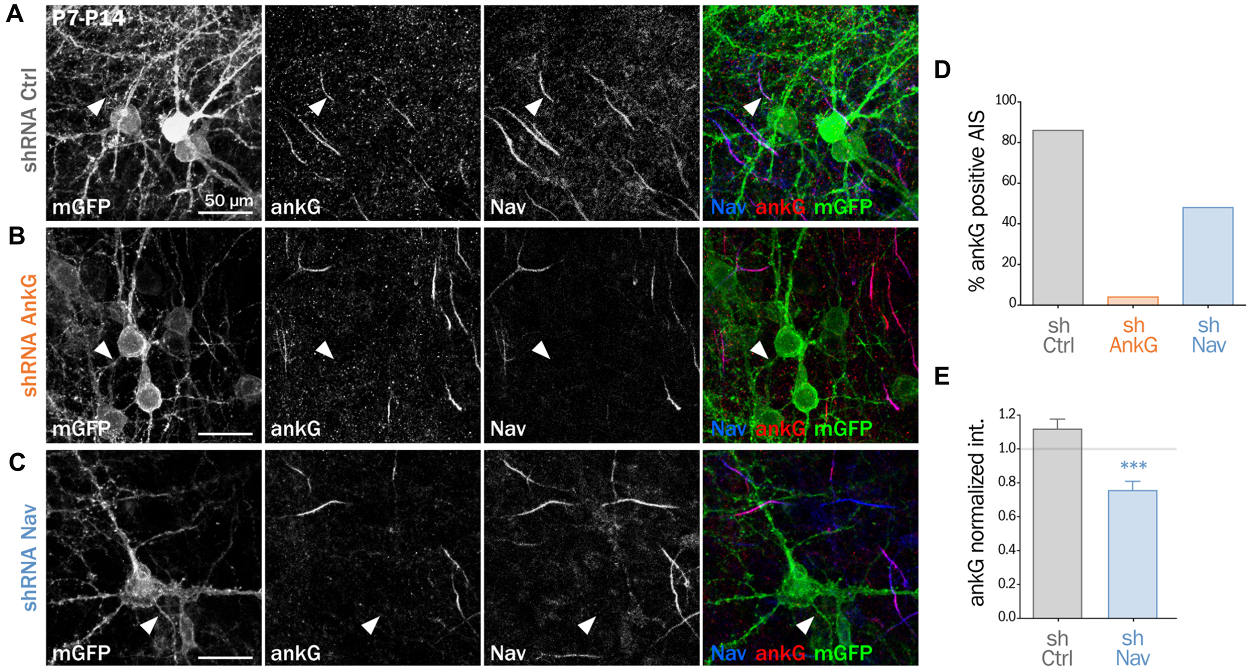

FIGURE 1 | Knockdown of Nav channels downregulates the axon initial segment (AIS) in organotypic slices. Organotypic cortical slices prepared from postnatal day 7 rats were infected with a lentivirus co-expressing membranous GFP (mGFP) and shRNA directed against ankG (shAnkG), Nav (shNav) or luciferase as control (shCtrl). Seven days post-infection, slices were fixed, immunostained for GFP, ankG and Nav. **(A–C)** Maximum intensity projection of 15–20 optical slices. Scale bar: 50 µm. **(D)** Percentage of infected neurons with an observable AIS (shCtrl *n* = 80; shAnkG *n* = 27; shNav *n* = 97; sum of three independent experiments). **(E)** Ratio of the mean fluorescence intensity for ankG labeling at the AIS in transfected neurons (where the AIS was still detected) compared to the surrounding untransfected cells (shCtrl 1.10 ± 0.06, *n* = 69; shNav: 0.72 ± 0.05, *n* = 47; three independent experiments).

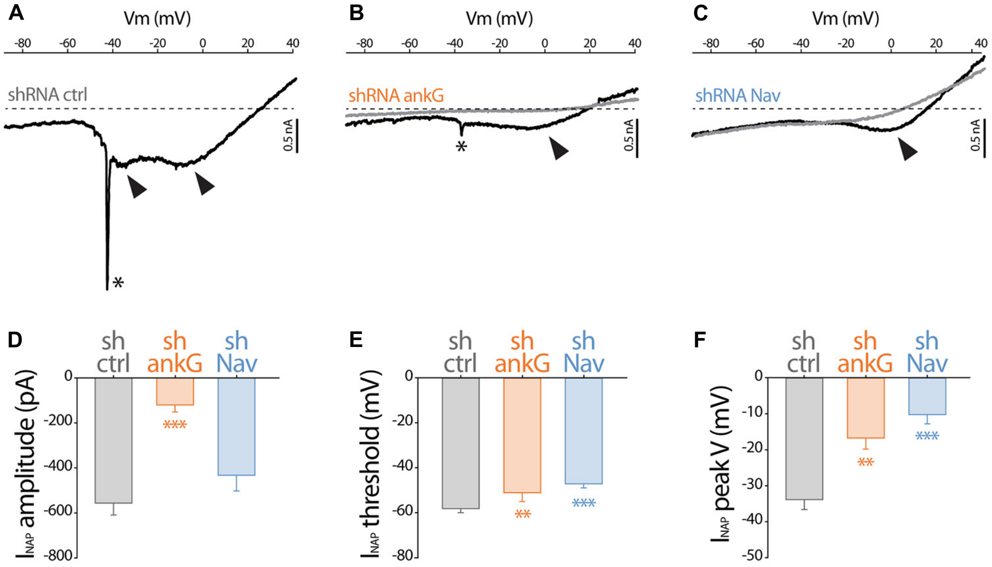

FIGURE 2 | Effect of ankG and Nav knockdown on sodium currents. Patch-clamp recordings obtained from mGFP expressing neurons from organotypic cortical slices, 7–8 days post infection with shCtrl, shAnkG or shNav. **(A–C)** Raw traces of Na^+ currents evoked by voltage ramps (from holding potential −90 mV to +40 mV at 0.2 mV/ms) in the absence (black) or presence (gray) of 500 nM TTX. The asterisks and arrows respectively indicate transient Na^+ currents and components of the Na^+ persistent current (INaP). **(D–F)** Characteristics of the INaP in the different conditions (shCtrl *n* = 19; shAnkG *n* = 5; shNav *n* = 9). **(D)** averaged peak amplitude; **(E)** peak threshold; **(F)** maximum peak voltage.

at −58.2 ± 1.8 mV (**Figures 2A,D**) and exhibited usually two components (**Figure 2A**), with the largest peaking at −33.9 ± 2.7 mV (**Figure 2D**). As expected, in most of these neurons (13/19), unclamped INaT were also generated and appeared as a single spike (star in **Figure 2A**; average threshold: −48.5 ± 1.4 mV; average peak amplitude: 2467 ± 648 pA). In neurons expressing shAnkG, INaP was affected both in terms of amplitude (strong reduction in 4/5 neurons and null current in 1/5 neuron; **Figures 2B,D**) and in terms of voltage dependence (depolarizing shift of the activation threshold and peak voltage; **Figures 2E,F**). In addition, in these ankG depleted neurons, INaT was in most cases absent (4/5 neurons) or extremely small (1/5 neurons, trace presented in **Figure 2B**; threshold: −39 mV; peak amplitude: 208 pA). In the neurons expressing shRNA against Nav, INaP exhibited significant changes in voltage dependence (more depolarized threshold and peak voltage, **Figures 2E,F**), but its average amplitude was not significantly lower than in shCtrl neurons (**Figure 2D**). Remarkably, INaT was absent in all the Nav-depleted neurons (9/9 neurons). Altogether these results confirm that Nav channels were functionally eliminated in our shRNA experiments.

Nav or Nfasc186 Knockdown Impair AIS Maintenance in Cultured Neurons

To decipher the mechanisms involved in the interplay between Nav and ankG, we tested the effect of Nav depletion in cultured hippocampal neurons, an amenable model for the analysis of neuronal morphology and polarity (Kaech and Banker, 2006). Neurons were maintained for 8 div, ensuring that polarity was well established, then transfected with shRNA constructs, and fixed 6 days later (14 div; **Figure 3**). We first verified that the ankG labeling intensity was strongly reduced in shAnkG transfected neurons, compared to untransfected surrounding neurons (**Figure 3B**): ankG intensity ratio between transfected and untransfected neurons was 0.97 ± 0.03 for shCtrl, but only 0.15 ± 0.01 for shAnkG (**Figure 3F**). Similarly, we checked the efficiency of Nav depletion and found that the Nav intensity ratio was 0.96 ± 0.04 for shCtrl and 0.37 ± 0.04 for shNav (**Figure 3E**). As expected, AnkG depletion also resulted in Nav disappearance (Nav ratio 0.35 ± 0.03, **Figure 3E**). Consistently with our results in slices, Nav1 depletion was accompanied by a ∼50% decrease in ankG labeling in the AIS (ankG ratio 0.48 ± 0.04, **Figure 3F**), but did not affect the position and length of the AIS that remained unchanged. Thus, Nav1 expression is required for ankG concentration at the AIS, and therefore for AIS maintenance. We reasoned that Nav could have a stabilizing effect by anchoring ankG to the membrane. Since the MBD of ankG can bind both to Nav and CAMs such as Nfasc186, we examined whether Nfasc186 can also participate in ankG stabilization at the AIS, as suggested by data obtained after conditional genetic depletion (Zonta et al., 2011). Six days after transfection of 8 div neurons with a validated shRNA against Nfasc186 (Hedstrom et al., 2007), ankG accumulation at the AIS was quantitatively analyzed. AnkG labeling was significantly reduced in neurons depleted for Nfasc186 (1.02 ± 0.05 for shCtrl, 0.59 ± 0.03 for shNF, **Figures 3D,G**). This additional observation suggests that elimination of membrane partners of ankG (Nav or CAMs) is sufficient to induce AIS destabilization in polarized neurons.

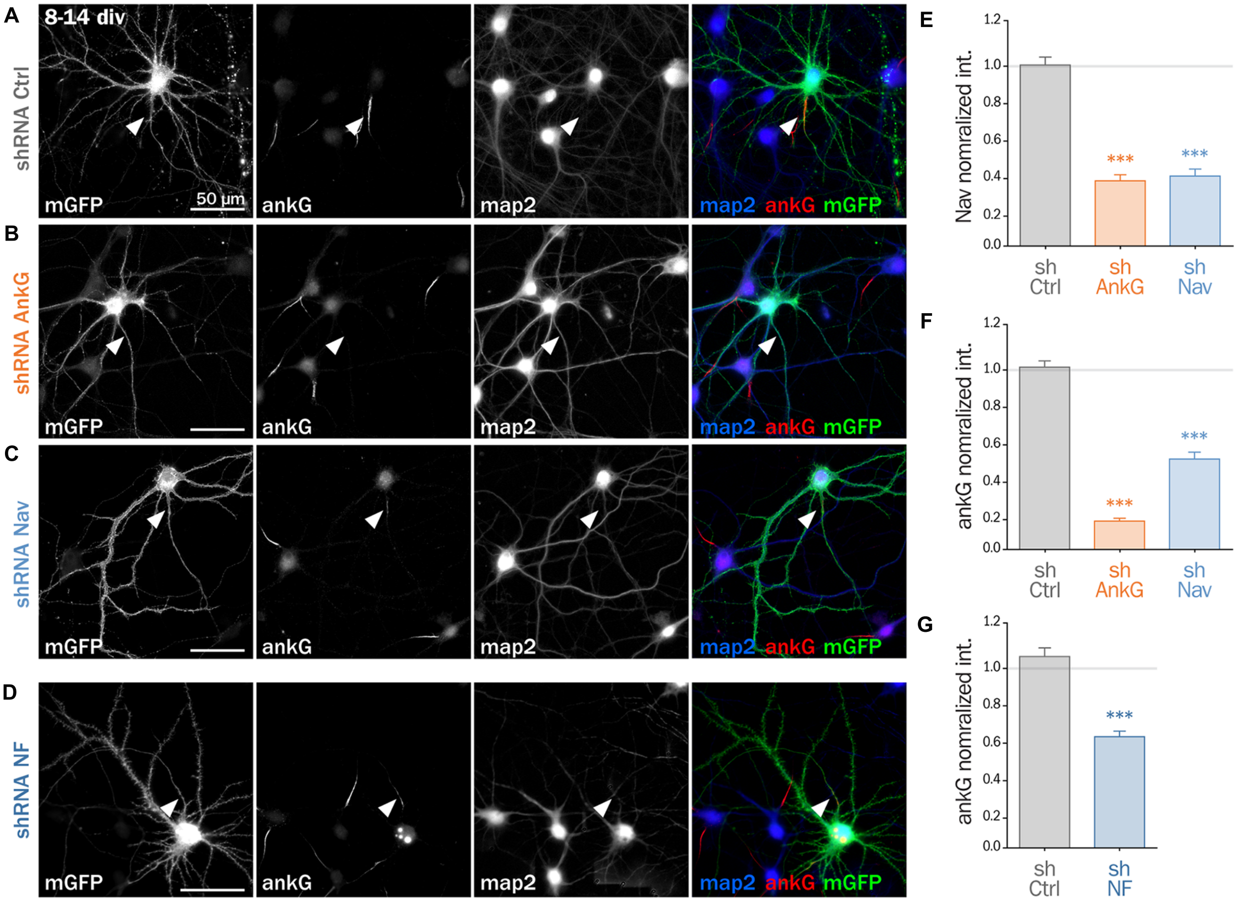

FIGURE 3 | Knockdown of AIS membrane components perturbs AIS maintenance. Cultured rat hippocampal neurons transfected at 8 days *in vitro* (8 div) with mGFP and shCtrl **(A)**, shAnkG **(B)**, shNav **(C)** or shNF **(D)**, fixed 6 days later (14 div) and then immunostained for GFP, ankG, map2 and Nav. Arrowheads indicate the AIS of transfected neurons. **(E)** Ratio of the mean fluorescence intensity for Nav1 labeling at the AIS of transfected cells compared to surrounding untransfected cells (shCtrl 0.96 ± 0.04, *n* = 43; shAnkG 0.35 ± 0.03, *n* = 43; shNav 0.37 ± 0.04, *n* = 40; three independent experiments). **(F,G)** Ratio of the mean fluorescence intensity for ankG labeling at the AIS in transfected neurons compared to surrounding untransfected cells (**F**: shCtrl 0.97 ± 0.03, *n* = 116; shAnkG *n* = 0.15 ± 0.01, *n* = 94; shNav 0.48 ± 0.04, *n* = 123; six independent experiments. **G**: shCtrl 1.02 ± 0.05, *n* = 36; shNF 0.59 ± 0.03, *n* = 64; three independent experiments).

Nav or Nfasc186 Knockdown Impairs AIS Formation

Next, we assessed if ankG membrane partners are also required for proper AIS formation in young neurons. In developing hippocampal neurons in culture, polarity is established around 2 div and is quickly followed by AIS assembly (Dotti et al., 1988; Hedstrom et al., 2007). Freshly dissociated hippocampal neurons were thus nucleofected in order to express shRNA prior to AIS formation and then fixed after 7 div (**Figures 4A–E**). We first checked that the expression of each shRNA led to the specific down regulation of its corresponding targets: ankG (ankG ratio 1.08 ± 0.04 for shCtrl; 0.12 ± 0.03 for shAnkG, **Figure 4G**), Nav1 (Nav ratio 1.08 ± 0.12 for shCtrl; 0.30 ± 0.03 for shNav, **Figure 4F**) or Nfasc186 (Nfasc186 ratio 1.12 ± 0.09 for shCtrl, 0.26 ± 0.03 for shNF, **Figure 4H**). As observed in mature neurons, ankG concentration was impaired in neurons depleted for either Nav channels (ankG ratio 0.65 ± 0.05 for shNav, **Figure 4G**) or Nfasc186 (ankG ratio 0.75 ± 0.03 for shNF, **Figure 4I**). In addition, we found that the effects of Nav or Nfasc186 depletion on AIS formation were cumulative, as simultaneous depletions using both shRNAs (shNav + shNF) further reduced ankG concentration at the AIS (0.47 ± 0.03, **Figure 4I**). Altogether, these data demonstrate that the membrane partners of ankG, Nav and Nfasc186 are essential for AIS assembly.

Nav1.6-GFP Expression Rescues the AnkG Downregulation Induced by Depleting Nav or Nfasc186

If Nav channels specifically contribute to AIS formation and integrity, ankG downregulation induced by Nav depletion should be rescued by the co-expression of an shRNA-resistant Nav construct. To test this hypothesis, we used a full length Nav1.6-GFP that is resistant to our shRNA construct against Nav (three bases mismatch; Gasser et al., 2012). Nav1.6-GFP and a

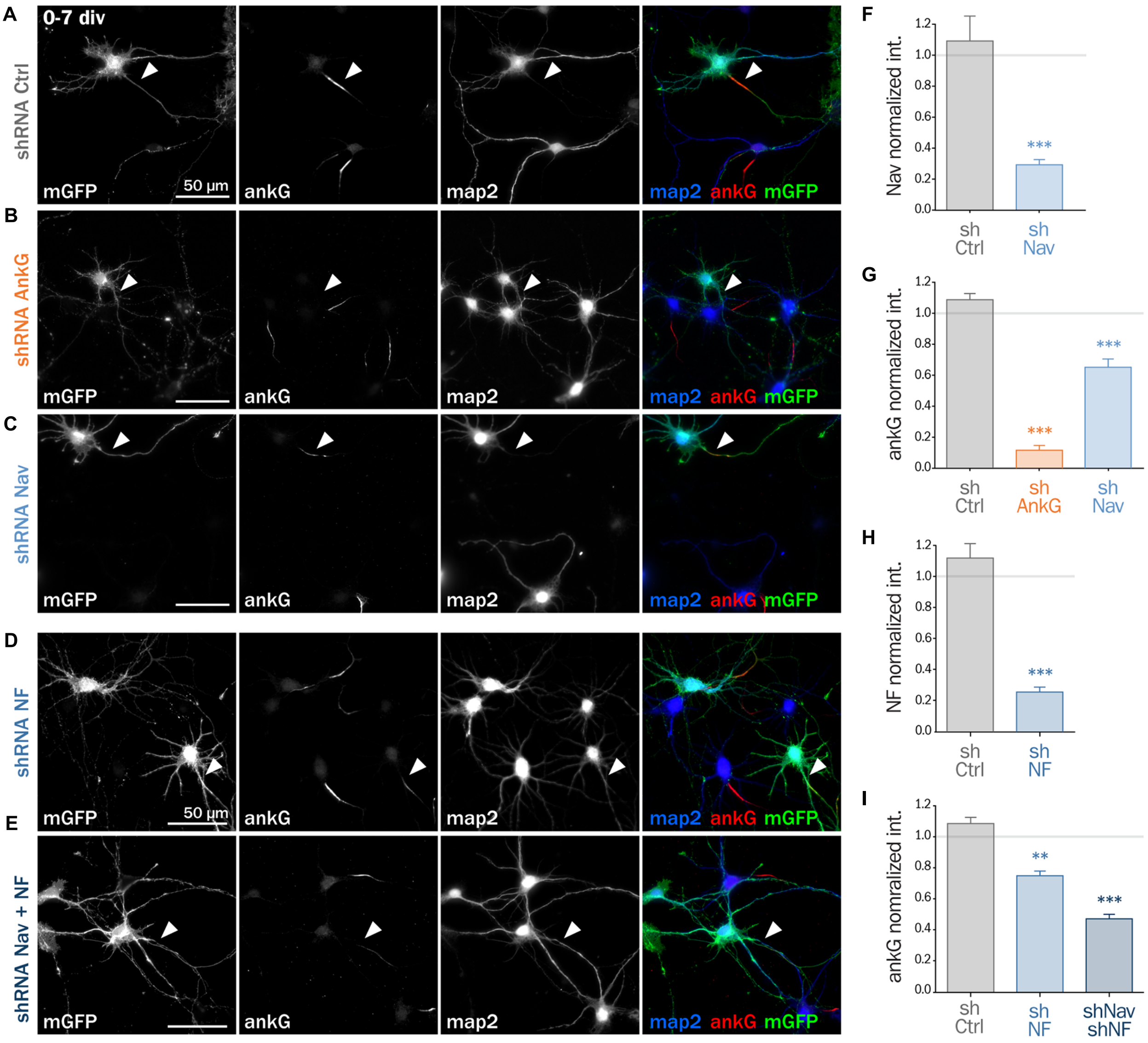

FIGURE 4 | Knockdown of AIS membrane components impairs AIS formation. Rat hippocampal neurons were transfected before plating (0 div) with mGFP and shCtrl **(A)**, shAnkG **(B)**, shNav **(C)**, shNF **(D)** or shNav + shNF **(E)**. Seven days later (7 div), neurons were fixed and immunostained for GFP, ankG, map2 and Nav or Nfasc186. Arrowheads indicate the AIS of transfected neurons. **(F)** Ratio of the mean fluorescence intensity for Nav1 labeling at the AIS of transfected neurons compared to surrounding untransfected neurons (shCtrl 1.08 ± 0.12, *n* = 41; shNav 0.30 ± 0.03, *n* = 55; three independent experiments). **(H)** Ratio of the mean fluorescence intensity for Nfasc186 labeling at the AIS of transfected neurons compared to surrounding untransfected neurons (shCtrl 1.12 ± 0.09, *n* = 20; shNF 0.25 ± 0.03, *n* = 25; two independent experiments). **(G,I)** Ratio of the mean fluorescence intensity for ankG labeling at the AIS of transfected neurons compared to surrounding untransfected neurons (**G**: shCtrl 1.08 ± 0.04, *n* = 80; shAnkG 0.12 ± 0.03, *n* = 40; shNav 0.65 ± 0.05, *n* = 39; three independent experiments. **I**: shCtrl 1.08 ± 0.04, *n* = 80; shNF 0.75 ± 0.03, *n* = 43 shNav + shNF 0.47 ± 0.03, *n* = 109; three independent experiments).

shNav plasmid containing soluble Td-Tomato as transfection marker were co-expressed either in freshly dissociated or mature (8 div) hippocampal neurons that were analyzed 6–7 days later. By contrast with mGFP that filled the entire neuron, Nav1.6-GFP was concentrated in the soma and at the AIS of co-transfected cells (**Figures 5A–C**). Notably, over-expression of Nav1.6-GFP alone did not alter the AIS morphology or ankG content (not shown). Quantitative analysis showed that ankG concentration was restored at the AIS by Nav1.6-GFP co-expression either in young neurons (0.56 ± 0.07 for shNav + mGFP, 1.09 ± 0.08 for shNav + Nav1.6-GFP, **Figure 5F**) or in mature neurons (0.37 ± 0.05 for shNav + mGFP, 0.92 ± 0.06 for shNav + Nav1.6-GFP, **Figure 5G**). These data validate the specificity of the effects observed with the shNav.

If ankG stabilization depends on ankG membrane anchoring *per se* and not on the partner identity, the overexpression of Nav1.6-GFP should also be able to cross-rescue Nf186 depletion (**Figures 5D,E**). When Nav1.6-GFP was co-expressed with

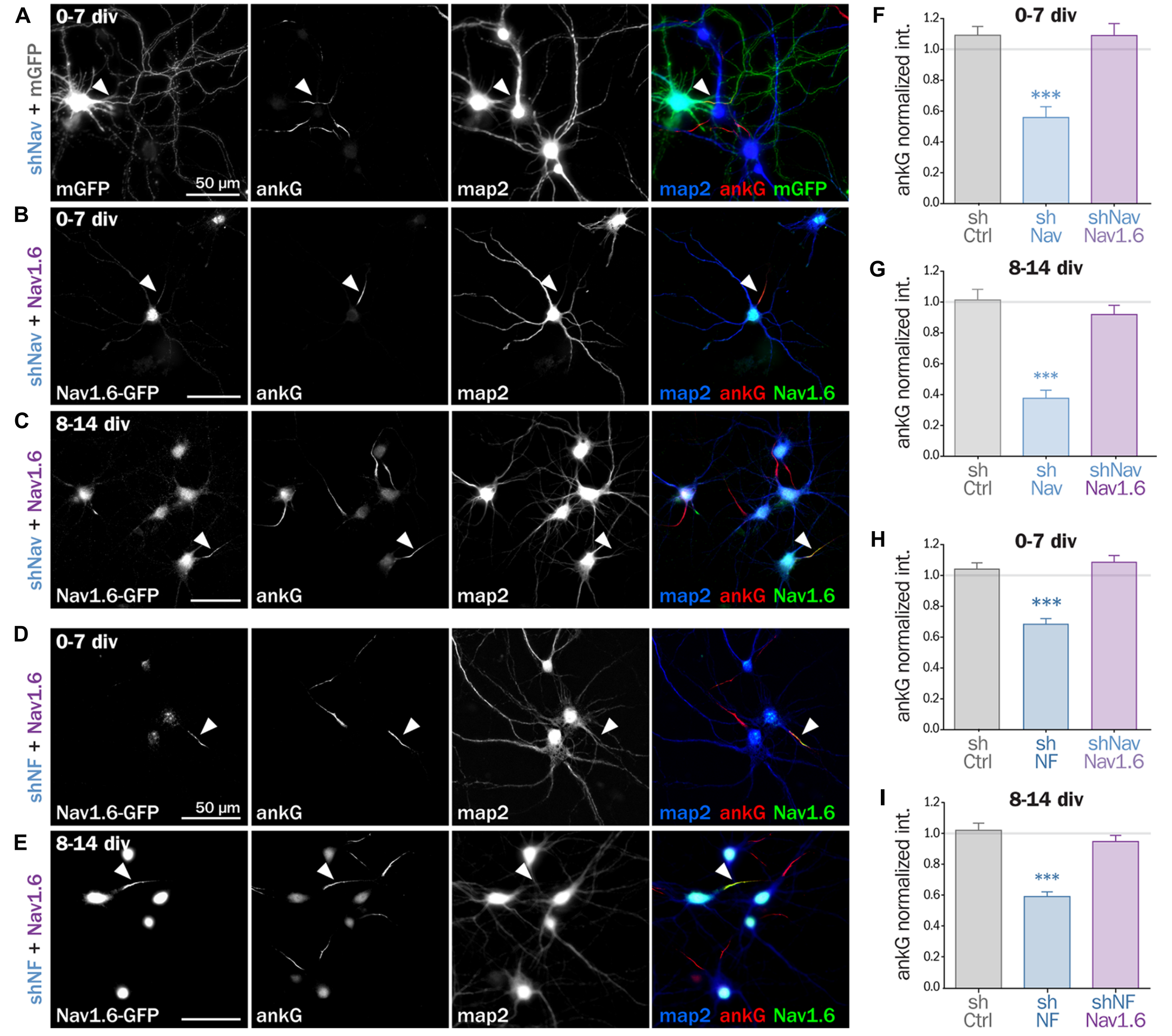

FIGURE 5 | Nav1.6 rescue the AIS downregulation induced by Nav knockdown, but also by Nfasc186 knockdown. Rat hippocampal neurons co-transfected at 0 div or 8 div with mGFP or Nav1.6-GFP and shNav **(A–C)** or shNF **(D,E)** and fixed 6 or 7 days later (0–7 div or 8–14 div) for subsequent immunostaining for GFP, ankG and map2. Arrowheads indicate the AIS of transfected neurons. **(F–I)** Normalized mean fluorescence intensity for ankG labeling at the AIS of 0–7 div **(F,H)** or 8–14 div **(G,I)** transfected neurons. (**F**: shCtrl 1.09 ± 0.06, *n* = 54; shNav 0.56 ± 0.07, *n* = 21, shNav + Nav1.6 1.09 ± 0.07, *n* = 41; three independent experiments. **G**: shCtrl 1.01 ± 0.07, *n* = 28; shNav 0.37 ± 0.05, *n* = 39; shNav + Nav1.6 0.92 ± 0.06, *n* = 30; two independent experiments. **H**: shCtrl 1.04 ± 0.04, *n* = 61; shNF 0.68 ± 0.04, *n* = 64; shNF + Nav1.6 1.09 ± 0.04, *n* = 68; three independent experiments. **I**: shCtrl 1.02 ± 0.05, *n* = 36; shNF 0.59 ± 0.03, *n* = 64; shNF + Nav1.6 0.95 ± 0.04, *n* = 58; three independent experiments).

the shRNA against Nfasc186, we indeed observed that ankG concentration at the AIS was restored in both young (0.68 ± 0.03 for shNF + mGFP, 1.09 ± 0.04 for shNF + Nav1.6-GFP, **Figure 5H**) and mature neurons (0.59 ± 0.03 for shNF + mGFP, 0.95 ± 0.04 for shNF + Nav1.6-GFP **Figure 5I**). This cross-rescue experiment demonstrates that one ankG membrane partner can be replaced by another and that the identity of the partner is less important than the membrane anchoring itself to drive AIS formation and maintenance.

Expression of a Chimeric Membrane-Anchored AnkG Partner Rescues AIS Formation

Next, we wanted to directly prove that ankG association to the membrane *via* a protein partner contributes to ankG targeting and assembly. We devised a minimal chimeric protein bearing the well-described ABD from the intracellular loop II-III of Nav1.2 (Garrido et al., 2003; Lemaillet et al., 2003; Gasser et al., 2012) fused to the farnesylated form of GFP that associates to the plasma membrane (**Figures 6A,B**). When this membrane ABD (mABD) construct was expressed in freshly dissociated hippocampal neurons, it was highly concentrated along the proximal axon with an AIS/dendrite ratio of 5.46 ± 0.53 (**Figures 6C,F**). As ABD binding to ankG is known to be impaired by the mutation of glutamate residue Nav1.2 E1111 or the four serine residues implicated in CK2 regulation (Bréchet et al., 2008), we produced three mutant constructs where E1111, the four serine residues or all these five amino-acids were replaced by alanine (mABD-EA, mABD-4SA and mABD-E4S; **Figure 6B**). These mutations abolished the ability of mABD to be concentrated to the AIS, resulting in an AIS/dendrite ratio close to 1 (**Figure 6F**). This indicates that mABD concentration at the AIS is under the control of a phospho-dependent interaction with ankG. We next assessed whether the expression of mABD was able to rescue the ankG downregulation induced by either Nav or Nf186 depletion. In young neurons, mABD expression rescued the deficit in ankG accumulation caused by depletion of either Nav (ankG ratio 1.47 ± 0.15 for shNav + mABD; **Figures 6D,F,G**) or Nfasc186 (ankG ratio 1.27 ± 0.07 for shNF + mABD, **Figures 6E,H**). Notably, we observed that the over-expression of mABD by itself up-regulated AIS components such as ankG, ß4-spectrin and Nfasc186 (ratios of 1.50 ± 0.04 for ankG, 1.52 ± 0.09 for ß4 spectrin, and 1.62 ± 0.14 for NF, **Figures 6I,J,L**). By opposition, endogenous Nav were strongly downregulated, indicating that the ABD domain acts as a dominant negative on endogenous Nav targeting or anchoring during AIS formation (Nav ratio 0.67 ± 0.04, **Figures 6K,L**). In addition, mABD expression affected the morphology of the AISs that were wider, but not longer, than those of untransfected neurons (length 17.7 ± 0.8 μm for untransfected, 18.4 ± 0.7 μm for mABD, width 0.76 ± 0.02 μm for untransfected, 1.78 ± 0.07 μm for mABD, **Figures 6M,N**). Altogether, these experiments performed during AIS formation show that mABD is able to rescue the absence of Nav or Nfasc186, and that its overexpression upregulates the whole AIS assembly, leading to a wider AIS that accumulates a higher density of components at the exception of Nav channels.

mABD Expression in Mature Neurons Results in AnkG Ectopic Localization

Next, we assessed the effect of mABD expression in mature neurons. First, we turned back to post-natal cortical organotypic slices, and examined neurons transduced with mABD (together with a control shRNA). In these mature neurons with an already assembled AIS, mABD was localized in the whole neuron, with no concentration at the AIS (**Figure 7A**). This contrasted with the AIS localization observed when expressing mABD during AIS formation in cultured neurons (see above). Interestingly, this non-polarized expression of mABD was accompanied by a partial delocalization of ankG, which was found to accumulate in the soma and proximal dendrites in addition to the AIS (**Figure 7A**). This was evidenced by the drop of the AIS/soma polarity index for ankG labeling in neurons expressing mABD compared to neurons expressing the neutral marker mGFP (0.88 ± 0.03 for mGFP, 0.14 ± 0.09 for mABD, **Figure 7C**). We reasoned that this difference in mABD localization observed during AIS formation compared to the already assembled AIS could be explained by the presence, in the AIS of mature neurons, of strongly anchored endogenous Nav that compete with the mABD construct for ankG binding sites. To test this hypothesis, the mABD together with the shRNA against Nav channels were expressed in organotypic slices. In contrast to control neurons, in the Nav-depleted neurons, the mABD was concentrated to the AIS and did not delocalize ankG (**Figures 7B,C**; ankG polarity index for mABD + shNav: 0.79 ± 0.03). Thus, the expression of mABD in mature neurons depleted for Nav results in a proper stabilization of ankG at the AIS. This also means that mABD expression in organotypic slices rescues the ankG downregulation observed in neurons depleted for Nav (see **Figure 1**). To functionally confirm that Nav depletion did occur in these neurons having a morphologically normal AIS, we performed electrophysiological experiments on neurons co-expressing shNav and mABD (**Figures 7D,E**). In these neurons, no INaT could be recorded (7/7 neurons). More remarkably, INaP was either absent (4/7 neurons) or extremely small with an average amplitude as small as 42, 3 ± 21, 5 pA (3/7 neurons; **Figures 7D,E**). In the seven slices from which these mABD positive neurons were patched, we also recorded Na^+ currents from non-transfected neurons in which the electrophysiological parameters of both INaT and INaP were similar to the currents recorded in control neurons as shown in **Figure 2**. These results demonstrate that a morphologically normal AIS can be maintained in neurons devoid of Na^+ currents. To confirm the ectopic localization of ankG observed in organotypic slices, we assessed the effect of overexpressing mABD in cultured mature hippocampal neurons (**Figures 7F–J**). In these neurons, mABD was also localized in the whole neuron with no preferential accumulation at the AIS (AIS/dendrite ratio for mABD 1.15 ± 0.09, **Figures 7F,I**). mABD over-expression also produced a mislocalization of ankG, that appeared in the cell body and proximal dendrites in addition to the AIS (AIS/dendrite ratio from 10.79 ± 0.73 in control neurons to 6.64 ± 0.57 in mABD-expressing neurons, **Figures 7F,J**). We determined if the two properties of the mABD construct (membrane association and ankG binding) were necessary for this delocalization of ankG. The ABD construct devoid of the farnesylation motif was expressed in a non-polarized manner, and was not able to mislocalize ankG (**Figures 7G,J**). Similarly, the mABD-E4S mutant that lacks ankG binding was localized in a non-polarized manner, and did not delocalize ankG from the AIS (**Figures 7H,J**). Overall, the expression of mABD in mature neurons from slices and cultures shows that binding of ankG to its membrane partners is important for its stabilization at the AIS. Furthermore, the ectopic localization of ankG after mABD expression suggests that ankG binding by mABD is sufficiently strong to perturb ankG targeting and that the association of ankG with its membrane partners occurs upstream of their insertion into the AIS scaffold.

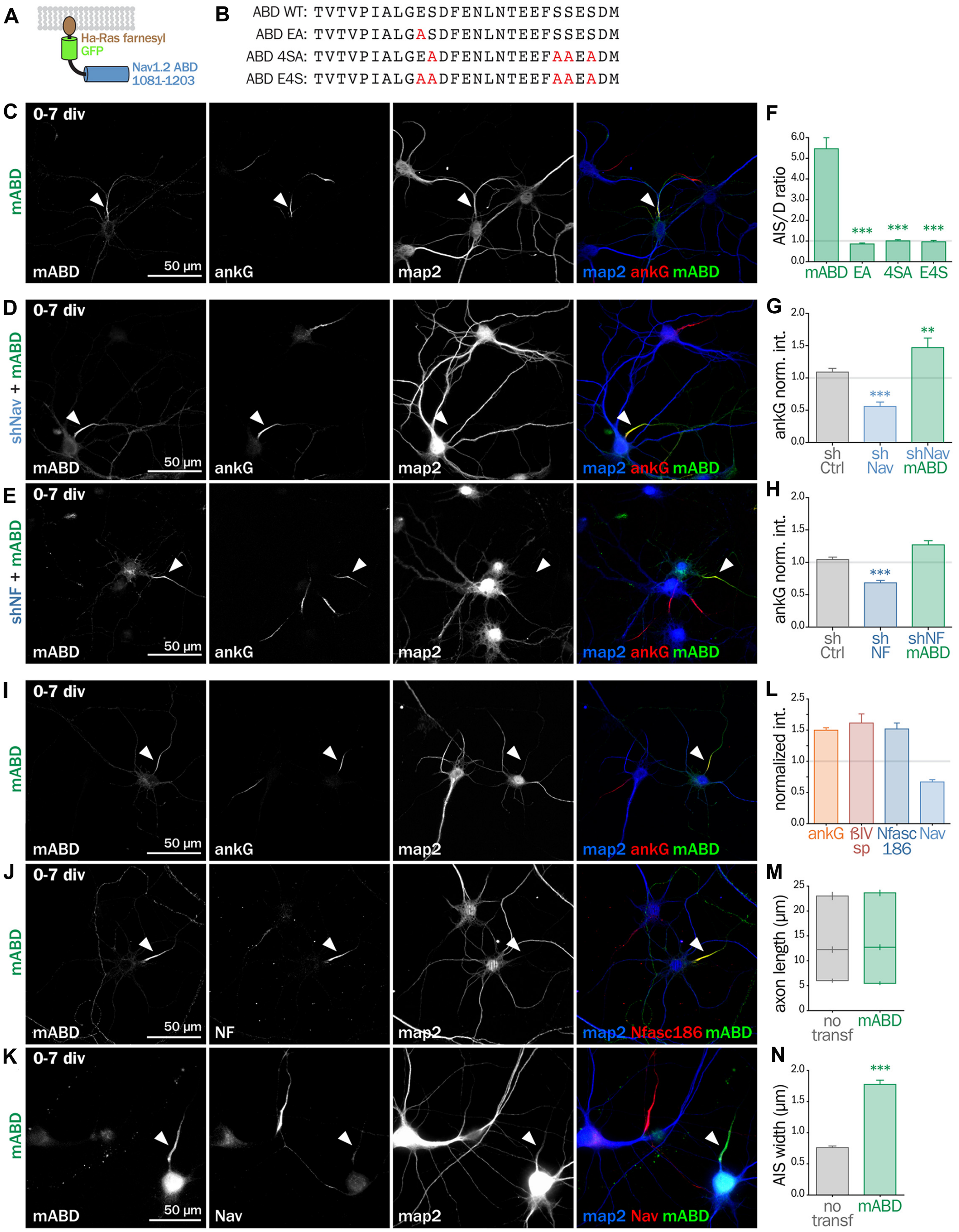

FIGURE 6 | Synthetic mABD construct rescues Nav or Nfasc186 knockdown and upregulates AIS formation. (A) Schematic representation of the mABD construct composed of the amino-acids 1081–1203 of rat Nav1.2 fused to a GFP with a farnesylation motif from Ha-Ras in its C-terminal. **(B)** Alignment of wild type (WT) and mutated sequences corresponding to the rat Nav1.2 (aa 1102–1128) Ankyrin Binding Domain (ABD). The mutated amino-acids involved in ankG binding are in red. Rat hippocampal neurons transfected at 0 div with mABD alone **(C,I,J,K)** or in association with shNav **(D)** or shNF **(E)**, fixed 7 days later (div 7), and immunostained for GFP, map2 and ankG **(C–E,I)**, Nfasc186 **(J)** or Nav **(K)**. Arrowheads indicate the AIS of transfected neurons. **(F)** Ratio of the mean fluorescence intensity for GFP labeling in the proximal axon compared to the mean of three dendrites **(D)** in each transfected neuron (mABD 5.46 ± 0.54, *n* = 77, mABD-EA 0.86 ± 0.06, *n* = 37, mABD-4SA 1.01 ± 0.05, *n* = 36; mABD-E4S 0.96 ± 0.07, *n* = 32; two independent experiments). **(G,H)** Ratio of the mean fluorescence intensity for ankG labeling at the AIS of transfected neurons compared to surrounding untransfected neurons (**G**: shCtrl 1.09 ± 0.06, *n* = 54; shNav 0.56 ± 0.07, *n* = 21; shNav + mABD 1.47 ± 0.15, *n* = 23; two independent experiments. **H**: shCtrl 1.04 ± 0.04, *n* = 61; shNF 0.68 ± 0.04; *n* = 64; shNF + mABD 1.27 ± 0.07, *n* = 49; two independent experiments). **(L)** Ratio of the mean fluorescence intensity for ankG, βIV-spectrin (βIVsp), Nfasc186 or Nav labeling at the AIS of transfected neurons compared to surroundings untransfected neurons (ankG 1.50 ± 0.04, *n* = 146; βIVsp 1, 52 ± 0.10, *n* = 49; NF 1, 62 ± 0.14, *n* = 26; Nav0.67 ± 0.04; *n* = 33; 2–6 independent experiments). **(M,N)** Length and width of the AIS in mABD-transfected neurons (untransfected cells AIS width 0.76 ± 0.03 µm, *n* = 61; mABD 1.78 ± 0.07 µm, *n* = 60; two independent experiments).

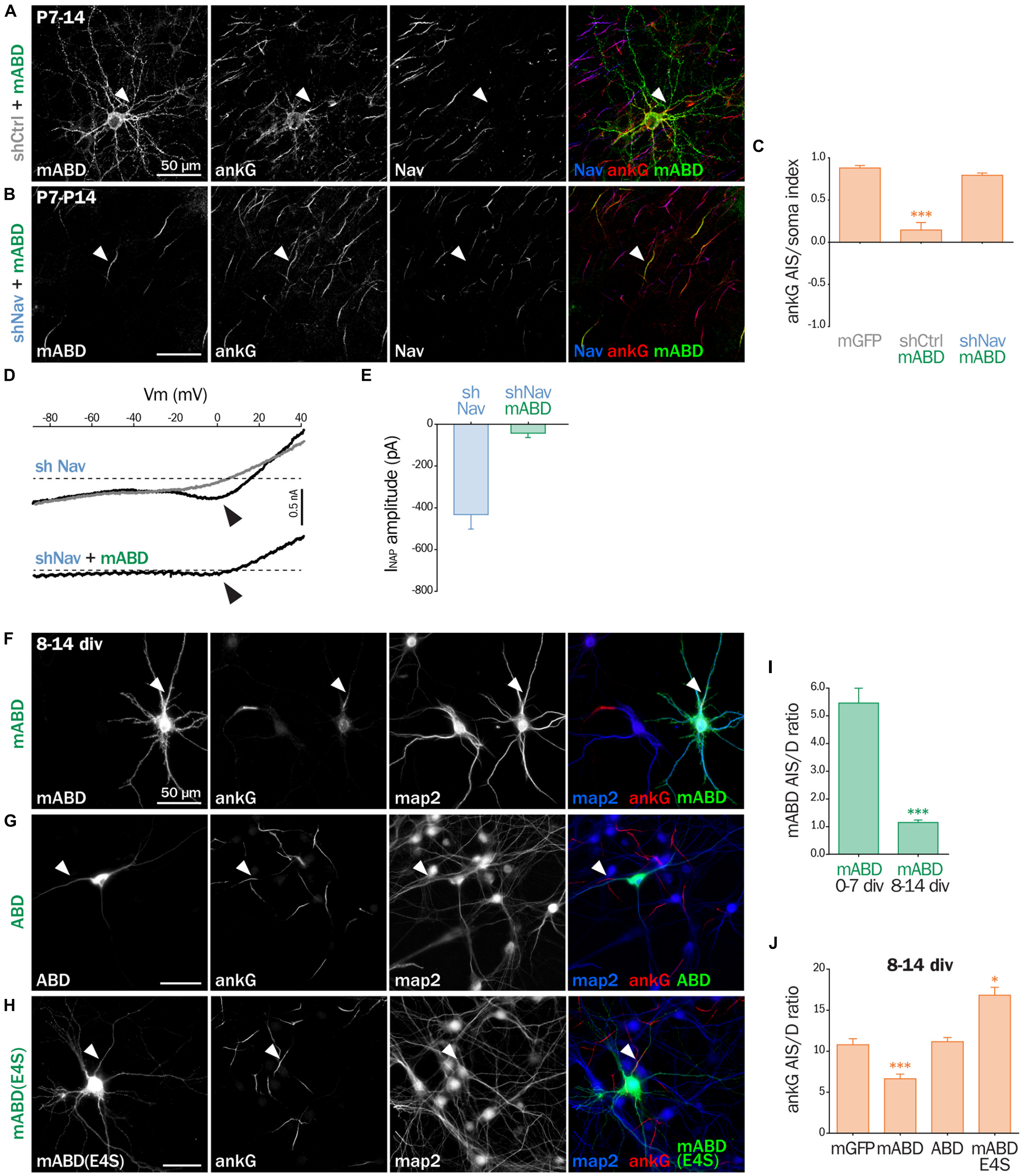

FIGURE 7 | mABD expression in mature neurons results in ankG mislocalization. (A–E) Organotypic cortical slices prepared from postnatal day 7 rats infected with a lentivirus co-expressing mABD and shCtrl or shNav and either treated for immunostaining for GFP, ankG and Nav **(A–C)** or used for patch-clamp recording **(D,E)** 7–8 days post-infection. **(A,B)** Maximum-intensity projection of 15–20 optical slices: arrowheads indicate the AIS of transfected neurons. **(C)** Polarity index of ankG labeling in the AIS vs. the soma obtained from infected neurons (mGFP alone 0.88 ± 0.03, *n* = 8; mABD + shCtrl 0.15 ± 0.09, *n* = 10; mABD + shNav 0.79 ± 0.03, *n* = 10; two independent experiments). **(D)** Raw traces of INaP evoked by voltage ramps in the absence (black) or presence (gray) of 500 nM TTX. Arrowheads indicate the INaP. **(E)** Averaged INaP peak amplitude (shNav *n* = 9; shNav + mABD: *n* = 3/7). **(F–J)** Rat hippocampal neurons transfected at 8 div with mGFP, mABD, ABD (mABD devoid of its membrane anchor) or mABD-E4S (mABD invalidated for ankG interaction, see **Figure 6B**) fixed 6 days later (8–14 div) and

(Continued)

FIGURE 7 | Continued
immunostained for GFP, map2 and ankG. Arrowheads indicate the AIS of transfected neurons. **(I)** Ratio of the mean fluorescence intensity for GFP labeling in the proximal axon compared to the mean intensity of three dendrites in each transfected neuron (mABD expressed from 0 div to 7 div from **Figure 6F** for comparison, mABD expressed from 8 div to 14 div 1.15 ± 0.09, *n* = 66, two independent experiments). **(J)** Ratio of the mean fluorescence intensity for ankG labeling in the proximal axon compared to the mean intensity of three dendrites in each transfected neuron (mGFP 10.79 ± 0.73, *n* = 30; mABD 6.64 ± 0.57, *n* = 114; ABD 11.16 ± 0.51, *n* = 58; mABD-E4S 16.83 ± 0.95, *n* = 66; 2–4 independent experiments).

DISCUSSION

The AIS is a highly specialized neuronal compartment that plays a key role in neuronal development and excitability. Many studies have highlighted the central role of ankG in the establishment and maintenance of the AIS molecular scaffold, since it targets and anchors most, if not all, known AIS components. Such central role in AIS building and stabilization have been demonstrated by Hedstrom et al. (2007) that obtained disappearance of the AIS only with ankG knockdown, as we show in **Figure 3B**. However, the converse role of the AIS components on ankG trafficking and stabilization is still poorly understood. Although many studies have reported that the down-regulation of non-membranous AIS proteins drives no or weak ankG concentration decrease (Leterrier et al., 2011b; Hien et al., 2014; Papandréou et al., 2015; Fréal et al., 2016; Pablo et al., 2016), we have demonstrated here that Nav and Nfasc186 knockdown in both developing and mature neurons induced a significant and cumulative decrease of ankG. This suggests that the membranous partners of ankG play a cardinal role in the interactome constituted by the AIS resident proteins. Thus, although ankG is unquestionably necessary for AIS construction and stabilization, it is not sufficient by itself to ensure the complete assembly of the AIS.

Both Nav and Nfasc186 are membrane proteins that bind directly to the MBD of ankG *via* their ABD. Their individual knockdown produced a similar decrease of ankG concentration at the AIS, whereas their simultaneous depletion had a cumulative effect (although their ABD are different). The very low transfection rate in our neuronal cultures prevented to determine whether this decrease of ankG concentration at the AIS reflects loss of expression, degradation or mislocalization. Nevertheless, this significant down-regulation indicates that the ability of Nav and Nfasc186 to anchor ankG to the plasma membrane plays a role in ankG targeting and maintenance at the AIS. Furthermore, the ankG down-regulation induced by Nfasc186 depletion is rescued by expressing recombinant Nav channels, which demonstrates that, regardless the identity of the anchoring membrane partner, membrane association is a crucial step in ankG targeting. Such a role of the association between ankG and Nav or Nfasc186 is consistent with recent data from Wang et al. (2014) who resolved the MBD structure. Indeed, mutations in two sites of the MBD that mediate binding to Nfasc186 also prevent the correct targeting of recombinant ankG to the AIS of cultured hippocampal neurons. Interestingly, a direct ankG association with the plasma membrane was also showed to be necessary by He et al. (2012). These authors observed that the suppression of the cysteine 70 of ankG, which is required for its S-palmitoylation, led to a loss of ankG accumulation to the AIS. We have not tested whether other AIS membrane partners contribute to ankG targeting. Nevertheless, we can suspect that KCNQ2/3 (Kv7.2/Kv7.3) channels, which have an ABD very similar to that of Nav channels, could have a similar stabilizing effect (Pan et al., 2006; Hill et al., 2008; Xu and Cooper, 2015).

To pinpoint the features required for ankG stabilization by its membrane partners, we designed a minimal chimeric protein consisting in a membrane-anchored ankyrin binding domain (mABD). This chimeric protein had a dominant negative effect on the concentration of endogenous Nav channels at the AIS. This effect was confirmed by our electrophysiological data obtained in cultured organotypic cortex slices. In this model, neurons expressing shNav alone exhibited a residual INaP (likely produced by Nav1.6 that is not targeted by our shRNA) that was suppressed in neurons co-expressing shNav and mABD. Although mABD expression had a dominant negative effect on endogenous Nav, it rescued the ankG downregulation induced by the shNav and drove the reestablishment of an AIS morphologically indistinguishable from the AIS of naive neurons (see **Figure 7B**). This demonstrates that a properly assembled AIS can be reconstituted by mABD in neurons devoid of Na^+ currents. Thus, the membrane-anchoring effect of Nav channels is essential for ankG targeting and anchoring to the AIS, independently of their ability to produce Na^+ currents.

Our study unravels two mechanisms regarding AIS components assembly and maintenance. First, we evidenced an unexpected ability of the AIS structure to be plastic in young neurons. Indeed, when mABD is overexpressed during AIS formation, a larger amount of ankG is positioned at the proximal axon, promoting a wider AIS. These observations suggest that the diameter of the AIS is subjected to a modulation regulated by the amount of available membrane components. These data fit with the observation that the level of Nav channels expressed to the membrane is regulated by a combination of mechanisms involving numerous Nav interacting partners such as ankG, CK2, VGSC beta subunits, FGF13- and 14 (Hien et al., 2014; Montersino et al., 2014; O'Malley and Isom, 2015; Pablo et al., 2016). This AIS diameter change could influence electrogenesis properties, as shown for AIS length and position plasticity in developing neurons (Galiano et al., 2012; Gutzmann et al., 2014; Kuba et al., 2014). On the opposite, in mature neurons the assembled AIS exhibit very little plasticity unless they are destabilized. Indeed, overexpression of mABD in mature cortical neurons leads to an ectopic localization of ankG that is rescued by a concomitant knockdown for Nav channels. Our data are consistent with the observed stability of AIS components in mature neurons (Hedstrom et al., 2008; Akin et al., 2015) and the preferential regulation of channels immobilization by CK2 in young neurons

(Brachet et al., 2010). A second important finding is the fact that ankG could interact with its membrane partners outside the AIS. Indeed, the ability of mABD to mistarget ankG in mature neurons suggests that ankG and its membrane partners, in particular Nav channels, can physically interact with each other upstream of their insertion into the AIS scaffold, and are likely co-transported to the AIS. The mechanisms for the targeting of AIS proteins are the subject of an ongoing debate. On the one hand, a "diffusion trapping" model has been proposed in which Nav and KCNQ2/3 channels are transported to the plasma membrane and diffuse to the AIS where they are immobilized by ankG (Leterrier et al., 2011a; Xu and Cooper, 2015). On the other hand, a "direct insertion" model was put forward in which Nav channels are directly targeted to the AIS where they are immediately immobilized (Barry et al., 2014; Akin et al., 2015). Our model of a co-transport of ankG associated to its membrane partners is in line with the latter hypothesis. We propose that ankG is targeted to vesicular membranes by a tight association with its membranous partners. This implies that the ankG/membrane partner complexes are co-transported to the axon, presumably via kinesin-1 (Barry et al., 2014), and inserted into the AIS scaffold during AIS formation and maintenance.

AUTHOR CONTRIBUTIONS

CL, NC and FC: conception and design; experiments and data acquisition; analysis and interpretation of data; draft and revision of the article. FR-B: experiments and data acquisition. AM: experiments and data acquisition; analysis and interpretation of data. BD: conception and design; draft and revision of the article.

FUNDING

This work was supported by the Centre National pour la Recherche Scientifique, by grants to BD from the French Agence Nationale de la Recherche (ANR-2011-BSV4-001-1) and from Conseil Regional PACA (N°2011-10925).

ACKNOWLEDGMENTS

We thank Dr. Sulayman Dib-Hajj for providing the Nav1.6-GFP plasmid; Aziz Moqrich for critical reading of the manuscript; Hélène Babski and Constance Manso for technical help; Gisèle Froment, Didier Nègre and Caroline Costa (lentivectors production facility/SFR BioSciences Gerland—Lyon Sud (UMS3444/US8)) for the production of lentiviruses.

REFERENCES

Abad, X., Razquin, N., Abad, A., and Fortes, P. (2010). Combination of RNA interference and U1 inhibition leads to increased inhibition of gene expression. *Nucleic Acids Res.* 38:e136. doi: 10.1093/nar/gkq299

Akin, E. J., Solé, L., Dib-Hajj, S. D., Waxman, S. G., and Tamkun, M. M. (2015). Preferential targeting of $Na_v1.6$ voltage-gated Na^+ channels to the axon initial segment during development. *PLoS One* 10:e0124397. doi: 10.1371/journal.pone.0124397

Barry, J., Gu, Y., Jukkola, P., O'Neill, B., Gu, H., Mohler, P. J., et al. (2014). Ankyrin-G directly binds to kinesin-1 to transport voltage-gated Na^+ channels into axons. *Dev. Cell* 28, 117–131. doi: 10.1016/j.devcel.2013.11.023

Brachet, A., Leterrier, C., Irondelle, M., Fache, M.-P., Racine, V., Sibarita, J.-B., et al. (2010). Ankyrin G restricts ion channel diffusion at the axonal initial segment before the establishment of the diffusion barrier. *J. Cell Biol.* 191, 383–395. doi: 10.1083/jcb.201003042

Bréchet, A., Fache, M.-P., Brachet, A., Ferracci, G., Baude, A., Irondelle, M., et al. (2008). Protein kinase CK2 contributes to the organization of sodium channels in axonal membranes by regulating their interactions with ankyrin G. *J. Cell Biol.* 183, 1101–1114. doi: 10.1083/jcb.200805169

Clark, B. D., Goldberg, E. M., and Rudy, B. (2009). Electrogenic tuning of the axon initial segment. *Neuroscientist* 15, 651–668. doi: 10.1177/1073858409341973

Dotti, C. G., Sullivan, C. A., and Banker, G. A. (1988). The establishment of polarity by hippocampal neurons in culture. *J. Neurosci.* 8, 1454–1468.

Dull, T., Zufferey, R., Kelly, M., Mandel, R. J., Nguyen, M., Trono, D., et al. (1998). A third-generation lentivirus vector with a conditional packaging system. *J. Virol.* 72, 8463–8471.

Estacion, M., and Waxman, S. G. (2013). The response of $Na_{(V)}1.3$ sodium channels to ramp stimuli: multiple components and mechanisms. *J. Neurophysiol.* 109, 306–314. doi: 10.1152/jn.00438.2012

Fréal, A., Fassier, C., Le Bras, B., Bullier, E., De Gois, S., Hazan, J., et al. (2016). Cooperative interactions between 480 kDa Ankyrin-G and EB proteins assemble the axon initial segment. *J. Neurosci.* 36, 4421–4433. doi: 10.1523/JNEUROSCI.3219-15.2016

Galiano, M. R., Jha, S., Ho, T. S.-Y., Zhang, C., Ogawa, Y., Chang, K.-J., et al. (2012). A distal axonal cytoskeleton forms an intra-axonal boundary that controls axon initial segment assembly. *Cell* 149, 1125–1139. doi: 10.1016/j.cell.2012.03.039

Garrido, J. J., Giraud, P., Carlier, E., Fernandes, F., Moussif, A., Fache, M.-P., et al. (2003). A targeting motif involved in sodium channel clustering at the axonal initial segment. *Science* 300, 2091–2094. doi: 10.1126/science.1085167

Gasser, A., Ho, T. S.-Y., Cheng, X., Chang, K.-J., Waxman, S. G., Rasband, M. N., et al. (2012). An ankyring-binding motif is necessary and sufficient for targeting Nav1.6 sodium channels to axon initial segments and nodes of Ranvier. *J. Neurosci.* 32, 7232–7243. doi: 10.1523/JNEUROSCI.5434-11.2012

Grubb, M. S., and Burrone, J. (2010). Activity-dependent relocation of the axon initial segment fine-tunes neuronal excitability. *Nature* 465, 1070–1074. doi: 10.1038/nature09160

Gutzmann, A., Ergül, N., Grossmann, R., Schultz, C., Wahle, P., and Engelhardt, M. (2014). A period of structural plasticity at the axon initial segment in developing visual cortex. *Front. Neuroanat.* 8:11. doi: 10.3389/fnana.2014.00011

He, M., Jenkins, P., and Bennett, V. (2012). Cysteine 70 of Ankyrin-G is S-palmitoylated and is required for function of ankyrin-G in membrane domain assembly. *J. Biol. Chem.* 287, 43995–44005. doi: 10.1074/jbc.M112.417501

Hedstrom, K. L., Ogawa, Y., and Rasband, M. N. (2008). AnkyrinG is required for maintenance of the axon initial segment and neuronal polarity. *J. Cell Biol.* 183, 635–640. doi: 10.1083/jcb.200806112

Hedstrom, K. L., Xu, X., Ogawa, Y., Frischknecht, R., Seidenbecher, C. I., Shrager, P., et al. (2007). Neurofascin assembles a specialized extracellular matrix at the axon initial segment. *J. Cell Biol.* 178, 875–886. doi: 10.1083/jcb.200705119

Hien, Y. E., Montersino, A., Castets, F., Leterrier, C., Filhol, O., Vacher, H., et al. (2014). CK2 accumulation at the axon initial segment depends on sodium channel Nav1. *FEBS Lett.* 588, 3403–3408. doi: 10.1016/j.febslet.2014.07.032

Hill, A. S., Nishino, A., Nakajo, K., Zhang, G., Fineman, J. R., Selzer, M. E., et al. (2008). Ion channel clustering at the axon initial segment and node of ranvier evolved sequentially in early chordates. *PLoS Genet.* 4:e1000317. doi: 10.1371/journal.pgen.1000317

Jenkins, S. M., and Bennett, V. (2001). Ankyrin-G coordinates assembly of the spectrin-based membrane skeleton, voltage-gated sodium channels and L1 CAMs at Purkinje neuron initial segments. *J. Cell Biol.* 155, 739–746. doi: 10.1083/JCB.200109026

Kaech, S., and Banker, G. (2006). Culturing hippocampal neurons. *Nat. Protoc.* 1, 2406–2415. doi: 10.1038/nprot.2006.356

Kole, M. H. P., and Stuart, G. J. (2012). Signal processing in the axon initial segment. *Neuron* 73, 235–247. doi: 10.1016/j.neuron.2012.01.007

Kuba, H., Adachi, R., and Ohmori, H. (2014). Activity-dependent and activity-independent development of the axon initial segment. *J. Neurosci.* 34, 3443–3453. doi: 10.1523/JNEUROSCI.4357-13.2014

Lemaillet, G., Walker, B., and Lambert, S. (2003). Identification of a conserved ankyrin-binding motif in the family of sodium channel α subunits. *J. Biol. Chem.* 278, 27333–27339. doi: 10.1074/jbc.M303327200

Leterrier, C. (2016). "The axon initial segment, 50 years later," in *Current Topics in Membranes*, (Elsevier), 185–233. Available online at: http://linkinghub.elsevier.com/retrieve/pii/S1063582315000691

Leterrier, C., Brachet, A., Dargent, B., and Vacher, H. (2011a). Determinants of voltage-gated sodium channel clustering in neurons. *Semin. Cell Dev. Biol.* 22, 171–177. doi: 10.1016/j.semcdb.2010.09.014

Leterrier, C., Vacher, H., Fache, M.-P., d'Ortoli, S. A., Castets, F., Autillo-Touati, A., et al. (2011b). End-binding proteins EB3 and EB1 link microtubules to ankyrin G in the axon initial segment. *Proc. Natl. Acad. Sci. U S A* 108, 8826–8831. doi: 10.1073/pnas.1018671108

Leterrier, C., Potier, J., Caillol, G., Debarnot, C., Rueda Boroni, F., and Dargent, B. (2015). Nanoscale architecture of the axon initial segment reveals an organized and robust scaffold. *Cell Rep.* 13, 2781–2793. doi: 10.1016/j.celrep.2015.11.051

Lois, C., Hong, E. J., Pease, S., Brown, E. J., and Baltimore, D. (2002). Germline transmission and tissue-specific expression of transgenes delivered by lentiviral vectors. *Science* 295, 868–872. doi: 10.1126/science.1067081

Mantegazza, M., Yu, F. H., Powell, A. J., Clare, J. J., Catterall, W. A., and Scheuer, T. (2005). Molecular determinants for modulation of persistent sodium current by G-protein βγ subunits. *J. Neurosci.* 25, 3341–3349. doi: 10.1523/JNEUROSCI.0104-05.2005

Montersino, A., Brachet, A., Ferracci, G., Fache, M.-P., Angles d'Ortoli, S., Liu, W., et al. (2014). Tetrodotoxin-resistant voltage-gated sodium channel Na_v 1.8 constitutively interacts with ankyrin G. *J. Neurochem.* 131, 33–41. doi: 10.1111/jnc.12785

Del Negro, C. A., Koshiya, N., Butera, R. J., and Smith, J. C. (2002). Persistent sodium current, membrane properties and bursting behavior of pre-bötzinger complex inspiratory neurons *in vitro*. *J. Neurophysiol.* 88, 2242–2250. doi: 10.1152/jn.00081.2002

O'Malley, H. A., and Isom, L. L. (2015). Sodium channel β subunits: emerging targets in channelopathies. *Annu. Rev. Physiol.* 77, 481–504. doi: 10.1146/annurev-physiol-021014-071846

Pablo, J. L., Wang, C., Presby, M. M., and Pitt, G. S. (2016). Polarized localization of voltage-gated Na^+ channels is regulated by concerted FGF13 and FGF14 action. *Proc. Natl. Acad. Sci. U S A* 113, E2665–E2674. doi: 10.1073/pnas.1521194113

Pan, Z., Kao, T., Horvath, Z., Lemos, J., Sul, J.-Y., Cranstoun, S. D., et al. (2006). A common ankyrin-G-based mechanism retains KCNQ and NaV channels at electrically active domains of the axon. *J. Neurosci.* 26, 2599–2613. doi: 10.1523/JNEUROSCI.4314-05.2006

Papandréou, M.-J., Vacher, H., Fache, M.-P., Klingler, E., Rueda-Boroni, F., Ferracci, G., et al. (2015). CK2-regulated schwannomin-interacting protein IQCJ-SCHIP-1 association with AnkG contributes to the maintenance of the axon initial segment. *J. Neurochem.* 134, 527–537. doi: 10.1111/jnc.13158

Rasband, M. N. (2010). The axon initial segment and the maintenance of neuronal polarity. *Nat. Rev. Neurosci.* 11, 552–562. doi: 10.1038/nrn2852

Rush, A. M., Dib-Hajj, S. D., and Waxman, S. G. (2005). Electrophysiological properties of two axonal sodium channels, Nav1.2 and Nav1.6, expressed in mouse spinal sensory neurones. *J. Physiol.* 564, 803–815. doi: 10.1113/jphysiol.2005.083089

Sobotzik, J.-M., Sie, J. M., Politi, C., Del Turco, D., Bennett, V., Deller, T., et al. (2009). AnkyrinG is required to maintain axo-dendritic polarity *in vivo*. *Proc. Natl. Acad. Sci. U S A* 106, 17564–17569. doi: 10.1073/pnas.0909267106

Stoppini, L., Buchs, P.-A., and Muller, D. (1991). A simple method for organotypic cultures of nervous tissue. *J. Neurosci. Methods* 37, 173–182. doi: 10.1016/0165-0270(91)90128-m

Wang, C., Wei, Z., Chen, K., Ye, F., Yu, C., Bennett, V., et al. (2014). Structural basis of diverse membrane target recognitions by ankyrins. *Elife* 3:e04353. doi: 10.7554/eLife.04353

Xu, M., and Cooper, E. C. (2015). An ankyrin-G N-terminal gate and protein kinase CK2 dually regulate binding of voltage-gated sodium and KCNQ2/3 potassium channels. *J. Biol. Chem.* 290, 16619–16632. doi: 10.1074/jbc.M115.638932

Xu, X., and Shrager, P. (2005). Dependence of axon initial segment formation on Na^+ channel expression. *J. Neurosci. Res.* 79, 428–441. doi: 10.1002/jnr.20378

Xu, K., Zhong, G., and Zhuang, X. (2013). Actin, spectrin and associated proteins form a periodic cytoskeletal structure in axons. *Science* 339, 452–456. doi: 10.1126/science.1232251

Zonta, B., Desmazieres, A., Rinaldi, A., Tait, S., Sherman, D. L., Nolan, M. F., et al. (2011). A critical role for neurofascin in regulating action potential initiation through maintenance of the axon initial segment. *Neuron* 69, 945–956. doi: 10.1016/j.neuron.2011.02.021

Conflict of Interest Statement: The authors declare that the research was conducted in the absence of any commercial or financial relationships that could be construed as a potential conflict of interest.

The reviewer DM and handling Editor declared their shared affiliation, and the handling Editor states that the process nevertheless met the standards of a fair and objective review.

frontiers in Cellular Neuroscience

ORIGINAL RESEARCH
published: 06 November 2017
doi: 10.3389/fncel.2017.00332

Heterogeneity of the Axon Initial Segment in Interneurons and Pyramidal Cells of Rodent Visual Cortex

Felix Höfflin[1]†, Alexander Jack[2]†, Christian Riedel[2], Julia Mack-Bucher[3]‡, Johannes Roos[1], Corinna Corcelli[1], Christian Schultz[1], Petra Wahle[2]* and Maren Engelhardt[1]*

[1] *Institute of Neuroanatomy, Medical Faculty Mannheim, Center for Biomedicine and Medical Technology Mannheim (CBTM), Heidelberg University, Heidelberg, Germany,* [2] *Developmental Neurobiology, Department of Zoology and Neurobiology, Ruhr-University Bochum, Bochum, Germany,* [3] *Live Cell Imaging Core Mannheim (LIMA), Medical Faculty Mannheim, Center for Biomedicine and Medical Technology Mannheim (CBTM), Heidelberg University, Heidelberg, Germany*

The microdomain that orchestrates action potential initiation in neurons is the axon initial segment (AIS). It has long been considered to be a rather homogeneous domain at the very proximal axon hillock with relatively stable length, particularly in cortical pyramidal cells. However, studies in other brain regions paint a different picture. In hippocampal CA1, up to 50% of axons emerge from basal dendrites. Further, in about 30% of thick-tufted layer V pyramidal neurons in rat somatosensory cortex, axons have a dendritic origin. Consequently, the AIS is separated from the soma. Recent *in vitro* and *in vivo* studies have shown that cellular excitability is a function of AIS length/position and somatodendritic morphology, undermining a potentially significant impact of AIS heterogeneity for neuronal function. We therefore investigated neocortical axon morphology and AIS composition, hypothesizing that the initial observation of seemingly homogeneous AIS is inadequate and needs to take into account neuronal cell types. Here, we biolistically transfected cortical neurons in organotypic cultures to visualize the entire neuron and classify cell types in combination with immunolabeling against AIS markers. Using confocal microscopy and morphometric analysis, we investigated axon origin, AIS position, length, diameter as well as distance to the soma. We find a substantial AIS heterogeneity in visual cortical neurons, classified into three groups: (I) axons with somatic origin with proximal AIS at the axon hillock; (II) axons with somatic origin with distal AIS, with a discernible gap between the AIS and the soma; and (III) axons with dendritic origin (axon-carrying dendrite cell, AcD cell) and an AIS either starting directly at the axon origin or more distal to that point. Pyramidal cells have significantly longer AIS than interneurons. Interneurons with vertical columnar axonal projections have significantly more distal AIS locations than all other cells with their prevailing phenotype as an AcD cell. In contrast, neurons with perisomatic terminations display most often an axon originating from the soma. Our data contribute to the emerging understanding that AIS morphology is highly variable, and potentially a function of the cell type.

Keywords: axon initial segment, interneuron, pyramidal neuron, βIV-spectrin, axon-carrying dendrite cell, basket cell

Edited by:
Arianna Maffei,
Stony Brook University, United States

Reviewed by:
Heiko J. Luhmann,
Johannes Gutenberg-Universität Mainz, Germany
Andreas Vlachos,
Albert Ludwigs University of Freiburg, Germany

***Correspondence:**
Maren Engelhardt
maren.engelhardt@medma.uni-heidelberg.de
Petra Wahle
petra.wahle@rub.de

†*These authors have contributed equally to this work.*

‡***Present address:***
Julia Mack-Bucher,
Institute of Pharmacology,
Heidelberg University, Germany

Received: *14 July 2017*
Accepted: *09 October 2017*
Published: *06 November 2017*

Citation:
Höfflin F, Jack A, Riedel C, Mack-Bucher J, Roos J, Corcelli C, Schultz C, Wahle P and Engelhardt M (2017) Heterogeneity of the Axon Initial Segment in Interneurons and Pyramidal Cells of Rodent Visual Cortex.
Front. Cell. Neurosci. 11:332.
doi: 10.3389/fncel.2017.00332

INTRODUCTION

A common assumption is that the axon initial segment (AIS) in most cortical neurons spans the very proximal portion of the axon that emerges from the soma at the axon hillock. This position is of importance for its general function: the initiation, propagation, and backpropagation of action potentials (APs). Consequently, the AIS is characterized by a high density clustering of voltage-gated sodium and potassium channels (Kole and Stuart, 2012), rendering it the ideal site for AP initiation in a neuron (Debanne et al., 2011). These channels are tethered in the axonal membrane by specific membrane scaffolding proteins, particularly ankyrin G and its binding partner βIV-spectrin, which then connect to the axonal cytoskeleton, building a stable, periodic structure (Rasband, 2010; D'Este et al., 2015; Leterrier, 2016).

Axon onset and AIS emergence at neurons is often described as generally proximal to the soma (Rasband, 2010; Grubb et al., 2011). However, different axon onsets in various neuron classes have been described previously, going back as far as the works of Ramón y Cajal (Cajal, 1909). More recently, several studies pointed out varying degrees of heterogeneity in axon onset, e.g., in dopaminergic neurons of the rodent substantia nigra (Häusser et al., 1995; Gentet and Williams, 2007), hippocampal oriens-alveus interneurons (Martina et al., 2000), and hypothalamic neuroendocrine neurons (Herde et al., 2013). In cortex, the current knowledge is incomplete. Subpopulations of cortical principal neurons in both primate (Sloper and Powell, 1979) and cat (Peters et al., 1968) have been shown to harbor axons off a dendrite (for review see Triarhou, 2014). Lorincz and Nusser (2010) showed that in CA1 pyramidal neurons, the apical dendrite can serve as origin for the axon. In roughly 50% of CA1 pyramidal cells, the axon arises from a basal dendrite, and Thome et al. (2014) coined the term "axon-carrying dendrite cell", AcD cell. Interneurons of different types often carry axons on dendrites, and some even have more than one axon (Meyer and Wahle, 1988). Also, bipolar cells give rise to vertically projecting axons mainly from a more substantial and longer descending dendrite (Peters and Kimerer, 1981; Meyer, 1983). The dendritic origin of axons and hence their AIS has functional implications. For example, in hippocampus CA1, AcD cells show higher excitability to synaptic input and generate APs with lower activation thresholds (Thome et al., 2014). A similar phenomenon was recently observed after electrophysiological recording and modeling of mouse cerebellar granule cells (Houston et al., 2017). Further, about 1/3 of all evaluated thick-tufted pyramidal cells in somatosensory cortex layer V give rise to axons from dendrites and are further characterized by a reduced dendritic complexity and thinner main apical dendrites (Hamada et al., 2016). The authors provide evidence that the AIS location in these cells is correlated with the somatodendritic capacitance load, and suggest it to be a mechanism for homeostatic scaling of somatic APs.

Several studies have shown that the AIS is not a static microdomain. Rather, its structural and functional plasticity is believed to contribute to homeostatic mechanisms and neuronal function (reviewed in Yamada and Kuba, 2016). A recent study applying computational modeling of realistic neuronal cell types indicated that intrinsic excitability correlates with the somatodendritic domain that corresponds to a certain AIS location and length (Gulledge and Bravo, 2016). Further, in the nucleus laminaris of the avian auditory system, AIS length and location varies according to functional cell specialization: Neurons responding to high-frequency sounds have short AIS that are located distally on the axon. In contrast, neurons processing low-frequency sounds tend to have longer and more proximal AIS (Kuba et al., 2006). Also, a significant body of evidence from *in vitro* studies underlines our understanding of the AIS as a dynamically regulated, adaptive microdomain with the potential to regulate cellular input-output relationships and thus impact neuronal network state (reviewed in Wefelmeyer et al., 2016; Jamann et al., 2017).

Assuming that AIS morphology correlates with cellular function and that neurons utilize AIS plasticity to regulate excitability, we hypothesize that AIS length and location have to be significantly more heterogeneous in sensory cortex than it is currently acknowledged. In addition, current data on AIS length and position particularly in interneurons is limited. Therefore, we set out to investigate AIS morphology, first characterizing three distinct axon morphologies *in vivo*. We then used biolistic gene transfection in organotypic cultures derived from postnatal rat visual cortex to analyze these morphological classes in more detail. Our data indicate that three major morphological groups exist into which pyramidal neurons and interneurons can be separated. Analyzing AIS length, we find that pyramidal neurons in total have significantly longer AIS than interneurons. Interestingly, interneurons with vertical columnar axonal projections display significantly more distal AIS locations than all other cells in that their prevailing phenotype is that of an AcD cell.

MATERIALS AND METHODS

All antibodies used in this study (*in vivo*, *ex vivo*, *in vitro*) are summarized in **Table 1**.

AIS Morphological Phenotypes in Mouse Visual Cortex *in Vivo*

To assess AIS phenotypes *in vivo*, perfusion-fixed brains from reporter mice for pyramidal neurons (B6.Cg-Tg(Thy1-GFP)16Jrs/J (Feng et al., 2000), kind gift from Tina Sackmann and Andreas Draguhn, Institute of Physiology and Pathophysiology, Heidelberg University) and interneurons (PVcre/Rosa tomato) were obtained for immunohistochemical analysis (PVcre/Rosa tomato line was a kind gift from Mirko Witte and Jochen Staiger, Institute of Anatomy, University of Göttingen, Germany). All animal procedures were carried out in accordance with the recommendations of the Animal Research Council of Medical Faculty Mannheim, Heidelberg University, and University of Göttingen, respectively. All procedures were approved by the Animal Research Boards of the States of Northrhine-Westfalia and Lower Saxony, respectively. After deep anesthesia with ketamine (120 mg/kg/xylazine (16 mg/kg)), animals were transcardially perfused with 0.9% saline, followed by 1% and 4% phosphate-buffered paraformaldehyde (PFA, pH 7.4), respectively. Brains were removed, cryoprotected in 10% at 4°C sucrose overnight, followed by 30% sucrose for 48 h, and cut on a cryotome at 25 μm. The sections were processed for immunofluorescence as previously described (Gutzmann et al., 2014; Schlüter et al., 2017). Briefly, brains were trimmed to a block including visual cortex and embedded in Tissue Tek® (Sakura Finetek). Double and triple immunofluorescence was performed directly on slides using a fish skin gelatine blocking buffer for all antibodies (0.1% fish skin gelatine (Sigma, Hamburg, Germany), 1% BSA, 0.1% Triton X-100 in PBS).

Preparation, Transfection and Staining of Rat Visual Cortex Organotypic Cultures

All animal protocols were approved by the Ruhr-University Animal Research Board and the State of Northrhine-Westfalia and Baden-Württemberg. Pigmented Long-Evans rats were used to prepare organotypic tissue cultures (OTCs) of the visual cortex as described previously (Hamad et al., 2014). Briefly, rats were decapitated at the day of birth (P0/P1) and brains were explanted. Blocks from visual cortex were cut into 350 μm slices using a McIlwain tissue chopper (Ted Pella, Redding, CA, USA). Slices were placed on coverslips with a plasma/thrombine coagulate. Cultures were kept in medium consisting of 25% adult horse serum, 25% HBSS, 50% Eagle's Basal Medium, 1 mM L-Glutamine (all from Life Technologies, Karlsruhe, Germany), and 0.65% D-Glucose (Merck, Darmstadt, Germany). Medium was exchanged two times a week. At the second day *in vitro* (DIV 2), 10 μl of a solution containing 1 mM of uridine, cytosine-ß-D-arabino-furanosid and 5-fluordeoxyuridine (each stock 1 mM, all from Sigma) was added for 24 h to inhibit glial growth. OTCs were transfected at DIV 10 and fixed for immunostaining at DIV 20.

To achieve visualization of complete neuronal morphology, OTCs were transfected with mCherry (under the CMV-promoter, Clontech, Hamburg, Germany) as described (Wirth et al., 2003; Hamad et al., 2011). Briefly, gold particles (Biorad, Munich, Germany) were coated with plasmid DNA encoding mCherry (pmCherry-N1, cat# 632523; Clontech, Heidelberg, Germany) and transfection was carried out at DIV 10 using a hand-held Helios Gene Gun (Bio-Rad, Munich, Germany) with 130 psi helium blast pressure. Subsequently, OTCs were cultured for an additional 10 days before processing for further analysis. A total of 48 OTCs derived from three different preparations (each of six pups) were used in this study.

At DIV 20, OTCs were fixed with prewarmed 4% PFA for 2 h. OTCs were blocked with 3% bovine serum albumin, 3% normal goat serum, and 0.5% Triton X-100 in TBS. Primary antibodies (**Table 1**) were incubated overnight at 4°C. After several washing steps with 1× TBS, secondary antibodies were applied (for 60 min each). After incubation, OTCs were rinsed several times with 1× TBS and finally switched to PBS. Cultures were mounted on glass coverslips using Roti®–Mount (Carl Roth, Karlsruhe, Germany) and sealed with nail polish. To test for antibody specificity, primary antibodies were omitted in control experiments, which completely abolished all stainings.

After confocal assessment was completed, selected cultures were de-coverslipped, rehydrated and incubated in PBS and PBS-Tween-20 (0.05%) for 48 h to elute antibodies. Cultures were blocked with TBS-BSA, and re-incubated in mouse anti mCherry antibody overnight followed by biotinylated goat anti mouse for 3 h, followed by ABC reagent for 2 h (Vector Laboratories Inc., Burlingame, CA, USA, RRID:AB_2336827), and reacted with 3,3′-diaminobenzidine (Sigma) and H_2O_2. The reaction product was enhanced with OsO_4 (Sigma). Cultures were dehydrated and coverslipped in DPX (Sigma). To demonstrate the major cell types, selected neurons and their axonal fields were reconstructed manually at 1000× (Neurolucida, MicroBrightField, Inc., Williston, VT, USA).

OTC for assessment of AIS development were prepared as described above at P0/P1, but cultured on filters (Stoppini et al., 1991). Culture conditions and staining procedures were identical to the roller tube cultures as outlined in the previous section and different culture preparations did not lead to differences in data obtained. Cultures were maintained until DIV 3, 7, 15, 21 and 35.

Primary Cultures of Cortical Neurons

Cortices of embryonic day 18.5 mice (bl6/C57) were removed and dissected in ice-cold HBSS substituted with 25 mM glucose (Thermo Fisher, Dreieich, Germany). Tissue was

TABLE 1 | Specification of antibodies used in the study with indication of catalog number, clone, working dilution, sources and references or research resource identifiers (RRID) where available.

Antibody (species), Catalog No., Clone/type	Dil.	Source	RRID or Reference
Ankyring (rb), sc-28561, H-215	1:500	UC Davis/NIH NeuroMab Facility, CA, USA	AB_633909
ßIV-spectrin (rb)	1:500	Selfmade, directed against amino acids 2237–2256 of human βIV spectrin	Gutzmann et al. (2014), Thome et al. (2014), Schlüter et al. (2017)
mCherry (ms), 632543	1:500	Living Colors®, Clontech, Hamburg, Germany	AB_2307319
panNaV (ms), S8809, clone K58/35	1:500	Sigma, St. Louis, MO, USA	Gottlieb and Keller (1997), Gutzmann et al. (2014), Thome et al. (2014)
map2 (gp),188 004	1:500	Synaptic Systems, Göttingen, Germany	Gumy et al. (2017)
gt anti rb ALEXA, 488, A-11008	1:1000	Molecular Probes, Karlsruhe, Germany	AB_143165
gt anti ms (biotinylated), P0447	1:500	DAKO Agilent, Glostrup, Denmark	AB_2617137
Streptavidin 594, S11227	1:1000	Thermo Scientific, Waltham, MA, USA	AB_2619631

Rb, rabbit; ms, mouse; gt, goat; gp, guinea pig.

further dissociated by enzymatic digestion in Accutase (Thermo Fisher) for 10 min at room temperature and then triturated with a fire-polished Pasteur pipette. Cells were plated on coverslips coated with poly-L-lysine (30 μg/ml) and laminin (2 μg/ml) at a density of 75,000/well for immunofluorescence at DIV 7. Cultures were maintained in Neurobasal medium supplemented with B27, 0.5 mM glutamine, 12.5 μM glutamate and 0.5% penicillin/streptomycin (all compounds from Gibco). For immunofluorescence, cells were fixed in 2% PFA for 10 min, washed, and blocked in fish skin gelatine buffer (see "AIS Morphological Phenotypes in Mouse Visual Cortex *in Vivo*" section) before primary antibody incubation overnight.

Image Acquisition and Criteria for AIS Onset

A Zeiss AxioImager microscope was used to obtain low magnification survey maps of transfected OTC, highlighting the specific location of all mCherry-positive neurons of each OTC so that cells could later be matched with their original image files. Confocal imaging of transfected and immunostained OTCs was carried out on a Leica SP5 MP using the Leica HC PL APO 63×/1.30 NA Glycerin matched objective and a C1 Nikon confocal microscope with a 60× objective (oil immersion, 1.4 NA), respectively. Scans of mCherry and Alexa 488 signals were acquired sequentially to clearly separate two channels (laser lines: 561 nm and 488 nm, respectively). Z-stacks of various sizes, dependent on OTC thickness between 3 μm and 18 μm, were spaced by 0.5 μm. Image size was 1024 × 1024 pixels (pixel dwell time 720 ns, two frames average), stitched into tiles to cover the entirety of the neuron of interest, and thick optical sections were merged to a maximum intensity projection and saved as tiff and jpg formats. Automatically tiled images were analyzed using Fiji/ImageJ (Rasband, 1997–2012) and enhanced for brightness and contrast in Photoshop CS4 when processed for figure preparation.

Only neurons with a clearly detectable AIS (overlapping signal of mCherry and ßIV-spectrin) were used for further investigation. Soma borders were defined manually. Depending on where the AIS (the ßIV-spectrin positive domain) began, cells were classified into three groups: group I cells with axons of somatic origin, and with proximal AIS at the axon hillock, group II cells with axons of somatic origin, but with distal AIS and a discernible gap between the start of the AIS and the soma, and group III cells with axons with dendritic origin (axon-carrying dendrite cell, AcD) and an AIS either located directly at the origin of the axon or more distal to that point. Several neurochemically distinct types of interneurons can give rise to more than one axon (Meyer and Wahle, 1988); in these cases, each axon and AIS, respectively, was analyzed separately and values were not averaged.

Neuron Classification

In OTC, neurons were classified as pyramidal neuron (abbreviated as PYR in all figures) or interneuron (abbreviated as IN in all figures) by the following criteria: location in upper or lower cortical layers, soma shape, dendrite configuration (polarized or multipolar), spine density and the initial axonal branching pattern (Ascoli et al., 2008; Hamad et al., 2014). Neurons with apical dendritic polarity, variable numbers of shorter basal dendrites, high spine density, and a descending primary axon with a few obliquely ascending fine collaterals with gracile boutons were classified as pyramidal neurons of supragranular and infragranular layers (Wirth et al., 2003; Hamad et al., 2014). Supragranular pyramidal cells have the soma in the outer 1/3 of the culture and an apical dendrite reaching into or coming close to layer I. Infragranular pyramidal cells have the soma in the lower 2/3 of the cultures and apical dendrites end in middle layers without reaching layer I. We also included pyramidal cells of the layer VIb/subplate with horizontal or oblique orientation in this group. Large cortico-midbrain projecting layer V pyramidal cells with prominent apical tufts in layer I are rarely transfected, because they are less frequent than those with local or callosal axons, and none are in the current sample. Supplementary Figure S1 gives representative examples of the major cell types assessed in the present study; Supplementary Table S1 summarizes other relevant cellular parameters of these representative cells such as soma area, axon length, number of nodes, length of dendrites, number of segments and branch order of the individual dendrites.

A few heavily spiny non-polarized neurons with >6 primary dendrites from middle layers were classified as spiny stellates and were not considered for analysis. Neurons with multipolar or polarized dendritic fields with dendrites being more varicose than those of pyramidal cells, less spiny or rather smooth, and with axons initially branching more profusely within the cell's dendritic field were classified as non-pyramidal IN.

In about 40% of the non-pyramidal neurons, the axon was sufficiently well stained to classify the type based on the axonal pattern. Neurons giving rise to a local plexus that may extend horizontally and with larger boutons of irregular size forming short terminal elements around neighboring somata suggestive of perisomatic endings were classified as basket cells (BC), many of which are fast-spiking (FS; Ascoli et al., 2008; DeFelipe et al., 2013; Jiang et al., 2015). We therefore grouped large BCs with longer horizontal collaterals and smaller BCs with more restricted axonal fields together. Neurons giving rise to vertical projections either by frequent recurrent branching and thin collaterals with fine boutons not entering layer I were classified as bitufted neurons (BT). Neurons giving rise to an ascending axon branching into an ascending bundle of collaterals reaching into layer I where they adopt a horizontal trajectory were classified as Martinotti cells (MC). BT and MC both target the dendrites of pyramidal neurons and are non-FS cells (Wang et al., 2004; Ascoli et al., 2008; DeFelipe et al., 2013; Jiang et al., 2015). We therefore pooled the BT and MC together as dendrite-targeting neurons. Chandelier cells were not identified in the current samples, likely because they appear in far fewer numbers compared to BCs, which comprise about half of all cortical interneurons, and because they are known to mature later than other interneurons types in various mammalian species (Meyer and Ferres-Torres, 1984; Cruz et al., 2003). Likewise, we could not safely identify bipolar cells, which are rarely transfected because they have very small somata.

Morphological Analysis of the AIS in OTC

AIS length was determined using a previously described self-written macro (Gutzmann et al., 2014; Schlüter et al., 2017). We used the standard settings of the program to pre-process images by histogram stretching and a sharpening filter to enhance edges. AIS were traced with overlapping ends on proximal and distal sections. The macro automatically straightened each line and data was saved in Excel (Microsoft), plotting number of pixels vs. intensity of ßIV-spectrin signal. To determine AIS length, the open source tool Anaconda (Continuum Analytics) containing the Jupyter Notebook App was utilized. The Jupyter Notebook App allows editing and running notebook documents through a web browser. The coding language Python was employed to write an analysis script in one of these notebook documents. This script determines the AIS length of each cell by evaluating the individual Excel files containing the information about ßIV-spectrin signal plotted vs. number of pixels in the following pattern: all values of ßIV-spectrin are combined and the highest value is used to calculate the cut-off for AIS onset and end. The cut-off was set to 30% of the individual maximum intensity. To avoid taking upward outliers into account, the script checks triplets of AIS signal values. The proximal beginning of AIS is set as the first value of a triplet containing only values that are higher than the calculated cut-off. The distal end of the AIS is determined similarly, starting from the last value of the chart. Pixel difference between beginning and ending is computed and converted into length in micrometer based on the microscope's calibration.

Neurons with a distal AIS or an AcD were additionally analyzed for the length of the gap between soma and AIS-beginning. Single color channel mode in Photoshop CS4 was used to delete the ßIV-spectrin signal of interfering AIS along the gap. The plotting line in Fiji was started at the individually set soma border, drawn over the whole gap and AIS and finished just beyond the distal AIS end. Gap lengths were defined as the distance between soma border and proximal beginning of the AIS. Only neurons with a clearly defined soma border and a traceable dendrite or axon to the first AIS segment were collected for statistical analysis of gap length.

For the axon diameter calculations, we used a novel approach using a self-written GUI application utilizing Python and the open-source modules matplotlib, opencv, python-bioformats, pyqt and numpy. The maximum intensity projection of the AIS to be measured is used to determine the respective intensity curve. Meta data is saved for pixel to physical dimension conversion. For every neighboring two points on the trace, a virtual rectangle with a width of the distance between the two points and a height of 20 pixels is created and overlaid on the image. The corner points of each rectangle are used to resolve the traced AIS using opencv-transformation tools. The multiple rectangles of the trace are then joined horizontally to a rectangular image spanning the length of the entire trace and height of 20 pixels. This image, now containing only the AIS and its surroundings, is used to determine the diameter of the AIS. Start and end of the AIS are calculated by selecting the first/last pixel with intensity over a 30% threshold (normalized on the channels' maximum). For the calculation of the diameter, a canny edge filter is applied to the image, which is then divided into vertical slices, each with a thickness of 1 pixel. For each vertical slice, the distance between the first lit pixel (that is the upper edge of the AIS) and last lit pixel (lower edge) is measured, resulting in an overlay of computed diameters on the image. The regions where the overlay fitted the AIS and no noise was interfering were selected. Finally, the mean diameter of these regions was calculated.

Three-dimensional projections from stacks were processed first by blind iterative deconvolution (theoretical PSF based on the optical properties of the microscope and the sample, 10× iteration) according to standard procedures in AutoQuant X3 (Media Cybernetics, Rockville, MD, USA). Subsequently, to visualize x-y-z information and dimensions of AIS in neuronal subtypes, deconvolved files were reconstructed (surface) using Imaris 8.1.2 (Bitplane, Zurich).

Statistical Analysis

Mean values and standard error of the mean (SEM) of AIS length, gap size and diameter were calculated, plotted and analyzed in Sigma Plot 12.5 Software (Systat Software GmbH). *T*-test and Wilcoxon rank-sum test was carried out for comparison of only two groups. Kruskal-Wallis one-way analysis of variance was applied when comparing three or more groups, followed by Dunn's correction. Error bars indicate SEM; *p* values and number of samples are given in each graph.

RESULTS

AIS Phenotypes *in Vivo*

In Thy1-GFP reporter mice, where a subset of cortical pyramidal neurons is GFP-positive, we found three AIS location phenotypes (**Figure 1**). In group I cells, the axon emerges from the soma and the AIS locates at the most proximal part of the axon directly at the soma with no discernible gap (**Figures 1A–A2**, cartoon insert). In group II cells, the axon emerges from the soma, but the AIS is located further distally on the axon with a clearly discernible gap between the first βIV-spectrin immunosignal and the soma (**Figures 1B–B2**, cartoon insert). The gap is devoid of βIV-spectrin, ankyrinG and voltage-gated sodium channels (panNaV; data not shown). In group III cells, the axon emerges from a dendrite and consequently, the AIS is located far distally from the soma (**Figures 1C–C2**, cartoon insert).

We next analyzed parvalbumin-tdTomato reporter mice (PV-tdTomato, **Figure 1**) in which BCs and chandelier cells are labeled (Walker et al., 2016). Parvalbumin (PARV)-expressing interneurons give rise to axons from the soma with AIS residing either proximal directly at the axon hillock (**Figures 1D–D2**) or distally with a gap to the soma (**Figures 1E–E2**). We also observed axons off dendrites (**Figures 1F–F2**), and the AIS can begin directly at the axon origin, or at some distance to the axon origin (**Figure 1F2**). Consequently, in these

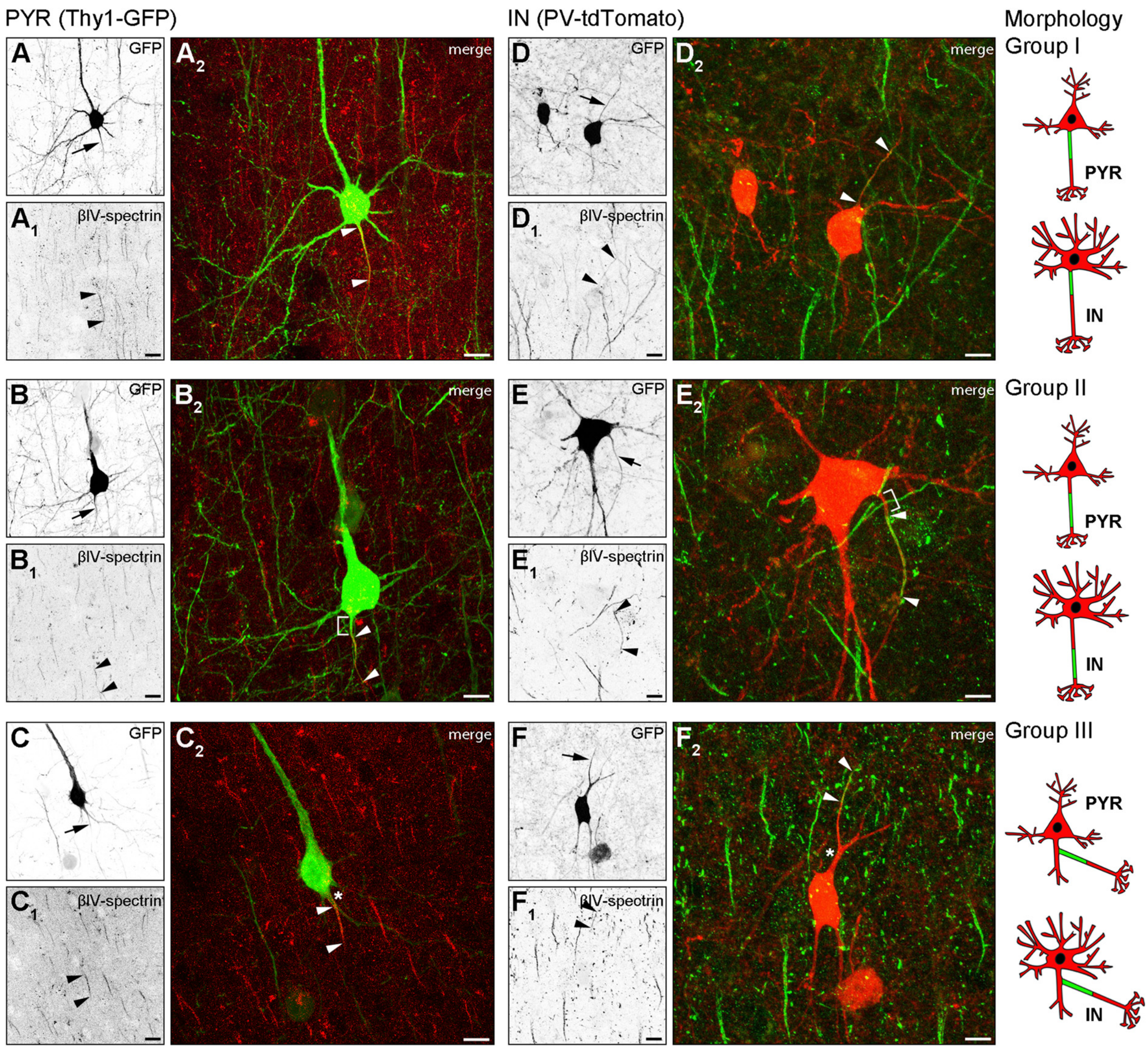

FIGURE 1 | Axon initial segment (AIS) heterogeneity in pyramidal (PYR) neurons and interneurons (IN) *in vivo*. **(A–C)** Layer V PYR neurons in visual cortex sections of adult Thy1-GFP reporter mice, immunostained for βIV-spectrin (red). **(A–A2)** Representative image of a Group I morphology: proximal AIS; arrow in **(A)** shows axon, arrowheads in **(A1+2)** delineate AIS. **(B–B2)** Representative image of a Group II morphology: distal AIS on axon emerging at the soma; arrow in **(B)** shows axon, arrowheads in **(B1+2)** delineate the AIS, bracket in **(B2)** indicates the gap on the axon between soma and AIS onset. **(C–C2)** Representative image of a Group III morphology: axon off a dendrite (AcD), therefore the AIS is located distally from the soma; arrow in **(C)** shows axon, arrowheads in **(C1+2)** delineate AIS, asterisk in **(C2)** indicates dendritic shaft. Scale bars **(A–C)** = 20 μm. **(D–F)** Layer V IN in visual cortex sections of adult PV-tdTomato reporter mice, immunostained for βIV-spectrin (green). **(D–D2)** Representative image of a Group I morphology: proximal AIS; arrow in **(D)** shows axon, arrowheads in **(D1+2)** delineate AIS. **(E–E2)** Representative image of a Group II morphology: distal AIS on axon emerging at the soma; arrow in **(E)** shows axon, arrowheads in **(E1+2)** delineate the AIS, bracket in **(E2)** indicates the gap on the axon between soma and AIS onset. **(F–F2)** Representative image of a Group III morphology: axon off a dendrite (AcD); therefore the AIS is located distally from the soma; arrow in **(F)** shows axon, arrowheads in **(F1+2)** delineate AIS, asterisk in **(F2)** indicates dendritic shaft. Scale bars **(D–F)** = 20 μm, in **(E)** = 15 μm. Cartoons illustrate the three main morphological groups observed.

cases the distance between AIS and soma is quite substantial. In histological sections, in particular in interneurons, the AIS is either not present nor represented in full extent.

AIS Development in Rat Visual Cortex OTC

OTC are fully regenerated, all structural elements are contained within the culture, and all neuron types develop in OTC as they do *in vivo*. Accordingly, OTC have long been established as a relevant tool to study structure and function under precisely-to-control conditions (Gähwiler et al., 1997; Wirth et al., 2003; Del Turco and Deller, 2007; Mori et al., 2007; Humpel, 2015). Therefore, we next utilized rat visual cortex-derived OTC to test if the AIS heterogeneity develops in network of cells that are spontaneously active, but lack patterned input from subcortical sources. First, we performed a quantitative analysis of AIS

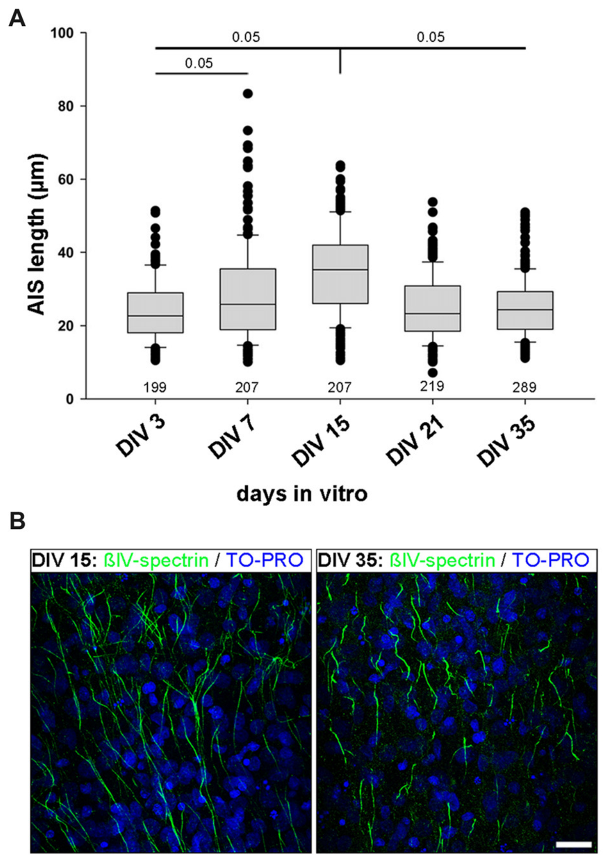

FIGURE 2 | AIS length development in organotypic tissue culture (OTC). **(A)** AIS length measurements at various developmental stages *in vitro* ranging from DIV 3 to DIV 35. Initially AIS elongate until P15, followed by length reduction, which reaches mature states around P35. Note the wider scatter of length distribution already at DIV 7 and overall longer AIS at DIV 15 compared to DIV 35. Kruskal-Wallis one way analysis of variance (ANOVA) followed by *post hoc* Dunn's correction, *p* value indicated in graph. Length at DIV 15 is significant when compared to all other time points. Length at DIV 3 is significant when compared to DIV 7. Data derived from at least nine cultures per time point from three different preparations. Number of AIS per time point indicated in graph. **(B)** Representative images of AIS lengths in cultures at DIV 15 (left) and DIV 35 (right). AIS are immunostained against βIV-spectrin (green) with nuclear counterstain TO-PRO (blue). Scale bar = 20 µm.

development in OTC in order to determine if OTC undergo a similar AIS maturation as *in vivo* and thus can be seen as equivalent to the *in vivo* situation (Gutzmann et al., 2014). OTC were fixed and stained for AIS scaffolding proteins βIV-spectrin and ankyrinG at 3, 7, 15, 21 and 35 days *in vitro* (DIV). Length measurements were carried out as described previously (Gutzmann et al., 2014). We found that AIS undergo a significant length increase from on average 24.1 µm at DIV 3 to a peak of 34.5 µm at DIV 15 (**Figure 2A**). Subsequently, AIS shorten to mature levels at DIV 21, which were also seen at DIV35 (**Figure 2A**). Representative photomicrographs of these different lengths are shown in **Figure 2B**. This maturational profile largely corresponds to the *in vivo* situation (Gutzmann et al., 2014).

AIS Phenotypes in Rat Visual Cortex OTC

In total, we analyzed 178 pyramidal neurons classified as 81 supragranular and 85 infragranular as well as 85 non-pyramidal bona fide interneurons. Neurons were sampled from 48 OTC derived from three preparations each from six animals.

In approximately 50% of all interneurons, the quality of the mCherry immunosignal in distal axonal arbors was not optimal, and hence unequivocal subclassification was not possible. These cells were not considered for subtype analysis. From the rest, 16 cells were classified as BC with local or horizontal axon plexus and perisomatic endings, and 24 were dendrite-targeting bitufted and MC (BT/MC).

Our observation of three major AIS location phenotypes from the *in vivo* assessment was confirmed in OTC. Group I (somatic axon with proximal AIS), group II (somatic axon with distal AIS) and group III (dendritic axon origin, AcD, with distal AIS) were found in both pyramidal neurons (**Figures 3A–A2,B–B2,C–C2**) and interneurons (**Figures 3D–D2,E–E2,F–F2,G–G2**). Interestingly, we observed two distinct types of AcD cells, especially in interneurons. In one, the AIS starts directly at the point of origin of the axon from the dendrite (**Figures 3F–F2**), and in the other, the AIS is located distally from the point of origin, adding further to the gap between soma and AIS (**Figures 3G–G2**). Further, we confirmed that the visible gap between the axon onset and the soma in the AcD phenotype is indeed of dendritic origin as shown by immunostaining against MAP2, panNaV and ankG (Supplementary Figures S2A–A3, B–B3). Using deconvolution and surface reconstruction, we then determined the three-dimensional expansion of AIS in all three morphological classes in pyramidal cells and interneurons (Supplementary Figure S3).

Interneurons More Often Have Distal AIS Phenotypes than Pyramidal Neurons

When comparing all pyramidal cells to all interneurons, the AIS phenotype groups I, II and III occurred with the same frequency (**Figures 4A,D**). In both cell classes, about 60% display a distal AIS on an axon with somatic (group II) or dendritic (group III) origin, while somewhat surprisingly, less than 40% of cells fit into the "classical" proximal axon/AIS location group I (**Figures 4A,D**; PYR 38.5% group I, 15.5% group II, 46% group III; IN 39% group I, 16.7% group II, 44.4% group III). In the cases where a neuron has a distal AIS (regardless of somatic or dendritic axon origin), it is most often an AcD. When looking at pyramidal neurons from supragranular vs. infragranular layers, we observed an almost identical overall distribution of proximal vs. distal AIS, but notably, infragranular neurons more often fall within the AcD classification than supragranular neurons (supragranular: 42.3%; infragranular: 49%; **Figures 4B,C**). A striking observation was made when comparing the distribution of AIS location phenotypes in interneurons. Here, perisomatic-targeting BCs belong predominantly into group I (50%; **Figure 4E**). By contrast, dendrite-targeting BT/MCs belong predominantly to group III in that a majority of these interneurons are AcD cells (50% distal AIS, 60% of those group III; **Figure 4F**).

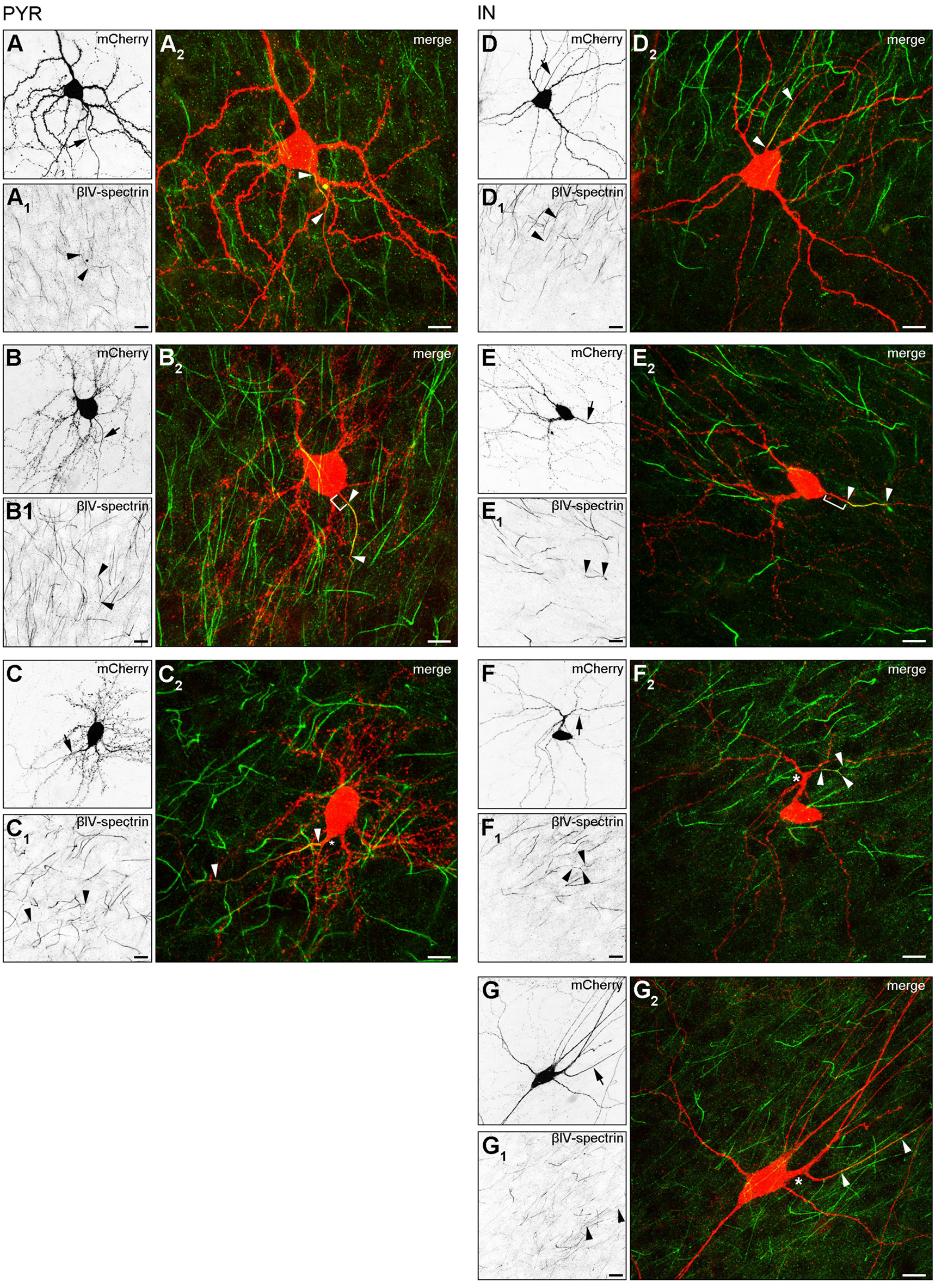

FIGURE 3 | AIS heterogeneity in pyramidal neurons **(A–C)** and interneurons **(D–G)** in OTC. **(A–A2)** Representative image of a pyramidal neuron classified in Group I: proximal AIS; arrow in **(A)** shows axon, arrowheads in **(A1+2)** delineate AIS (mCherry, red; βIV-spectrin, green). The same cell was reconstructed in Imaris to highlight the 3D expansion of the AIS (Supplementary Figure S3A). **(B–B2)** Representative image of a pyramidal neuron classified in Group II: distal AIS on axon emerging at the soma (mCherry, red; βIV-spectrin, green); arrow in **(B)** shows axon, arrowheads in **(B1+2)** delineate the AIS, bracket in **(B2)** indicates gap between AIS and soma. The same cell was reconstructed in Imaris to highlight the 3D expansion of the AIS (Supplementary Figure S3B). **(C–C2)** Representative image of a pyramidal neuron classified in Group III: axon off a dendrite (AcD), therefore the AIS is located distally from the soma; arrow in **(C)** shows axon, arrowheads in **(C1+2)** delineate AIS, asterisk in **(C2)** indicates dendritic shaft.The same cell was reconstructed in Imaris to highlight the 3D expansion of the AIS (Supplementary Figure S3C). Scale bars **(A–C)** = 20 µm. **(D–D2)** Representative image of an interneuron classified in Group I (mCherry, red; βIV-spectrin, green); arrow in **(D)** shows axon, arrowheads in **(D1+2)** delineate the AIS. **(E–E2)** Representative image of an interneuron classified in Group II (mCherry, red; βIV-spectrin, green); arrow in **(E)** shows axon, arrowheads in **(E1+2)** delineate AIS, bracket in **E2** indicates distance from the soma to the onset of the AIS. The same cell was reconstructed in Imaris to highlight the 3D expansion of the AIS (Supplementary Figure S3E). **(F–F2)** Representative image of an interneuron classified in Group III (mCherry, red; βIV-spectrin, green); arrow in **(F)** shows axon, arrowheads in **(F1+2)** delineate AIS with a bifurcation, asterisk in **(F2)** indicates dendritic shaft. The same cell was reconstructed in Imaris to highlight the 3D expansion of the AIS (Supplementary Figure S3F). **(G–G2)** Representative image of an interneuron classified in Group III, with a notably gap between axon onset on dendritic shaft and the beginning of the AIS (mCherry, red; βIV-spectrin, green); arrow in **(G)** shows axon, arrowheads in **(G1+2)** delineate AIS with a clear gap between AIS onset and point of origin of the axon at the dendrite, asterisk in **(G2)** indicates dendritic shaft. Scale bars **(D–G)** = 20 µm.

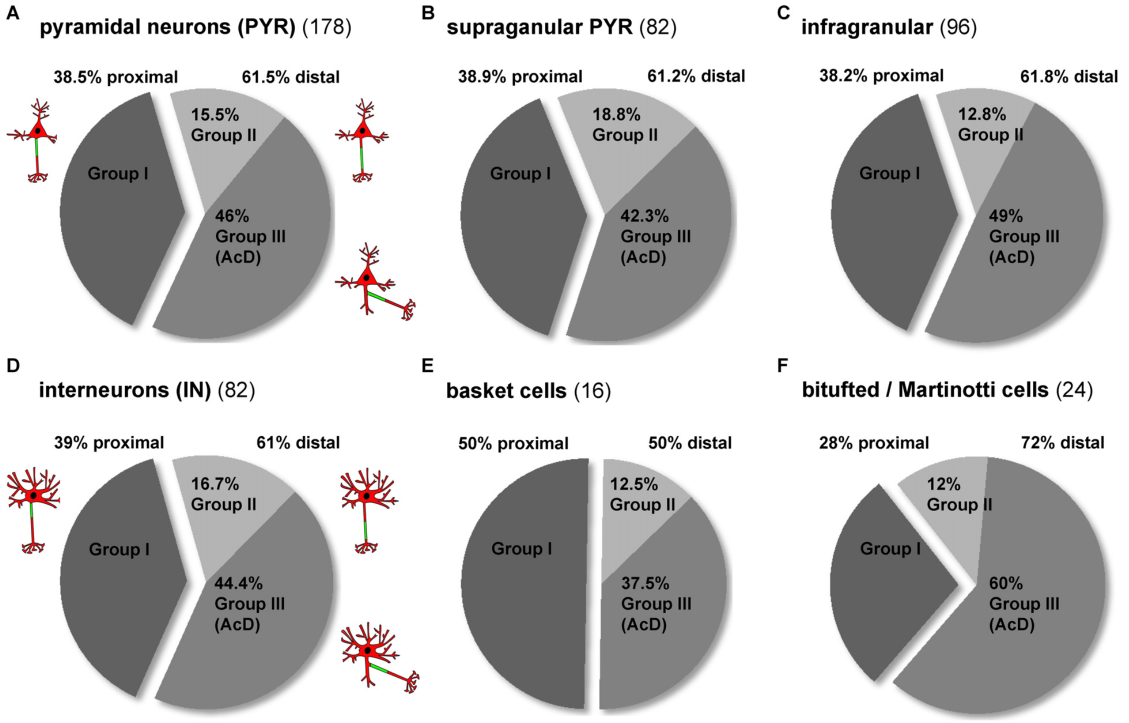

FIGURE 4 | Distribution of AIS location phenotypes among subtypes of pyramidal neurons and interneurons. **(A)** The overall distribution of the three major AIS phenotypes is almost identical in pyramidal neurons and (D) interneurons (dark gray = group I, proximal AIS; light gray = group II, distal AIS, axon with somatic origin; medium gray = group III, axon with dendritic origin). The distribution of distal subtypes (AIS on somatic axon, AIS on dendritc axon (AcD)) favors group III. **(B)** The distribution of AIS phenotypes in supragranular and **(C)** infragranular pyramidal neurons is similar, with a slight trend towards more AcDs in infragranular pyramidal neurons. **(D)** The distribution of AIS phenotypes in interneurons resembles that seen in pyramidal neurons, but the distribution differs for the major subgroups. **(E)** Group I proximal AIS are the dominant phenotype of perisomatically targeting (basket) interneurons, whereas group III AcD are the dominant form (60%) of the **(F)** dendrite-targeting (bitufted and Martinotti) interneurons. Distal AIS on axons with somatic origin occur at an equal proportion (12%) in the two subgroups in **(E,F)**.

Pyramidal Neurons Have Significantly Longer AIS than Interneurons

Apart from location, another AIS parameter can have significant influence on cellular excitability and function: AIS length. In fact, shortening and elongation are a hallmark feature of developmental and experimentally evoked AIS plasticity *in vivo* and *in vitro* (Cruz et al., 2009; Kuba et al., 2010; Hinman et al., 2013; Gutzmann et al., 2014; Wefelmeyer et al., 2016). When comparing all pyramidal neurons with all interneurons, regardless of AIS location, we found that pyramidal neurons have significantly longer AIS than interneurons (PYR 28.5 μm ± 10.7 vs. IN 25.7 μm ± 11.1; $p = 0.012$; **Figure 5A**). A similar trend in length difference also occurred when comparing individual neurons classified by AIS group: AIS tended to be shorter in interneurons of group I (PYR: 27.9 ± 10 vs. IN: 25 ± 10.3, $p = 0.119$). No differences were observed for cells in group II (PYR: 25.1 ± 8.7 vs. IN: 26.2 ± 11.6, $p = 0.894$). AIS of group III interneurons again were significantly shorter than those of pyramidal neurons in the same group (PYR: 30.2 ± 11.6 vs. IN: 26 ± 11.7, $p = 0.049$; **Figure 5A**). When looking at the three major AIS location groups across supragranular and infragranular pyramidal cells, we observed significant length differences for group I only. Here, supragranular neurons have significantly longer AIS than infragranular neurons (supra: 31.1 μm ± 11.9 vs. *infra*: 25.1 μm ± 7.5; $p = 0.03$; **Figure 5B**), a finding confirming quantitative data from layer 2/3 and layer 5 pyramidal neurons of visual cortex (Gutzmann et al., 2014) and somatosensory cortex (Vascak et al., 2017) *in vivo*. A similar, albeit non-significant trend was observed for group II, where AIS of supragranular pyramidal cells tended to be longer than those of infragranular cells (supra: 26.6 μm ± 8.6 vs. *infra*: 23.1 μm ± 8.8; $p = 0.303$; **Figure 5B**). No difference was observed for group III (supra: 29.9 μm ± 11.7 vs. *infra*: 30.4 μm ± 11.7; $p = 0.808$; **Figure 5B**). Within the cohort of classified interneurons, we saw no significant AIS length difference between perisomatic BCs and dendrite-targeting BT/MCs, although a trend for shorter AIS in BCs was apparent (BC: 20.8 μm ± 10.3 vs. BT/MC: 26.4 μm ± 13.7; $p = 0.136$; data not shown).

The Gap Length between AIS Onset and Soma as well as Axon Diameter Is Similar in Pyramidal Neurons and Interneurons

In any cell with a distal AIS, irrespective of whether the axon is of somatic or dendritic origin, the physical gap between the soma and the AIS most likely has significant impact on cellular function. It is hypothesized that even small changes

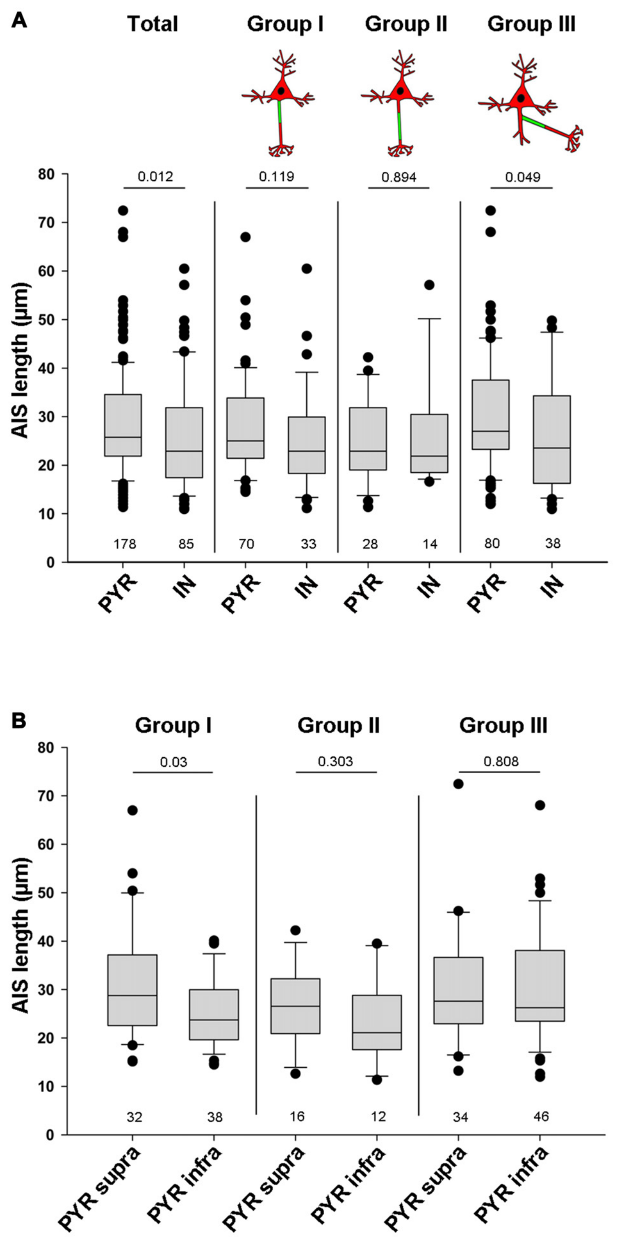

FIGURE 5 | Quantification of overall AIS length in pyramidal and interneuron populations. **(A)** AIS length (in μm) plotted for all pyramidal neurons (PYR) and all interneurons (IN; total, left pair of bars). AIS in PYR are significantly longer than those in IN. No significant differences for AIS length were observed when comparing proximal vs. distal AIS location. However, when comparing AcDs, where the AIS emerges off a basal dendrite, those of PYR are significantly longer. Wilkoxon rank-sum test with *post hoc* correction applying Dunn's post test, *p* values and *n*-numbers indicated in graph. **(B)** Comparison of the three major AIS phenotypes in supragranular vs. infrgranular pyramidal neurons showed significantly longer AIS in supragranular vs. infragranular neurons. Wilkoxon rank-sum test with *post hoc* correction applying Dunn's post test, *p* values and *n*-numbers indicated in graph.

in gap length can have dramatic effects on intrinsic firing properties and/or response times to synaptic input (Gulledge and Bravo, 2016; Hamada et al., 2016). Therefore, we analyzed the length of the gap. It was defined as the distance between the soma and beginning of immunostaining against AIS markers (**Figures 6A1–3**, Group II; **Figures 6B1–3**, Group III). We excluded gaps >70 μm from the analysis in order to not skew the distribution towards false positive results, since some cells displayed extremely large gaps of 90–113 μm (see "Noncanonical AIS Morphologies" section). First, we compared all pyramidal neurons with all interneurons, and saw no significant difference in gap length (PYR: 13.5 μm ± 12.6 vs. IN: 14.3 μm ± 10.9, $p = 0.239$; groups II and III were pooled; **Figure 6C**). No significant difference in gap length was observed when comparing supragranular and infragranular pyramidal neurons (supra: 12.2 μm ± 11.2 vs. *infra*: 13.5 μm ± 11.9, $p = 0.344$). Likewise, no significant difference in gap length between the interneuron classes (perisomatic vs. dendrite-targeting) was seen (BC: 14.4 μm ± 8.8 μm, BT/MC: 12.9 μm ± 8.6 μm, $p = 0.505$). Likewise, axon diameter did not differ significantly between PYR and IN, irrespective of morphological group (PYR non AcD (Groups I + II): 0.92 μm ± 0.02 vs. IN: 0.93 μm ± 0.02; PYR AcD (Group III): 0.92 ± 0.01 vs. IN: 0.92 ± 0.02; **Figure 6D**).

Noncanonical AIS Morphologies

Several rather atypical AIS morphologies were observed *in vivo* and in OTC, examples of which are shown in **Figure 7** and Supplementary Figures S2C–C3. A number of interneurons showed specific AIS-staining along axonal bifurcations and branch points (**Figure 7A**). This was not observed in pyramidal neurons. Furthermore, a noteworthy proportion of both pyramidal cells and interneurons exhibited high-intensity spot-like immunoreactivity against βIV-spectrin often at a remarkable distance to the end of the actual AIS, which we tentatively termed "extra domains" (**Figure 7B**). These occurred in cells that morphologically appeared normal and healthy. Third, we observed what others and we have termed as "leaky" AIS in hippocampal AcD cells (Thome et al., 2014) and dendritic "hot spots" in PARV-positive cells of the olfactory bulb (Kosaka et al., 2008; Thome et al., 2014), showing more or less clearly visible immunoreaction to AIS markers along the basal dendritic shaft and into the emerging axon (**Figure 7C**, signal delineated by white arrowheads). These qualitative observations were made in a significant proportion of cells, suggesting that these phenotypes unlikely result from culture effects, but rather reflect the significant heterogeneity of AIS in cortical neurons. In fact, extra domains and leaky AIS were seen quite frequently in up to 45% of neurons and merit further investigation. As mentioned above, we also observed several pyramidal neurons and interneurons with extremely long gaps between the proximal AIS border and the axon origin, ranging from 90 μm to 113 μm (**Figure 7D**). Such extreme cases could result from axonal remodeling after injury induced by lesions during the sectioning process.

DISCUSSION

Heterogeneity in Axon Origin

Why is AIS heterogeneity an important subject? A growing number of studies investigating AIS plasticity describe events

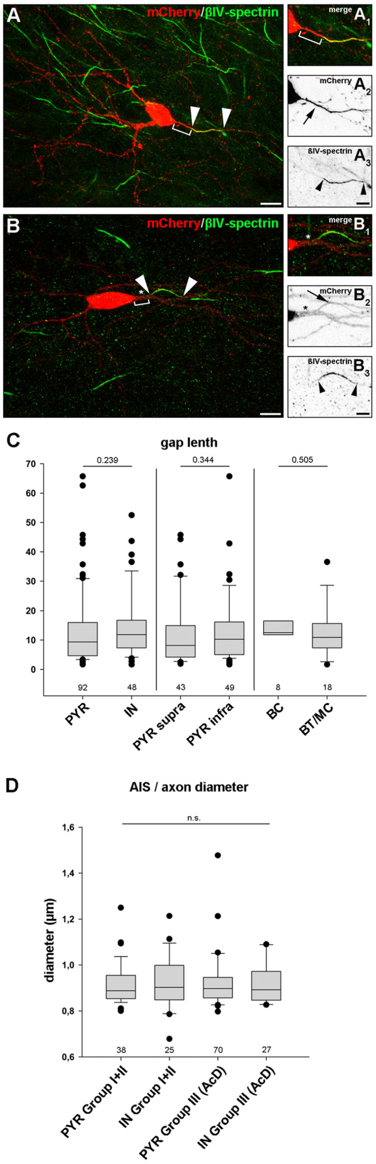

FIGURE 6 | Gap length between AIS and soma is similar in pyramidal neurons and interneurons. **(A–A3)** Representative image of an interneuron classified in group II (distal AIS on somatic axon) to illustrate the gap (bracket in **A+A1**) between soma (mCherry, red; **A–A2**) and proximal AIS (βIV-spectrin, green; **A–A3**). AIS indicated by arrowheads, arrow points to axon. The same cell was reconstructed in Imaris to highlight the 3D expansion of the AIS (Supplementary Figure S3E). **(B–B3)** Representative image of a group III interneuron (AcD). Gap delineated by bracket **(B+B1)**. The dendritic shaft is highlighted by an asterisk. Arrowheads outline the AIS (βIV spectrin, green; **B–B3**) on an axon with dendritic origin (mCherry, red; **B–B2**). **(C)** Gap length was not significantly longer in pyramidal neurons (PYR) compared to interneurons (IN) irrespective of supragranular vs. infragranular location of IN subtype. Pyramidal neurons showed a tendency for a more heterogeneous gap length distribution. Wilkoxon rank-sum test with *post hoc* correction applying Dunn's post test, *p* values and *n*-numbers indicated in graph. **(D)** Comparison of axon diameter in PYR vs. IN (data pooled for Groups I and II) and AcDs in both cell classes. No significant difference was observed. Wilkoxon rank-sum test with *post hoc* correction applying Dunn's post test, *p* values and *n*-numbers indicated in graph. Scale bar **(A,B)** = 20 µm, scale bar **(A1–3)** = 10 µm, scale bar **(B1–3)** = 5 µm.

that indicate an active shifting and/or elongation and shortening of the AIS (reviewed in Adachi et al., 2015; Wefelmeyer et al., 2016; Yamada and Kuba, 2016; Jamann et al., 2017). However, the actual baseline morphology in these systems studies is almost never taken into account. Since a robust AIS live label is currently just emerging (Dumitrescu et al., 2016), the so far reported dynamic range of AIS motion during events of plasticity should be handled with caution. For instance, the shifting and elongating of AIS so far has been observed predominantly in cells where the axon emerges from the soma and the AIS is close to the soma. This configuration is seen in just about one-third of all neurons in the current study. All other neurons where this is not fulfilled have not been analyzed for these forms of structural plasticity as of yet. A fundamental question regarding AIS plasticity is therefore not yet fully answered. Further, the question of whether the various interneuron types undergo comparable forms of plasticity has not been analyzed to date.

Some incoherence exists with regard to the nomenclature of AIS on axons emanating from dendrites, a long known phenomenon in vertebrate neurons, and much more common in non-vertebrates (Triarhou, 2014). We refrained from coining new terms to describe known phenomena, and classified neurons into three distinct axon/AIS groups as outlined in Supplementary Figure S4, using the term AcD cell introduced previously (Thome et al., 2014). The authors showed that roughly 50% of CA1 neurons in mouse hippocampus possess AIS beginning either directly at the point of origin of the axon or with a discernible gap to that point. More recently, Hamada et al. (2016) published experimental and modeling data showing that axon/AIS location should not be viewed isolated from the morphology of the somatodendritic domain. The authors show that in combination with the complexity of the dendritic tree, the location of the axon/AIS is correlated with the somatodendritic capacitance load, and suggest it to be a mechanism for homeostatic scaling of somatic APs (Hamada et al., 2016). The functional consequence of a gap between the AIS and the soma, regardless of whether this gap results from a distal AIS on an axon with somatic origin (Group II) or from a distal AIS/axon emerging off a dendrite (Group III, AcD) is still a matter of debate. It seems logical that the further the AIS is located distally from the soma, the more the AP generation is uncoupled from somatic input. In fact, as shown by recent studies, this results in higher excitability to synaptic input and decreased activation thresholds for AP generation in hippocampal AcD cells (Thome et al., 2014) and cerebellar granule cells of this morphology (Houston et al., 2017). Generally speaking, the optimal AIS length and/or location (that of the most excitability, regardless of whether this is positive or negative for the cell) should be depending on the balance of depolarizing drive and its electrical isolation from the conductance load via the somatodendritic domain (Kuba et al., 2006; Baranauskas et al., 2013). Indeed, a comprehensive modeling study utilizing realistic neurons indicated that there is a physiological optimum for AIS distance to the soma, depending on the cell type and somatodendritic morphology (Gulledge and Bravo, 2016). The authors demonstrate that AIS length and location have different impact on the rheobase: in

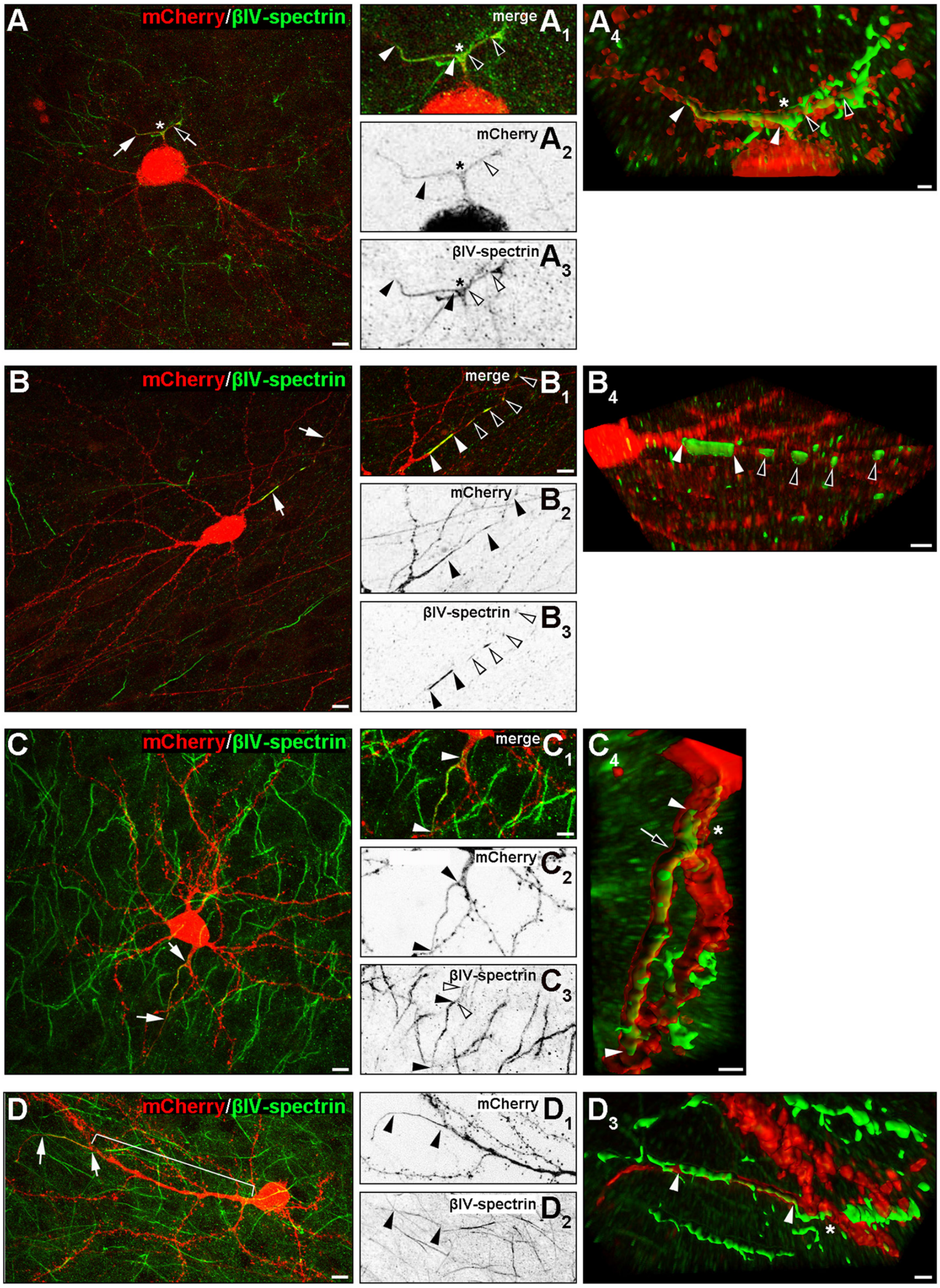

FIGURE 7 | Noncanonical AIS phenotypes in PYR and IN. **(A–A4)** Representative image of an interneuron with a proximal axon bifurcation (asterisk in **A–A4**), along which an AIS is developed, expanding into the two processes after a shared basal shaft (white and black arrows and arrowheads). The length of both AIS is delineated by white and black arrowheads in (**B3**; βIV-spectrin signal). Panel **(A4)** shows the AIS of this cell after deconvolution and surface reconstruction in Imaris to highlight the 3D aspect of the AIS branch point (white and black arrowheads). **(B–B4)** Representative image of βIV-spectrin-positive clusters along the axon of an interneuron (group III, AcD). White arrows in **(B)** indicate the axon, white arrowheads in **(B1)** delineate the length of the primary AIS of this cell (βIV-spectrin, green). Additional immunoreactive clusters termed “extra domains” are outlined by black and white arrowheads, respectively, in **(B1,B3)**. Panel **(B4)** shows the AIS and extra domains of this cell after deconvolution and surface reconstruction in Imaris. **(C–C4)** Representative image of a pyramidal neuron classified in group III (AcD) with a βIV-spectrin-immunoreactive basal dendrite before axon/AIS onset. White arrows in **(C)** and white arrowheads in **(C1)** outline the actual AIS and the proximal “leak” of βIV-spectrin into the basal dendritic shaft (also delineated by white arrowheads in **(C3+4)**, with black arrowheads showing the actual AIS). Panel **(C4)** shows the AIS of this cell after deconvolution and surface reconstruction in Imaris to highlight the actual expansion of βIV-spectrin immunosignal into the dendritic shaft (the proximal beginning of the AIS is highlighted by a black arrow). **(D–D3)** Example of a pyramidal neuron with an extremely large gap between soma and AIS (bracket in **D**). White arrows in **(D)** and black arrowheads in **(D1+2)** delineate the actual AIS. Panel **(D3)** shows the AIS (white arrowheads) at its dendritic origin after deconvolution and surface reconstruction in Imaris. Scale bar **(A–D,D1+2)** = 10 μm, scale bars in **(A1–C3)** for all small inserts = 5 μm, scale bars in 3D reconstruction **(A4)** = 2 μm, **(B4)** = 5 μm, **(C4+D3)** = 3 μm.

neurons with a large somatodendritic domain, a longer and more distally located AIS is more optimal, while in smaller neurons, a relatively short and more proximal AIS renders neurons more excitable. Likewise, as shown by Hamada et al. (2016) the gap (measured as branch path length from the soma) is inversely correlated with dendritic tree size and complexity. In fact, "blind" electrophysiological recordings alone gave no indication of which cell type (proximal or distal AIS) was being analyzed (Thome et al., 2014; Hamada et al., 2016), leading to the assumption that AIS position alone cannot determine cellular excitability. So while the distance of the AIS to the soma possibly has direct physiological implications, the corresponding somatodendritic domain seems to be a determining factor as well.

Methodological Considerations

OTCs are well established culture systems maintaining a 3D environment for long periods *in vitro* to study structure and function under easy-to-control conditions. A majority of processes like development of activity, synaptogenesis, and dendritogenesis occur along the same time line as in cortex *in vivo* (Gähwiler et al., 1997; Wirth et al., 2003; Berghuis et al., 2004; Del Turco and Deller, 2007; Mori et al., 2007; Humpel, 2015). For instance, interneurons develop their typical FS and regular-spiking patterns and connect to regular-spiking pyramidal cells in an adult excitation/inhibition balance by DIV 20 in visual cortex OTC (Klostermann and Wahle, 1999). The activity drives expression of trophic factors like BDNF similar to the *in vivo* situation, with the exception that peak levels evoked by sensory inputs are missing (Gorba and Wahle, 1999; Gorba et al., 1999).

A peculiar observation was the βIV-spectrin positive "extra domains" downstream of the AIS. Such spots could appear as break-down products from AIS or nodes of Ranvier in unhealthy cells, which occur under poor culturing conditions in dissociated neurons and disappear with more optimal culture conditions. However, we now find them in a substantial fraction of cells in DIV 20 OTC long after ontogenetic cell death periods in cultures that are fully recovered and could potentially live on for many further weeks (Humpel, 2015). The corresponding neurons did not display symptoms of degeneration such as nuclear break-down, leakage of mCherry protein, or vacuoles. Although not yet systematically assessed, the distance and periodicity with which the extra domains occur to where AIS scaffolds would normally be found (closer to soma) might imply a more relevant and functional role. One possibility is that these sites represent soon-to-be nodes or preassembled multiprotein "node" packages up for anterograde transport, although their size seems quite large. However, such large microdomains have been observed. In frog spinal cord and cerebral cortex, long nodes of Ranvier of >10 μm in length have been described (Gray, 1970).

Developmental Aspects and Potential Impact of Species Differences

The developmental profile revealed that overall the AIS of neurons in OTC start out rather short, then elongate to peak values at DIV 15, and shorten until DIV 21 to a final length also seen at DIV 35. Excitability and spontaneous AP firing is initially low and infrequent in OTC, but at DIV 20 neurons display stable membrane potentials, cell type-specific action potential wave forms and spike rates, all of which remain constant in neurons recorded until DIV 140 (Klostermann and Wahle, 1999). Also, in visual cortex of mice *in vivo*, AIS steadily increase in length from shortly after birth until P15 which is around or shortly after eye opening (Gutzmann et al., 2014). Afterwards, AIS undergo a dramatic shortening until the beginning of the critical period of cortical ocular dominance plasticity at P21. By the end of the critical period around P35, AIS have re-elongated to the length which is also observed in the adult cortex, and the variability of individual lengths is much narrower (Gutzmann et al., 2014). A far less dynamic AIS length increase occurred in the non-sensory cingulate cortex, where no influence of visual experience was observed (Gutzmann et al., 2014). Thus, the maturation profile determined here in OTC corresponds in two aspects with the *in vivo* situation, namely the increase to peak lengths until DIV 15 and the wider scatter of individual AIS lengths between DIV 7 and DIV 15. These aspects are either genetically encoded and cell-autonomous or driven by intrinsic cues e.g., depending on the electrical activity developing in OTC. A reason for the wide scatter of length distribution could be the observation in mouse cortex at P8–13 that layer V pyramidal cells display an enormous heterogeneity in firing rate responses and excitability, which seems to be intrinsic to the cells and partly persists into adulthood (Zerlaut et al., 2016). However, layer V in motor cortex harbors four major groups of pyramidal cells distinguished by projection target and their electrophysiological properties (Oswald et al., 2013). This may contribute to the wide scatter of AIS length distribution. It remains to be seen if AIS length and position correlate with the individual functional state of a given neuron, or with target-specificity of a given subset. The previously observed substantial length reduction followed by re-elongation does not occur in OTC, most likely because it is influenced by sensory input (Gutzmann et al., 2014; Schlüter et al., 2017) absent in OTC. Overall, the average length of AIS in rat visual cortex OTC (cultured on filters) is quite similar to the averages determined *in vivo* in mouse visual cortex.

Functional Consequences of AIS Heterogeneity

The pyramidal cell types in supra- and infragranular layers have clearly different axonal projection targets and projection distances, differ in electrophysiology (Gottlieb and Keller, 1997), in the density of symmetric BC synapses (Fariñas and DeFelipe, 1991; Melchitzky et al., 1997), in mechanisms regulating intrinsic excitability and plasticity (Nataraj et al., 2010), and in the excitatory output to the various types of interneurons (Xu and Callaway, 2009). Yet, they display AIS of similar length, and the AIS phenotypes (Group 1–III) occur in similar proportions, suggesting that these parameters are neither correlated with a cell's specializations nor constitute a prerequisite for the ability of a cell to undergo plastic changes. This hypothesis is supported by data showing that the onset of an axon either from the soma or a basal dendrite is not driven developmentally by the target region (Hamada et al., 2016).

In mouse visual cortex *in vivo*, AIS of supragranular pyramidal cells are barely longer on average by about 2 μm than those in infragranular layers in mouse visual cortex (Gutzmann et al., 2014). At the structural level, activity-dependent reorganization of the axonal arbors can be elicited, e.g., in the barrel cortex in supragranular cells towards the end of the first postnatal month (Broser et al., 2008). However, AIS length significantly differs between cortical cell classes. Interneurons overall have shorter AIS than pyramidal cells. Whether or not this is genetically or functionally determined has not been addressed yet.

BT/MCs are non-FS neurons (Wang et al., 2004), activated by recurrent pyramidal cell axons, inhibited by interneuron-selective bipolar cells and by BCs (Jiang et al., 2015; Walker et al., 2016), and regulate information processing in pyramidal cell dendrites. They are known to frequently display axons emerging from primary, secondary or even tertiary dendrites (Wahle and Meyer, 1989). These cells being predominantly AcD with distal AIS may be an efficient design principle, because rather few excitatory inputs converging on just the dendrite carrying the axon could trigger the inhibitory output towards the pyramidal cell. Indeed, it was suggested that there is a physiological range of "ideal" AIS distance to the soma; whether or not this accounts for interneurons remains to be determined (Gulledge and Bravo, 2016).

Neurons of all interneuron types may give rise to more than just one axon (Meyer and Wahle, 1988). These axons may arise both from the soma, or both from the same or from different dendrites, or from a soma and a dendrite, and the two axon hillocks can reside close together such that the axon seems to branch within a few micrometer after its point of origin (Meyer and Wahle, 1988). We now show that both axons have an AIS and that their respective lengths are similar. Whether or not the two axons work as independent units on the same cell remains to be determined. The close neighborhood of two axon hillocks on one cell possibly explains some of the noncanonical AIS observed in the present study, namely, βIV-spectrin-immunoreactivity along the entire T-shaped branch point of an axon. However, we also observed βIV-spectrin positive axonal branch points further away from the axon hillock. Multiaxonic cells can be produced *in vitro* by altering proteins essential for neuronal polarity, and these axons are positive for tau and the AIS marker ankyrinG (Muñoz-Llancao et al., 2015). In addition, βIV-spectrin, ankyrinG and voltage-gated sodium channels may be localized in the dendrite which carries the axon. This is another phenomenon previously observed as a "leaky" AIS (Thome et al., 2014). Dendrites carrying an axon are asymmetric in that a fasciculation of microtubules occurs along the side of the dendrite where the axon emerges, whereas the other side of the dendritic cytosol contains microtubulues in the dendrite-typical homogeneous distribution (Peters et al., 1968). However, PARV-positive neurons in the rodent olfactory bulb have been shown to frequently express AIS scaffolding proteins and sodium channels in dendritic "hot spots" 7–50 μm distal from the soma (Kosaka et al., 2008). Interestingly, the membrane undercoating of these particular dendritic segments at the ultrastructural level resembled that of typical AIS (Kosaka et al., 2008).

Perisomatic BCs are feed-forward activated by incoming afferents. Faithful recruitment is enabled by a high density of calcium-permeable AMPA receptors and highly reliable AP firing to deliver feed-forward inhibition, which hyperpolarizes local pyramidal cell groups. BCs containing PARV are FS interneurons and essential for gamma oscillations (Hu et al., 2014). Also in OTC, large BCs respond to very small current injections with strong firing (Klostermann and Wahle, 1999). Interestingly, 50% of BCs had axons originating from the soma and a proximal AIS. AIS location *in vitro* has been recently shown to be regulated by BDNF such that high TrkB signaling moves the AIS proximally towards the soma (Guo et al., 2017). The FS PARV-containing large BCs express mainly TrkB receptors and depend heavily on BDNF derived from pyramidal cells (Gorba and Wahle, 1999; Berghuis et al., 2004; Patz et al., 2004). This suggests that in BCs, a strong and steady BDNF supply stabilizes the AIS close to the soma. It remains to be tested if this "classical" axon/AIS configuration is an essential requirement for FS cell properties.

Why then do we observe just 50% of the BCs with the Group I- phenotype? Likely this is owing to an inhomogeneity of our sample because BCs comprises neurons with very local axons and as well as with long horizontal axonal fields in layers II/III–V, and FS and non-FS types (Battaglia et al., 2013; Jiang et al., 2015; Feldmeyer et al., 2017). Already the PARV-positive BCs are inhomogeneous in mice, with a subset projecting across the corpus callosum (Rock et al., 2017). In the absence of further neurochemical, hodological or electrophysiological markers, we are at this moment unable to divide this group any further. For instance, non-PARV non-FS cholecystokinin-positive BCs employ cannabinoid-1 receptor (CB1R) mediated signaling to enlarge dendritic fields and facilitate synapse development (Berghuis et al., 2004). Thus, AIS location or length may be regulated differently in these cells compared to the BDNF-dependent FS PARV BCs. Interestingly, albeit not residing at the AIS, CB1R signaling influences the AIS during early differentiation in that inhibition of CB1R signaling decreases ankyrinG expression in dissociated hippocampal (mostly pyramidal) neurons, resulting in shorter AIS (Tapia et al., 2017). Presence and strength of such early influences may explain why *in vivo* and *in vitro* as well as in neurons from different species, the overall AIS length varies.

Taken together, these reflections argue for the necessity of a much more detailed analysis of AIS phenotypes in functionally and neurochemically well-delineated neuronal subsets. This future work will then also address the question, how the observed AIS heterogeneity could contribute to neuronal excitability, adaptation and network homeostasis.

AUTHOR CONTRIBUTIONS

ME and PW: conceptualization and design of the study. FH, AJ, CR, JM-B, JR, CC, PW and ME: data acquisition and programming. FH, AJ, PW and ME: data analysis. FH, AJ, CS, PW and ME: data interpretation. FH, ME and PW: preparation of manuscript. FH, AJ, CR, JM-B, JR, CC, CS, PW and ME: final approval of the version to be published.

FUNDING

This work was supported by a project grant from the ProRetina Foundation to ME, a grant from the Schram-Stiftung to PW, and the Deutsche Forschungsgemeinschaft (SFB 1134/A03) to CS. We further acknowledge the support of the Core Facility Life Cell Imaging Mannheim at the CBTM (DFG-INST 91027/10-1 FUGG and DFG INST 91027/9-1 FUGG). This publication was supported by the Deutsche Forschungsgemeinschaft and Heidelberg University within the funding program Open Access Publishing.

ACKNOWLEDGMENTS

The authors would like to thank Andrea Räk and Sabine Schönfelder (Bochum) as well as Alexander Bott (Mannheim) for technical support and Nora Jamann (Mannheim) for graphics support. We thank Mirko Witte and Jochen Staiger, Institute of Anatomy, Justus-Liebig-University Göttingen, Germany, for the tissue of PV-tdTomato mice, and Tina Sackmann and Andreas Draguhn, Institute of Physiology and Pathophysiology, Heidelberg University, Germany, for the tissue of Thy1-GFP mice.

SUPPLEMENTARY MATERIAL

The Supplementary Material for this article can be found online at: https://www.frontiersin.org/articles/10.3389/fncel.2017.00332/full#supplementary-material

REFERENCES

Adachi, R., Yamada, R., and Kuba, H. (2015). Plasticity of the axonal trigger zone. *Neuroscientist* 21, 255–265. doi: 10.1177/1073858414535986

Ascoli, G. A., Alonso-Nanclares, L., Anderson, S. A., Barrionuevo, G., Benavides-Piccione, R., Burkhalter, A., et al. (2008). Petilla terminology: nomenclature of features of GABAergic interneurons of the cerebral cortex. *Nat. Rev. Neurosci.* 9, 557–568. doi: 10.1038/nrn2402

Baranauskas, G., David, Y., and Fleidervish, I. A. (2013). Spatial mismatch between the Na^+ flux and spike initiation in axon initial segment. *Proc. Natl. Acad. Sci. U S A* 110, 4051–4056. doi: 10.1073/pnas.1215125110

Battaglia, D., Karagiannis, A., Gallopin, T., Gutch, H. W., and Cauli, B. (2013). Beyond the frontiers of neuronal types. *Front. Neural Circuits* 7:13. doi: 10.3389/fncir.2013.00013

Berghuis, P., Dobszay, M. B., Ibanez, R. M., Ernfors, P., and Harkany, T. (2004). Turning the heterogeneous into homogeneous: studies on selectively isolated GABAergic interneuron subsets. *Int. J. Dev. Neurosci.* 22, 533–543. doi: 10.1016/j.ijdevneu.2004.07.012

Broser, P., Grinevich, V., Osten, P., Sakmann, B., and Wallace, D. J. (2008). Critical period plasticity of axonal arbors of layer 2/3 pyramidal neurons in rat somatosensory cortex: layer-specific reduction of projections into deprived cortical columns. *Cereb. Cortex* 18, 1588–1603. doi: 10.1093/cercor/bhm189

Cajal, S. F. R. (1909). *Histologie du Système Nerveux de L'homme and des Vertébrés.* Paris: Maloine.

Cruz, D. A., Eggan, S. M., and Lewis, D. A. (2003). Postnatal development of pre- and postsynaptic GABA markers at chandelier cell connections with pyramidal neurons in monkey prefrontal cortex. *J. Comp. Neurol.* 465, 385–400. doi: 10.1002/cne.10833

Cruz, D. A., Lovallo, E. M., Stockton, S., Rasband, M., and Lewis, D. A. (2009). Postnatal development of synaptic structure proteins in pyramidal neuron axon initial segments in monkey prefrontal cortex. *J. Comp. Neurol.* 514, 353–367. doi: 10.1002/cne.22006

Debanne, D., Campanac, E., Bialowas, A., Carlier, E., and Alcaraz, G. (2011). Axon physiology. *Physiol. Rev.* 91, 555–602. doi: 10.1152/physrev.00048.2009

DeFelipe, J., López-Cruz, P. L., Benavides-Piccione, R., Bielza, C., Larrañaga, P., Anderson, S., et al. (2013). New insights into the classification and nomenclature of cortical GABAergic interneurons. *Nat. Rev. Neurosci.* 14, 202–216. doi: 10.1038/nrn3444

Del Turco, D., and Deller, T. (2007). Organotypic entorhino-hippocampal slice cultures—a tool to study the molecular and cellular regulation of axonal regeneration and collateral sprouting *in vitro*. *Methods Mol. Biol.* 399, 55–66. doi: 10.1007/978-1-59745-504-6_5

D'Este, E., Kamin, D., Göttfert, F., El-Hady, A., and Hell, S. W. (2015). STED nanoscopy reveals the ubiquity of subcortical cytoskeleton periodicity in living neurons. *Cell Rep.* 10, 1246–1251. doi: 10.1016/j.celrep.2015.02.007

Dumitrescu, A. S., Evans, M. D., and Grubb, M. S. (2016). Evaluating tools for live imaging of structural plasticity at the axon initial segment. *Front. Cell. Neurosci.* 10:268. doi: 10.3389/fncel.2016.00268

Fariñas, I., and DeFelipe, J. (1991). Patterns of synaptic input on corticocortical and corticothalamic cells in the cat visual cortex. II. The axon initial segment. *J. Comp. Neurol.* 304, 70–77. doi: 10.1002/cne.903040106

Feldmeyer, D., Qi, G., Emmenegger, V., and Staiger, J. F. (2017). Inhibitory interneurons and their circuit motifs in the many layers of the barrel cortex. *Neuroscience* doi: 10.1016/j.neuroscience.2017.05.027 [Epub ahead of print].

Feng, G., Mellor, R. H., Bernstein, M., Keller-Peck, C., Nguyen, Q. T., Wallace, M., et al. (2000). Imaging neuronal subsets in transgenic mice expressing multiple spectral variants of GFP. *Neuron* 28, 41–51. doi: 10.1016/s0896-6273(00)00084-2

Gähwiler, B. H., Capogna, M., Debanne, D., McKinney, R. A., and Thompson, S. M. (1997). Organotypic slice cultures: a technique has come of age. *Trends Neurosci.* 20, 471–477. doi: 10.1016/s0166-2236(97)01122-3

Gentet, L. J., and Williams, S. R. (2007). Dopamine gates action potential backpropagation in midbrain dopaminergic neurons. *J. Neurosci.* 27, 1892–1901. doi: 10.1523/JNEUROSCI.5234-06.2007

Gorba, T., Klostermann, O., and Wahle, P. (1999). Development of neuronal activity and activity-dependent expression of brain-derived neurotrophic factor mRNA in organotypic cultures of rat visual cortex. *Cereb. Cortex* 9, 864–877. doi: 10.1093/cercor/9.8.864

Gorba, T., and Wahle, P. (1999). Expression of TrkB and TrkC but not BDNF mRNA in neurochemically identified interneurons in rat visual cortex *in vivo* and in organotypic cultures. *Eur. J. Neurosci.* 11, 1179–1190. doi: 10.1046/j.1460-9568.1999.00551.x

Gottlieb, J. P., and Keller, A. (1997). Intrinsic circuitry and physiological properties of pyramidal neurons in rat barrel cortex. *Exp. Brain Res.* 115, 47–60. doi: 10.1007/pl00005684

Gray, E. G. (1970). The fine structure of nerve. *Comp. Biochem. Physiol.* 36, 419–448. doi: 10.1016/0010-406X(70)91021-2

Grubb, M. S., Shu, Y., Kuba, H., Rasband, M. N., Wimmer, V. C., and Bender, K. J. (2011). Short- and long-term plasticity at the axon initial segment. *J. Neurosci.* 31, 16049–16055. doi: 10.1523/JNEUROSCI.4064-11.2011

Gulledge, A. T., and Bravo, J. J. (2016). Neuron morphology influences axon initial segment plasticity. *eNeuro* 3:ENEURO.0085-15.2016. doi: 10.1523/ENEURO.0085-15.2016

Gumy, L. F., Katrukha, E. A., Grigoriev, I., Jaarsma, D., Kapitein, L. C., Akhmanova, A., et al. (2017). MAP2 defines a pre-axonal filtering zone to regulate KIF1- versus KIF5-dependent cargo transport in sensory neurons. *Neuron* 94, 347.e7–362.e7. doi: 10.1016/j.neuron.2017.03.046

Guo, Y., Su, Z. J., Chen, Y. K., and Chai, Z. (2017). Brain-derived neurotrophic factor/neurotrophin 3 regulate axon initial segment location and affect neuronal excitability in cultured hippocampal neurons. *J. Neurochem.* 142, 260–271. doi: 10.1111/jnc.14050

Gutzmann, A., Ergül, N., Grossmann, R., Schultz, C., Wahle, P., and Engelhardt, M. (2014). A period of structural plasticity at the axon initial segment in developing visual cortex. *Front. Neuroanat.* 8:11. doi: 10.3389/fnana.2014.00011

Hamada, M. S., Goethals, S., de Vries, S. I., Brette, R., and Kole, M. H. (2016). Covariation of axon initial segment location and dendritic tree normalizes the somatic action potential. *Proc. Natl. Acad. Sci. U S A* 113, 14841–14846. doi: 10.1073/pnas.1607548113

Hamad, M. I., Jack, A., Klatt, O., Lorkowski, M., Strasdeit, T., Kott, S., et al. (2014). Type I TARPs promote dendritic growth of early postnatal neocortical pyramidal cells in organotypic cultures. *Development* 141, 1737–1748. doi: 10.1242/dev.099697

Hamad, M. I., Ma-Högemeier, Z. L., Riedel, C., Conrads, C., Veitinger, T., Habijan, T., et al. (2011). Cell class-specific regulation of neocortical dendrite and spine growth by AMPA receptor splice and editing variants. *Development* 138, 4301–4313. doi: 10.1242/dev.071076

Häusser, M., Stuart, G., Racca, C., and Sakmann, B. (1995). Axonal initiation and active dendritic propagation of action potentials in substantia nigra neurons. *Neuron* 15, 637–647. doi: 10.1016/0896-6273(95)90152-3

Herde, M. K., Iremonger, K. J., Constantin, S., and Herbison, A. E. (2013). GnRH neurons elaborate a long-range projection with shared axonal and dendritic functions. *J. Neurosci.* 33, 12689–12697. doi: 10.1523/JNEUROSCI.0579-13.2013

Hinman, J. D., Rasband, M. N., and Carmichael, S. T. (2013). Remodeling of the axon initial segment after focal cortical and white matter stroke. *Stroke* 44, 182–189. doi: 10.1161/STROKEAHA.112.668749

Houston, C. M., Diamanti, E., Diamantaki, M., Kutsarova, E., Cook, A., Sultan, F., et al. (2017). Exploring the significance of morphological diversity for cerebellar granule cell excitability. *Sci. Rep.* 7:46147. doi: 10.1038/srep46147

Hu, H., Gan, J., and Jonas, P. (2014). Interneurons. Fast-spiking, parvalbumin$^+$ GABAergic interneurons: from cellular design to microcircuit function. *Science* 345:1255263. doi: 10.1126/science.1255263

Humpel, C. (2015). Organotypic brain slice cultures: a review. *Neuroscience* 305, 86–98. doi: 10.1016/j.neuroscience.2015.07.086

Jamann, N., Jordan, M., and Engelhardt, M. (2017). Activity-dependent axonal plasticity in sensory systems. *Neuroscience* doi: 10.1016/j.neuroscience.2017.07.035 [Epub ahead of print].

Jiang, X., Shen, S., Cadwell, C. R., Berens, P., Sinz, F., Ecker, A. S., et al. (2015). Principles of connectivity among morphologically defined cell types in adult neocortex. *Science* 350:aac9462. doi: 10.1126/science.aac9462

Klostermann, O., and Wahle, P. (1999). Patterns of spontaneous activity and morphology of interneuron types in organotypic cortex and thalamus-cortex cultures. *Neuroscience* 92, 1243–1259. doi: 10.1016/s0306-4522(99)00009-3

Kole, M. H., and Stuart, G. J. (2012). Signal processing in the axon initial segment. *Neuron* 73, 235–247. doi: 10.1016/j.neuron.2012.01.007

Kosaka, T., Komada, M., and Kosaka, K. (2008). Sodium channel cluster, βIV-spectrin and ankyrinG positive "hot spots" on dendritic segments of parvalbumin-containing neurons and some other neurons in the mouse and rat main olfactory bulbs. *Neurosci. Res.* 62, 176–186. doi: 10.1016/j.neures.2008.08.002

Kuba, H., Ishii, T. M., and Ohmori, H. (2006). Axonal site of spike initiation enhances auditory coincidence detection. *Nature* 444, 1069–1072. doi: 10.1038/nature05347

Kuba, H., Oichi, Y., and Ohmori, H. (2010). Presynaptic activity regulates Na$^+$ channel distribution at the axon initial segment. *Nature* 465, 1075–1078. doi: 10.1038/nature09087

Leterrier, C. (2016). The axon initial segment, 50 years later: a nexus for neuronal organization and function. *Curr. Top. Membr.* 77, 185–233. doi: 10.1016/bs.ctm.2015.10.005

Lorincz, A., and Nusser, Z. (2010). Molecular identity of dendritic voltage-gated sodium channels. *Science* 328, 906–909. doi: 10.1126/science.1187958

Martina, M., Vida, I., and Jonas, P. (2000). Distal initiation and active propagation of action potentials in interneuron dendrites. *Science* 287, 295–300. doi: 10.1126/science.287.5451.295

Melchitzky, D. S., Sesack, S. R., and Lewis, D. A. (1997). Axosomatic input to subpopulations of cortically projecting pyramidal neurons in primate prefrontal cortex. *Synapse* 25, 326–334. doi: 10.1002/(sici)1098-2396(199704)25:4< 326::aid-syn3>3.3.co;2-3

Meyer, G. (1983). Axonal patterns and topography of short-axon neurons in visual areas 17, 18, and 19 of the cat. *J. Comp. Neurol.* 220, 405–438. doi: 10.1002/cne.902200405

Meyer, G., and Ferres-Torres, R. (1984). Postnatal maturation of nonpyramidal neurons in the visual cortex of the cat. *J. Comp. Neurol.* 228, 226–244. doi: 10.1002/cne.902280209

Meyer, G., and Wahle, P. (1988). Early postnatal development of cholecystokinin-immunoreactive structures in the visual cortex of the cat. *J. Comp. Neurol.* 276, 360–386. doi: 10.1002/cne.902760304

Mori, M., Gähwiler, B. H., and Gerber, U. (2007). Recruitment of an inhibitory hippocampal network after bursting in a single granule cell. *Proc. Natl. Acad. Sci. U S A* 104, 7640–7645. doi: 10.1073/pnas.0702164104

Muñoz-Llancao, P., Henríquez, D. R., Wilson, C., Bodaleo, F., Boddeke, E. W., Lezoualc'h, F., et al. (2015). Exchange protein directly activated by cAMP (EPAC) regulates neuronal polarization through Rap1B. *J. Neurosci.* 35, 11315–11329. doi: 10.1523/JNEUROSCI.3645-14.2015

Nataraj, K., Le Roux, N., Nahmani, M., Lefort, S., and Turrigiano, G. (2010). Visual deprivation suppresses L5 pyramidal neuron excitability by preventing the induction of intrinsic plasticity. *Neuron* 68, 750–762. doi: 10.1016/j.neuron.2010.09.033

Oswald, M. J., Tantirigama, M. L., Sonntag, I., Hughes, S. M., and Empson, R. M. (2013). Diversity of layer 5 projection neurons in the mouse motor cortex. *Front. Cell. Neurosci.* 7:174. doi: 10.3389/fncel.2013.00174

Patz, S., Grabert, J., Gorba, T., Wirth, M. J., and Wahle, P. (2004). Parvalbumin expression in visual cortical interneurons depends on neuronal activity and TrkB ligands during an Early period of postnatal development. *Cereb. Cortex* 14, 342–351. doi: 10.1093/cercor/bhg132

Peters, A., and Kimerer, L. M. (1981). Bipolar neurons in rat visual cortex: a combined Golgi-electron microscope study. *J. Neurocytol.* 10, 921–946. doi: 10.1007/bf01258522

Peters, A., Proskauer, C. C., and Kaiserman-Abramof, I. R. (1968). The small pyramidal neuron of the rat cerebral cortex. The axon hillock and initial segment. *J. Cell Biol.* 39, 604–619. doi: 10.1083/jcb.39.3.604

Rasband, M. N. (2010). The axon initial segment and the maintenance of neuronal polarity. *Nat. Rev. Neurosci.* 11, 552–562. doi: 10.1038/nrn2852

Rasband, W. S. (1997–2012). ImageJ. National Institutes of Health, Bethesda, MD, USA. Available online at: https://imagej.nih.gov/ij/

Rock, C., Zurita, H., Lebby, S., Wilson, C. J., and Apicella, A. J. (2017). Cortical circuits of callosal gabaergic neurons. *Cereb. Cortex* doi: 10.1093/cercor/bhx025 [Epub ahead of print].

Schlüter, A., Del Turco, D., Deller, T., Gutzmann, A., Schultz, C., and Engelhardt, M. (2017). Structural plasticity of synaptopodin in the axon initial segment during visual cortex development. *Cereb. Cortex* 27, 4662–4675. doi: 10.1093/cercor/bhx208

Sloper, J. J., and Powell, T. P. (1979). A study of the axon initial segment and proximal axon of neurons in the primate motor and somatic sensory cortices. *Philos. Trans. R. Soc. Lond. B Biol. Sci.* 285, 173–197. doi: 10.1098/rstb.1979.0004

Stoppini, L., Buchs, P. A., and Muller, D. (1991). A simple method for organotypic cultures of nervous tissue. *J. Neurosci. Methods* 37, 173–182. doi: 10.1016/0165-0270(91)90128-m

Tapia, M., Dominguez, A., Zhang, W., Del Puerto, A., Ciorraga, M., Benitez, M. J., et al. (2017). Cannabinoid receptors modulate neuronal morphology and ankyring density at the axon initial segment. *Front. Cell. Neurosci.* 11:5. doi: 10.3389/fncel.2017.00005

Thome, C., Kelly, T., Yanez, A., Schultz, C., Engelhardt, M., Cambridge, S. B., et al. (2014). Axon-carrying dendrites convey privileged synaptic input in hippocampal neurons. *Neuron* 83, 1418–1430. doi: 10.1016/j.neuron.2014.08.013

Triarhou, L. C. (2014). Axons emanating from dendrites: phylogenetic repercussions with Cajalian hues. *Front. Neuroanat.* 8:133. doi: 10.3389/fnana.2014.00133

Vascak, M., Sun, J., Bear, M., Jacobs, K. M., and Povlishock, J. T. (2017). Mild traumatic brain injury evokes pyramidal neuron axon initial segment plasticity and diffuse presynaptic inhibitory terminal loss. *Front. Cell. Neurosci.* 11:157. doi: 10.3389/fncel.2017.00157

Wahle, P., and Meyer, G. (1989). Early postnatal development of vasoactive intestinal polypeptide- and peptide histidine isoleucine-immunoreactive structures in the cat visual cortex. *J. Comp. Neurol.* 282, 215–248. doi: 10.1002/cne.902820206

Walker, F., Möck, M., Feyerabend, M., Guy, J., Wagener, R. J., Schubert, D., et al. (2016). Parvalbumin- and vasoactive intestinal polypeptide-expressing neocortical interneurons impose differential inhibition on Martinotti cells. *Nat. Commun.* 7:13664. doi: 10.1038/ncomms13664

Wang, Y., Toledo-Rodriguez, M., Gupta, A., Wu, C., Silberberg, G., Luo, J., et al. (2004). Anatomical, physiological and molecular properties of Martinotti cells in the somatosensory cortex of the juvenile rat. *J. Physiol.* 561, 65–90. doi: 10.1113/jphysiol.2004.073353

Wefelmeyer, W., Puhl, C. J., and Burrone, J. (2016). Homeostatic plasticity of subcellular neuronal structures: from inputs to outputs. *Trends Neurosci.* 39, 656–667. doi: 10.1016/j.tins.2016.08.004

Wirth, M. J., Brun, A., Grabert, J., Patz, S., and Wahle, P. (2003). Accelerated dendritic development of rat cortical pyramidal cells and interneurons after biolistic transfection with BDNF and NT4/5. *Development* 130, 5827–5838. doi: 10.1242/dev.00826

Xu, X., and Callaway, E. M. (2009). Laminar specificity of functional input to distinct types of inhibitory cortical neurons. *J. Neurosci.* 29, 70–85. doi: 10.1523/JNEUROSCI.4104-08.2009

Yamada, R., and Kuba, H. (2016). Structural and functional plasticity at the axon initial segment. *Front. Cell. Neurosci.* 10:250. doi: 10.3389/fncel.2016.00250

Zerlaut, Y., Telenczuk, B., Deleuze, C., Bal, T., Ouanounou, G., and Destexhe, A. (2016). Heterogeneous firing rate response of mouse layer V pyramidal neurons in the fluctuation-driven regime. *J. Physiol.* 594, 3791–3808. doi: 10.1113/JP272317

Conflict of Interest Statement: The authors declare that the research was conducted in the absence of any commercial or financial relationships that could be construed as a potential conflict of interest.

frontiers
in Cellular Neuroscience

ORIGINAL RESEARCH
published: 23 November 2016
doi: 10.3389/fncel.2016.00268

Evaluating Tools for Live Imaging of Structural Plasticity at the Axon Initial Segment

*Adna S. Dumitrescu, Mark D. Evans† and Matthew S. Grubb **

Centre for Developmental Neurobiology, King's College London, London, UK

The axon initial segment (AIS) is a specialized neuronal compartment involved in the maintenance of axo-dendritic polarity and in the generation of action potentials. It is also a site of significant structural plasticity—manipulations of neuronal activity *in vitro* and *in vivo* can produce changes in AIS position and/or size that are associated with alterations in intrinsic excitability. However, to date all activity-dependent AIS changes have been observed in experiments carried out on fixed samples, offering only a snapshot, population-wide view of this form of plasticity. To extend these findings by following morphological changes at the AIS of individual neurons requires reliable means of labeling the structure in live preparations. Here, we assessed five different immunofluorescence-based and genetically-encoded tools for live-labeling the AIS of dentate granule cells (DGCs) in dissociated hippocampal cultures. We found that an antibody targeting the extracellular domain of neurofascin provided accurate live label of AIS structure at baseline, but could not follow rapid activity-dependent changes in AIS length. Three different fusion constructs of GFP with full-length AIS proteins also proved unsuitable: while neurofascin-186-GFP and $Na_V\beta4$-GFP did not localize to the AIS in our experimental conditions, overexpressing 270kDa-AnkyrinG-GFP produced abnormally elongated AISs in mature neurons. In contrast, a genetically-encoded construct consisting of a voltage-gated sodium channel intracellular domain fused to yellow fluorescent protein (YFP-Na_VII–III) fulfilled all of our criteria for successful live AIS label: this construct specifically localized to the AIS, accurately revealed plastic changes at the structure within hours, and, crucially, did not alter normal cell firing properties. We therefore recommend this probe for future studies of live AIS plasticity *in vitro* and *in vivo*.

Keywords: axon initial segment, plasticity, imaging, dentate granule cell

Edited by:
Maren Engelhardt,
Heidelberg University, Germany

Reviewed by:
Paul M. Jenkins,
University of Michigan, USA
Kevin Bender,
University of California, San Francisco, USA

****Correspondence:***
Matthew S. Grubb
matthew.grubb@kcl.ac.uk

†Present address:
Mark D. Evans,
Gladstone Institute of Neurological Disease, San Francisco, CA, USA

Received: *05 August 2016*
Accepted: *04 November 2016*
Published: *23 November 2016*

Citation:
Dumitrescu AS, Evans MD and Grubb MS (2016) Evaluating Tools for Live Imaging of Structural Plasticity at the Axon Initial Segment. Front. Cell. Neurosci. 10:268. doi: 10.3389/fncel.2016.00268

INTRODUCTION

In neurons, the axon initial segment (AIS) is a molecularly-defined portion of the proximal axon with unique structural and functional properties. It serves as a barrier that maintains distinct somatodendritic vs. axonal neuronal polarity (Rasband, 2010), and is a key regulator of neuronal excitability—in almost all neuronal cell types, and under almost all circumstances, the AIS is the site of action potential initiation (Bender and Trussell, 2012; Kole and Stuart, 2012).

It is also a highly dynamic structure. Over short-term timescales, the AIS can be modified by intrinsic conductances and intracellular signaling pathways, as well as by extrinsic synaptic and neuromodulatory inputs, to alter the initiation, patterning and spike waveform features of action potential firing (Bender et al., 2010, 2011; Grubb et al., 2011; Cotel et al., 2013; Martinello et al., 2015). Over longer timescales of hours to days, the structural and positional features of the AIS can also undergo modifications in response to sustained perturbations in neuronal activity. These structural forms of AIS plasticity—which can include changes in AIS length, position and/or ion channel distribution in both excitatory and inhibitory neurons (Grubb and Burrone, 2010a; Kuba et al., 2010; Muir and Kittler, 2014; Chand et al., 2015; Evans et al., 2015; Wefelmeyer et al., 2015)—have been shown to be associated with changes in neuronal excitability, and may form part of a repertoire of compensatory mechanisms acting to maintain network activity within set limits.

However, the evidence for structural AIS plasticity has thus far been limited to static snapshots, where plasticity is revealed *post hoc* by comparing fixed AIS label in separate groups of neurons subjected to different activity manipulations. Put simply, no individual AIS has ever been observed to change. This is despite the many potential benefits to be gained from live imaging of structural AIS plasticity. Following AISs live over time would allow us to definitively reveal local structural plasticity in individual neurons. It would also reduce the effects of cell-to-cell and experiment-to-experiment heterogeneity, permitting the detection of fine-scale changes that can be obscured in all but the largest of independent group datasets. It would allow studies of AIS plasticity to be combined with simultaneous live interrogation of neuronal function via electrophysiological and/or functional imaging techniques. And, finally, it has the potential to give us new insight into the mechanisms by which AIS plasticity is produced.

Here we characterize five alternative methodological approaches designed to live-label the AIS for timelapse imaging of activity-dependent plasticity. We find that, unlike other immunofluorescence-based and genetically-encoded probes, the fluorescently-tagged sodium channel motif YFP-Na$_V$II–III meets our three criteria for a successful AIS live-label tool: (1) it accurately labels AIS structure under baseline conditions; (2) it reveals hours-scale AIS structural plasticity; and (3) it leaves neuronal excitability unperturbed.

MATERIALS AND METHODS

Dissociated Cultures

Humane killing for tissue collection conformed to local King's College London ethical approval under the UK Supplementary Code of Practice, The Humane Killing of Animals under Schedule 1 to the Animals (Scientific Procedures) Act 1986. Hippocampi were rapidly dissected from embryonic day (E18) Wistar rat embryos (Charles River) of either sex in ice-cold Hank's balanced salt solution (HBSS). Tissue was trypsin digested (Worthington, 0.5 mg/ml; 15 min at 37°C), then triturated by repeatedly pipetting the cells using fire-polished Pasteur pipettes, and finally plated at a density of ~230 cells/mm^2 on 13 mm coverslips (45,000 cells/coverslip; VWR) coated with poly-l-lysine (50 μg/ml, Sigma) and laminin (40 μg/ml). Cells were incubated at 37°C with 5% CO$_2$ in Neurobasal medium containing 1% B27, 1% foetal calf serum and 500 μM Glutamax. At 4 days *in vitro* (DIV) half the media was changed with Neurobasal plus 2% B27 and 500 μM Glutamax. At 7 DIV media was topped up to 1 ml (13 mm coverslips) with fresh Neurobasal plus 2% B27 and 500 μM Glutamax. All experiments were carried out between 10–14 DIV. Unless otherwise stated, all cell culture reagents were obtained from Invitrogen.

Depolarization Treatment

We carried out all treatments and analyses blind to experimental group. Depolarization was induced using the same protocol described by Evans et al. (2015). Briefly, neurons were treated in fully conditioned media by adding 15 mM KCl, or 15 mM NaCl as an osmolarity control.

AIS Live-Labeling

Antibody

The mouse anti-pan-neurofascin antibody (extNF; A12/18, Neuromab) was generated against the rat-specific extracellular domain common to NF155 and NF186 (amino acids 25-1110). Our labeling protocol was very similar to that employed by Evans et al. (2015; see **Table 1**). Briefly, cells were pre-incubated for 5 min in 50:50 conditioned media: fresh Neurobasal, and 50 μM APV (NB-APV, Invitrogen) to protect against cell death (Hogins et al., 2011). After this, coverslips were briefly washed three times in NB-APV, after which they were placed in primary antibody

TABLE 1 | List of publications that have used extNF as a live axon initial segment (AIS) marker.

Study	Cell culture source	Culture age	extNF ab conc.	Incubation time	2° ab conc.	Incubation time
Hedstrom et al. (2008)	E18 rat hippocampus	10 DIV	Not specified	30 min at 4°C	Not specified	Not specified
Schafer et al. (2009)	E18 rat hippocampus	10 DIV	1:200	30 min at 37°C	1:500	30 min at 37°C
Lukinavčius et al. (2014)[1]	P0–P1 rat hippocampus	Not specified	1:100	5 min at RT	Not specified	30 s at RT
Evans et al. (2015)	E18 rat hippocampus	10 DIV	1:200	3 min at 37°C	1:500	10 s at RT
Muir and Kittler (2014)[2]	E18 rat hippocampus	10 DIV	1:100	8 min at RT	1:350	8 min at RT
Current project	E18 rat hippocampus	10 DIV	1:200	30 min at 37°C	1:500	1 min at 37°C

[1] *D'Este et al. (2015) used the same live-labeling protocols.* [2] *For this experiment the primary and secondary antibody mix were pre-incubated for 15 min on ice, after which they were applied to cells in an imaging media buffer containing 10% horse serum.*

solution (extNF, 1:200) diluted in NB-APV for 30 mins at 37°C. Next, cells were washed 3× in Neurobasal after which they were placed in secondary antibody (anti-mouse 488, 1:500, Invitrogen) diluted in NB-APV, for 1 min at room temperature (RT). After three final Neurobasal washes coverslips were transferred to the fully conditioned media in which they were situated prior to antibody labeling. For a subset of experiments we used an extNF antibody pre-bound with an Alexa488 antibody labeling kit (Thermo Fisher).

Genetically-Encoded Fluorescent Probes

All genetically-encoded means of live-labeling the AIS were achieved via transfections with lipofectamine 2000 (Thermo Fisher), usually at 7 DIV (see **Table 2**). On the day of transfection, half of the conditioned cell media was removed from each well, after which cells were topped up with Neurobasal containing 2% B27 and 500 μM Glutamax, and placed back in the incubator (5% CO_2, 37°C; 1 ml total volume) for a minimum of 30 min. The transfection solution mix was made by pre-incubating DNA constructs together with lipofectamine 2000 (0.5 μl/well) for 30 min at RT in Optimem media. Next, cells were treated with the DNA/lipofectamine 2000 mix (50 μl/well) for 10 or 5 min at 5% CO_2, 37°C. Post transfection, cells were kept in a 1:1 solution containing conditioned cell media and Neurobasal containing 2% B27 and 500 μM Glutamax, usually until 10–12 DIV (see **Table 2**).

The full-length rat neurofascin-186 construct expressing EGFP at the COOH terminus and a concomitant HA tag (NF186-GFP) was a gift from Matt Rasband (Baylor College of Medicine). The DNA plasmids containing the rat sodium channel β4 subunit fused with GFP at the C-terminal tail (full sequence, Na_Vβ4-FL-GFP, C-terminal tail deletion Na_Vβ4-ΔCT-GFP, gifts from the Rasband lab) were previously described by Buffington and Rasband (2013). The full-length rat 270kDa Ankyrin-G (AnkG) fused with EGFP at the COOH tail (270kDa-AnkG-GFP; a gift from Vann Bennett, Duke University) was originally described by Zhang and Bennett (1998). We excised the CMV promoter driving expression of the original 270kDa-AnkG-GFP plasmid via a restriction digest with AseI and EcoRI, and replaced it with the neuron-specific synapsin promoter.

The rat sodium channel 1.2 (Na_V1.2) loop between the 2nd and the 3rd transmembrane domains fused to YFP at the C-terminus (YFP-Na_VII–III) was subcloned via the following steps:

1. A synapsin promoter-driven YFP construct was made from the ChR2-YFP-Na_VII–III plasmid previously described in Grubb and Burrone (2010b; Addgene deposit #26057) by using the 5′ primer CTACCGGTGCCACCATGGTGAGCAAGGGCGAGGAGCTGTTCA together with a 3′ primer TCGAATTCTTACTTGTACAGCTCGTCCATGCCG to PCR clone the YFP region. Next, the ChR2-YFP-Na_VII–III region from another sample of ChR2-YFP-Na_VII–III plasmid was excised, creating a synapsin promoter-only backbone construct which was then ligated with the YFP sequence.
2. The synapsin-YFP-Na_VII–III construct used here was made by first excising the Na_VII–III region via a Bsrg1 digest of a CMV promoter-driven YFP-Na_VII–III plasmid (Addgene deposit #26056). Next, this region was blunt ligated with a Bsrg1-linearized synapsin promoter-driven YFP plasmid.

Immunocytochemistry

Cells were fixed immediately after 3 h or 6 h treatment in 4% paraformaldehyde (PFA, TAAB Laboratories; in 3% sucrose,

TABLE 2 | Transfection protocols for genetically-encoded AIS markers.

DNA plasmid	Culture age: transfection—fixation	Transfection duration at 37°C	DNA concentration/coverslip	AIS localization?
YFP-Na_VII–III	7–10 DIV	10 min	0.5 μg/ml	Yes
270kDa-AnkG-GFP	7–10 DIV	10 min	0.5 μg/ml	Yes
NF186-GFP	7–11 DIV	10 min	0.5 μg/ml	No
	7–14 DIV			No
	4–10 DIV			No
	4–14 DIV			No
Na_Vβ4FL-GFP	7–10 DIV	10 min	0.5 μg/ml	No
			0.1 μg/ml	No
			0.3 μg/ml	No
		5 min	0.3 μg/ml	No
	11–14 DIV	10 min	0.3 μg/ml	No
			0.5 μg/ml	No
	11–12 DIV	10 min	0.1 μg/ml	No
			0.2 μg/ml	No
Na_Vβ4-ΔCT-GFP	7–10 DIV	10 min	0.5 μg/ml	No
			0.3 μg/ml	No
			0.1 μg/ml	No
		5 min	3 μg/ml	No
	11–14 DIV	10 min	0.3 μg/ml	No
			0.5 μg/ml	No

60 mM PIPES, 25 mM HEPES, 5 mM EGTA, 1 mM $MgCl_2$) for 20 min at RT. Permeabilization was carried out in 0.25% Triton X-100 (Sigma) in PBS for 5 min at RT and the block step was carried out in 10% Normal Goat Serum (NGS, Sigma) in PBS for 1 h at RT. 1° antibody incubation was in 2% NGS in PBS for 1 h at RT with the following antibodies: rabbit anti-prox1 (1:1000, Sigma), mouse IgG1 or mouse IgG2B anti-AnkG (1:500, N106/43 and N106/65, Neuromab). This was followed by 5× PBS washes, after which coverslips were incubated with the appropriate Alexa Fluor 2° antibody for 1 h at RT: anti-rabbit 594, anti-mouse IgG1 or IgG2B 633. Stained coverslips were mounted on glass slides with Mowiol (Calbiochem).

AIS Imaging and Analysis

The transfection efficiency of our genetically encoded AIS live-label constructs was not uniform. For this reason, we selected only DGCs which displayed a high, AIS-specific increase of fluorescence signal with a low overall signal in the soma, dendrites and the rest of the axon. We did not analyze cells in which the construct was over-expressed indiscriminately throughout the entire extent of the neuron. Once a suitable cell was identified, all images were obtained with a Zeiss LSM 710 confocal microscope, using a 40× oil immersion objective and appropriate laser excitation and filters. Image size was 512 × 512 pixels, with 0.138μm/pixel XY resolution, and Z steps of 0.664 μm. *Z*-stack images were then converted into maximum intensity projections and exported into Matlab (Mathworks) for AIS length measurements using custom-made scripts (Evans et al., 2015; freely available at Matlab Central). AIS length was calculated by measuring fluorescence intensity along a line drawn by hand starting at the soma, down the axon, through and past the AIS. Fluorescence intensity measures were averaged over a 3 × 3-pixel square centered on the pixel of interest. Averaged profiles were smoothed using a ∼5 μm sliding mean and normalized between 1 and 0. AIS start and end positions were the proximal and distal axonal locations where the normalized, smoothed profile declined to 0.33. AIS length was calculated as the axonal distance between the start and end positions. For all experiments where an AIS was labeled with two different markers, e.g., YFP-Na_VII–III and AnkG, AIS lengths for both labels were obtained concomitantly from the same axonal drawn line profile.

Electrophysiology

Whole-cell patch-clamp recordings were obtained from both untransfected and YFP-Na_VII–III + Tag-RFP-expressing DGCs identified based on morphology (Evans et al., 2013, 2015) at 10–12 DIV. Cells were patched at RT in an HBS extracellular solution (pH 7.4, ∼290 mOsm) which contained: 136 mM NaCl, 2.5 mM KCl, 10 mM HEPES, 10 mM D-glucose, 2 mM $CaCl_2$, 1.3 mM $MgCl_2$, 0.01 mM SR-95531 (gabazine, Sigma), 0.02 mM NBQX and 0.025 mM APV. Pipettes with a 3–7 MΩ resistance were pulled from borosilicate glass (1.17 mm inner diameter, 1.5 mm outer diameter, Harvard Apparatus), fire polished (Narishige microforge) and filled with an internal solution that contained: 130 mM K-gluconate, 10 mM NaCl, 1 mM EGTA, 0.133 mM $CaCl_2$, 2 mM $MgCl_2$, 10 mM HEPES, 3.5 mM NaATP, 1 mM NaGTP (pH 7.4, ∼290 mOsm). Signals were measured with a Heka EPC10 amplifier coupled to Patchmaster software. Signals were Bessel filtered at 10 kHz (filter 1) and 2.9 kHz (filter 2, active filters used in voltage-clamp only), digitized and sampled at 20–200 kHz (5–50 μs sample interval) depending on the protocol. Fast capacitance was compensated in the on-cell configuration, slow capacitance was compensated after membrane rupture, and 100% bridge balance was employed during current-clamp recordings. Data are uncorrected for an estimated liquid junction potential of ∼15 mV.

Series resistance (R_s) was calculated as a cell's response to a 10-mV hyperpolarization step in voltage clamp with slow capacitance compensation disabled. Membrane resistance (R_m) was obtained from the steady holding current at the new step, and membrane capacitance (C_m) was the area under the exponentially decaying current from peak to holding. Series resistance was used as a proxy for patch quality as only cells with $R_s < 25$ MΩ were selected for analysis. R_s was measured several times during the recording session and any data in which the following R_s varied by more than 20% from the initial value were excluded. To look at single spike properties we evoked spikes in current-clamp mode at V_{hold} -60 ± 3 mV. For action potential waveform measures, we injected 10-ms-duration current steps of increasing amplitude until we reached the current threshold at which the neuron reliably fired an action potential ($V_m > 0$ mV). For multiple spiking measures, we injected 500-ms current steps of increasing amplitude with 2-s inter-sweep interval until the neuron passed its maximum spike number.

Exported traces were analyzed using custom-written MATLAB routines. To determine voltage threshold, 5-μs sample interval recordings of spikes fired at threshold 10-ms current injection were smoothed using a 20-point (100-μs) sliding filter, before differentiation for dV/dt. Voltage threshold was taken as the unsmoothed potential at which dV/dt first passed 10 V/s. AP height was calculated as the difference between V_{max} and $V_{threshold}$. Spike width was measured at the midpoint between $V_{threshold}$ and V_{max}.

Statistics

Statistical analysis was carried out with Prism (Graphpad) and SPSS (IBM). Sample distributions were first assessed for normality with the D'Agostino and Pearson omnibus test. Details regarding the specific parametric or non-parametric tests carried out are reported in the results section. α values were set to 0.05 unless otherwise stated, and tests were two-tailed for all experiments.

RESULTS

We screened several candidate approaches for live imaging of structural plasticity at the AIS. Key criteria for successful live label with a given probe were that it revealed AIS structure accurately—even after activity-dependent plasticity—and that

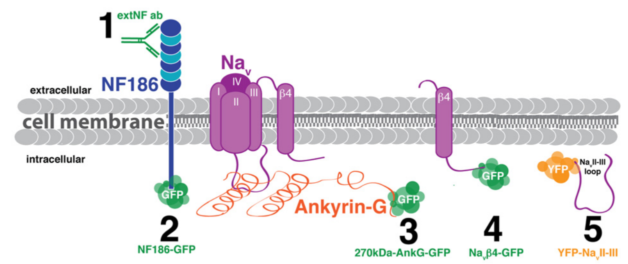

FIGURE 1 | Schematic of candidate methods for live labeling the axon initial segment (AIS) *in vitro*. (1) Antibody targeted against the neurofascin extracellular domain (extNF ab). **(2)** Plasmid DNA fusion construct of neurofascin and GFP (NF186-GFP). **(3)** Plasmid DNA fusion construct of 270kDa-ankyrin-G (AnkG) and GFP (270kDa-AnkG-GFP). **(4)** Plasmid DNA fusion construct of the sodium channel β4 subunit and GFP (Na_Vβ4-GFP). **(5)** Plasmid DNA fusion construct of the sodium channel loop between the II and III α subunits and YFP (YFP-Na_VII–III).

it did not itself alter AIS structure or function. In other words, we were looking for a probe that was accurate, plastic, and benign. We trialed five separate probes in dissociated cultures of rat hippocampal cells: one based on immunocytochemistry, and four that were genetically-encoded (**Figure 1**). To reduce cell-type heterogeneity, we focused exclusively on DGCs. These hippocampal glutamatergic projection neurons retain many of their distinctive morphological and functional features in dissociated culture, and can be readily identified either on the basis of gross morphology or by post-fixation immunocytochemical label for the transcription factor prox1 (Williams et al., 2011; Evans et al., 2013, 2015; Lee et al., 2013).

Live AIS Label with a Neurofascin Antibody Is Accurate at Baseline but Does Not Report Rapid Structural Plasticity

An immunohistochemical approach to labeling the AIS in live neurons has clear theoretical benefits. It has the potential to provide comprehensive label of every AIS in a given sample, and, unlike genetically-encoded probes, can be achieved in minutes without invasively introducing any foreign intracellular material (Schafer et al., 2009; Evans et al., 2015). It does, though, rely on the availability of an antibody that recognizes an extracellular epitope of an AIS-localized protein. Here we used a rat-specific monoclonal antibody designed to recognize the extracellular domain of neurofascin isoforms 186 (found at the AIS and the node of Ranvier) and 155 (found at the paranode; Tait et al., 2000). This "extNF" antibody has been previously employed to reveal baseline AIS position and length in live dissociated rat neurons (Hedstrom et al., 2008; Lukinavičius et al., 2014; Muir and Kittler, 2014; D'Este et al., 2015; Evans et al., 2015), and also to report live injury-induced alterations in AIS structure (Schafer et al., 2009; **Table 1**).

However, although extNF label is a reasonably accurate indicator of baseline AIS features in live neurons, we found that it was unable to follow rapid structural AIS plasticity. As an initial test of this probe's suitability, we live-labeled 10 DIV hippocampal cells with extNF and an appropriate Alexa-conjugated secondary antibody, then induced chronic depolarization for 3 h with elevated external potassium (+15 mM KCl, **Figure 2A**). In previous comparisons vs. control cells treated with +15 mM NaCl, this manipulation produced rapid structural AIS plasticity: post-fix immunocytochemical labeling of the key AIS scaffolding molecule AnkG, of voltage-gated sodium channels (Pan-Na_V), or of neurofascin using extNF itself, all consistently revealed a ∼5 µm (25%) reduction in DGC AIS length (Evans et al., 2015). Indeed, in DGCs live-labeled with extNF throughout the treatment period we again observed this rapid form of structural AIS plasticity, with AnkG distributions significantly shorter in depolarized compared to control neurons (**Figures 2B,C**; 3 h treatment two-way repeated-measures ANOVA; treatment, $F_{(1,350)} = 9.02$ $p = 0.0029$; label type, $F_{(1,350)} = 23.57$ $p < 0.0001$; interaction, $F_{(1,350)} = 1.41$ $p = 0.24$; Bonferroni post-test AnkG control vs. depolarized $t = 2.96$ $p < 0.01$). However, in the very same cells the shortening effect was not observed in the live-applied extNF label distribution (**Figures 2B,C** left panel, Bonferroni post-test extNF control vs. depolarized $t = 1.28$ $p > 0.05$).

Assessing correlations between AnkG and live-applied extNF label on a cell-by-cell basis further underscored this mismatch under plastic conditions. When both antibodies were applied post-fixation, AIS lengths measured from AnkG and extNF label correlated extremely well in both control and depolarized DGCs (Evans et al., 2015; **Figure 2D**; controls Spearman's $r = 0.91$, $p < 0.0001$, $n = 37$; depolarized Spearman's $r = 0.89$, $p < 0.0001$, $n = 35$). A significant correlation was still present for control cells when the extNF label was applied throughout the 3 h +15 mM NaCl treatment, but was weaker than for dual fixed label (**Figure 2D**; extNF vs. AnkG in control cells Spearman's $r = 0.69$, $p < 0.0001$, $n = 92$). This shows that extNF label provides a less accurate picture of AIS structure when applied to live neurons, an unsurprising result given the shorter antibody incubation times and lack of blocking step that are necessary in this protocol. In 3 h depolarized cells, however, the correlation between AnkG- and live-extNF-defined AIS lengths was even weaker (**Figure 2D** right panel; extNF vs. AnkG in depolarized cells Spearman's $r = 0.29$, $p < 0.0080$, $n = 85$), providing further evidence that this live labeling approach cannot be used to accurately report structural AIS plasticity.

We reasoned that live extNF immunolabel might still be capable of revealing AIS plasticity over longer timescales. We therefore live-labeled 10 DIV cultures with extNF before exposing them to extended 6 h treatments with +15 mM NaCl or KCl. Similar to 3 h manipulations, 6 h depolarization was again associated with significantly shorter DGC AISs measured with post-fixation AnkG label (**Figures 2B,C** right panel; 6 h treatment two-way repeated-measures ANOVA; treatment, $F_{(1,91)} = 19.98$ $p < 0.0001$; label type, $F_{(1,91)} = 6.43$ $p < 0.013$; interaction, $F_{(1,91)} = 2.502$ $p = 0.12$; Bonferroni post-test AnkG control vs. depolarized $t = 4.63$ $p < 0.0001$). Now, 6 h-depolarized DGCs also had significantly shorter AISs than their control counterparts as assessed by live extNF label (**Figure 2C** right panel; Bonferroni post-test extNF control vs. depolarized $t = 2.95$ $p < 0.01$). However, the live extNF axonal distributions did

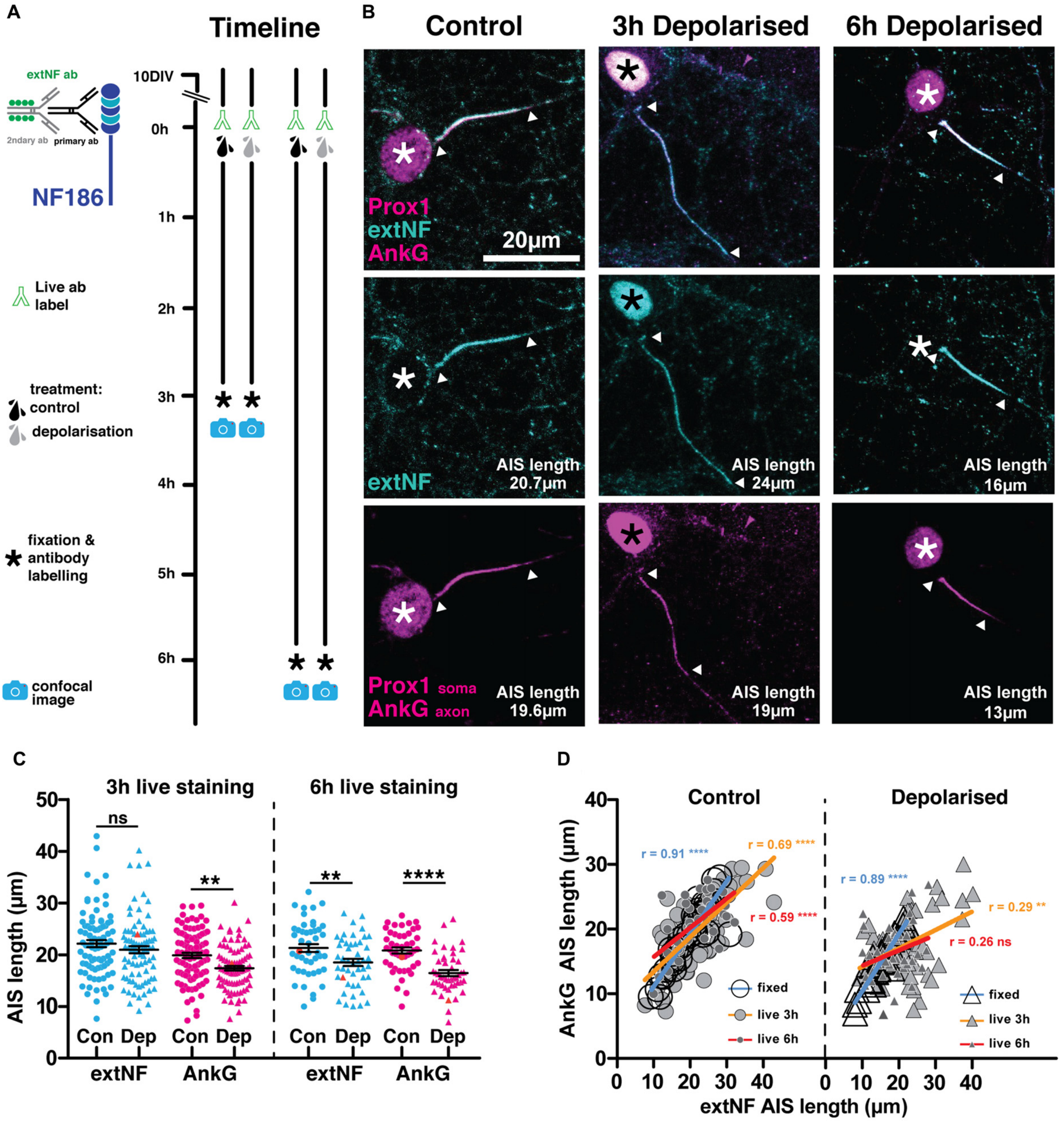

FIGURE 2 | Live AIS label with a neurofascin antibody does not report rapid structural plasticity. (A) Diagram of the experimental timeline used to test the extNF antibody as an AIS live label method. **(B)** Example maximum intensity projections of control or 3 h/6 h depolarized dentate granule cells (DGCs) bearing extNF live-labeled AISs (cyan) and stained post fixation with antibodies against AnkG (magenta, axonal) or prox1 (magenta, nuclear, white asterisks; cyan nuclear, black asterisks—due to secondary antibody contamination); arrowheads, DGC AIS start and end positions. **(C)** Plot shows distributions of AIS lengths measured with extNF applied live for either 3 or 6 h (blue) and AnkG (magenta) from control (Con) or depolarized (Dep) DGCs. Each point represents a single cell; black lines show mean ± SEM; orange symbols, values from example cells displayed in **(B)**; Bonferroni post-test after two-way repeated measures ANOVA; ns, non-significant; $^{**}p < 0.01$; $^{****}p < 0.0001$. **(D)** Correlation analysis for AISs labeled with both extNF and AnkG in the same neuron under control (dotted symbols) or depolarized (triangle symbols) conditions in three separate experiments: extNF post fixation (large open circles and triangles), extNF applied live for the duration of a 3 h treatment (medium sized light gray filled dots and triangles), extNF applied live for the duration of a 6 h treatment (small, dark gray filled dots and triangles). Lines show best linear regression fit for extNF applied post fixation (blue), live for 3 h (orange) or live for 6 h (red); Pearson's correlation; $^{**}p = 0.008$; $^{****}p < 0.0001$; ns, non-significant.

not shorten as much as the AnkG distributions in the same neurons, to the extent that the correlation between the two labeling approaches was no longer significant in the depolarized group (**Figure 2D** right panel; depolarized cells extNF vs. AnkG Spearman's $r = 0.25$, $p = 0.0798$, $n = 47$). Even after more prolonged perturbations of neuronal activity, then, live-applied extNF label cannot provide an accurate representation of plastic changes in AIS structure.

Live immunolabeling approaches using standard, multivalent probes suffer the potential risk of crosslinking antigen molecules at the levels of both primary and secondary antibodies, thereby altering mobility or function of the bound antigen. If neurofascin molecules live-labeled with extNF were somehow rendered more stable by such crosslinking, this may explain the inaccuracy of the approach in labeling plastic changes in AIS structure. We therefore ruled out the possibility of cross-linking at the secondary antibody level by pre-conjugating the extNF primary antibody with an Alexa 488 fluorophore before applying it to our neurons in a single labeling step (**Figure 3A**). However, this pre-conjugated extNF-488 live label was no more accurate in reporting rapid activity-dependent AIS shortening. While AnkG-defined DGC AIS lengths were again significantly shorter in the 3 h-depolarized group, distributions of pre-conjugated, live-applied extNF-488 label did not differ between treatment groups (**Figures 3B,C**; two-way repeated measured ANOVA; treatment, $F_{(1,73)} = 0.77$ $p = 0.38$; label type, $F_{(1,73)} = 7.42$ $p = 0.008$; interaction $F_{(1,73)} = 13.73$ $p = 0.0004$; Bonferroni post-test, extNF-488 control vs. depolarized treatments $t = 1.07$ $p > 0.05$; AnkG control vs. depolarized treatment $t = 2.6$ $p < 0.05$). Moreover, correlations between AIS length measured by AnkG and pre-conjugated extNF-488 label were relatively weak in both control and depolarized cells (**Figure 3D**; control cells Pearson's $r = 0.47$ $p = 0.003$ $n = 38$; depolarized cells Pearson's $r = 0.56$ $p = 0.0003$ $n = 37$).

So, despite the potential advantages of live-labeling the AIS with an immunocytochemical approach, and despite the fact

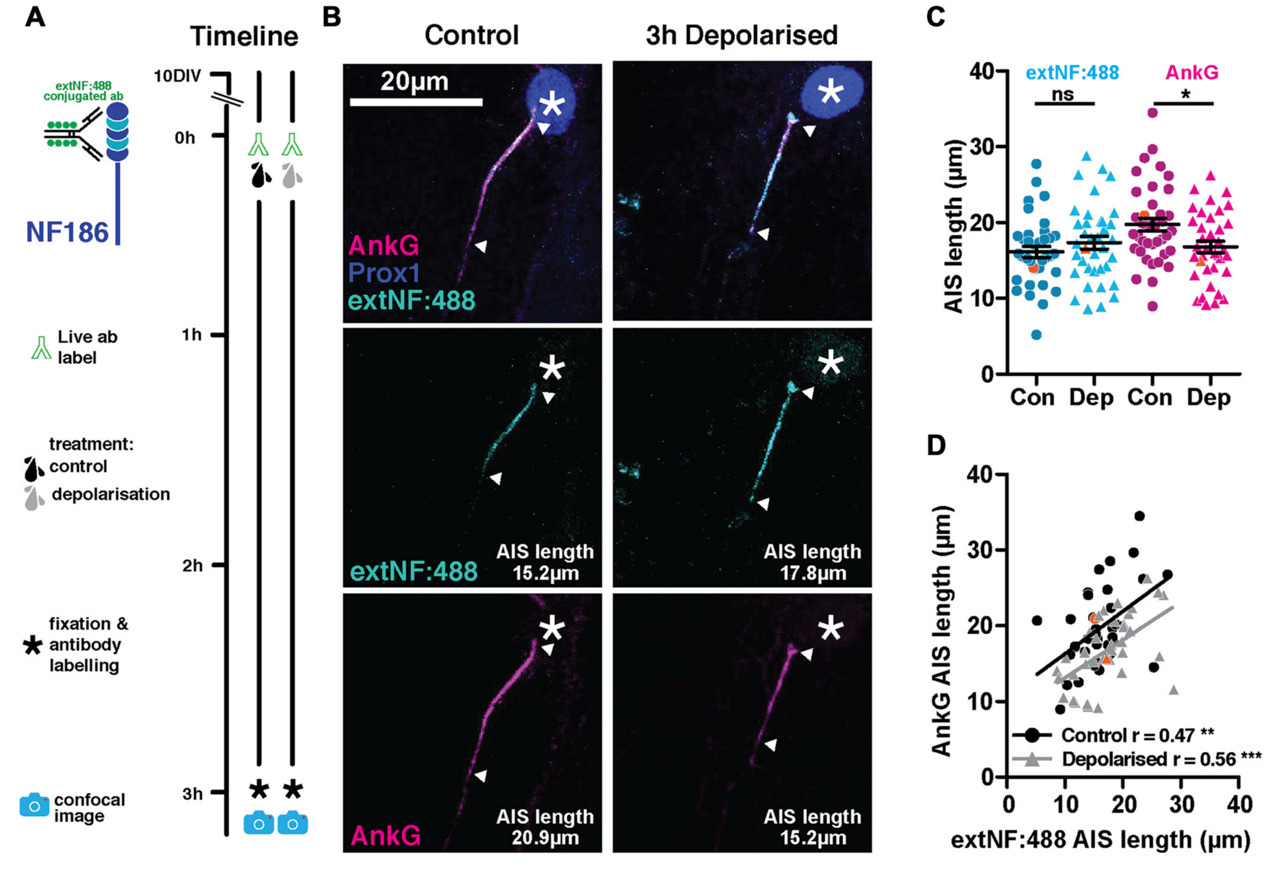

FIGURE 3 | ExtNF antibody conjugated with Alexa-488 does not track AIS plasticity. (A) Diagram of AIS live label method used and experimental timeline. **(B)** Maximum intensity projections of example neurons labeled live with the extNF antibody conjugated to Alexa-488, after which they were subjected to either a 3 h control or depolarization treatment. Following fixation, cells were stained with antibodies against AnkG (magenta) and Prox1 (dark blue). Asterisks, nucleus; arrowheads, DGC AIS start and end positions. **(C)** Distributions of AIS lengths measured with extNF-488 conjugated antibody and AnkG from control or depolarized DGCs. Each dot or triangle represents a single cell; orange symbols, values from example cells displayed in **(B)**; dark lines show mean ± SEM; Bonferroni post-test after two-way repeated measures ANOVA; ns, non-significant; $^{*}p < 0.05$. **(D)** Correlation analysis for AISs labeled with both the extNF-488 conjugated antibody label and AnkG under control or depolarized conditions. Orange symbols, values from example cells displayed in **(B)**; lines show best linear regression fit for control (black) or depolarized cells (gray); $^{**}p < 0.01$; $^{***}p < 0.001$.

that extNF label might reveal some aspects of AIS plasticity under longer activity perturbations, for an accurate readout of structural AIS changes in live neurons we needed to consider alternative, genetically-encoded strategies.

Lack of AIS Label with Neurofascin-186-GFP or Na$_V$β4-GFP

We tested four genetically-encoded probes for their potential to live-label the AIS. For two of these constructs—fusion proteins of GFP with full-length neurofascin-186 or the Na$_V$β4 subunit—we were unfortunately unable to find the experimental conditions for successful AIS localization.

We used a rat-specific, full-length neurofascin-186 construct tagged with GFP at its C-terminal domain (NF186-GFP), first described by Zhang and Bennett (1998) and used more recently by Dzhashiashvili et al. (2007). We reasoned that over-expression of NF186-GFP starting at a stage at which most AISs have already been established in culture (7 DIV) should not disrupt AIS assembly or disturb cell function. To test its expression pattern we initially transfected cells according to our standard lipofection protocol at 7 DIV (see "Materials and Methods" Section; **Table 2**), after which at 10 DIV we fixed and stained with an antibody against AnkG to check co-localization with endogenous AIS labeling, and prox1 to confirm DGC identity. We also ran several trials in which: (1) the transfection protocol was started earlier at 4 DIV, and (2) allowed cells a longer developmental time until 14 DIV (**Figure 4A**; **Table 2**). In all experiments, we failed to see precise co-localization between NF186-GFP and AnkG antibody label (**Figure 4**). The NF186-GFP signal tended to be strongly expressed in the cell soma and in a punctate fashion across the dendrites and the axon (**Figure 4**). Even in the best example of AnkG co-localization, NF186-GFP did not specifically localize to the AIS (**Figure 4B**), thereby failing to fulfil our first condition as a suitable AIS live-label.

Na$_V$β4 is an auxiliary sodium channel subunit, thought to be responsible for the resurgent Na$^+$ current through the action of its C-terminal tail as an open-channel blocker (Grieco et al., 2005; Bant and Raman, 2010). Due to the high concentration of sodium channels found at the AIS, it was previously shown that overexpression of Na$_V$β4-GFP labels AISs in fixed tissue from multiple brain regions, including the hippocampus in both slices and dissociated *in vitro* cultures (Buffington and Rasband, 2013). We tested two constructs where Na$_V$β4 was fused with GFP: (1) the full-length channel subunit (Na$_V$β4-FL-GFP, **Figure 5B**) and (2) a version with a truncation of the functionally important C-terminal tail (Na$_V$β4-ΔCT-GFP, **Figure 5C**). DGCs do not express Na$_V$β4 (Yu et al., 2003; Castelli et al., 2007), so we reasoned that these constructs—especially the functionally null Na$_V$β4-ΔCT-GFP version—might be a benign way of labeling AISs live. We therefore transfected cells with Na$_V$β4-FL-GFP or Na$_V$β4-ΔCT-GFP at several stages: either at 7 DIV followed by fixation at 10 DIV as per our normal protocol, or at 11 DIV followed by fixation at 12 or 14 DIV in order to match previously published expression methods (Buffington and Rasband, 2013, **Figure 5**; **Table 2**). All cells were immuno-labeled against AnkG and prox1 post fixation. Unfortunately, we were not able to see clear co-localization of either Na$_V$β4-GFP probe with endogenous AnkG label. Regardless of the transfection protocol used, both constructs were strongly expressed in the cell soma and in a

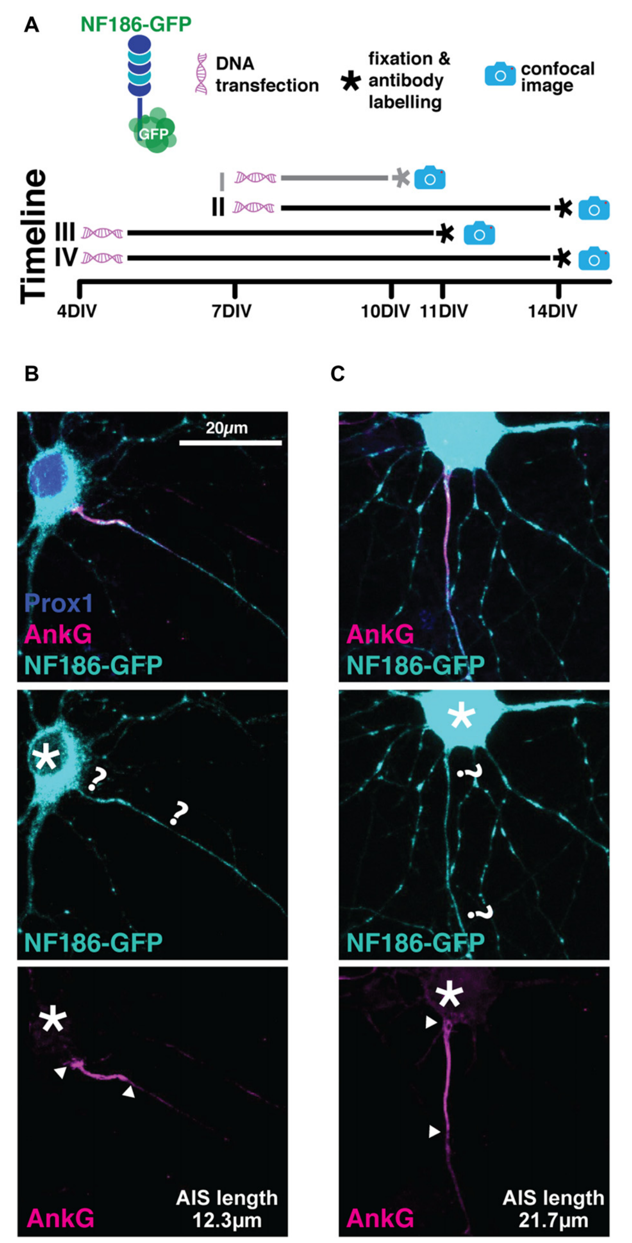

FIGURE 4 | NF186-GFP does not localize specifically to the AIS. **(A)** Diagram of experimental timeline for all the four transfection methods attempted (see **Table 2**); gray line highlights method used for the cells displayed in panel **(B,C)**. **(B)** Maximum intensity projection of the best observed co-localization between the NF186-GFP construct (cyan) and AnkG (magenta). Asterisks, soma; question marks, putative start and end of NF186-GFP-labeled AIS; arrowheads, AnkG-labeled AIS start and end positions. **(C)** As in **(B)**, but showing the most commonly observed expression pattern of NF186-GFP.

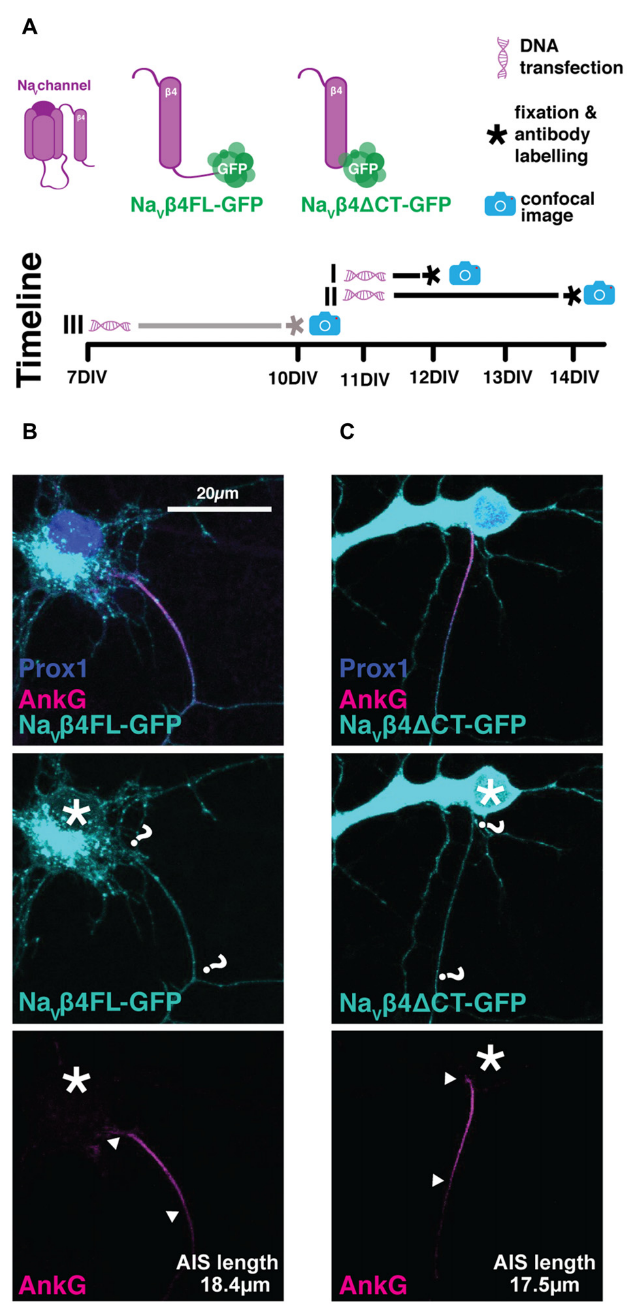

FIGURE 5 | Lack of AIS specificity with the $\text{Na}_{\text{V}}\beta4$-GFP constructs. **(A)** Diagram of experimental timeline for the three transfection methods attempted (see **Table 2**); gray line highlights method used for the cells displayed in panels **(B,C)**. **(B)** Maximum intensity projection of the usual expression pattern of $\text{Na}_{\text{V}}\beta4$FL-GFP (cyan) and lack of co-localization with AIS marker AnkG (magenta). Asterisks, soma; question marks, presumptive location of $\text{Na}_{\text{V}}\beta4$-GFP AIS; arrowheads, AnkG AIS start and end positions. **(C)** As in **(B)**, but for the Na4ΔCT-GFP construct.

punctate fashion throughout dendrites and axons (**Figure 5**). We therefore concluded that—at least in our hands—neither of the $\text{Na}_{\text{V}}\beta4$-GFP plasmids was suitable for use as a live AIS marker.

Overexpression of 270kDa-AnkG-GFP Alters AIS Structure in Mature Neurons

Our third genetically-encoded probe consisted of GFP fused to the C-terminus of the 270kDa isoform of AnkG (270kDa-AnkG-GFP). We were aware that overexpressing this AnkG isoform in very young neurons (Galiano et al., 2012) or in AnkG-null cells (Jenkins et al., 2015) was previously shown to produce abnormally elongated AISs. However, we reasoned that overexpressing 270kDa-AnkG-GFP in more mature wild-type neurons (**Figure 6A**; **Table 2**), in the presence of higher levels of endogenous AnkG and after the establishment of the AnkG-ankyrin-B boundary at the distal AIS (Galiano et al., 2012), might allow accurate live label of normal-length AISs. We also drove 270kDa-AnkG-GFP from the synapsin promoter, in order to achieve both neuronal specificity and activity-independent expression (see "Materials and Methods" Section). With this probe, localization to the AIS was good, with a significant correlation between AIS length revealed by the live marker and immunocytochemical label for total AnkG distribution (**Figure 6E**; 270kDa-AnkG-GFP vs. AnkG antibody Pearson's $r = 0.59$ $p = 0.0002$ $n = 35$). However, under baseline conditions overexpression of 270kDa-AnkG-GFP from 7 DIV still produced a marked increase in AIS length when compared to neighboring non-transfected DGCs (**Figures 6B–D**; unpaired t-test on AIS AnkG antibody length from transfected vs. untransfected cells $t = 4.1$ $p = 0.0001$). Since this approach therefore broke our key requirement that live label should leave baseline AIS structure unperturbed, it was rapidly abandoned.

YFP-Na_{V}II–III Provides Accurate Live AIS Label That Is Both Plastic and Functionally Benign

Rather than overexpressing fluorescently-tagged full-length AIS proteins, our final genetically-encoded strategy for live AIS label involved a highly conserved sub-region of vertebrate Na_{V} channels. The intracellular loop between Na_{V} transmembrane domains II and III (Na_{V}II–III) is both necessary and sufficient for these channels to bind AnkG and localize to the AIS (Garrido et al., 2003; Lemaillet et al., 2003; Gasser et al., 2012), and under the control of the CMV promoter it can be used to accurately report long-term (48 h) activity-dependent changes in AIS position (Grubb and Burrone, 2010a). Here we employed this fusion protein under the control of the neuron-specific and non-activity-dependent synapsin promoter. Sparse expression in hippocampal neurons under control conditions resulted in YFP-Na_{V}II–III specifically accumulating at the AIS, with markedly lower expression levels in the soma (**Figures 7A,B**). Live-labeled in this way, DGC AISs at baseline were of normal length and correlated extremely well with post-fixation immunocytochemical label for AnkG (**Figure 7D** left panel; 3 h control treatment YFP-Na_{V}II–III post fix vs. AnkG antibody Pearson's $r = 0.94$ $p < 0.0001$ $n = 18$). This probe therefore offers highly accurate labeling without morphological distortion of the AIS under baseline conditions.

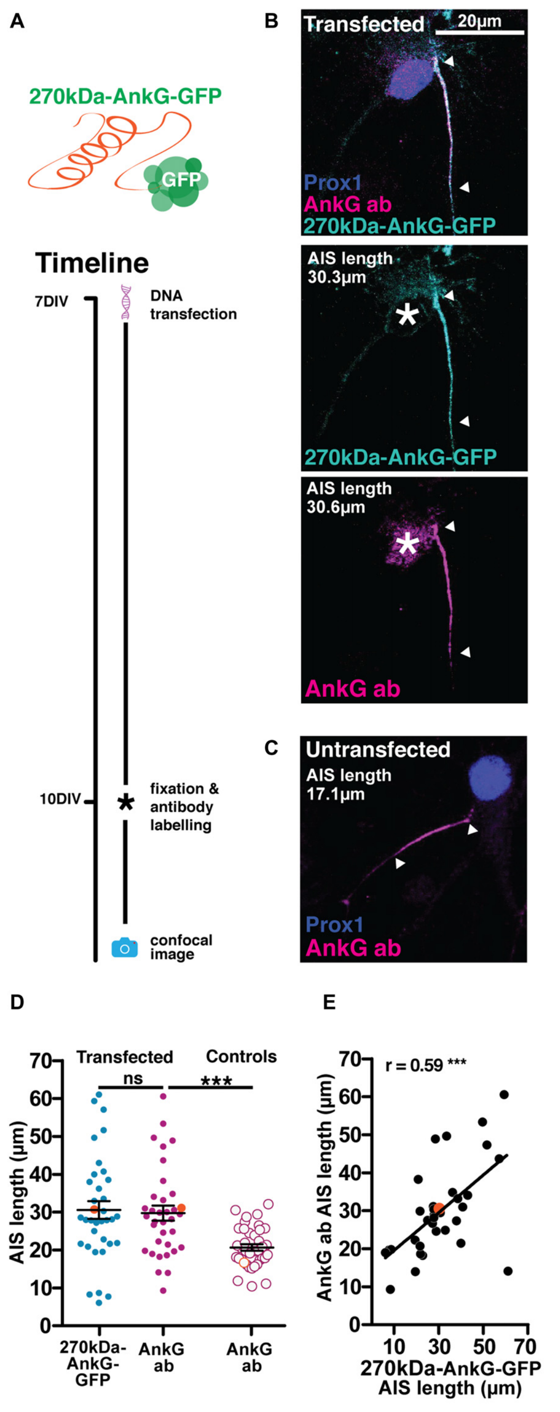

FIGURE 6 | The 270kDa-AnkG-GFP construct artificially increases AIS length in mature neurons. (A) Diagram of construct used and transfection method timeline. **(B)** Maximum intensity projection of a DGC expressing 270kDa-AnkG-GFP (cyan) which co-localizes with an anti-AnkG antibody (magenta). Asterisks, nucleus; arrowheads, DGC AIS start and end positions. **(C)** Maximum intensity projection of an untransfected DGC bearing an AIS of normal length. Arrowheads DGC AIS start and end positions. **(D)** Distributions of AIS lengths measured from 270kDa-AnkG-GFP transfected neurons and control untransfected DGCs. Each dot or triangle represents a single cell; orange symbols represent cells from panel **(B)**; dark lines show mean ± SEM;

(Continued)

FIGURE 6 | Continued
paired *t*-test AnkG-GFP and AnkG ab, $p = 0.68$; ns, non-significant; unpaired *t*-test AIS length via AnkG ab from transfected vs. control untransfected cells, $^{***}p = 0.002$. **(E)** Correlation analysis for AISs labeled with both the AnkG-GFP construct and AnkG antibody. Each dot represents one cell; orange symbol, example cell from panel **(B)**; line; best fit linear regression; Pearson's correlation; $^{***}p < 0.001$.

We next asked if YFP-Na$_V$II–III is also an accurate reporter of structural AIS plasticity. However, although 3 h depolarization with +15 mM KCl produced a significant reduction in AIS length revealed by post-fixation AnkG label in non-transfected cells, the YFP-Na$_V$II–III distribution in neighboring transfected neurons showed no evidence of shortening (**Figure 7C** left panel; two-way repeated measured ANOVA; treatment, $F_{(1,33)} = 1.99$ $p = 0.17$; label type, $F_{(1,33)} = 14.45$ $p = 0.0006$; interaction $F_{(1,33)} = 3.13$ $p = 0.09$; Bonferroni post-test, YFP-Na$_V$II–III transfected control vs. depolarized treatments $t = 0.48$ $p > 0.05$; AnkG AIS length in transfected control vs. depolarized cells $t = 1.82$ $p > 0.05$; AnkG AIS length in untransfected cells unpaired *t*-test control vs. depolarized $t = 3.20$ $p = 0.0020$ $n = 72$). With an extended 6 h depolarization treatment, though, the probe did accurately reflect structural AIS plasticity: the YFP-Na$_V$II–III distribution was significantly shorter in 6 h-depolarized vs. control neurons (**Figure 7C** right panel; two-way repeated measures ANOVA; treatment, $F_{(1,41)} = 35.47$ $p < 0.0001$; label type, $F_{(1,41)} = 15.37$ $p = 0.0003$; interaction $F_{(1,41)} = 4.2$ $p = 0.047$; Bonferroni post-test, YFP-Na$_V$II–III transfected control vs. depolarized treatments $t = 5.08$ $p < 0.0001$; AnkG transfected control vs. depolarized cells $t = 6.29$ $p < 0.0001$; AnkG AIS length in untransfected cells unpaired *t*-test control vs. depolarized $t = 7.31$ $p < 0.0001$ $n = 76$), and was strongly and significantly correlated with AnkG immunocytochemical label in both treatment groups (**Figure 7D** red lines; 6 h control treatment YFP-Na$_V$II–III vs. AnkG antibody Pearson's $r = 0.87$ $p < 0.0001$ $n = 25$; 6 h depolarized treatment YFP- Na$_V$II–III vs. AnkG antibody Pearson's $r = 0.74$ $p = 0.0005$ $n = 18$).

Over a slightly longer, but still hours-scale timeframe, YFP-Na$_V$II–III is therefore an accurate reporter of activity-dependent structural change at the AIS. But, like all genetic probes, its use has the drawbacks of requiring the introduction of foreign material into neurons, a lack of temporal specificity, overexpression of biologically active proteins, and sparse expression. While the latter might be beneficial under certain circumstances, the others raise the concern that the probe could adversely affect neuronal function. We therefore assayed the key AIS-dependent function of action potential initiation, via targeted whole-cell patch-clamp recordings in YFP-Na$_V$II–III-transfected vs. untransfected DGCs (**Figure 8A**). With the synapsin-YFP-Na$_V$II–III construct expressed under our experimental conditions, we found no difference in any parameter related to single or multiple spike firing (**Figure 8**; **Table 3**). In addition, we profited from the presence of accurate live AIS label in our recorded neurons to investigate structure-function relationships between AIS length and spike characteristics in cultured DGCs. In this dataset we replicated a previous observation obtained with recordings in control-

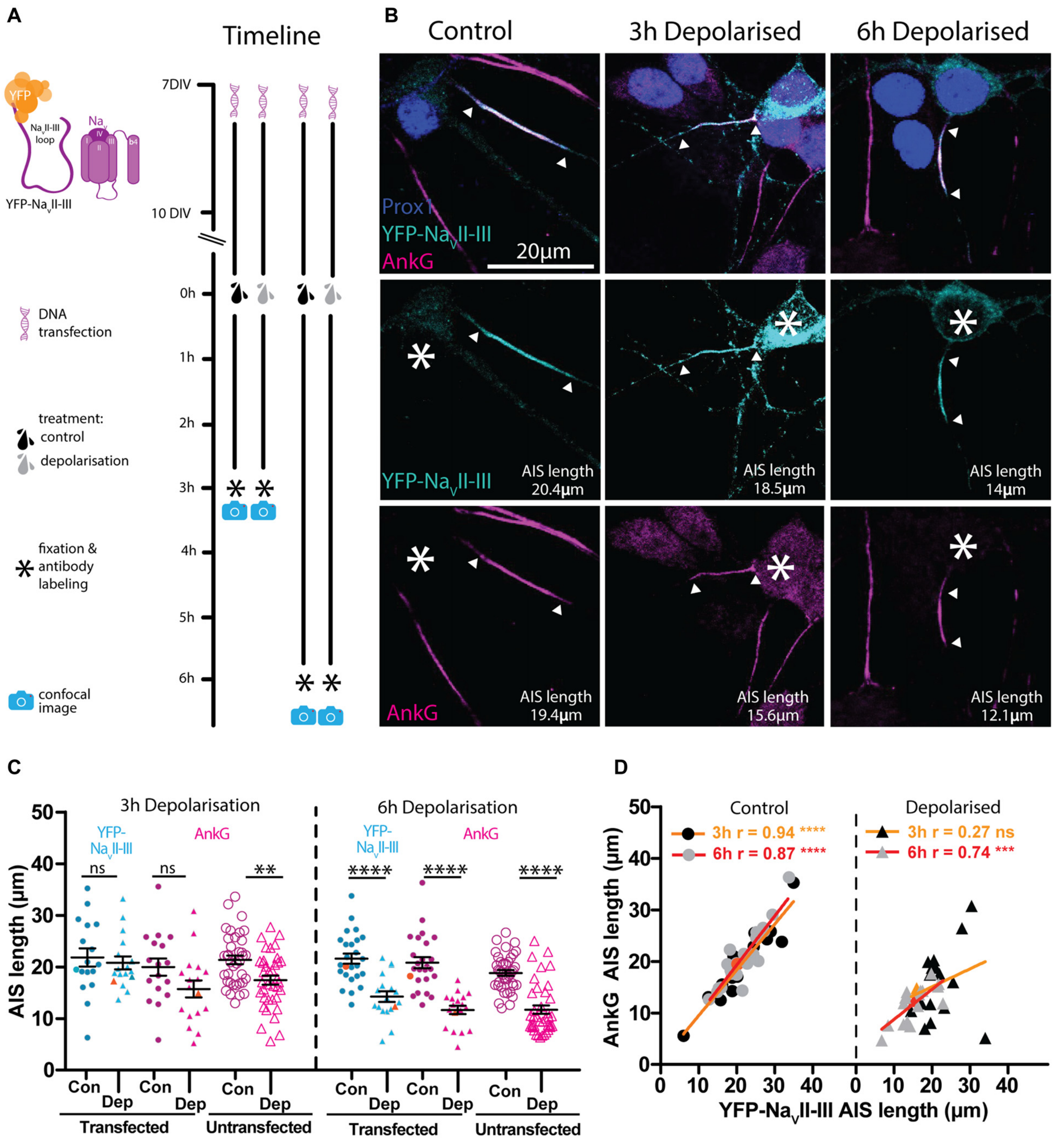

FIGURE 7 | YFP-Na_VII–III has a high degree of correlation with AnkG and is able to accurately track AIS plasticity following a 6 h depolarization treatment. (A) Diagram of the experimental timeline used to test the YFP-Na_VII–III construct as an AIS live label. **(B)** Maximum intensity projections of control or 3 h and 6 h depolarized DGCs bearing YFP-Na_VII–III live-labeled AISs (cyan) and stained post fixation with antibodies against AnkG (magenta) or prox1 (dark blue). Asterisks, soma; arrowheads, DGC AIS start and end positions. **(C)** Distributions of AIS lengths determined from YFP-Na_VII–III (blue) and AnkG (magenta) from control (Con) or depolarized (Dep) DGCs. Each symbol represents a single cell; black lines show mean ± SEM; orange symbols represent cells from panel **(B)**; Bonferroni post-test after two-way repeated measures ANOVA; ns, non-significant; $^{**}p < 0.01$; $^{****}p < 0.0001$. **(D)** Correlation analysis for AISs labeled with YFP-Na_VII–III and AnkG under control (dotted symbols) or depolarized (triangle symbols) conditions. Lines show best linear regression fit for a 3 h (orange) or 6 h treatment (red); orange symbols represent cells from panel **(B)**; Pearson's correlation; ns, non-significant; $^{***}p < 0.001$; $^{****}p < 0.0001$.

treated, extNF-labeled neurons (Evans et al., 2015): a negative relationship between AIS length and single-spike voltage threshold (**Figure 8D**, right panel). We also found a significant negative correlation between YFP-Na_VII–III-labeled AIS length and single spike current threshold (**Figure 8C**, right panel), as well as a significant positive correlation between AIS length and

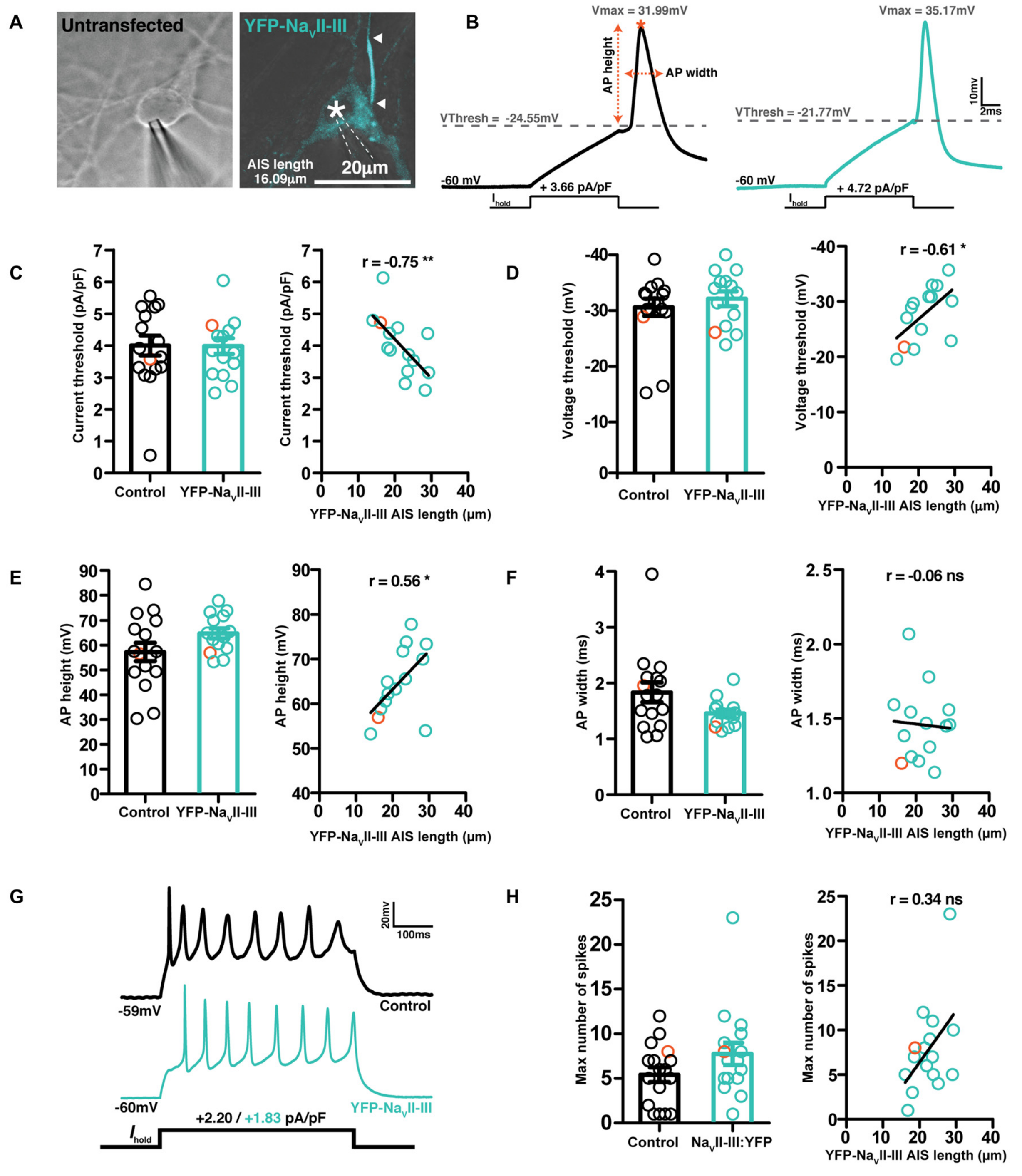

FIGURE 8 | YFP-Na$_V$II–III labeled cells exhibit normal spike firing properties. (A) Brightfield image of a control untransfected neuron, and a maximum intensity projection of a cell expressing YFP-Na$_V$II–III (cyan), both patched in whole-cell mode. Asterisks, nucleus; arrowheads, DGC AIS start and end positions. **(B)** Example whole-cell current-clamp recordings of threshold APs fired to 10-ms somatic current injection from neurons displayed in **(A)**; orange asterisk, V max; orange dotted lines, AP height and width calculation. **(C)** Single action potential current threshold; left, each dot represents a single cell from either the control untransfected group (black) or YFP-Na$_V$II–III expressing (cyan) group; orange colored symbols represent values from the example cells presented in panel **(A)**; bars show mean ± SEM; unpaired *t*-test $p = 0.76$. Right, correlation of current threshold vs. AIS length revealed by live label with YFP-Na$_V$II-III; each dot shows one cell; orange dot shows the example cell from panel **(A)**; line shows best fit linear regression; $^{**}p < 0.01$. **(D)** Single action potential voltage threshold; details same as panel **(C)**; left, $p = 0.37$; right, $^{*}p < 0.05$. **(E)** Action potential height; details same as panel **(C)**; left, $p = 0.1$; right, $^{*}p < 0.05$. **(F)** Action potential width at half height; details same as panel **(C)**; left, $p = 0.1$; right, ns, non-significant. **(G)** Example traces of maximum firing elicited via a 500 ms duration current injection used to probe repetitive spiking. **(H)** Maximum number of spikes fired to a 500 ms current injection pulse; details same as panel **(C)**; left, $p = 0.2$; right, ns, non-significant.

TABLE 3 | Physiological parameters of control or YFP-Na$_V$II–III expressing dentate granule cells (DGCs) recorded under baseline conditions.

Parameter	Mean ± SEM (*n*)		Group comparison	YFP-Na$_V$II–III AIS length correlation
	Control	YFP-Na$_V$II–III		
R_s (MΩ)	16.42 ± 0.59 (17)	14.63 ± 0.82 (18)	$t = 1.77$, $p = 0.09$	N/A
R_m (MΩ)	1300 ± 385.4 (17)	711.1 ± 87.75 (18)	$U = 110$, $p = 0.16$	Sr = 0.43, $p = 0.07$
C_m (pF)	33.37 ± 1.89 (17)	41.63 ± 2.57 (18)	**$t = 2.56$, $p = 0.02$**	Pr = −0.07, $p = 0.79$
Ithresh (pA/pF)	3.99 ± 0.31 (16)	3.98 ± 0.25 (14)	$U = 104.0$, $p = 0.76$	**Sr = −0.75, $p = 0.003$**
Vthresh (mV)	−25.95 ± 1.54 (16)	−27.83 ± 1.33 (14)	$U = 90.00$, $p = 0.37$	**Sr = −0.61, $p = 0.02$**
Vmax (mV)	31.32 ± 2.65 (16)	36.94 ± 1.22 (14)	$t = 1.84$, $p = 0.08$	Pr = 0.32, $p = 0.26$
AP height (mV)	57.27 ± 3.68 (16)	64.77 ± 2.07 (14)	$t = 1.71$, $p = 0.1$	**Pr = 0.56, $p = 0.04$**
AP width (ms)	1.84 ± 0.18 (16)	1.46 ± 0.07 (14)	$U = 72.50$, $p = 0.1$	Sr = −0.06, $p = 0.84$
Max dV/dt (V/s)	105 ± 18.39 (16)	134.2 ± 12.39 (14)	$t = 1.28$, $p = 0.21$	Pr = 0.28, $p = 0.33$
Max no of spikes	5.41 ± 0.82 (17)	7.75 ± 1.25 (16)	$U = 100.0$, $p = 0.2$	Sr = 0.34, $p = 0.19$

Group comparisons show results of Mann-Whitney U test or unpaired t-test, and correlations report Spearman's r (Sr) or Pearson's r (Pr), for non-parametric and parametric datasets, respectively. Bold text highlights tests where $p < 0.05$.

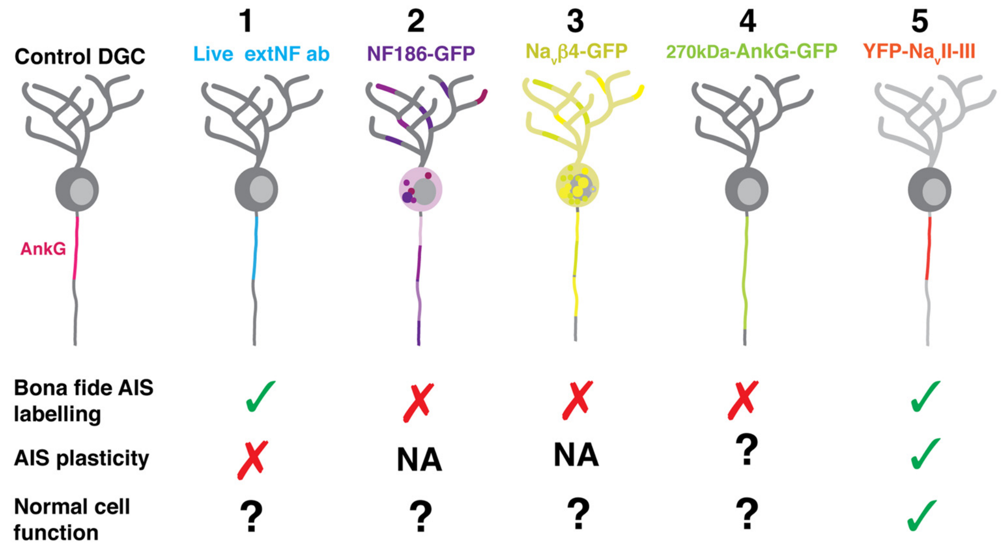

FIGURE 9 | Diagram summarizing the expression pattern of all five live *in vitro* AIS markers tested. (1) The live extNF antibody localized at the presumptive AIS endogenous site; however, it did not recapitulate the plasticity phenotype. The same was true for a version of the label conjugated with a 488 nm secondary antibody. **(2)** The NF186-GFP construct did not localize specifically to the AIS. **(3)** The 270kDa-Na$_V$β4-GFP construct, in both the full length or the C-terminal tail deletion versions, did not localize specifically to the AIS. **(4)** The 270kDa-AnkG-GFP construct did become localized specifically; however, it artificially lengthened the AIS. **(5)** The YFP-Na$_V$II–III fusion construct was localized specifically at the AIS, displayed a shortening phenotype following a 6 h depolarization treatment, and was also shown not to alter neuronal excitability.

AP height (**Figure 8E**, right panel). Finally, in multiple-spiking responses we observed a positive correlation between AIS length and maximum spike number, but in this relatively small sample this effect fell short of statistical significance (**Figures 8G,H**, left panel; **Table 3**).

DISCUSSION

To enable live imaging of AIS structure, we assessed five different labeling approaches. Of these, the YFP-Na$_V$II–III construct was clearly the most suitable—it accurately revealed both baseline and activity-altered AIS structure, and did not affect intrinsic neuronal excitability (**Figure 9**). This probe may therefore prove useful in future studies investigating alterations in AIS structure in individual neurons over time.

Live Label with the extNF Antibody Does Not Accurately Track Structural Plasticity at the AIS

There are significant advantages associated with an immunocytochemical approach to live AIS label in cell culture, including comprehensive coverage across all neurons in a given preparation, labeling that is rapidly effective after minutes, and protocols that do not require disruption of neuronal membrane integrity. Indeed, we found that live application of the extNF antibody is a reasonable, though far from perfect, indicator of baseline AIS length (**Figures 2**, **3**), and it remains entirely suitable for use in conjunction with electrophysiology (Evans et al., 2015) or other acute protocols where it is used to reveal AIS structure live at one single snapshot in time.

However, extNF label does not accurately follow AIS plasticity. After 3 h depolarization its distribution did not shorten at all, and after 6 h it not only underestimated the degree of shortening but also correlated very poorly with AnkG staining (**Figure 3**). Here our data contrast somewhat with a previous study that found local calcium uncaging at the AIS to produce a 50% reduction in live-labeled extNF fluorescence within 30 min (Schafer et al., 2009). However this calpain-dependent response to injury requires higher levels of calcium entry (Schafer et al., 2009; see also Friedrich, 2004), whereas the calcineurin-dependent AIS plasticity studied here can potentially be activated by much lower levels of calcium influx (Stemmer and Klee, 1994; Graupner and Brunel, 2007; Forbes et al., 2012). It may be, therefore, that the more dramatic process of protease-driven AIS degradation can be more readily reported by the live extNF probe.

Nevertheless, it is surprising that live extNF label does not accurately report hours-scale plastic AIS alterations, given that neurofascin-186 binds directly to AnkG (Davis and Bennett, 1994; Garver et al., 1997; Boiko et al., 2007) and might be expected to follow its distribution faithfully. The molecular features and mechanisms of neurofascin dynamics at the AIS remain entirely unknown, but a prime candidate to explain extNF's inability to track rapid structural AIS plasticity is cross-linking at the primary antibody level. An effect of cross-linking at the secondary antibody level was ruled out by our experiment showing a lack of live-labeled AIS shortening with monovalently tagged extNF (**Figure 3**). We can speculate, though, that primary antibody-level extracellular cross-linking of neurofascin molecules may make them resistant to internalization and/or promote de-coupling from the intracellular AnkG scaffold. It is possible, though not trivial, to produce monovalent F_{ab}-fragment extNF primary antibodies that would not cross-link neurofascin in this way (Bruce et al., 2016) and this may yet prove a fruitful avenue for future studies.

Unsuccessful AIS Label with NF186-GFP or $Na_V\beta 4$-GFP

Our initial attempts to live-label the AIS with genetically-encoded probes were unsuccessful, with neither NF186-GFP nor $Na_V\beta 4$-GFP localizing specifically to the proximal axon. These approaches may have suffered from common problems associated with overexpressing sizeable fluorophore fusion proteins, including issues with cellular trafficking or alterations in molecular interactions. The location of fused GFP at the C-terminal tail of neurofascin-186, for example, may have disrupted its FIGQY AnkG-binding motif and prevented successful AIS targeting (Dzhasiashvili et al., 2007). In the case of $Na_V\beta 4$-GFP, we cannot account for our inability to replicate previous reports of AIS localization with these same probes (Buffington and Rasband, 2013). We can only speculate that notorious variability in lipofection efficiency, and the associated large difference in transfection reagent exposure times (5–10 min here; 4 h in Buffington and Rasband, 2013) may have contributed to the different results we obtained. It is also worth noting that in the previous publication, the $Na_V\beta 4$-GFP signal was amplified via immunocytochemistry with antibodies against GFP (Buffington and Rasband, 2013). It is possible that we have missed potential cells that have a low and specific $Na_V\beta 4$-GFP signal that cannot be picked up live, prior to antibody staining. Extensive optimization of these protocols for individual experimental settings might allow successful AIS label with these probes in future studies.

Overexpression of 270kDa-AnkG-GFP Produces AIS Elongation in Mature Neurons

We found that an alternative, genetically-encoded live AIS reporter—270kDa-AnkG-GFP—was well localized to the AIS, but elongated the structure by ∼40%. A similar effect of this construct has been reported by two previous studies in dissociated hippocampal neurons, although both under somewhat different conditions. When over-expressed from the time of plating and throughout the initial stages of AIS development, 270kDa-AnkG-GFP was found to significantly elongate the structure (Galiano et al., 2012). This supported a model of the AIS specification in which the distal AIS boundary is established by the relative timing of ankyrin-B (AnkB) vs. AnkG expression. In this developmental scheme, AnkB is normally expressed early and located in the distal axon, with AnkG later "filling back" the proximal axonal region that is not yet AnkB-occupied (Galiano et al., 2012). Our data show that starting the overexpression of 270kDa-AnkG-GFP at 7 DIV, well past the time of initial AIS formation *in vitro* (Boiko et al., 2003; Yang et al., 2007), can also significantly elongate the structure (**Figure 4**). They suggest that if the distal AnkG-AnkB boundary still operates after the AIS has initially formed, this boundary is rather flexible.

However, the elongating effects of 270kDa-AnkG-GFP overexpression may be more due to the specific isoform utilized than to overexpression *per se*. When expressed from 3 DIV in cells where all endogenous AnkG expression had been knocked out, 270kDa-AnkG-GFP still produced longer AISs compared to control WT neurons (Jenkins et al., 2015). This effect was not observed with a GFP-fused version of the longer 480 kDa-AnkG isoform, which produced AISs of normal length when expressed from 3 DIV in AnkG-null neurons (Jenkins et al., 2015). It remains to be seen whether this fluorophore-tagged "giant" AnkG is benign when overexpressed in WT conditions, alongside endogenous AnkG production. However, given the importance of this 480 kDa AnkG isoform in AIS formation (Jenkins et al., 2015), overexpressing the 480 kDa-AnkG-GFP construct, or generating transgenic animals that constitutively express 480 kDa-AnkG-GFP (ideally from the endogenous AnkG locus) might be a very promising AIS live-label approach for future investigations.

YFP-$\mathrm{Na_V}$II–III is a Suitable Tool for Following AIS Plasticity Live

The most appropriate of our five candidate live-labeling approaches was overexpression of YFP-$\mathrm{Na_V}$II–III, a construct containing a combination of AIS-localization mechanisms employed by native $\mathrm{Na_V}$ channels via this intracellular motif (Garrido et al., 2003; Lemaillet et al., 2003; Fache et al., 2004; Bréchet et al., 2008; Gasser et al., 2012). YFP-$\mathrm{Na_V}$II–III provided accurate label of AIS length under baseline conditions and also after activity-dependent shortening. The genetically-encoded nature of this probe means it may also prove suitable for use in *in vivo* settings.

However, the axonal distribution of this probe was slower to change than those of endogenous proteins. Whilst native AIS components including AnkG and $\mathrm{Na_V}$ can shorten their distributions after just 3 h of elevated activity (Evans et al., 2015), the YFP-$\mathrm{Na_V}$II–III distribution took longer to shorten (**Figure 7**). This is extremely puzzling, given that the $\mathrm{Na_V}$II–III loop binds directly to AnkG, and is not membrane bound—it should be free to disperse with AnkG, or in unbound form, once the scaffolding molecule is removed from the AIS. We can only speculate that, once localized via an AnkG-dependent interaction, YFP-$\mathrm{Na_V}$II–III might also have as-yet unidentified associations with more stable non-AIS-specific axonal proteins, or other AIS components that do not shorten (e.g., the microtubule associated protein labeled by the "pIκBα" antibody, Evans et al., 2015).

At first glance, it is also puzzling that overexpression of YFP-$\mathrm{Na_V}$II–III does not affect neuronal excitability (**Figure 8**). The construct uses the same mechanism as $\mathrm{Na_V}$ channels for AnkG binding and AIS localization, so, under the assumption that $\mathrm{Na_V}$ binding sites on AnkG are normally saturated in DGCs at 10–12 DIV, it might be expected to at least partially out-compete native channels. The resulting reduction in AIS $\mathrm{Na_V}$ density would then be predicted, on the basis of previous experimental and theoretical work, to impact on action potential initiation (Khaliq and Raman, 2006; Laezza et al., 2007; Kole et al., 2008; Kress et al., 2010; Tapia et al., 2013; Del Puerto et al., 2015). A reduction in whole-cell $\mathrm{Na_V}$ current was indeed reported with overexpression of GFP-$\mathrm{Na_V}$II–III in hippocampal neurons of similar maturational status (Garrido et al., 2003), although that study did not assess the construct's impact on spike firing. In contrast, using $\mathrm{Na_V}$II–III to localize channelrhodopsin-2 to the AIS did not significantly reduce either whole-cell $\mathrm{Na_V}$ current or excitability of single or multiple spiking (Grubb and Burrone, 2010b). These differences may be reconciled by cross-study variations in transfection efficiency and therefore expression level: stronger $\mathrm{Na_V}$II–III overexpression would be more likely to out-compete native channel localization, and while localization of YFP-$\mathrm{Na_V}$II–III was excellent here, label intensity was certainly on the weaker side. Additionally, it may be possible that AnkG binding sites for $\mathrm{Na_V}$ are not fully saturated in DGCs at this stage in their maturation, and/or that $\mathrm{Na_V}$II–III-based constructs do not only out-compete native $\mathrm{Na_V}$ channels. $\mathrm{K_V}$7 channels also rely on a similar motif for AnkG binding (Pan et al., 2006; Rasmussen et al., 2007) and act in DGCs to dampen excitability (Martinello et al., 2015). Displacing a mixed population of native $\mathrm{Na_V}$ and $\mathrm{K_V}$7 channels might therefore result in balanced effects on action potential initiation.

Overall, we find that synapsin-driven YFP-$\mathrm{Na_V}$II–III has all the attributes required of a probe for following live structural change at the AIS, at least over longer (>6 h) timescales. When appropriately expressed, it localizes accurately to the AIS without altering baseline length or neuronal excitability, and it can reliably track plastic alterations in the structure. We envisage it being employed in future work to investigate activity-dependent and/or pathological AIS alterations in individual neurons, both *in vitro* and *in vivo*. However, we urge investigators using this probe to take inter-preparation variability into account, and to start by fully characterizing the suitability of label obtained with YFP-$\mathrm{Na_V}$II–III in their model system of choice.

AUTHOR CONTRIBUTIONS

ASD performed all experiments and analysis. MDE produced the synapsin-driven YFP-$\mathrm{Na_V}$II–III and 270kDa-AnkG-GFP constructs. All authors designed experiments and discussed results. ASD and MSG wrote the article.

FUNDING

This research was supported by a Wellcome Trust Research Career Development Fellowship (088301) to MSG, and Medical Research Council 4-year PhD studentships to ASD and MDE.

ACKNOWLEDGEMENTS

We thank Annisa Chand and Mideia Kotsogianni for assistance with cell culture, Vann Bennett for the CMV-driven 270kD-AnkG-GFP construct, and Matt Rasband for the NF186-GFP and $\mathrm{Na_V}\beta$4-GFP constructs.

REFERENCES

Bant, J. S., and Raman, I. M. (2010). Control of transient, resurgent, and persistent current by open-channel block by Na channel β4 in cultured cerebellar granule neurons. *Proc. Natl. Acad. Sci. U S A* 107, 12357–12362. doi: 10.1073/pnas.1005633107

Bender, K. J., Ford, C. P., and Trussell, L. O. (2010). Dopaminergic modulation of axon initial segment calcium channels regulates action potential initiation. *Neuron* 68, 500–511. doi: 10.1016/j.neuron.2010.09.026

Bender, K. J., and Trussell, L. O. (2012). The physiology of the axon initial segment. *Annu. Rev. Neurosci.* 35, 249–265. doi: 10.1146/annurev-neuro-062111-150339

Bender, K. J., Uebele, V. N., Renger, J. J., and Trussell, L. O. (2011). Control of firing patterns through modulation of axon initial segment T-type calcium channels. *J. Physiol.* 1, 109–118. doi: 10.1113/jphysiol.2011.218768

Boiko, T., Vakulenko, M., Ewers, H., Yap, C. C., Norden, C., and Winckler, B. (2007). Ankyrin-dependent and -independent mechanisms orchestrate axonal compartmentalization of L1 family members neurofascin and L1/neuron—glia cell adhesion molecule. *J. Neurosci.* 27, 590–603. doi: 10.1523/JNEUROSCI.4302-06.2007

Boiko, T., Van Wart, A., Caldwell, J. H., Levinson, S. R., Trimmer, J. S., and Matthews, G. (2003). Functional specialization of the axon initial segment by isoform-specific sodium channel targeting. *J. Neurosci.* 23, 2306–2313.

Bréchet, A., Fache, M. P., Brachet, A., Ferracci, G., Baude, A., Irondelle, M., et al. (2008). Protein kinase CK2 contributes to the organization of sodium channels in axonal membranes by regulating their interactions with ankyrin G. *J. Cell Biol.* 183, 1101–1114. doi: 10.1083/JCB.200805169

Bruce, A. V., Ta, A., and McNaughton, B. (2016). Minimalist antibodies and mimetics: an update and recent applications. *Chembiochem* 17, 1892–1899. doi: 10.1002/cbic.201600303

Buffington, S. A., and Rasband, M. N. (2013). Na+ channel-dependent recruitment of $Na_v\beta4$ to axon initial segments and nodes of Ranvier. *J. Neurosci.* 33, 6191–6202. doi: 10.1523/JNEUROSCI.4051-12.2013

Castelli, L., Nigro, M. J., and Magistretti, J. (2007). Analysis of resurgent sodium-current expression in rat parahippocampal cortices and hippocampal formation. *Brain Res.* 1163, 44–55. doi: 10.1016/j.brainres.2007.05.065

Chand, A. N., Galliano, E., Chesters, R. A., and Grubb, M. S. (2015). A distinct subtype of dopaminergic interneuron displays inverted structural plasticity at the axon initial segment. *J. Neurosci.* 35, 1573–1590. doi: 10.1523/JNEUROSCI.3515-14.2015

Cotel, F., Exley, R., Cragg, S. J., and Perrier, J. F. (2013). Serotonin spillover onto the axon initial segment of motoneurons induces central fatigue by inhibiting action potential initiation. *Proc. Natl. Acad. Sci. U S A* 110, 4774–4779. doi: 10.1073/pnas.1216150110

Davis, J. Q., and Bennett, V. (1994). Ankyrin binding activity shared by the neurofascin/L1/NrCAM family of nervous system cell adhesion molecules. *J. Biol. Chem.* 269, 27163–27166.

Del Puerto, A., Fronzaroli-Molinieres, L., Perez-Alvarez, M. J., Giraud, P., Carlier, E., Wandosell, F., et al. (2015). ATP-P2X7 receptor modulates axon initial segment composition and function in physiological conditions and brain injury. *Cereb. Cortex* 25, 2282–2294. doi: 10.1093/cercor/bhu035

D'Este, E., Kamin, D., Göttfert, F., El-Hady, A., and Hell, S. W. (2015). STED nanoscopy reveals the ubiquity of subcortical cytoskeleton periodicity in living neurons. *Cell Rep.* 10, 1246–1251. doi: 10.1016/j.celrep.2015.02.007

Dzhashiashvili, Y., Zhang, Y., Galinska, J., Lam, I., Grumet, M., and Salzer, J. L. (2007). Nodes of Ranvier and axon initial segments are ankyrin G-dependent domains that assemble by distinct mechanisms. *J. Cell Biol.* 177, 857–870. doi: 10.1083/jcb.200612012

Evans, M. D., Dumitrescu, A. S., Kruijssen, D. L. H., Taylor, S. E., and Grubb, M. S. (2015). Rapid modulation of axon initial segment length influences repetitive spike firing. *Cell Rep.* 13, 1233–1245. doi: 10.1016/j.celrep.2015.09.066

Evans, M. D., Sammons, R. P., Lebron, S., Dumitrescu, A. S., Watkins, T. B. K., Uebele, V. N., et al. (2013). Calcineurin signaling mediates activity-dependent relocation of the axon initial segment. *J. Neurosci.* 33, 6950–6963. doi: 10.1523/JNEUROSCI.0277-13.2013

Fache, M.-P., Moussif, A., Fernandes, F., Giraud, P., Garrido, J. J., and Dargent, B. (2004). Endocytotic elimination and domain-selective tethering constitute a potential mechanism of protein segregation at the axonal initial segment. *J. Cell Biol.* 166, 571–578. doi: 10.1083/JCB.200312155

Forbes, E. M., Thompson, A. W., Yuan, J., and Goodhill, G. J. (2012). Calcium and cAMP levels interact to determine attraction versus repulsion in axon guidance. *Neuron* 74, 490–503. doi: 10.1016/j.neuron.2012.02.035

Friedrich, P. (2004). The intriguing Ca^{2+} requirement of calpain activation. *Biochem. Biophys. Res. Commun.* 323, 1131–1133. doi: 10.1016/j.bbrc.2004.08.194

Galiano, M. R., Jha, S., Ho, T. S., Zhang, C., Ogawa, Y., Chang, K., et al. (2012). A distal axonal cytoskeleton forms an intra-axonal boundary that controls axon initial segment assembly. *Cell* 149, 1125–1139. doi: 10.1016/j.cell.2012.03.039

Garrido, J., Giraud, P., Carlier, E., Fernandes, F., Moussif, A., Fache, M. P., et al. (2003). A targeting motif involved in sodium channel clustering at the axonal initial segment. *Science* 300, 2091–2094. doi: 10.1126/science.1085167

Garver, T. D., Ren, Q., Tuvia, S., and Bennett, V. (1997). Tyrosine phosphorylation at a site highly conserved in the L1 family of cell adhesion molecules abolishes ankyrin binding and increases lateral mobility of neurofascin. *J. Cell Biol.* 137, 703–714. doi: 10.1083/JCB.137.3.703

Gasser, A., Ho, T. S., Cheng, X., Chang, K. J., Waxman, S. G., Rasband, M. N., et al. (2012). An ankyrinG-binding motif is necessary and sufficient for targeting Nav1.6 sodium channels to axon initial segments and nodes of Ranvier. *J. Neurosci.* 32, 7232–7243. doi: 10.1523/JNEUROSCI.5434-11.2012

Graupner, M., and Brunel, N. (2007). STDP in a bistable synapse model based on CaMKII and associated signaling pathways. *PLoS Comput. Biol.* 3:e221. doi: 10.1371/journal.pcbi.0030221

Grieco, T. M., Malhotra, J. D., Chen, C., Isom, L. L., and Raman, I. M. (2005). Open-channel block by the cytoplasmic tail of sodium channel β4 as a mechanism for resurgent sodium current. *Neuron* 45, 233–244. doi: 10.1016/j.neuron.2004.12.035

Grubb, M. S., and Burrone, J. (2010a). Activity-dependent relocation of the axon initial segment fine-tunes neuronal excitability. *Nature* 465, 1070–1074. doi: 10.1038/nature09160

Grubb, M. S., and Burrone, J. (2010b). Channelrhodopsin-2 localised to the axon initial segment. *PLoS One* 5:e13761. doi: 10.1371/journal.pone.0013761

Grubb, M. S., Shu, Y., Kuba, H., Rasband, M. N., Wimmer, V. C., and Bender, K. J. (2011). Short and long-term plasticity at the axon initial segment. *J. Neurosci.* 31, 16049–16055. doi: 10.1523/JNEUROSCI.4064-11.2011

Hedstrom, K. L., Ogawa, Y., and Rasband, M. N. (2008). AnkyrinG is required for maintenance of the axon initial segment and neuronal polarity. *J. Cell Biol.* 183, 635–640. doi: 10.1083/jcb.200806112

Hogins, J., Crawford, D. C., Zorumski, C. F., and Mennerick, S. (2011). Excitotoxicity triggered by Neurobasal culture medium. *PLoS One* 6:e25633. doi: 10.1371/journal.pone.0025633

Jenkins, P. M., Kim, N., Jones, S. L., Tseng, W. C., Svitkina, T. M., Yin, H. H., et al. (2015). Giant ankyrin-G: a critical innovation in vertebrate evolution of fast and integrated neuronal signaling. *Proc. Natl. Acad. Sci. U S A* 112, 957–964. doi: 10.1073/pnas.1416544112

Khaliq, Z. M., and Raman, I. M. (2006). Relative contributions of axonal and somatic Na channels to action potential initiation in cerebellar Purkinje neurons. *J. Neurosci.* 26, 1935–1944. doi: 10.1523/JNEUROSCI.4664-05.2006

Kole, M. H. P., Ilschner, S. U., Kampa, B. M., Williams, S. R., Ruben, P. C., and Stuart, G. J. (2008). Action potential generation requires a high sodium channel density in the axon initial segment. *Nat. Neurosci.* 11, 178–186. doi: 10.1038/nn2040

Kole, M. H. P., and Stuart, G. J. (2012). Signal processing in the axon initial segment. *Neuron* 73, 235–247. doi: 10.1016/j.neuron.2012.01.007

Kress, G. J., Dowling, M. J., Eisenman, L. N., and Mennerick, S. (2010). Axonal sodium channel distribution shapes the depolarized action potential threshold of dentate granule neurons. *Hippocampus* 20, 558–571. doi: 10.1002/hipo.20667

Kuba, H., Oichi, Y., and Ohmori, H. (2010). Presynaptic activity regulates Na^+ channel distribution at the axon initial segment. *Nature* 465, 1075–1078. doi: 10.1038/nature09087

Laezza, F., Gerber, B. R., Lou, J., Kozel, M. A., Hartman, H., Craig, A. M., et al. (2007). The FGF14 F145S mutation disrupts the interaction of FGF14 with voltage-gated Na^+ channels and impairs neuronal excitability. *J. Neurosci.* 27, 12033–12044. doi: 10.1523/JNEUROSCI.2282-07.2007

Lee, K. J., Queenan, B. N., Rozeboom, A. M., Bellmore, R., Lim, S. T., Vicini, S., et al. (2013). Mossy fiber-CA3 synapses mediate homeostatic plasticity in mature hippocampal neurons. *Neuron* 77, 99–114. doi: 10.1016/j.neuron.2012.10.033

Lemaillet, G., Walker, B., and Lambert, S. (2003). Identification of a conserved ankyrin-binding motif in the family of sodium channel β subunits. *J. Biol. Chem.* 278, 27333–27339. doi: 10.1074/jbc.M303327200

Lukinavičius, G., Reymond, L., D'Este, E., Masharina, A., Göttfert, F., Ta, H., et al. (2014). Fluorogenic probes for live-cell imaging of the cytoskeleton. *Nat. Methods* 11, 731–733. doi: 10.1038/nmeth.2972

Martinello, K., Huang, Z., Lujan, R., Tran, B., Watanabe, M., Cooper, E. C., et al. (2015). Cholinergic afferent stimulation induces axonal function plasticity in adult hippocampal granule cells. *Neuron* 85, 346–363. doi: 10.1016/j.neuron.2014.12.030

Muir, J., and Kittler, J. T. (2014). Plasticity of GABA A receptor diffusion dynamics at the axon initial segment. *Front. Cell. Neurosci.* 8:151. doi: 10.3389/fncel.2014.00151

Pan, Z., Kao, T., Horvath, Z., Lemos, J., Sul, J., Cranstoun, S. D., et al. (2006). A common ankyrin-G-based mechanism retains KCNQ and NaV channels at electrically active domains of the axon. *J. Neurosci.* 26, 2599–2613. doi: 10.1523/JNEUROSCI.4314-05.2006

Rasband, M. N. (2010). The axon initial segment and the maintenance of neuronal polarity. *Nat. Rev. Neurosci.* 11, 552–562. doi: 10.1038/nrn2852

Rasmussen, H. B., Frøkjaer-Jensen, C., Jensen, C. S., Jensen, H. S., Jørgensen, N. K., Misonou, H., et al. (2007). Requirement of subunit co-assembly and ankyrin-G for M-channel localization at the axon initial segment. *J. Cell Sci.* 120, 953–963. doi: 10.1242/jcs.03396

Schafer, D. P., Jha, S., Liu, F., Akella, T., McCullough, L. D., and Rasband, M. N. (2009). Disruption of the axon initial segment cytoskeleton is a new mechanism for neuronal injury. *J. Neurosci.* 29, 13242–13254. doi: 10.1523/JNEUROSCI.3376-09.2009

Stemmer, P. M., and Klee, C. B. (1994). Dual calcium ion regulation of calcineurin by calmodulin and calcineurin B. *Biochemistry* 33, 6859–6866. doi: 10.1021/bi00188a015

Tait, S., Gunn-Moore, F., Collinson, J. M., Huang, J., Lubetzki, C., Pedraza, L., et al. (2000). An oligodendrocyte cell adhesion molecule at the site of assembly of the paranodal axo-glial junction. *J. Cell Biol.* 150, 657–666. doi: 10.1083/jcb.150.3.657

Tapia, M., Del Puerto, A., Puime, A., Sanchez-Ponce, D., Fronzaroli-Molinieres, L., Pallas-Bazarra, N., et al. (2013). GSK3 and β-catenin determines functional expression of sodium channels at the axon initial segment. *Cell. Mol. Life Sci.* 70, 105–120. doi: 10.1007/s00018-012-1059-5

Wefelmeyer, W., Cattaert, D., and Burrone, J. (2015). Activity-dependent mismatch between axo-axonic synapses and the axon initial segment controls neuronal output. *Proc. Natl. Acad. Sci. U S A* 112, 9757–9762. doi: 10.1073/pnas.1502902112

Williams, M. E., Wilke, S. A., Daggett, A., Davis, E., Otto, S., Ravi, D., et al. (2011). Cadherin-9 regulates synapse-specific differentiation in the developing hippocampus. *Neuron* 71, 640–655. doi: 10.1016/j.neuron.2011.06.019

Yang, Y., Ogawa, Y., Hedstrom, K. L., and Rasband, M. N. (2007). β-IV spectrin is recruited to axon initial segments and nodes of Ranvier by ankyrinG. *J. Cell Biol.* 176, 509–519. doi: 10.1083/jcb.200610128

Yu, F. H., Westenbroek, R. E., Silos-Santiago, I., McCormick, K. A., Lawson, D., Ge, P., et al. (2003). Sodium channel β4, a new disulfide-linked auxiliary subunit with similarity to β2. *J. Neurosci.* 23, 7577–7585.

Zhang, X., and Bennett, V. (1998). Restriction of 480/270-kD ankyrin $_G$ to axon proximal segments requires multiple ankyrin $_G$-specific domains. *J. Cell Biol.* 142, 1571–1581. doi: 10.1083/jcb.142.6.1571

Conflict of Interest Statement: The authors declare that the research was conducted in the absence of any commercial or financial relationships that could be construed as a potential conflict of interest.

frontiers
in Cellular Neuroscience

REVIEW
published: 09 May 2017
doi: 10.3389/fncel.2017.00136

Axonal Membranes and Their Domains: Assembly and Function of the Axon Initial Segment and Node of Ranvier

Andrew D. Nelson[1] **and Paul M. Jenkins**[1,2]*

[1] *Department of Pharmacology, University of Michigan Medical School, Ann Arbor, MI, USA,* [2] *Department of Psychiatry, University of Michigan Medical School, Ann Arbor, MI, USA*

Neurons are highly specialized cells of the nervous system that receive, process and transmit electrical signals critical for normal brain function. Here, we review the intricate organization of axonal membrane domains that facilitate rapid action potential conduction underlying communication between complex neuronal circuits. Two critical excitable domains of vertebrate axons are the axon initial segment (AIS) and the nodes of Ranvier, which are characterized by the high concentrations of voltage-gated ion channels, cell adhesion molecules and specialized cytoskeletal networks. The AIS is located at the proximal region of the axon and serves as the site of action potential initiation, while nodes of Ranvier, gaps between adjacent myelin sheaths, allow rapid propagation of the action potential through saltatory conduction. The AIS and nodes of Ranvier are assembled by ankyrins, spectrins and their associated binding partners through the clustering of membrane proteins and connection to the underlying cytoskeleton network. Although the AIS and nodes of Ranvier share similar protein composition, their mechanisms of assembly are strikingly different. Here we will cover the mechanisms of formation and maintenance of these axonal excitable membrane domains, specifically highlighting the similarities and differences between them. We will also discuss recent advances in super resolution fluorescence imaging which have elucidated the arrangement of the submembranous axonal cytoskeleton revealing a surprising structural organization necessary to maintain axonal organization and function. Finally, human mutations in axonal domain components have been associated with a growing number of neurological disorders including severe cognitive dysfunction, epilepsy, autism, neurodegenerative diseases and psychiatric disorders. Overall, this review highlights the assembly, maintenance and function of axonal excitable domains, particularly the AIS and nodes of Ranvier, and how abnormalities in these processes may contribute to disease.

Keywords: axon initial segment, nodes of Ranvier, ankyrin-G, spectrin, cytoskeleton, excitable membrane domains, sodium channels

Edited by:
Maren Engelhardt,
Heidelberg University, Germany

Reviewed by:
Michael E. Hildebrand,
Carleton University, Canada
Keiichiro Susuki,
Wright State University, USA

***Correspondence:**
Paul M. Jenkins
pjenkins@umich.edu

Received: *03 March 2017*
Accepted: *21 April 2017*
Published: *09 May 2017*

Citation:
Nelson AD and Jenkins PM (2017) Axonal Membranes and Their Domains: Assembly and Function of the Axon Initial Segment and Node of Ranvier. Front. Cell. Neurosci. 11:136. doi: 10.3389/fncel.2017.00136

INTRODUCTION

Neurons are polarized cells made up of structurally and functionally distinct processes, dendrites and axons, which direct the flow of information throughout the nervous system. The dendrites are often composed of multiple branches and dendritic spines that receive signals from upstream synaptic inputs and transmit this information to the axon. The axon propagates electrical signals, known as action potentials, to downstream neurons by the opening of voltage gated-sodium channels at specialized excitable microdomains referred to as the axon initial segment (AIS) and nodes of Ranvier (**Figure 1**). Action potential initiation at the AIS and efficient propagation across the nodes of Ranvier requires the localization of high concentrations of voltage-gated ion channels. In addition, the AIS and nodes also contain high densities of cell adhesion molecules and scaffolding proteins that anchor these critical ion channels to the underlying cytoskeleton networks.

Despite similar structural composition between the AIS and the nodes, the mechanisms by which these microdomains form are quite different. The formation of the nodes of Ranvier is strongly influenced by both intrinsic and extrinsic factors, whereas localization of these same proteins to the AIS relies mainly on factors intrinsic to the neuron. The intricate formation and function of excitable axonal microdomains of the vertebrate nervous system plays a critical role in fast neuronal signaling and higher order cognitive processing. Several excellent detailed reviews about the structural organization and physiology of the AIS and nodes of Ranvier have been published (see: Leterrier and Dargent, 2014; Yoshimura and Rasband, 2014; Rasband and Peles, 2015). This review focuses on the recent advances in our understanding of structural and functional mechanisms underlying the formation and function of AIS and nodes of Ranvier and how disruptions in these mechanisms influence neurological health and disease.

OVERVIEW OF THE FUNCTION AND INTRINSIC ASSEMBLY OF THE AIS

The AIS is a specialized membrane domain approximately 10–60 μm long and is generally located at the most proximal region of the axon (Palay et al., 1968). This domain is characterized by high-densities of voltage-gated ion channels and functions as the gatekeeper of action potential initiation as well as axonal polarity (Kole et al., 2008; Bender and Trussell, 2012; Kole and Stuart, 2012; Jones and Svitkina, 2016; **Figure 1**). AIS assembly is an intrinsic process within the neuron, in contrast to the formation of nodes of Ranvier, which also require extracellular glial-derived signals. The scaffolding protein ankyrin-G is regarded as the master organizer of the AIS as it coordinates the localization of all known AIS components (Bennett and Baines, 2001; Jenkins and Bennett, 2001; Leterrier et al., 2017). Other critical proteins involved in AIS assembly and function include Nav channels (Kordeli et al., 1995; Zhou et al., 1998), neuronal KCNQ potassium channels (Pan et al., 2006), the cell adhesion molecule neurofascin-186 (NF186; Davis and Bennett, 1994; Jenkins and Bennett, 2001; Ango et al., 2004; Dzhashiashvili et al., 2007), casein kinase II (CK2; Bréchet et al., 2008) and βIV spectrin-actin cytoskeletal proteins (Komada and Soriano, 2002; Yang et al., 2007; **Figure 1**).

Work from Gary Banker and others with cultured hippocampal neurons has established the nomenclature for stages of neuronal development (Dotti et al., 1988). At the start of neuron development, referred to as stage 1, multiple lamellipodia protrude around the entire circumference of the cell. In stage 2, the lamellipodia progress into several short and identical neurites within 12–24 h of plating. Neuronal polarity begins to develop at 24–48 h in stage 3 during which one of the immature neurites rapidly elongates and subsequently acquires axonal properties. Stage 4 occurs shortly after the formation of the axon, where the remaining immature neurites slowly transition into the dendrites at 3–4 days (Dotti et al., 1988). The AIS first forms in cultured hippocampal neurons between stages 3 and 4 (approximately 3–4 days *in vitro*) indicated by the clustering of ankyrin-G, the first detectable marker of the AIS (Yoshimura and Rasband, 2014). *In utero* electroporation of GFP to label neurons *in vivo* revealed the first noticeable accumulation of ankyrin-G occurs in the proximal axon at approximately P1 after most neurons have migrated to their final destination in layer II/III of the cortex (Galiano et al., 2012). In contrast, Gutzmann et al. (2014) discovered ankyrin-G appears at the proximal axon at embryonic day 14.5 in the visual cortex. Further, analysis of AIS formation *in vivo* using spinal motor neurons, demonstrated that ankyrin-G is first expressed along the length of the axon before gradually becoming restricted to the proximal axon at embryonic day 13.5 (Le Bras et al., 2014). It is not clear whether these findings represent a difference in assembly of the AIS in a brain region-specific or cell type-specific manner (i.e., primary motor cortex vs. visual cortex vs. spinal motor neurons); however, in all cases ankyrin-G is the first resident protein of the AIS to appear.

GIANT ANKYRINS KEY TO AXONAL STRUCTURE AND FUNCTION

The vertebrate genome contains three members of the ankyrin gene family: *ANK1*, *ANK2* and *ANK3* (encoding ankyrin-R, ankyrin-B and ankyrin-G, respectively). Alternative splicing is a key mechanism underlying the functional diversity and cellular distribution of ankyrins. In addition to the canonical 190 kDa ankyrin-G, alternative splicing of the giant 7.8-kb exon produces a 270 kDa isoform, which only utilizes the first ∼2700 nucleotides of the giant exon due to in-frame splicing, and a giant 480 kDa isoform which utilizes the entire giant exon. Similar alternative splicing of *ANK2* gives rise to a 220 kDa isoform and a 440 kDA isoform of ankyrin-B. The giant ankyrin-G differs from the large isoform of ankyrin-B due to the presence of a 40 kDa serine and threonine rich domain located on the N-terminal side that is modified by O-linked *N*-acetylglucosamine residues with unknown function (Zhang and Bennett, 1996; Vosseller et al., 2006). Interestingly, giant

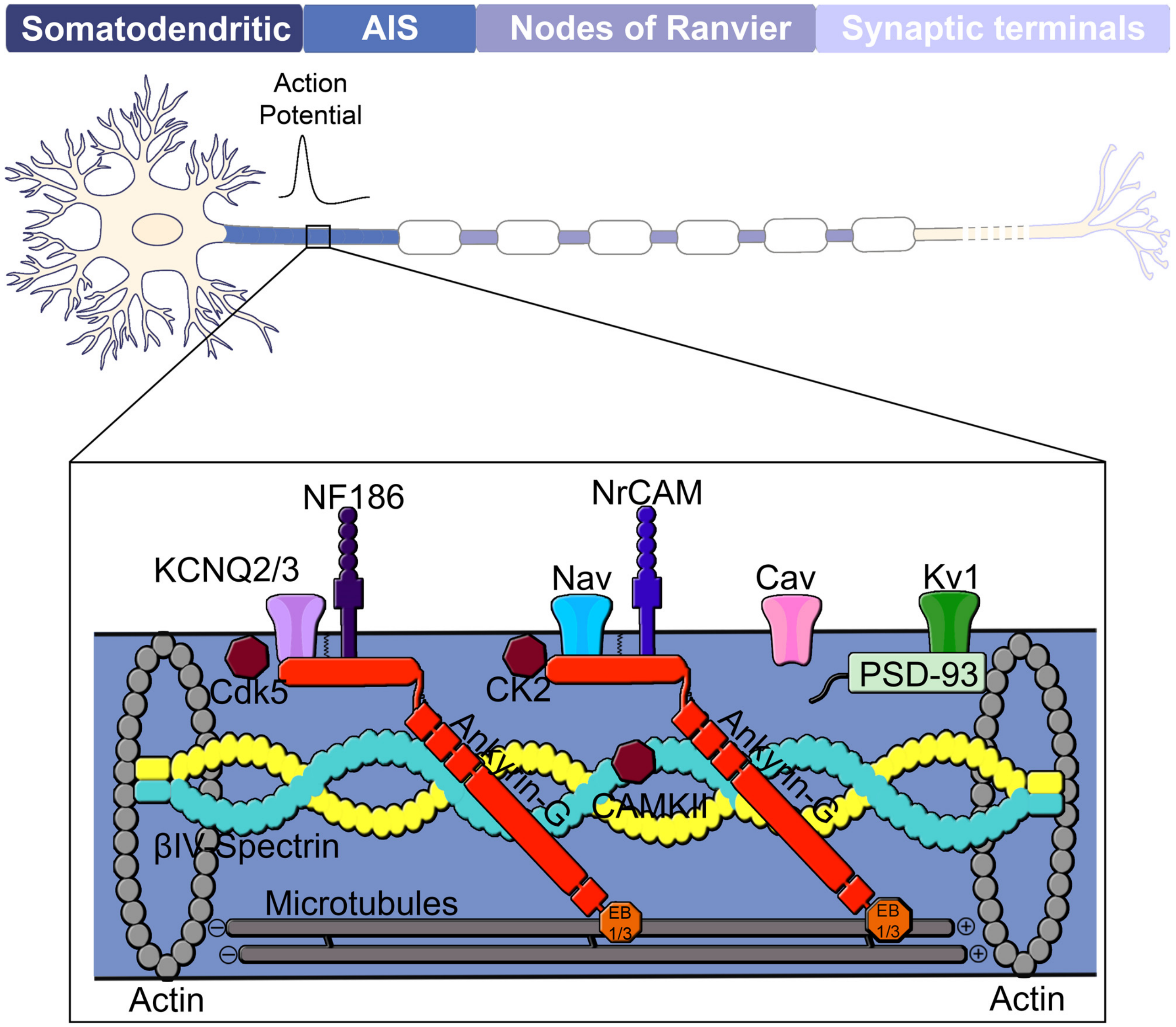

FIGURE 1 | Domain organization of a neuron. The neuron consists of a somatodendritic domain, the axon initial segment (AIS), nodes of Ranvier and presynaptic terminals. The action potential is generated at the AIS, located in the proximal region of the axon and propagates via saltatory conduction down the nodes of Ranvier of a myelinated axon to the presynaptic terminals. Ankyrin-G (red) is considered the master organizer of the AIS and controls localization of membrane-associated proteins such as Kv and Nav channels as well as the cell adhesion molecules NF186 and NrCAM. Nav channels found at the AIS include Nav 1.1, Nav1.2 and Nav1.6. Ankyrin-G is also linked to the underlying actin cytoskeleton through its interaction with βIV-spectrin and to the microtubule cytoskeleton through interactions with EB1/3 proteins. Other components of the AIS include protein kinases CK2, Cdk5 and CAMKII as well as Cav, Kv1 and PSD-93.

ankyrins are more prevalent in the genome throughout evolution than originally thought, with many bilaterians expressing giant isoforms with variation between species in the site of insertion (Jegla et al., 2016). Between three species that share homologous insertion sites (*Drosophila*, *Ciona intestinalis* and *Stronglyocentrotus purpuratus*), there is no significant sequence homology outside of a composition bias of increased usage of serine and glutamic acid and there is a huge variation in exon size (7.8 kb in vertebrates vs. 13.3 kb in *C. intestinalis* and 27.8 kb in *Drosophila*). Although the *Drosophila* giant splice variants also show some ability to restrict ion channel mobility within the axon (Jegla et al., 2016), more work is necessary to determine the functions of these different giant ankyrins.

In vertebrates, the 480 kDa isoform of ankyrin-G is localized to the AIS and nodes of Ranvier in myelinated axons. Recent studies demonstrated that, of all the *ANK3* isoforms, the giant 480 kDa ankyrin-G is specifically required for the proper localization of voltage-gated Nav channels, KCNQ2/3 channels, NF186 and βIV-spectrin to the AIS (Jenkins et al., 2015). The authors also identified a critical serine residue located within the giant exon, but outside of the canonical binding site of βIV-spectrin, that regulates spectrin localization via a likely phosphorylation-dependent mechanism. Surprisingly, mice lacking the giant 270 kDa and 480 kDa splice variants of ankyrin-G survive through weaning, whereas mice lacking all three main isoforms of ankyrin-G die immediately after birth (Jenkins et al., 2015). Survival of mice lacking the giant splice forms of ankyrin-G may be because of a compensatory increase in expression of the smaller 190 kDa isoform. Further, mice lacking giant ankyrin-G demonstrate severe movement defects and significant reductions in higher order cognitive processing such as working memory and sensory stimulation as compared to control littermates (Jenkins et al., 2015). These findings highlight the critical importance of the giant exon of ankyrin-G for normal neuronal function at both the cellular level and for synchronization of complex brain circuits.

In contrast to the giant splice variant of ankyrin-G, the 440 kDa variant of ankyrin-B is found in unmyelinated axons where it interacts with αII-spectrin and βII-spectrin to establish an intra-axonal barrier that limits ankyrin-G expansion within the axon (**Figure 2**; Galiano et al., 2012). During postnatal axonal development the majority of the 440 kDa ankyrin-B is replaced by the 220 kDa isoform, lacking the giant insert, which has been shown to be important for the long-range trafficking of cargo down the axon (Lorenzo et al., 2014). Future work will be necessary to fully elucidate the roles of the different splice variants of ankyrin-B and their relationships to ankyrin-G in the proper structure and function of the AIS.

Ankyrins and their spectrin counterparts play a central role in the formation of discrete plasma membrane domains by coordinating the specific subcellular localization of membrane-associated proteins. Ankyrins interact with their membrane-associated proteins through a membrane-binding domain that consists of 24 ANK repeats folded into an extended solenoid structure on the N-terminus (Bennett and Lorenzo, 2013). In canonical ankyrins, the membrane-binding domain is followed by two ZU5 domains, a UPA domain (Wang et al., 2012), a death domain (Wang et al., 2009) and an unstructured C-terminal regulatory domain. The membrane-binding domain of ankyrin-G directly binds to a highly conserved intracellular motif located in the II-III linker domain of Nav channels and to the C-terminus of Kv channels and recruits them to the AIS both *in vivo* and *in vitro* (Pan et al., 2006; Gasser et al., 2012). The cell adhesion molecules NF186 and NrCAM directly interact with the membrane-spanning domain of ankyrin-G through a conserved intracellular five amino acid motif (FIGQY; Zhang et al., 1998; Zhong et al., 2014).

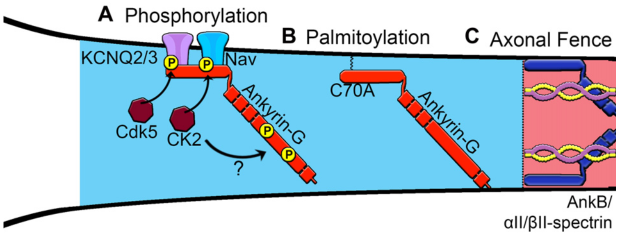

FIGURE 2 | Proposed mechanisms of assembly of the AIS.
(A) Phosphorylation of Nav channels by protein kinase casein kinase II (CK2) and KCNQ2/3 channels increases affinity for ankyrin-G. Phosphorylation sites within the giant exon of ankyrin-G (red), potentially regulated by CK2, are important for βIV-spectrin binding. **(B)** Palmitoylation of a critical cysteine 70 residue in the membrane-binding domain of ankyrin-G is necessary to target ankyrin-G to the AIS and recruit known binding partners. **(C)** Ankyrin-B interacts with αII-spectrin and βII-spectrin to establish an intracellular barrier or "axonal fence" and maintain ankyrin-G within the proximal axon.

The clustering of ion channels, including Nav and Kv channels, at the AIS is critical for normal neuronal function. The specific subtypes of Nav channels at the AIS include Nav1.1, Nav1.2 and Nav1.6. Early in AIS development, Nav1.2 is the predominant channel found at the AIS; however, as the neuron matures, Nav1.6 becomes the primary channel (Boiko et al., 2003; Osorio et al., 2005). The reason for this shift in Nav channel expression and its physiological impact remains poorly understood. Multiple subtypes of Kv channels have also been identified at the AIS, these include Kv1.1, Kv1.2, Kv1.4, Kv2.1, Kv2.2, Kv7.2 (KCNQ2) and Kv7.3 (KCNQ3), which are important for modulating neuronal excitability (Cooper, 2011).

Deletion of ankyrin-G prevents clustering of other AIS members including KCNQ2/3 channels, NF186, NrCAM, βIV-spectrin and Nav channels in the proximal axon (Zhou et al., 1998; Jenkins and Bennett, 2001; Pan et al., 2006; Jenkins et al., 2015). Genetic deletion of ankyrin-G in mice or silencing ankyrin-G using short hairpin RNA (shRNA) in dissociated neurons results in the loss of Nav channel clustering at the membrane (Zhou et al., 1998; Fache et al., 2004; Hedstrom et al., 2008). The assembly of the AIS through interaction of both the ion channels and cell adhesion molecules to ankyrin-G is regulated by phosphorylation. Interestingly, the phosphorylation of Nav channels is facilitated by protein kinase CK2, which greatly increases Nav affinity for ankyrin-G (**Figure 2**; Bréchet et al., 2008), whereas phosphorylation of the FIGQY motif on NF186 and NrCAM inhibits interaction with ankyrin-G (Tuvia et al., 1997). The NF186-ankyrin-G-Nav channel protein complex is linked to the underlying actin cytoskeleton through ankyrin-G's interactions with βIV-spectrin (Berghs et al., 2000).

Spectrins are a group of cytoskeletal proteins that contribute to the mechanical support of axons through direct interaction with ankyrins. βIV-spectrin is a member of the spectrin family, a group of flexible rod-shaped cytoskeletal proteins that exist as tetramers with two α and two β subunits (Ogawa et al., 2006; Uemoto et al., 2007; Galiano et al., 2012). In mammals, although β-spectrins are encoded by five different genes, only βIV-spectrin is found to be enriched at the AIS and nodes of Ranvier, and its recruitment to these sites depends on the direct interaction with ankyrin-G (Yang et al., 2007). Since all β-spectrins contain the canonical ankyrin-spectrin interaction site (Davis et al., 2009), what is unique about βIV-spectrin that allows its clustering at the AIS and nodes of Ranvier? Studies have shown that the first Zu5 domain of ankyrin is the canonical β-spectrin binding site since this is where βII-spectrin binds to ankyrin-B in neonatal cardiomyocytes and where βI-spectrin binds to ankyrin-R in erythrocytes (Mohler et al., 2004; Ipsaro and Mondragon, 2010; Ipsaro et al., 2010). However, the presence of the DAR999AAA mutation in the 480 kDa ankyrin-G, which is known to abolish ankyrin-spectrin binding at Zu5, had no effect on its ability to cluster βIV-spectrin to the proximal axon. In addition, knockout and rescue with the 270 kDa ankyrin-G failed to properly localize βIV-spectrin to the AIS despite the fact that all isoforms of ankyrin-G share the Zu5 domain and that 270 kDa ankyrin-G is capable of interacting with βIV-spectrin in immunoprecipitation experiments (Komada and Soriano, 2002; Hedstrom et al., 2008; Jenkins et al., 2015). Interestingly, mutation of a critical S2417A site found within the giant exon of the 480 kDa ankyrin-G greatly reduces βIV-spectrin localization to the AIS. These findings demonstrate that recruitment of βIV-spectrin to the AIS by ankyrin-G occurs independently of the canonical ankyrin-spectrin binding site in the first Zu5 domain and perhaps offers a novel mechanism as to why βIV-spectrin is localized to the AIS. In addition, the 270 residues between the last spectrin repeat and the PH domain of βIV-spectrin, which are not found in other β-spectrins, may play an important role in the noncanonical recruitment of βIV-spectrin to the AIS. Although this stretch is predominantly unstructured, there are ∼70 amino acids that are strongly predicted to form alpha helical coils and this may represent an important interaction surface. More work is necessary to determine the precise mechanisms by which ankyrin-G recruits βIV-spectrin to the AIS.

Despite the fact that βIV-spectrin can interact with αII-spectrin (Uemoto et al., 2007); αII-spectrin has not yet been identified at the AIS. In contrast, βII-spectrin and αII-spectrin assemble with one another in the distal axon (Uemoto et al., 2007). βII-spectrin has been implicated in the initial assembly of the AIS as genetic ablation of βII-spectrin in immature neurons alters βIV-spectrin's ability to appropriately accumulate at the AIS (Zhong et al., 2014). βII-spectrin becomes enriched in a periodic arrangement in the AIS very early in development, before the other AIS proteins are detectable, and then migrates to more distal regions within the axon. The migration of βII-spectrin down the axon coincides with the appearance of ankyrin-G and βIV-spectrin at the AIS (Zhong et al., 2014). If βII-spectrin is providing initial structural support, what is the function of the clustered βIV-spectrin? One potential role could be to function as the coordinator of a signaling platform for calcium-mediated signaling through calmodulin-dependent kinase II (Hund et al., 2010).

POTENTIAL MECHANISMS OF ANKYRIN-G RECRUITMENT TO THE AIS

Increasing evidence supports the role of ankyrin-G as the master organizer of the AIS; however, a major unresolved question is how ankyrin-G itself is recruited to the proximal axon to initiate this process (**Figure 2**). It has been shown that multiple domains of ankyrin-G cooperate with one another to drive its localization to the AIS (Zhang and Bennett, 1998). He et al. (2012) demonstrated that the addition of a fatty acid palmitate, termed S-palmitoylation, to a critical cysteine residue in the membrane-binding domain of the 190 kDa ankyrin-G is necessary for ankyrin-G membrane association and proper polarized localization in epithelial cells. In addition, palmitoylation of the 270 kDa ankyrin-G at the cysteine 70 site is necessary to target ankyrin-G to the AIS and the presence of a C70A mutation in ankyrin-G fails to cluster at the AIS and cannot recruit neurofascin or Nav channels (He et al., 2012). Of the 23 members of the aspartate-histidine-histidine-cysteine (DHHC)-containing protein palmitoylacyltransferases, zDHHC5 and zDHHC8 were identified as the only family members that localize to the lateral membrane and are responsible for the palmitoylation and targeting of ankyrin-G (He et al., 2014). Although the cysteine 70 residue is conserved within all major splice variants of ankyrin-G, it remains unknown which palmitoylacyltransferases localize the giant 480 kDa isoform to the AIS and whether palmitoylation of ankyrin-G occurs specifically at the AIS or within the cell body (**Figure 2**). Future studies are needed to characterize the palmitoylacyltransferases capable of palmitoylating neuronal ankyrin-G and to evaluate the spatial and temporal regulation of this process during AIS development.

Another important mechanism for the control of AIS formation is phosphorylation of ankyrin-G and its binding partners. Phosphorylation of KCNQ2/3 channels by cyclin-dependent kinase 5 (Cdk5) and phosphorylation of Nav channels by CK2 increase binding affinity to ankyrin-G. Bréchet et al. (2008) showed that CK2 phosphorylation of various serine residues (S1112, S1124 and S1126) and a glutamate residue (E1111) on Nav1.2 regulates Nav channel association with ankyrin-G. These data show that increasing the affinity of ion channels for ankyrin-G is an important regulatory step in the formation of the AIS. Overall, posttranslational modifications are an important step in AIS formation. It will be interesting to see if there are other posttranslational modifications on ankyrin-G and its partners and how these modifications are altered under different signaling conditions.

Lastly, the distal axon cytoskeleton, which is composed of ankyrin-B, αII-spectrin and βII-spectrin complexes, has been proposed to create a boundary that restricts ankyrin-G to the proximal axon (**Figure 2**). Manipulating the position of this boundary closer to the soma by overexpression of ankyrin or spectrin resulted in a shorter AIS, whereas shifting the boundary away from the soma caused the AIS to become elongated (Galiano et al., 2012). Silencing of ankyrin-B with shRNA inhibits AIS assembly and causes ankyrin-G to distribute throughout the distal axon in cultured neurons (Galiano et al., 2012). In contrast, Lorenzo et al. (2014) observed no gross detectable abnormalities in the AIS in 8 DIV hippocampal neurons derived from ankyrin-B-null mice lacking the 440 kDa and 220 kDa isoforms. Instead, deletion of ankyrin-B results in shortened axonal tracts and impaired axonal transport due to the loss of ankyrin-B association with dynactin and dynein mediated cargo transport (Lorenzo et al., 2014). Elucidating the role of the ankyrin-B/αII-spectrin/βII-spectrin network in the formation of the AIS *in vivo* will be important for the understanding of human diseases involving dysfunction of ankyrins and spectrins. In addition, it remains unclear how 480 kDa ankyrin-G, found both at the AIS and at the distal nodes of Ranvier, is able to avoid the restriction at the proximal axon by the ankyrin-B/spectrin cytoskeletal boundary. It is attractive to speculate that nascent ankyrin-G protein is locally translated at the node of Ranvier or perhaps locally palmitoylated; however, the exact mechanisms controlling AIS ankyrin-G vs. that found at the node of Ranvier remains poorly understood.

AIS MAINTENANCE AND ANALYSIS OF CYTOSKELETAL COMPOSITION THROUGH HIGH-RESOLUTION MICROSCOPY

A primary function of the AIS is to maintain polarity of the proximal axon. One potential mechanism is the role of the AIS as a diffusion barrier to inhibit the mobility of membrane-associated proteins from dispersing from one neuronal domain to another. To support this theory, Kobayashi et al. (1992) first suggested the presence of a diffusion barrier at the axonal hillock or AIS after they observed fluorescently labeled phospholipids are static within the axonal membrane in hippocampal cultures, whereas no labeling was observed within the somatodendritic domain. Winckler et al. (1999) then showed that the transmembrane protein L1CAM and the GPI-anchored protein Thy-1 display markedly reduced mobility at the AIS and they may be constrained by a cytoplasmic tether to actin filaments since the disruption of actin caused the proteins to freely distribute between the axonal and somatodendritic compartments. Nakada et al. (2003) further supported these findings by showing that ankyrin-G accumulation in the AIS at 7–10 DIV of developing hippocampal neurons correlates with a dramatic decrease in the rate of phospholipid and Nav channel diffusion.

A more recent study by Song et al. (2009) proposed a second role of the AIS in which ankyrin-G and actin filaments create a selective filter or intracellular sieve within the cytoplasm that blocks the passage of somatodendritic proteins and large macromolecule from entering the axon. For example, axonal motor proteins of the kinesin superfamily (KIFs) were allowed entry into the axon, whereas dendritic cargos and the microtubule-associated protein 2 (MAP2) were found exclusively in the somatodendritic domain of the neuron and become excluded from the AIS throughout the course of assembly (Song et al., 2009). Silencing ankyrin-G expression in hippocampal neurons or genetic deletion of ankyrin-G *in vivo* results in disassembly of the AIS and causes the proximal portion of the axon to acquire dendritic characteristics including dendritic spines and the presence of MAP2 (Hedstrom et al., 2008; Sobotzik et al., 2009). In addition, Jenkins et al. (2015) showed invasion of MAP2 into the axonal process in mice lacking only the giant isoforms 270/480 kDa of ankyrin-G, which indicates that the AIS does play a role in determining the site of axonal specification. Interestingly, however, the axonal process eventually excludes MAP2 and acquires the axonal marker, neurofilament, despite a complete lack of the AIS. These data demonstrate that the AIS is critical for maintaining axonal identity in the proximal axon, but also that a transition from dendritic to axonal character can occur in an ankyrin-G and AIS-independent manner. The exact mechanisms underlying this transition are unknown.

An important prediction of both the diffusion barrier and selective filter models is that dendritic and axonal cargos would randomly mix in the absence of the AIS. Studies evaluating the dendritic-specific cargos, transferrin receptor and TGN38, in neurons completely lacking ankyrin-G showed that these dendritic proteins maintain localization within the dendrites, but were excluded from the distal axon despite the absence of all known AIS components. In addition, the complete loss of the AIS in ankyrin-G-null neurons revealed anterograde and retrograde transport rates of LAMP-1, a relatively large (50–500 nm) lysosome, were indistinguishable between the AIS and distal axon in hippocampal neurons (Jenkins et al., 2015). These findings correspond with other work showing there is no difference in the trafficking of the neuronglia cell adhesion molecule (NgCAM) in the AIS as compared to the distal axon (Petersen et al., 2014). Furthermore, despite the loss of the AIS in total ankyrin-G-null or 480 kDa ankyrin-G-null neurons, MAP2 remains excluded from the distal axon (Jenkins et al., 2015), which suggests neurons may contain a secondary intrinsic property necessary to maintain distal axonal identity. The exclusion of dendritic cargo from the distal axon in cells lacking ankyrin-G is reminiscent of the separation of dendritic and axonal compartments seen before the AIS has been established (Silverman et al., 2001; Nakada et al., 2003; Petersen et al., 2014). Future studies need to evaluate additional AIS-independent mechanisms and how they may be critical to establish and maintain distinct axonal and dendritic polarized compartments.

While this work supports the existence of a diffusion barrier or selective filter that restricts phospholipids, membrane and cytoplasmic proteins and transport vesicles, the molecular composition of the cytoskeletal structure involved in the maintenance of neuronal polarity remains poorly understood. Recent work utilizing light and scanning microscopy showed that dense clusters of actin filaments within the AIS prevented the transport of vesicles that contain dendritic cargo from entering into the axon (Watanabe et al., 2012). Further, live-imaging experiments demonstrated that vesicles containing dendritic cargo enter the axon and dendrites with equal frequency; however, once inside the AIS the vesicles with dendritic proteins reverse directions and proceed toward the somatodendritic domain via an actin and myosin Va-dependent mechanism, whereas vesicles with axonal proteins proceed efficiently down the axon (Al-Bassam et al., 2012). These findings indicate actin filaments may be a key component for the transport of selective axonal cargo; however, there was still a lack in our understanding regarding actin organization within the AIS. Jones et al. (2014) recently sought to evaluate the sophisticated architecture of the AIS cytoskeleton in mature hippocampal neurons using platinum replica electron microscopy (PREM). The results showed an array of microtubule bundles covered in a dense submembranous coat comprised of known AIS proteins including ankyrin-G, βIV-spectrin, neurofascin, Nav channels and actin filaments (Jones et al., 2014). Interestingly, although they failed to identify a dense actin network within the AIS, they discovered subpopulations of actin that alternate between short, stable and longer, flexible filaments.

Recent advances in super resolution microscopy have revealed further insights to the arrangement of the submembranous axonal cytoskeleton and the mechanisms by which the AIS may maintain axonal polarity. A recent study quantitatively sought to determine the nanoscale organization of the AIS using Stochastic Optical Reconstruction Microscopy (STORM). They revealed the actin filaments form "actin rings" that distribute consecutively throughout the entire length of the AIS and are spaced roughly 190 nm apart. In addition, they also determined that ankyrin-B was also found to be periodically localized between the adjacent actin rings in the distal axon (Xu et al., 2013). This unique orientation occurs because βIV-spectrin connects between the adjacent actin rings in a lateral, head-to-head orientation. Further, implementation of 3D-STORM, utilizing antibodies directed against epitopes to either end of ankyrin-G, revealed βIV-spectrin binds periodically on the N-terminus of ankyrin-G, whereas the unstructured C-terminal tail extends ∼30 nm internally into the AIS cytoplasm where it may interact with additional cytoplasmic binding partners (Leterrier et al., 2015).

AXONAL POLARIZATION AND VESICLE TRAFFICKING

Besides ankyrin-G, βIV-spectrin and actin, what additional cytoskeletal proteins are important to maintain neuronal polarity? There is strong evidence that microtubule-based motor proteins influence the selective filtering of cargo transport into axons and dendrites, but the mechanisms underlying this process is not well understood (Witte et al., 2008; Hoogenraad and Bradke, 2009). Interestingly, Jacobson et al. (2006) showed that the axonal transport protein, kinesin-1, accumulates at a single immature neurite before polarization, which suggests that molecular differences between neurites exist long before the emergence of the axon. The selective transport of signaling proteins to the axon would allow for axon-specific growth from an individual neurite and the timing of this process throughout neuron development would be critical to initiate and maintain axonal polarity. One model suggests the pre-axonal exclusion zone (PAEZ), which is located within the axon hillock, distinguishes the AIS from the soma and may be important for the sorting of somatodendritic and axonal cargo (Farias et al., 2015). Here, the carrier vesicles bind to different microtubule motors that mediate transport either towards the dendrites or down the axon. Organelles that normally bind kinesin-1 or other axonal kinesins can migrate across the PAEZ and down the axon; however, vesicles that bind to dynein or other kinesins are directed to the dendrites.

Another model suggests that, since the microtubules within the AIS are primarily oriented with the plus-ends facing away from the cell body and in the dendrites the microtubules are of mixed orientation, the designated kinesins prefer one orientation over the other driving selective axonal or dendritic trafficking (Hirokawa and Takemura, 2005; Jacobson et al., 2006; Kapitein and Hoogenraad, 2011). In further support of this model, recent work showed that microtubule plus-end binding proteins EB1 and EB3 accumulate in the AIS through direct association with ankyrin-G. Following shRNA-mediated knockdown of ankyrin-G the AIS disassembles and results in a dramatic upregulation in the expression of EB1 and EB2. Thus, it is possible that the C-terminal tail of ankyrin-G extends within the axoplasm to control the proper formation of microtubule bundles and regulate AIS stability. This prediction is consistent with the loss of bundled microtubules seen in the proximal axon of mice lacking ankyrin-G (Sobotzik et al., 2009). Fréal et al. (2016) showed the cooperative interaction between 480 kDa isoform of ankyrin-G and end-binding proteins of the microtubule cytoskeleton drives AIS assembly and axon polarity and suggests another potential mechanism that drives ankyrin-G localization to the AIS.

Kinesins motors are mainly involved in the anterograde transport of dendritic cargo by migrating towards microtubule plus-ends, whereas dynein motors move in retrograde fashion towards microtubule minus-ends within axonal tracts. In support of this view, experiments using fluorescently-labeled mutant kinesin motors were conducted to monitor which subtypes of kinesin motors translocate to either dendritic or axonal domains (Nakata et al., 2011). Kuijpers et al. (2016) discovered that the Nuclear distribution element-like 1 (NDEL1) facilitates dynein activation on somatodendritic cargos that enter the proximal axon and reverses their movement to a retrograde manner. NDEL1 is highly concentrated in the AIS via a direct link with ankyrin-G through its C-terminus tail and with LIS1 through its N-terminus tail. LIS1 has been shown to be an important regulator of NDEL1-based dynein activity at the AIS (Vallee and Tsai, 2006). The knockdown of ankyrin-G, NDEL1, or LIS1 results in the entry of dendritic cargo into the proximal axon, thus these findings suggest a "quick-switch" mechanism for selective vesicle filtering at the AIS. In addition to kinesin and dynein transport, myosin motors have also been implicated to be important for the sorting of cargo between axonal or dendritic polarized domains by interacting directly with different microtubule components (Lewis et al., 2009).

ELECTRICAL ACTIVITY AND PLASTICITY AT THE AIS

In vertebrate neurons, the AIS is the site of action potential initiation (Palay et al., 1968; Kole et al., 2008). It has recently been proposed that changes in AIS length, location and/or ion channel expression may occur following varying degrees of neuronal activity (**Figure 3**; Yamada and Kuba, 2016). This striking plasticity of the AIS arises in an attempt to maintain homeostasis within individual neurons and balance synchronization between complex neuronal circuits. Changes in

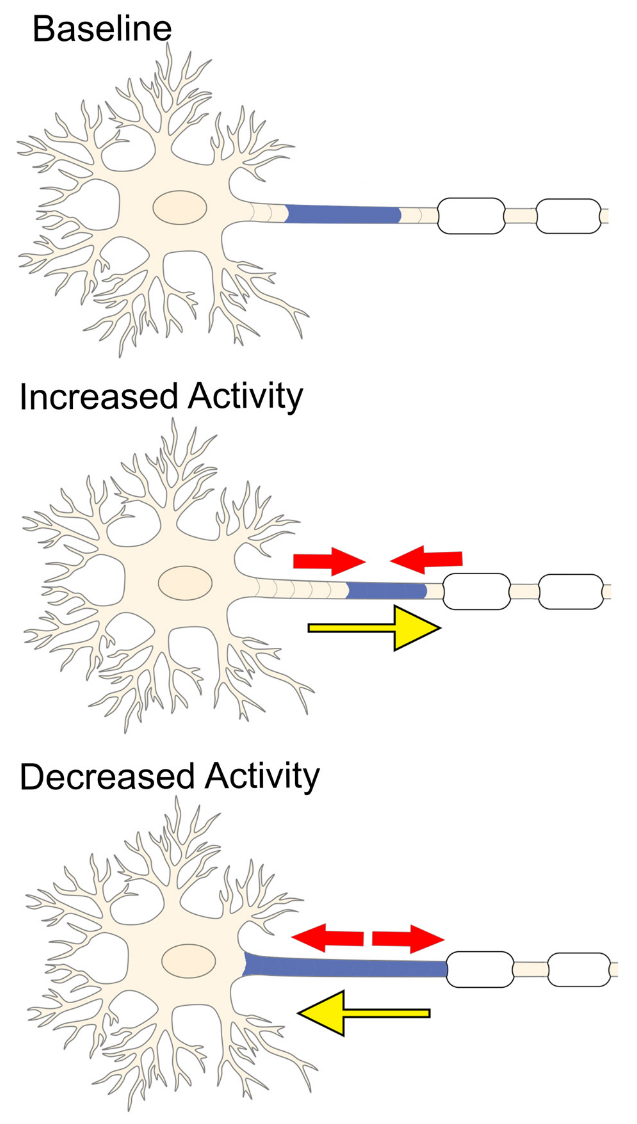

FIGURE 3 | Electrical activity and plasticity at the AIS. Increased neuronal activity causes the AIS to shrink (red arrows) and shift more distally away from the soma (yellow arrow). In contrast, inhibiting stimulation of the neuron promotes the AIS to elongate (red arrows) and causes the AIS to shift closer to the soma (yellow arrow).

AIS length were first observed in neurons removed from the avian cochlear nucleus (Kuba et al., 2010). Decreased stimulation of these neurons resulted in elongation of the AIS and an increase in the number of surface Nav channels, which, in turn, enhanced membrane excitability and promoted action potential firing (Kuba et al., 2010). In addition, low-frequency stimulation caused the AIS to shift within about 10 μm of the soma, whereas high-frequency stimulation shifted the AIS about 45 μm away from the soma (Kuba et al., 2006). A similar observation was seen after chronic stimulation of dissociated hippocampal neurons, which also caused a distal shift in the AIS and a corresponding decrease in membrane excitability (Grubb and Burrone, 2010; Evans et al., 2013). These findings suggest changes in electrical activity affect both the dynamics and location of the AIS, but what are the molecular mechanisms that contribute to this plasticity?

Recent studies demonstrated that prolonged depolarization activates L-type and T-type Ca^{2+} channels in pyramidal hippocampal neurons and that the subsequent increase in intracellular Ca^{2+} levels activate Ca^{2+}- and calmodulin-dependent protein phosphatases, which may ultimately be responsible for the distal migration and contraction of the AIS (Grubb and Burrone, 2010; Evans et al., 2013, 2015; Muir and Kittler, 2014). Increased intracellular Ca^{2+} has also been shown to activate cyclin-dependent kinase 5 (cdk5) in olfactory bulb dopaminergic interneurons. In addition, heightened cdk5 activity extended AIS length by as much as 100% in mushroom body neurons of *Drosophila*, while depleting cdk5 causes the AIS to significantly shrink or disappear altogether (Trunova et al., 2011). To date, the majority of studies that evaluated activity-dependent AIS plasticity and the underlying cellular mechanisms were conducted in fixed cells and these changes were analyzed amongst a population of neurons. The development of innovative tools capable of labeling the AIS for live-imaging experiments will be beneficial to examine AIS plasticity in individual neurons both *in vitro* and *in vivo*. Recently, Dumitrescu et al. (2016) used a construct consisting of the intracellular domain of a voltage-gated sodium channel Nav1.2 fused to a yellow-fluorescent protein (YFP-NavII-III) to examine the AIS in live neurons. This construct localized specifically to the AIS of dentate granule cells (DGCs) in dissociated hippocampal cultures as well as accurately demonstrated both baseline and activity-induced plasticity changes of the AIS without altering intrinsic neuronal excitability (Dumitrescu et al., 2016). This construct may be useful in future studies to investigate AIS plasticity in individual neurons. Live-imaging the AIS in individual neurons will reduce cell-to-cell and experimental heterogeneity and provide greater insight to the physiological impact underlying changes in AIS size and position.

Relatively little is known about what happens to the ankyrin-spectrin protein networks during periods of AIS plasticity and the physiological impact these changes have on action potential initiation. Post-translational modifications, such as phosphorylation of Nav channels by CK2 or palmitoylation of ankyrin-G and NF186, may be involved in this process (**Figure 2**; Ren and Bennett, 1998; Bréchet et al., 2008; He et al., 2012). In addition, the changes in the expression levels of ankyrin could underlie AIS plasticity. In dissociated hippocampal cultures, the overexpression of ankyrin-G was shown to elongate the length of the AIS, whereas overexpression of the distal axon cytoskeletal protein ankyrin-B shortened the AIS (Galiano et al., 2012). While phosphorylation is necessary to assemble and maintain proper AIS structure and function, the Ca^{2+}-dependent cysteine protease calpain works in opposition to promote the degradation and disassembly of the AIS. Calpain activates the proteolysis of the axonal cytoskeletal proteins including ankyrin-G and βIV-spectrin in the proximal axon and ankyrin-B, αII-spectrin and βII-spectrin in the distal axon

(Harada et al., 1997; Czogalla and Sikorski, 2005; Bevers and Neumar, 2008). In addition, Schafer et al. (2009) showed that pharmacological inhibition of calpain was sufficient to attenuate degradation and maintain the molecular organization of the AIS both *in vitro* and *in vivo*. It is also possible that the shortened and distal translocation of the AIS is caused by an overload of Ca^{2+} levels and the subsequent potentiation of calpain-mediated proteolysis.

What are the physiological impacts these changes in AIS structure and position may have on action potential generation? Jenkins et al. (2015) recently showed that mice lacking the giant isoforms (270/480 kDa) of ankyrin-G, and thus all other known components of the AIS, were still able to fire current-induced action potentials with modest effects on action potential frequency and dynamics. One possibility for this phenomenon is that the small 190 kDa ankyrin-G, which displayed a four- to five-fold increase in expression in the giant-exon null mice, is capable of compensating for the 480 kDa ankyrin-G and rescuing Nav channel localization to the plasma membrane. Another possibility is that the action potentials might be generated by Nav channels clustered locally in the somatodendritic domain (Lai and Jan, 2006). If the AIS is dispensable for action potential generation with only minor deficits, what is the evolutionary advantage of having an AIS? One potential answer to this question comes from the abnormalities seen in the gamma oscillations from the EEG recordings of the giant ankyrin-G knockout mice. Gamma oscillations arise through the activity of cortical GABAergic interneurons, which synapse directly on to the AIS and soma of pyramidal neurons and are essential for the proper synchronization of the cortical network (Somogyi, 1977; Markram et al., 2004; Bartos et al., 2007). The AIS thus provides a defined physical location to allow interneurons precise temporal and spatial modulation of action potentials.

NODES OF RANVIER

Following initiation at the AIS, action potentials must travel rapidly across long distances down the axon in order to reach the synapse. In myelinated axons, action potential regeneration occurs at the nodes of Ranvier, which are gaps between myelin sheaths characterized by very high densities of Nav channels (**Figure 1**). The molecular composition of the nodes of Ranvier and the AIS are very similar in that they both consist of similar ion channels, cell adhesion molecules and scaffolding proteins (**Figure 4**; Rasband, 2010). In contrast to the AIS, which is regulated solely by axonal intrinsic signaling, the proper assembly and function of nodes depend on both intrinsic and glial-derived extrinsic mechanisms.

MOLECULAR ORGANIZATION OF THE NODES OF RANVIER

The complex organization of the Nodes of Ranvier is accomplished in part by myelinating Schwann cells in the peripheral nervous system (PNS) and oligodendrocytes in the central nervous system (CNS). The clustering of Nav channels to the node is critically important for the rapid, saltatory propagation of action potentials. Myelination divides the axonal membrane into distinct domains including nodes of Ranvier, paranodes, juxtaparanodes and internodes. The nodes of Ranvier are the sites of action potential repolarization and depolarization due to the clustering of high concentrations of ion channels, including Nav and Kv channels. The complement of Nav and Kv channels at the node are diverse and can include Nav1.1, Nav1.2, Nav1.6, Nav1.7, Nav 1.8 and Nav1.9 which interact with β-subunits Navβ1, Navβ2 and Navβ4 (Fjell et al., 2000; Chen et al., 2002; Boiko et al., 2003; Henry et al., 2005; Duflocq et al., 2008; Black and Waxman, 2012). β2-subunits covalently bond with Nav channels via an extracellular disulfide bond and regulate their surface expression (Chen et al., 2012). Kv channels at the node include Kv3.1b, KCNQ2 and KCNQ3 (Cooper, 2011). In addition to ion channels, ankyrin-G and βIV-spectrin scaffolding proteins are also highly concentrated at the nodes and, similar to the AIS, anchor the ion channels and cell adhesion molecules NF186 and NrCAM to the underlying cytoskeleton network. Recent studies using Stimulated Emission Depleted (STED) microscopy demonstrated a periodic organization of ankyrin-G and βIV-spectrin with the underlying microtubule cytoskeleton at the nodes of Ranvier, similar to that seen in the AIS (D'Este et al., 2015). The paranode flanks the node of Ranvier and is the site where myelinating glial cells form septate-like junctions with the axonal membrane. Ankyrin-G has been shown to be highly enriched within oligodendrocytes on the glial side of the paranodal junction, whereas ankyrin-B is highly expressed at the Schwann cell paranodal membrane (Chang et al., 2014). Glial ankyrins bind to the cell adhesion molecule NF155 at the paranodal junction and contribute to the assembly and maintenance of nodes of Ranvier in both the CNS and PNS. Thus, mutations within *ANK2* or *ANK3* may lead to abnormalities in the AIS and axonal nodes of Ranvier as well as the paranodes within glia. The juxtaparanodes flank the paranodes and are enriched with dense populations of Kv channels known to module action potential conduction and help maintain internodal resting potential. Finally, the internodes make up the majority of the axon and are found underneath the myelin sheaths.

ASSEMBLY OF THE PNS NODES OF RANVIER

Although the molecular composition between PNS and CNS nodes of Ranvier are similar, the mechanisms involved in their assembly are different mainly due to the glial cells types involved in myelination (**Figure 4**). In PNS node assembly, Nav channels are initially clustered at the edges of developing myelin sheaths, referred to as the heminodes, by the extracellular matrix (ECM) molecules gliomedin and neuronal cell adhesion molecule (NrCAM) from Schwann cell microvilli interacting with axonal NF186 (Lambert et al., 1997; Eshed et al., 2005; Schafer et al., 2006; Feinberg et al., 2010). Secondly, Nav channels are restricted to the nodal gap by the paranodal junction, which consists of glial-derived NF155, found at paranodal region,

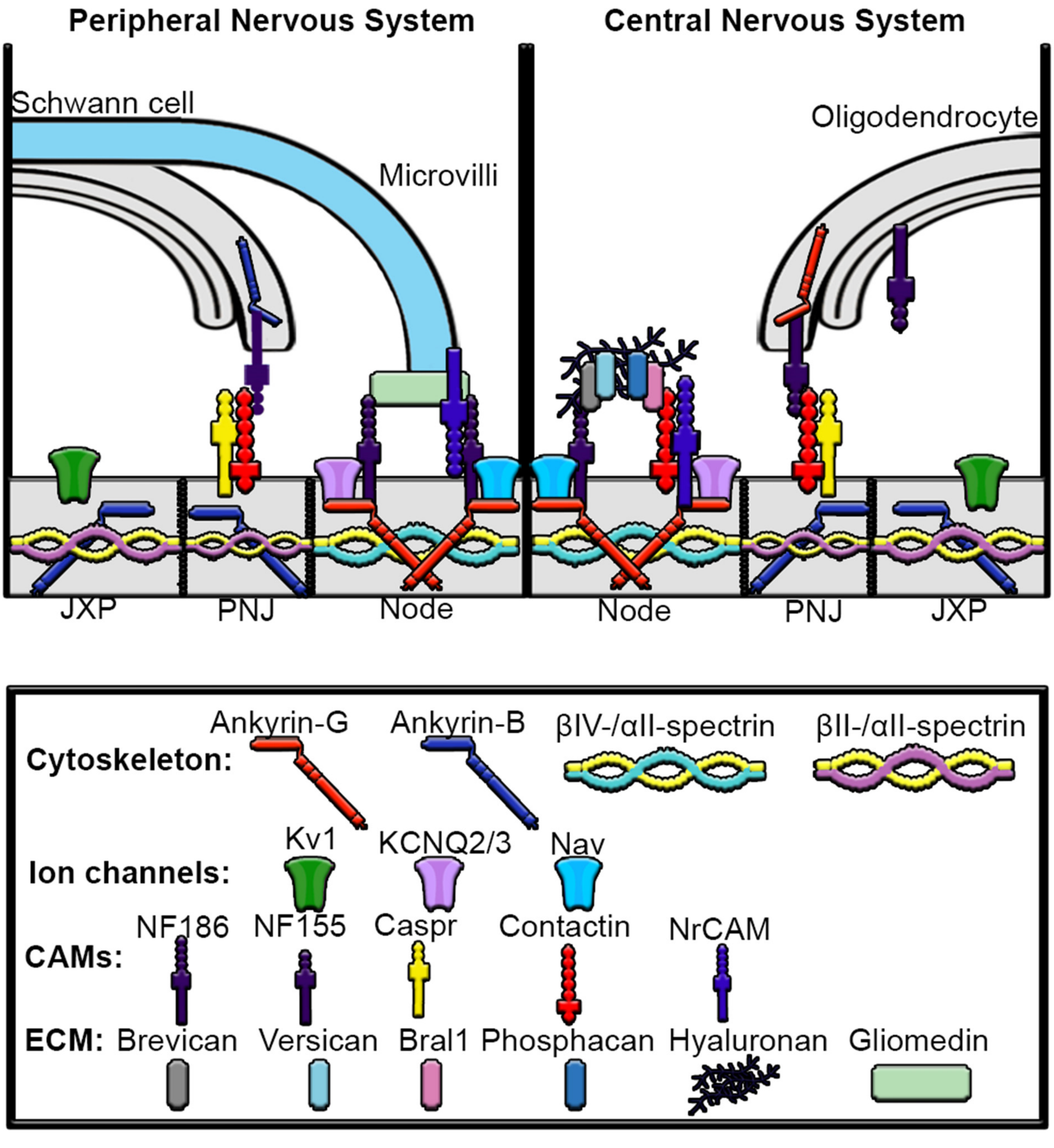

FIGURE 4 | Mechanisms underlying assembly of peripheral nervous system (PNS) and central nervous system (CNS) nodes of Ranvier. Axons are myelinated by Schwann cells in the PNS and oligodendrocytes in the CNS. The nodes are gaps in myelinated sheaths and are sites of action potential regeneration. In both the PNS and CNS the node contains high densities of Nav and KCNQ2/3 channels, ankyrin-G, βIV-spectrin, αII-spectrin, NF186 and NrCAM. In the PNS, gliomedin from the microvilli of myelinating Schwann cells directly interacts with NF186 and NrCAM at the node. In contrast, the node of the CNS contains an extracellular matrix (ECM) complex made up of chondroitin sulfate proteoglycans brevican, versican and phosphacan, which interact with contactin, Bral1, hyaluronan and NF186. The paranodal junction (PNJ) flanks the nodes of Ranvier and is the site of Schwann cell contact in the PNS and oligodendrocyte contact in the CNS. In the PNS, Ankyrin-B interacts with NF155 in Schwann cells, which then binds to contactin to connect the myelinating Schwann cell with the axon, whereas in the oligodendrocytes of the CNS, ankyrin-G associates with NF155. Within the paranodal axolemma, ankyrin-B binds βII and αII-spectrin cytoskeleton complexes that play important roles in maintaining paranode barriers. The juxtaparanodes (JXP) are characterized by high-density clustering of Kv1 channels as well as ankyrin-B and βII-spectrin and αII-spectrin tetramers.

in conjunction with Caspr and contactin within the axonal membrane. The interaction between NF155 and the Caspr-contactin complex mediates Schwann cell interaction with the axon and formation of the paranodal junction. These paranodal junctions are thought to act as a restriction barrier during node of Ranvier assembly as the nodes are fully capable of forming in NrCAM and gliomedin knockout-mice, despite the fact that NF186 fails to localize to the heminodes of these mice (Feinberg et al., 2010). In addition, the paranodal junction between myelinating Schwann cells of the PNS (and oligodendrocytes in the CNS) may function as a diffusion barrier to prevent the lateral movement of ion channels along the axonal plasma membrane (Rasband et al., 1999; Pedraza et al., 2001). In contrast, the significance of a diffusion barrier remains controversial since disturbing the paranodal junction only slightly perturbed Nav clustering (Bhat et al., 2001; Thaxton et al., 2011). Interestingly, Amor et al. (2017) recently showed that the paranodal junctions are sufficient to cluster Nav channels to the node of Ranvier in peripheral sensory neurons and retinal ganglion cells of knockout mice deficient of nodal NF186. Further, the authors demonstrate that βII-spectrin plays a role as a diffusion barrier within the paranodal junction to mediate Nav clustering at the node. These findings suggest that the intact paranode can function as a secondary mechanism for Nav nodal clustering independent of axonal NF186 localization by glial-derived proteins.

In addition to gliomedin, other ECM proteins involved in heminode formation include syndecans, laminins, NG2 and versican, all of which also directly interact with NF186 (Occhi et al., 2005). Additional proteins unique to the PNS nodal microvilli are exrin, radixin, moesin, EBP50, dystphin and utophin (Occhi et al., 2005). The paranodal junction then constrict leading to stabilization of the node by NF186 association with ankyrin-G, which subsequently interacts with and recruits Nav channels, Kv channels and βIV-spectrin. Nav and Kv channels bind with high affinity to the membrane-binding domain of ankyrin-G at the node via a CK2 phosphorylation-dependent mechanism as seen in the AIS (Wang et al., 2014; Xu and Cooper, 2015). Recent studies by Ho et al. (2014) discovered that in the absence of ankyrin-G, Nav channels are still clustered to the node of Ranvier by compensation of ankyrin-R and its binding partner βI-spectrin in peripheral sensory neurons and retinal ganglion cells. However, the ability of ankyrin-R to compensate for ankyrin-G at the node of Ranvier remains controversial (Saifetiarova et al., 2017).

ASSEMBLY OF CNS NODES OF RANVIER

Similar to the PNS, glial-derived extrinsic mechanisms contribute to CNS formation; however, in contrast to the microvilli of Schwann cells that make contact to the node in the PNS, the oligodendrocytes do not directly interact with the nodes in the CNS. Three important components have been proposed to be important for node of Ranvier assembly in the CNS (**Figure 4**). First, an ECM complex produced by glial cells promotes NF186 to cluster at the node. The ECM in the CNS contains the chondroitin sulfate proteoglycans brevican, versican, neurocan and phosphacan in addition to tenascin-R, BRal1 and NrCAM. The glial-derived ECM directly interacts with the axonal cell adhesion molecules NF186, NrCAM, contactin-1 and the β-subunit of sodium channel and are likely involved in the long-term maintenance of CNS nodes (Weber et al., 1999; Xiao et al., 1999; Oohashi et al., 2002; Bekku et al., 2009; Dours-Zimmermann et al., 2009; Susuki et al., 2013). Secondly, the paranodal axo-glial complex forms, which consists of three main cell adhesion molecules: neurofascin 155 kDa isoform (NF155) derived from glial cells, and Caspr (contactin-associated protein) and contactin which are generated in the neuron. Lastly, the axonal scaffolding protein ankyrin-G is necessary to cluster and stabilize Nav channels to the node (Gasser et al., 2012). Deletion of the giant splice variants of ankyrin-G resulted in an 80% loss in the number of nodes of Ranvier *in vivo* and the remaining nodes of the corpus callosum were malformed and elongated (Jenkins et al., 2015). Interestingly, while the remaining nodes lacked 480 kDa ankyrin-G and NF186, βIV-spectrin and Nav channels were still present and NF155 persisted at the paranode. Nav channels were clustered at the node, likely due to the dramatic upregulation seen in the 190 kDa isoform of ankyrin-G (Jenkins et al., 2015).

Ankyrin-G is referred to as the master organizer of the AIS; however, because the nodes require extrinsic regulation for their proper formation and function, the role of ankyrin-G as the master organizer of the node of Ranvier is less clear. The fact that ankyrin-G contains binding sites for all known nodal components supports the theory that ankyrin-G is necessary and sufficient for node formation (Hill et al., 2008; Gasser et al., 2012). In addition, mutation of the ankyrin-G-binding domain in NF186 inhibits its ability to cluster at the node (Susuki et al., 2013). Zonta et al. (2008) demonstrated that genetic deletion of both isoforms of NF186 and NF155 completely disrupted nodal and paranodal complexes; however, the authors show that rescue with either NF186 or NF155 independently can promote the assembly of the nodal complex and recruit Nav channels. Since Nav channels, their β subunits and ankyrin-G can interact with NF186 directly, it may not be a surprise that the addition of NF186 is capable of rescuing the node and may even subsequently promote more delivery of NF186. Rescuing with NF155 is more intriguing as NF155 is not found at the node with ankyrin-G or Nav channels, but is still sufficient to rescue assembly of the node (Zonta et al., 2008). Zhang et al. (2015) recently discovered a third isoform of neurofascin, NF140, which is highly expressed early in embryonic development and is capable of clustering Nav channels to the developing node of Ranvier independently of NF186 and NF155. Future research should expand on these findings to better understand how deletion of ankyrin-G or neurofascin disrupts Nav clustering throughout CNS, and how this loss of Nav channels at the node impacts brain function.

While the pioneering work on the AIS and nodes of Ranvier done in cultured cells *in vitro* has given us great insights into the formation and function of these critical subcellular domains, recent work has highlighted the need to examine these mechanisms *in vivo* (Komada and Soriano, 2002; Sherman et al., 2005; Zonta et al., 2008; Susuki et al., 2013; Chang et al., 2014; Jenkins et al., 2015; Amor et al., 2017; Saifetiarova et al., 2017). Specific knockout animal models have elucidated how the AIS and nodes of Ranvier are formed in the intact organisms and have supported many of the findings from *in vitro* studies. Importantly, animal models also give us the ability to examine whether the mechanisms are conserved between cell types. For example, much of the work on the mechanisms of CNS node of Ranvier formation has been done in spinal cord or optic nerve. Are these mechanisms conserved in myelinated axons in the brain?

AXONAL DOMAIN PROTEINS IN DISEASE AND INJURY

An increasing number of studies have shown that genetic mutations in components of both the AIS and nodes of Ranvier are involved in the pathophysiology of multiple diseases and injuries. As previously mentioned, ankyrin-G is absolutely essential to maintain the structural composition of the AIS and nodes of Ranvier and for normal axonal polarity. Thus, mutations or loss-of-function of *ANK3* might be expected to have a profound effect on neurological function. Consistent with this idea, genome-wide association studies have identified *ANK3* as one of the most significant risk loci for bipolar disorder, and to a lesser degree schizophrenia (Ferreira et al., 2008; Muhleisen et al., 2014; Roussos and Haroutunian, 2014). Post-mortem brains of schizophrenic patients revealed a 15%–20% decrease in ankyrin-G expression at the AIS of pyramidal neurons in the superficial cortical layer as compared to neurotypical controls, while no significant changes in AIS length were observed (Cruz et al., 2009). A recent study by Lopez et al. (2016) showed that the presence of a bipolar disorder-associated variant in *ANK3* results in reduced expression of the *ANK3* exon 1b isoform in the AIS of parvalbumin-positive (PV) GABAergic interneurons. Interestingly, mice lacking the exon 1b isoform loose Nav channel clustering at the AIS of PV interneurons and demonstrate behavioral characteristics of bipolar disorder, epilepsy and sudden death (Lopez et al., 2016). In addition, *de novo* missense mutations in *ANK3* have been identified in autistic patients as well as severe cognitive deficits, borderline intelligence, severe attention deficit hyperactivity disorder (ADHD) and sleeping problems (Awadalla et al., 2010; Hamdan et al., 2011; Talkowski et al., 2012). The presence of a homozygous premature stop codon predicted to abolish the 480 kDa isoform of ankyrin-G resulted in dramatic cognitive dysfunction and intellectual disability with IQ values below 50 (Iqbal et al., 2015). It will be important to elucidate the precise effects of *ANK3* mutations on neuronal function.

Mutations in voltage-gated sodium channel α subunits and their associated β subunits found at the AIS and nodes of Ranvier have a wide range of profound neurological effects, including epilepsy, neurodegeneration and sudden death. For example, mutations in *SCN1A* (Nav1.1) are associated with Dravet syndrome, a severe myoclonic epilepsy of infancy, as well as West syndrome, genetic epilepsy with febrile seizures plus (GEFS+) and others (Steinlein, 2014). *SCN2A* (Nav1.2) and *SCN8A* (Nav1.6) mutations are found in patients with early infantile epileptic encephalopathy (Steinlein, 2014; Wagnon and Meisler, 2015). Mutations in the sodium channel β subunits are associated with multiple neurological disorders, including GEFS+, Dravet syndrome and neurodegenerative disease (O'Malley and Isom, 2015). In addition to mutations in sodium channel genes, loss-of-function mutations in both KCNQ2 and KCNQ3 potassium channel genes are linked to benign familial neonatal convulsions (Singh et al., 2003).

Disruptions in spectrin cytoskeletal function and assembly have also been associated with neurological disease. The human spectrin family consists of two alpha- and five beta-spectrin subunits, which form heterodimers that assemble into tetramers through head-to-head and lateral associations (Bennett and Lorenzo, 2013). Human dominant in-frame duplications and deletion mutations in *SPTAN1* have been found in patients with early-onset epileptic encephalopathies, hypomyelination, intellectual disability and blindness starting in children under age 3 (Saitsu et al., 2010; Nicita et al., 2015). Mutations in βIII-spectrin, which is highly expressed in cerebellar Purkinje neurons, have been associated with spinocerebellar ataxia type 5 (Ikeda et al., 2006).

Increasing evidence also suggests degeneration of the axon is an important component underlying multiple sclerosis (MS) pathology; however, the mechanisms that contribute to axonal loss remain elusive (Dutta and Trapp, 2007). Patients suffering from MS demonstrated changes in expression and localization of Nav channels and neurofascin, as well as the paranodal protein Caspr (Wolswijk and Balesar, 2003; Craner et al., 2004; Coman et al., 2006; Howell et al., 2006). One potential mechanism that contributes to MS may be abnormal axo-glial interaction at the paranode, which would be expected to disrupt axonal transport and alter normal organization of myelinated axons (Sousa and Bhat, 2007). Mathey et al. (2007) identified autoantibodies from MS patients that specifically target the extracellular domains both axonal NF186 and glial NF155, disrupt conduction and ultimately lead to axonal injury that mimics the pathology of MS. In addition to the nodes of Ranvier, the effect of demyelination on the AIS may be another potential mechanism that contributes to MS. Hamada and Kole (2015) showed that demyelinating axons using cuprizone caused the AIS to shift more proximal to the soma and reduced action potential initiation. However, they observed no changes in ankyrin-G, βIV-spectrin and Nav1.6 expression at the AIS following demyelination (Hamada and Kole, 2015). Consistent with these findings, Clark et al. (2016) also found AIS components remained intact following cuprizone-induced demyelination. In contrast, the authors discovered the proper clustering of ankyrin-G, βIV-spectrin and Nav1.6 was lost at the AIS of mice after chronic exposure of experimental autoimmune encephalomyelitis (EAE), an inflammatory model of MS (Clark et al., 2016). Ultimately, the AIS is a primary target during inflammation and, in addition to demyelination of the distal axon, may contribute to inflammatory demyelinating diseases such as MS.

In a rat model of mild traumatic brain injury, Baalman et al. (2013) showed that exposure to a single blast wave results in long-term changes in memory within these rats and, at the cellular level, significant decreases in AIS length. These changes in the AIS perhaps highlight a potential mechanism underlying mild traumatic brain injury and future studies will be important to elucidate the specific molecular components that contribute to the structural and functional changes in the AIS.

Overall, changes in excitable domains of the axon or their constituent proteins have profound impact on neurological function. Although many of the proteins of the AIS and nodes of Ranvier have important functions in other cellular domains, the overlapping phenotypes seen with loss of function of different AIS and nodal components suggest that dysfunction of these axonal membrane domains is a major factor in the development of disease. As we increasingly understand the genetic basis of neurological disorders, we will likely uncover more genes involved in the formation and function of axonal domains that can give us more insight into the etiology of human disease.

CONCLUSION

The structural assembly and maintenance of the axon relies on the precise organization between ankyrins, spectrins, membrane-associated proteins and actin and microtubule cytoskeletal proteins. The mechanisms underlying the interaction between these components at the AISs and nodes of Ranvier are now becoming more apparent. A better understanding of the organization and maintenance of axonal excitable domains as well as how abnormalities in their signaling may lead to altered axonal function will provide insight to novel therapeutic targets for the treatment of human diseases of the nervous system.

AUTHOR CONTRIBUTIONS

ADN and PMJ wrote the manuscript.

ACKNOWLEDGMENTS

This work was supported by the following National Institute of General Medical Sciences, NIH training grant: "Michigan Predoctoral Training in Genetics (T32GM007544) (ADN) and the Heinz C. Prechter Bipolar Research Fund and the Richard Tam Foundation at the University of Michigan Depression Center". We would also like to thank Dr. Heather O'Malley for helpful comments on the manuscript.

REFERENCES

Al-Bassam, S., Xu, M., Wandless, T. J., and Arnold, D. B. (2012). Differential trafficking of transport vesicles contributes to the localization of dendritic proteins. *Cell Rep.* 2, 89–100. doi: 10.1016/j.celrep.2012.05.018

Amor, V., Zhang, C., Vainshtein, A., Zhang, A., Zollinger, D. R., Eshed-Eisenbach, Y., et al. (2017). The paranodal cytoskeleton clusters Na^+ channels at nodes of Ranvier. *Elife* 6:e21392. doi: 10.7554/eLife.21392

Ango, F., di Cristo, G., Higashiyama, H., Bennett, V., Wu, P., and Huang, Z. J. (2004). Ankyrin-based subcellular gradient of neurofascin, an immunoglobulin family protein, directs GABAergic innervation at Purkinje axon initial segment. *Cell* 119, 257–272. doi: 10.1016/j.cell.2004.10.004

Awadalla, P., Gauthier, J., Myers, R. A., Casals, F., Hamdan, F. F., Griffing, A. R., et al. (2010). Direct measure of the *de novo* mutation rate in autism and schizophrenia cohorts. *Am. J. Hum. Genet.* 87, 316–324. doi: 10.1016/j.ajhg.2010.07.019

Baalman, K. L., Cotton, R. J., Rasband, S. N., and Rasband, M. N. (2013). Blast wave exposure impairs memory and decreases axon initial segment length. *J. Neurotrauma* 30, 741–751. doi: 10.1089/neu.2012.2478

Bartos, M., Vida, I., and Jonas, P. (2007). Synaptic mechanisms of synchronized gamma oscillations in inhibitory interneuron networks. *Nat. Rev. Neurosci.* 8, 45–56. doi: 10.1038/nrn2044

Bekku, Y., Rauch, U., Ninomiya, Y., and Oohashi, T. (2009). Brevican distinctively assembles extracellular components at the large diameter nodes of Ranvier in the CNS. *J. Neurochem.* 108, 1266–1276. doi: 10.1111/j.1471-4159.2009.05873.x

Bender, K. J., and Trussell, L. O. (2012). The physiology of the axon initial segment. *Annu. Rev. Neurosci.* 35, 249–265. doi: 10.1146/annurev-neuro-062111-150339

Bennett, V., and Baines, A. J. (2001). Spectrin and ankyrin-based pathways: metazoan inventions for integrating cells into tissues. *Physiol. Rev.* 81, 1353–1392.

Bennett, V., and Lorenzo, D. N. (2013). Spectrin- and ankyrin-based membrane domains and the evolution of vertebrates. *Curr. Top. Membr.* 72, 1–37. doi: 10.1016/b978-0-12-417027-8.00001-5

Berghs, S., Aggujaro, D., Dirkx, R., Maksimova, E., Stabach, P., Hermel, J. M., et al. (2000). β IV spectrin, a new spectrin localized at axon initial segments and nodes of ranvier in the central and peripheral nervous system. *J. Cell Biol.* 151, 985–1002. doi: 10.1083/jcb.151.5.985

Bevers, M. B., and Neumar, R. W. (2008). Mechanistic role of calpains in postischemic neurodegeneration. *J. Cereb. Blood Flow Metab.* 28, 655–673. doi: 10.1038/sj.jcbfm.9600595

Bhat, M. A., Rios, J. C., Lu, Y., Garcia-Fresco, G. P., Ching, W., St Martin, M., et al. (2001). Axon-glia interactions and the domain organization of myelinated axons requires neurexin IV/Caspr/Paranodin. *Neuron* 30, 369–383. doi: 10.1016/s0896-6273(01)00294-x

Black, J. A., and Waxman, S. G. (2012). Sodium channels and microglial function. *Exp. Neurol.* 234, 302–315. doi: 10.1016/j.expneurol.2011.09.030

Boiko, T., Van Wart, A., Caldwell, J. H., Levinson, S. R., Trimmer, J. S., and Matthews, G. (2003). Functional specialization of the axon initial segment by isoform-specific sodium channel targeting. *J. Neurosci.* 23, 2306–2313.

Bréchet, A., Fache, M. P., Brachet, A., Ferracci, G., Baude, A., Irondelle, M., et al. (2008). Protein kinase CK2 contributes to the organization of sodium channels in axonal membranes by regulating their interactions with ankyrin G. *J. Cell Biol.* 183, 1101–1114. doi: 10.1083/jcb.200805169

Chang, K. J., Zollinger, D. R., Susuki, K., Sherman, D. L., Makara, M. A., Brophy, P. J., et al. (2014). Glial ankyrins facilitate paranodal axoglial junction assembly. *Nat. Neurosci.* 17, 1673–1681. doi: 10.1038/nn.3858

Chen, C., Bharucha, V., Chen, Y., Westenbroek, R. E., Brown, A., Malhotra, J. D., et al. (2002). Reduced sodium channel density, altered voltage dependence of inactivation and increased susceptibility to seizures in mice lacking sodium channel β 2-subunits. *Proc. Natl. Acad. Sci. U S A* 99, 17072–17077. doi: 10.1073/pnas.212638099

Chen, C. L., Calhoun, J. D., Zhang, Y. Q., Lopez-Santiago, L., Zhou, N., Davis, T. H., et al. (2012). Identification of the cysteine residue responsible for disulfide linkage of Na^+ channel α and β 2 subunits. *J. Biol. Chem.* 287, 39061–39069. doi: 10.1074/jbc.m112.397646

Clark, K. C., Josephson, A., Benusa, S. D., Hartley, R. K., Baer, M., Thummala, S., et al. (2016). Compromised axon initial segment integrity in EAE is preceded by microglial reactivity and contact. *Glia* 64, 1190–1209. doi: 10.1002/glia.22991

Coman, I., Aigrot, M. S., Seilhean, D., Reynolds, R., Girault, J. A., Zalc, B., et al. (2006). Nodal, paranodal and juxtaparanodal axonal proteins during demyelination and remyelination in multiple sclerosis. *Brain* 129, 3186–3195. doi: 10.1093/brain/awl144

Cooper, E. C. (2011). Made for "anchorin": Kv7.2/7.3 (KCNQ2/KCNQ3) channels and the modulation of neuronal excitability in vertebrate axons. *Semin. Cell Dev. Biol.* 22, 185–192. doi: 10.1016/j.semcdb.2010.10.001

Craner, M. J., Newcombe, J., Black, J. A., Hartle, C., Cuzner, M. L., and Waxman, S. G. (2004). Molecular changes in neurons in multiple sclerosis: altered axonal expression of $Na_V1.2$ and $Na_V1.6$ sodium channels and Na^+/Ca^{2+} exchanger. *Proc. Natl. Acad. Sci. U S A* 101, 8168–8173. doi: 10.1073/pnas.0402765101

Cruz, D. A., Weaver, C. L., Lovallo, E. M., Melchitzky, D. S., and Lewis, D. A. (2009). Selective alterations in postsynaptic markers of chandelier cell inputs to cortical pyramidal neurons in subjects with schizophrenia. *Neuropsychopharmacology* 34, 2112–2124. doi: 10.1038/npp.2009.36

Czogalla, A., and Sikorski, A. F. (2005). Spectrin and calpain: a 'target' and a 'sniper' in the pathology of neuronal cells. *Cell. Mol. Life Sci.* 62, 1913–1924. doi: 10.1007/s00018-005-5097-0

Davis, J. Q., and Bennett, V. (1994). Ankyrin binding-activity shared by the neurofascin/L1/nrcam family of nervous-system cell-adhesion molecules. *J. Biol. Chem.* 269, 27163–27166.

Davis, L., Abdi, K., Machius, M., Brautigam, C., Tomchick, D. R., Bennett, V., et al. (2009). Localization and structure of the ankyrin-binding site on β2-spectrin. *J. Biol. Chem.* 284, 6982–6987. doi: 10.1074/jbc.M809245200

D'Este, E., Kamin, D., Göttfert, F., El-Hady, A., and Hell, S. W. (2015). STED nanoscopy reveals the ubiquity of subcortical cytoskeleton periodicity in living neurons. *Cell Rep.* 10, 1246–1251. doi: 10.1016/j.celrep.2015.02.007

Dotti, C. G., Sullivan, C. A., and Banker, G. A. (1988). The establishment of polarity by hippocampal neurons in culture. *J. Neurosci.* 8, 1454–1468.

Dours-Zimmermann, M. T., Maurer, K., Rauch, U., Stoffel, W., Fässler, R., and Zimmermann, D. R. (2009). Versican V2 assembles the extracellular matrix surrounding the nodes of ranvier in the CNS. *J. Neurosci.* 29, 7731–7742. doi: 10.1523/JNEUROSCI.4158-08.2009

Duflocq, A., Le Bras, B., Bullier, E., Couraud, F., and Davenne, M. (2008). Nav1.1 is predominantly expressed in nodes of Ranvier and axon initial segments. *Mol. Cell. Neurosci.* 39, 180–192. doi: 10.1016/j.mcn.2008.06.008

Dumitrescu, A. S., Evans, M. D., and Grubb, M. S. (2016). Evaluating tools for live imaging of structural plasticity at the axon initial segment. *Front. Cell. Neurosci.* 10:268. doi: 10.3389/fncel.2016.00268

Dutta, R., and Trapp, B. D. (2007). Pathogenesis of axonal and neuronal damage in multiple sclerosis. *Neurology* 68, S22–S31; discussion S43–S54. doi: 10.1212/01.wnl.0000275229.13012.32

Dzhashiashvili, Y., Zhang, Y. Q., Galinska, J., Lam, I., Grumet, M., and Salzer, J. L. (2007). Nodes of Ranvier and axon initial segments are ankyrin G-dependent domains that assemble by distinct mechanisms. *J. Cell Biol.* 177, 857–870. doi: 10.1083/jcb.200612012

Eshed, Y., Feinberg, K., Poliak, S., Sabanay, H., Sarig-Nadir, O., Spiegel, I., et al. (2005). Gliomedin mediates Schwann cell-axon interaction and the molecular assembly of the nodes of Ranvier. *Neuron* 47, 215–229. doi: 10.1016/j.neuron.2005.06.026

Evans, M. D., Dumitrescu, A. S., Kruijssen, D. L. H., Taylor, S. E., and Grubb, M. S. (2015). Rapid modulation of axon initial segment length influences repetitive spike firing. *Cell Rep.* 13, 1233–1245. doi: 10.1016/j.celrep.2015.09.066

Evans, M. D., Sammons, R. P., Lebron, S., Dumitrescu, A. S., Watkins, T. B. K., Uebele, V. N., et al. (2013). Calcineurin signaling mediates activity-dependent relocation of the axon initial segment. *J. Neurosci.* 33, 6950–6963. doi: 10.1523/JNEUROSCI.0277-13.2013

Fache, M. P., Moussif, A., Fernandes, F., Giraud, P., Garrido, J. J., and Dargent, B. (2004). Endocytotic elimination and domain-selective tethering constitute a potential mechanism of protein segregation at the axonal initial segment. *J. Cell Biol.* 166, 571–578. doi: 10.1083/jcb.200312155

Farias, G. G., Guardia, C. M., Britt, D. J., Guo, X., and Bonifacino, J. S. (2015). Sorting of dendritic and axonal vesicles at the pre-axonal exclusion zone. *Cell Rep.* 13, 1221–1232. doi: 10.1016/j.celrep.2015.09.074

Feinberg, K., Eshed-Eisenbach, Y., Frechter, S., Amor, V., Salomon, D., Sabanay, H., et al. (2010). A glial signal consisting of gliomedin and NrCAM clusters axonal Na^+ channels during the formation of nodes of Ranvier. *Neuron* 65, 490–502. doi: 10.1016/j.neuron.2010.02.004

Ferreira, M. A. R., O'Donovan, M. C., Meng, Y. A., Jones, I. R., Ruderfer, D. M., Jones, L., et al. (2008). Collaborative genome-wide association analysis supports a role for ANK3 and CACNA1C in bipolar disorder. *Nat. Genet.* 40, 1056–1058. doi: 10.1038/ng.209

Fjell, J., Hjelmstrom, P., Hormuzdiar, W., Milenkovic, M., Aglieco, F., Tyrrell, L., et al. (2000). Localization of the tetrodotoxin-resistant sodium channel NaN in nociceptors. *Neuroreport* 11, 199–202. doi: 10.1097/00001756-200001170-00039

Fréal, A., Fassier, C., Le Bras, B., Bullier, E., De Gois, S., Hazan, J., et al. (2016). Cooperative interactions between 480 kDa ankyrin-G and EB proteins assemble the axon initial segment. *J. Neurosci.* 36, 4421–4433. doi: 10.1523/JNEUROSCI.3219-15.2016

Galiano, M. R., Jha, S., Ho, T. S. Y., Zhang, C. S., Ogawa, Y., Chang, K. J., et al. (2012). A distal axonal cytoskeleton forms an intra-axonal boundary that controls axon initial segment assembly. *Cell* 149, 1125–1139. doi: 10.1016/j.cell.2012.03.039

Gasser, A., Ho, T. S. Y., Cheng, X. Y., Chang, K. J., Waxman, S. G., Rasband, M. N., et al. (2012). An ankyrin-binding motif is necessary and sufficient for targeting $Na_V1.6$ sodium channels to axon initial segments and nodes of ranvier. *J. Neurosci.* 32, 7232–7243. doi: 10.1523/JNEUROSCI.5434-11.2012

Grubb, M. S., and Burrone, J. (2010). Activity-dependent relocation of the axon initial segment fine-tunes neuronal excitability. *Nature* 465, U1070–U1131. doi: 10.1038/nature09160

Gutzmann, A., Ergül, N., Grossmann, R., Schultz, C., Wahle, P., and Engelhardt, M. (2014). A period of structural plasticity at the axon initial segment in developing visual cortex. *Front. Neuroanat.* 8:11. doi: 10.3389/fnana.2014.00011

Hamada, M. S., and Kole, M. H. (2015). Myelin loss and axonal ion channel adaptations associated with gray matter neuronal hyperexcitability. *J. Neurosci.* 35, 7272–7286. doi: 10.1523/JNEUROSCI.4747-14.2015

Hamdan, F. F., Gauthier, J., Araki, Y., Lin, D. T., Yoshizawa, Y., Higashi, K., et al. (2011). Excess of *de novo* deleterious mutations in genes associated with glutamatergic systems in nonsyndromic intellectual disability. *Am. J. Hum. Genet.* 88, 306–316. doi: 10.1016/j.ajhg.2011.02.001

Harada, K., Fukuda, S., Kunimoto, M., and Yoshida, K. (1997). Distribution of ankyrin isoforms and their proteolysis after ischemia and reperfusion in rat brain. *J. Neurochem.* 69, 371–376. doi: 10.1046/j.1471-4159.1997.69010371.x

He, M., Abdi, K. M., and Bennett, V. (2014). Ankyrin-G palmitoylation and βII-spectrin binding to phosphoinositide lipids drive lateral membrane assembly. *J. Cell Biol.* 206, 273–288. doi: 10.1083/jcb.201401016

He, M., Jenkins, P., and Bennett, V. (2012). Cysteine 70 of ankyrin-G is S-palmitoylated and is required for function of ankyrin-G in membrane domain assembly. *J. Biol. Chem.* 287, 43995–44005. doi: 10.1074/jbc.M112.417501

Hedstrom, K. L., Ogawa, Y., and Rasband, M. N. (2008). AnkyrinG is required for maintenance of the axon initial segment and neuronal polarity. *J. Cell Biol.* 183, 635–640. doi: 10.1083/jcb.200806112

Henry, M. A., Sorensen, H. J., Johnson, L. R., and Levinson, S. R. (2005). Localization of the Na-v 1.8 sodium channel isoform at nodes of Ranvier in normal human radicular tooth pulp. *Neurosci. Lett.* 380, 32–36. doi: 10.1016/j.neulet.2005.01.017

Hill, A. S., Nishino, A., Nakajo, K., Zhang, G. X., Fineman, J. R., Selzer, M. E., et al. (2008). Ion channel clustering at the axon initial segment and node of ranvier evolved sequentially in early chordates. *PLoS Genet.* 4:e1000317. doi: 10.1371/journal.pgen.1000317

Hirokawa, N., and Takemura, R. (2005). Molecular motors and mechanisms of directional transport in neurons. *Nat. Rev. Neurosci.* 6, 201–214. doi: 10.1038/nrn1624

Ho, T. S., Zollinger, D. R., Chang, K. J., Xu, M., Cooper, E. C., Stankewich, M. C., et al. (2014). A hierarchy of ankyrin-spectrin complexes clusters sodium channels at nodes of Ranvier. *Nat. Neurosci.* 17, 1664–1672. doi: 10.1038/nn.3859

Hoogenraad, C. C., and Bradke, F. (2009). Control of neuronal polarity and plasticity—a renaissance for microtubules?. *Trends Cell Biol.* 19, 669–676. doi: 10.1016/j.tcb.2009.08.006

Howell, O. W., Palser, A., Polito, A., Melrose, S., Zonta, B., Scheiermann, C., et al. (2006). Disruption of neurofascin localization reveals early changes preceding demyelination and remyelination in multiple sclerosis. *Brain* 129, 3173–3185. doi: 10.1093/brain/awl290

Hund, T. J., Koval, O. M., Li, J., Wright, P. J., Qian, L., Snyder, J. S., et al. (2010). A β_{IV}-spectrin/CaMKII signaling complex is essential for membrane excitability in mice. *J. Clin. Invest.* 120, 3508–3519. doi: 10.1172/JCI43621

Ikeda, Y., Dick, K. A., Weatherspoon, M. R., Gincel, D., Armbrust, K. R., Dalton, J. C., et al. (2006). Spectrin mutations cause spinocerebellar ataxia type 5. *Nat. Genet.* 38, 184–190. doi: 10.1038/ng1728

Ipsaro, J. J., Harper, S. L., Messick, T. E., Marmorstein, R., Mondragon, A., and Speicher, D. W. (2010). Crystal structure and functional interpretation of the erythrocyte spectrin tetramerization domain complex. *Blood* 115, 4843–4852. doi: 10.1182/blood-2010-01-261396

Ipsaro, J. J., and Mondragon, A. (2010). Structural basis for spectrin recognition by ankyrin. *Blood* 115, 4093–4101. doi: 10.1182/blood-2009-11-255604

Iqbal, Z., Willemsen, M. H., Papon, M. A., Musante, L., Benevento, M., Hu, H., et al. (2015). Homozygous SLC6A17 mutations cause autosomal-recessive intellectual disability with progressive tremor, speech impairment, and behavioral problems. *Am. J. Hum. Genet.* 96, 386–396. doi: 10.1016/j.ajhg.2015.01.010

Jacobson, C., Schnapp, B., and Banker, G. A. (2006). A change in the selective translocation of the Kinesin-1 motor domain marks the initial specification of the axon. *Neuron* 49, 797–804. doi: 10.1016/j.neuron.2006.02.005

Jegla, T., Nguyen, M. M., Feng, C., Goetschius, D. J., Luna, E., van Rossum, D. B., et al. (2016). Bilaterian giant ankyrins have a common evolutionary origin and play a conserved role in patterning the axon initial segment. *PLoS Genet.* 12:e1006457. doi: 10.1371/journal.pgen.1006457

Jenkins, S. M., and Bennett, V. (2001). Ankyrin-G coordinates assembly of the spectrin-based membrane skeleton, voltage-gated sodium channels, and L1 CAMs at Purkinje neuron initial segments. *J. Cell Biol.* 155, 739–746. doi: 10.1083/jcb.200109026

Jenkins, P. M., Kim, N., Jones, S. L., Tseng, W. C., Svitkina, T. M., Yin, H. H., et al. (2015). Giant ankyrin-G: a critical innovation in vertebrate evolution of fast and integrated neuronal signaling. *Proc. Natl. Acad. Sci. U S A* 112, 957–964. doi: 10.1073/pnas.1416544112

Jones, S. L., Korobova, F., and Svitkina, T. (2014). Axon initial segment cytoskeleton comprises a multiprotein submembranous coat containing sparse actin filaments. *J. Cell Biol.* 205, 67–81. doi: 10.1083/jcb.201401045

Jones, S. L., and Svitkina, T. M. (2016). Axon initial segment cytoskeleton: architecture, development, and role in neuron polarity. *Neural Plast.* 2016:6808293. doi: 10.1155/2016/6808293

Kapitein, L. C., and Hoogenraad, C. C. (2011). Which way to go? Cytoskeletal organization and polarized transport in neurons. *Mol. Cell. Neurosci.* 46, 9–20. doi: 10.1016/j.mcn.2010.08.015

Kobayashi, T., Storrie, B., Simons, K., and Dotti, C. G. (1992). A functional barrier to movement of lipids in polarized neurons. *Nature* 359, 647–650. doi: 10.1038/359647a0

Kole, M. H., Ilschner, S. U., Kampa, B. M., Williams, S. R., Ruben, P. C., and Stuart, G. J. (2008). Action potential generation requires a high sodium channel density in the axon initial segment. *Nat. Neurosci.* 11, 178–186. doi: 10.1038/nn2040

Kole, M. H., and Stuart, G. J. (2012). Signal processing in the axon initial segment. *Neuron* 73, 235–247. doi: 10.1016/j.neuron.2012.01.007

Komada, M., and Soriano, P. (2002). βIV-spectrin regulates sodium channel clustering through ankyrin-G at axon initial segments and nodes of Ranvier. *J. Cell Biol.* 156, 337–348. doi: 10.1083/jcb.200110003

Kordeli, E., Lambert, S., and Bennett, V. (1995). AnkyrinG. A new ankyrin gene with neural-specific isoforms localized at the axonal initial segment and node of Ranvier. *J. Biol. Chem.* 270, 2352–2359.

Kuba, H., Ishii, T. M., and Ohmori, H. (2006). Axonal site of spike initiation enhances auditory coincidence detection. *Nature* 444, 1069–1072. doi: 10.1038/nature05347

Kuba, H., Oichi, Y., and Ohmori, H. (2010). Presynaptic activity regulates Na^+ channel distribution at the axon initial segment. *Nature* 465, U1075–U1136. doi: 10.1038/nature09087

Kuijpers, M., van de Willige, D., Freal, A., Chazeau, A., Franker, M. A., Hofenk, J., et al. (2016). Dynein regulator NDEL1 controls polarized cargo transport at the axon initial segment. *Neuron* 89, 461–471. doi: 10.1016/j.neuron.2016.01.022

Lai, H. C., and Jan, L. Y. (2006). The distribution and targeting of neuronal voltage-gated ion channels. *Nat. Rev. Neurosci.* 7, 548–562. doi: 10.1038/nrn1938

Lambert, S., Davis, J. Q., and Bennett, V. (1997). Morphogenesis of the node of Ranvier: co-clusters of ankyrin and ankyrin-binding integral proteins define early developmental intermediates. *J. Neurosci.* 17, 7025–7036.

Le Bras, B., Fréal, A., Czarnecki, A., Legendre, P., Bullier, E., Komada, M., et al. (2014). *in vivo* assembly of the axon initial segment in motor neurons. *Brain Struct. Funct.* 219, 1433–1450. doi: 10.1007/s00429-013-0578-7

Leterrier, C., Clerc, N., Rueda-Boroni, F., Montersino, A., Dargent, B., and Castets, F. (2017). Ankyrin G membrane partners drive the establishment and maintenance of the axon initial segment. *bioRxiv* 11:6. doi: 10.1101/073163

Leterrier, C., and Dargent, B. (2014). No Pasaran! Role of the axon initial segment in the regulation of protein transport and the maintenance of axonal identity. *Semin. Cell Dev. Biol.* 27C, 44–51. doi: 10.1016/j.semcdb.2013.11.001

Leterrier, C., Potier, J., Caillol, G., Debarnot, C., Boroni Rueda, F., and Dargent, B. (2015). Nanoscale architecture of the axon initial segment reveals an organized and robust scaffold. *Cell Rep.* 13, 2781–2793. doi: 10.1016/j.celrep.2015.11.051

Lewis, T. L., Mao, T. Y., Svoboda, K., and Arnold, D. B. (2009). Myosin-dependent targeting of transmembrane proteins to neuronal dendrites. *Nat. Neurosci.* 12, 568–576. doi: 10.1038/nn.2318

Lopez, A. Y., Wang, X., Xu, M., Maheshwari, A., Curry, D., Lam, S., et al. (2016). Ankyrin-G isoform imbalance and interneuronopathy link epilepsy and bipolar disorder. *Mol. Psychiatry* doi: 10.1038/mp.2016.233 [Epub ahead of print].

Lorenzo, D. N., Badea, A., Davis, J., Hostettler, J., He, J., Zhong, G. S., et al. (2014). A PIK3C3-ankyrin-B-dynactin pathway promotes axonal growth and multiorganelle transport. *J. Cell Biol.* 207, 735–752. doi: 10.1083/jcb.201407063

Markram, H., Toledo-Rodriguez, M., Wang, Y., Gupta, A., Silberberg, G., and Wu, C. (2004). Interneurons of the neocortical inhibitory system. *Nat. Rev. Neurosci.* 5, 793–807. doi: 10.1152/jn.00520.2004

Mathey, E. K., Derfuss, T., Storch, M. K., Williams, K. R., Hales, K., Woolley, D. R., et al. (2007). Neurofascin as a novel target for autoantibody-mediated axonal injury. *J. Exp. Med.* 204, 2363–2372. doi: 10.1084/jem.20071053

Mohler, P. J., Yoon, W., and Bennett, V. (2004). Ankyrin-B targets β_2-spectrin to an intracellular compartment in neonatal cardiomyocytes. *J. Biol. Chem.* 279, 40185–40193. doi: 10.1074/jbc.M406018200

Muhleisen, T. W., Leber, M., Schulze, T. G., Strohmaier, J., Degenhardt, F., Treutlein, J., et al. (2014). Genome-wide association study reveals two new risk loci for bipolar disorder. *Nat. Commun.* 5:3339. doi: 10.1038/ncomms4339

Muir, J., and Kittler, J. T. (2014). Plasticity of $GABA_A$ receptor diffusion dynamics at the axon initial segment. *Front. Cell. Neurosci.* 8:151. doi: 10.3389/fncel.2014.00151

Nakata, T., Niwa, S., Okada, Y., Perez, F., and Hirokawa, N. (2011). Preferential binding of a kinesin-1 motor to GTP-tubulin-rich microtubules underlies polarized vesicle transport. *J. Cell Biol.* 194, 245–255. doi: 10.1083/jcb.201104034

Nakada, C., Ritchie, K., Oba, Y., Nakamura, M., Hotta, Y., Iino, R., et al. (2003). Accumulation of anchored proteins forms membrane diffusion barriers during neuronal polarization. *Nat. Cell Biol.* 5, 626–632. doi: 10.1038/ncb1009

Nicita, F., Ulgiati, F., Bernardini, L., Garone, G., Papetti, L., Novelli, A., et al. (2015). Early myoclonic encephalopathy in 9q33–q34 deletion encompassing STXBP1 and SPTAN1. *Ann. Hum. Genet.* 79, 209–217. doi: 10.1111/ahg.12106

Occhi, S., Zambroni, D., Del Carro, U., Amadio, S., Sirkowski, E. E., Scherer, S. S., et al. (2005). Both laminin and Schwann cell dystroglycan are necessary for proper clustering of sodium channels at nodes of Ranvier. *J. Neurosci.* 25, 9418–9427. doi: 10.1523/JNEUROSCI.2068-05.2005

Ogawa, Y., Schafer, D. P., Horresh, I., Bar, V., Hales, K., Yang, Y., et al. (2006). Spectrins and ankyrinB constitute a specialized paranodal cytoskeleton. *J. Neurosci.* 26, 5230–5239. doi: 10.1523/JNEUROSCI.0425-06.2006

O'Malley, H. A., and Isom, L. L. (2015). Sodium channel beta subunits: emerging targets in channelopathies. *Annu. Rev. Physiol.* 77, 481–504. doi: 10.1146/annurev-physiol-021014-071846

Oohashi, T., Hirakawa, S., Bekku, Y., Rauch, U., Zimmermann, D. R., Su, W. D., et al. (2002). Bral1, a brain-specific link protein, colocalizing with the versican V2 isoform at the nodes of Ranvier in developing and adult mouse central nervous systems. *Mol. Cell. Neurosci.* 19, 43–57. doi: 10.1006/mcne.2001.1061

Osorio, N., Alcaraz, G., Padilla, F., Couraud, F., Delmas, P., and Crest, M. (2005). Differential targeting and functional specialization of sodium channels in cultured cerebellar granule cells. *J. Physiol.* 569, 801–816. doi: 10.1113/jphysiol.2005.097022

Palay, S. L., Sotelo, C., Peters, A., and Orkand, P. M. (1968). Axon hillock and initial segment. *J. Cell Biol.* 38, 193–201. doi: 10.1083/jcb.38.1.193

Pan, Z., Kao, T., Horvath, Z., Lemos, J., Sul, J. Y., Cranstoun, S. D., et al. (2006). A common ankyrin-G-based mechanism retains KCNQ and Na$_V$ channels at electrically active domains of the axon. *J. Neurosci.* 26, 2599–2613. doi: 10.1523/JNEUROSCI.4314-05.2006

Pedraza, L., Huang, J. K., and Colman, D. R. (2001). Organizing principles of the axoglial apparatus. *Neuron* 30, 335–344. doi: 10.1016/s0896-6273(01)00306-3

Petersen, J. D., Kaech, S., and Banker, G. (2014). Selective microtubule-based transport of dendritic membrane proteins arises in concert with axon specification. *J. Neurosci.* 34, 4135–4147. doi: 10.1523/JNEUROSCI.3779-13.2014

Rasband, M. N. (2010). The axon initial segment and the maintenance of neuronal polarity. *Nat. Rev. Neurosci.* 11, 552–562. doi: 10.1038/nrn2852

Rasband, M. N., and Peles, E. (2015). The nodes of ranvier: molecular assembly and maintenance. *Cold Spring Harb. Perspect. Biol.* 8:a020495. doi: 10.1101/cshperspect.a020495

Rasband, M. N., Peles, E., Trimmer, J. S., Levinson, S. R., Lux, S. E., and Shrager, P. (1999). Dependence of nodal sodium channel clustering on paranodal axoglial contact in the developing CNS. *J. Neurosci.* 19, 7516–7528.

Ren, Q., and Bennett, V. (1998). Palmitoylation of neurofascin at a site in the membrane-spanning domain highly conserved among the L1 family of cell adhesion molecules. *J. Neurochem.* 70, 1839–1849. doi: 10.1046/j.1471-4159.1998.70051839.x

Roussos, P., and Haroutunian, V. (2014). Schizophrenia: susceptibility genes and oligodendroglial and myelin related abnormalities. *Front. Cell. Neurosci.* 8:5. doi: 10.3389/fncel.2014.00005

Saifetiarova, J., Liu, X., Taylor, A. M., Li, J., and Bhat, M. A. (2017). Axonal domain disorganization in Caspr1 and Caspr2 mutant myelinated axons affects neuromuscular junction integrity, leading to muscle atrophy. *J. Neurosci. Res.* doi: 10.1002/jnr.24052 [Epub ahead of print].

Saitsu, H., Tohyama, J., Kumada, T., Egawa, K., Hamada, K., Okada, I., et al. (2010). Dominant-negative mutations in alpha-II spectrin cause West syndrome with severe cerebral hypomyelination, spastic quadriplegia and developmental delay. *Am. J. Hum. Genet.* 86, 881–891. doi: 10.1016/j.ajhg.2010.04.013

Schafer, D. P., Custer, A. W., Shrager, P., and Rasband, M. N. (2006). Early events in node of Ranvier formation during myelination and remyelination in the PNS. *Neuron Glia Biol.* 2, 69–79. doi: 10.1017/S1740925X06000093

Schafer, D. P., Jha, S., Liu, F. D., Akella, T., McCullough, L. D., and Rasband, M. N. (2009). Disruption of the axon initial segment cytoskeleton is a new mechanism for neuronal injury. *J. Neurosci.* 29, 13242–13254. doi: 10.1523/JNEUROSCI.3376-09.2009

Sherman, D. L., Tait, S., Melrose, S., Johnson, R., Zonta, B., Court, F. A., et al. (2005). Neurofascins are required to establish axonal domains for saltatory conduction. *Neuron* 48, 737–742. doi: 10.1016/j.neuron.2005.10.019

Silverman, M. A., Kaech, S., Jareb, M., Burack, M. A., Vogt, L., Sonderegger, P., et al. (2001). Sorting and directed transport of membrane proteins during development of hippocampal neurons in culture. *Proc. Natl. Acad. Sci. U S A* 98, 7051–7057. doi: 10.1073/pnas.111146198

Singh, N. A., Westenskow, P., Charlier, C., Pappas, C., Leslie, J., Dillon, J., et al. (2003). KCNQ2 and KCNQ3 potassium channel genes in benign familial neonatal convulsions: expansion of the functional and mutation spectrum. *Brain* 126, 2726–2737. doi: 10.1093/brain/awg286

Sobotzik, J. M., Sie, J. M., Politi, C., Turco Del, D., Bennett, V., Deller, T., et al. (2009). AnkyrinG is required to maintain axo-dendritic polarity *in vivo*. *Proc. Natl. Acad. Sci. U S A* 106, 17564–17569. doi: 10.1073/pnas.0909267106

Somogyi, P. (1977). A specific 'axo-axonal' interneuron in the visual cortex of the rat. *Brain Res.* 136, 345–350. doi: 10.1016/0006-8993(77)90808-3

Song, A. H., Wang, D., Chen, G., Li, Y., Luo, J., Duan, S., et al. (2009). A selective filter for cytoplasmic transport at the axon initial segment. *Cell* 136, 1148–1160. doi: 10.1016/j.cell.2009.01.016

Sousa, A. D., and Bhat, M. A. (2007). Cytoskeletal transition at the paranodes: the Achilles′ heel of myelinated axons. *Neuron Glia Biol.* 3, 169–178. doi: 10.1017/S1740925X07000415

Steinlein, O. K. (2014). Mechanisms underlying epilepsies associated with sodium channel mutations. *Prog. Brain Res.* 213, 97–111. doi: 10.1016/b978-0-444-63326-2.00005-3

Susuki, K., Chang, K. J., Zollinger, D. R., Liu, Y. H., Ogawa, Y., Eshed-Eisenbach, Y., et al. (2013). Three mechanisms assemble central nervous system nodes of ranvier. *Neuron* 78, 469–482. doi: 10.1016/j.neuron.2013.03.005

Talkowski, M. E., Rosenfeld, J. A., Blumenthal, I., Pillalamarri, V., Chiang, C., Heilbut, A., et al. (2012). Sequencing chromosomal abnormalities reveals neurodevelopmental loci that confer risk across diagnostic boundaries. *Cell* 149, 525–537. doi: 10.1016/j.cell.2012.03.028

Thaxton, C., Pillai, A. M., Pribisko, A. L., Dupree, J. L., and Bhat, M. A. (2011). Nodes of Ranvier act as barriers to restrict invasion of flanking paranodal domains in myelinated axons. *Neuron* 69, 244–257. doi: 10.1016/j.neuron.2010.12.016

Trunova, S., Baek, B., and Giniger, E. (2011). Cdk5 regulates the size of an axon initial segment-like compartment in mushroom body neurons of the drosophila central brain. *J. Neurosci.* 31, 10451–10462. doi: 10.1523/JNEUROSCI.0117-11.2011

Tuvia, S., Garver, T. D., and Bennett, V. (1997). The phosphorylation state of the FIGQY tyrosine of neurofascin determines ankyrin-binding activity and patterns of cell segregation. *Proc. Natl. Acad. Sci. U S A* 94, 12957–12962. doi: 10.1073/pnas.94.24.12957

Uemoto, Y., Suzuki, S., Terada, N., Ohno, N., Ohno, S., Yamanaka, S., et al. (2007). Specific role of the truncated betaIV-spectrin Sigma6 in sodium channel clustering at axon initial segments and nodes of ranvier. *J. Biol. Chem.* 282, 6548–6555. doi: 10.1074/jbc.m609223200

Vallee, R. B., and Tsai, J. W. (2006). The cellular roles of the lissencephaly gene LIS1 and what they tell us about brain development. *Gene Dev.* 20, 1384–1393. doi: 10.1101/gad.1417206

Vosseller, K., Trinidad, J. C., Chalkley, R. J., Specht, C. G., Thalhammer, A., Lynn, A. J., et al. (2006). O-linked N-acetylglucosamine proteomics of postsynaptic density preparations using lectin weak affinity chromatography and mass spectrometry. *Mol. Cell. Proteomics* 5, 923–934. doi: 10.1074/mcp.t500040-mcp200

Wagnon, J. L., and Meisler, M. H. (2015). Recurrent and non-recurrent mutations of SCN8A in epileptic encephalopathy. *Front. Neurol.* 6:104. doi: 10.3389/fneur.2015.00104

Wang, C., Wei, Z., Chen, K., Ye, F., Yu, C., Bennett, V., et al. (2014). Structural basis of diverse membrane target recognitions by ankyrins. *Elife* 3:e04353. doi: 10.7554/elife.04353

Wang, R., Wei, Z. Y., Jin, H., Wu, H., Yu, C., Wen, W. Y., et al. (2009). Autoinhibition of UNC5b revealed by the cytoplasmic domain structure of the receptor. *Mol. Cell* 33, 692–703. doi: 10.1016/j.molcel.2009.02.016

Wang, C., Yu, C., Ye, F., Wei, Z. Y., and Zhang, M. J. (2012). Structure of the ZU5-ZU5-UPA-DD tandem of ankyrin-B reveals interaction surfaces necessary for ankyrin function. *Proc. Natl. Acad. Sci. U S A* 109, 4822–4827. doi: 10.1073/pnas.1200613109

Watanabe, K., Al-Bassam, S., Miyazaki, Y., Wandless, T. J., Webster, P., and Arnold, D. B. (2012). Networks of polarized actin filaments in the axon initial segment provide a mechanism for sorting axonal and dendritic proteins. *Cell Rep.* 2, 1546–1553. doi: 10.1016/j.celrep.2012.11.015

Weber, P., Bartsch, U., Rasband, M. N., Czaniera, R., Lang, Y., Bluethmann, H., et al. (1999). Mice deficient for tenascin-R display alterations of the extracellular matrix and decreased axonal conduction velocities in the CNS. *J. Neurosci.* 19, 4245–4262.

Winckler, B., Forscher, P., and Mellman, I. (1999). A diffusion barrier maintains distribution of membrane proteins in polarized neurons. *Nature* 397, 698–701. doi: 10.1038/17806

Witte, H., Neukirchen, D., and Bradke, F. (2008). Microtubule stabilization specifies initial neuronal polarization. *J. Cell Biol.* 180, 619–632. doi: 10.1083/jcb.200707042

Wolswijk, G., and Balesar, R. (2003). Changes in the expression and localization of the paranodal protein Caspr on axons in chronic multiple sclerosis. *Brain* 126, 1638–1649. doi: 10.1093/brain/awg151

Xiao, Z. C., Ragsdale, D. S., Malhotra, J. D., Mattei, L. N., Braun, P. E., Schachner, M., et al. (1999). Tenascin-R is a functional modulator of sodium channel beta subunits. *J. Biol. Chem.* 274, 26511–26517. doi: 10.1074/jbc.274.37.26511

Xu, M., and Cooper, E. C. (2015). An ankyrin-G N-terminal gate and protein kinase CK2 dually regulate binding of voltage-gated sodium and KCNQ2/3 potassium channels. *J. Biol. Chem.* 290, 16619–16632. doi: 10.1074/jbc.M115.638932

Xu, K., Zhong, G., and Zhuang, X. (2013). Actin, spectrin and associated proteins form a periodic cytoskeletal structure in axons. *Science* 339, 452–456. doi: 10.1126/science.1232251

Yamada, R., and Kuba, H. (2016). Structural and functional plasticity at the Axon initial segment. *Front. Cell. Neurosci.* 10:250. doi: 10.3389/fncel.2016.00250

Yang, Y., Ogawa, Y., Hedstrom, K. L., and Rasband, M. N. (2007). β IV spectrin is recruited to axon initial segments and nodes of Ranvier by ankyrinG. *J. Cell Biol.* 176, 509–519. doi: 10.1083/jcb.200610128

Yoshimura, T., and Rasband, M. N. (2014). Axon initial segments: diverse and dynamic neuronal compartments. *Curr. Opin. Neurobiol.* 27, 96–102. doi: 10.1016/j.conb.2014.03.004

Zhang, X., and Bennett, V. (1996). Identification of O-linked N-acetylglucosamine modification of ankyrin(G) isoforms targeted to nodes of Ranvier. *J. Cell Biol.* 271, 31391–31398. doi: 10.1074/jbc.271.49.31391

Zhang, X., and Bennett, V. (1998). Restriction of 480/270-kD ankyrin G to axon proximal segments requires multiple ankyrin G-specific domains. *J. Cell Biol.* 142, 1571–1581. doi: 10.1083/jcb.142.6.1571

Zhang, X., Davis, J. Q., Carpenter, S., and Bennett, V. (1998). Structural requirements for association of neurofascin with ankyrin. *J. Biol. Chem.* 273, 30785–30794. doi: 10.1074/jbc.273.46.30785

Zhang, A., Desmazieres, A., Zonta, B., Melrose, S., Campbell, G., Mahad, D., et al. (2015). Neurofascin 140 is an embryonic neuronal neurofascin isoform that promotes the assembly of the node of Ranvier. *J. Neurosci.* 35, 2246–2254. doi: 10.1523/JNEUROSCI.3552-14.2015

Zhong, G., He, J., Zhou, R., Lorenzo, D., Babcock, H. P., Bennett, V., et al. (2014). Developmental mechanism of the periodic membrane skeleton in axons. *Elife* 3:e04581. doi: 10.7554/eLife.04581

Zhou, D. X., Lambert, S., Malen, P. L., Carpenter, S., Boland, L. M., and Bennett, V. (1998). Ankyrin$_G$ is required for clustering of voltage-gated Na channels at axon initial segments and for normal action potential firing. *J. Cell Biol.* 143, 1295–1304. doi: 10.1083/jcb.143.5.1295

Zonta, B., Tait, S., Melrose, S., Anderson, H., Harroch, S., Higginson, J., et al. (2008). Glial and neuronal isoforms of Neurofascin have distinct roles in the assembly of nodes of Ranvier in the central nervous system. *J. Cell Biol.* 181, 1169–1177. doi: 10.1083/jcb.200712154

Conflict of Interest Statement: The authors declare that the research was conducted in the absence of any commercial or financial relationships that could be construed as a potential conflict of interest.

frontiers
in Cellular Neuroscience

ORIGINAL RESEARCH
published: 14 February 2017
doi: 10.3389/fncel.2017.00028

Encoding of High Frequencies Improves with Maturation of Action Potential Generation in Cultured Neocortical Neurons

Evgeny S. Nikitin[1], Natalia V. Bal[1], Aleksey Malyshev[1,2], Victor N. Ierusalimsky[1], Yulia Spivak[1], Pavel M. Balaban[1] and Maxim Volgushev[1,2]*

[1]Institute of Higher Nervous Activity and Neurophysiology, Russian Academy of Sciences, Moscow, Russia, [2]Department of Psychological Sciences, University of Connecticut, Storrs, CT, USA

The ability of neocortical neurons to detect and encode rapid changes at their inputs is crucial for basic neuronal computations, such as coincidence detection, precise synchronization of activity and spike-timing dependent plasticity. Indeed, populations of cortical neurons can respond to subtle changes of the input very fast, on a millisecond time scale. Theoretical studies and model simulations linked the encoding abilities of neuronal populations to the fast onset dynamics of action potentials (APs). Experimental results support this idea, however mechanisms of fast onset of APs in cortical neurons remain elusive. Studies in neuronal cultures, that are allowing for accurate control over conditions of growth and microenvironment during the development of neurons and provide better access to the spike initiation zone, may help to shed light on mechanisms of AP generation and encoding. Here we characterize properties of AP encoding in neocortical neurons grown for 11–25 days in culture. We show that encoding of high frequencies improves upon culture maturation, which is accompanied by the development of passive electrophysiological properties and AP generation. The onset of APs becomes faster with culture maturation. Statistical analysis using correlations and linear model approaches identified the onset dynamics of APs as a major predictor of age-dependent changes of encoding. Encoding of high frequencies strongly correlated also with the input resistance of neurons. Finally, we show that maturation of encoding properties of neurons in cultures is similar to the maturation of encoding in neurons studied in slices. These results show that maturation of AP generators and encoding is, to a large extent, determined genetically and takes place even without normal micro-environment and activity of the whole brain *in vivo*. This establishes neuronal cultures as a valid experimental model for studying mechanisms of AP generation and encoding, and their maturation.

Keywords: neocortical neurons, cultures, slices, development, action potential, encoding, transfer function

Edited by:
Maren Engelhardt,
Heidelberg University, Germany

Reviewed by:
Qian Sun,
Columbia University, USA
Hiroshi Kuba,
Nagoya University, Japan

****Correspondence:***
Maxim Volgushev
maxim.volgushev@uconn.edu

Received: *14 December 2016*
Accepted: *31 January 2017*
Published: *14 February 2017*

Citation:
Nikitin ES, Bal NV, Malyshev A, Ierusalimsky VN, Spivak Y, Balaban PM and Volgushev M (2017) Encoding of High Frequencies Improves with Maturation of Action Potential Generation in Cultured Neocortical Neurons. Front. Cell. Neurosci. 11:28. doi: 10.3389/fncel.2017.00028

INTRODUCTION

Cortical neurons can encode rapidly changing stimuli by phase-locking their spiking to high-frequency components of signals (Köndgen et al., 2008; Boucsein et al., 2009; Higgs and Spain, 2009; Tchumatchenko et al., 2011; Broicher et al., 2012; Ilin et al., 2013). Populations of cortical neurons can detect and respond to subtle changes of the input very fast, on a millisecond time scale (Tchumatchenko et al., 2011; Ilin et al., 2013, 2014; Malyshev et al., 2013). Theoretical studies and results of model simulations linked these abilities to the properties of action potential (AP) generators, specifically to the fast onset dynamics of APs (Brunel et al., 2001; Fourcaud-Trocmé et al., 2003; Naundorf et al., 2005; Wei and Wolf, 2011; Huang et al., 2012; Ilin et al., 2013). This idea is supported by experimental results showing that manipulations which slow down the onset of APs disturb the ability of neurons to phase-lock their spiking to high frequencies and decrease the speed of population responses to fast changes of the input (Ilin et al., 2013; for review see Volgushev, 2016).

Despite the established relationship between encoding of high frequencies, response speed and onset dynamics of APs, the mechanisms of fast onset of APs in cortical neurons remain elusive (Naundorf et al., 2006; Yu et al., 2008). APs in neocortical neurons are initiated in the axon initial segment, about 30–50 μm away from the soma (Stuart and Sakmann, 1994; Stuart et al., 1997; Palmer and Stuart, 2006; Fleidervish et al., 2010; Kole and Stuart, 2012; Baranauskas et al., 2013). Poor accessibility of the axon initial segment in slices hinders further progress in understanding intrinsic mechanisms of AP initiation and encoding. Experimental preparations allowing better access to the spike initiation zone might help to address these questions. Neuronal cultures may provide such an experimental model. The use of cultures proved to be a powerful tool to study diverse aspects of axon initial segment functioning, such as trafficking of channel proteins and other molecules, structural plasticity or changes of excitability (e.g., Grubb and Burrone, 2010; Muir and Kittler, 2014; Evans et al., 2015; Albrecht et al., 2016). Moreover, there are important similarities in development of neurons in cultures and *in vivo*, including development of dendritic morphology, synaptogenesis, maturation of synapses and network activity (Li et al., 1998; De Simoni et al., 2003; Harrill et al., 2015; Schneider et al., 2015).

Here we set to characterize encoding properties of cultured neocortical neurons, and to clarify whether cultures represent a valid experimental model for studying mechanisms of neuronal encoding in the brain. We ask: (i) How coding abilities of cultured neurons change with time *in vitro*; (ii) How these changes are related to maturation of AP generation mechanisms; and (iii) How development of encoding in cultured neurons is related to maturation of neuronal encoding in the whole brain?

MATERIALS AND METHODS

All experimental procedures of this study are in compliance with the Guide for the Care and Use of Laboratory Animals approved by the Department of Humanitarian Expertise and Bioethics of RAS, and the US National Institutes of Health regulations. Procedures for preparation of slices were approved by the Institutional Animal Care and Use Committee of the University of Connecticut.

Cell Cultures

Wistar rat pups (P0–P2) were euthanized by decapitation with sharp scissors. The brains were removed, than cortical tissue was dissected and gently cut into pieces with a sharp blade in ice-cold Hank's balanced salt solution (Gibco). After having it centrifuged, we treated the tissue with TripLE (Gibco) for 5 min at 36°C. TripLE was inactivated by adding ice-cold Neurobasal Medium (Gibco). Cells were dissociated by trituration and washed with Neurobasal medium followed by centrifugation at 2000 rpm for 2 min. Then the tissue was resuspended in Neurobasal Medium (Gibco) with B-27 supplement (Gibco), GlutaMax (Gibco), and cells were plated onto 12 mm glass coverslips coated with poly-D-lysine (Sigma). The initial plating density of cultures was about 1000 cells per square millimeter in a monolayer. Cultures were housed in a CO_2 incubator prior to electrophysiological experiments (Aseyev et al., 2013).

For electrophysiological recording the glass coverslips with cultured neurons (or brain slices, see below) were placed into a chamber continuously perfused with ASCF containing (in mM): 125 NaCl, 25 $NaHCO_3$, 27.5 glucose, 2.5 KCl, 1.25 NaH_2PO_4, 2 $CaCl_2$ and 1.5 $MgCl_2$ (All Sigma Ultra graded), pH 7.4 and preaerated with 95% O_2, 5% CO_2. Experiments were performed at near physiological temperature (32–34°C). Recording chamber was mounted on an Olympus BX50W microscope with DIC infrared optics. For recording we selected large cells, and after establishing whole-cell recording configuration, cells with spike shapes similar to those of pyramidal neurons were selected for encoding experiments. Patch pipettes with tip resistances of 5–6 MΩ were filled with a solution containing (in mM): 132 K-Gluconate, 20 KCl, 4 Mg-ATP, 0.3 Na_2GTP, 10 Na-Phosphocreatine, 10 HEPES, pH 7.25 (all from Sigma, USA). Membrane potential recording and current injection were performed in current clamp mode (**Figure 1**) using Axoclamp 2B amplifier. Capacitance was compensated for recording APs evoked by depolarizing current steps in the beginning of experiment. These recordings were used to measure parameters of the APs. After that capacitance compensation was reduced to ∼60%–70% to avoid occasional overcompensation during recording responses to injection of fluctuating current. Series resistance was not compensated. Recordings were filtered at 10 kHz and digitized at 20 kHz using ADC Digidata 1440 (Axon Instruments, CA, USA) and pCLAMP software (Molecular Devices).

Immunohistochemistry and Confocal Imaging

Cell cultures were fixed in 2% paraformaldehyde in phosphate-buffered saline for 10 min at room temperature. Prior to the incubation with primary antibodies, the cultures were

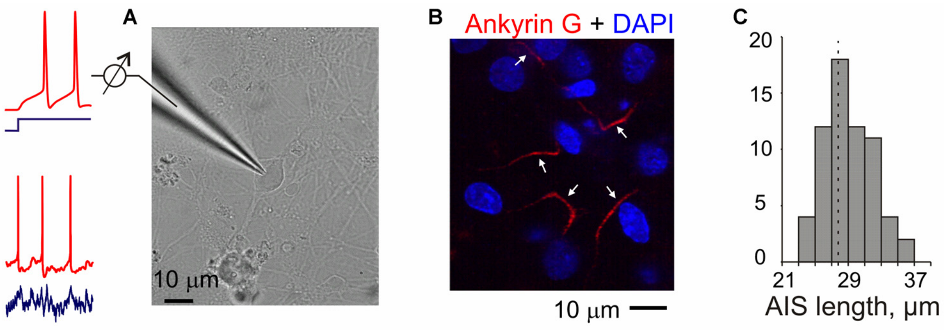

FIGURE 1 | Experiments in neuron cultures. (A) Membrane potential responses of cultured neurons to injection of current steps or fluctuating currents were recorded in a whole-cell configuration. **(B)** Example of combined DAPI nuclear staining (blue) and ankyrin-G staining with antibodies labeled with Alexa Fluor Red in the axons of cultured neurons (17 days in culture). Arrows indicate presumable axon initial segments of cultured neurons. Note that a region with small number of clearly isolated axons was selected for illustration and axons of some neurons may be outside of this region; some of the DAPI-staining may also be due to glial cells. **(C)** Distribution of the lengths of axon initial segments measured using ankyrin-G staining in $N = 63$ cultured neurons. Mean length 27.7 ± 0.4 μm.

washed in the blocking solution (0.5% Triton X-100, 0.01% sodium azide, 5% normal goat serum, and 1% BSA in PBS, all from Sigma) for 2 h. Staining was performed in the blocking solution at 4°C in two stages: primary antibodies overnight with washing in for 1 h; secondary antibodies for 12 h with washing in for 1 h. Primary mouse monoclonal anti-ankyrin G antibodies (Calbiochem) were used at 1:500 dilution. Secondary goat anti-mouse Alexa-546-conjugated IgG antibodies (Invitrogen) were used at 1:100 dilution. The sections were embedded in SlowFade Gold antifade reagent with DAPI (Invitrogen). Confocal imaging was performed using Axiovision software. Stacks of images were acquired at 0.6–1 μm steps with the LSM 5 Live confocal scanning microscope and 63×/1.4 N.A. oil objective (Zeiss, Germany) to produce a detailed 3D-reconstruction.

Experiments in Slices

Procedures for preparation of slices were approved by the Institutional Animal Care and Use Committee of the University of Connecticut. Details of slice preparation are similar to those used in previous studies (Volgushev et al., 2000; Lee et al., 2012; Ilin et al., 2013). Slices were prepared from male Wistar rats (two age groups, P9–P13 and P17–P25) obtained from Charles-River or Harlan. Rats were anesthetized with isoflurane, decapitated, and the brain quickly removed and placed into an ice-cold oxygenated artificial cerebrospinal fluid solution (ACSF), containing, in mM: 125 NaCl, 25 $NaHCO_3$, 25 glucose, 3 KCl, 1.25 NaH_2PO_4, 2 $CaCl_2$, 1 $MgCl_2$, bubbled with 95% O_2/5% CO_2, pH 7.4. Coronal slices (350 μm thickness) containing the visual cortex were prepared from the right hemisphere. After at least 1 h recovery at room temperature, individual slices were transferred to a recording chamber mounted on an Olympus BX-50WI microscope equipped with IR-DIC optics.

Whole-cell recordings using patch electrodes were made at 28–32°C. Layer 2/3 pyramidal neurons in the visual cortex were selected under visual control using infrared videomicroscopy. The patch electrodes were filled with K-gluconate based solution (in mM: 130 K-Gluconate, 20 KCl, 4 Mg-ATP, 0.3 Na_2-GTP, 10 Na-Phosphocreatine, 10 HEPES) and had a resistance of 4−6 MΩ. Recordings were made using Axoclamp-2A (Axon Instruments, CA, USA) or Dagan BVC-700A (Dagan Corporation, MN, USA) amplifier. Similar to recordings from cultured neurons, capacitance was compensated for recording APs evoked by depolarizing current steps, and capacitance compensation was reduced to ∼60–70% after that, for recording responses to injection of fluctuating current. Series resistance was not compensated. After amplification and low-pass filtering at 10 kHz, data were digitized at 20 kHz and fed into a computer (Digidata 1440A interface and pCLAMP software, Molecular Devices).

Current Injection and Calculation of Transfer Function

To calculate the frequency transfer function of individual neurons, we injected fluctuating current that mimics the effect produced in the soma by numerous balanced excitatory and inhibitory synaptic inputs (Destexhe et al., 2003). Fluctuating current for injection was synthetized as a summed activity of large population of model presynaptic excitatory ($N = 512$) and inhibitory ($N = 512$) neurons, each firing at mean rate of 5 Hz (Ilin et al., 2014). Individual excitatory and inhibitory postsynaptic currents were generated as a difference of two exponentials with a rise time of 0.5 ms and decay time of 5 ms. Because of the same number of excitatory and inhibitory neurons and same amplitudes (but for the sign) of excitatory and inhibitory currents the resulting fluctuating current was balanced. Injected current was scaled to produce membrane potential fluctuations of 15–20 mV amplitude, similar to membrane potential fluctuations recorded in neocortical neurons *in vivo* (Destexhe et al., 2003; Volgushev et al., 2003). Current injections lasted 46 s, and were separated by a recovery period of 60–100 s. We used 20 different realizations of 46 s-episodes of fluctuating current for injection in neurons in this study.

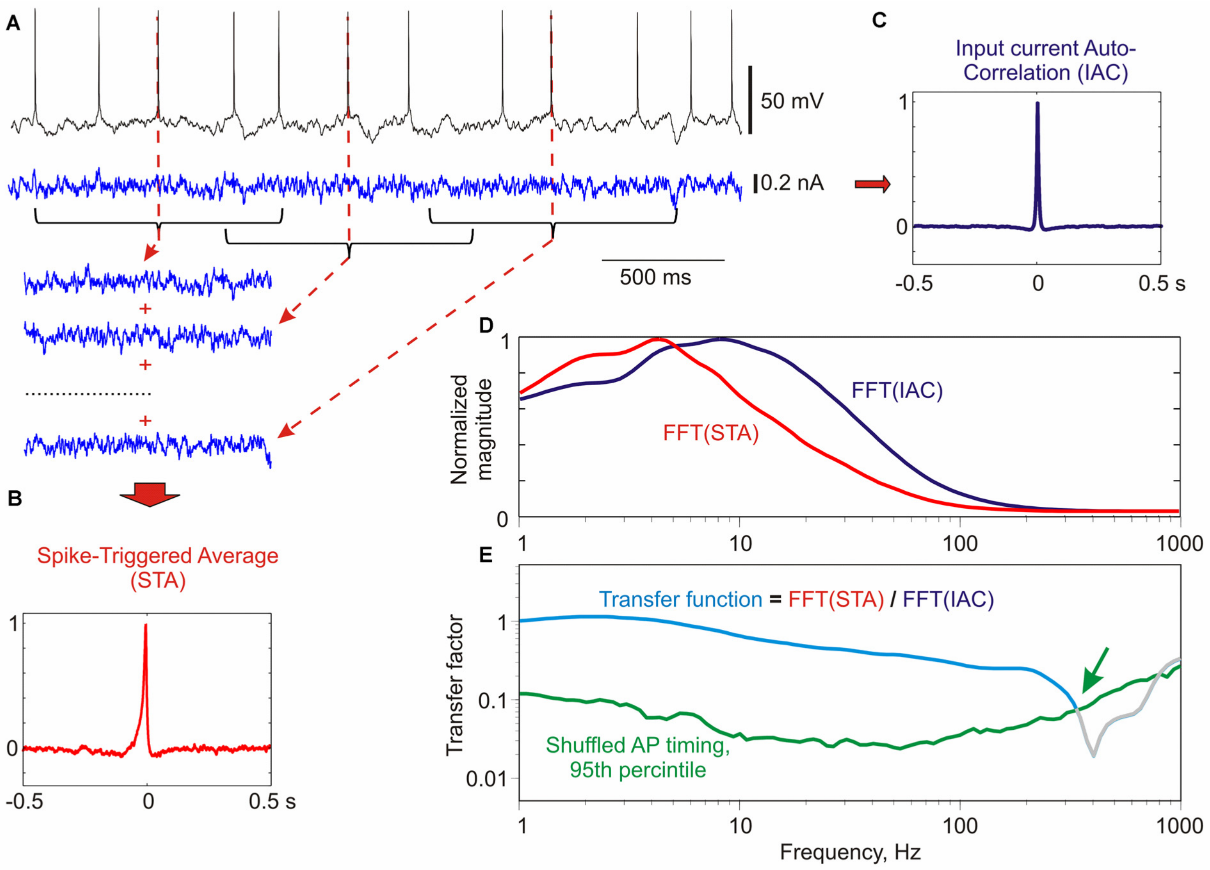

FIGURE 2 | Calculation of frequency transfer function of a culture neuron using noise injection. (A) Response of a neuron in culture to injection of fluctuating current. For calculation of spike-triggered average (STA) 1 s portions of the injected current centered at each spike were used. Three such segments are shown for clarity. **(B)** Normalized STA of the injected current. **(C)** Normalized auto-correlation function of the injected current (IAC). **(D)** Normalized Fast Fourier Transformation (FFT) transforms of the spike-triggered average FFT(STA), and of the input auto-correlation FFT(IAC). **(E)** Transfer function (cyan) calculated as the ratio of the normalized FFT transforms of the STA and the input auto-correlation. Green line shows 95th percentile of "shuffled" transfer functions (*N* = 500), calculated as above, but using shuffled instead of real timings of spikes. Values above the 95th percentile of shuffled transfer function are considered significant. The transfer function was cut at the intersection with the 95th percentile (green arrow). Method of calculation of transfer function is based on Higgs and Spain (2009); significance estimation as in Ilin et al. (2013).

In the recorded responses to injected current we calculated timing of each AP as a positive-slope crossing of zero potential. Using spike timings we calculated normalized spike triggered average of the injected current and power spectrum of the spike-triggered average (STA) using Fast Fourier Transformation (FFT). Next, normalized autocorrelation function of the injected current and its FFT were calculated. Frequency transfer function of a neuron was then calculated as the ratio of the FFT transfers of the STA and the autocorrelation function of the input current. Significance of the transfer function was calculated as following. The same procedure of calculation of transfer function as above was repeated 500 times, but with shuffled spike times. We then calculated 95th percentile of these "shuffled" transfer functions and used it as a significance margin, above which the transfer function was considered significant. Further details of this method are provided in Ilin et al. (2013). In this prior work we have also demonstrated that transfer function calculated using this noise-injection method is similar to the transfer function calculated using a sine-wave immersed in noise paradigm (Ilin et al., 2013).

Database

In the final analysis we included 29 neurons recorded in cultures. Most cultured neurons displayed rare spontaneous spiking, and to avoid contamination of STA by spontaneous spikes we only used for analysis neurons with the spontaneous firing rate lower than one spike per minute. Other criteria included stability of the membrane potential, input resistance and responses to injection of fluctuation current. In preliminary experiments we tested if addition of blockers of synaptic transmission changes the transfer function. Because no significant differences between transfer functions measured with or without blockers were found, we pooled results together. For comparison we used data for 25 neurons from slice experiments, some of which were used in a prior study (Ilin et al., 2013).

Statistical Analysis

Correlations (Spearman-Rho) and their significance were calculated using IBM SPSS Statistics package (PASW Statistics version 18.0.0). Analysis using linear models was done in R (version 3.2.3 (2015-12-10), The R Foundation for Statistical Computing), functions *regsubsets* and *lm*.

RESULTS

Action Potential Encoding of High Frequencies Improves with Maturation of Neurons in Culture

To verify that neurons in our cultures developed normal axon initial segments we used anti-ankyrin-G staining. Ankyrin-G is selectively expressed in the axon initial segment of neurons, and is an established label for the axon initial segments (Lorincz and Nusser, 2008; Kole and Stuart, 2012). Staining neurons in 17-day old cultures with anti-ankyrin-G antibodies revealed a characteristic pattern of linear, 20–35 μm long (mean 27.7 ± 0.4 μm, $N = 63$) smooth stripes near the soma, but no staining in the soma, dendrites or dendritic spines (**Figures 1B,C**). This pattern of staining is similar to that reported in other studies of neurons from brain tissue (Lorincz and Nusser, 2008; Kole and Stuart, 2012; Gutzmann et al., 2014) and in cultures (Grubb and Burrone, 2010; Wefelmeyer et al., 2015), indicating no abnormalities in the development of axon initial segments in our cultures.

We measured encoding properties of cultured neurons using frequency transfer function. Frequency transfer function provides a comprehensive characterization of the ability of neurons to encode periodic signals of different frequencies by phase-locking the generation of APs to a specific phase of the sine wave (Köndgen et al., 2008; Higgs and Spain, 2009; Ilin et al., 2013). The transfer function was calculated as following (**Figure 2**; for details see Ilin et al., 2013). We measured membrane potential response of neurons to injection of fluctuating noise through the recording electrode, and determined the timing of APs generated by the neuron. Next, we calculated the spike triggered average (**Figure 2B**) and autocorrelation function (**Figure 2C**) of the injected current. Transfer function was then calculated as the ratio of the FFT transforms of the STA and the autocorrelation function of the input current (**Figures 2D,E**). Calculated transfer function shows that the cultured neuron in this example was able to phase-lock generation of APs to signal frequencies of up to ∼300 Hz (**Figure 2E**, green arrow).

How does spike encoding change with development of neurons in culture? **Figure 3A** shows transfer functions of three neurons recorded after growing in culture for 13, 17 or 25 days. The ability of neurons to phase-lock their spiking to high frequencies systematically increases with age. While the neuron from 13-day old culture was not able to phase-lock spiking to signal frequencies above 100 Hz (**Figure 3A**, cyan), in neurons from older cultures the range of encoded frequencies expanded and transfer factors for higher frequency range increased. In the neuron from 25 day-old culture the range of encoded frequencies reached 400–500 Hz (**Figure 3A**, green). The improvement of encoding of high frequencies with culture age is further illustrated by the group-averaged transfer functions of neurons grown in culture for 11–15 days, 16–20 days and 21–25 days (**Figure 3B**). To quantify the ability of neurons to encode high frequencies we calculated the ratio of the transfer factors at 100 Hz to 13 Hz, and at 150 Hz to 13 Hz. Both measures were strongly correlated with the age of culture (Spearman-Rho 0.72, $p < 0.001$ and 0.73, $p < 0.001$; $N = 29$; **Figures 3C,D**).

Thus, encoding of high frequencies correlated with the age of culture, and improved significantly over the period from 11 to 25 days.

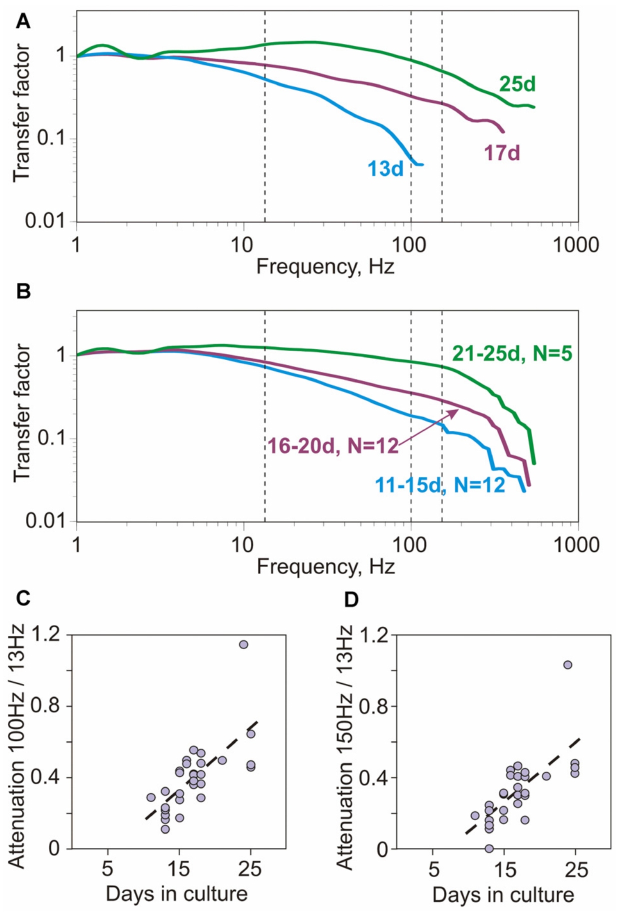

FIGURE 3 | Encoding of high frequencies in cultured neurons improves with age (days in culture). (A) Example transfer functions of three neurons, cultured for 13, 17 and 25 days. Vertical dashed lines show 13 Hz, 100 Hz and 150 Hz. Averaged firing rate for the three neurons was 4.18 Hz; 5.08 Hz and 4.6 Hz, respectively. **(B)** Group-averages of transfer functions of neurons cultured for 11–15 days ($N = 12$), 16–20 days ($N = 12$) and 21–25 days ($N = 5$). **(C,D)** Correlation between the attenuation of encoding of high frequencies and age (days in culture). Attenuation of encoding of high frequencies was quantified using the ratio of transfer factor at 100 Hz over the transfer factor at 13 Hz (**C**, 100 Hz/13 Hz) or the ratio of factors at 150 Hz over 13 Hz (**D**, 150 Hz/13 Hz). Both measures were strongly correlated with age (Spearman-Rho 0.72, $p < 0.001$ and 0.73, $p < 0.001$; $N = 29$).

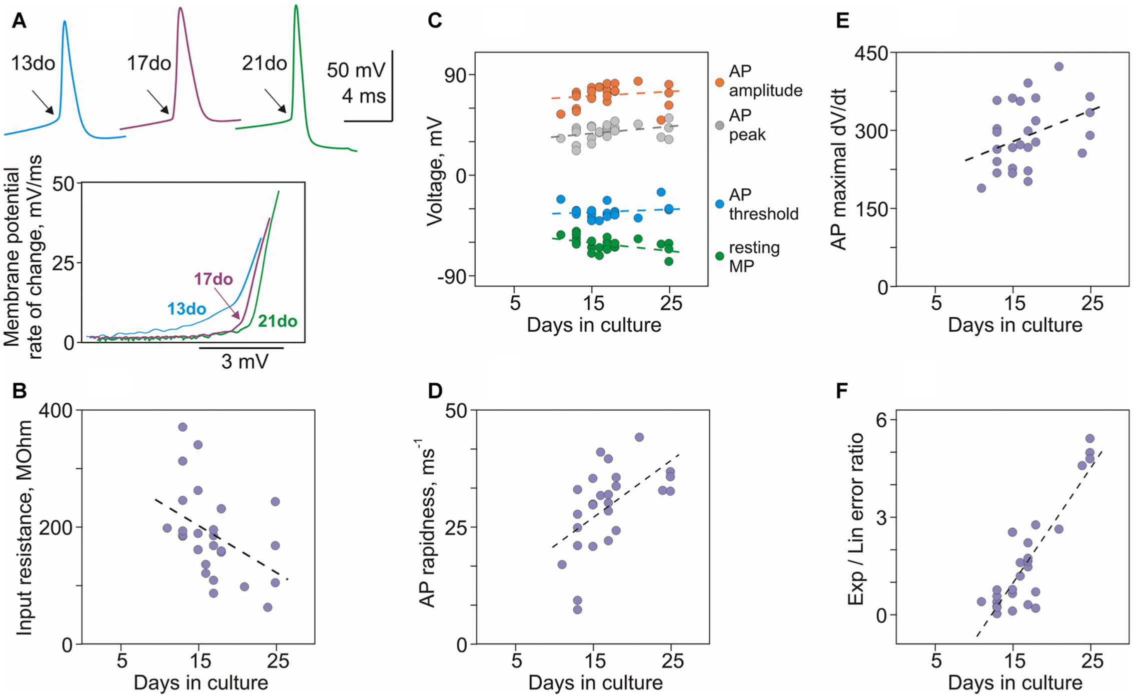

FIGURE 4 | Maturation of membrane properties and action potential (AP) generation in cultured neurons. (A) APs from three neurons cultured for 13, 17 and 21 days, and their onsets in phase plots. In the phase plots, APs were shifted along the X-scale (voltage) to facilitate comparison of their onset dynamics. **(B)** Decrease of input resistance with age ($r = -0.49$, $p = 0.006$, $N = 29$). **(C)** Correlation of resting membrane potential ($r = -0.50$, $p = 0.006$), and AP threshold ($r = 0.003$, $p = 0.99$), peak ($r = 0.36$, $p = 0.053$) and amplitude ($r = 0.42$, $p = 0.024$) with age of cultured neurons. **(D)** AP rapidness increases with age ($r = 0.65$, $p < 0.001$). **(E)** Maximal rate of rise of APs increases with age ($r = 0.46$, $p = 0.013$). **(F)** The ratio of errors of the exponential and the linear fits of AP onset increases with age ($r = 0.63$, $p < 0.001$).

Maturation of Membrane Properties and Action Potential (AP) Generation in Neurons in Culture

A number of basic electrophysiological properties and characteristics of APs changed dramatically in neurons between 11 and 25 days in culture, and were significantly correlated with the culture age (**Figures 4A–F**). Resting membrane potential, input resistance and membrane time constant were negatively correlated with age: neurons became more hyperpolarized ($r = -0.50$, $p = 0.006$; $N = 29$; **Figure 4C**, green circles), their input resistance decreased ($r = -0.49$, $p = 0.006$; **Figure 4B**), and time constant had a tendency to become shorter ($r = -0.27$, $p = 0.15$). Most prominent changes in the generation of APs were their more rapid onset and faster rising front. A characteristic kink at the onset of an AP in conventional voltage-over-time plots became more evident in spikes generated by older neurons (**Figure 4A**, top traces, arrows). Faster onset in older neurons was especially clear in the phase-plots of initial portions of spikes (**Figure 4A**). For quantification of onset dynamics of spikes we used two measures: rapidness (slope of the phase plot at 20 mV/ms; Naundorf et al., 2006) and the ratio of errors of the exponential and linear fits of AP onset in the phase plot (Volgushev et al., 2008). Both measures strongly correlated with culture age (rapidness: $r = 0.65$, $p < 0.001$, **Figure 4D**; ratio of exponential-to-linear fit errors: $r = 0.63$, $p < 0.001$, **Figure 4F**). Increase of the speed of AP rise with age is evidenced by strong positive correlation between culture age and maximal rate of voltage increase (maximal dV/dt, **Figure 4E**, $r = 0.46$, $p = 0.013$).

Other characteristics of APs either weakly correlated or did not change with age of cultures. Weak correlations with age were found for AP amplitude ($r = 0.42$, $p = 0.024$) and peak ($r = 0.36$, $p = 0.053$; **Figure 4C**). No correlation with age was found for AP threshold ($r = 0.003$, $p = 0.99$; **Figure 4C**) and width at half-amplitude ($r = -0.072$, $p = 0.71$; not shown).

Thus, development of neurons between 11 and 25 days in culture is associated with increasingly hyperpolarized membrane potential, decreasing input resistance and faster onset and upstroke of APs.

Which Factors Determine Encoding Properties of Neurons in Culture?

We used several statistical approaches to reveal which factors determine maturation of encoding properties of neurons in culture, specifically the improvement of encoding of high frequencies by neurons from older cultures.

In the first approach we analyzed correlations between a quantitative measure of high frequency encoding, the ratio of transfer factors for 150 Hz and 13 Hz on the one hand,

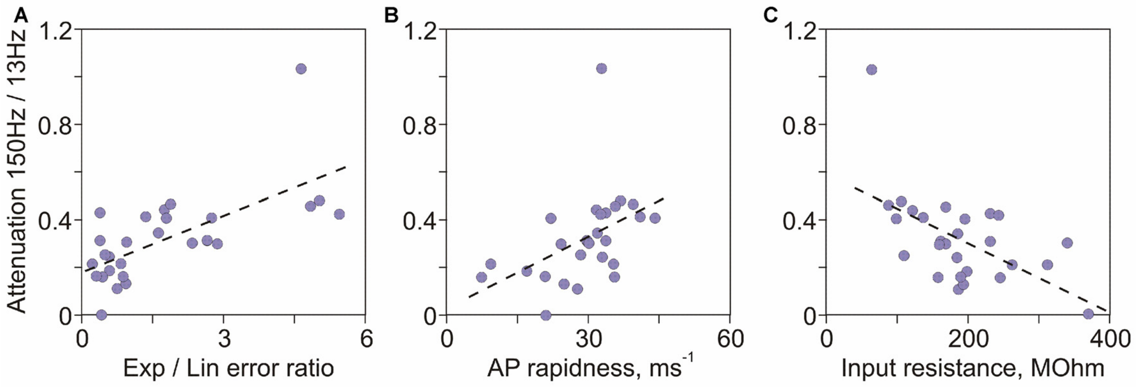

FIGURE 5 | Factors determining encoding of high frequencies in cultured neurons. (A) Correlation between the attenuation of high frequency encoding (ratio of transfer factors at 150 Hz over 13 Hz) and the ratio of errors of exponential to linear fits of AP onset ($r = 0.65$, $p < 0.001$). **(B)** Correlation between the attenuation of 150 Hz/13 Hz encoding and AP onset rapidness ($r = 0.64$, $p < 0.001$). **(C)** Correlation between the attenuation of 150 Hz/13 Hz encoding and input resistance ($r = -0.53$, $p = 0.003$).

and age of culture and electrophysiological characteristics of neurons on the other. The ratio of 150 Hz/13 Hz transfer factors correlated most strongly with age of cultures (Spearman-Rho = 0.73, $R^2 = 0.54$, $p < 0.001$; **Figure 3D**), indicating that age of neurons in culture accounts for >50% of the variance of their encoding abilities. The strongest predictive power of age is not surprising, because age is the common factor that governs changes of all electrophysiological properties of neurons. Other significant factors, in the order of R^2 values were: ratio of errors of exponential to linear fits of the AP onset ($R^2 = 0.42$, $p < 0.001$; **Figure 5A**), AP rapidness ($R^2 = 0.41$, $p < 0.001$; **Figure 5B**), input resistance ($R^2 = 0.28$, $p = 0.003$; **Figure 5C**), followed by resting membrane potential ($R^2 = 0.2$, $p = 0.015$) and AP amplitude ($R^2 = 0.15$, $p = 0.038$). Ability to encode high frequencies did not correlate with other measured characteristics of APs: maximal rate of rise ($R^2 = 0.09$, $p = 0.12$), peak ($R^2 = 0.08$, $p = 0.13$), threshold ($R^2 = 0.001$, $p = 0.89$) and width at half amplitude ($R^2 = 0.0002$, $p = 0.94$). Thus, among measured electrophysiological characteristics of neurons, two measures of the onset of AP—the ratio of errors of exponential to linear fits and onset rapidness—were strongest predictors of abilities of neurons to encode high frequencies. The next strongest factor was input resistance.

In the second approach we used linear model, in which the ratio of 150 Hz/13 Hz transfer factors was considered a response, and all other measured electrophysiological characteristics of neurons (resting membrane potential, input resistance, AP threshold, rapidness, maximal rate of rise, peak, amplitude, width at half height and the ratio of errors of exponential to linear fits) were considered predictors. For subsets of each size (1–8) the optimal combination of these predictors that minimized the residual standard error was determined (function *regsubsets* in R version 3.2.3 (2015-12-10), The R Foundation for Statistical Computing). Optimal subsets of all sizes (from 1 up to 8) contained the quantitative measure of AP onset dynamics, the ratio of exponential-to-linear fit errors, supporting the conclusion that onset dynamics was the strongest predictor of the neurons' ability to encode high frequencies.

Finally, in the linear model which included all nine of the above predictors of encoding of high frequencies ($F_{DF(9,18)} = 3.256$, $p = 0.016$) the strongest predictor was again the ratio of exponential to linear fit errors ($t = 2.592$, $p = 0.018$; all other factors $p > 0.1$; function *lm* in R version 3.2.3).

Thus, results of all three statistical approaches identified onset dynamics of APs as the major factor determining abilities of neurons to encode high frequency signals.

Similarity of Age-Dependent Improvement of Encoding in Neurons in Culture and in Acute Slices

In prior work with neurons in slices we found that encoding of high frequencies improves with age (Ilin et al., 2013). Here we ask, how does maturation of encoding properties of neurons in cultures compares to that during normal development in the whole brain *in vivo*, assessed with recordings from slices prepared from animals of different ages. We found several marked similarities between maturation of encoding in cultures and *in vivo*. First, comparison of transfer functions of neurons in slices prepared from animals of two age groups, P9–P13 and P17–P25, revealed clear improvement of encoding of high frequencies with age (**Figure 6A**). Second, there was a strong correlation between quantitative measures of encoding of high frequencies (ratio of transfer factors at 100 Hz/13 Hz and at 230 Hz/13 Hz) on the one hand, and age on the other (**Figure 6B**, cultures: $r = 0.72$, $p < 0.001$, slices: $r = 0.35$, $p = 0.056$ and **Figure 6C**, cultures: $r = 0.63$, $p < 0.001$, slices: $r = 0.72$, $p < 0.001$). Improvement of encoding with age was also strongly correlated with the decrease of the input resistance (**Figure 6D**, cultures: $r = -0.71$, $p < 0.001$, slices: $r = -0.41$, $p = 0.022$; and **Figure 6E**, cultures: $r = -0.45$, $p = 0.013$; slices: $r = -0.62$, $p < 0.001$).

Third, in neurons both from slices and cultures, encoding of high frequencies correlated with measures of AP onset, the ratio of errors of exponential and linear fits of AP onset (**Figures 6H,I**, cultures: $r = 0.69$, $p < 0.001$ and $r = 0.53$, $p = 0.003$; slices: $r = 0.55$, $p = 0.001$ and $r = 0.75$, $p < 0.001$) and the AP rapidness (**Figures 6F,G**, cultures: $r = 0.71$, $p < 0.001$ and $r = 0.54$, $p = 0.002$; slices: $r = 0.28$, $p = 0.12$ and $r = 0.72$, $p < 0.001$).

Aside from these clear similarities, one notable difference was a better encoding of high frequencies by neurons from slices as compared to matched-age neurons from cultures. This is evidenced by comparison of transfer functions of group-averages (**Figure 6A**). Further, in the plots of encoding against age, input resistance and AP rapidness data-points representing neurons from slices and from cultures form separable clouds, with data-points for slices shifted upwards relative to those from cultures (**Figures 6B–G**, red vs. lilac symbols). In contrast, in the plots of encoding against the ratio of errors of exponential and linear fits of AP onset all data points form one cloud, with similar regression lines for data from slices and from cultures. Neurons from slices had faster onset of APs as evidenced by higher values of the error ratio, and encoded high frequencies better than neurons from cultures (**Figures 6H,I**). Thus the reason for better encoding in neurons from slices could be faster onset of their APs. We interpret these results as an indication that, among the parameters considered above, the AP onset quantified with

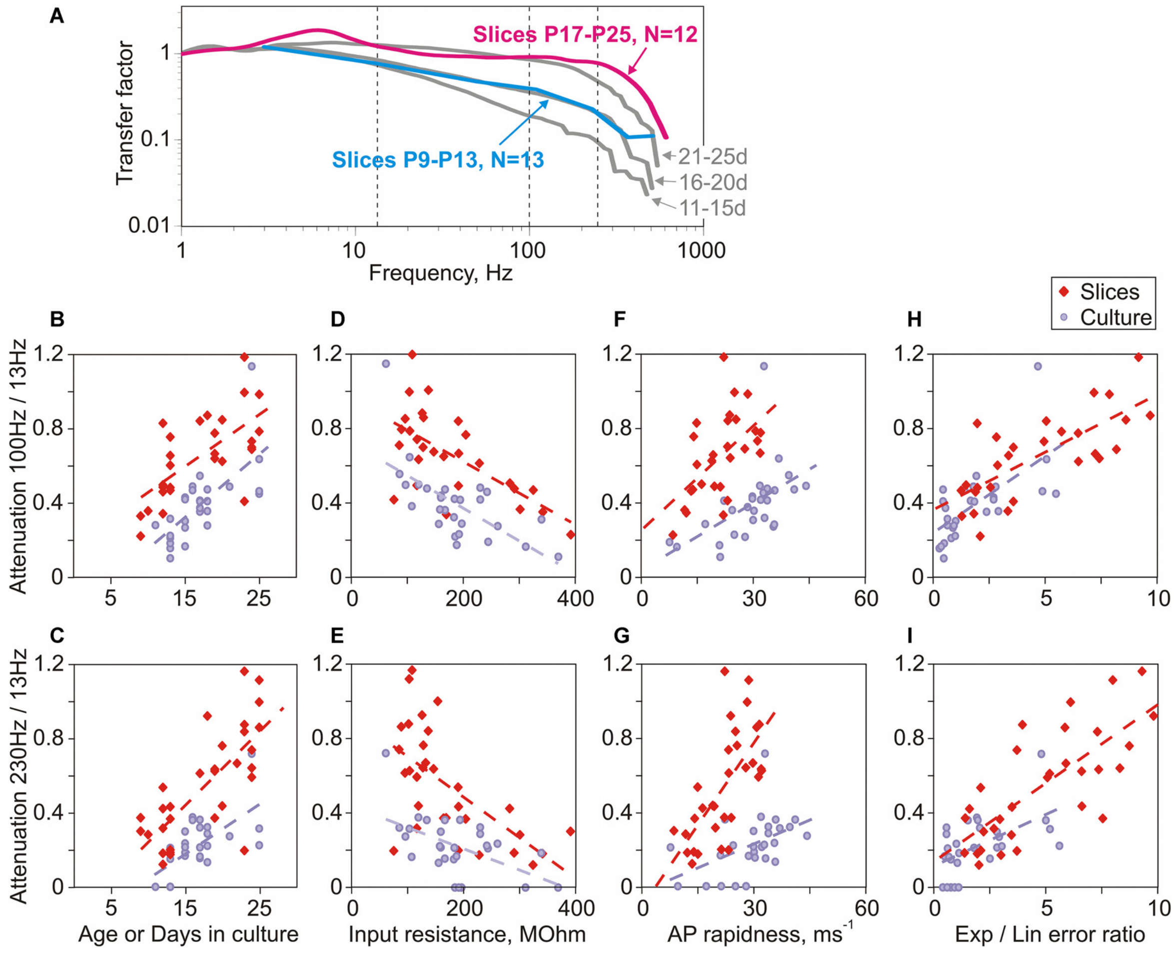

FIGURE 6 | Parallels in the age-dependent improvement of encoding of high frequencies in neurons in slices and in cultures. (A) Averaged transfer functions for two groups of neurons in slices prepared from 9 to 13 day old rats (cyan, $N = 13$) and 17–25 day old animals (magenta, $N = 12$). For comparison, transfer functions for three age groups of cultured neurons are shown (gray; 11–15 day; 16–20 day and 21–25 day; data from **Figure 3B**). **(B,C)** Correlation between attenuation of encoding of high frequencies (**B**: 100 Hz/13 Hz; **C**: 230 Hz/13 Hz) and age for slice neurons (red diamond symbols, **B**: $r = 0.35$, $p = 0.056$; **C**: $r = 0.72$, $p < 0.001$) or days in culture for cultured neurons (lilac circles, **B**: $r = 0.72$, $p < 0.001$; **C**: $r = 0.63$, $p < 0.001$). **(D,E)** Correlation between attenuation of encoding of high frequencies (**D**: 100 Hz/13 Hz; **E**: 230 Hz/13 Hz) and input resistance for neurons in slices (red diamonds, **D**: $r = -0.41$, $p = 0.022$; **E**: $r = -0.62$, $p < 0.001$) and in cultures (lilac circles, **D**: $r = -0.71$, $p < 0.001$; **E**: $r = -0.45$, $p = 0.013$). **(F,G)** Correlation between attenuation of encoding of high frequencies (**F**: 100 Hz/13 Hz; **G**: 230 Hz/13 Hz) and AP onset rapidness for neurons in slices (red diamonds, **F**: $r = 0.28$, $p = 0.12$; **G**: $r = 0.72$, $p < 0.001$) and in cultures (lilac circles, **F**: $r = 0.71$, $p < 0.001$; **G**: $r = 0.54$, $p = 0.002$). **(H,I)** Correlation between attenuation of encoding of high frequencies (**H**: 100 Hz/13 Hz; **I**: 230 Hz/13 Hz) and the ratio of errors of exponential to linear fits for neurons in slices (red diamonds, **H**: $r = 0.55$, $p = 0.001$; **I**: $r = 0.75$, $p < 0.001$) and in cultures (lilac circles, **H**: $r = 0.69$, $p < 0.001$; **I**: $r = 0.53$, $p = 0.003$).

the error ratio is the strongest predictor of encoding of high frequencies.

To summarize, neurons developed in cultures or in the whole brain express clear similarities of the maturation of AP onset dynamics and encoding. Notably, this similarity occurs in spite of dramatically different environment to which neurons are exposed during the development.

DISCUSSION

Results of the present study demonstrate that, in cultured neocortical neurons: (i) encoding of high frequencies improves with maturation of the cultures, in parallel with development of passive electrophysiological properties and AP generation; (ii) the major predictor of encoding is the onset dynamics of APs; and (iii) maturation of encoding properties is similar to developmental changes of encoding in neurons studied in slices.

Electrophysiological Properties and Action Potential Generation in Neurons in Cultures

Passive membrane properties and generation of APs change between 11 and 25 days in culture. Neurons become more hyperpolarized, their input resistance decreases, and membrane time constant becomes shorter. These changes suggest an increase of potassium conductance at rest. An additional factor contributing to a decrease of input resistance might be an increase of size and membrane area of neurons, as reported for both organotypic and dissociated cultures (De Simoni et al., 2003; Harrill et al., 2015). At the same time, threshold for AP generation remained stable over that period. This combination of changes implies a decrease of excitability of neurons: the distance from a more hyperpolarized membrane potential to the unchanged threshold potential increases, and because of the decreased input resistance more input (synaptic) current would be needed to depolarize the membrane to the threshold.

Several lines of evidence indicate changes of the spike generation mechanisms in cultured neurons over the studied period. First, because the rate of rise of an AP is proportional to sodium current density, the increase of the maximal rate of rise implies an increase of the density of sodium current (and sodium channels). Faster onset of APs, documented by the increase of the rapidness and the ratio of errors of exponential and linear fits of AP onset can be due to a shift of the initiation zone of APs down the axon initial segment, leading to the "invasion current" from the generation site recorded at the beginning of the AP in the soma (McCormick et al., 2007; Yu et al., 2008). Both the increase of the maximal rate of rise and faster onset of APs can be also suggestive of a faster gating kinetics of sodium channels in the axon initial segment (Baranauskas and Martina, 2006; Naundorf et al., 2006; Schmidt-Hieber and Bischofberger, 2010). Identifying how each of these three factors change during development of neurons in cultures, and how their interaction leads to the observed changes of spike generation requires further investigation.

Which Factors Mediate the Enhancement of Encoding with Age of Neurons in Culture?

Clear improvement of encoding of high frequencies in cultured neurons and its strong correlation with age over the studied period (from day 11 to day 25 in culture) provide an opportunity to analyze which factors determine age-dependent changes of encoding. Theoretical studies predicted that major determinant of encoding properties of neuronal populations is the onset dynamics of APs (Fourcaud-Trocmé et al., 2003; Naundorf et al., 2005; Wei and Wolf, 2011; Huang et al., 2012). Prior research provided several lines of evidence in support of this prediction. Experiments with neurons in slices showed that encoding of high frequencies correlated with the onset rapidness of APs, and manipulations that slowed-down the onset of spikes impaired the ability of neurons to encode high frequencies (Ilin et al., 2013). Mature neurons with fast-onset spikes encoded high frequencies better than neurons in slices from younger animals with immature spike generators and slow-onset spikes (Ilin et al., 2013). Results of the present study provide further support to this idea. Statistical analysis using correlations and linear model approaches identified the quantitative measure of AP onset dynamic—the ratio of errors of exponential and linear fits of spike onset, as major predictor of age-dependent changes of encoding. Encoding of high frequencies was also strongly correlated with a second measure of onset dynamics, AP rapidness.

Recent modeling work predicted that dendritic load is one further factor that determines encoding: with increasing dendritic load, model neurons were able to encode progressively higher frequencies (Eyal et al., 2014). Experimental results showing better encoding of high frequencies by large L5 pyramids than by small L2/3 pyramids support this conjecture (Volgushev, 2016). Present results lend further support to this notion: improvement of encoding of high frequencies with age was correlated with the decrease of input resistance, which might be at least partially related to the larger dendritic tree of neurons from older cultures (De Simoni et al., 2003; Harrill et al., 2015) and thus increased dendritic load.

Other electrophysiological properties of neurons measured in this study expressed only a weak or no correlation with the ability to encode high frequencies (resting potential $r = -0.45$, $p = 0.15$; AP amplitude $r = 0.39$, $p = 0.038$; no correlation for membrane time constant, AP threshold, maximal rate of rise, peak and width). Notably, linear model approach did not identify AP amplitude and rate of rise as significant predictors of encoding abilities. Because AP rate of rise is proportional to the density of sodium current (and channels), this result indicates that density of sodium channels as such is not a significant predictor of encoding. This is consistent with modeling results which demonstrated that increasing sodium current density in model neurons did not lead to significant improvement of encoding (Huang et al., 2012; Ilin et al., 2013).

Changes of excitability, AP generation and encoding abilities of neurons might alter the ability of neuronal networks in cultures to generate precisely patterned activity and thus contribute to the reported changes of activity patterns with age of cultures (Maeda et al., 1995; Harrill et al., 2015; Schneider et al., 2015). Such age-dependent changes might also have implications for recently suggested construction of large scale logical devices exploiting geometrical design of neural cultures *in vitro* (Feinerman et al., 2008; Kato-Negishi et al., 2013). The observed dependence of the AP generation and encoding on culture age may negatively affect the reproducibility of computations in such devices.

Outlook: Cultured Neurons as an Experimental Model for Studying Action Potential Encoding

Results of the present study revealed clear similarity between the development of encoding properties in neurons in cultures and maturation of encoding properties *in vivo*, as accessed in experiments in acute slices prepared from animals of different ages. In both cases ability of neurons to encode high frequencies was significantly correlated with age, improving with maturation of neurons. Further, encoding of high frequencies correlated with the onset dynamics of APs, and was enhanced in neurons with faster AP onset dynamics. Quantitative measures of AP onset dynamics were the strongest predictors of the encoding properties of neurons. These similarities were present despite strikingly different conditions in which neurons developed: cellular micro-environment, interactions with other neurons and activity in cultures is dramatically simplified compared to the whole brain *in vivo*. Parallels in maturation of AP generation and encoding in neurons in cultures and *in vivo* indicate that these processes are to a large extent determined by genetic mechanisms governing development of nerve cells. Support to this notion comes from studies which demonstrated further similarities between development of neurons in cultures and *in vivo*, including dendritic growth, synaptogenesis, and maturation of synaptic and network activity (Li et al., 1998; De Simoni et al., 2003; Harrill et al., 2015; Schneider et al., 2015). This makes cultures a suitable and valuable experimental model to study the development of AP generation and encoding, and allows to exploit advantages of cultures over experiments in slices. These advantages include accurate control over conditions of growth and microenvironment throughout the development, a possibility to precisely modify these conditions (e.g., Grubb and Burrone, 2010), and enhanced access to the axon initial segment (e.g., Albrecht et al., 2016; Muir and Kittler, 2014). Further, experiments in cultures expand the range of genetic tools applicable to study AP generation and encoding, e.g., allowing the use of mutations that affect sodium channels and have severe physiological consequences (e.g., Scn8a mutation, in which Nav1.6 do not replace Nav1.2, leading to severe dysfunction and lethality around PD21; Burgess et al., 1995; Meisler et al., 2001).

Interestingly, results from cultured neurons had a better correspondence with the predictions of computer models. Similar to computer models (Huang et al., 2012; Ilin et al., 2013), encoding in cultured neurons correlated with AP onset and input resistance, but not with other parameters of AP, such as rate of rise or amplitude. Prior work in slices found correlation of encoding with AP rate of rise and amplitude (Ilin et al., 2013). Possible reasons for this discrepancy may include influence of natural environment and natural activity of the whole brain on the development of neurons. Lower number of synapses and less elaborated dendritic tree of neurons in cultures as compared to slices (De Simoni et al., 2003; Harrill et al., 2015) could be one of the reasons why models with simple morphology (Ilin et al., 2013) better captured properties of cultured neurons. One further reason could be that during normal development in the whole brain *in vivo* factors additional to genetically-determined program executed in cultures were activated, leading to a faster onset of APs and better encoding of high frequencies as our results show, but also to deviations of real neuron behavior from that of a simple model. Among these factors could be up-regulation and redistribution of potassium channels and increased density of sodium channels in the axon initial segment, as well as a shift of the AP generation zone. Indeed, these factors change during normal development, and sensory deprivation disrupts refinement of the structure and location of the axon initial segment (Gutzmann et al., 2014; Kuba et al., 2014; Adachi et al., 2015; Yamada and Kuba, 2016), pointing at the involvement of activity-dependent mechanisms in final shaping of spike generation zone (Grubb and Burrone, 2010; Evans et al., 2015; Wefelmeyer et al., 2015). A further reason for enhanced encoding of high frequencies in neurons in slices could be higher dendritic load (Eyal et al., 2014), due to both, larger dendritic trees and higher level of spontaneous activity in neurons in acute slices as compared to cultures (De Simoni et al., 2003). Experiments with neuronal cultures, in which conditions of growth can be precisely controlled and modified, provide a unique opportunity to disentangle the contribution of genetically-determined program and activity-dependent mechanisms to the development of AP generators and encoding. Understanding these factors might provide further insights into mechanisms of AP generation and encoding in cortical neurons and their maturation.

AUTHOR CONTRIBUTIONS

ESN, AM, PMB and MV: designed the study; ESN, NVB, AM, VNI and YS: performed experiments; ESN, AM, VNI and MV: processed results; ESN and MV: wrote the manuscript. All authors have read and approved the submitted version of the manuscript.

ACKNOWLEDGMENTS

This work was supported by the grant R01 MH087631 from National Institutes of Health (NIH) to MV, Russian Foundation for Basic Research (RFBR; grant no. 16-04-00490) to ESN, Russian Science Foundation (RSF; grant no. 16-15-00291, experiments in slices) to AM, Molecular and Cell Biology Program of Russian Academy of Sciences (to ESN). MV was partially supported by the Humboldt Research Award from the Alexander von Humboldt-Foundation. We are grateful to Stanislav Volgushev for his help with statistical analysis.

REFERENCES

Adachi, R., Yamada, R., and Kuba, H. (2015). Plasticity of the axonal trigger zone. *Neuroscientist* 21, 255–265. doi: 10.1177/1073858414535986

Albrecht, D., Winterflood, C. M., Sadeghi, M., Tschager, T., Noé, F., and Ewers, H. (2016). Nanoscopic compartmentalization of membrane protein motion at the axon initial segment. *J. Cell Biol.* 215, 37–46. doi: 10.1083/jcb.201603108

Aseyev, N., Roshchin, M., Ierusalimsky, V. N., Balaban, P. M., and Nikitin, E. S. (2013). Biolistic delivery of voltage-sensitive dyes for fast recording of membrane potential changes in individual neurons in rat brain slices. *J. Neurosci. Methods* 212, 17–27. doi: 10.1016/j.jneumeth.2012.09.008

Baranauskas, G., David, Y., and Fleidervish, I. A. (2013). Spatial mismatch between the Na^+ flux and spike initiation in axon initial segment. *Proc. Natl. Acad. Sci. U S A* 110, 4051–4056. doi: 10.1073/pnas.1215125110

Baranauskas, G., and Martina, M. (2006). Sodium currents activate without a Hodgkin and Huxley type delay in central mammalian neurons. *J. Neurosci.* 26, 671–684. doi: 10.1523/JNEUROSCI.2283-05.2006

Boucsein, C., Tetzlaff, T., Meier, R., Aertsen, A., and Naundorf, B. (2009). Dynamical response properties of neocortical neuron ensembles: multiplicative versus additive noise. *J. Neurosci.* 29, 1006–1010. doi: 10.1523/JNEUROSCI.3424-08.2009

Broicher, T., Malerba, P., Dorval, A. D., Borisyuk, A., Fernandez, F. R., and White, J. A. (2012). Spike phase locking in CA1 pyramidal neurons depends on background conductance and firing rate. *J. Neurosci.* 32, 14374–14388. doi: 10.1523/JNEUROSCI.0842-12.2012

Brunel, N., Chance, F. S., Fourcaud, N., and Abbott, L. F. (2001). Effects of synaptic noise and filtering on the frequency response of spiking neurons. *Phys. Rev. Lett.* 86, 2186–2189. doi: 10.1103/physrevlett.86.2186

Burgess, D. L., Kohrman, D. C., Galt, J., Plummer, N. W., Jones, J. M., Spear, B., et al. (1995). Mutation of a new sodium channel gene, *Scn8a*, in the mouse mutant 'motor endplate disease'. *Nat Genet.* 10, 461–465. doi: 10.1038/ng0895-461

De Simoni, A., Griesinger, C. B., and Edwards, F. A. (2003). Development of rat CA1 neurones in acute versus organotypic slices: role of experience in synaptic morphology and activity. *J. Physiol.* 550, 135–147. doi: 10.1113/jphysiol.2003.039099

Destexhe, A., Rudolph, M., and Paré, D. (2003). The high-conductance state of neocortical neurons *in vivo*. *Nat. Rev. Neurosci.* 4, 739–751. doi: 10.1038/nrn1198

Evans, M. D., Dumitrescu, A. S., Kruijssen, D. L., Taylor, S. E., and Grubb, M. S. (2015). Rapid modulation of axon initial segment length influences repetitive spike firing. *Cell Rep.* 13, 1233–1245. doi: 10.1016/j.celrep.2015.09.066

Eyal, G., Mansvelder, H. D., de Kock, C. P., and Segev, I. (2014). Dendrites impact the encoding capabilities of the axon. *J. Neurosci.* 34, 8063–8071. doi: 10.1523/JNEUROSCI.5431-13.2014

Feinerman, O., Rotem, A., and Moses, E. (2008). Reliable neuronal logic devices from patterned hippocampal cultures. *Nat. Phys.* 4, 967–973. doi: 10.1038/nphys1099

Fleidervish, I. A., Lasser-Ross, N., Gutnick, M. J., and Ross, W. N. (2010). Na^+ imaging reveals little difference in action potential-evoked Na^+ influx between axon and soma. *Nat. Neurosci.* 13, 852–860. doi: 10.1038/nn.2574

Fourcaud-Trocmé, N., Hansel, D., van Vreeswijk, C., and Brunel, N. (2003). How spike generation mechanisms determine the neuronal response to fluctuating inputs. *J. Neurosci.* 23, 11628–11640.

Grubb, M. S., and Burrone, J. (2010). Activity-dependent relocation of the axon initial segment fine-tunes neuronal excitability. *Nature* 465, 1070–1074. doi: 10.1038/nature09160

Gutzmann, A., Ergül, N., Grossmann, R., Schultz, C., Wahle, P., and Engelhardt, M. (2014). A period of structural plasticity at the axon initial segment in developing visual cortex. *Front. Neuroanat.* 8:11. doi: 10.3389/fnana.2014.00011

Harrill, J. A., Chen, H., Streifel, K. M., Yang, D., Mundy, W. R., and Lein, P. J. (2015). Ontogeny of biochemical, morphological and functional parameters of synaptogenesis in primary cultures of rat hippocampal and cortical neurons. *Mol. Brain* 8:10. doi: 10.1186/s13041-015-0099-9

Higgs, M. H., and Spain, W. J. (2009). Conditional bursting enhances resonant firing in neocortical layer 2-3 pyramidal neurons. *J. Neurosci.* 29, 1285–1299. doi: 10.1523/JNEUROSCI.3728-08.2009

Huang, M., Volgushev, M., and Wolf, F. (2012). A small fraction of strongly cooperative sodium channels boosts neuronal encoding of high frequencies. *PLoS One* 7:e37629. doi: 10.1371/journal.pone.0037629

Ilin, V., Malyshev, A., Wolf, F., and Volgushev, M. (2013). Fast computations in cortical ensembles require rapid initiation of action potentials. *J. Neurosci.* 33, 2281–2292. doi: 10.1523/JNEUROSCI.0771-12.2013

Ilin, V., Stevenson, I. H., and Volgushev, M. (2014). Injection of fully-defined signal mixtures: a novel high-throughput tool to study neuronal encoding and computations. *PLoS One* 9:e109928. doi: 10.1371/journal.pone.0109928

Kato-Negishi, M., Morimoto, Y., Onoe, H., and Takeuchi, S. (2013). Millimeter-sized neural building blocks for 3D heterogeneous neural network assembly. *Adv. Healthc. Mater.* 12, 1564–1570. doi: 10.1002/adhm.201300052

Kole, M. H., and Stuart, G. (2012). Signal processing in the axon initial segment. *Neuron* 73, 235–247. doi: 10.1016/j.neuron.2012.01.007

Köndgen, H., Geisler, C., Fusi, S., Wang, X. J., Lüscher, H. R., and Giugliano, M. (2008). The dynamical response properties of neocortical neurons to temporally modulated noisy inputs *in vitro*. *Cereb. Cortex* 18, 2086–2097. doi: 10.1093/cercor/bhm235

Kuba, H., Adachi, R., and Ohmori, H. (2014). Activity-dependent and activity-independent development of the axon initial segment. *J. Neurosci.* 34, 3443–3453. doi: 10.1523/JNEUROSCI.4357-13.2014

Lee, C. M., Stoelzel, C., Chistiakova, M., and Volgushev, M. (2012). Heterosynaptic plasticity induced by intracellular tetanization in layer 2/3 pyramidal neurons in rat auditory cortex. *J. Physiol.* 590, 2253–2271. doi: 10.1113/jphysiol.2012.228247

Li, J. H., Wang, Y. H., Wolfe, B. B., Krueger, K. E., Corsi, L., Stocca, G., et al. (1998). Developmental changes in localization of NMDA receptor subunits in primary cultures of cortical neurons. *Eur. J. Neurosci.* 10, 1704–1715. doi: 10.1046/j.1460-9568.1998.00169.x

Lorincz, A., and Nusser, Z. (2008). Cell-type dependent molecular composition of the axon initial segment. *J. Neurosci.* 28, 14329–14340. doi: 10.1523/JNEUROSCI.4833-08.2008

Maeda, E., Robinson, H. P. C., and Kawana, A. (1995). The mechanisms of generation and propagation of synchronized bursting in developing networks of cortical neurons. *J. Neurosci.* 15, 6834–6845.

Malyshev, A., Tchumatchenko, T., Volgushev, S., and Volgushev, M. (2013). Energy-efficient encoding by shifting spikes in neocortical neurons. *Eur. J. Neurosci.* 38, 3181–3188. doi: 10.1111/ejn.12338

McCormick, D. A., Shu, Y., and Yu, Y. (2007). Neurophysiology: hodgkin and huxley mode–still standing? *Nature* 445, E1–E2; discussion E2–E3. doi: 10.1038/nature05523

Meisler, M. H., Kearney, J., Escayg, A., MacDonald, B. T., and Sprunger, L. K. (2001). Sodium channels and neurological disease: insights from Scn8a mutations in the mouse. *Neuroscientist* 7, 136–145. doi: 10.1177/107385840100700208

Muir, J., and Kittler, J. T. (2014). Plasticity of $GABA_A$ receptor diffusion dynamics at the axon initial segment. *Front. Cell. Neurosci.* 8:151. doi: 10.3389/fncel.2014.00151

Naundorf, B., Geisel, T., and Wolf, F. (2005). Action potential onset dynamics and the response speed of neuronal populations. *J. Comput. Neurosci.* 18, 297–309. doi: 10.1007/s10827-005-0329-8

Naundorf, B., Wolf, F., and Volgushev, M. (2006). Unique features of action potential initiation in cortical neurons. *Nature* 440, 1060–1063. doi: 10.1038/nature04610

Palmer, L. M., and Stuart, G. J. (2006). Site of action potential initiation in layer 5 pyramidal neurons. *J. Neurosci.* 26, 1854–1863. doi: 10.1523/JNEUROSCI.4812-05.2006

Schmidt-Hieber, C., and Bischofberger, J. (2010). Fast sodium channel gating supports localized and efficient axonal action potential initiation. *J. Neurosci.* 30, 10233–10242. doi: 10.1523/JNEUROSCI.6335-09.2010

Schneider, J., Lewen, A., Ta, T. T., Galow, L. V., Isola, R., Papageorgiou, I. E., et al. (2015). A reliable model for gamma oscillations in hippocampal tissue. *J. Neurosci. Res.* 93, 1067–1078. doi: 10.1002/jnr.23590

Stuart, G. J., and Sakmann, B. (1994). Active propagation of somatic action potentials into neocortical pyramidal cell dendrites. *Nature* 367, 69–72. doi: 10.1038/367069a0

Stuart, G., Spruston, N., Sakmann, B., and Häusser, M. (1997). Action potential initiation and backpropagation in neurons of the mammalian CNS. *Trends Neurosci.* 20, 125–131. doi: 10.1016/s0166-2236(96)10075-8

Tchumatchenko, T., Malyshev, A., Wolf, F., and Volgushev, M. (2011). Ultrafast population encoding by cortical neurons. *J. Neurosci.* 31, 12171–12179. doi: 10.1523/JNEUROSCI.2182-11.2011

Volgushev, M. (2016). Cortical specializations underlying fast computations. *Neuroscientist* 22, 145–164. doi: 10.1177/1073858415571539

Volgushev, M., Malyshev, A., Balaban, P., Chistiakova, M., Volgushev, S., and Wolf, F. (2008). Onset dynamics of action potentials in rat neocortical neurons and identified snail neurons: quantification of the difference. *PLoS One* 3:e1962. doi: 10.1371/journal.pone.0001962

Volgushev, M., Pernberg, J., and Eysel, U. T. (2003). Gamma-frequency fluctuations of the membrane potential and response selectivity in visual cortical neurons. *Eur. J. Neurosci.* 17, 1768–1776. doi: 10.1046/j.1460-9568.2003.02609.x

Volgushev, M., Vidyasagar, T. R., Chistiakova, M., Yousef, T., and Eysel, U. T. (2000). Membrane properties and spike generation in rat visual cortical cells during reversible cooling. *J. Physiol.* 522, 59–76. doi: 10.1111/j.1469-7793.2000.0059m.x

Wefelmeyer, W., Cattaert, D., and Burrone, J. (2015). Activity-dependent mismatch between axo-axonic synapses and the axon initial segment controls neuronal output. *Proc. Natl. Acad. Sci. U S A* 112, 9757–9762. doi: 10.1073/pnas.1502902112

Wei, W., and Wolf, F. (2011). Spike onset dynamics and response speed in neuronal populations. *Phys. Rev. Lett.* 106:088102. doi: 10.1103/physrevlett.106.088102

Yamada, R., and Kuba, H. (2016). Structural and functional plasticity at the axon initial segment. *Front. Cell. Neurosci.* 10:250. doi: 10.3389/fncel.2016.00250

Yu, Y., Shu, Y., and McCormick, D. A. (2008). Cortical action potential backpropagation explains spike threshold variability and rapid-onset kinetics. *J. Neurosci.* 28, 7260–7272. doi: 10.1523/JNEUROSCI.1613-08.2008

Conflict of Interest Statement: The authors declare that the research was conducted in the absence of any commercial or financial relationships that could be construed as a potential conflict of interest.

frontiers
in Cellular Neuroscience

ORIGINAL RESEARCH
published: 25 January 2017
doi: 10.3389/fncel.2017.00005

Cannabinoid Receptors Modulate Neuronal Morphology and AnkyrinG Density at the Axon Initial Segment

Mónica Tapia[1]*†, Ana Dominguez[1], Wei Zhang[1], Ana del Puerto[1], María Ciorraga[1], María José Benitez[1,2], Carmen Guaza[1] and Juan José Garrido[1]*

[1] Instituto Cajal, Consejo Superior de Investigaciones Científicas (CSIC), Madrid, Spain, [2] Department of Quimica Fisica Aplicada,Universidad Autónoma de Madrid, Madrid, Spain

OPEN ACCESS

Edited by:
Vann Bennett,
Howard Hughes Medical Institute,
USA

Reviewed by:
Maarten H. P. Kole,
Netherlands Institute for
Neuroscience (KNAW), Netherlands
Matthew S. Grubb,
King's College London, UK
Christian Schultz,
Heidelberg University, Germany

Correspondence:
Mónica Tapia
monica.tapia-pacheco@univ-amu.fr
Juan José Garrido
jjgarrido@cajal.csic.es

†Present address:
Mónica Tapia,
Faculté de Médecine Secteur Nord,
Inserm UMR 1072, Aix Marseille
University, Boulevard Pierre Dramard,
Marseille, France

Received: *20 September 2016*
Accepted: *10 January 2017*
Published: *25 January 2017*

Citation:
Tapia M, Dominguez A, Zhang W, del Puerto A, Ciorraga M, Benitez MJ, Guaza C and Garrido JJ (2017) Cannabinoid Receptors Modulate Neuronal Morphology and AnkyrinG Density at the Axon Initial Segment.
Front. Cell. Neurosci. 11:5.
doi: 10.3389/fncel.2017.00005

Neuronal polarization underlies the ability of neurons to integrate and transmit information. This process begins early in development with axon outgrowth, followed by dendritic growth and subsequent maturation. In between these two steps, the axon initial segment (AIS), a subcellular domain crucial for generating action potentials (APs) and maintaining the morphological and functional polarization, starts to develop. However, the cellular/molecular mechanisms and receptors involved in AIS initial development and maturation are mostly unknown. In this study, we have focused on the role of the type-1 cannabinoid receptor (CB1R), a highly abundant G-protein coupled receptor (GPCR) in the nervous system largely involved in different phases of neuronal development and differentiation. Although CB1R activity modulation has been related to changes in axons or dendrites, its possible role as a modulator of AIS development has not been yet explored. Here we analyzed the potential role of CB1R on neuronal morphology and AIS development using pharmacological and RNA interference approaches in cultured hippocampal neurons. CB1R inhibition, at a very early developmental stage, has no effect on axonal growth, yet CB1R activation can promote it. By contrast, subsequent dendritic growth is impaired by CB1R inhibition, which also reduces ankyrinG density at the AIS. Moreover, our data show a significant correlation between early dendritic growth and ankyrinG density. However, CB1R inhibition in later developmental stages after dendrites are formed only reduces ankyrinG accumulation at the AIS. In conclusion, our data suggest that neuronal CB1R basal activity plays a role in initial development of dendrites and indirectly in AIS proteins accumulation. Based on the lack of CB1R expression at the AIS, we hypothesize that CB1R mediated modulation of dendritic arbor size during early development indirectly determines the accumulation of ankyrinG and AIS development. Further studies will be necessary to determine which CB1R-dependent mechanisms can coordinate these two domains, and what may be the impact of these early developmental changes once neurons mature and are embedded in a functional brain network.

Keywords: axon initial segment, cannabinoids, CB1R, 2-AG, ankyrinG, dendrites, axon, hippocampal neurons

INTRODUCTION

The establishment of a functional brain network depends on the ability of neurons to reach and activate their specific targets via the growth and elongation of their axons. Axonal outgrowth is the first morphological event of neuronal polarization, followed by the development of dendrites and axon initial segment (AIS) formation (Ramón Y Cajal, 1897; Kaech and Banker, 2006). The AIS plays an essential role in maintaining neuronal polarity and axon integrity and identity (Hedstrom et al., 2008). Functionally, the AIS is a unique neuronal domain comprising high densities of Na^+, K^+ and Ca^{2+} voltage-gated ion channels (for a review see Bender and Trussell, 2012). These voltage-gated ion channels are anchored in the AIS by interactions with scaffold cytoskeletal proteins, such as ankyrinG or PSD-93 (Garrido et al., 2003; Pan et al., 2006; Ogawa et al., 2008). Among other factors, the high density of ion channels confers on the AIS the property of being the site of action potential (AP) initiation (Stuart et al., 1997; Kole et al., 2008). In fact, the AIS acts as an electrical gatekeeper, becoming the decision point for initiation of APs. The AIS performs this function by summing all excitatory and inhibitory inputs from thousands of synapses until a critical firing threshold is reached and the AP is irreversibly triggered. The scaffold protein ankyrinG is the AIS master regulator and is necessary for its assembly and maintenance, such that ankyrinG suppression leads to a loss of axonal identity characterized by the appearance of dendritic spines in former axonal structures (Hedstrom et al., 2008; Sobotzik et al., 2009). Over the past 20 years, many studies have contributed to describe AIS molecular structure, function and some regulatory mechanisms (some examples and reviews are: Kobayashi et al., 1992; Zhou et al., 1998; Garrido et al., 2003; Rasband, 2010; Grubb et al., 2011; Sanchez-Ponce et al., 2011; Bender and Trussell, 2012; Zollinger et al., 2015; Huang and Rasband, 2016). Furthermore, the discovery of AIS structural plasticity (changes in position or length) and its capacity to adapt in response to different physiological and pathological conditions in order to maintain neuronal survival and excitability shed light on the dynamical complexity of the AIS (Schafer et al., 2009; Grubb and Burrone, 2010; Kuba et al., 2010). Besides AIS structural plasticity, AIS proteins density also can change in response to physiological or pathological stimuli (Kuba et al., 2015; del Puerto et al., 2015).

However, it is now important to understand which neuronal or glial mechanisms, and which membrane receptors, contribute to different types of AIS modulation. Moreover, the mechanisms involved in the targeting and modulation of AIS proteins during the very early stages of neuronal development remain elusive. Recent studies have shown that the purinergic system (del Puerto et al., 2015), serotonin receptors (Ko et al., 2016) or GABAergic innervation (Muir and Kittler, 2014) influence and modulate AIS proteins and neuronal excitability. However, the role of another important neuromodulatory system, the cannabinoid system, has not been analyzed in the context of AIS development and maturation.

The endocannabinoid system (ECS) comprises endocannabinoids (eCB) such as 2-arachidonoyl glycerol (2-AG) and n-arachidonoyl ethanolamine (AEA or anandamide), the enzymes responsible for their synthesis/degradation and the cannabinoid receptors. Among cannabinoid receptors, type-1 cannabinoid receptor (CB1R) is abundantly expressed in the central nervous system, particularly in the cortex, basal ganglia, hippocampus and cerebellum (Mackie, 2005), and is considered one of the most abundant G protein-coupled receptors (GPCRs) expressed in the brain (Matsuda et al., 1990; Kano et al., 2009). CB1R coupling to Gi/o proteins leads to multiple downstream events depending on the cell type: adenylyl cyclase inhibition, voltage-gated calcium channel inhibition, activation of inwardly rectifying potassium channels and activation of mitogen-activated protein kinases (Howlett, 2005). Despite the lack of highly specific pharmacology for the study of cannabinoid receptors, several studies have suggested that CB1Rs are mostly present in axon terminals, and also in astrocytes (Navarrete and Araque, 2010), and control a wide spectrum of physiological and pathological conditions (Katona and Freund, 2012; Mechoulam and Parker, 2013). The type-2 cannabinoid receptors (CB2Rs) are considered the predominant cannabinoid receptor in the immune system and their neuronal expression has only been described under certain pathological conditions (Viscomi et al., 2009). Besides their well-known functions as neuromodulators, controlling both neuronal excitability and synaptic plasticity at different scales (Chevaleyre et al., 2006; Kano et al., 2009; Marinelli et al., 2009; Katona and Freund, 2012), eCB also seem to be involved in brain development and axonal pathfinding (Mulder et al., 2008; Keimpema et al., 2011). Indeed, CB1Rs are highly expressed in the developing brain (Vitalis et al., 2008), and axon development and pathfinding are disrupted during pre- and post natal brain development in CB1R knock out mice (Mulder et al., 2008; Wu et al., 2010). CB1Rs are also involved in the regulation of adult neurogenesis, such that their loss inhibits neuronal progenitor cell proliferation *in vivo* and *in vitro*. Moreover CB1R expression in neural progenitors increases along neuronal differentiation, allowing eCBs to control neuronal specification and morphogenesis (reviewed in Galve-Roperh et al., 2013).

Thus, a tempting idea is that cannabinoid receptors play an important role during the early stages of neuronal domain development and maturation. In this article, we will focus on new data concerning the role of the cannabinoid system in the modulation of AIS and its relation with axonal and dendritic development. We demonstrate a differential neuronal CB1R modulation of axonal and dendritic development, as well as a role of CB1R on the modulation of ankyrinG density at the AIS at different early developmental stages. Moreover, our data suggest that glial CB2Rs also participate in ankyrinG density maintenance.

MATERIALS AND METHODS

Reagents and Plasmids

2-AG, AM-251, AM630 and SR141716A were obtained from Tocris. UCM-03025 was a gift from María Luz Lopez Rodriguez laboratory (Complutense University, Madrid; Hernández-Torres et al., 2014). CB1R interference RNA and scrambled RNA plasmids (Origene) were a kind gift of Dr. Ismael Galve-Ropert (Universidad Complutense, Madrid) and were previously validated (Diaz-Alonso et al., 2012).

Animals

Animals were housed in a room at controlled temperature and relative humidity with alternating 12 h light and dark cycles and free access to food and water "*ad libitum*". Animal care protocols used in our laboratory are in conformity with the appropriate national legislation (53/2013, BOE no. 1337) and guidelines of the Council of the European Communities (2010/63/UE). All protocols were previously approved by the CSIC bioethics committee.

Neuronal Culture

Mouse hippocampal neurons were prepared as previously described (del Puerto et al., 2012, 2015). Neurons were obtained from E17 mouse hippocampi, which were incubated in a 0.25% trypsin solution in Ca^{2+}/Mg^{2+} free Hank's buffered salt solution (HBSS) and dissociated using fire-polished Pasteur pipettes. The cells were plated on polylysine-coated coverslips (1 mg/mL) at a density of 5000 cells/cm^2 for 2 h in plating medium (minimum essential medium [MEM], 10% horse serum, 0.6% glucose, Glutamax-I and antibiotics). Then coverslips were inverted and transferred to culture dishes containing astrocytes. Astrocyte medium was replaced by neuronal culture medium 24 h before neuronal culture (Neurobasal medium, B27 supplement, Glutamax-I). To avoid contact between neurons and astrocytes, paraffin beads were placed on coverslips before neuronal plating. 5 μM 1-β-D-arabinofuranosylcytosine (AraC) was added after 2 days in culture to avoid glial proliferation. Pharmacological treatments were applied as described in the "Results" Section. In the case of pharmacological treatments in the absence of glial cell layer, coverslips were transferred to plates containing glial cell-conditioned medium. Primary hippocampal neurons were nucleofected using the Amaxa nucleofector kit for primary mammalian neural cells (Amaxa Bioscience) according to the manufacturer's instructions. Nucleofection was performed using 3 μg of total DNA and 3×10^6 cells for each nucleofection. Neurons were plated at a density of 10,000 cells/cm^2 as described above. Nucleofection efficiency was ∼15% of neurons, based on the number of GFP-positive neurons. For Western-blot experiments, neurons were plated at a density of 50,000 cells/cm^2 and processed as previously described (Tapia et al., 2013).

Immunofluorescence

Neurons were fixed in 4% PFA, then coverslips were treated for 10 min with 50 mM NH4Cl and incubated in blocking buffer (0.22% gelatin, 0.1% Triton X-100 in PBS) for 30 min, before incubation with primary antibodies for 1 h at room temperature in blocking buffer. For CB1R staining, neurons were incubated for 30 min at 37°C with anti-CB1R antibody, then rinsed three times and fixed to continue the procedure with other antibody staining. The primary antibodies used were: chicken anti-MAP2 (1:10,000, Abcam), mouse anti-ankyrinG (1:100) from NeuroMab, anti-Tau-1 from Millipore (1:1000) and rabbit anti-CB1R (1:50) from Cayman (Cat. 101500). The secondary antibodies used were a donkey anti-mouse, anti-rabbit or anti-chicken Alexa-Fluor 488, 594, or 647 (1:1000). Phalloidin Alexa-Fluor 594 was used at a concentration of 1:100. Nuclei were stained using 4′,6-diamidino-2-phenylindole, and coverslips were mounted in Fluoromount G. Images were acquired on a vertical Axioskop-2 plus microscope (Zeiss) or a Leica SP5 confocal microscope under the same conditions to compare intensities. Figures were prepared for presentation using the Adobe CS4 software.

Dendrites, Axon and AIS Measurements

Quantification of fluorescence intensity at the AIS was performed in neurons from at least three independent experiments. Measurements of ankyrinG fluorescence intensity were performed on confocal images. Using ImageJ software we drew a line starting at the limit of neuronal soma identified by MAP2 staining, and extended it along the ankyrinG staining or the GFP signal of the axon. Data from every 0.16 μm along the first 40 μm were obtained and smoothed using the Sigmaplot software to obtain average ankyrinG fluorescence intensity every 1 μm. Data were normalized in each neuron considering the value of maximum mean fluorescence in control neurons to be 100%. Total fluorescence intensity for each neuron was obtained by adding ankyrinG fluorescence values from 0 μm to 40 μm. AIS start, end and maximum fluorescence intensity were determined following the criteria described in Grubb and Burrone (2010). Taking 100% fluorescence as the maximum fluorescence intensity point, start and end points were defined as the points were fluorescence intensity is lower than 33%.

Dendrite and axon lengths were obtained based on MAP2 or Tau-1 staining using NeuronJ software to measure the length of dendritic arbor in each neuron or the axonal length including ramifications. In order to study correlations between dendrites and AIS fluorescence, both data were obtained from the same neurons.

Statistical Analysis

All statistical analyses were carried out in Sigmaplot v12.5 (Systat Software Inc., San Jose, CA, USA) and Prism 6 (GraphPad Software, Inc., La Jolla, CA, USA). Data for each independent sample were obtained from at least three independent experiments. Data from each experiment were collected from at least 30 cells (between 30 and 50 cells) in each experimental condition. Statistical analysis was performed by *t*-test for two group comparisons and one-way ANOVA for multiple group comparisons. When data were non-normally distributed, non-parametric tests were used: Mann-Whitney Rank test for two independent samples and Kruskal-Wallis for analysis of multiple groups. In the analysis of multiple comparison, a *post hoc* analysis was performed using Bonferroni's (in the case of ANOVA) or Dunn's test (in the case of Kruskal-Wallis). All *p*-values were adjusted to account for multiple comparison. Cell-to-cell analysis of dendrite length and ankyrinG fluorescence was performed using Prism 6 and Sigmaplot v12.5 with a Pearson product moment test. Differences were considered significant when $p < 0.05$.

RESULTS

CB1Rs Modulate Axonal and Dendritic Development

In order to understand how cannabinoids may modulate neuronal development, we studied their role during axonal growth and dendrite development. First, we analyzed the expression of CB1R in cultured hippocampal neurons using a polyclonal antibody directed against the N-terminus of the receptor (Howlett et al., 1998). CB1R was detected by Western-blot after 2 days *in vitro* (2 DIV) and its expression progressively and markedly increased until 13 DIV (**Figure 1A**). Next, we analyzed its membrane subcellular localization by immunocytochemistry at different developmental stages. Consistent with previous reports (Irving et al., 2000), the analysis of receptor immunoreactivity revealed a punctate pattern along the axon and at the growth cone in 2-DIV neurons (**Figure 1B**). While the same pattern of staining was conserved in older neurons (6 DIV), no CB1R expression was detected in dendrites or in the AIS (**Figure 1C**). Based on this specific pattern of subcellular localization of CB1R, we sought to determine whether CB1R could be involved in axonal elongation. Hippocampal neurons were cultured since plating until 2 DIV in the presence of 2-AG (3 μM) alone or in combination with the CB1R antagonists AM251 (3 μM) or SR141716A (1 μM; **Figure 1D**). Axon length was increased by 40% in neurons treated with only 2-AG (408.03 ± 19.92 μm compared to 288.12 ± 12.97 μm in non-treated control neurons, Kruskal-Wallis, Dunn's multiple comparison test, $p < 0.0001$, **Figure 1E**). However, treatment of neurons with two different CB1 antagonists had no effect on axonal growth (286.74 ± 13.07 μm for AM251 and 282.03 ± 19.52 μm for SR141716A vs. 288.12 ± 12.97 μm in control neurons, Kruskal-Wallis, Dunn's multiple comparisons test, **Figure 1E**). In order to demonstrate that axonal elongation following 2-AG application was specifically due to CB1R activation, neurons were pre-incubated for 1 h with the CB1R antagonists AM251 or SR141716A before 2-AG application (**Figure 1E**). The addition of CB1R antagonists prevented the 2-AG-mediated increase in axonal elongation (273.21 ± 18.1 μm for 2-AG + AM251 and 283.28 ± 23.1 μm for 2-AG + SR141716A vs. 408.03 ± 19.92 μm in 2-AG treated neurons, $p < 0.0001$ and $p < 0.05$, and 288.12 ± 12.97 μm in control neurons, Kruskal-Wallis, Dunn's multiple comparisons test, **Figure 1E**), confirming that CB1R activation promotes axonal elongation. In addition, 2-AG treatment also increased axonal ramification and, as observed for axonal elongation, this increase was prevented when neurons were pre-incubated for 1 h with the CB1R antagonists (**Figure 1F**). Moreover, we tested the effect of increasing endogenous levels of 2-AG by using UCM-03025, a monoacylglycerol lipase (MAGL) inhibitor that prevents 2-AG degradation (Hernández-Torres et al., 2014). Similar to what occurred when neurons were treated with 2-AG, MAGL inhibition also promoted axonal elongation (467.54 ± 25.35 μm for UCM 1 μM vs. 324.15 ± 14.42 μm in control neurons, Kruskal-Wallis, Dunn's multiple comparisons test, $p < 0.0001$, **Figure 1G**).

Our results are in agreement with the increased density of axonal markers observed during the development of zebrafish treated with the CB1 agonist WIN55212-2 (Gilbert and Soderstrom, 2014). However, while these authors showed an increased density of dendritic proteins after CB1R activation during development (but not in adult), we did not detect CB1R expression in dendrites. In this regard, while somatodendritic CB1R visualization is difficult using immunocytochemical and/or immunohistochemical approaches, new evidence of functional CB1Rs in postsynaptic dendritic domains have been provided by electrophysiological (Bacci et al., 2004; Marinelli et al., 2009) and live imaging studies (Leterrier et al., 2006; Ladarre et al., 2015). To test whether CB1R had an effect on dendritic development, hippocampal neurons were cultured until 6 DIV and treated at 0, 2 and 4 DIV with 2-AG or CB1R antagonists alone or combined (**Figure 2A**). Unlike what was observed for axonal growth, neither 2-AG nor UCM-03025 treatments did significantly modify the total dendritic length (433.18 ± 22.75 μm for 2-AG and 524.8 ± 34.28 μm for UCM μm vs. 422.06 ± 20.25 μm in control neurons, Kruskal-Wallis, Dunn's multiple comparisons test, **Figure 2B**). However, when neurons were treated with CB1R antagonists, total dendritic length was reduced to less than 50% of the control value (204.18 ± 14.06 μm for AM251 and 191.07 ± 16.56 μm for SR1141716A vs. 422.06 ± 20.25 μm in control neurons, Kruskal-Wallis, Dunn's multiple comparisons test, $p < 0.0001$ **Figure 2B**). The same result was obtained when antagonists were applied in combination with 2-AG. Altogether, these data suggest a differential modulation of somatodendritic and axonal morphologies by CB1Rs: CB1R basal activity seems necessary for adequate dendrite development, while axon growth does not require CB1R activity, although application of exogenous 2-AG can potentiate axon growth.

Cannabinoid Receptors and Axon Initial Segment Development

Since theoretical mathematical models have shown that dendritic size and/or morphology influence AP onset and AIS plasticity (Eyal et al., 2014; Gulledge and Bravo, 2016), we hypothesized that the basal CB1R activity related to dendritic development described here could also influence AIS development. Thus, we investigated whether CB1R had an effect on AIS formation and maturation. For that purpose we analyzed the density of one of the main proteins of the AIS, ankyrinG, in different experimental conditions modulating both the activity and the expression of CB1Rs. First, we analyzed the possible role of CB1R on the formation and initial development of the AIS. We treated hippocampal neurons every other

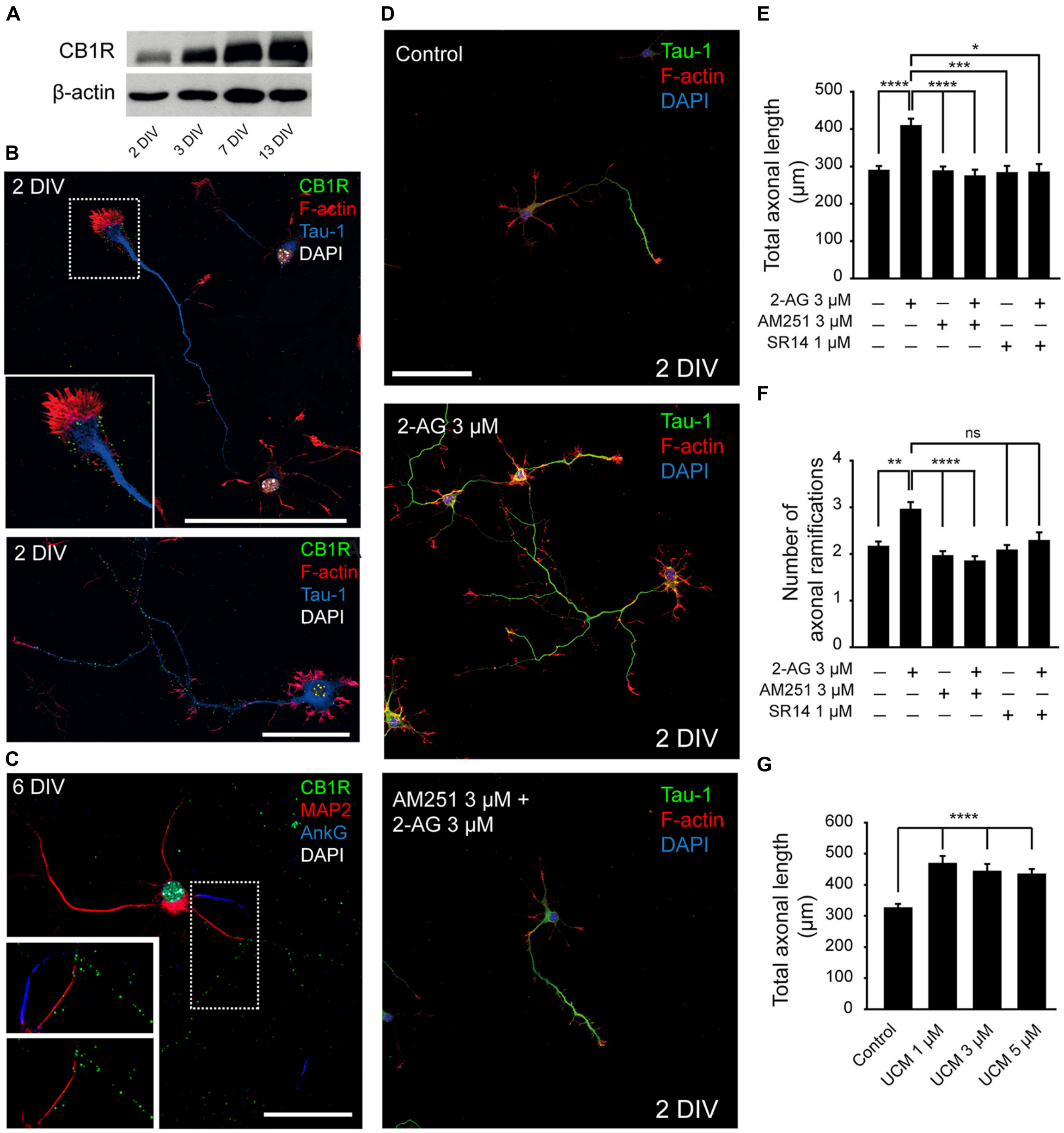

FIGURE 1 | Modulation of axonal growth by the type-1 cannabinoid receptor (CB1R). (A) Western-blot showing CB1 receptor total expression levels on 2, 3, 7 and 13-days *in vitro* (DIV) hippocampal neurons. **(B)** CB1 receptor (green) expression in 2-DIV hippocampal neurons. Growth cones are stained with phalloidin-Alexa 594 (red), axons with Tau-1 antibody (blue) and nuclei with DAPI (white). The inset shows a magnification of the growth cone region. Note that CB1 receptors show a punctate staining and are mainly concentrated in the axonal growth cone and along the axonal shaft (image below). **(C)** CB1 receptor (green) expression in 6-DIV hippocampal neurons. CB1 receptors are expressed along the axon and are not detected by immunofluorescence in the dendrites (red) or the axon initial segment (AIS; blue). Magnification of the image is shown below with or without AIS marker staining (AnkyrinG, blue). **(D)** 2-DIV hippocampal neurons treated with 2-Arachidonylglycerol (2-AG) or 2-AG in combination with AM251 from plating until 2 days. Neurons were stained using a Tau-1 antibody and Phalloidin for better recognition of neuronal and axonal morphology. Scale bar = 100 μm. **(E–G)** Bar plots representing the mean ± SEM of axonal length or total number of axonal ramifications of 2-DIV hippocampal neurons treated with CB1R antagonists, and/or agonist **(E,F)** or treated with monoacylglycerol lipase (MAGL) inhibitor UCM03025 **(G)**. Data were acquired from three independent experiments (30 neurons/experimental condition in each experiment). Kruskal-Wallis, Dunn's multiple comparisons test. Adjusted p values: $^{*}p < 0.05$, $^{**}p < 0.01$, $^{***}p < 0.001$, $^{****}p < 0.0001$; ns, non-significant.

day (0, 2 and 4 DIV) until 6 DIV with 2-AG and CB1R antagonists alone or combined, as mentioned above for the analysis of dendrites (**Figures 3A,B**). As shown for dendritic development, 2-AG or UCM-03025 treatments did not modify the ankyrinG fluorescence signal compared to control neurons (100 ± 3.58% for control neurons vs. 98.93 ± 2.62% for 2-AG and 92.87 ± 2.24% for UCM, ANOVA, Bonferroni multiple comparisons test, **Figure 3C**). By contrast, CB1R inhibition with

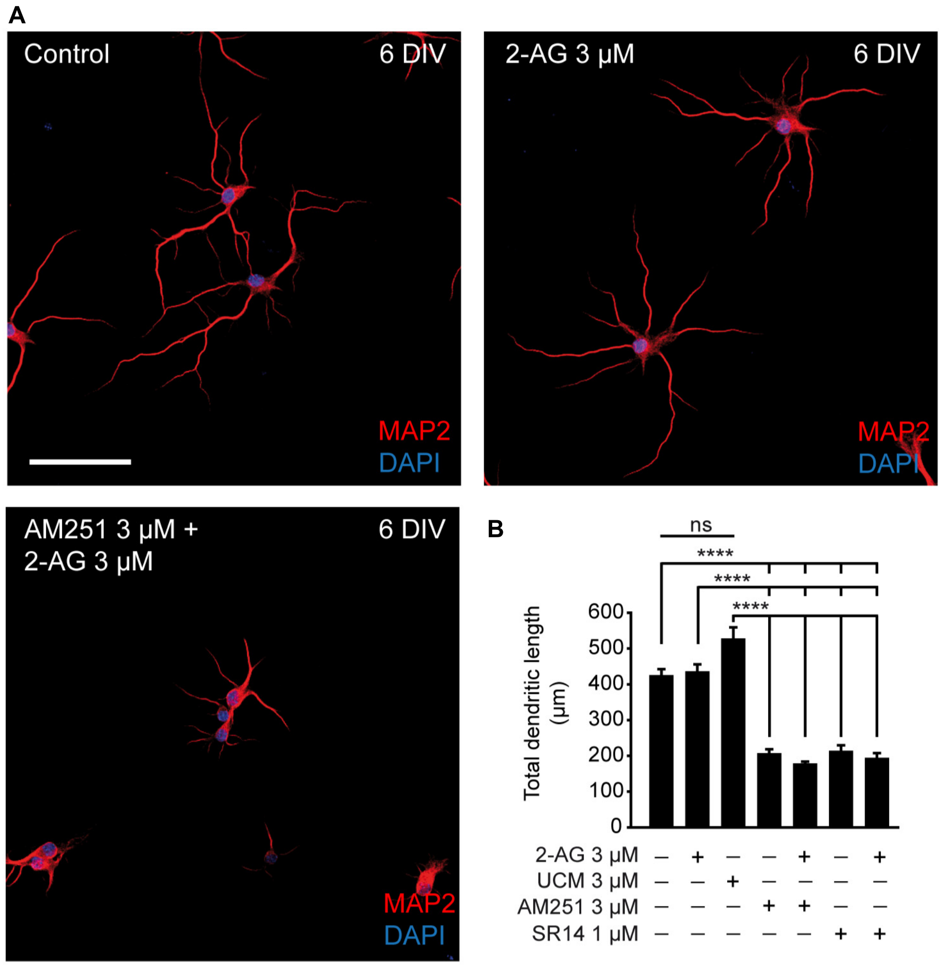

FIGURE 2 | CB1R activity is necessary for dendritic development. (A) 6-DIV hippocampal neurons treated with CB1R antagonists, and/or agonist or treated with the MAGL inhibitor UCM03025. Drugs were first added after plating and treatment was repeated every other day. After 6 days in culture, neurons were stained with MAP2 antibody to detect the somatodendritic domain and DAPI for nuclei. Scale bar = 100 μm. **(B)** Bar plots representing the mean ± SEM of total dendritic length. Data were acquired from three independent experiments (30 neurons/experimental condition in each experiment). Kruskal-Wallis, Dunn's multiple comparisons test. Adjusted p values: $^{****}p < 0.0001$; ns, non-significant.

AM251 or SR141716A alone or in combination with 2-AG reduced the ankyrinG signal by ~30% (70.39 ± 3.16% for AM251, 69.73 ± 1.76% for SR141716A, 71.29 ± 4.97% for AM251 + 2-AG and 70.48 ± 6.73% for SR141716A + 2-AG vs. 100 ± 3.58% in control neurons, ANOVA, Bonferroni multiple comparisons test, $p < 0.01$ **Figure 3C**). These results clearly suggest that CB1R activity modulates AIS formation during early development *in vitro*, and that a basal CB1R activity is necessary for initial dendritic formation and AIS accumulation of ankyrinG.

We then wondered whether CB1R activity could also participate in AIS maintenance and maturation at later stages of development after dendritic maturation has started. Thus we treated 7-DIV hippocampal neurons daily for 3 days, until 10 DIV, with 3 μM 2-AG or 3 μM AM251 (**Figures 4A,B**) and then we analyzed the expression of ankyrinG along the AIS (**Figure 4C**) and the total ankyrinG expression in the AIS (**Figure 4D**). As had been observed for dendrites, treatment with 2-AG did not significantly increase ankyrinG intensity in the AIS (110.28 ± 3.17% vs. 100 ± 2.72% in control neurons), whereas CB1 inhibition with AM251 decreased ankyrinG intensity by ~20% (82.94 ± 2.9%, Kruskal-Wallis, Dunn's multiple comparisons test, $p < 0.0001$, **Figure 4E**). No change in AIS length or position was observed (**Figure 4E**). However, the maximum fluorescence intensity position shifted slightly and significantly by 2 μm towards the soma in AM251-treated neurons compared to control neurons (Kruskal-Wallis, Dunn's multiple comparisons test, $p < 0.05$). In addition, no apparent changes in dendritic arbor were observed after 2-AG or AM251 treatments. Thus, while CB1R activity modulates the initial development of dendrites, at least *in vitro*, CB1R inhibition after 7 DIV does not affect the growth of dendrites, and is only necessary for AIS maturation.

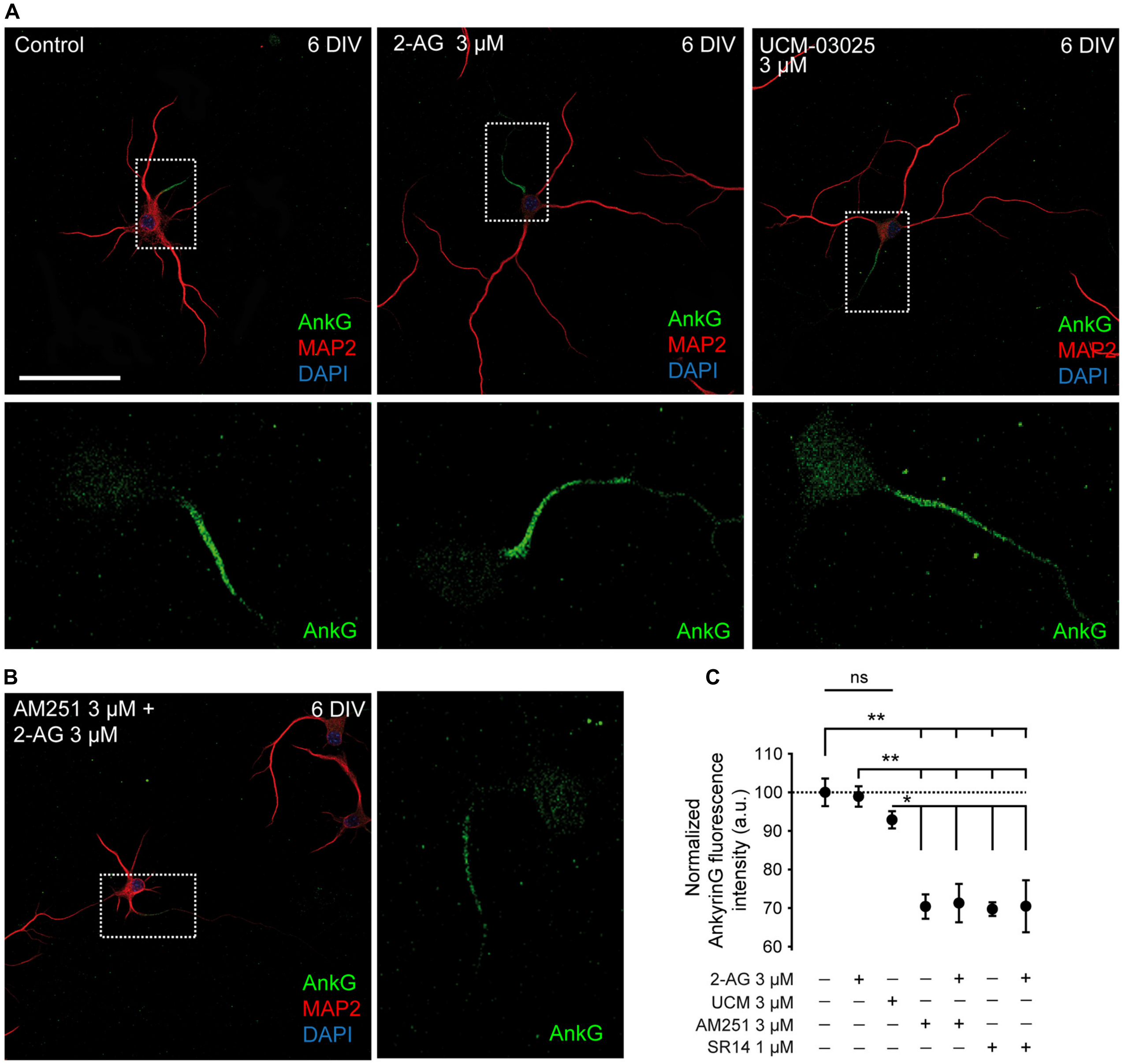

FIGURE 3 | CB1R inhibition decreases ankyrinG expression at the developing AIS. (A,B) 6-DIV hippocampal neurons treated with 2-AG or UCM-03025 **(A)**, or 2-AG in combination with AM251 **(B)**. AIS domain stained for ankyrinG is included in a box and its magnification shown below **(A)** or in the right **(B)** for every image. Drugs were first added after cell plating and treatment was repeated every other day. After 6 days in culture, neurons were fixed and stained for MAP2 (red) to visualize somatodendritic compartment, and ankyrinG (AnkG, green) to visualize the AIS. All images were acquired using the same fluorescence parameters. Scale bar = 100 μm. **(C)** Bar plots representing the mean ± SEM of normalized AnkyrinG total fluorescence intensity along the AIS. Data were acquired from three independent experiments (30 neurons/experimental condition in each experiment). ANOVA, Bonferroni multiple comparisons test. Adjusted *p* values: $^{**}p < 0.01$; $^{*}p < 0.05$; ns, non-significant; a.u., arbitrary units.

One more point that needs to be considered is the fact that CB1R expression and activity in astrocytes (Navarrete and Araque, 2010) may be essential at these developmental stages for proper control of neuronal excitability. Indeed, CB1R activation in astrocytes can trigger the astrocytic release of neurotransmitters onto neurons (Gómez-Gonzalo et al., 2015). On the other hand, while CB2R expression in astrocytes and neurons in physiological conditions is controversial (Stella, 2010), this receptor has a role in embryonic and neural progenitors (Palazuelos et al., 2012). Thus, we tested whether CB2R activation by 2-AG or any possible non-CB1 effect of AM-251 on CB2R (Pertwee, 2005) could be responsible for AIS changes. First, we cultured 7-DIV hippocampal neurons for 3 days in the presence or absence of a layer of astroglial cells (**Figures 5A,B**). In the absence of glial cells, neurons were cultured in glial cell-conditioned medium. Neurons were

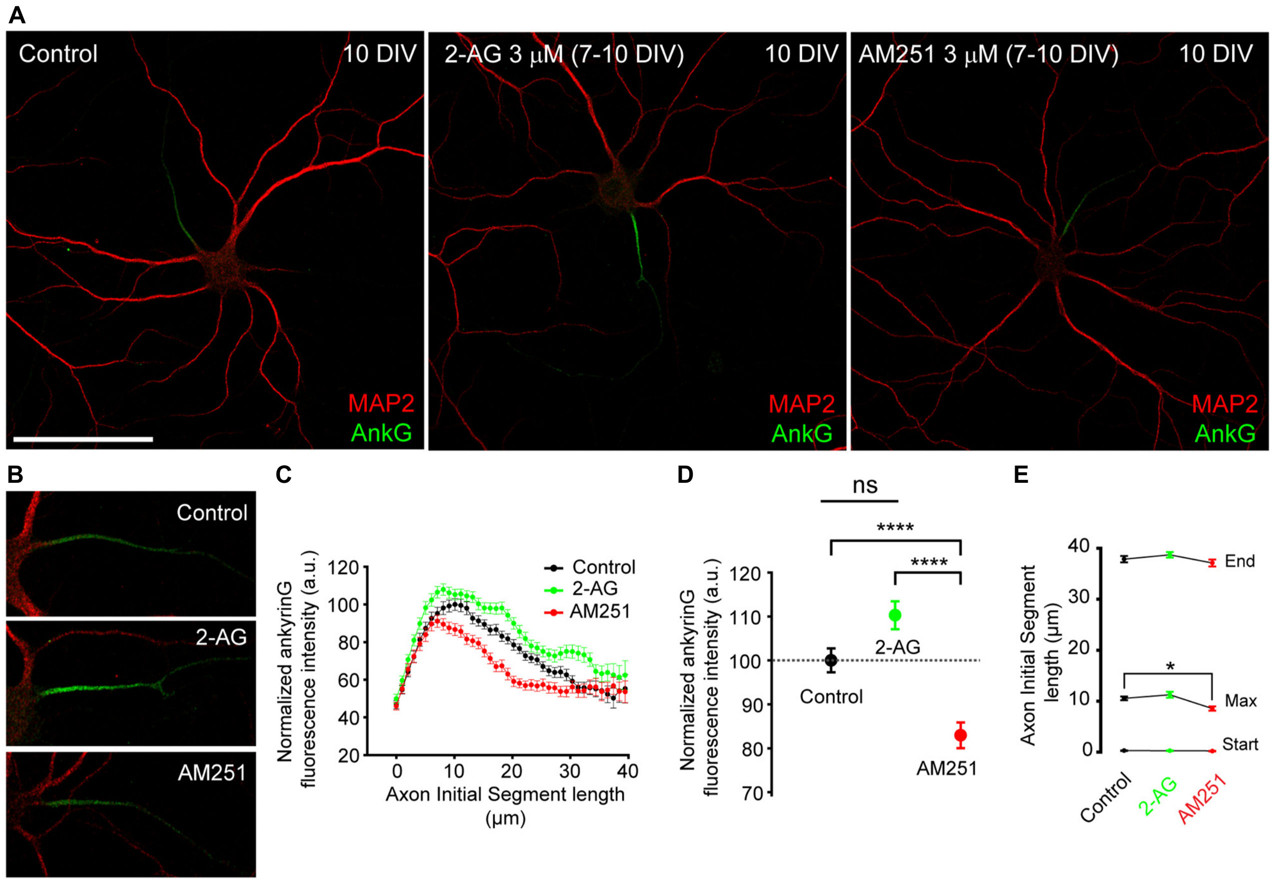

FIGURE 4 | CB1R inhibition, after dendrites formation, diminishes ankyrinG expression at the AIS. (A,B) 10-DIV hippocampal neurons treated daily with cannabinoid receptor agonist 2-AG or CB1R antagonist AM251 from 7 to 10 days. High-magnification pictures of the AIS of each neuron are shown in **(B)**. Scale bar = 100 μm. **(C)** AnkyrinG fluorescence intensity profile along the AIS in control, 2-AG- or AM251-treated neurons. Data were acquired from three independent experiments (30 neurons/experimental condition in each experiment). **(D)** Normalized ankyrinG total fluorescence intensity at the AIS of neurons represented in **(C)**. **(E)** Graph representing the mean ± SEM of the start and end positions of the AIS, as well as, the position of the maximum fluorescence intensity at the AIS for each experimental condition. Kruskal-Wallis, Dunn's multiple comparisons test. Adjusted *p* values: $^{*}p < 0.05$; $^{****}p < 0.0001$, ns, non-significant; a.u., arbitrary units.

treated daily for 3 days with the CB2R antagonist AM630 (100 nM) and then we analyzed ankyrinG intensity along the AIS (**Figures 5C,D**). Interestingly, the presence of a glial cell layer reduced ankyrinG maximal intensity by 20% when CB2 receptor was inhibited (83.55 ± 2.72% vs. 100 ± 2.75% in control neurons, Mann-Whitney Rank test, $p < 0.05$, **Figure 5E**). However, no change in ankyrinG intensity was detected in neurons treated in the absence of glial cells (95.61 ± 2.16% vs. 100 ± 2.95% in control neurons, Mann-Whitney Rank test, **Figure 5E**). Hence, while a neuron-specific CB2R effect on AIS maturation can be discarded, glial CB2Rs may also regulate the AIS.

In order to rule out that ankyrinG reduction due to CB1R antagonist could be due to CB1Rs expressed by glial cells, we nucleofected hippocampal neurons with plasmids expressing the CB1R interference RNA (shCB1) or its corresponding scrambled RNA (shScr). We used previously validated shRNAs that were able to suppress ∼50% of CB1R protein and mRNA expression in P19 cells (Diaz-Alonso et al., 2012). CB1R reduction in hippocampal neurons was confirmed by assessing CB1R expression in 3 DIV neurons nucleofected with shCB1 or shScr plasmids (**Figure 6A**) using a CB1R antibody that recognizes the extracellular N-terminal domain. CB1R signal was detected at the distal region of the axon only in shScr control neurons, while it was not detectable in shCB1 expressing neurons, confirming the validity of our plasmids. Then, we analyzed ankyrinG expression and dendrite length in nucleofected neurons kept for 5 DIV (**Figure 6B**). In 5-DIV shCB1 neurons, ankyrinG signal at the AIS was almost absent (2.46 ± 0.74% compared to 100 ± 13.73% shScr neurons, Mann-Whitney Rank test, $p < 0.001$, **Figure 6C**). Analysis of dendrite length in the same neurons showed a reduction in dendritic length of more than 50% in shCB1 neurons (159.88 ± 13.33 μm compared to 341.55 ± 24.35 μm in shScr neurons, Mann-Whitney Rank test, $p < 0.001$, **Figure 6D**). In order to confirm these results in neurons with a higher degree of dendritic development, we analyzed the data in

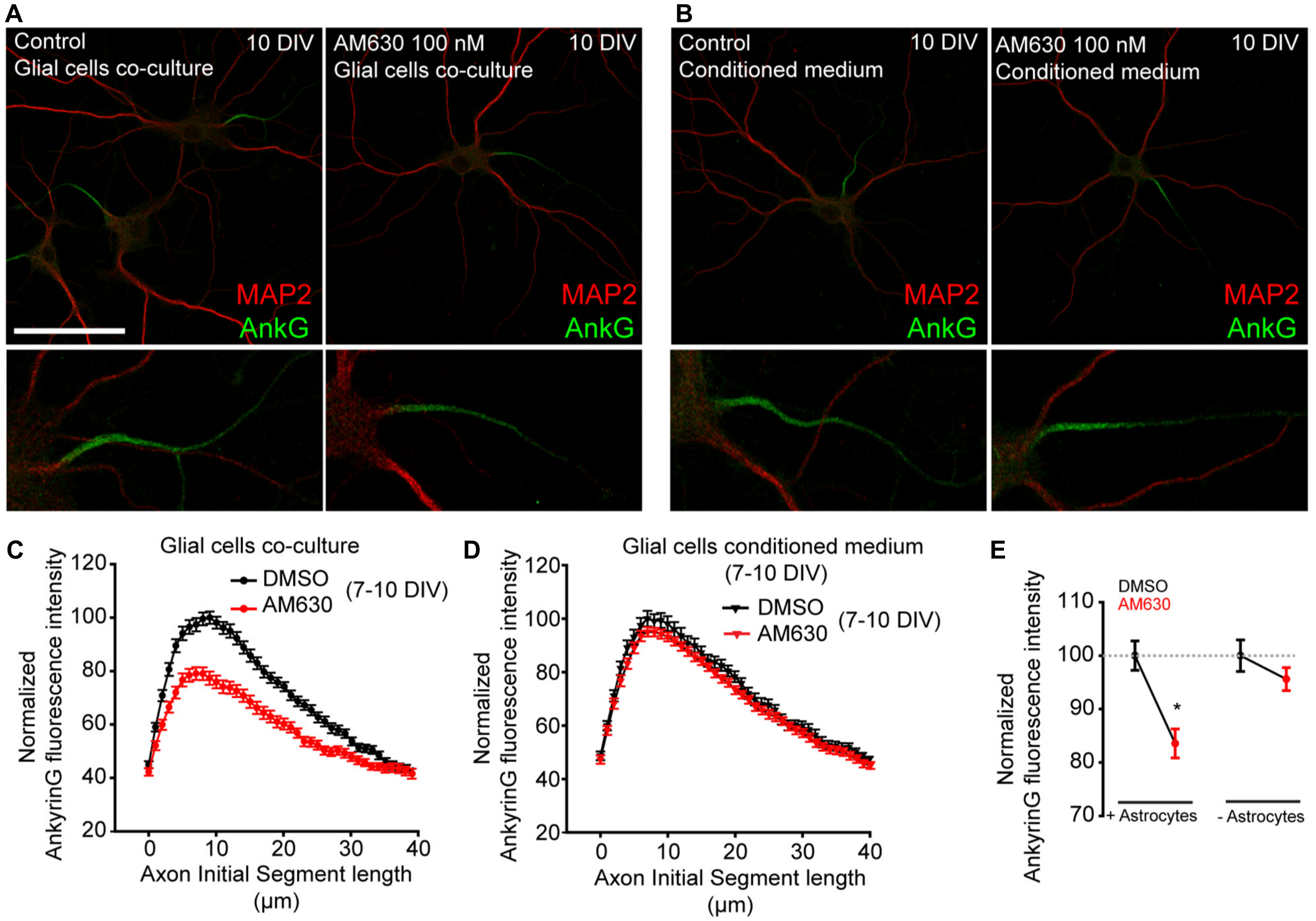

FIGURE 5 | Glial type-2 cannabinoid receptors (CB2Rs) modulation of AIS. (A,B) 10-DIV hippocampal neurons treated daily with the CB2R antagonist AM630 from 7 to 10 days. Neurons were grown in the presence of a glial cell layer until 7 days (co-culture). Then, one group was treated in the presence of glial cells **(A)** and the second group was transferred to other plates containing only conditioned medium **(B)**. Neurons were stained with the somatodendritic marker MAP2 (red) and ankyrinG (green). Scale bar = 100 µm. **(C,D)** Graphs representing normalized ankyrinG fluorescence intensity profile along the AIS in control or AM630-treated neurons in the presence **(C)** or absence **(D)** of glial cells. **(E)** Graph representing the normalized total ankyrinG fluorescence intensity at the AIS of neurons represented in **(C,D)**. Data were acquired from three independent experiments (30 neurons/experimental condition in each experiment). Mann-Whitney Rank test. $^{*}p < 0.05$.

9-DIV nucleofected neurons (**Figure 6E**). shCB1 neurons showed a clear reduction of ankyrinG staining all along the AIS (**Figure 6F**), and a total ankyrinG fluorescence intensity 30% lower than in shScr control neurons (69.2 ± 5.4% vs. 100 ± 6.24% in shScr neurons, Mann-Whitney Rank test, $p < 0.001$, **Figure 6G**), in line with the results obtained previously with CB1R antagonists (**Figure 3**). This reduction was not associated to any change in position, length or maximum fluorescence position. Therefore, these experiments demonstrate that the effects of CB1R antagonists are due to neuronal CB1R inhibition. Next, we analyzed dendrite length in 76 of these neurons (36 shScr; 40 shCB1) and, as had been observed for 5-DIV nucleofected neurons (**Figure 6D**) and 6-DIV neurons treated with CB1R antagonists (**Figure 2B**), dendrite length was significantly reduced. While control shScr 9-DIV neurons had a mean total dendritic length of 710.31 ± 44.7 µm, mean dendritic length of shCB1 neurons was only 518.96 ± 35.38 µm (**Figure 6H**, bar plot on the right, Mann-Whitney Rank test, $p < 0.01$). To test a possible relationship between dendrites and AIS, we performed a cell-to-cell correlation of these two parameters in both conditions (**Figure 6H**). Dendritic length and AnkyrinG intensity were found to be positively correlated in the whole neuronal population ($p < 0.001$, $n = 76$), but also in neurons of each experimental condition taken separately ($p < 0.005$ for 36 shScr neurons and $p < 0.01$ for 40 shCb1 neurons). Moreover, a positive correlation was also obtained between ankyrinG fluorescence intensity and dendritic length in 5-DIV neurons ($p < 0.0001$, Pearson product moment test). Altogether these results confirm that functional neuronal CB1Rs contribute, likely through dendritic growth regulation, to ankyrinG accumulation at the AIS in hippocampal neurons at both early and late stages of development. Moreover, our results also show that CB1R-mediated changes in AIS composition and dendritic growth are correlated at initial dendritic development

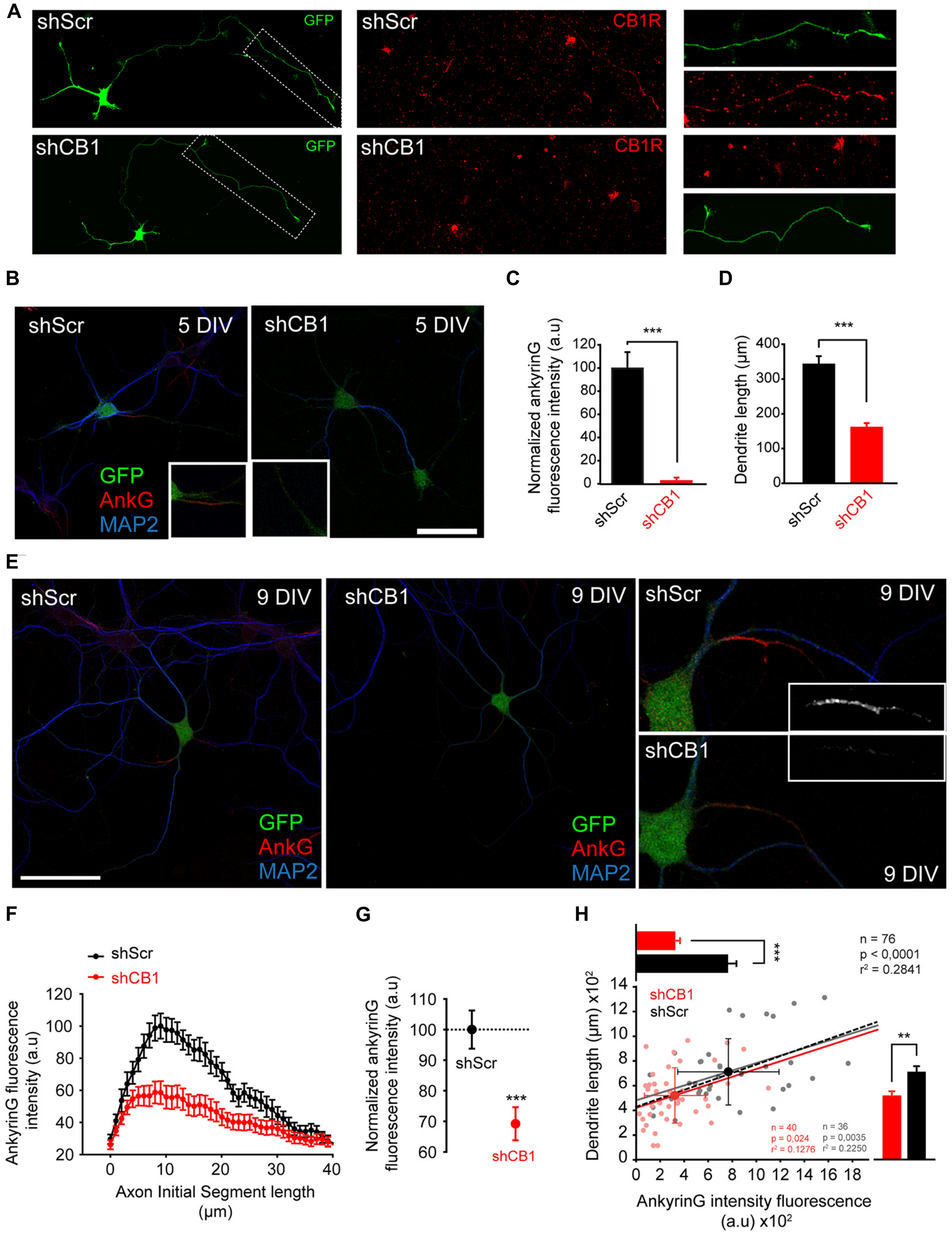

FIGURE 6 | Early CB1R suppression decreases ankyrinG concentration at the AIS and reduces dendritic length. (A) 3-DIV hippocampal neurons nucleofected with scrambled interference RNA (shScr) or CB1R interference RNA (shCB1). Nucleofected neurons were identified based on GFP fluorescence. Surface CB1 receptor expression (red) was identified using a CB1R antibody that recognizes an extracellular epitope at the N-terminal domain. Note that CB1R staining was performed in living neurons at 37°C and neurons were rinsed quickly before fixation, generating the observed background. **(B)** Representative images of 5-DIV hippocampal neurons nucleofected with CB1R interference RNA (shCB1) or scrambled interference RNA (shScr). Neurons were stained with MAP2 antibody (blue) and ankyrinG antibody (red). Nucleofected neurons were identified based on GFP fluorescence. Insets show the AIS region. Note the strong reduction of ankyrinG staining and dendritic length in 5 DIV shCB1 neurons compared to shScr neurons. **(C,D)** Bar plots representing the mean ± SEM of normalized total

(Continued)

FIGURE 6 | Continued
AnkyrinG fluorescence intensity along the AIS **(C)** and total dendritic length of 5-DIV nucleofected neurons (**D**, $n = 24$, 13 shScr, 11 shCB1).
(E) Representative images of 9-DIV hippocampal neurons nucleofected with CB1R interference RNA (shCB1) or scrambled interference RNA (shScr). Scale bar = 100 μm. The right panels show higher-magnification images of the AIS for the nucleofected neurons represented on the left panels. **(F)** AnkyrinG fluorescence intensity profile along the AIS of shScr- or shCB1-nucleofected neurons. Data were obtained from at least 40 neurons of each condition from three independent experiments. **(G)** Normalized ankyrinG total fluorescence intensity at the AIS for the neurons represented in **(B)**. Mann-Whitney Rank test *** $p < 0.001$. **(H)** Cell-to-cell analysis of the relationship between dendrite length and ankyrinG total fluorescence intensity at the AIS in 9-DIV nucleofected neurons. Scatter plot illustrating the significant correlation between ankyrinG intensity fluorescence (x-axis) and dendrite length (y-axis) of 76 nucleofected neurons (36 shScr, gray dots; 40 shCB1, light red dots). Regression lines and the r^2 and p values for all neurons (black), for shScr neurons (gray) and shCB1 neurons (red) are indicated on the graph (Pearson product moment test). Bright colored dots represent the average (± SD) for the two groups. The bar plots shown on the right and top of the graph represent the mean (± SEM) for the cells plotted for each group, and significant statistical differences are represented. Mann-Whitney Rank test. ***$p < 0.001$, **$p < 0.01$. a.u., arbitrary units.

stages. Thus, a CB1 basal activity is necessary during very early neuronal development for AIS development and maturation. Further studies are necessary to understand which role pre- and post-synaptic CB1Rs may play on AIS maturation and plasticity within intact networks.

DISCUSSION

The ECS was initially characterized as a retrograde synaptic signaling system in the adult brain, where postsynaptically released eCBs bound to presynaptic CB1 receptors in GABAergic terminals (Katona et al., 1999; Ohno-Shosaku et al., 2001; Wilson and Nicoll, 2001). However, the classical view of the ECS in the CNS has dramatically changed over the last two decades, and in this new scenario the eCB system has been reported to regulate functions in many neuronal subtypes, in different subcellular locations, and to be associated with a plethora of down-stream modulators (Busquets Garcia et al., 2016; Lu and Mackie, 2016). Moreover, during CNS development the eCB system undergoes readjustments at multiple levels, showing the tremendous complexity of its effects on neuronal physiology (Katona and Freund, 2012).

In this study, we focused on the role of the eCB system during different stages of *in vitro* axonal, dendritic and AIS development. We show for the first time that neuronal CB1R basal activity indirectly contributes to AIS proteins accumulation during AIS initial development through the modulation of early developmental dendritic growth. Our data demonstrate that neuronal CB1Rs modulate axonal and dendritic morphology in very early stages of development. Moreover, our results demonstrate a correlated influence of these receptors on dendritic length and ankyrinG density at the AIS. In addition, we have identified a more modest role for glial CB2R in AIS modulation. These results suggest that a fine-tuned eCB signaling early in neuronal development acts as a modulator and coordinator of neuronal morphology and AIS composition (**Figure 7**).

Modulation of Axonal and Dendritic Development by Cannabinoids

Our results show that CB1R is immunodetected in the distal part of the axon. However CB1R activity is not essential for axon establishment or the proper elongation of the axon at initial developmental stages, although its activation by 2-AG potentiates axonal growth and ramification in cultured hippocampal neurons. Several groups have suggested that CB1R antagonism/agonism can either promote or inhibit axon elongation and/or ramification depending on the agonist or antagonist used, the time of exposure, the age of culture and the type of neurons used (Gaffuri et al., 2012). Moreover, the strength of coupling of CB1Rs to downstream signaling pathways seems to also depend on the neuronal population considered: while CB1Rs are expressed at lower densities in glutamatergic neurons compared to GABAergic neurons, they are more strongly coupled to G-protein signaling in the first cell type (Steindel et al., 2013). These glutamatergic neurons represent 95% of the neurons in our primary cultures (Benson et al., 1994). Thus, differences between experimental models may partially explain the heterogeneity of data. In this study, we clearly demonstrate that an increase in 2-AG levels (exogenous or endogenous—induced by MAGL inhibition) potentiates axonal growth of hippocampal neurons *in vitro* in a CB1R-dependent manner. The question remains whether the effect of CB1R on axon elongation and ramification is direct or indirect. CB1R activation has been shown to induce the expression of trophic factors, such as BDNF, that promote axon growth and branching (Danzer et al., 2002; Derkinderen et al., 2003; Marsicano et al., 2003). Moreover, several studies showed a crosstalk between tyrosine kinase receptors and the eCB system in several neuronal subtypes: CB1R can form complexes and trans-activate TrkB receptors (Berghuis et al., 2005) or couple activated FGF receptors to an axonal growth response in cultured neurons (Williams et al., 2003). In addition, CB1R is also linked to other signaling pathways involved in neuronal differentiation and axonal growth (Keimpema et al., 2011; Galve-Roperh et al., 2013), such as the PI3K-Akt-GSK3 pathway (Ozaita et al., 2007) or JNK (Rueda et al., 2000).

Regarding dendritic development and unlike what happens during axonal development, triggering CB1R activation by 2-AG has no effect on dendritic elongation. However, our results point to a basal CB1R activity necessary for dendritic development, suggesting a CB1R differential regulation of axonal and dendritic development. Although our results show an axonal distribution of CB1R by immunofluorescence, CB1R may have a transient expression in dendrites after which somatodendritic endocytosis may contribute to target the receptor to the axon (Leterrier et al., 2006; McDonald et al., 2007). This axonal polarization process due to somatodendritic endocytosis has been described for other proteins in neurons (Garrido et al., 2001; Sampo et al., 2003). This differential regulation of axon and dendrites development by CB1R can be explained by differential basal

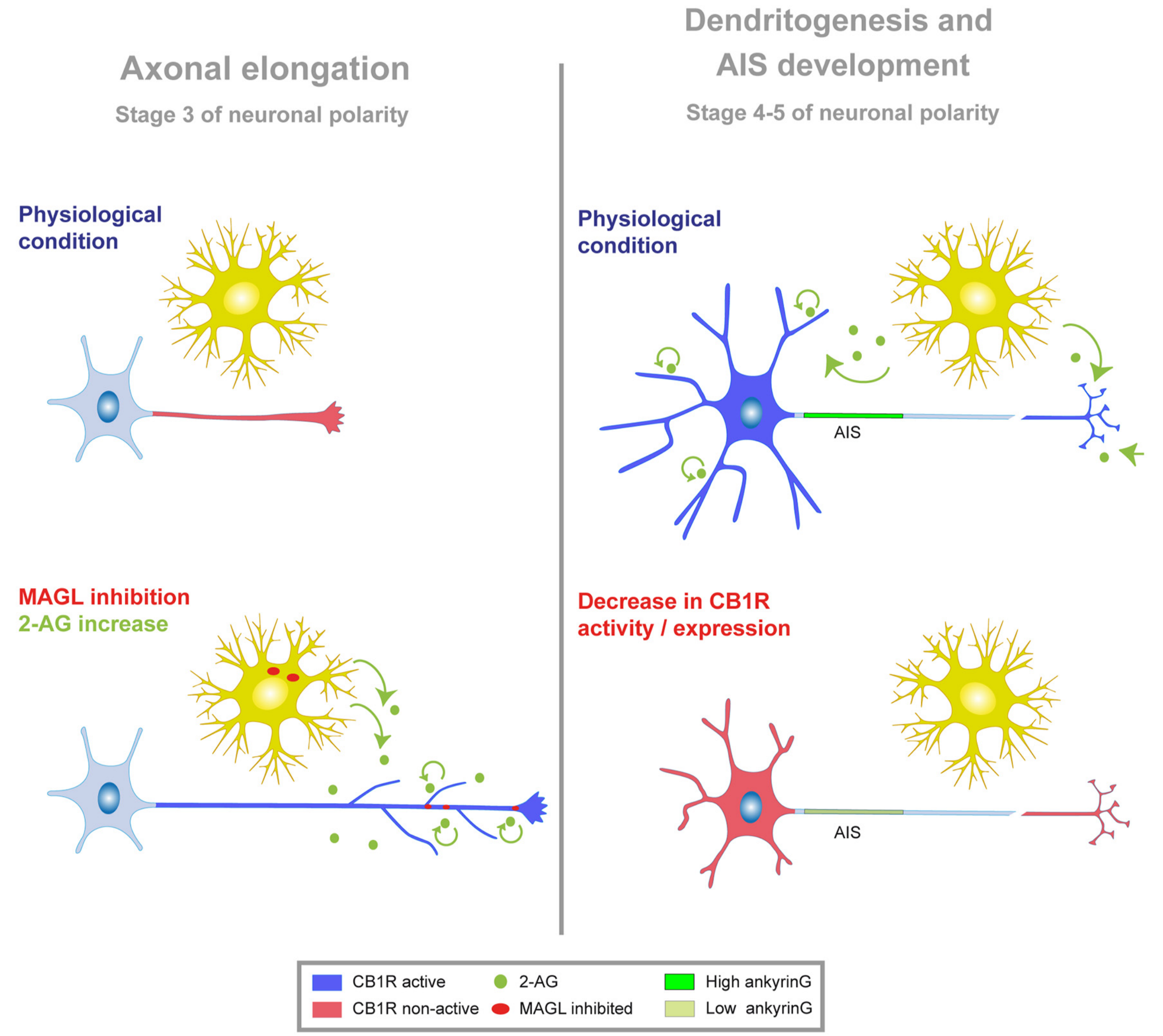

FIGURE 7 | Model of CB1R modulation of neuronal morphology and AIS. Schematic showing the functional implication of CB1R activity at different stages of neuronal development *in vitro*. Neuronal developmental stages 1–5 have been defined previously by Dotti et al. (1988). Stage 3 is characterized by axonal polarization and elongation, while dendritogenesis and AIS development occurs from stages 4–5. In both cases, figures represent the effect of CB1R inhibition or suppression at stage 1, when neurons are not yet polarized. Left, during initial stages of neuronal polarization and axonal elongation, CB1Rs display low or negligible activity (red) in the axon. Exogenous or endogenous increase of 2-AG level (through MAGL inhibition, red dots; or exogenous application, green dots) promotes axonal elongation and branching through CB1R activation (blue). Evidence so far suggests that endogenous 2-AG may come from glial or neuronal cells. Right, at later stages of neuronal development (stages 4–5), CB1R activity (blue) in the dendrites and/or in the axons terminals and synapses contributes to dendritic and AIS development. Reducing CB1R activity or expression (red) impedes dendritic growth and reduces ankyrinG levels in the AIS.

activity of the receptor in each domain. CB1Rs are constitutively active in dendrites due to 2-AG local production, while axonal CB1Rs are not constitutively active (Ladarre et al., 2015). Local dendritic 2-AG production may explain why exogenous addition of 2-AG does not promote dendritic growth, while CB1R inhibition impairs dendritic elongation. On the other hand, the fact that axonal CB1Rs have no basal activity may explain why CB1R antagonists have no effect, and why only exogenous CB1R activation promotes axonal growth. This subcellular difference in CB1R activity may lead to differential inhibition of adenylyl cyclases and differences in cAMP and cGMP concentrations in both neuronal compartments. In fact, higher cAMP levels in axons are associated with axon formation and elongation, while dendritic development correlates with lower cAMP levels and higher cGMP levels (Shelly et al., 2010). Thus, the difference of CB1R activity and signaling between both compartments may explain the opposite results obtained with 2-AG and CB1R antagonists between axons and dendrites.

Endocannabinoid System and Axon Initial Segment Formation and Maturation

Development of neuronal domains follow a well-defined time course in cultured hippocampal neurons (Dotti et al., 1988), where AIS initial formation and maturation take place after early axonal elongation and coincides with initial dendritic development. In this study, we demonstrate that functional neuronal CB1Rs participate in the regulation of AIS proteins composition, through the modulation of dendritic development. CB1R inhibition or knockdown reduced ankyrinG expression at the AIS, while CB1R activation had no significant effect on ankyrinG levels. Since CB1R location at the AIS has not been detected so far, we can hypothesize that axonal or dendritic CB1R activity is responsible for the changes in ankyrinG density we observed. In our low-density cultures and during early stages of development, neurons have not yet developed dendritic spines and neuronal connectivity is very low, making the hypothesis of a CB1R effect on dendrites the most plausible hypothesis to explain AIS changes during these stages. In fact, we demonstrate a significant positive correlation between dendritic length and ankyrinG levels in both control neurons expressing CB1R or neurons where CB1R expression was knocked down using RNA interference. In other words, our results show that a tonic CB1R activation would be critical for a proper initial dendrite growth, which modulate subsequent AIS development and maturation. This dendritic-AIS correlation only occurs when CB1R activity is impaired from very early stages of development. Nevertheless, CB1R inhibition at later stages of development (6 DIV, after dendrite maturation has started and neuronal connectivity increases) affects the AIS by reducing ankyrinG density. Thus, at later stages, we cannot rule out that reduced CB1R presynaptic activity may also participate in the modulation of AIS when dendritic development is not impaired by CB1R inhibition. Previous studies have shown a relationship between axonal and dendritic growth and ankyrinG density at the AIS. For example, impaired activity of the tubulin deacetylase HDAC6 reduces axonal and dendritic growth in early stages of development, and at the same time reduces AIS protein density (Kim et al., 2009; Tapia et al., 2010). Also, a recent study from the Südhof laboratory described a tight relationship between dendritic size, axonal growth and ankyrinG density at the AIS in neurons after L1CAM conditional deletion (Patzke et al., 2016). Moreover, a very recent study demonstrates that AIS distance to the soma in cortical layer 5 pyramidal adult neurons inversely correlates with dendritic complexity (Hamada et al., 2016), supporting the idea that dendritic morphology and AIS might be regulated in a coordinated manner in several neuronal types. Taking these studies and our results into account, change in dendritic morphology induced by CB1R lack of function is the more plausible hypothesis to explain AIS changes. However, we cannot rule out the existence of a direct effect on AIS due to unknown mechanisms.

These results raise the question of which mechanisms, and related molecules and receptors, are involved in the CB1R-mediated modulation of the AIS. CB1R signaling mechanisms are highly complex and diverse, and these receptors have many other effectors apart from their canonical targets (see "Introduction" Section). Somatodendritic CB1Rs play a key role in short-term regulation of intrinsic excitability through the activation of GIRK channels (Bacci et al., 2004; Marinelli et al., 2009) but also by regulating the baseline levels of the I_h current (hyperpolarization-activated cationic current) in pyramidal hippocampal neurons (Maroso et al., 2016). Moreover, presynaptic CB1Rs are widely involved in short and long-term plasticity events at inhibitory and excitatory synapses (Chevaleyre et al., 2006; Kano et al., 2009). Thus, secondary changes in AIS maybe attributed to CB1R mediated changes in intrinsic excitability and/or in synaptic strength. CB1R may exert these neuromodulatory effects cooperating with other receptors, such as glutamate receptors (Varma et al., 2001), or even modulating the release of neurotransmitters, such as glutamate (Gerdeman and Lovinger, 2001). For instance, a crosstalk between purinergic receptors and the ECS has been proposed. In fact, several groups have recently reported that the purinergic system may participate in cannabinoid-dependent synaptic modulation, thus demonstrating the existence of a crosstalk between these two families of receptors (Kovacs et al., 2011; Ievglevskyi et al., 2012). Similar to what has been observed for CB1Rs, purinergic receptors are absent from the AIS but are expressed in the somatodendritic domain and axon terminals (del Puerto et al., 2012; Shrivastava et al., 2013; Pougnet et al., 2014). Moreover, P2X7 receptors modulate the density of ankyrinG and sodium channels at the AIS (del Puerto et al., 2015). Whether the crosstalk between CB1R and P2X7 receptors is involved in AIS modulation remains elusive, however both are able to modulate G proteins (Howlett et al., 1998; del Puerto et al., 2012) and signaling molecules like GSK3 (Ozaita et al., 2007; del Puerto et al., 2012), which participates in AIS modulation (Tapia et al., 2013).

Regarding our results showing an astroglial CB2R-dependent modulation of the AIS, one study in a GFP-CB2R transgenic mouse has detected the expression of CB2R in microglia cells, but not in astrocytes or neurons (Schmöle et al., 2015). We assessed whether microglia cells were present in our glial cultures by detecting a specific microglial marker, Iba-1, and found only a few (or none) microglia cells that are unlikely to explain the observed effect. Nevertheless, it is still possible that cultured astrocytes express very low levels of CB2Rs, even though CB2Rs have only been detected in astrocytomas (Sánchez et al., 2001). Further studies and the development of tools for CB2R detection will be necessary to investigate the potential role of CB2R in the regulation of AIS and neuronal excitability in physiological and pathological conditions. In fact, CB2Rs have been detected in neurons and glial cells only in pathological conditions (Viscomi et al., 2009; Choi et al., 2013).

CONCLUSION

Our results show that cannabinoid receptors play an important role in coordinating dendritic development and maturation of the AIS, which may influence future events during neuronal maturation. While CB1Rs have been thoroughly studied at presynaptic and postsynaptic sites, our study show that CB1R modulation of dendritic growth also modulates ankyrinG density, and therefore voltage-gated sodium channel density at the AIS. Further studies regarding cannabinoid receptors are necessary to understand the role the ECS may have in the regulation of AIS structure and plasticity, and its relation with the presynaptic and postsynaptic domains. Furthermore, understanding AIS modulation in response to brain disorders, diseases or injury also requires to consider changes in other neuronal compartments.

AUTHOR CONTRIBUTIONS

JJG and MT conceived and designed experiments. MT, JJG and AD performed experiments and data acquisition. MT, JJG and AD analyzed and interpreted data. MT and JJG wrote the manuscript. WZ, AP and MJB and MC contributed to acquiring and analyzing data. CG contributed to data comprehension. All authors read and approved the final manuscript.

ACKNOWLEDGMENTS

We thank María Luz López-Rodríguez for kindly supplying the monoacylglycerol lipase (MAGL) selective inhibitor UCM-03025, Ismael Galve-Roperh for CB1 interference RNA plasmids and people from CG laboratory for their kind help and advice. We also thank Jean-Marc Goaillard for critical reading and helpful suggestions on the manuscript. This work was supported by research grants from Ministerio de Economia y Competitividad (MINECO to JJG) (SAF2015-65315-R) and CG (SAF- 2013-42784-R).

REFERENCES

Bacci, A., Huguenard, J. R., and Prince, D. A. (2004). Long-lasting self-inhibition of neocortical interneurons mediated by endocannabinoids. *Nature* 431, 312–316. doi: 10.1038/nature02913

Bender, K. J., and Trussell, L. O. (2012). The physiology of the axon initial segment. *Annu. Rev. Neurosci.* 35, 249–265. doi: 10.1146/annurev-neuro-062111-150339

Benson, D. L., Watkins, F. H., Steward, O., and Banker, G. (1994). Characterization of GABAergic neurons in hippocampal cell cultures. *J. Neurocytol.* 23, 279–295. doi: 10.1007/bf01188497

Berghuis, P., Dobszay, M. B., Wang, X., Spano, S., Ledda, F., Sousa, K. M., et al. (2005). Endocannabinoids regulate interneuron migration and morphogenesis by transactivating the TrkB receptor. *Proc. Natl. Acad. Sci. U S A* 102, 19115–19120. doi: 10.1073/pnas.0509494102

Busquets Garcia, A., Soria-Gomez, E., Bellocchio, L., and Marsicano, G. (2016). Cannabinoid receptor type-1: breaking the dogmas. *F1000Res.* 5:990. doi: 10.12688/f1000research.8245.1

Chevaleyre, V., Takahashi, K. A., and Castillo, P. E. (2006). Endocannabinoid-mediated synaptic plasticity in the CNS. *Annu. Rev. Neurosci.* 29, 37–76. doi: 10.1146/annurev.neuro.29.051605.112834

Choi, I. Y., Ju, C., Anthony Jalin, A. M., Lee, D. I., Prather, P. L., and Kim, W. K. (2013). Activation of cannabinoid CB_2 receptor-mediated AMPK/CREB pathway reduces cerebral ischemic injury. *Am. J. Pathol.* 182, 928–939. doi: 10.1016/j.ajpath.2012.11.024

Danzer, S. C., Crooks, K. R., Lo, D. C., and Mcnamara, J. O. (2002). Increased expression of brain-derived neurotrophic factor induces formation of basal dendrites and axonal branching in dentate granule cells in hippocampal explant cultures. *J. Neurosci.* 22, 9754–9763.

Derkinderen, P., Valjent, E., Toutant, M., Corvol, J. C., Enslen, H., Ledent, C., et al. (2003). Regulation of extracellular signal-regulated kinase by cannabinoids in hippocampus. *J. Neurosci.* 23, 2371–2382.

Diaz-Alonso, J., Aguado, T., Wu, C. S., Palazuelos, J., Hofmann, C., Garcez, P., et al. (2012). The CB_1 cannabinoid receptor drives corticospinal motor neuron differentiation through the Ctip2/Satb2 transcriptional regulation axis. *J. Neurosci.* 32, 16651–16665. doi: 10.1523/JNEUROSCI.0681-12.2012

Dotti, C. G., Sullivan, C. A., and Banker, G. A. (1988). The establishment of polarity by hippocampal neurons in culture. *J. Neurosci.* 8, 1454–1468.

Eyal, G., Mansvelder, H. D., de Kock, C. P., and Segev, I. (2014). Dendrites impact the encoding capabilities of the axon. *J. Neurosci.* 34, 8063–8071. doi: 10.1523/JNEUROSCI.5431-13.2014

Gaffuri, A. L., Ladarre, D., and Lenkei, Z. (2012). Type-1 cannabinoid receptor signaling in neuronal development. *Pharmacology* 90, 19–39. doi: 10.1159/000339075

Galve-Roperh, I., Chiurchiù, V., Díaz-Alonso, J., Bari, M., Guzmán, M., and Maccarrone, M. (2013). Cannabinoid receptor signaling in progenitor/stem cell proliferation and differentiation. *Prog. Lipid Res.* 52, 633–650. doi: 10.1016/j.plipres.2013.05.004

Garrido, J. J., Fernandes, F., Giraud, P., Mouret, I., Pasqualini, E., Fache, M. P., et al. (2001). Identification of an axonal determinant in the C-terminus of the sodium channel $Na_v1.2$. *EMBO J.* 20, 5950–5961. doi: 10.1093/emboj/20.21.5950

Garrido, J. J., Giraud, P., Carlier, E., Fernandes, F., Moussif, A., Fache, M. P., et al. (2003). A targeting motif involved in sodium channel clustering at the axonal initial segment. *Science* 300, 2091–2094. doi: 10.1126/science.1085167

Gerdeman, G., and Lovinger, D. M. (2001). CB1 cannabinoid receptor inhibits synaptic release of glutamate in rat dorsolateral striatum. *J. Neurophysiol.* 85, 468–471.

Gilbert, M. T., and Soderstrom, K. (2014). Developmental but not adult cannabinoid treatments persistently alter axonal and dendritic morphology within brain regions important for zebra finch vocal learning. *Brain Res.* 1558, 57–73. doi: 10.1016/j.brainres.2014.02.039

Gómez-Gonzalo, M., Navarrete, M., Perea, G., Covelo, A., Martín-Fernández, M., Shigemoto, R., et al. (2015). Endocannabinoids induce lateral long-term potentiation of transmitter release by stimulation of gliotransmission. *Cereb. Cortex* 25, 3699–3712. doi: 10.1093/cercor/bhu231

Grubb, M. S., and Burrone, J. (2010). Activity-dependent relocation of the axon initial segment fine-tunes neuronal excitability. *Nature* 465, 1070–1074. doi: 10.1038/nature09160

Grubb, M. S., Shu, Y., Kuba, H., Rasband, M. N., Wimmer, V. C., and Bender, K. J. (2011). Short- and long-term plasticity at the axon initial segment. *J. Neurosci.* 31, 16049–16055. doi: 10.1523/JNEUROSCI.4064-11.2011

Gulledge, A. T., and Bravo, J. J. (2016). Neuron morphology influences axon initial segment plasticity. *eNeuro* 3, 1–24. doi: 10.1523/eneuro.0085-15.2016

Hamada, M. S., Goethals, S., de Vries, S. I., Brette, R., and Kole, M. H. (2016). Covariation of axon initial segment location and dendritic tree normalizes the somatic action potential. *Proc. Natl. Acad. Sci. U S A* 113, 14841–14846. doi: 10.1073/pnas.1607548113

Hedstrom, K. L., Ogawa, Y., and Rasband, M. N. (2008). AnkyrinG is required for maintenance of the axon initial segment and neuronal polarity. *J. Cell Biol.* 183, 635–640. doi: 10.1083/jcb.200806112

Hernández-Torres, G., Cipriano, M., Hedén, E., Björklund, E., Canales, Á., Zian, D., et al. (2014). A reversible and selective inhibitor of monoacylglycerol lipase ameliorates multiple sclerosis. *Angew. Chem. Int. Ed. Engl.* 53, 13765–13770. doi: 10.1002/anie.201407807

Howlett, A. C. (2005). Cannabinoid receptor signaling. *Handb. Exp. Pharmacol.* 168, 53–79. doi: 10.1007/3-540-26573-2_2

Howlett, A. C., Song, C., Berglund, B. A., Wilken, G. H., and Pigg, J. J. (1998). Characterization of CB1 cannabinoid receptors using receptor peptide fragments and site-directed antibodies. *Mol. Pharmacol.* 53, 504–510. doi: 10.1124/mol.53.3.504

Huang, Y. M., and Rasband, M. N. (2016). Organization of the axon initial segment: actin like a fence. *J. Cell Biol.* 215, 9–11. doi: 10.1083/jcb.201609084

Ievglevskyi, O., Palygin, O., Kondratskaya, E., Grebenyuk, S., and Krishtal, O. (2012). Modulation of ATP-induced LTP by cannabinoid receptors in rat hippocampus. *Purinergic Signal.* 8, 705–713. doi: 10.1007/s11302-012-9296-5

Irving, A. J., Coutts, A. A., Harvey, J., Rae, M. G., Mackie, K., Bewick, G. S., et al. (2000). Functional expression of cell surface cannabinoid CB_1 receptors on presynaptic inhibitory terminals in cultured rat hippocampal neurons. *Neuroscience* 98, 253–262. doi: 10.1016/s0306-4522(00)00120-2

Kaech, S., and Banker, G. (2006). Culturing hippocampal neurons. *Nat. Protoc.* 1, 2406–2415. doi: 10.1038/nprot.2006.356

Kano, M., Ohno-Shosaku, T., Hashimotodani, Y., Uchigashima, M., and Watanabe, M. (2009). Endocannabinoid-mediated control of synaptic transmission. *Physiol. Rev.* 89, 309–380. doi: 10.1152/physrev.00019.2008

Katona, I., and Freund, T. F. (2012). Multiple functions of endocannabinoid signaling in the brain. *Annu. Rev. Neurosci.* 35, 529–558. doi: 10.1146/annurev-neuro-062111-150420

Katona, I., Sperlágh, B., Sík, A., Käfalvi, A., Vizi, E. S., Mackie, K., et al. (1999). Presynaptically located CB1 cannabinoid receptors regulate GABA release from axon terminals of specific hippocampal interneurons. *J. Neurosci.* 19, 4544–4558.

Keimpema, E., Mackie, K., and Harkany, T. (2011). Molecular model of cannabis sensitivity in developing neuronal circuits. *Trends Pharmacol. Sci.* 32, 551–561. doi: 10.1016/j.tips.2011.05.004

Kim, A. H., Puram, S. V., Bilimoria, P. M., Ikeuchi, Y., Keough, S., Wong, M., et al. (2009). A centrosomal Cdc20-APC pathway controls dendrite morphogenesis in postmitotic neurons. *Cell* 136, 322–336. doi: 10.1016/j.cell.2008.11.050

Ko, K. W., Rasband, M. N., Meseguer, V., Kramer, R. H., and Golding, N. L. (2016). Serotonin modulates spike probability in the axon initial segment through HCN channels. *Nat. Neurosci.* 19, 826–834. doi: 10.1038/nn.4293

Kobayashi, T., Storrie, B., Simons, K., and Dotti, C. G. (1992). A functional barrier to movement of lipids in polarized neurons. *Nature* 359, 647–650. doi: 10.1038/359647a0

Kole, M. H., Ilschner, S. U., Kampa, B. M., Williams, S. R., Ruben, P. C., and Stuart, G. J. (2008). Action potential generation requires a high sodium channel density in the axon initial segment. *Nat. Neurosci.* 11, 178–186. doi: 10.1038/nn2040

Kovacs, F. E., Illes, P., and Szabo, B. (2011). Purine receptor-mediated endocannabinoid production and retrograde synaptic signalling in the cerebellar cortex. *Br. J. Pharmacol.* 162, 974–988. doi: 10.1111/j.1476-5381.2010.01106.x

Kuba, H., Oichi, Y., and Ohmori, H. (2010). Presynaptic activity regulates Na^+ channel distribution at the axon initial segment. *Nature* 465, 1075–1078. doi: 10.1038/nature09087

Kuba, H., Yamada, R., Ishiguro, G., and Adachi, R. (2015). Redistribution of Kv1 and Kv7 enhances neuronal excitability during structural axon initial segment plasticity. *Nat. Commun.* 6:8815. doi: 10.1038/ncomms9815

Ladarre, D., Roland, A. B., Biedzinski, S., Ricobaraza, A., and Lenkei, Z. (2015). Polarized cellular patterns of endocannabinoid production and detection shape cannabinoid signaling in neurons. *Front. Cell. Neurosci.* 8:426. doi: 10.3389/fncel.2014.00426

Leterrier, C., Lainé, J., Darmon, M., Boudin, H., Rossier, J., and Lenkei, Z. (2006). Constitutive activation drives compartment-selective endocytosis and axonal targeting of type 1 cannabinoid receptors. *J. Neurosci.* 26, 3141–3153. doi: 10.1523/JNEUROSCI.5437-05.2006

Lu, H. C., and Mackie, K. (2016). An introduction to the endogenous cannabinoid system. *Biol. Psychiatry* 79, 516–525. doi: 10.1016/j.biopsych.2015.07.028

Mackie, K. (2005). Distribution of cannabinoid receptors in the central and peripheral nervous system. *Handb. Exp. Pharmacol.* 168, 299–325. doi: 10.1007/3-540-26573-2_10

Marinelli, S., Pacioni, S., Cannich, A., Marsicano, G., and Bacci, A. (2009). Self-modulation of neocortical pyramidal neurons by endocannabinoids. *Nat. Neurosci.* 12, 1488–1490. doi: 10.1038/nn.2430

Maroso, M., Szabo, G. G., Kim, H. K., Alexander, A., Bui, A. D., Lee, S. H., et al. (2016). Cannabinoid control of learning and memory through HCN channels. *Neuron* 89, 1059–1073. doi: 10.1016/j.neuron.2016.01.023

Marsicano, G., Goodenough, S., Monory, K., Hermann, H., Eder, M., Cannich, A., et al. (2003). CB1 cannabinoid receptors and on-demand defense against excitotoxicity. *Science* 302, 84–88. doi: 10.1126/science.1088208

Matsuda, L. A., Lolait, S. J., Brownstein, M. J., Young, A. C., and Bonner, T. I. (1990). Structure of a cannabinoid receptor and functional expression of the cloned cDNA. *Nature* 346, 561–564. doi: 10.1038/346561a0

McDonald, N. A., Henstridge, C. M., Connolly, C. N., and Irving, A. J. (2007). An essential role for constitutive endocytosis, but not activity, in the axonal targeting of the CB1 cannabinoid receptor. *Mol. Pharmacol.* 71, 976–984. doi: 10.1124/mol.106.029348

Mechoulam, R., and Parker, L. A. (2013). The endocannabinoid system and the brain. *Annu. Rev. Psychol.* 64, 21–47. doi: 10.1146/annurev-psych-113011-143739

Muir, J., and Kittler, J. T. (2014). Plasticity of $GABA_A$ receptor diffusion dynamics at the axon initial segment. *Front. Cell. Neurosci.* 8:151. doi: 10.3389/fncel.2014.00151

Mulder, J., Aguado, T., Keimpema, E., Barabás, K., Ballester Rosado, C. J., Nguyen, L., et al. (2008). Endocannabinoid signaling controls pyramidal cell specification and long-range axon patterning. *Proc. Natl. Acad. Sci. U S A* 105, 8760–8765. doi: 10.1073/pnas.0803545105

Navarrete, M., and Araque, A. (2010). Endocannabinoids potentiate synaptic transmission through stimulation of astrocytes. *Neuron* 68, 113–126. doi: 10.1016/j.neuron.2010.08.043

Ogawa, Y., Horresh, I., Trimmer, J. S., Bredt, D. S., Peles, E., and Rasband, M. N. (2008). Postsynaptic density-93 clusters Kv1 channels at axon initial segments independently of Caspr2. *J. Neurosci.* 28, 5731–5739. doi: 10.1523/JNEUROSCI.4431-07.2008

Ohno-Shosaku, T., Maejima, T., and Kano, M. (2001). Endogenous cannabinoids mediate retrograde signals from depolarized postsynaptic neurons to presynaptic terminals. *Neuron* 29, 729–738. doi: 10.1016/s0896-6273(01)00247-1

Ozaita, A., Puighermanal, E., and Maldonado, R. (2007). Regulation of PI3K/Akt/GSK-3 pathway by cannabinoids in the brain. *J. Neurochem.* 102, 1105–1114. doi: 10.1111/j.1471-4159.2007.04642.x

Palazuelos, J., Ortega, Z., Díaz-Alonso, J., Guzmán, M., and Galve-Roperh, I. (2012). CB_2 cannabinoid receptors promote neural progenitor cell proliferation via mTORC1 signaling. *J. Biol. Chem.* 287, 1198–1209. doi: 10.1074/jbc.m111.291294

Pan, Z., Kao, T., Horvath, Z., Lemos, J., Sul, J. Y., Cranstoun, S. D., et al. (2006). A common ankyrin-G-based mechanism retains KCNQ and Na_V channels at electrically active domains of the axon. *J. Neurosci.* 26, 2599–2613. doi: 10.1523/JNEUROSCI.4314-05.2006

Patzke, C., Acuna, C., Giam, L. R., Wernig, M., and Südhof, T. C. (2016). Conditional deletion of L1CAM in human neurons impairs both axonal and dendritic arborization and action potential generation. *J. Exp. Med.* 213, 499–515. doi: 10.1084/jem.20150951

Pertwee, R. G. (2005). Inverse agonism and neutral antagonism at cannabinoid CB1 receptors. *Life Sci.* 76, 1307–1324. doi: 10.1016/j.lfs.2004.10.025

Pougnet, J. T., Toulme, E., Martinez, A., Choquet, D., Hosy, E., and Boué-Grabot, E. (2014). ATP P2X receptors downregulate AMPA receptor trafficking and postsynaptic efficacy in hippocampal neurons. *Neuron* 83, 417–430. doi: 10.1016/j.neuron.2014.06.005

del Puerto, A., Díaz-Hernández, J. I., Tapia, M., Gomez-Villafuertes, R., Benitez, M. J., Zhang, J., et al. (2012). Adenylate cyclase 5 coordinates the action of ADP, P2Y1, P2Y13 and ATP-gated P2X7 receptors on axonal elongation. *J. Cell. Sci.* 125, 176–188. doi: 10.1242/jcs.091736

del Puerto, A., Fronzaroli-Molinieres, L., Perez-Alvarez, M. J., Giraud, P., Carlier, E., Wandosell, F., et al. (2015). ATP-P2X7 receptor modulates axon initial segment composition and function in physiological conditions and brain injury. *Cereb. Cortex* 25, 2282–2294. doi: 10.1093/cercor/bhu035

Ramón Y Cajal, S. (1897). Leyes de la morfología y el dinamismo de las células nerviosas. *Rev. Trimest. Micrográfica* 2, 1–28.

Rasband, M. N. (2010). The axon initial segment and the maintenance of neuronal polarity. *Nat. Rev. Neurosci.* 11, 552–562. doi: 10.1038/nrn2852

Rueda, D., Galve-Roperh, I., Haro, A., and Guzman, M. (2000). The CB_1 cannabinoid receptor is coupled to the activation of c-Jun N-terminal kinase. *Mol. Pharmacol.* 58, 814–820. doi: 10.1124/mol.58.4.814

Sampo, B., Kaech, S., Kunz, S., and Banker, G. (2003). Two distinct mechanisms target membrane proteins to the axonal surface. *Neuron* 37, 611–624. doi: 10.1016/s0896-6273(03)00058-8

Sanchez-Ponce, D., Muñoz, A., and Garrido, J. J. (2011). Casein kinase 2 and microtubules control axon initial segment formation. *Mol. Cell. Neurosci.* 46, 222–234. doi: 10.1016/j.mcn.2010.09.005

Sánchez, C., De Ceballos, M. L., Gomez Del Pulgar, T., Rueda, D., Corbacho, C., Velasco, G., et al. (2001). Inhibition of glioma growth *in vivo* by selective activation of the CB_2 cannabinoid receptor. *Cancer Res.* 61, 5784–5789.

Schafer, D. P., Jha, S., Liu, F., Akella, T., Mccullough, L. D., and Rasband, M. N. (2009). Disruption of the axon initial segment cytoskeleton is a new mechanism for neuronal injury. *J. Neurosci.* 29, 13242–13254. doi: 10.1523/JNEUROSCI.3376-09.2009

Schmöle, A. C., Lundt, R., Gennequin, B., Schrage, H., Beins, E., Kramer, A., et al. (2015). Expression analysis of CB_2-GFP BAC transgenic mice. *PLoS One* 10:e0138986. doi: 10.1371/journal.pone.0138986

Shelly, M., Lim, B. K., Cancedda, L., Heilshorn, S. C., Gao, H., and Poo, M. M. (2010). Local and long-range reciprocal regulation of cAMP and cGMP in axon/dendrite formation. *Science* 327, 547–552. doi: 10.1126/science.1179735

Shrivastava, A. N., Rodriguez, P. C., Triller, A., and Renner, M. (2013). Dynamic micro-organization of P2X7 receptors revealed by PALM based single particle tracking. *Front. Cell. Neurosci.* 7:232. doi: 10.3389/fncel.2013.00232

Sobotzik, J. M., Sie, J. M., Politi, C., del Turco, D., Bennett, V., Deller, T., et al. (2009). AnkyrinG is required to maintain axo-dendritic polarity *in vivo*. *Proc. Natl. Acad. Sci. U S A* 106, 17564–17569. doi: 10.1073/pnas.0909267106

Steindel, F., Lerner, R., Haring, M., Ruehle, S., Marsicano, G., Lutz, B., et al. (2013). Neuron-type specific cannabinoid-mediated G protein signalling in mouse hippocampus. *J. Neurochem.* 124, 795–807. doi: 10.1111/jnc.12137

Stella, N. (2010). Cannabinoid and cannabinoid-like receptors in microglia, astrocytes and astrocytomas. *Glia* 58, 1017–1030. doi: 10.1002/glia.20983

Stuart, G., Schiller, J., and Sakmann, B. (1997). Action potential initiation and propagation in rat neocortical pyramidal neurons. *J. Physiol.* 505, 617–632. doi: 10.1111/j.1469-7793.1997.617ba.x

Tapia, M., Del Puerto, A., Puime, A., Sánchez-Ponce, D., Fronzaroli-Molinieres, L., Pallas-Bazarra, N., et al. (2013). GSK_3 and β-catenin determines functional expression of sodium channels at the axon initial segment. *Cell. Mol. Life Sci.* 70, 105–120. doi: 10.1007/s00018-012-1059-5

Tapia, M., Wandosell, F., and Garrido, J. J. (2010). Impaired function of HDAC6 slows down axonal growth and interferes with axon initial segment development. *PLoS One* 5:e12908. doi: 10.1371/journal.pone.0012908

Varma, N., Carlson, G. C., Ledent, C., and Alger, B. E. (2001). Metabotropic glutamate receptors drive the endocannabinoid system in hippocampus. *J. Neurosci.* 21:RC188.

Viscomi, M. T., Oddi, S., Latini, L., Pasquariello, N., Florenzano, F., Bernardi, G., et al. (2009). Selective CB2 receptor agonism protects central neurons from remote axotomy-induced apoptosis through the PI3K/Akt pathway. *J. Neurosci.* 29, 4564–4570. doi: 10.1523/JNEUROSCI.0786-09.2009

Vitalis, T., Laine, J., Simon, A., Roland, A., Leterrier, C., and Lenkei, Z. (2008). The type 1 cannabinoid receptor is highly expressed in embryonic cortical projection neurons and negatively regulates neurite growth *in vitro*. *Eur. J. Neurosci.* 28, 1705–1718. doi: 10.1111/j.1460-9568.2008.06484.x

Wilson, R. I., and Nicoll, R. A. (2001). Endogenous cannabinoids mediate retrograde signalling at hippocampal synapses. *Nature* 410, 588–592. doi: 10.1038/35082121

Williams, E. J., Walsh, F. S., and Doherty, P. (2003). The FGF receptor uses the endocannabinoid signaling system to couple to an axonal growth response. *J. Cell Biol.* 160, 481–486. doi: 10.1083/jcb.200210164

Wu, C. S., Zhu, J., Wager-Miller, J., Wang, S., O'Leary, D., Monory, K., et al. (2010). Requirement of cannabinoid CB_1 receptors in cortical pyramidal neurons for appropriate development of corticothalamic and thalamocortical projections. *Eur. J. Neurosci.* 32, 693–706. doi: 10.1111/j.1460-9568.2010.07337.x

Zhou, D., Lambert, S., Malen, P. L., Carpenter, S., Boland, L. M., and Bennett, V. (1998). AnkyrinG is required for clustering of voltage-gated Na channels at axon initial segments and for normal action potential firing. *J. Cell Biol.* 143, 1295–1304. doi: 10.1083/jcb.143.5.1295

Zollinger, D. R., Baalman, K. L., and Rasband, M. N. (2015). The ins and outs of polarized axonal domains. *Annu. Rev. Cell Dev. Biol.* 31, 647–667. doi: 10.1146/annurev-cellbio-100913-013107

Conflict of Interest Statement: The authors declare that the research was conducted in the absence of any commercial or financial relationships that could be construed as a potential conflict of interest.

frontiers
in Cellular Neuroscience

MINI REVIEW
published: 05 December 2016
doi: 10.3389/fncel.2016.00278

Dynamic Control of Neurotransmitter Release by Presynaptic Potential

*Mickael Zbili, Sylvain Rama and Dominique Debanne**

UNIS, UMR_S 1072, Institut National de la Santé et de la Recherche Médicale (INSERM), Aix-Marseille Université, Marseille, France

Action potentials (APs) in the mammalian brain are thought to represent the smallest unit of information transmitted by neurons to their postsynaptic targets. According to this view, neuronal signaling is all-or-none or digital. Increasing evidence suggests, however, that subthreshold changes in presynaptic membrane potential before triggering the spike also determines spike-evoked release of neurotransmitter. We discuss here how analog changes in presynaptic voltage may regulate spike-evoked release of neurotransmitter through the modulation of biophysical state of voltage-gated potassium, calcium and sodium channels in the presynaptic compartment. The contribution of this regulation has been greatly underestimated and we discuss the impact for information processing in neuronal circuits.

Keywords: axon, sodium channels, synaptic transmission, brain circuit

OPEN ACCESS

Edited by:
Maren Engelhardt,
Heidelberg University, Germany

Reviewed by:
Michael Beierlein,
University of Texas Health Science Center at Houston, USA
Andreas Draguhn,
Heidelberg University, Germany

Correspondence:
Dominique Debanne
dominique.debanne@univ-amu.fr

Received: *10 October 2016*
Accepted: *21 November 2016*
Published: *05 December 2016*

Citation:
Zbili M, Rama S and Debanne D (2016) Dynamic Control of Neurotransmitter Release by Presynaptic Potential. Front. Cell. Neurosci. 10:278. doi: 10.3389/fncel.2016.00278

INTRODUCTION: DIGITAL, ANALOG AND ANALOG-DIGITAL SIGNALING

Neuronal information in the mammalian brain is usually conveyed by action potentials (APs). The axon initial segment (AIS) expresses a high density of sodium channels, and therefore it constitutes a hot spot for generation of APs. Once initiated the spike propagates along the axon to the presynaptic terminals where it causes release of neurotransmitter. Neuronal information is thus transmitted to the post-synaptic neurons as discrete spike-evoked packets of neurotransmitter in an all-or-none mode of signaling. Thus, neuronal signaling is considered to be digital: if the spike threshold is crossed the neuron fires and generates an output but if the spike threshold is not reached no output is observed, and neurotransmitter release follows a binary mode of signaling (**Figure 1A**, left). Digital signaling presents several advantages. First, information is carried over long distances without dissipation because the AP is regenerated all along the axon (Debanne et al., 2011). Another advantage of digital signaling resides in its low energy cost. In fact, kinetics of voltage-gated sodium and potassium currents underlying the action potential are tuned to constrain energy consumption. The Na^+ excess during APs is found to be close to the theoretical minimum (i.e., it varies between 1.3 and 2 fold, depending on axon type (Alle et al., 2009; Hallermann et al., 2012)). If digital signaling presents advantages, it has also limitations. The coding of information by a digital synapse is generally poor because of the discrete nature of digital signaling (Borst and Theunissen, 1999).

Neuronal information is not only transmitted in digital mode and subthreshold activity originating from the dendrites and the soma can be conveyed by the axon to the presynaptic terminal where the flow of information is coded in an analog mode (**Figure 1A**, middle). Pure analog transmission has been reported in invertebrate neurons and in the inner ear or in the retina of mammalians where sensory stimulation produces graded changes in membrane potential without APs (Werblin and Dowling, 1969; Heidelberger, 2007). These cells release transmitter in a tonic mode and their rate of release is a function of the presynaptic

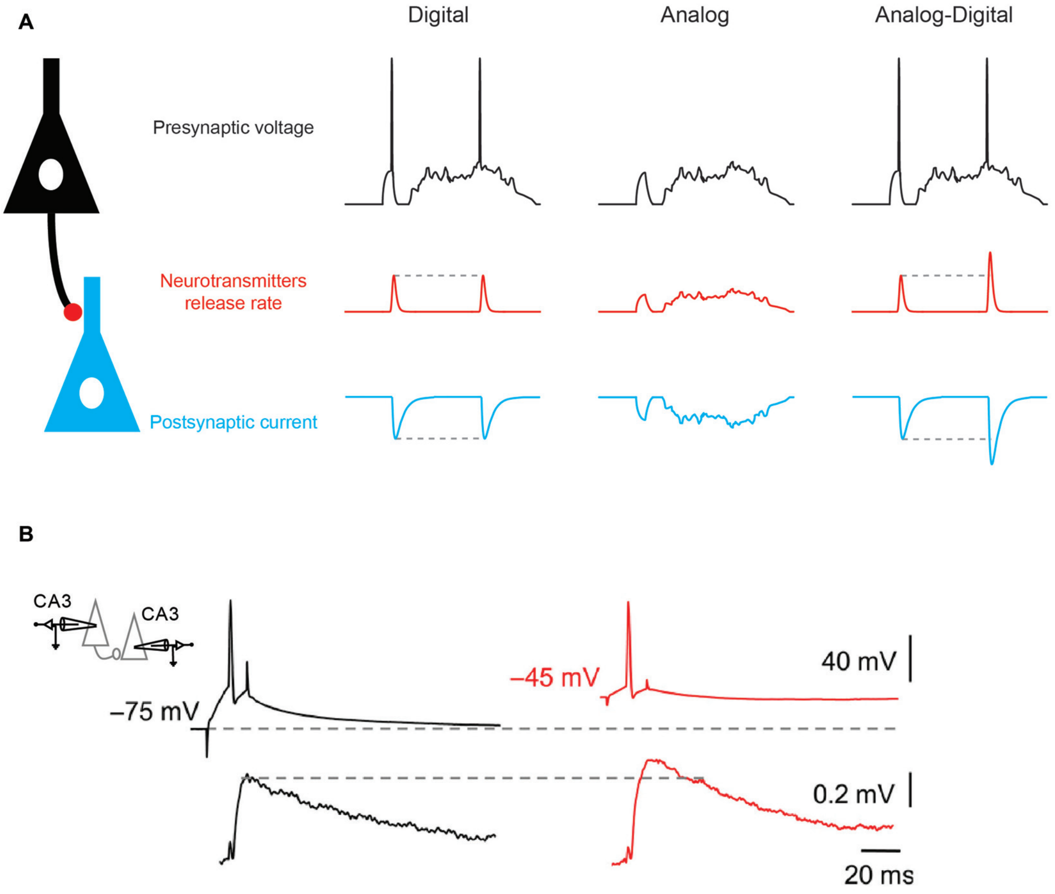

FIGURE 1 | Analog-digital (AD) mode of synaptic transmission. (A) Digital, analog and hybrid (AD) modes of synaptic transmission. Left: digital mode of synaptic transmission. Transmission is stereotyped and occurs only if a presynaptic action potential (AP) is elicited. Middle: analog mode of synaptic transmission (graded transmission of presynaptic voltage fluctuations). Right: hybrid AD transmission. Both subthreshold fluctuations and spiking activity are transmitted. Note that when the presynaptic spike is produced after a prolonged period of depolarization (second spike) the spike-evoked synaptic response is enhanced compared with when there is no prolonged depolarization (first spike). **(B)** Depolarization-induced AD facilitation (d-ADF) of synaptic transmission at a CA3 –CA3 connection. Average excitatory post-synaptic potential (EPSP) traces (bottom) evoked by action potentials APs triggered from control (black traces) and depolarized presynaptic membrane potentials (red traces). Adapted from Bialowas et al. (2015).

membrane potential. Compared to digital synapses, analog synapses display a much higher rate of information transfer (Borst and Theunissen, 1999). However, the energy consumption and voltage dissipation along neuronal processes represent two major drawbacks of analog signaling (Debanne et al., 2013).

It has been recently shown that analog signals modulate the function of digital synapses. In fact, subthreshold activity in the presynaptic element modulates spike-evoked transmission, leading to the emergence of the concept of hybrid analog-digital (AD) synaptic transmission (**Figure 1A**, right). Initially described in invertebrates (Takeuchi and Takeuchi, 1962; Kusano et al., 1967; Shimahara and Tauc, 1975), AD facilitation (ADF) of synaptic transmission has been reported in many mammalian synapses including cortical (Shu et al., 2006; Kole et al., 2007; Zhu et al., 2011; Rama et al., 2015a), cerebellar (Bouhours et al., 2011; Christie et al., 2011) and hippocampal synapses (Saviane et al., 2003; Alle and Geiger, 2006; Sasaki et al., 2012; Kim, 2014; Bialowas et al., 2015; Rama et al., 2015a). Most of ADF reported so far has been induced by long (0.3–10 s) subthreshold depolarization of the soma (Saviane et al., 2003; Alle and Geiger, 2006; Shu et al., 2006; Kole et al., 2007; Bouhours et al., 2011; Christie et al., 2011; Sasaki et al., 2012; Bialowas et al., 2015) and correspond to depolarization-induced ADF (d-ADF; **Figure 1B**). In the other few cases, ADF has been induced by a transient hyperpolarization (15–200 ms) before the action potential (Cowan and Stricker, 2004; Thio and Yamada, 2004; Rama et al., 2015a). This form of plasticity corresponds to hyperpolarization-induced ADF (h-ADF).

In both cases, the principle underlying ADF is that membrane potential fluctuations in the cell body is electrically transmitted by the axon over hundreds of micrometers to the terminals where they modulate the biophysical state of voltage-gated potassium, calcium or sodium channels (Alle and Geiger, 2006; Shu et al., 2006; Christie et al., 2011; Sasaki et al., 2012; Debanne et al., 2013; Rama et al., 2015a,b). Thus, these forms of ADF can be found only in local circuits such as L5-L5 synapses in the cortex or CA3-CA3 synapses in the hippocampus where both the short axonal distance and the limited number of branch-points represent favorable conditions to an optimal transmission of voltage to the presynaptic terminal (Sasaki et al., 2012). Long distance connections with many branch points such as CA3-CA1 synapses usually do not express ADF (Sasaki et al., 2012).

DEPOLARIZATION-INDUCED AD FACILITATION (d-ADF)

Two mechanisms have been identified to account for d-ADF. The first mechanism relies on inactivation of shaker-type voltage-gated potassium channels (Kv1). Kv1 channels are present in the axon of L5 and CA3 neurons where they control the spike duration and subsequently, neurotransmitter release (Kole et al., 2007; Shu et al., 2007; Boudkkazi et al., 2011; Foust et al., 2011; Kim, 2014; Bialowas et al., 2015). Inactivation of Kv1 channel is, however, a very slow process and depolarizations of ∼5–10 s are usually required to fully inactivate Kv1 channels and produce a significant (i.e., ∼30%) increase in neurotransmitter release (Kole et al., 2007; Bialowas et al., 2015). Thus, slow oscillations of network activity such as up and down states usually occurring during slow-wave sleep may represent a physiological condition in which d-ADF occurs (Shu et al., 2006). However, up-states affect equally all neurons thus creating conjoint shifts in membrane potential of 10–20 mV in presynaptic and postsynaptic neuron. Therefore, during up-states the driving force of the excitatory post-synaptic potential (EPSP) is reduced by ∼30%. One may thus propose that d-ADF rather constitutes a homeostatic process to compensate for the loss of driving force of the EPSP due to the up-state.

The second mechanism is based on the activation of voltage gated calcium channels (Cav) by the subthreshold depolarization. In the axon of cerebellar interneurons, slow subthreshold depolarizations have been found to activate P/Q type (Cav2.1) Cav channels thus producing an elevation in basal Ca^{2+} concentration and subsequently an increase in spike-evoked transmission (Bouhours et al., 2011). Because, these Cav channels are activated by high levels of depolarization, their contribution to d-ADF is limited to short axons such as cerebellar axons (Bouhours et al., 2011) or to very proximal synapses (Bialowas et al., 2015).

HYPERPOLARIZATION-INDUCED AD FACILITATION (h-ADF)

Analog modulation by changes in presynaptic membrane potential is not restricted to voltage-gated K^+ and Ca^{2+} channels. In fact, in excitatory neurons, a large portion of the voltage-gated Na^+ (Nav) current in the axon and presynaptic terminal is inactivated at rest. In the axon terminal or the axon proper from dentate granule cells or from L5 pyramidal neurons, the inactivated fraction of Nav channels may reach 70%–80% (Engel and Jonas, 2005; Hu et al., 2009; Schmidt-Hieber and Bischofberger, 2010). In comparison, somatic Nav channels display much less inactivation (∼20% in cortical layer five pyramidal cells (Hu et al., 2009)). The origin of this difference in Nav channel inactivation is not well established but it may result from the nature of the subunits. Nav1.6 is principally found in the distal axon whereas Nav1.2 is found in the proximal part of the axon and in the soma (Hu et al., 2009).

The consequence of this elevated Nav channel inactivation in the axon is multiple. First, it may extend the spike initiation site to a wider axonal zone (Scott et al., 2014). But most importantly, it will largely modulate the amplitude of the action potential in the axon upon changes in membrane potential in the cell body (Rama et al., 2015a). In fact, it was shown in this study that hyperpolarizing the somatic potential enhanced the amplitude of the action potential recorded in the axon (**Figures 2A,B**). As a consequence, the spike-evoked calcium influx was found to be increased, and synaptic transmission was augmented (Rama et al., 2015a). This h-ADF was found to be present at both CA3-CA3 and L5-L5 connections (**Figures 2C,D**), suggesting that h-ADF might be a general feature in local brain circuits. Nav channel inactivation is a key factor in the expression of h-ADF because the increase in spike amplitude result from the recovery of Nav channel from inactivation. Thus, increasing Nav channel inactivation with carbamazepine or reducing the number of activatable Nav channels with tetrodotoxin (TTX) that subsequently enhances the modulation of the presynaptic spike amplitude by the hyperpolarization was found to augment the amplitude of h-ADF (Rama et al., 2015a).

h-ADF and d-ADF were found at the same connections and were found to be additive (Rama et al., 2015a). Compared to d-ADF, h-ADF is three orders of magnitude faster. Indeed, h-ADF can be induced by 15 ms hyperpolarization. This feature has important consequences in terms of network dynamics. First, h-ADF can be triggered by a hyperpolarizing inhibitory post-synaptic potential (IPSP; **Figure 2E**). In addition, h-ADF can be induced by 4 Hz theta oscillations (Rama et al., 2015a). The maximal facilitation was found to occur in the troughs of the oscillation (**Figure 2F**). Thus, in contrast with d-ADF, h-ADF adds on the post-synaptic modulation of the EPSP due to the increase in driving force during hyperpolarization of the network. *in vivo*, APs triggered in the troughs of theta oscillations are thought to improve the accuracy of spatial coding (O'Keefe and Recce, 1993). We suggest that phase-unlocked spikes would produce a stronger post-synaptic response through h-ADF, and hence would promote further the spatial coding. Finally, in a model of interconnected pyramidal cells and interneurons that expresses spontaneous gamma oscillations, addition of h-ADF was found to promote network synchrony at gamma frequency (Rama et al., 2015a).

CONCLUSION AND FUTURE DIRECTIONS

The recent identification of h-ADF adds a new form of plasticity in local circuits such as CA3-CA3 or L5-L5 synapses. As a fast process, h-ADF may impact the network properties during

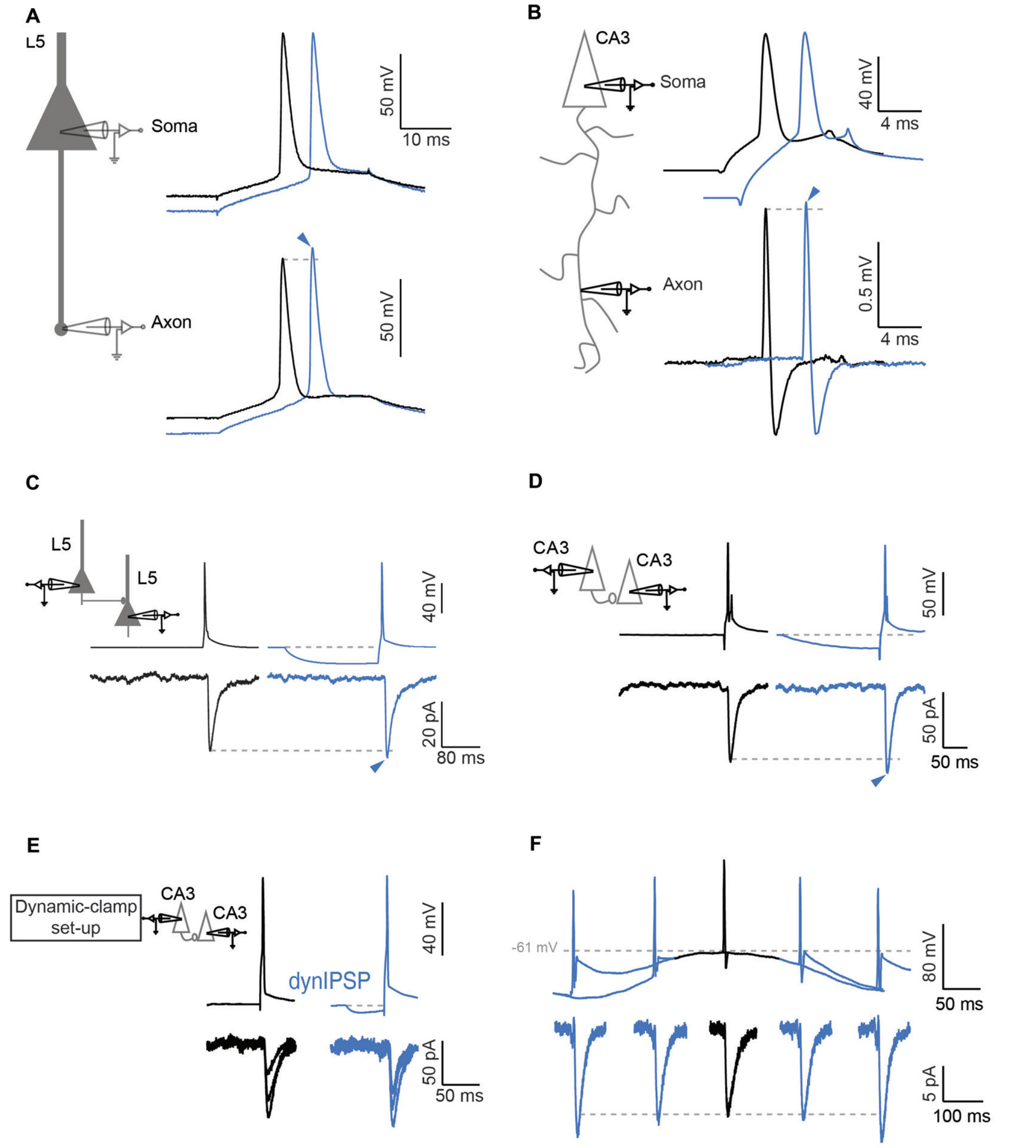

FIGURE 2 | Hyperpolarization induced ADF (h-ADF). (A,B) Dual recording from the soma and the axon in L5 **(A)** and CA3 **(B)** pyramidal neurons. Left: scheme of experimental setup showing double recording from the soma and the axon. Right: soma–axon recording (in whole-cell in **A** and in cell-attached recording in **B**). Hyperpolarization of the soma (blue traces) enhances the spike amplitude measured in the axon but not in the soma. **(C,D)** Paired recording of synaptically connected L5 **(C)** and CA3 **(D)** pyramidal neurons. Note that a brief hyperpolarization of the presynaptic cell (blue traces) enhances the amplitude of the postsynaptic response. **(E)** Induction of h-ADF with presynaptic inhibitory post-synaptic potentials (IPSPs). Left: scheme of the dynamic-clamp system used to inject a current that mimics a GABAergic input in the presynaptic cell. Right: recording from a pair of CA3 neurons in the absence (black traces) and in the presence of a simulated GABAergic input injected into the presynaptic neuron before the spike (blue traces). The two groups of EPSCs are representative of the two conditions. Note that an IPSP waveform injection before the presynaptic spike enhances the amplitude of the postsynaptic response (blue traces). **(F)** θ oscillation induces h-ADF in CA3 neurons. Presynaptic APs are triggered at different phases of a subthreshold oscillation of the membrane potential at 4 Hz. h-ADF is observed when the spike is triggered in the trough of the oscillation. Adapted from Rama et al. (2015a).

rapid activity regimes such as theta or gamma activity. In contrast, the impact of d-ADF on network properties is probably less important because of its slow kinetics. Rather, it can be seen as a homeostatic process that maintain stable synaptic strength during slow depolarization shifts. It will be important to incorporate these forms of short-term plasticity in realistic models of cortical circuits (Markram et al., 2015).

Will other forms of ADF be identified in the near future? There are serious reasons to believe that this will be the case. The study of functional properties of ion channels in the axon is only at its beginning. And the recent development of direct recordings from thin axons and presynaptic terminals (Novak et al., 2013; Kawaguchi and Sakaba, 2015; Begum et al., 2016; Rowan et al., 2016) together with the development of genetically-encoded voltage indicators (Hoppa et al., 2014) will certainly open new investigation opportunities about the role and function of ion channels in the presynaptic compartment.

AUTHOR CONTRIBUTIONS

MZ, SR and DD wrote the manuscript. MZ built the figures.

FUNDING

Supported by Institut National de la Santé et de la Recherche Médicale (INSERM), Centre National de la Recherche Scientifique (CNRS), Fondation pour la Recherche Médicale (FRM) (doctoral grant FDT20150532147 to MZ) and Agence Nationale de la Recherche (ANR) (AXODE-14-CE13-0003-02).

REFERENCES

Alle, H., and Geiger, J. R. (2006). Combined analog and action potential coding in hippocampal mossy fibers. *Science* 311, 1290–1293. doi: 10.1126/science.1119055

Alle, H., Roth, A., and Geiger, J. R. P. (2009). Energy-efficient action potentials in hippocampal mossy fibers. *Science* 325, 1405–1408. doi: 10.1126/science.1174331

Begum, R., Bakiri, Y., Volynski, K. E., and Kullmann, D. M. (2016). Action potential broadening in a presynaptic channelopathy. *Nat. Commun.* 7:12102. doi: 10.1038/ncomms12102

Bialowas, A., Rama, S., Zbili, M., Marra, V., Fronzaroli-Molinieres, L., Ankri, N., et al. (2015). Analog modulation of spike-evoked transmission in CA3 circuits is determined by axonal Kv1.1 channels in a time-dependent manner. *Eur. J. Neurosci.* 41, 293–304. doi: 10.1111/ejn.12787

Borst, A., and Theunissen, F. E. (1999). Information theory and neural coding. *Nat. Neurosci.* 2, 947–957. doi: 10.1038/14731

Boudkkazi, S., Fronzaroli-Molinieres, L., and Debanne, D. (2011). Presynaptic action potential waveform determines cortical synaptic latency. *J. Physiol.* 589, 1117–1131. doi: 10.1113/jphysiol.2010.199653

Bouhours, B., Trigo, F. F., and Marty, A. (2011). Somatic depolarization enhances GABA release in cerebellar interneurons via a calcium/protein kinase C pathway. *J. Neurosci.* 31, 5804–5815. doi: 10.1523/JNEUROSCI.5127-10.2011

Christie, J. M., Chiu, D. N., and Jahr, C. E. (2011). Ca^{2+}-dependent enhancement of release by subthreshold somatic depolarization. *Nat. Neurosci.* 14, 62–68. doi: 10.1038/nn.2718

Cowan, A. I., and Stricker, C. (2004). Functional connectivity in layer IV local excitatory circuits of rat somatosensory cortex. *J. Neurophysiol.* 92, 2137–2150. doi: 10.1152/jn.01262.2003

Debanne, D., Bialowas, A., and Rama, S. (2013). What are the mechanisms for analogue and digital signalling in the brain? *Nat. Rev. Neurosci.* 14, 63–69. doi: 10.1038/nrn3361

Debanne, D., Campanac, E., Bialowas, A., Carlier, E., and Alcaraz, G. (2011). Axon physiology. *Physiol. Rev.* 91, 555–602. doi: 10.1152/physrev.00048.2009

Engel, D., and Jonas, P. (2005). Presynaptic action potential amplification by voltage-gated Na^+ channels in hippocampal mossy fiber boutons. *Neuron* 45, 405–417. doi: 10.1016/j.neuron.2004.12.048

Foust, A. J., Yu, Y., Popovic, M., Zecevic, D., and Mccormick, D. A. (2011). Somatic membrane potential and Kv1 channels control spike repolarization in cortical axon collaterals and presynaptic boutons. *J. Neurosci.* 31, 15490–15498. doi: 10.1523/JNEUROSCI.2752-11.2011

Hallermann, S., de Kock, C. P., Stuart, G. J., and Kole, M. H. (2012). State and location dependence of action potential metabolic cost in cortical pyramidal neurons. *Nat. Neurosci.* 15, 1007–1014. doi: 10.1038/nn.3132

Heidelberger, R. (2007). Mechanisms of tonic, graded release: lessons from the vertebrate photoreceptor. *J. Physiol.* 585, 663–667. doi: 10.1113/jphysiol.2007.137927

Hoppa, M. B., Gouzer, G., Armbruster, M., and Ryan, T. A. (2014). Control and plasticity of the presynaptic action potential waveform at small CNS nerve terminals. *Neuron* 84, 778–789. doi: 10.1016/j.neuron.2014.09.038

Hu, W., Tian, C., Li, T., Yang, M., Hou, H., and Shu, Y. (2009). Distinct contributions of $Na_v1.6$ and $Na_v1.2$ in action potential initiation and backpropagation. *Nat. Neurosci.* 12, 996–1002. doi: 10.1038/nn.2359

Kawaguchi, S. Y., and Sakaba, T. (2015). Control of inhibitory synaptic outputs by low excitability of axon terminals revealed by direct recording. *Neuron* 85, 1273–1288. doi: 10.1016/j.neuron.2015.02.013

Kim, S. (2014). Action potential modulation in CA1 pyramidal neuron axons facilitates OLM interneuron activation in recurrent inhibitory microcircuits of rat hippocampus. *PLoS One* 9:e113124. doi: 10.1371/journal.pone.0113124

Kole, M. H., Letzkus, J. J., and Stuart, G. J. (2007). Axon initial segment Kv1 channels control axonal action potential waveform and synaptic efficacy. *Neuron* 55, 633–647. doi: 10.1016/j.neuron.2007.07.031

Kusano, K., Livengood, D. R., and Werman, R. (1967). Correlation of transmitter release with membrane properties of the presynaptic fiber of the squid giant synapse. *J. Gen. Physiol.* 50, 2579–2601. doi: 10.1085/jgp.50.11.2579

Markram, H., Muller, E., Ramaswamy, S., Reimann, M. W., Abdellah, M., Sanchez, C. A., et al. (2015). Reconstruction and simulation of neocortical microcircuitry. *Cell* 163, 456–492. doi: 10.1016/j.cell.2015.09.029

Novak, P., Gorelik, J., Vivekananda, U., Shevchuk, A. I., Ermolyuk, Y. S., Bailey, R. J., et al. (2013). Nanoscale-targeted patch-clamp recordings of functional presynaptic ion channels. *Neuron* 79, 1067–1077. doi: 10.1016/j.neuron.2013.07.012

O'Keefe, J., and Recce, M. L. (1993). Phase relationship between hippocampal place units and the EEG theta rhythm. *Hippocampus* 3, 317–330. doi: 10.1002/hipo.450030307

Rama, S., Zbili, M., Bialowas, A., Fronzaroli-Molinieres, L., Ankri, N., Carlier, E., et al. (2015a). Presynaptic hyperpolarization induces a fast analogue modulation of spike-evoked transmission mediated by axonal sodium channels. *Nat. Commun.* 6:10163. doi: 10.1038/ncomms10163

Rama, S., Zbili, M., and Debanne, D. (2015b). Modulation of spike-evoked synaptic transmission: the role of presynaptic calcium and potassium channels. *Biochim. Biophys. Acta* 1853, 1933–1939. doi: 10.1016/j.bbamcr.2014.11.024

Rowan, M. J., DelCanto, G., Yu, J. J., Kamasawa, N., and Christie, J. M. (2016). Synapse-level determination of action potential duration by K^+ channel clustering in axons. *Neuron* 91, 370–383. doi: 10.1016/j.neuron.2016.05.035

Sasaki, T., Matsuki, N., and Ikegaya, Y. (2012). Effects of axonal topology on the somatic modulation of synaptic outputs. *J. Neurosci.* 32, 2868–2876. doi: 10.1523/JNEUROSCI.5365-11.2012

Saviane, C., Mohajerani, M. H., and Cherubini, E. (2003). An ID-like current that is downregulated by Ca^{2+} modulates information coding at CA3-CA3 synapses in the rat hippocampus. *J. Physiol.* 552, 513–524. doi: 10.1113/jphysiol.2003.051045

Schmidt-Hieber, C., and Bischofberger, J. (2010). Fast sodium channel gating supports localized and efficient axonal action potential initiation. *J. Neurosci.* 30, 10233–10242. doi: 10.1523/JNEUROSCI.6335-09.2010

Scott, R. S., Henneberger, C., Padmashri, R., Anders, S., Jensen, T. P., and Rusakov, D. A. (2014). Neuronal adaptation involves rapid expansion of the action potential initiation site. *Nat. Commun.* 5:3817. doi: 10.1038/ncomms4817

Shimahara, T., and Tauc, L. (1975). Multiple interneuronal afferents to the giant cells in Aplysia. *J. Physiol.* 247, 299–319. doi: 10.1113/jphysiol.1975.sp010933

Shu, Y., Hasenstaub, A., Duque, A., Yu, Y., and McCormick, D. A. (2006). Modulation of intracortical synaptic potentials by presynaptic somatic membrane potential. *Nature* 441, 761–765. doi: 10.1038/nature04720

Shu, Y., Yu, Y., Yang, J., and McCormick, D. A. (2007). Selective control of cortical axonal spikes by a slowly inactivating K^+ current. *Proc. Natl. Acad. Sci. U S A* 104, 11453–11458. doi: 10.1073/pnas.0702041104

Takeuchi, A., and Takeuchi, N. (1962). Electrical changes in pre- and postsynaptic axons of the giant synapse of Loligo. *J. Gen. Physiol.* 45, 1181–1193. doi: 10.1085/jgp.45.6.1181

Thio, L. L., and Yamada, K. A. (2004). Differential presynaptic modulation of excitatory and inhibitory autaptic currents in cultured hippocampal neurons. *Brain Res.* 1012, 22–28. doi: 10.1016/j.brainres. 2004.02.077

Werblin, F. S., and Dowling, J. E. (1969). Organization of the retina of the mudpuppy, necturus maculosus. II. Intracellular recording. *J. Neurophysiol.* 32, 339–355.

Zhu, J., Jiang, M., Yang, M., Hou, H., and Shu, Y. (2011). Membrane potential-dependent modulation of recurrent inhibition in rat neocortex. *PLoS Biol.* 9:e1001032. doi: 10.1371/journal.pbio.1001032

Conflict of Interest Statement: The authors declare that the research was conducted in the absence of any commercial or financial relationships that could be construed as a potential conflict of interest.

The reviewer AD and handling Editor declared their shared affiliation, and the handling Editor states that the process nevertheless met the standards of a fair and objective review.

frontiers in Cellular Neuroscience

MINI REVIEW
published: 25 October 2016
doi: 10.3389/fncel.2016.00250

Structural and Functional Plasticity at the Axon Initial Segment

Rei Yamada and Hiroshi Kuba *

Department of Cell Physiology, Graduate School of Medicine, Nagoya University, Nagoya, Japan

The axon initial segment (AIS) is positioned between the axonal and somato-dendritic compartments and plays a pivotal role in triggering action potentials (APs) and determining neuronal output. It is now widely accepted that structural properties of the AIS, such as length and/or location relative to the soma, change in an activity-dependent manner. This structural plasticity of the AIS is known to be crucial for homeostatic control of neuronal excitability. However, it is obvious that the impact of the AIS on neuronal excitability is critically dependent on the biophysical properties of the AIS, which are primarily determined by the composition and characteristics of ion channels in this domain. Moreover, these properties can be altered via phosphorylation and/or redistribution of the channels. Recently, studies in auditory neurons showed that alterations in the composition of voltage-gated K^+ (Kv) channels at the AIS coincide with elongation of the AIS, thereby enhancing the neuronal excitability, suggesting that the interaction between structural and functional plasticities of the AIS is important in the control of neuronal excitability. In this review, we will summarize the current knowledge regarding structural and functional alterations of the AIS and discuss how they interact and contribute to regulating the neuronal output.

Keywords: axon initial segment, plasticity, excitability, action potential, ion channel

Edited by:
Maren Engelhardt,
Heidelberg University, Germany

Reviewed by:
Dominique Debanne,
University of the Mediterranean,
France
Maxim Volgushev,
University of Connecticut, USA

Correspondence:
Hiroshi Kuba
kuba@med.nagoya-u.ac.jp

Received: *30 August 2016*
Accepted: *12 October 2016*
Published: *25 October 2016*

Citation:
Yamada R and Kuba H
(2016) Structural and Functional
Plasticity at the Axon Initial Segment.
Front. Cell. Neurosci. 10:250.
doi: 10.3389/fncel.2016.00250

INTRODUCTION

The axon initial segment (AIS) is an excitable neuronal domain that separates the axonal and somatodendritic compartments and is involved in the initiation of action potentials (APs). The biophysical and structural characteristics of the AIS are considered ideal for AP initiation. In particular, the AIS has the lowest threshold for APs within neurons, due to the high density of voltage-gated Na^+ (Nav) channels (for review, Debanne et al., 2011), which is accomplished through an interaction with a molecular complex composed of membrane scaffolds, cell adhesion molecules and cytoskeletal proteins (for review, Ogawa and Rasband, 2008). In addition, the AIS is located proximally in the axon; the isolation from the soma makes the domain electrically compact, while the proximity to the soma maximizes the charge reaching the domain from the soma, thereby increasing its excitability and making this domain further preferable for AP initiation (for review, Kole and Stuart, 2012). Importantly, these biophysical and structural characteristics of the AIS vary among individual neurons (for review, Kuba, 2012). Moreover, they even change in a manner dependent on neural activity, indicating that the AIS is a site of plasticity and contributes to the fine regulation of neuronal output (for review, Grubb et al., 2011). Furthermore, recent studies have revealed that these biophysical and structural changes can interact with each other, emphasizing the necessity of understanding the interactions to interpret their effects on the neuronal output.

BIOPHYSICAL EFFECTS ON EXCITABILITY

Our understanding of the mechanisms by which the AIS regulates neuronal activity was advanced greatly by various findings regarding the subtypes, distributions and roles of ion channels at the AIS.

Three types of Nav channels are found at the AIS. Among them, Nav1.6 is the most common subtype (Jenkins and Bennett, 2001; Lorincz and Nusser, 2008) and has the lowest activation threshold (Colbert and Pan, 2002; Rush et al., 2005), thus being the primary contributor to AP initiation in most neurons. Notably, Nav1.6 is located distally within the AIS (Van Wart et al., 2007; Hu et al., 2009), and this segregation from the soma also makes it suitable for AP initiation (Palmer and Stuart, 2006; Kole et al., 2008; Hu et al., 2009; Baranauskas et al., 2013). On the other hand, Nav1.1 and Nav1.2 are expressed in a cell-type-specific manner and are located proximally within the AIS (Van Wart et al., 2007; Lorincz and Nusser, 2008; Hu et al., 2009). One possible role of these subtypes is to promote back-propagation of APs to dendrites (Hu et al., 2009).

Several types of voltage-gated K^+ (Kv) channels are reported at the AIS (Pan et al., 2006; Lorincz and Nusser, 2008). Since these Kv channels are expressed at different levels and in different combinations among neurons, they play a major role in determining the firing behavior of individual neurons (Johnston et al., 2010). In general, Kv1 (Kv1.1 and 1.2) and Kv7 (Kv7.2 and 7.3) channels have low activation thresholds and suppress AP generation by counteracting Nav channels either actively or passively as a shunt (Dodson et al., 2002; Goldberg et al., 2008; Shah et al., 2008; for review, Clark et al., 2009). In addition, Kv1 channels are known to be critical for shortening APs (Kole et al., 2007; Shu et al., 2007), and Kv7 channels contribute to maintaining availability of Nav channels by setting the resting potential (Battefeld et al., 2014). On the other hand, Kv2 (Kv2.1 and Kv2.2) channels have high activation thresholds. Therefore, Kv2 channels are preferentially activated by APs and promote repetitive firing by accelerating the repolarization of APs (Johnston et al., 2008).

Voltage-gated Ca^{2+} (Cav) channels, which were recently identified at the AIS, contribute to shaping the firing behavior of neurons in various ways. Cav2.3 and Cav3 have relatively low activation thresholds and promote AP generation by augmenting after-depolarization (Bender and Trussell, 2009), whereas Cav2.1 and Cav2.2 have high activation thresholds and suppress AP generation and facilitate AP repolarization by increasing shunting conductance via activation of Ca^{2+}-activated K^+ (BK) channels (Yu et al., 2010). Thus, multiple ion channels are expressed at the AIS, and their composition and distribution are strategically determined to shape the firing behavior of individual neurons.

STRUCTURAL EFFECTS ON EXCITABILITY

Structural characteristics of the AIS, such as length and distance from the soma, strongly affect the excitability and firing behavior of neurons (Kuba et al., 2006; Fried et al., 2009; Kuba and Ohmori, 2009; Kress et al., 2010). Effects of the AIS structure on neuronal excitability have been examined extensively in the nucleus laminaris, which is the third-order nucleus in the avian auditory pathway that is involved in sound localization (Kuba et al., 2006; for review Adachi et al., 2015). In this nucleus, the length of the AIS and its distance from the soma vary depending on the tuning frequency of the neurons, such that the AIS is shorter and more distal from the soma in neurons with higher tuning frequencies. This negative correlation between AIS length and distance from the soma is considered optimal for maximizing the excitability of the neurons.

The location of the AIS is related to the extent of its isolation from the soma, and greater distance increases the isolation. This isolation affects the excitability in two ways. First, it reduces the effects of the conductive and capacitive loads of somato-dendritic compartments on the AIS, thereby increasing the excitability. Second, it increases the dissipation of charges along the axon during propagation from the soma, thereby decreasing the excitability. Accordingly, the highest excitability of the AIS occurs at a certain distance from the soma, but a further increase in the distance reduces excitability because more charge is required to overcome the charge dissipation and generate APs (threshold current).

The surface area of the AIS is associated with the number of ion channels in this domain. This implies that elongation of the AIS increases both Na^+ and K^+ conductances in the AIS; the latter acts as a shunt around the resting potential (see above). In this situation, a longer AIS shows higher excitability, particularly when the AIS is located near the soma. This occurs because the increase in Na^+ conductance at the AIS helps the domain to overcome the effects of somato-dendritic loads, while the short distance enables the AIS to overcome the large shunting conductance in the domain. However, when the AIS is located distally from the soma, the long AIS becomes less excitable because the charge dissipation increases with the distance, making it difficult to depolarize the AIS above the AP threshold in the presence of the shunting conductance. On the other hand, a shorter AIS becomes more excitable at a distal location because it has a relatively small shunting conductance, and the effects of somato-dendritic loads are milder in this location. Thus, a negative correlation between the AIS length and distance from the soma can maximize excitability, and this relationship is critically influenced by the conductances at both the AIS and the somato-dendritic compartments. The importance of somato-dendritic compartments to this relationship is also reported in models with realistic neuronal morphologies (Gulledge and Bravo, 2016).

BIOPHYSICAL MODULATION OF THE AIS

Biophysical and structural characteristics of the AIS can change over different time scales, which endows neurons with efficient ways of adjusting their output. In many cases, biophysical changes are mediated through the modulation of ion channels via synaptic potentials and/or the activation of metabotropic receptors in the AIS and can proceed within milliseconds or seconds.

MODULATION VIA IONOTROPIC RECEPTORS

Glutamatergic excitatory synapses are not formed at the AIS. However, barrages of excitatory inputs to the somato-dendritic compartments temporally summate and cause a prolonged depolarization at the AIS. This alters the balance between Na^+ and K^+ conductances and affects the output of neurons. One prominent example is the inactivation of Kv1 channels during the depolarization, which broadens APs at the AIS and strengthens the synaptic output from cortical pyramidal neurons (Kole et al., 2007; Shu et al., 2007). Nav channels are also subjected to inactivation during the prolonged depolarization. This inactivation decreases with increasing distance from the soma, due to an electrotonic decrement of the depolarization. Accordingly, neurons overcome the effects of this inactivation and maintain their excitability by transient expansion of AP initiation areas at the AIS (hippocampus, Scott et al., 2014), or by localizing the AIS at a distal location (nucleus laminaris, see above, Kuba et al., 2006).

In cortical and hippocampal excitatory neurons, the AIS is innervated by GABAergic fast-spiking interneurons, and AP generation is directly modulated at the AIS (for review, Howard et al., 2005). This axo-axonic GABAergic input depolarizes the membrane (Szabadics et al., 2006; Woodruff et al., 2006) because potassium-chloride co-transporters, KCC2, which are the key molecules to extrude intracellular Cl^-, are very few at the AIS (Szabadics et al., 2006; Khirug et al., 2008). Although it is still debated, this GABAergic input has been suggested to decrease the output of neurons via an increase in the shunting conductance at the AIS, particularly during *in vivo*-like membrane potential depolarization (Woodruff et al., 2011).

MODULATION VIA METABOTROPIC RECEPTORS

Several metabotropic modulations are reported at the AIS. Modulation of Nav channels is mediated via $5HT_{1A}$ receptors (Cotel et al., 2013). Notably, however, the effects of this serotonergic modulation differ among neurons. In cortical pyramidal neurons, activation of $5HT_{1A}$ receptors decreases Na^+ conductance at the AIS via a positive shift in the activation curve of Nav channels (Yin et al., 2015). As this effect is specific to Nav1.2, this modulation suppresses back-propagation of APs with minimal effects on forward propagation in the axons. On the other hand, in auditory neurons of the medial superior olivary nucleus, activation of $5HT_{1A}$ receptors increases Na^+ conductance at the AIS and enhances AP generation (Ko et al., 2016). This occurs because activation of these receptors inhibits hyperpolarization- and cyclic-nucleotide-gated (HCN) channels, thereby hyperpolarizing the membrane at the AIS and decreasing the inactivation of Nav channels.

Cav channels are also the targets of modulation. In inhibitory interneurons of the dorsal cochlear nucleus, Cav3.2 is coupled with dopaminergic D3 receptors at the AIS and is inhibited via the activation of protein kinase C in a β-arrestin-dependent manner (Bender et al., 2010; Yang et al., 2016). Consequently, dopamine suppresses burst firing by eliminating after-depolarization and reduces neuronal output. In hippocampal granule cells, on the other hand, Cav3.2 is activated by muscarinic M1 receptors at the AIS and elevates $[Ca^{2+}]_i$ in this domain (Martinello et al., 2015). This elevation of $[Ca^{2+}]_i$ causes a negative shift in the activation curve of Kv7 channels, thereby reducing the shunting conductance and augmenting AP generation. Thus, ion channels at the AIS are modulated in a cell-type-specific manner, which enables the appropriate adjustment of output in individual neurons.

STRUCTURAL PLASTICITY OF THE AIS

Structural characteristics of the AIS change depending on neuronal activity, which contributes to homeostatic control of excitability. This is rather slow in time course, and it requires hours or days to proceed. Two types of structural plasticity of the AIS are reported.

CHANGE IN LOCATION

Changes in AIS location were first observed in dissociated hippocampal culture (Grubb and Burrone, 2010; Evans et al., 2013). With chronic depolarization (2 days) via photo-stimulation or high $[K^+]_o$ media, all types of excitatory neurons in the culture move the entire AIS distally, resulting in a decrease in their excitability. Importantly, in dissociated culture of the olfactory bulb, chronic depolarization causes reciprocal movements of the AIS in excitatory and inhibitory neurons; the AIS moves proximally in inhibitory interneurons, whereas it moves distally in excitatory neurons (Chand et al., 2015), implying the cell-type-specific nature of the AIS plasticity. These reciprocal movements of the AIS may counterbalance the excess activity in the circuit. Indeed, changes in AIS locations are found in various disease models that are associated with hyperexcitability of neurons, such as epilepsy and demyelination (Harty et al., 2013; Hamada and Kole, 2015), supporting the idea that the AIS plasticity works as a negative-feedback mechanism to maintain homeostasis of the neural circuit.

CHANGE IN LENGTH

Changes in AIS length are also observed in pathological conditions. In the avian cochlear nucleus, in which neurons are innervated by the auditory nerve and send their projections to nucleus laminaris, the AIS elongates within several days after deprivation of auditory input (Kuba et al., 2010). This elongation adds Na^+ conductance to the distal location and enhances the excitability, allowing the neurons to compensate for the loss of auditory nerve activity. Elongation also occurs in a mouse model of Angelman syndrome, which is a neurodevelopmental disorder associated with autism (Kaphzan et al., 2011), whereas shortening occurs after demyelination, stroke and traumatic brain injury (Baalman et al., 2013; Harty et al., 2013; Hamada and Kole, 2015). These alterations in AIS length would be critical in adjusting activity and maintaining homeostasis of neural circuits. In addition to the pathological conditions, length of the AIS changes in immature animals, particularly after the appearance of afferent inputs, implicating the involvement of AIS plasticity in the refinement of neural circuits during development (Cruz et al., 2009; Gutzmann et al., 2014; Kuba et al., 2014).

BIOPHYSICAL INTERACTION DURING STRUCTURAL PLASTICITY

Recent studies have revealed that structural plasticity of the AIS coincides with changes in expression and/or modulation of ion channels at the domain. This is reasonable because the effects of AIS structure on excitability are tightly regulated by biophysical characteristics of the AIS.

In the avian cochlear nucleus, deprivation of auditory inputs elongates the AIS (see above). This elongation is accompanied by subtype-specific changes in expression of Kv channels: Kv1 decreases, whereas Kv7 increases at the AIS, resulting in complementary changes in their expression levels (**Figure 1A**; Kuba et al., 2015). Kv1 has rapid kinetics and is activated strongly with depolarization, while Kv7 has slow kinetics and behaves rather like passive conductance. Accordingly, these complementary changes in Kv channels reduce the shunting conductance during AP initiation, allowing the elongated AIS to compensate for the loss of auditory inputs more efficiently, with minimal effects on resting potential. This implies that these structural and biophysical changes in the AIS work synergistically and maintain the homeostasis of central auditory circuits after hearing loss.

In dentate granule cells of hippocampal cultures, on the other hand, structural and biophysical changes in the AIS are antagonistic (**Figure 1B**; Evans et al., 2015). Depolarizing the neurons for 3 h causes a shortening of the AIS, which is accompanied by de-phosphorylation of Nav channels in this domain; the shortening reduces excitability, whereas the de-phosphorylation of Nav channels increases excitability. Accordingly, these alterations counteract each other and maintain the excitability at a constant level. Nevertheless, the physiological role of this interaction remains elusive.

Notably, a longer depolarization (2 days) moves the AIS distally and suppresses excitability in the hippocampal neurons (see above; Evans et al., 2013). Although this movement is not accompanied by changes in the ion channel composition at the AIS (Grubb and Burrone, 2010), nor in the location of axo-axonic GABAergic synapses (**Figure 1C**; Wefelmeyer et al., 2015), it results in a spatial mismatch between the axo-axonic synapses and the AIS, augmenting the suppressive effects of

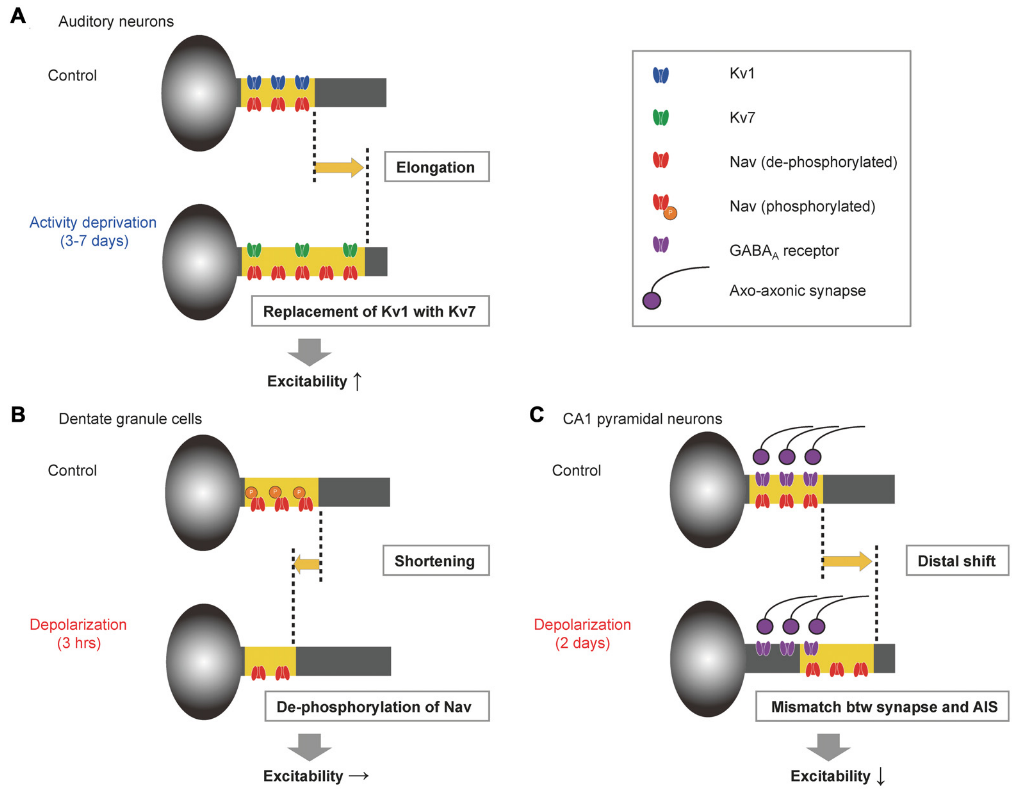

FIGURE 1 | Examples of structural and biophysical interaction during axon initial segment (AIS) plasticity. (A) In neurons of the avian cochlear nucleus, elongation of the AIS is accompanied by replacement of Kv1 with Kv7 at the AIS, which augments the effects of elongation on excitability (Kuba et al., 2015). **(B)** In hippocampal dentate granule cells, depolarization for 3 h shortens the AIS but simultaneously de-phosphorylates voltage-gated Na$^+$ (Nav) channels, which offsets the effects of shortening on excitability (Evans et al., 2015). **(C)** In hippocampal CA1 pyramidal neurons, depolarization for 2 days moves the AIS distally, but axo-axonic synapses remain at the original location, augmenting the suppressive effects of distal movement on excitability (Wefelmeyer et al., 2015).

the AIS movement. This augmentation occurs because the remaining synapses increase the shunting conductance between the soma and the AIS and reduce the charges reaching the AIS.

Structural plasticity of the AIS depends on changes in $[Ca^{2+}]_i$ via L-type Ca^{2+} channels (Grubb and Burrone, 2010), but their downstream signaling differs according to the types of plasticity. Key molecules are the calcium-dependent phosphatase calcineurin and cyclin-dependent kinase 5 (cdk5); calcineurin mediates the distal movement of the AIS in hippocampal neurons (Evans et al., 2013), whereas cdk5 mediates the proximal movement in olfactory bulb inhibitory interneurons (Chand et al., 2015). Although the precise mechanisms by which these molecules reorganize the AIS structure remain unknown, the mechanisms may involve post-translational modification of AIS proteins (Yoshimura and Rasband, 2014). Interestingly, it has been reported that calcineurin causes shortening of the AIS and simultaneously de-phosphorylates Nav channels in dentate granule cells (Evans et al., 2015). In addition, a blockade of cdk5 decreases the length of the AIS-like structure in mushroom body neurons in *Drosophila* (Trunova et al., 2011), whereas accumulation of Kv1 at the AIS requires phosphorylation via cdk2 and/or cdk5 (Vacher et al., 2011). These findings may indicate that structural and biophysical changes in the AIS share the same signaling molecules.

CONCLUSION

Biophysical changes in the AIS are rapid, proceeding within milliseconds or seconds, and they can therefore contribute to modulating neuronal signal processing. On the other hand, structural changes are much slower, generally on the order of days, and would contribute to stability or refinement of neural circuits. Further, it is now evident that some structural changes can occur with a much faster time scale (within hours), allowing them to interact with other forms of plasticity, including long-term potentiation or depression, and shape neuronal signal processing. In addition, biophysical changes in the AIS occur simultaneously with structural changes and determine the effects of modulation. This indicates that the structural and functional plasticities of the AIS provide multiple and efficient methods of regulating neuronal excitability over various time scales and would enable the fine adjustment of neural activity during both physiological and pathological conditions.

However, many questions remain. Why do different types of AIS plasticity occur in individual cell types, e.g., resizing with redistribution of Kv channels in auditory neurons vs. relocation without redistribution of ion channels in hippocampal neurons? What is the mechanism for determining the types of plasticity implemented? How is the plasticity temporally and spatially regulated? How does it interact with other forms of plasticity? It is also important to see the impact of AIS plasticity on the function of neural circuits as well as its roles in the signal processing of individual neurons. As the AIS is the site of AP generation, and given that its abnormalities are associated with various neuropsychiatric disorders (Wimmer et al., 2010; Buffington and Rasband, 2011), exploring these issues will help us to understand the mechanisms by which activity is regulated in the brain during health and disease.

AUTHOR CONTRIBUTIONS

HK and RY wrote the manuscript.

ACKNOWLEDGMENTS

This work was supported by Grants-in-aid from the MEXT (16K08493 to RY and 15H04257 to HK).

REFERENCES

Adachi, R., Yamada, R., and Kuba, H. (2015). Plasticity of the axonal trigger zone. *Neuroscientist* 21, 255–265. doi: 10.1177/1073858414535986

Baalman, K. L., Cotton, R. J., Rasband, S. N., and Rasband, M. N. (2013). Blast wave exposure impairs memory and decreases axon initial segment length. *J. Neurotrauma* 30, 741–751. doi: 10.1089/neu.2012.2478

Baranauskas, G., David, Y., and Fleidervish, I. A. (2013). Spatial mismatch between the Na^+ flux and spike initiation in axon initial segment. *Proc. Natl. Acad. Sci. U S A* 110, 4051–4056. doi: 10.1073/pnas.1215125110

Battefeld, A., Tran, B. T., Gavrilis, J., Cooper, E. C., and Kole, M. H. (2014). Heteromeric kv7.2/7.3 channels differentially regulate action potential initiation and conduction in neocortical myelinated axons. *J. Neurosci.* 34, 3719–3732. doi: 10.1523/jneurosci.4206-13.2014

Bender, K. J., Ford, C. P., and Trussell, L. O. (2010). Dopaminergic modulation of axon initial segment calcium channels regulates action potential initiation. *Neuron* 68, 500–511. doi: 10.1016/j.neuron.2010.09.026

Bender, K. J., and Trussell, L. O. (2009). Axon initial segment Ca^{2+} channels influence action potential generation and timing. *Neuron* 61, 259–271. doi: 10.1016/j.neuron.2008.12.004

Buffington, S. A., and Rasband, M. N. (2011). The axon initial segment in nervous system disease and injury. *Eur. J. Neurosci.* 34, 1609–1619. doi: 10.1111/j.1460-9568.2011.07875.x

Chand, A. N., Galliano, E., Chesters, R. A., and Grubb, M. S. (2015). A distinct subtype of dopaminergic interneuron displays inverted structural plasticity at the axon initial segment. *J. Neurosci.* 35, 1573–1590. doi: 10.1523/jneurosci.3515-14.2015

Clark, B. D., Goldberg, E. M., and Rudy, B. (2009). Electrogenic tuning of the axon initial segment. *Neuroscientist* 15, 651–668. doi: 10.1177/1073858409341973

Colbert, C. M., and Pan, E. (2002). Ion channel properties underlying axonal action potential initiation in pyramidal neurons. *Nat. Neurosci.* 5, 533–538. doi: 10.1038/nn857

Cotel, F., Exley, R., Cragg, S. J., and Perrier, J. F. (2013). Serotonin spillover onto the axon initial segment of motoneurons induces central fatigue by inhibiting action potential initiation. *Proc. Natl. Acad. Sci. U S A* 110, 4774–4779. doi: 10.1073/pnas.1216150110

Cruz, D. A., Lovallo, E. M., Stockton, S., Rasband, M., and Lewis, D. A. (2009). Postnatal development of synaptic structure proteins in pyramidal neuron axon initial segments in monkey prefrontal cortex. *J. Comp. Neurol.* 514, 353–367. doi: 10.1002/cne.22006

Debanne, D., Campanac, E., Bialowas, A., Carlier, E., and Alcaraz, G. (2011). Axon physiology. *Physiol. Rev.* 91, 555–602. doi: 10.1152/physrev.00048.2009

Dodson, P. D., Barker, M. C., and Forsythe, I. D. (2002). Two heteromeric Kv1 potassium channels differentially regulate action potential firing. *J. Neurosci.* 22, 6953–6961.

Evans, M. D., Dumitrescu, A. S., Kruijssen, D. L., Taylor, S. E., and Grubb, M. S. (2015). Rapid modulation of axon initial segment length influences repetitive spike firing. *Cell Rep.* 13, 1233–1245. doi: 10.1016/j.celrep.2015.09.066

Evans, M. D., Sammons, R. P., Lebron, S., Dumitrescu, A. S., Watkins, T. B. K., Uebele, V. N., et al. (2013). Calcineurin signaling mediates activity-dependent relocation of the axon initial segment. *J. Neurosci.* 33, 6950–6963. doi: 10.1523/JNEUROSCI.0277-13.2013

Fried, S. I., Lasker, A. C., Desai, N. J., Eddington, D. K., and Rizzo, J. F. III. (2009). Axonal sodium-channel bands shape the response to electric stimulation in retinal ganglion cells. *J. Neurophysiol.* 101, 1972–1987. doi: 10.1152/jn.91081.2008

Goldberg, E. M., Clark, B. D., Zagha, E., Nahmani, M., Erisir, A., and Rudy, B. (2008). K^+ channels at the axon initial segment dampen near-threshold excitability of neocortical fast-spiking GABAergic interneurons. *Neuron* 58, 387–400. doi: 10.1016/j.neuron.2008.03.003

Grubb, M. S., and Burrone, J. (2010). Activity-dependent relocation of the axon initial segment fine-tunes neuronal excitability. *Nature* 465, 1070–1074. doi: 10.1038/nature09160

Grubb, M. S., Shu, Y., Kuba, H., Rasband, M. N., Wimmer, V. C., and Bender, K. J. (2011). Short- and long-term plasticity at the axon initial segment. *J. Neurosci.* 31, 16049–16055. doi: 10.1523/jneurosci.4064-11.2011

Gulledge, A. T., and Bravo, J. J. (2016). Neuron morphology influences axon initial segment plasticity. *eNeuro* 3:e0085–15.2016. doi: 10.1523/eneuro.0085-15.2016

Gutzmann, A., Ergül, N., Grossmann, R., Schultz, C., Wahle, P., and Engelhardt, M. (2014). A period of structural plasticity at the axon initial segment in developing visual cortex. *Front. Neuroanat.* 8:11. doi: 10.3389/fnana.2014.00011

Hamada, M. S., and Kole, M. H. (2015). Myelin loss and axonal ion channel adaptations associated with gray matter neuronal hyperexcitability. *J. Neurosci.* 35, 7272–7286. doi: 10.1523/jneurosci.4747-14.2015

Harty, R. C., Kim, T. H., Thomas, E. A., Cardamone, L., Jones, N. C., Petrou, S., et al. (2013). Axon initial segment structural plasticity in animal models of genetic and acquired epilepsy. *Epilepsy Res.* 105, 272–279. doi: 10.1016/j.eplepsyres.2013.03.004

Howard, A., Tamas, G., and Soltesz, I. (2005). Lighting the chandelier: new vistas for axo-axonic cells. *Trends Neurosci.* 28, 310–316. doi: 10.1016/j.tins.2005.04.004

Hu, W., Tian, C., Li, T., Yang, M., Hou, H., and Shu, Y. (2009). Distinct contributions of Na(v)1.6 and Na(v)1.2 in action potential initiation and backpropagation. *Nat. Neurosci.* 12, 996–1002. doi: 10.1038/nn.2359

Jenkins, S. M., and Bennett, V. (2001). Ankyrin-G coordinates assembly of the spectrin-based membrane skeleton, voltage-gated sodium channels and L1 CAMs at Purkinje neuron initial segments. *J. Cell Biol.* 155, 739–746. doi: 10.1083/jcb.200109026

Johnston, J., Forsythe, I. D., and Kopp-Scheinpflug, C. (2010). Going native: voltage-gated potassium channels controlling neuronal excitability. *J. Physiol.* 588, 3187–3200. doi: 10.1113/jphysiol.2010.191973

Johnston, J., Griffin, S. J., Baker, C., Skrzypiec, A., Chernova, T., and Forsythe, I. D. (2008). Initial segment Kv2.2 channels mediate a slow delayed rectifier and maintain high frequency action potential firing in medial nucleus of the trapezoid body neurons. *J. Physiol.* 586, 3493–3509. doi: 10.1113/jphysiol.2008.153734

Kaphzan, H., Buffington, S. A., Jung, J. I., Rasband, M. N., and Klann, E. (2011). Alterations in intrinsic membrane properties and the axon initial segment in a mouse model of angelman syndrome. *J. Neurosci.* 31, 17637–17648. doi: 10.1523/jneurosci.4162-11.2011

Khirug, S., Yamada, J., Afzalov, R., Voipio, J., Khiroug, L., and Kaila, K. (2008). GABAergic depolarization of the axon initial segment in cortical principle neurons is caused by the Na–K–2Cl cotransporter NKCC1. *J. Neuroci.* 28, 4635–4639. doi: 10.1523/JNEUROSCI.0908-08.2008

Ko, K. W., Rasband, M. N., Meseguer, V., Kramer, R. H., and Golding, N. L. (2016). Serotonin modulates spike probability in the axon initial segment through HCN channels. *Nat. Neurosci.* 19, 826–834. doi: 10.1038/nn.4293

Kole, M. H., Ilschner, S. U., Kampa, B. M., Williams, S. R., Ruben, P. C., and Stuart, G. J. (2008). Action potential generation requires a high sodium channel density in the axon initial segment. *Nat. Neurosci.* 11, 178–186. doi: 10.1038/nn2040

Kole, M. H., Letzkus, J. J., and Stuart, G. J. (2007). Axon initial segment Kv1 channels control axonal action potential waveform and synaptic efficacy. *Neuron* 55, 633–647. doi: 10.1016/j.neuron.2007.07.031

Kole, M. H. P., and Stuart, G. J. (2012). Signal processing in the axon initial segment. *Neuron* 73, 235–247. doi: 10.1016/j.neuron.2012.01.007

Kress, G. J., Dowling, M. J., Eisenman, L. N., and Mennerick, S. (2010). Axonal sodium channel distribution shapes the depolarized action potential threshold of dentate granule neurons. *Hippocampus* 20, 558–571. doi: 10.1002/hipo.20667

Kuba, H. (2012). Structural tuning and plasticity of the axon initial segment in auditory neurons. *J. Physiol.* 590, 5571–5579. doi: 10.1113/jphysiol.2012.237305

Kuba, H., Adachi, R., and Ohmori, H. (2014). Activity-dependent and activity-independent development of the axon initial segment. *J. Neurosci.* 34, 3443–3453. doi: 10.1523/jneurosci.4357-13.2014

Kuba, H., Ishii, T. M., and Ohmori, H. (2006). Axonal site of spike initiation enhances auditory coincidence detection. *Nature* 444, 1069–1072. doi: 10.1038/nature05347

Kuba, H., and Ohmori, H. (2009). Roles of axonal sodium channels in precise auditory time coding at nucleus magnocellularis of the chick. *J. Physiol.* 587, 87–100. doi: 10.1113/jphysiol.2008.162651

Kuba, H., Oichi, Y., and Ohmori, H. (2010). Presynaptic activity regulates Na^+ channel distribution at the axon initial segment. *Nature* 465, 1075–1078. doi: 10.1038/nature09087

Kuba, H., Yamada, R., Ishiguro, G., and Adachi, R. (2015). Redistribution of Kv1 and Kv7 enhances neuronal excitability during structural axon initial segment plasticity. *Nat. Commun.* 6:8815. doi: 10.1038/ncomms9815

Lorincz, A., and Nusser, Z. (2008). Cell-type-dependent molecular composition of the axon initial segment. *J. Neurosci.* 28, 14329–14340. doi: 10.1523/jneurosci.4833-08.2008

Martinello, K., Huang, Z., Lujan, R., Tran, B., Watanabe, M., Cooper, E. C., et al. (2015). Cholinergic afferent stimulation induces axonal function plasticity in adult hippocampal granule cells. *Neuron* 85, 346–363. doi: 10.1016/j.neuron.2014.12.030

Ogawa, Y., and Rasband, M. N. (2008). The functional organization and assembly of the axon initial segment. *Curr. Opin. Neurobiol.* 18, 307–313. doi: 10.1016/j.conb.2008.08.008

Palmer, L. M., and Stuart, G. J. (2006). Site of action potential initiation in layer 5 pyramidal neurons. *J. Neurosci.* 26, 1854–1863. doi: 10.1523/jneurosci.4812-05.2006

Pan, Z., Kao, T., Horvath, Z., Lemos, J., Sul, J.-Y., Cranstoun, S. D., et al. (2006). A common ankyrin-G-based mechanism retains KCNQ and Nav channels at electrically active domains of the axon. *J. Neurosci.* 26, 2599–2613. doi: 10.1523/jneurosci.4314-05.2006

Rush, A. M., Dib-Hajj, S. D., and Waxman, S. G. (2005). Electrophysiological properties of two axonal sodium channels, Nav1.2 and Nav1.6, expressed in mouse spinal sensory neurones. *J. Physiol.* 564, 803–815. doi: 10.1113/jphysiol.2005.083089

Scott, R. S., Henneberger, C., Padmashri, R., Anders, S., Jensen, T. P., and Rusakov, D. A. (2014). Neuronal adaptation involves rapid expansion of the action potential initiation site. *Nat. Commun.* 5:3817. doi: 10.1038/ncomms4817

Shah, M. M., Migliore, M., Valencia, I., Cooper, E. C., and Brown, D. A. (2008). Functional significance of axonal Kv7 channels in hippocampal pyramidal neurons. *Proc. Natl. Acad. Sci. U S A* 105, 7869–7874. doi: 10.1073/pnas.0802805105

Shu, Y., Yu, Y., Jang, J., and McCormick, D. A. (2007). Selective control of cortical axonal spikes by a slowly inactivating K^+ current. *Proc. Natl. Acad. Sci. U S A* 104, 11453–11458. doi: 10.1073/pnas.0702041104

Szabadics, J., Varga, C., Molnár, G., Oláh, S., Barzó, P., and Tamás, G. (2006). Excitatory effect of GABAergic axo-axonic cells in cortical microcircuits. *Science* 311, 233–235. doi: 10.1126/science.1121325

Trunova, S., Baek, B., and Giniger, E. (2011). Cdk5 regulates the size of an axon initial segment-like compartment in mushroom body neurons of the Drosophila central brain. *J. Neurosci.* 31, 10451–10462. doi: 10.1523/jneurosci.0117-11.2011

Vacher, H., Yang, J. W., Cerda, O., Autillo-Touati, A., Dargent, B., and Trimmer, J. S. (2011). Cdk-mediated phosphorylation of the Kvβ2 auxiliary subunit regulates Kv1 channel axonal targeting. *J. Cell Biol.* 192, 813–824. doi: 10.1083/jcb.201007113

Van Wart, A., Trimmer, J. S., and Matthews, G. (2007). Polarized distribution of Ion channels within microdomains of the axon initial segment. *J. Comp. Neurol.* 500, 339–352. doi: 10.1002/cne.21173

Wefelmeyer, W., Cattaert, D., and Burrone, J. (2015). Activity-dependent mismatch between axo-axonic synapses and the axon initial segment controls neuronal output. *Proc. Natl. Acad. Sci. U S A* 112, 9757–9762. doi: 10.1073/pnas.1502902112

Wimmer, V. C., Reid, C. A., So, E. Y., Berkovic, S. F., and Petrou, S. (2010). Axon initial segment dysfunction in epilepsy. *J. Physiol.* 588, 1829–1840. doi: 10.1113/jphysiol.2010.188417

Woodruff, A. R., McGarry, L. M., Vogels, T. P., Inan, M., Anderson, S. A., and Yuste, R. (2011). State-dependent function of neocortical chandelier cells. *J. Neurosci.* 31, 17872–17886. doi: 10.1523/jneurosci.3894-11.2011

Woodruff, A. R., Monyer, H., and Sah, P. (2006). GABArgic excitation in the basolateral amygdala. *J. Neurosci.* 26, 11881–11887. doi: 10.1523/JNEUROSCI.3389-06.2006

Yang, S., Ben-Shalom, R., Ahn, M., Liptak, A. T., van Rijn, R. M., Whistler, J. L., et al. (2016). β-arrestin-dependent dopaminergic regulation of calcium channel activity in the axon initial segment. *Cell Rep.* 16, 1518–1526. doi: 10.1016/j.celrep.2016.06.098

Yin, L., Rasch, M. J., He, Q., Wu, S., Dou, F., and Shu, Y. (2015). Selective modulation of axonal sodium channel subtypes by 5-HT1A receptor in cortical pyramidal neuron. *Cereb. Cortex* doi: 10.1093/cercor/bhv245 [Epub ahead of print].

Yoshimura, T., and Rasband, M. N. (2014). Axon initial segments: diverse and dynamic neuronal compartments. *Curr. Opin. Neurobiol.* 27, 96–102. doi: 10.1016/j.conb.2014.03.004

Yu, Y., Maureira, C., Liu, X., and McCormick, D. (2010). P/Q and N channels control baseline and spike-triggered calcium levels in neocortical axons and synaptic boutons. *J. Neurosci.* 30, 11858–11869. doi: 10.1523/jneurosci.2651-10.2010

Conflict of Interest Statement: The authors declare that the research was conducted in the absence of any commercial or financial relationships that could be construed as a potential conflict of interest.

frontiers in Cellular Neuroscience

ORIGINAL RESEARCH
published: 27 February 2017
doi: 10.3389/fncel.2017.00045

Loss of Saltation and Presynaptic Action Potential Failure in Demyelinated Axons

Mustafa S. Hamada[1,2], Marko A. Popovic[1] and Maarten H. P. Kole[1,2]*

[1]Department of Axonal Signaling, Netherlands Institute for Neuroscience, Royal Netherlands Academy of Arts and Sciences, Amsterdam, Netherlands, [2]Cell Biology, Faculty of Science, Utrecht University, Utrecht, Netherlands

In cortical pyramidal neurons the presynaptic terminals controlling transmitter release are located along unmyelinated axon collaterals, far from the original action potential (AP) initiation site, the axon initial segment (AIS). Once initiated, APs will need to reliably propagate over long distances and regions of geometrical inhomogeneity like branch points (BPs) to rapidly depolarize the presynaptic terminals and confer temporally precise synaptic transmission. While axon pathologies such as demyelinating diseases are well established to impede the fidelity of AP propagation along internodes, to which extent myelin loss affects propagation along BPs and axon collaterals is not well understood. Here, using the cuprizone demyelination model, we performed optical voltage-sensitive dye (VSD) imaging from control and demyelinated layer 5 pyramidal neuron axons. In the main axon, we find that myelin loss switches the modality of AP propagation from rapid saltation towards a slow continuous wave. The duration of single AP waveforms at BPs or nodes was, however, only slightly briefer. In contrast, by using two-photon microscopy-guided loose-seal patch recordings from axon collaterals we revealed a presynaptic AP broadening in combination with a reduced velocity and frequency-dependent failure. Finally, internodal myelin loss was also associated with *de novo* sprouting of axon collaterals starting from the primary (demyelinated) axon. Thus, the loss of oligodendrocytes and myelin sheaths bears functional consequences beyond the main axon, impeding the temporal fidelity of presynaptic APs and affecting the functional and structural organization of synaptic connectivity within the neocortex.

Keywords: axon, axon collaterals, boutons, node of Ranvier, action potential, demyelination

OPEN ACCESS

Edited by:
Vann Bennett,
Howard Hughes Medical Institute,
USA

Reviewed by:
Mark Bevan,
Northwestern University, USA
Jason M. Christie,
Max Planck Florida Institute for
Neuroscience, USA

Correspondence:
Maarten H. P. Kole
m.kole@nin.knaw.nl

Received: *25 November 2016*
Accepted: *09 February 2017*
Published: *27 February 2017*

Citation:
Hamada MS, Popovic MA and Kole MHP (2017) Loss of Saltation and Presynaptic Action Potential Failure in Demyelinated Axons. Front. Cell. Neurosci. 11:45. doi: 10.3389/fncel.2017.00045

INTRODUCTION

Action potentials (APs) are the primary signals by which neural information is electrically encoded and distributed throughout the nervous system to provide temporally precise neurotransmitter release at the presynaptic terminals. In most neurons, the presynaptic terminals are anatomically dispersed along the branches of axon collaterals, far away from the original AP initiation site in the axon initial segment (AIS; Kole and Stuart, 2012). Such anatomical organization requires the AP voltage transient to reliably propagate when covering long distances from the AIS until the transmitter release sites. Such reliability is particularly important considering that neural coding strategies in the neocortex are often relying on a sparse coding scheme, in which low mean firing rates of individual neurons represent features of sensory modalities (Brecht et al., 2004; Harris and Mrsic-Flogel, 2013), the temporal fidelity of how APs propagate from their initiation site into complex branched axonal trees and the presynaptic terminal limits the capacity for neural information encoding.

AP propagation is well known to fail at low-safety conduction points including branch points (BPs), regions of inhomogeneity or abrupt diameter changes in an activity-dependent manner (Goldstein and Rall, 1974; Parnas and Segev, 1979; Deschênes and Landry, 1980; Manor et al., 1991; Ducreux et al., 1993; Debanne et al., 1997). These observations led to the general notion that the temporal features of neuronal firing in highly branched axon terminals may differ from their main axon (Deschênes and Landry, 1980). AP propagation fidelity is furthermore strongly compromised in axon pathologies such as demyelinating diseases. In the spinal cord, optic nerve, corpus callosum and neocortex myelin loss causes a substantial slowing in conduction velocity (McDonald and Sears, 1970; Bostock and Sears, 1978; Felts et al., 1997; Crawford et al., 2009; Hamada and Kole, 2015). However, whether AP propagation into the higher-order small-diameter collaterals, where all synaptic terminals reside, is equally impaired remains poorly understood. Axon collaterals are typically unmyelinated but given their complex branched geometries, we hypothesized that they may be particularly sensitive to demyelination-induced failures in high-frequency firing (Bostock and Sears, 1978; Kim et al., 2013). In addition, demyelination produces a large variability in both nodal anchoring proteins (Ankyrin G and βIV-spectrin) and their voltage-gated ion channel expression (Nav and Kv7) along individual axons (Hamada and Kole, 2015), possibly impairing invasion of collaterals. Transmission failures at BPs could also arise from local Nav channel inactivation causing frequency-dependent failure during high-frequency firing in axons (Monsivais et al., 2005; Khaliq and Raman, 2006).

In order to determine the impact of myelin loss on AP fidelity in the main axon and their collateral branches, we performed optical voltage-sensitive dye (VSD) imaging and two-photon microscopy-guided patch-clamp recordings from en passant presynaptic boutons in layer 5 axon collaterals. We find that myelin loss causes a frequency-dependent failure of APs at the presynaptic terminals. In addition, axon collaterals in demyelinated axons showed *de novo* sprouting. Taken together, demyelination affects intra-cortical synaptic transmission beyond a slowing of AP signaling in the originally myelinated main axon.

MATERIALS AND METHODS

Electrophysiological Recordings and Two-Photon Imaging

Male C57BL/6 mice were kept on a 12:12 h light-dark cycle and brain slices prepared at ∼3 h after onset of the light period. A total of 20 mice were used (control, $n = 9$, 11 weeks; cuprizone, $n = 11$, 11 weeks). Mice in the cuprizone experimental group were fed with 0.2% cuprizone for 5 weeks supplemented in the diet and acute slice preparation and recording from layer 5 pyramidal neurons in somatosensory cortex were performed in cortical slices (300 μm) as previously described (Hamada and Kole, 2015). All experiments and protocols were in compliance with the European Communities Council Directive of 24 November 1986 (86/609/EEC) and were reviewed and approved by the animal welfare and ethics committee (DEC) of the Royal Netherlands Academy of Arts and Sciences (KNAW) under the protocol number NIN 11.70.

Two-photon (2P) visualization and electrophysiological recordings were performed using galvanometer-based laser-scanning microscope (Femto3D-RC, Femtonics Inc., Budapest, Hungary). A Ti:Sapphire pulsed laser (Chameleon Ultra II, Coherent Inc., Santa Clara, CA, USA) tuned to 800 nm was used for two-photon excitation. Three photomultipliers (PMTs, Hamamatsu Photonics Co., Hamamatsu, Japan) were used for signal detection, two were used to collect the fluorescence signals and one to scan the transmitted IR-light (800 nm). The two signals were overlaid for fluorescence-assisted patching from axons. Whole-cell somatic patch-clamp pipettes were filled with intracellular solution containing 200 μM Alexa Fluor 568 hydrazide (Sigma-Aldrich) to visualize cellular morphology. Layer 5 pyramidal neurons in the primary somato-sensory cortex were filled for at least 30 min in whole-cell configuration before commencing with dual soma-axon recording approaches. For axonal loose-seal patch-clamp recordings the signals were filtered at 2 kHz using a Multiclamp 700B (Molecular Devices Co., Sunnyvale, CA, USA). Loose-seal recordings from visually identified BPs and *en passant* boutons were accomplished by gently pressing the pipette tip (∼10 MΩ open tip resistance) against the membrane and applying negative pressure to form a seal resistance between ∼30 and 50 MΩ. All recordings were made at 32 ± 1°C. Electrophysiological data were digitized (ITC-18 InstruTECH, HEKA Elektronik GmbH) at 100 kHz and acquired using AxoGraph X (v. 1.5.4, Molecular Devices Co., Sunnyvale, CA, USA). APs were analyzed using custom-written routines in MatLab (The MathWorks Inc., Natick, MA, USA). High frequency somatic APs were evoked by brief (1 ms) square currents pulses with decreasing inter-pulse intervals. To convert loose-seal recorded APs into binary probability values, the failure of propagation was determined using a semi-automatic routine with a threshold set at ∼25% of the maximal amplitude of the first evoked bouton AP, confirmed by visual inspection of each individual spike.

Immunohistochemistry and Confocal Microscopy

Live imaging of primary axons of layer 5 pyramidal neurons was done using 2P laser-scanning microscope (Femto3D-RC, Femtonics Inc., Budapest, Hungary). Neurons were loaded with dye (200 μM Alexa 568) for at least 30 min to allow sufficient diffusion into the primary axon and collaterals. For morphological analysis, a z-stack with a 300 × 300 μm field of view was scanned at a resolution of 1000 × 1000 pixels (1 μm z-step) using a 60× (NA1.0) water-immersion objective.

Images were saved as TIFF files and later processed using Fiji (ImageJ) graphics software (v1.47p, NIH). Immediately after recording and imaging slices were transferred to a fixative containing 4% paraformaldehyde (20 min). Brain slices were then blocked with 10% bovine serum albumin (BSA), 5% normal goat serum (NGS) and 2% Triton X-100 for 2 h at room temperature (RT) before incubation with mouse anti-myelin basic protein (MBP; 1:250; Covance Inc., Princeton, NJ, USA), rabbit anti-βIV-spectrin (1:250, gift from M. N. Rasband, Baylor College of Medicine, Houston, TX, USA), fluorophore-conjugated streptavidin (1:500; Invitrogen B.V., Groningen, Netherlands) for 24 h, followed by second antibody incubation for 2 h (488 goat anti-rabbit, streptavidin-conjugated 568, and 633 goat anti-mouse, Invitrogen B.V., Groningen, Netherlands). Confocal images of labeled neurons were collected with a Leica TCS SP8 X confocal laser-scanning microscope (Leica Microsystems GmbH) at 2048 × 2048 pixels (0.5 μm z-step) using a 40× (1.3 N.A., 0.75–1.0 digital zoom) oil-immersion objective. To avoid bleed-through between emission wavelengths, automated sequential acquisition of multiple channels was used.

Optical Voltage-Sensitive Dye Recordings

Individual layer 5 pyramidal neurons from somatosensory cortex were selectively labeled with a membrane impermeable VSD by allowing free diffusion of the probe from a somatic patch pipette in the whole-cell configuration. We used the most successful voltage probe for intracellular application, JPW3028, which is a doubly positively charged analog of the ANEP series of lipophilic styryl dyes that is still sufficiently water soluble to be used for microinjection. Its close analog JPW1114 characterized by the same voltage sensitivity is commercially available (Catalog number D6923, Invitrogen, ThermoFisher Scientific Inc., Waltham, MA, USA). Patch pipettes were first filled with the dye-free solution to about three quarters of the pipette taper and then filled with the solution containing the indicator dye (0.8 mM). Intracellular filling was accomplished in 30–60 min. To stimulate and obtain electrical recordings from the soma, the cell body was re-patched using an electrode filled with dye-free intracellular solution before making optical measurements. We used a stationary upright microscope (Olympus BX51WI, Olympus, Japan) equipped with two camera ports. One camera port had a high spatial resolution CCD camera for oblique contrast video-microscopy (CoolSNAP EZ, Photometrics). The second camera port had a fast data acquisition camera with relatively low spatial resolution (80 × 80 pixels) but outstanding dynamic range (14 bits) and exceptionally low read noise (NeuroCCD-SM, RedShirtImaging LLC, Decatur, GA, USA).

The brain slice was placed on the stage of the microscope and the fluorescent image of the stained neuron projected by a water immersion objective (100×/1.1 NA, Nikon, Japan) onto the fast data acquisition CCD positioned in the primary image plane. This objective was selected as a compromise between imaging area, spatial resolution, and signal-to-noise ratio (S/N). Optical recording of VSD signals from the axonal arbor was carried out in the wide-field epifluorescence microscopy mode. A frequency-doubled 500 mW diode-pumped Nd:YVO4 continuous wave laser emitting at 532 nm (MLL532, Changchun New Industries Optoelectronics Tech. Co., Ltd., Changchun, China) was the source of excitation light. The laser beam was directed to a light guide coupled to the microscope via a single-port epifluorescence condenser designed to provide approximately uniform illumination of the object plane (assembly adapted from X-Cite® 120Q lamp, Excelitas Technologies Co., Waltham, MA, USA). The fractional noise of low-noise solid-state lasers (RMS < 0.5%) is below typical fractional shot-noise in fluorescence VSD recordings. The laser was used as a light source in place of a conventional Xenon arc-lamp to maximize the sensitivity of optical V_m imaging by: (1) using a monochromatic excitation light at the red wing of the absorption spectrum to maximize V_m sensitivity of the dye; and (2) increasing the intensity of the excitation light beyond the level that can be achieved by an arc-lamp. The excitation light was reflected to the preparation by a dichroic mirror with the central wavelength of 560 nm, and the fluorescence light was passed through a 610 nm barrier filter (parts of Olympus U-MWG filter assembly cube). The image of a stained neuron was projected onto a CCD chip via a 2× intermediate zoom (U-ECA, Olympus) and 0.1× de-magnifier (RedShirtImaging LLC, Decatur, GA, USA). The CCD frame (26 × 4 pixels) corresponded to approximately an 82.5 × 12.7 μm area in the object plane with each individual pixel receiving light from an area of ∼3.2 × 3.2 μm. To measure the AP shape in the nodes of Ranvier (noR) changes in the light intensity were recorded while an AP was evoked by brief (3 ms) transmembrane current pulse with the intensity tuned to trigger an AP in the cell delivered via a recording electrode attached to the soma in whole-cell current-clamp configuration. Signal averaging (∼80–100 trials) was used to improve the S/N further.

Statistical Analysis

Data are given as mean ± SEM, and were statistically analyzed with MatLab 2014a (The MathWorks, Natick, MA, USA) or IGOR Pro 6, WaveMetrics). When $n \geq 6$, data were tested for normal distribution with a Shapiro-Wilk test and when positive, we applied an unpaired t-test subsequently. Not normally distributed experiments with $n < 6$ were tested with non-parametric unpaired Mann-Whitney (M-W) test. Cut-off significance level (P) was set to 0.05. Pearson correlation coefficients were determined using IBM SPSS (v.23; IBM Co., New York, NY, USA).

RESULTS

Non-Saltatory Reliable Propagation of APs in the Demyelinated Main Axon

In order to study the forward propagation of the AP in single layer 5 axons, we made targeted recordings from visually identified layer 5 neurons in the primary somatosensory hindlimb region (S1HL) of demyelinated brain slices (**Figures 1A,B**). Widefield imaging of parasagittal slices including neocortex and hippocampus revealed that 5 weeks of 0.2% cuprizone treatment causes widespread loss of MBP, in particular in lamina 2/3 and 5 of the neocortex as well as in the hippocampus (Clarner et al., 2012; Dutta et al., 2013; Hamada and Kole, 2015). Confocal *z*-projected images of electrophysiologically recorded and biocytin-filled thick-tufted layer 5 neurons shows the extent of myelin loss at internodes of cuprizone-treated animals (**Figure 1C**). At the single axon resolution the first 3–5 internodes were rarely covered by myelin, consistent with previous work (Hamada and Kole, 2015). Therefore, the proximal region of the main layer 5 pyramidal neuron axon provides a reliable and reproducible domain to explore mechanisms and consequences of myelin loss in internodes and the associated axon collaterals (**Figure 1D**).

Although direct whole-cell patch-clamp recordings from axon blebs (Kole et al., 2007; Kole and Popovic, 2016) provides the best possible temporal resolution to examine axonal APs, mouse axons are small in diameter (<1.0 μm) making this approach technically challenging. In addition, demyelination is accompanied by a significant diminution of axon diameter (Mason et al., 2001), as well as aberrant axon neurofilament (de-) phosphorylation (de Waegh et al., 1992; Smith et al., 2013), which may explain the lack of swellings at the cut ends of axons. As an alternative, we here used the approach of optical VSD imaging (Popovic et al., 2011). We obtained reliable optical signals of V_m in the main axon and correlated signals with the expression of anti-βIV-spectrin in these axons (**Figure 2A**). Optical signals of V_m were observed in internodes and noR from control axons ($n = 5$ cells; **Figures 2B,C**, top), in βIV-spectrin-negative BPs in demyelinated axons ($n = 3$ cells; **Figures 2B,C**, middle) as well as in βIV-spectrin-enriched BPs ($n = 2$ cells; **Figures 2B,C**, bottom). To improve the S/N ratio, up to 100 trials were averaged for individual recordings. In all control axons saltatory AP conduction could be observed as V_m in the node always temporally preceded the previous internodal AP signal (**Figure 2C**, top). These findings confirm previous observations of saltation in adult myelinated layer 5 axons in mice (Popovic et al., 2011). In contrast, spatiotemporal analysis of the AP waveforms in axons from cuprizone-treated animals revealed a continuously propagating wave compared to the preceding and succeeding internodes (**Figure 2C**, middle and bottom). Continuous propagation occurred independent of the presence or absence of βIV-spectrin expression suggesting that only the myelin sheath is essential for temporal saltation. Interestingly, *post hoc* immunolabeling of one axon, which did show saltatory conduction, revealed partial internodal (re-) myelination (data not shown). Taken together, these results suggest that the presence of myelin is crucial for saltatory conduction.

In addition to probing the spatial properties of the AP propagation, optical V_m recording with the voltage probe JPW3028 also enables reliable assessment of the intracellular AP shape at ∼20 μs resolution (Popovic et al., 2011). As every BP in demyelinated axons showed APs, we compared the half-widths of the optical V_m signals from putative nodal BPs (**Figures 2D,E**). Interestingly, the AP half width was significantly ∼100 μs narrower in the BPs from demyelinated axons (**Figure 2F**). Taken together, these results indicate reliable, albeit slow, propagation

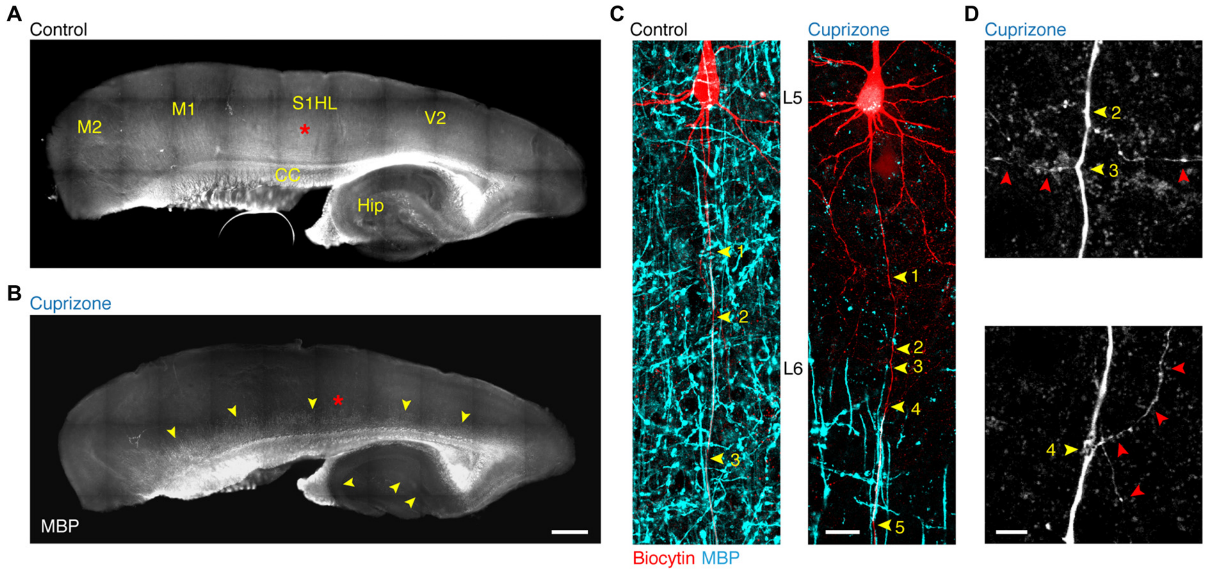

FIGURE 1 | Demyelination of the main axon of thick-tufted layer 5 pyramidal neurons. (A,B) Overview fluorescent image of a myelinated **(A)** demyelinated **(B)** parasagittal brain section immunolabeled for myelin basic protein (MBP). *Red asterisks*, indicate the locations of the recorded thick-tufted layer 5 neuron shown in **(C)**. Note that cuprizone-induced gray matter demyelination (*yellow arrowheads*) occurs across the entire cerebral cortex. S1HL, primary somatosensory hindlimb cortex; V2, secondary visual cortex; M1, primary motor cortex; M2, secondary motor cortex; CC, corpus collosum; Hip, hippocampus. Scale bar, 700 μm, **(C)** *z*-projected confocal images of layer 5 axons co-labeled for biocytin (*red*) and MBP expression (*cyan*). *Yellow arrowheads*, indicate branch points (BPs) along the main axon. Scale bar, 20 μm. **(D)** Magnified *z*-projected confocal images of BPs of the demyelinated primary axon shown in **(C)**. *Yellow arrowheads*, BPs. *Red arrowheads*, trajectory of the primary and secondary axon collaterals. Scale bar, 5 μm.

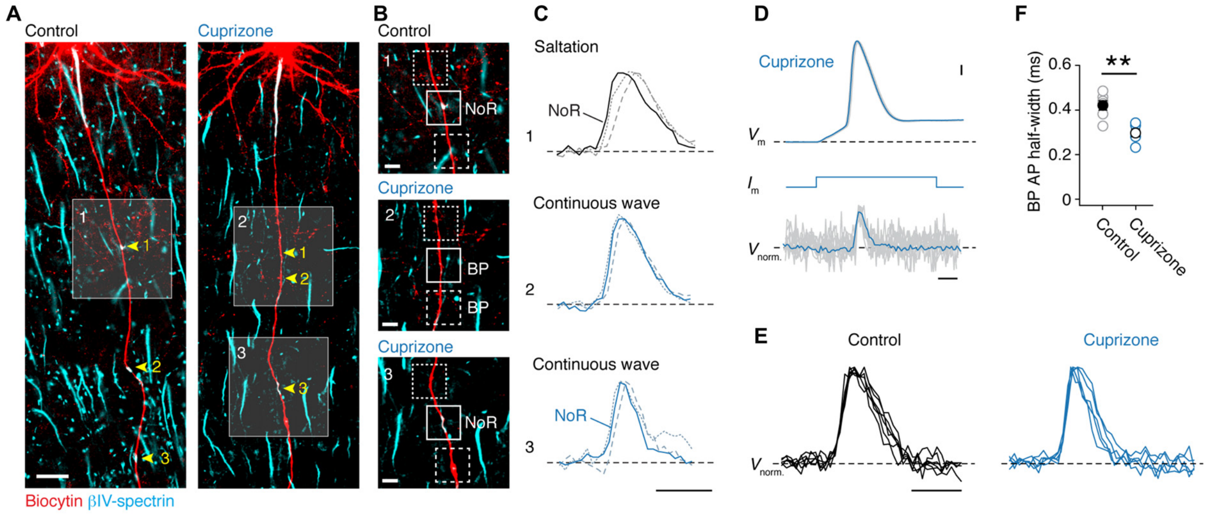

FIGURE 2 | Loss of saltatory propagation and narrowing of nodal action potentials (APs) in demyelinated axons. (A) *Z*-projected confocal images of primary layer 5 axons immuno-labeled for (biocytin, *red*) and βIV-spectrin (*cyan*). Nodes of Ranvier (noR) in myelinated (*left*) and BPs in demyelinated (right) axons are highlighted. Scale bar, 20 μm. **(B)** Zoomed in regions of interest indicated by white squares in **(A)**. Examples of normal noR pattern in control mice (*top*) and BPs from cuprizone treated mice: lacking βIV-spectrin (*middle*) and βIV-spectrin enriched (*bottom*). Scale bar, 5 μm. **(C)** *Top*: normalized voltage-sensitive dye (VSD) traces from noR (*solid line*), preceding internode (*dotted line*) and following internode (*dashed line*). *Middle* and *bottom*: normalized VSD traces from BP (*solid line*), more proximal area (*dotted line*) and more distal area (*dashed line*). Scale bar, 0.5 ms. **(D)** Align and overlay of nine example (out of 100) somatic APs and their corresponding BP spikes (VSD recorded at 20 kHz, gray) and the average of all 100 recorded traces (*black*). Somatic single APs (*top*) were elicited through brief (3 ms; *middle*) square current pulse. BP, branch point. Scale bar, 0.5 ms; 10 mV. **(E)** Normalized VSD traces from control (5 noR; *n* = 5 cells) and cuprizone-treated mice (6 BPs; *n* = 5 cells). Scale bar, 0.5 ms. **(F)** Comparison of BP AP half-widths in control and cuprizone treated mice obtained from VSD data. APs in cuprizone treated mice are significantly narrower (control, *n* = 5 noR; cuprizone, *n* = 6 BPs; Mann-Whitney (M-W) test, ***P* = 0.0087). Individual cells plotted as open circles.

of APs in demyelinated main axons, which are slightly shorter in half-width duration.

Single APs Successfully Invade the Axon Collaterals of Demyelinated Axons

If APs are detectable in all nodes of demyelinated axons, independent of spectrin expression, this suggests they will reliable invade collaterals. As JPW3028 diffusion into the thin axon collaterals is limited (but see Rowan et al., 2016) we made simultaneous somatic and two-photon (2P)-targeted loose-seal patch recordings from en passant presynaptic boutons (**Figure 3A**). After approximately 30 min of somatic whole-cell recording with a fluorescent dye (200 μM Alexa 568), BPs of layer 5 axons, which commonly arise at noR (Sloper and Powell, 1979; Fraher and Kaar, 1984), could be imaged with 2P laser scanning microscopy and collaterals with visually detectable boutons targeted for loose-seal voltage-clamp recordings under continuous 2P imaging at distances between 90–580 μm from the AP initiation site (26 μm from the soma (Hamada and Kole, 2015); *n* = 31 boutons from 30 cells). Somatically elicited APs were visible in the boutons as rapid capacitive currents corresponding to the depolarizing and repolarizing phase of the underlying AP. An overlay of all somatic and bouton APs shows that each event in the collateral was associated with an AP triggered at the soma, confirming a near 100% reliability in propagation (31 out of 31 boutons; **Figures 3A,B**). While the local APs waveforms at boutons from control and demyelinated axons were not different in amplitude (Inward current amplitude: cuprizone, −18.8 ± 4.0 pA, *n* = 16; control, −12.1 ± 1.4 pA, *n* = 15; *P* = 0.1160; outward current amplitude: cuprizone, 10.7 ± 1.0 pA; control, 8.0 ± 1.3 pA; *P* = 0.3726) they showed a significantly longer half-width duration in both the inward and outward component compared to control (**Figures 3C,D**; *P* = 0.010 and *P* = 0.0002, respectively). These data suggest that presynaptic APs in the unmyelinated collaterals are broader and thereby oppositely affected when compared to the nodal APs in the main axon.

We next investigated the AP conduction velocity in axon collaterals. Average spike-triggered current transients recorded near each en passant bouton were aligned to the peak $dV\,dt^{-1}$ of the somatic AP. Axo-somatic conduction delays were calculated relative to the 20% rise point of each averaged bouton spike (Hamada and Kole, 2015) and plotted vs. the distance from the AP initiation site in micrometers measured in 3D image stacks (**Figures 4A,B**). The AP latencies were fitted with a linear function yielding an estimate of axon-collateral conduction velocity of 0.56 ms^{-1} in demyelinated axons, a two-fold velocity reduction compared with the control velocity of 1.2 ms^{-1} (**Figure 4C**).

Increased AP Failure in Demyelinated Axon Collaterals during High-Frequency Stimulation

As shown in **Figure 3B**, single APs propagate into the axon collateral with 100% fidelity. However, at higher frequencies

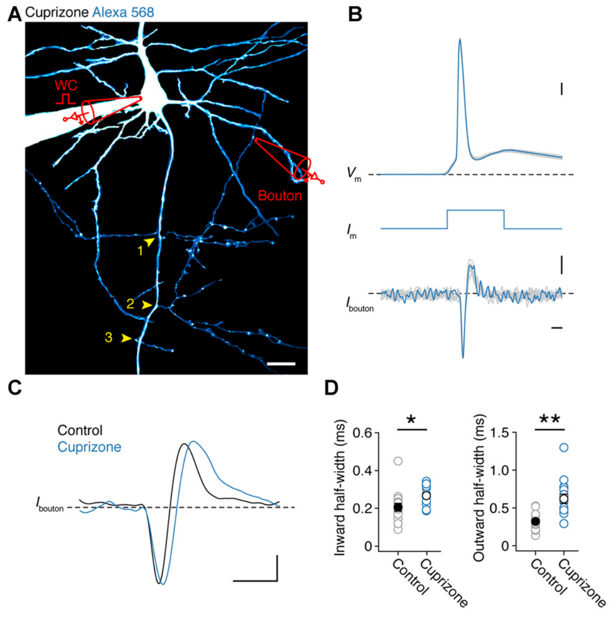

FIGURE 3 | Presynaptic bouton recordings reveal AP broadening in axon collaterals. (A) 2P fluorescence overview image of a demyelinated layer 5 pyramidal neuron loaded with Alexa 568 (200 μM), *Yellow arrows*, BP locations. Image has been modified for clarity by subtracting the background noise extensively to highlight the collateral tree. A loose-seal recording is indicated schematically. Scale bar, 20 μm. **(B)** Temporally aligned overlay of eight somatic APs and their corresponding bouton axonal spikes. Bouton loose-seal patch APs (*bottom*) were recorded by repetitively eliciting somatic single APs (*top*) through brief (3 ms; *middle*) square current pulse. Scale bar, 0.5 ms; 10 mV; 5 pA. **(C)** Example traces of aligned APs recorded in control (*black*) and demyelinated (*blue*) axon collaterals (~149 μm from the AP initiation). Scale bar, 1 ms; 5 pA. **(D)** Plots of the average half-widths of the inward and outward current components of the recorded bouton APs. Cuprizone, *blue circles*, $n = 16$ boutons from 14 cells. Control, *gray circles*, $n = 15$ boutons from 14 cells. Individual recordings plotted as open circles. M-W test, $^{*}P = 0.0010$, $^{**}P = 0.0002$, respectively. Data are presented as mean ± SEM.

we noticed that spikes within a train started to show failures (**Figure 5A**). To probe this relationship between frequency and failures quantitatively, we elicited APs by injecting 10 square current steps in the soma (amplitude range: 4–6 nA; duration: 1 ms), with increasing frequencies (50, 100 to 600 Hz, steps of 100 Hz) and repeated these ~40 times to average the traces and increase the S/N ratio. To quantify the frequency at which failures occur, we examined whether the somatic compartment can faithfully track APs during high-frequency current injection (**Figure 5B**). By comparing the amplitude of the last AP (10th) to the first initiated AP (1st), we found a sharp drop in the somatic AP amplitude at 300 Hz, and at higher frequencies the soma failed completely to initiate APs in both groups. However, control neurons displayed less amplitude attenuation at 200 Hz at the soma when compared to demyelinated neurons (**Figure 5B**).

Recordings at the axon showed that AP amplitude attenuation was less prominent at higher input frequencies (400–600 Hz) when compared to the soma consistent with the possibility of axonal Nav channels to recover more quickly from Nav channel inactivation and the depolarized voltage threshold for activation of the somatodendritic spike component (Kole and Stuart, 2008; Popovic et al., 2011; **Figures 5A,C**). However, in this frequency range, presynaptic AP recordings from demyelinated axons showed significantly larger amplitude attenuation when compared to control axons (**Figure 5C**). Finally, we examined the inward amplitude component of the axonal signals, converted the analog axonal signals into binary data and plotted AP probability against the input frequency (**Figure 5D**; see *Experimental Procedures*). The results showed that presynaptic AP recordings from demyelinated axons. The axonal AP failures occurred in the same range of input frequencies but for significantly more APs in the train (at 600 Hz, cuprizone ~70% failure vs. control 30%; $P = 0.0063$; **Figure 5D**). Furthermore, axonal AP failures at any given input frequency did not correlate with recording distance from the soma (Pearson correlation; control: $r = -0.1669$, $P = 0.6449$ (500 Hz); cuprizone, $r = -0.2585$, $P = 0.5365$ (500 Hz)).

Structural Plasticity of Axon Collaterals

Based on the axon morphologies acquired during 2P imaging we noticed that BPs in demyelinated axons appeared denser. To test the hypothesis that myelin loss affects the anatomical organization of the main (de-)myelinated axon arbor we examined the BP locations within the first 300 μm from the soma using high-resolution two-photon imaging (**Figure 6A**). Similar to a previous anatomical study of thick-tufted layer 5 axons in the adult rat (Romand et al., 2011), we found that the main axon has approximately three BPs from which horizontal collaterals emerge. On average, the total number of BPs were not different between control and demyelinated axons (M-W test, $P = 0.3715$; control, 3.2 ± 0.2 BPs, $n = 11$ axons; cuprizone, 3.6 ± 0.3 BPs, $n = 14$ axons; **Figure 6A**, yellow arrowheads). Interestingly, a few demyelinated axons showed a large number of BPs and were characterized by protrusions indicative of axonal sprouting ($n = 2$ sprouting axons, **Figure 6B**; red arrowhead). When plotting the BP locations as a function of distance from the soma demyelinated axons showed a significant shift towards a more proximal onset for both the second and third BP ($P = 0.0079$, $P = 0.030$, respectively; **Figure 6C**). Furthermore, while the average inter-BP distance was not different between the two groups (control, 48.1 ± 6.0 μm; cuprizone, 36.0 ± 4.6 μm; $P = 0.1670$; **Figure 6D**), the first inter-BP distance was on average ~30 μm shorter in demyelinated axons (control, 57.0 ± 9.0 μm; cuprizone, 29.0 ± 4.8 μm; *t*-test, $P = 0.0095$). This was not different anymore for the second inter-BP length (control, 40.8 ± 7.9 μm; cuprizone, 31.8 ± 7.3 μm; *t*-test, $P = 0.4112$). These data indicate that collaterals and internodes around the first BPs from the soma undergo structural plasticity in demyelinated axons.

DISCUSSION

In this study we addressed how APs are propagating along demyelinated internodes and variably reorganized nodal domains to reach the presynaptic terminals. Axon-glia interactions at the contact sites between the axon and myelin

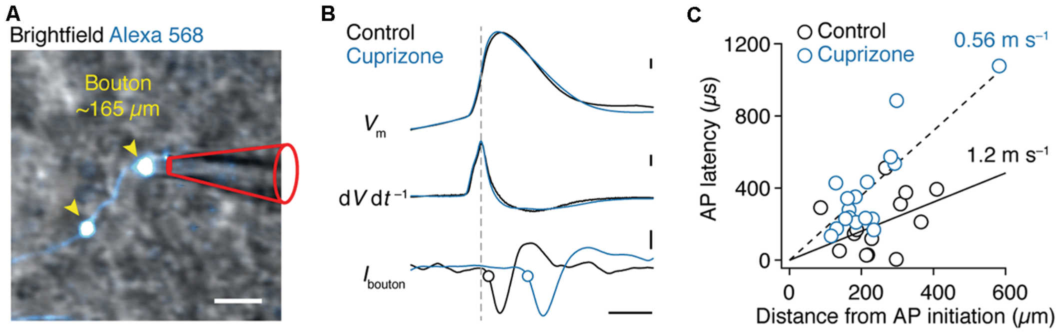

FIGURE 4 | Reduced conduction velocity in axon collaterals of demyelinated layer 5 axons. (A) Magnified 2P scan overlaid with the brightfield image from a demyelinated layer 5 axon a distance of ~165 μm from the soma. Scale bar, 2 μm. **(B)** Top, somatically evoked single APs from control and demyelinated layer 5 neurons. Middle, time derivative of the somatic APs aligned at peak amplitude. Bottom, loose-seal patch recording of bouton APs recorded at ~300 μm from the soma of respective neurons. Note the delay of the AP in demyelinated axon due to reduced conduction velocity as a consequence of myelin loss. *Closed circles* indicate the 20% onset of the local spike maxima. Scale bar, 0.5 ms; 10 mV; 1 kV s^{-1}; 5 pA. **(C)** Axosomatic latency plotted vs. total measured bouton distance (measured from the AP initiation site, 26 μm). Control (*n* = 13 boutons from 13 cells; *open circles*) and cuprizone data sets (*n* = 17 boutons from 15 cells; *blue open circles*) are fitted with a linear function.

sheath are critical for the proper assembly and maintenance of the microdomains of the node of Ranvier (Poliak and Peles, 2003; Chang et al., 2014). As a consequence of the loss of the myelin sheath in experimental demyelination models or in MS, nodal regions are characterized by a large redistribution or *de novo* expression of anchoring proteins and voltage-gated ion channels (Rasband et al., 1998; Arroyo et al., 2002; Craner et al., 2004; Black et al., 2006; Hamada and Kole, 2015). Interestingly, along the successive BPs of a single axon a large diversity in the expression of ion channel proteins can be found from node to node (Hamada and Kole, 2015). Here, we found that molecular variation in nodes did, however, not greatly impact on conduction along the main axon; independent of βIV-spectrin myelin loss was found to switch the optically recorded AP from rapid saltation into a continuous non-saltatory wave (**Figure 2**). Continuation of AP propagation in demyelinated main axons is consistent with the observation that even low Nav channel densities at the denuded internode axolemma suffice to ensure propagation of axonal APs (Shrager, 1993).

The biophysical basis underlying the ~120 μs narrower half-width at demyelinated BPs most likely relies on redistribution of juxtaparanodal Kv channels (Rasband et al., 1998; Arroyo et al., 2002; Black et al., 2006; Bagchi et al., 2014). However, technical errors in measuring voltage accurately at these small domains may also play a confounding factor. First, the local amplitude of optically recorded APs is unknown because the fractional fluorescence change depends on the surface to volume ratio of imaged compartments. Secondly, the pixel size encompassing a region of 3.2 μm^2, is slightly larger compared to the ~2.5 μm^2 size of the noR in control axons (Hamada and Kole, 2015) and thus may contain fluorescence emitted from the internode either under the myelin sheath or, in the case of cuprizone, the exposed internodal axolemma. Decreasing the pixel size would, however, either reduce the temporal resolution, causing undersampling and aggravate the averaging jitter, or require further zooming which would reduce the field of view to <50 μm, decrease the fluorescence light intensity and, hence, the S/N ratio. To compensate for such light loss, tissue-damaging levels of excitation light would be required. Taken together, the current approach was the best available compromise between pixel size, temporal resolution and S/N ratio.

The most likely explanation for the optically recorded narrower AP is the increased expression and redistribution of fast-activating Kv1.1/Kv1.2 channels in demyelinated axons (Rasband et al., 1998; Arroyo et al., 2002; Black et al., 2006; Bagchi et al., 2014). This hypothesis remains to be tested by comparing recordings with and without Kv1 channel blockers. Kv1 channels are typically clustered at the juxta-paranodal domains, but with myelin loss disperse into the paranodes and nodal axolemma or in opposite direction into the internode (Rasband et al., 1999; Rasband and Shrager, 2000). Furthermore, in the demyelinated optic nerve in cuprizone mouse model, Kv1.1 homo-tetramers undergo *de novo* expression in denuded axons (Bagchi et al., 2014). Additionally, the same study also showed that Kv1.1 subunit homo-tetramers confer a decrease in the activation voltage threshold and accelerate the activation kinetics. Since axonal Kv1 voltage-gated potassium channels play a key role in repolarizing the axonal AP (Kole et al., 2007; Foust et al., 2011), their expression in the nodal axolemma may significantly shorten the AP half-width duration and rapid repolarization would act to increase the Nav channel availability during repetitive firing.

In striking contrast to the AP waveform in the main axon recordings from the presynaptic boutons revealed a broadening of the presynaptic AP current components (**Figure 3**). The molecular changes underlying presynaptic AP broadening are not clear but, similar to the main axon, may depend on expression changes in Kv1- or Kv3-subtype potassium channels. Staining and/or recording Kv1/3 channels in presynaptic terminals is challenging and there is no information about their

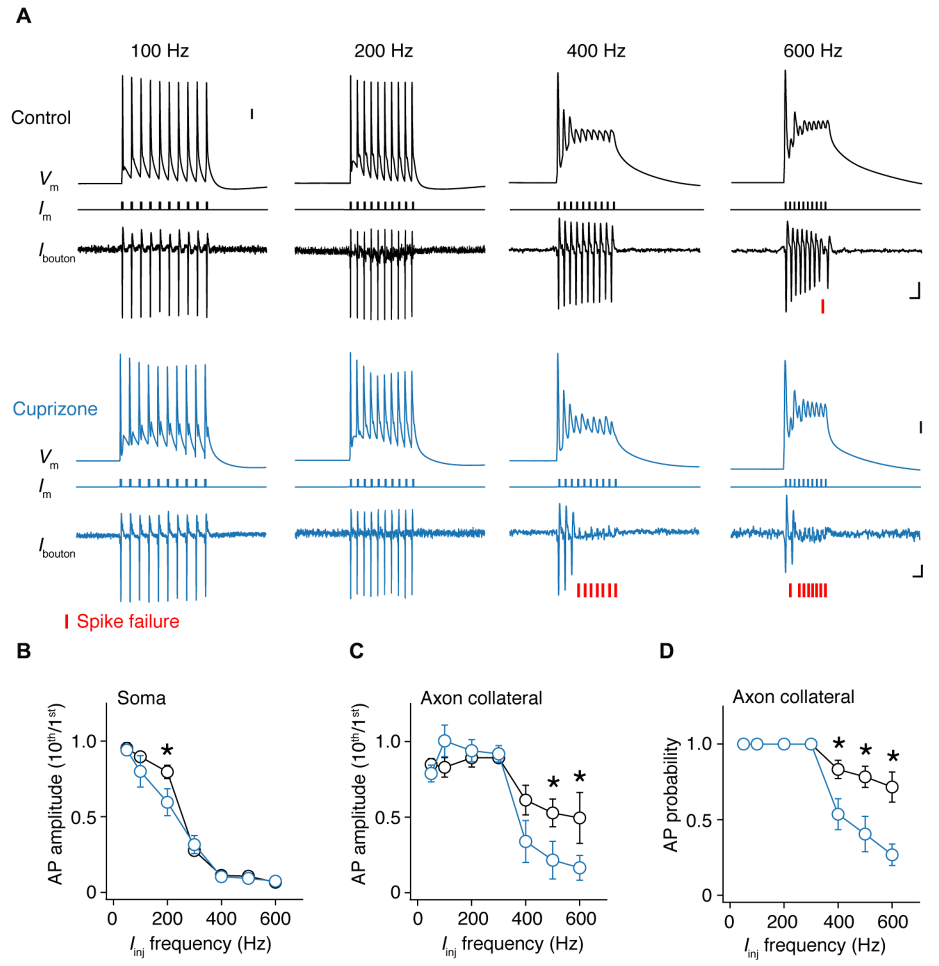

FIGURE 5 | Frequency-dependent AP failures in presynaptic boutons of demyelinated axons. (A) Simultaneous somatic whole-cell and axonal loose-seal recording from control (*black*) and demyelinated neurons (*blue*) during somatic current injections (1 ms pulses) at increasing frequencies. Note the increased failure rate in demyelinated axons. *Asterisks*, spike failure. Scale bar, 5 ms; 10 mV; 10 pA. Somatic capacitive transients are blanked for clarity reasons. **(B)** Normalized somatic AP amplitude vs. injected current frequency. *t*-test, $*P = 0.0432$. **(C)** Collateral AP amplitude vs. evoked injected current frequency. M-W test, $*P = 0.0446$ (500 Hz); $*P = 0.0426$ (600 Hz). **(D)** Relationship between AP probability vs. somatic step frequency in control ($n = 16$ boutons from 16 cells; *black open circles*) and demyelinated axons ($n = 14$ boutons from 14 cells; *black open circles*). Data presented as average ± SEM. M-W test, $P = 0.0185$ (400 Hz); $P = 0.0098$ (500 Hz); $P = 0.0063$ (600 Hz).

expression in demyelination models. Recently, it was shown that bouton-specific expression of fast-activating Kv3 channels causes large heterogeneity of presynaptic AP durations along successive boutons of axon collaterals (Rowan et al., 2014, 2016). In addition to the broadening of presynaptic APs at boutons from demyelinated axons the conduction velocity was also significantly lower, indicating that myelin loss at the main axon affects arrival times into the axon collaterals impeding on the temporal precision of glutamatergic excitation of the target cells (**Figure 4**).

While at frequencies near 300 Hz AP failure at the soma rapidly increases with successive spikes, neocortical axons can generate higher firing rates (**Figure 5**; Popovic et al., 2011). Interestingly, in comparison to control neurons demyelinated axons showed substantially lower fidelity for input frequencies ≥400 Hz. The results raise the question, where APs in demyelinated axons fail? The underlying mechanisms and location of propagation failures may be complex. Increased failures in collaterals from demyelinated axons may be an integrated result of slower propagation and AP waveform changes. Indeed, the measured broad presynaptic AP predicts a longer duration to recover from Nav channel inactivation and delay the availability of inward current for the next spike. In addition, loss of voltage-gated Nav channels in demyelinated nodes preceding the presynaptic AP also will deteriorate AP regeneration at the BP and as a consequence limit invasion during high frequency spiking. In neocortical pyramidal neurons every AP during a high-frequency burst of ~250 Hz is initiated within the AIS (Kole, 2011). However, our results are not excluding the possibility that very high-frequency APs ≥400 Hz are actually initiated downstream the AIS, within the noR. Strong depolarization evoked at the soma electrotonically spreads

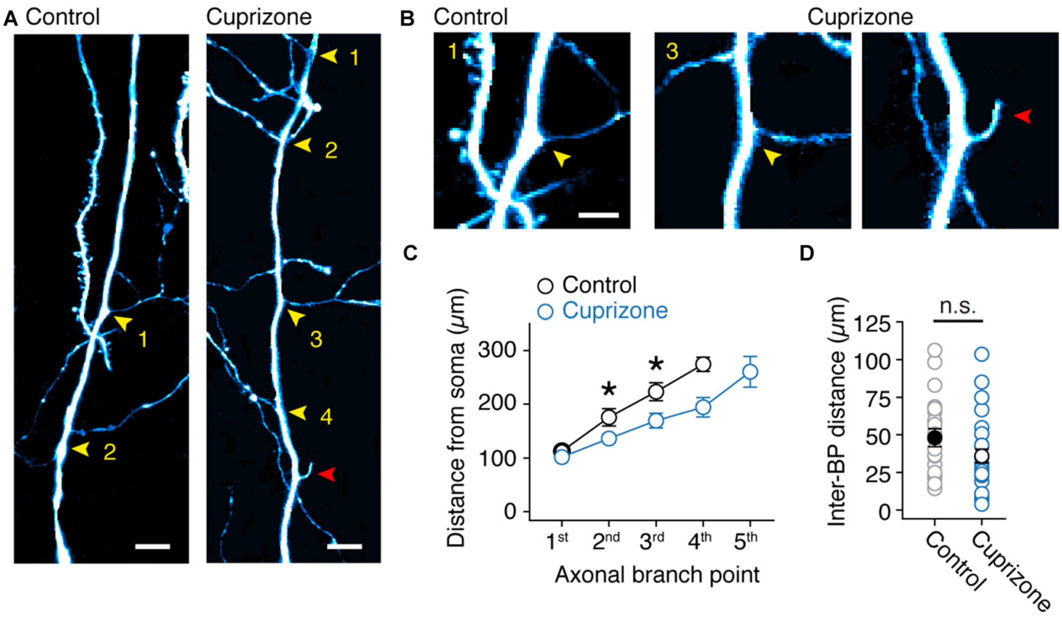

FIGURE 6 | Sprouting of new axon collaterals in demyelinated axons. (A) Fluorescent 2P images of the proximal BPs in control and demyelinated layer 5 axons. Note the larger number of BPs in demyelinated axon compared to control. *Yellow arrowheads*, BPs. *Red arrowhead*, putative *de novo* axon outgrowth. Scale bar, 10 μm. **(B)** Magnified 2P images of the same images shown in **(A)**. *Yellow arrowheads*, BPs; *Red arrowhead*, putative *de novo* axon outgrowth. Scale bar, 5 μm. **(C)** Plot of the BP locations within the first 350 μm of primary axon (measured from the soma). M-W test, **P* = 0.0301 (control, *n* = 11 BPs; cuprizone, *n* = 13 BPs; 2nd branch point); **P* = 0.0079 (control, *n* = 10 BPs; cuprizone, *n* = 11 BPs; 3rd branch point). Data presented as mean ± SEM. **(D)** Plot of the average inter-BP distance. Control, *black open circles*, *n* = 24 inter-BP distances from 11 cells. Cuprizone, *blue open circles*, *n* = 28 inter-BP distances from 12 cells. M-W test *P* = 0.1670.

down the axon and may increase the time to recover from Nav channel inactivation in the most proximal regions of the axon. A better detectability of high-frequency spikes has been described in distal axons of CA1 neurons during the complex spike (Apostolides et al., 2016). In this view, the failure of high-frequency presynaptic APs in demyelinated axons may be an *initiation*- rather then *propagation* failure. To identify the specific location where failure (or re-initiation) of the AP occurs during presynaptically recorded failures is technically challenging. Testing this hypothesis would require multiple loose-seal recordings from the axon proper, BPs and collaterals. These approaches are in particular difficult due to the extremely narrow stretch of exposed membrane accessible to the patch pipette tip in myelinated axons.

The observation of both structural and functional changes within the collaterals of demyelinated axons raises the question what the long-lasting functional consequences are for synaptic transmission. Dynamic reorganization of the presynaptic terminals is likely to impact on synaptic transmission and analysis of these sites may increase our understanding of the computational capacity of demyelinated neural circuits. Indeed, cuprizone-induced demyelination reduces the AMPA receptors in the hippocampus (Dutta et al., 2013). Furthermore, axon sprouting is consistent with the observed structural plasticity of axons within the cortico-spinal tract in the experimental autoimmune encephalomyelitis (EAE) model (Kerschensteiner et al., 2004). In the adult mammalian central nervous system myelin exerts an inhibitory influence on axon elongation and regeneration (Schwab and Bartholdi, 1996; Horner and Gage, 2000) mediated, among other players, by oligodendrocyte myelin-associated glycoprotein (MAG; McKerracher et al., 1994; Mukhopadhyay et al., 1994), and Nogo-A (Chen et al., 2000; GrandPré et al., 2000). These proteins are thought to limit axon growth and confine plasticity within restricted regions, preventing the formation of aberrant connections. Unlike EAE the cuprizone model is a toxicological model, which induces demyelination by selectively killing mature oligodendrocytes with minimal inflammatory responses (Kipp et al., 2009). It is possible that in both demyelination models the axons are no longer exposed to the growth inhibition mediated by myelin-associated proteins, possibly permitting structural plasticity along the previously myelinated internodes. Consistent with this idea previous studies have reported a significant decrease of Nogo-A levels in cuprizone-treated animals (Kuhlmann et al., 2007; Skripuletz et al., 2010).

Taken together, the present results show that oligodendrocyte loss in the gray matter causes a wide range of site-specific structural and functional changes throughout the axon arborization including its presynaptic boutons. While demyelinated axons show a loss of rapid impulse saltation they are also characterized by geometrical *de novo* branch outgrowth and reduced ability to propagate APs at high frequencies. Structural reorganization of the glutamatergic axonal collateral network may explain the aberrant intra-cortical excitation and hyperexcitability of demyelinated cortical neural circuits (Hamada and Kole, 2015).

AUTHOR CONTRIBUTIONS

MHPK: conceptualization, visualization, supervision, and funding acquisition; MSH, MAP and MHPK: methodology, analysis, review writing and editing; MSH and MAP: investigation; MSH and MHPK: writing the original draft.

FUNDING

This work has been funded by a National Multiple Sclerosis Society Grant (RG 4924A1/1) and European Research Council Starting Grant (ERC StG 261114, EU 7th Framework) to MHPK.

ACKNOWLEDGMENTS

We are indebted to Sharon I. de Vries for her support.

REFERENCES

Apostolides, P. F., Milstein, A. D., Grienberger, C., Bittner, K. C., and Magee, J. C. (2016). Axonal filtering allows reliable output during dendritic plateau-driven complex spiking in CA1 neurons. *Neuron* 89, 770–783. doi: 10.1016/j.neuron.2015.12.040

Arroyo, E. J., Xu, T., Grinspan, J., Lambert, S., Levinson, S. R., Brophy, P. J., et al. (2002). Genetic dysmyelination alters the molecular architecture of the nodal region. *J. Neurosci.* 22, 1726–1737.

Bagchi, B., Al-Sabi, A., Kaza, S., Scholz, D., O'Leary, V. B., Dolly, J. O., et al. (2014). Disruption of myelin leads to ectopic expression of $K_V1.1$ channels with abnormal conductivity of optic nerve axons in a cuprizone-induced model of demyelination. *PLoS One* 9:e87736. doi: 10.1371/journal.pone.0087736

Black, J. A., Waxman, S. G., and Smith, K. J. (2006). Remyelination of dorsal column axons by endogenous Schwann cells restores the normal pattern of Nav1.6 and Kv1.2 at nodes of Ranvier. *Brain* 129, 1319–1329. doi: 10.1093/brain/awl057

Bostock, H., and Sears, T. A. (1978). The internodal axon membrane: electrical excitability and continuous conduction in segmental demyelination. *J. Physiol.* 280, 273–301. doi: 10.1113/jphysiol.1978.sp012384

Brecht, M., Schneider, M., Sakmann, B., and Margrie, T. W. (2004). Whisker movements evoked by stimulation of single pyramidal cells in rat motor cortex. *Nature* 427, 704–710. doi: 10.1038/nature02266

Chang, K.-J., Zollinger, D. R., Susuki, K., Sherman, D. L., Makara, M. A., Brophy, P. J., et al. (2014). Glial ankyrins facilitate paranodal axoglial junction assembly. *Nat. Neurosci.* 17, 1673–1681. doi: 10.1038/nn.3858

Chen, M. S., Huber, A. B., van der Haar, M. E., Frank, M., Schnell, L., Spillmann, A. A., et al. (2000). Nogo-A is a myelin-associated neurite outgrowth inhibitor and an antigen for monoclonal antibody IN-1. *Nature* 403, 434–439. doi: 10.1038/35000219

Clarner, T., Diederichs, F., Berger, K., Denecke, B., Gan, L., van der Valk, P., et al. (2012). Myelin debris regulates inflammatory responses in an experimental demyelination animal model and multiple sclerosis lesions. *Glia* 60, 1468–1480. doi: 10.1002/glia.22367

Craner, M. J., Newcombe, J., Black, J. A., Hartle, C., Cuzner, M. L., and Waxman, S. G. (2004). Molecular changes in neurons in multiple sclerosis: altered axonal expression of Nav1.2 and Nav1.6 sodium channels and Na^+/Ca^{2+} exchanger. *Proc. Natl. Acad. Sci. U S A* 101, 8168–8173. doi: 10.1073/pnas.0402765101

Crawford, D. K., Mangiardi, M., Xia, X., López-Valdés, H. E., and Tiwari-Woodruff, S. K. (2009). Functional recovery of callosal axons following demyelination: a critical window. *Neuroscience* 164, 1407–1421. doi: 10.1016/j.neuroscience.2009.09.069

Debanne, D., Guérineau, N. C., Gähwiler, B. H., and Thompson, S. M. (1997). Action-potential propagation gated by an axonal I(A)-like K^+ conductance in hippocampus. *Nature* 389, 286–289. doi: 10.1038/38502

Deschênes, M., and Landry, P. (1980). Axonal branch diameter and spacing of nodes in the terminal arborization of identified thalamic and cortical neurons. *Brain Res.* 191, 538–544. doi: 10.1016/0006-8993(80)91302-5

de Waegh, S. M., Lee, V. M., and Brady, S. T. (1992). Local modulation of neurofilament phosphorylation, axonal caliber, and slow axonal transport by myelinating Schwann cells. *Cell* 68, 451–463. doi: 10.1016/0092-8674(92)90183-d

Ducreux, C., Reynaud, J. C., and Puizillout, J. J. (1993). Spike conduction properties of T-shaped C neurons in the rabbit nodose ganglion. *Pflugers Arch.* 424, 238–244. doi: 10.1007/bf00384348

Dutta, R., Chomyk, A. M., Chang, A., Ribaudo, M. V., Deckard, S. A., Doud, M. K., et al. (2013). Hippocampal demyelination and memory dysfunction are associated with increased levels of the neuronal microRNA miR-124 and reduced AMPA receptors. *Ann. Neurol.* 73, 637–645. doi: 10.1002/ana.23860

Felts, P. A., Baker, T. A., and Smith, K. J. (1997). Conduction in segmentally demyelinated mammalian central axons. *J. Neurosci.* 17, 7267–7277.

Foust, A. J., Yu, Y., Popovic, M. A., Zecevic, D., and McCormick, D. A. (2011). Somatic membrane potential and kv1 channels control spike repolarization in cortical axon collaterals and presynaptic boutons. *J. Neurosci.* 31, 15490–15498. doi: 10.1523/JNEUROSCI.2752-11.2011

Fraher, J. P., and Kaar, G. F. (1984). The transitional node of Ranvier at the junction of the central and peripheral nervous systems: an ultrastructural study of its development and mature form. *J. Anat.* 139, 215–238.

Goldstein, S. S., and Rall, W. (1974). Changes of action potential shape and velocity for changing core conductor geometry. *Biophys. J.* 14, 731–757. doi: 10.1016/s0006-3495(74)85947-3

GrandPré, T., Nakamura, F., Vartanian, T., and Strittmatter, S. M. (2000). Identification of the Nogo inhibitor of axon regeneration as a Reticulon protein. *Nature* 403, 439–444. doi: 10.1038/35000226

Hamada, M. S., and Kole, M. H. P. (2015). Myelin loss and axonal ion channel adaptations associated with gray matter neuronal hyperexcitability. *J. Neurosci.* 35, 7272–7286. doi: 10.1523/JNEUROSCI.4747-14.2015

Harris, K. D., and Mrsic-Flogel, T. D. (2013). Cortical connectivity and sensory coding. *Nature* 503, 51–58. doi: 10.1038/nature12654

Horner, P. J., and Gage, F. H. (2000). Regenerating the damaged central nervous system. *Nature* 407, 963–970. doi: 10.1038/35039559

Kerschensteiner, M., Bareyre, F. M., Buddeberg, B. S., Merkler, D., Stadelmann, C., Brück, W., et al. (2004). Remodeling of axonal connections contributes to recovery in an animal model of multiple sclerosis. *J. Exp. Med.* 200, 1027–1038. doi: 10.1084/jem.20040452

Khaliq, Z. M., and Raman, I. M. (2006). Relative contributions of axonal and somatic Na channels to action potential initiation in cerebellar Purkinje neurons. *J. Neurosci.* 26, 1935–1944. doi: 10.1523/JNEUROSCI.4664-05.2006

Kim, J. H., Renden, R., and von Gersdorff, H. (2013). Dysmyelination of auditory afferent axons increases the jitter of action potential timing during high-frequency firing. *J. Neurosci.* 33, 9402–9407. doi: 10.1523/JNEUROSCI.3389-12.2013

Kipp, M., Clarner, T., Dang, J., Copray, S., and Beyer, C. (2009). The cuprizone animal model: new insights into an old story. *Acta Neuropathol.* 118, 723–736. doi: 10.1007/s00401-009-0591-3

Kole, M. H. P. (2011). First node of ranvier facilitates high-frequency burst encoding. *Neuron* 71, 671–682. doi: 10.1016/j.neuron.2011.06.024

Kole, M. H. P., Letzkus, J. J., and Stuart, G. J. (2007). Axon initial segment Kv1 channels control axonal action potential waveform and synaptic efficacy. *Neuron* 55, 633–647. doi: 10.1016/j.neuron.2007.07.031

Kole, M. H. P., and Popovic, M. A. (2016). "Patch-clamp recording from myelinated central axons," in *Advanced Patch-Clamp Analysis for Neuroscientists*, ed. A. Korngreen (New York, NY: Springer), 123–138.

Kole, M. H. P., and Stuart, G. J. (2008). Is action potential threshold lowest in the axon? *Nat. Neurosci.* 11, 1253–1255. doi: 10.1038/nn.2203

Kole, M. H. P., and Stuart, G. J. (2012). Signal processing in the axon initial segment. *Neuron* 73, 235–247. doi: 10.1016/j.neuron.2012.01.007

Kuhlmann, T., Remington, L., Maruschak, B., Owens, T., and Brück, W. (2007). Nogo-A is a reliable oligodendroglial marker in adult human and mouse CNS and in demyelinated lesions. *J. Neuropathol. Exp. Neurol.* 66, 238–246. doi: 10.1097/01.jnen.0000248559.83573.71

Manor, Y., Koch, C., and Segev, I. (1991). Effect of geometrical irregularities on propagation delay in axonal trees. *Biophys. J.* 60, 1424–1437. doi: 10.1016/s0006-3495(91)82179-8

Mason, J. L., Langaman, C., Morell, P., Suzuki, K., and Matsushima, G. K. (2001). Episodic demyelination and subsequent remyelination within the murine central nervous system: changes in axonal calibre. *Neuropathol. Appl. Neurobiol.* 27, 50–58. doi: 10.1046/j.0305-1846.2001.00301.x

McDonald, W. I., and Sears, T. A. (1970). The effects of experimental demyelination on conduction in the central nervous system. *Brain* 93, 583–598. doi: 10.1093/brain/93.3.583

McKerracher, L., David, S., Jackson, D. L., Kottis, V., and Dunn, R. J. (1994). Identification of myelin-associated glycoprotein as a major myelin-derived inhibitor of neurite growth. *Neuron* 13, 805–811. doi: 10.1016/0896-6273(94)90247-x

Monsivais, P., Clark, B. A., Roth, A., and Häusser, M. (2005). Determinants of action potential propagation in cerebellar Purkinje cell axons. *J. Neurosci.* 25, 464–472. doi: 10.1523/JNEUROSCI.3871-04.2005

Mukhopadhyay, G., Doherty, P., Walsh, F. S., Crocker, P. R., and Filbin, M. T. (1994). A novel role for myelin-associated glycoprotein as an inhibitor of axonal regeneration. *Neuron* 13, 757–767. doi: 10.1016/0896-6273(94)90042-6

Parnas, I., and Segev, I. (1979). A mathematical model for conduction of action potentials along bifurcating axons. *J. Physiol.* 295, 323–343. doi: 10.1113/jphysiol.1979.sp012971

Poliak, S., and Peles, E. (2003). The local differentiation of myelinated axons at nodes of Ranvier. *Nat. Rev. Neurosci.* 4, 968–980. doi: 10.1038/nrn1253

Popovic, M. A., Foust, A. J., McCormick, D. A., and Zecevic, D. (2011). The spatio-temporal characteristics of action potential initiation in layer 5 pyramidal neurons: a voltage imaging study. *J. Physiol.* 589, 4167–4187. doi: 10.1113/jphysiol.2011.209015

Rasband, M. N., Peles, E., Trimmer, J. S., Levinson, S. R., Lux, S. E., and Shrager, P. (1999). Dependence of nodal sodium channel clustering on paranodal axoglial contact in the developing CNS. *J. Neurosci.* 19, 7516–7528.

Rasband, M. N., and Shrager, P. (2000). Ion channel sequestration in central nervous system axons. *J. Physiol.* 525, 63–73. doi: 10.1111/j.1469-7793.2000.00063.x

Rasband, M. N., Trimmer, J. S., Schwarz, T. L., Levinson, S. R., Ellisman, M. H., Schachner, M., et al. (1998). Potassium channel distribution, clustering and function in remyelinating rat axons. *J. Neurosci.* 18, 36–47.

Romand, S., Wang, Y., Toledo-Rodriguez, M., and Markram, H. (2011). Morphological development of thick-tufted layer v pyramidal cells in the rat somatosensory cortex. *Front. Neuroanat.* 5:5. doi: 10.3389/fnana.2011.00005

Rowan, M. J. M., DelCanto, G., Yu, J. J., Kamasawa, N., and Christie, J. M. (2016). Synapse-level determination of action potential duration by K^+ channel clustering in axons. *Neuron* 91, 370–383. doi: 10.1016/j.neuron.2016.05.035

Rowan, M. J. M., Tranquil, E., and Christie, J. M. (2014). Distinct Kv channel subtypes contribute to differences in spike signaling properties in the axon initial segment and presynaptic boutons of cerebellar interneurons. *J. Neurosci.* 34, 6611–6623. doi: 10.1523/JNEUROSCI.4208-13.2014

Schwab, M. E., and Bartholdi, D. (1996). Degeneration and regeneration of axons in the lesioned spinal cord. *Physiol. Rev.* 76, 319–370.

Shrager, P. (1993). Axonal coding of action potentials in demyelinated nerve fibers. *Brain Res.* 619, 278–290. doi: 10.1016/0006-8993(93)91622-y

Skripuletz, T., Bussmann, J.-H., Gudi, V., Koutsoudaki, P. N., Pul, R., Moharregh-Khiabani, D., et al. (2010). Cerebellar cortical demyelination in the murine cuprizone model. *Brain Pathol.* 20, 301–312. doi: 10.1111/j.1750-3639.2009.00271.x

Sloper, J. J., and Powell, T. P. (1979). A study of the axon initial segment and proximal axon of neurons in the primate motor and somatic sensory cortices. *Philos. Trans. R. Soc. Lond. B Biol. Sci.* 285, 173–197. doi: 10.1098/rstb.1979.0004

Smith, C. M., Cooksey, E., and Duncan, I. D. (2013). Myelin loss does not lead to axonal degeneration in a long-lived model of chronic demyelination. *J. Neurosci.* 33, 2718–2727. doi: 10.1523/JNEUROSCI.4627-12.2013

Conflict of Interest Statement: The authors declare that the research was conducted in the absence of any commercial or financial relationships that could be construed as a potential conflict of interest.

frontiers in Cellular Neuroscience

ORIGINAL RESEARCH
published: 06 June 2017
doi: 10.3389/fncel.2017.00157

Mild Traumatic Brain Injury Evokes Pyramidal Neuron Axon Initial Segment Plasticity and Diffuse Presynaptic Inhibitory Terminal Loss

Michal Vascak, Jianli Sun, Matthew Baer, Kimberle M. Jacobs and John T. Povlishock*

Department of Anatomy and Neurobiology, Virginia Commonwealth University School of Medicine, Richmond, VA, United States

The axon initial segment (AIS) is the site of action potential (AP) initiation, thus a crucial regulator of neuronal activity. In excitatory pyramidal neurons, the high density of voltage-gated sodium channels (NaV1.6) at the distal AIS regulates AP initiation. A surrogate AIS marker, ankyrin-G (ankG) is a structural protein regulating neuronal functional via clustering voltage-gated ion channels. In neuronal circuits, changes in presynaptic input can alter postsynaptic output via AIS structural-functional plasticity. Recently, we showed experimental mild traumatic brain injury (mTBI) evokes neocortical circuit disruption via diffuse axonal injury (DAI) of excitatory and inhibitory neuronal systems. A key finding was that mTBI-induced neocortical electrophysiological changes involved non-DAI/ intact excitatory pyramidal neurons consistent with AIS-specific alterations. In the current study we employed Thy1-yellow fluorescent protein (YFP)-H mice to test if mTBI induces AIS structural and/or functional plasticity within intact pyramidal neurons 2 days after mTBI. We used confocal microscopy to assess intact YFP+ pyramidal neurons in layer 5 of primary somatosensory barrel field (S1BF), whose axons were continuous from the soma of origin to the subcortical white matter (SCWM). YFP+ axonal traces were superimposed on ankG and NaV1.6 immunofluorescent profiles to determine AIS position and length. We found that while mTBI had no effect on ankG start position, the length significantly decreased from the distal end, consistent with the site of AP initiation at the AIS. However, NaV1.6 structure did not change after mTBI, suggesting uncoupling from ankG. Parallel quantitative analysis of presynaptic inhibitory terminals along the postsynaptic perisomatic domain of these same intact YFP+ excitatory pyramidal neurons revealed a significant decrease in GABAergic bouton density. Also within this non-DAI population, patch-clamp recordings of intact YFP+ pyramidal neurons showed AP acceleration decreased 2 days post-mTBI, consistent with AIS functional plasticity.

Edited by:
Maren Engelhardt,
Heidelberg University, Germany

Reviewed by:
Matthew N. Rasband,
Baylor College of Medicine,
United States
Lisa Mapelli,
University of Pavia, Italy

***Correspondence:**
John T. Povlishock
john.povlishock@vcuhealth.org

Received: 21 February 2017
Accepted: 17 May 2017
Published: 06 June 2017

Citation:
Vascak M, Sun J, Baer M, Jacobs KM and Povlishock JT (2017) Mild Traumatic Brain Injury Evokes Pyramidal Neuron Axon Initial Segment Plasticity and Diffuse Presynaptic Inhibitory Terminal Loss. Front. Cell. Neurosci. 11:157. doi: 10.3389/fncel.2017.00157

Abbreviations: aCSF, artificial cerebral spinal fluid; AIS, axon initial segment; ankG, ankyrin-G; AP, action potential(s); BPM, beats per minute; cFPI, central fluid percussion injury; CI, confidence interval; DAI, diffuse axonal injury; d_{SCWM}, coefficient of distance from subcortical white mater; FOV, field-of-view; GAD67, glutamate decarboxylase (67 kDa); Kv1, voltage-gated potassium channel; mTBI, mild traumatic brain injury; NaV, voltage-gated sodium channel; PBS, phosphate buffered saline; PV, parvalbumin; ROI, region-of-interest; RPM, respirations per minute; S1BF, primary somatosensory barrel field; SCWM, subcortical white matter; SD, standard deviation; SEM, standard error of the mean; TBI, traumatic brain injury; YFP, yellow fluorescent protein.

Simulations of realistic pyramidal neuron computational models using experimentally determined AIS lengths showed a subtle decrease is NaV1.6 density is sufficient to attenuate AP acceleration. Collectively, these findings highlight the complexity of mTBI-induced neocortical circuit disruption, involving changes in extrinsic/presynaptic inhibitory perisomatic input interfaced with intrinsic/postsynaptic intact excitatory neuron AIS output.

Keywords: mild traumatic brain injury, axon initial segment, GABAergic synapse, plasticity, action potential initiation, layer 5 pyramidal neurons, transgenic mouse models, excitation-inhibition balance

INTRODUCTION

Traumatic brain injury (TBI) constitutes a major global healthcare problem that extracts a devastating personal and societal toll (Langlois et al., 2006). Historically, TBI research focused on severe head injuries associated with high-speed motor vehicle incidents. In the last decade, the incidence of severe TBI decreased dramatically (Thurman et al., 1999; Coronado et al., 2011), with milder forms of TBI elicited by contact sports and blast waves during combat now predominating (Borg et al., 2004; Cassidy et al., 2004; Styrke et al., 2007; Hoge et al., 2008). Mild TBI (mTBI) is frequently termed the "silent epidemic" because of its relatively subtle nature typically occurring without any evidence of macroscopic brain damage such as contusion or hematoma formation (Alexander, 1995; Povlishock and Katz, 2005). However, recent findings in patients with mTBI linking acute cognitive network dysfunction with potential life-long morbidity have captured the attention of media and raised public concern (Mannix et al., 2016). Despite the focus of research shifting to mTBI (CDC, 2003), its cellular and physiological substrates remain controversial (Shaw, 2002; Büki and Povlishock, 2006; Cohen et al., 2007; Andriessen et al., 2010; Johnson et al., 2013).

Using advanced structural neuroimaging of patients with TBI ranging from mild-to-severe, multiple groups have demonstrated that diffuse axonal injury (DAI) occurs within various subcortical white matter (SCWM) tracts and callosal domains (Salmond et al., 2006; Bazarian et al., 2007; Mayer et al., 2010; Kinnunen et al., 2011). These findings led to the inference that white matter DAI causes cortical network dysfunction that underlies acute and/or chronic cognitive impairment (Bonnelle et al., 2011; Sharp et al., 2011, 2014; Johnson et al., 2013). However, other groups using the same imaging tools have not confirmed this finding in well-controlled studies of patients with mTBI and clinically significant cognitive dysfunction (Zhang et al., 2010; Mac Donald et al., 2011; Ilvesmäki et al., 2014; Wäljas et al., 2014). In fact, some reports suggest the potential for primary neocortical gray involvement (Newcombe et al., 2011; Bouix et al., 2013; Ling et al., 2013), wherein local information processing relies on balanced excitatory and inhibitory unitary neuronal activity to support function of large-scale distributed neurocognitive networks (Mountcastle, 1979; Mesulam, 1990; Douglas et al., 1995; Varela et al., 2001; Hasenstaub et al., 2005; Raichle, 2010). Several multi-modal studies using functional MRI and electrophysiological approaches have reported local neocortical network dysfunction following mTBI, supporting this premise (Mayer et al., 2011; Sponheim et al., 2011; Tremblay et al., 2011; Bashir et al., 2012; Huang et al., 2017; Palacios et al., 2017).

Although these issues are extremely difficult to rigorously assess in humans, our laboratory critically evaluated the potential for mTBI-induced neocortical change in a well-controlled animal model. Specifically, following experimental mTBI using transgenic mice, we observed primary neocortical damage involving scattered DAI within a subset of layer 5 pyramidal neurons expressing a yellow variant of green fluorescent protein (YFP) labeling the soma as well as their dendrites and axons (Greer et al., 2011). Perhaps even more biologically significant was our parallel observation that the non-DAI (intact) YFP+ neuronal population showed altered electrophysiological properties without any evidence of overt structural damage (Greer et al., 2012; Hånell et al., 2015a; Sun and Jacobs, 2016). Over time, these same intact YFP+ pyramidal neurons became hyperexcitable, entirely consistent with some form of mTBI-induced circuit disruption within local neocortical networks (Zhang and Raichle, 2010; Wolf and Koch, 2016).

At present, the neurobiological basis for this hyperexcitability in this intact neuronal population remains unknown. While several different mechanisms can alter neuronal excitability, our observations are most consistent with structural-functional changes within the axon initial segment (AIS), the site of action potential (AP) generation (Stuart et al., 1997; Palmer and Stuart, 2006). The AIS is a critical subdomain regulating neuronal excitability by integrating synaptic input to determine whether to fire an AP, thereby acting as a gatekeeper of neuronal output (Bender and Trussell, 2012; Kole and Stuart, 2012). Specifically, the high density of voltage-gated sodium channels (NaV) at the distal AIS sets the threshold for AP generation (Kole et al., 2008; Hu et al., 2009; Popovic et al., 2011). Ankyrin-G (ankG), a widely used AIS marker, is the master structural organizer that clusters ion channels via linkage to the subaxolemmal cytoskeleton (Zhou et al., 1998; Jenkins and Bennett, 2001; Yang et al., 2007). In sensory circuits, presynaptic input fine-tunes AIS structure (Kuba, 2012; Gutzmann et al., 2014; Kuba et al., 2014) altering neuronal excitability (Kuba et al., 2010). Because pyramidal neuron AIS function is strongly regulated by perisomatic GABAergic synaptic transmission from parvalbumin (PV)-expressing interneurons (Cobb et al., 1995; Pouille and Scanziani, 2001; Freund, 2003; Klausberger et al., 2003; Klausberger and Somogyi, 2008; Cardin et al., 2009; Atallah et al., 2012; Pouille et al., 2013; Lazarus et al., 2015; Wefelmeyer et al., 2015), concomitant involvement of these inhibitory inputs could potentially induce changes in AIS structure-function after mTBI (Buffington and Rasband, 2011; Baalman et al., 2013).

To address these AIS-related issues, the current report builds upon our previous studies that utilized YFP-expressing transgenic mice in a well-characterized model of mTBI to examine the potential for changes in layer 5 pyramidal neuron AIS and its associated perisomatic domain, both of which are critical for regulating neuronal excitability. Specifically, to assess AIS structural plasticity, immunohistochemical approaches targeting ankG and NaV1.6 distribution were quantitatively assessed in the early stage post-mTBI using confocal microscopy. These assessments of AIS structural plasticity in non-DAI/intact layer 5 pyramidal neurons were also accompanied by parallel morphological studies examining presynaptic GABAergic bouton density. Lastly, these imaging studies were interfaced with patch-clamp electrophysiology and computational modeling of layer 5 pyramidal neurons to establish a functional match with the AIS structural plasticity posited above. Using these multifaceted approaches, we show for the first time that mTBI evokes structural plasticity at the distal AIS, occurring independent of detectable changes in sodium channel distribution, in a specific subset of neocortical neurons with intact axons. These same events within intact neurons were also recognized to occur in concert with PV+ GABAergic terminal loss at their perisomatic domain. Lastly, the observed intrinsic/postsynaptic (AIS) and extrinsic/presynaptic (perisomatic) structural plasticity within intact neurons were also accompanied by a reduction in AP acceleration, likely reflecting a change in NaV1.6 density. Collectively, these findings reshape our understanding of mTBI and have major implications as we continue to better understand the brain's response to milder injury in terms of the functionality of its intrinsic networks within neocortex.

MATERIALS AND METHODS

Animal maintenance and experimental protocols were approved by the Virginia Commonwealth University Institutional Animal Care and Use Committee and complied with principles in the National Research Council *Guide for the Care and Use of Laboratory Animals: 8th Edition*.

Breeding and Genotyping of YFP-H Transgenic Mice

The Thy1-YFP-H line [B6Cg-TgN(Thy1-YFP-H)2Jrs, stock number 003782] was obtained from Jackson Laboratories (Bar Harbor, ME) and maintained as heterozygotes upon a C57BL/6J background. Inheritance of the fluorescent transgene in these was determined from an ear punch taken at weaning (∼21 days). The tissue from the ear punch was mounted on a glass slide and examined using a FITC filter on an Olympus DP71 digital camera (Olympus, Center Valley, PA, USA) where YFP expression could easily be identified in mice that inherited the transgene (YFP-H mice). Transgene expression in these mice is under the control of the neuronal specific Thy1 promoter, resulting in YFP expression within the neocortex that is primarily restricted to layer 5 pyramidal neurons (Feng et al., 2000).

Experimental Design

This study used a total of 18 young adult (age: 6–10 weeks; weight: 20–24 g) male mice randomly assigned[1] to either sham-injury (control) or mTBI (experimental) groups. Based on our previous work showing mTBI consistently generates DAI within primary somatosensory barrel field (S1BF), we assessed layer 5 intact YFP+ pyramidal neurons for AIS structural-functional changes at 2 days postinjury within this well-characterized region of neocortical gray matter (Greer et al., 2011, 2013; Hånell et al., 2015b). For confocal microscopy studies, a total of 11 mice (age 8–10 weeks) were surgically prepared for sham-injury (*n* = 5) or mTBI (*n* = 6) and perfused for immunohistochemical labeling of tissue sections. To identify the AIS we fluorescently labeled ankG, the master scaffolding protein that is widely used as a surrogate marker for AIS position and length (Hedstrom et al., 2008; Grubb and Burrone, 2010; Gutzmann et al., 2014). Additionally, we targeted NaV1.6, which sets the threshold for AP generation (Kole et al., 2008), to structurally assess the membrane channels underpinning AIS function/output. In addition to intrinsic/postsynaptic AIS structural plasticity within intact YFP+ pyramidal neurons, we assessed their perisomatic domain for extrinsic/presynaptic changes in GABAergic bouton density. To probe for any AIS functional plasticity correlated with potential structural changes we recorded intrinsic electrophysiological data from intact YFP+ pyramidal neurons in layer 5 of S1BF within *ex vivo* slice preparations from a total of 7 mice (age 6–8 weeks) at 2 days following sham-injury (*n* = 3) or mTBI (*n* = 4). Lastly, we determined the functional consequences of any potential AIS structural changes using a realistic computational model of a layer 5 pyramidal neuron based on experimentally derived properties (Hallermann et al., 2012).

Surgical Preparation and Central Fluid Percussion Injury

To model mTBI we used midline central fluid percussion injury (cFPI) first described by Dixon and associates using rats (Dixon et al., 1987), which our lab modified for mice as described previously (Greer et al., 2011). Briefly, anesthetized mice were surgically prepared for cFPI induction by installing a hub surrounding a craniectomy centered on the superior sagittal suture, midway between bregma and lambda. Intraoperative rectal temperature was maintained at 37 ± 0.2°C using a thermostatically controlled heating pad (Harvard Apparatus). Additionally, heart rate beats per minute (BPM), respiratory rate (RPM) and arterial blood oxygenation (SpO_2) were monitored using a thigh-clamp pulse oximeter sensor (MouseOx; STARR Life Sciences) to ensure maintenance of physiological homeostasis. After a post-operative recovery (∼1.5 h), mice were re-anesthetized and then connected to the fluid percussion apparatus (Custom Design and Fabrication, Virginia Commonwealth University)

---

[1] www.random.org

forming a closed mechanical system. Releasing the pendulum, striking the piston in the fluid-filled cylinder generated a mild pressure wave (~12 ms) that was delivered onto the intact dura. This action simulates human brain inertial loading during trauma-induced rapid acceleration-deceleration causing a mild diffuse brain injury (Dixon et al., 1987). The mean ± standard error of the mean (SEM) of the peak amplitude of the pressure wave (1.6 ± 0.03 atmospheres, n = 10 mice) was measured by a transducer and displayed on an oscilloscope (Tektronix TDS 210). For sham-injury, an identical procedure was used with the exception of the pendulum's release. Mice were disconnected from the apparatus immediately postinjury and visually monitored while removing the hub, suturing the incision and checking reflexes. None of the mice showed signs of seizure or apnea. Severity of injury (peak amplitude) and duration of loss of righting reflex, a rodent behavioral surrogate of loss of consciousness, were recorded for each animal (Grimm et al., 2015). We determined the degree of mTBI by comparing loss of righting reflex duration with shams (Morehead et al., 1994). After recovering from loss of righting reflex, animals were transferred to a warmed cage to maintain normothermia and monitored before returned to the vivarium.

Perfusion and Tissue Processing

Mice received a lethal dose of sodium pentobarbital (1.6 mg/g IP) 2 days postinjury. After loss of pain reflexes mice were transcardially perfused, first with heparinized (10 units/ml) saline for 1 min then 4% paraformaldehyde in Millonig's buffer pH 7.4 for 20 min. Brains were dissected and then sectioned coronally at 60 μm using a vibratome (Leica VT1000S). Sections directly below the craniectomy (bregma level −0.6 to −2.4 mm) were collected in 24-well plates filled with Millonig's buffer pH 7.4. To quantitatively assess for intrinsic AIS and extrinsic/synaptic perisomatic structural plasticity, for each animal, we labeled ankG, NaV1.6 and double-labeled glutamate decarboxylase-67 (GAD67) with PV in sections taken from a randomly selected and two adjacent wells, respectively, containing caudal S1BF (bregma level −1.5 to −2.0). This was done because of the consistency with which cFPI generates DAI within this well characterized area of neocortex, which was also the rational for choosing this region-of-interest (ROI) in our previously published electrophysiological studies (Greer et al., 2012; Hånell et al., 2015a; Sun and Jacobs, 2016).

Immunohistochemistry

Free-floating sections were rinsed with phosphate buffered saline (PBS). Heat-induced epitope retrieval was performed by incubating sections in 10 mM sodium citrate buffer pH 8.5 for 10 min in an 80°C water bath (Jiao et al., 1999). After cooling to room temperature sections were rinsed with PBS then incubated for 1 h at room temperature with 10% normal goat serum, 2% fish skin gelatin and 0.5% Triton X-100 in PBS. To mask any potential endogenous mouse immunoglobulin, the blocking buffer was supplemented with Mouse-on-Mouse reagent (Vector Laboratories, MKB-2213). Then, sections were rinsed with 1% normal goat serum, 1% fish skin gelatin, and 0.5% Triton X-100 in PBS (working buffer). Primary antibody solutions were prepared by dilution with working buffer and the sections were incubated overnight at 4°C with agitation. Specifically, we used monoclonal antibodies against ankG (1:500; mouse IgG2a, clone N106/36; NeuroMab), NaV1.6 (1:200; mouse IgG1, clone K87A/10; NeuroMab), PV (1:2000; mouse IgG1; Swant, PV235) and GAD67 (1:1000; mouse IgG2a, clone 1G10.2; Millipore, MAB5406). For qualitative double-labeled overview images, we used a polyclonal antibody against NaV1.6 (1:200; Alomone). The following day, sections were rinsed with working buffer and incubated with isotype-specific goat-derived secondary antibodies conjugated to Alexa Fluor 568 for quantitative analyses and a combination of Alexa Fluor 568 and 633 for qualitative colocalization (1:500: ThermoFisher Scientific) for 2 h at room temperature. After final rinses using working buffer then PBS, sections were mounted on glass slides and cover-slipped using non-hardening Vectashield with DAPI (Vector Laboratories, H-1200) to prevent shrinkage and preserve morphology of tissue.

The AIS quantitative analysis on the YFP+ background used separate single-labeled sections opposed to double-labeled single sections in an effort to match the fluorescent quantum yield and stoichiometry via monoclonal primary antibodies to immunolabel ankG and NaV1.6, which were both visualized using Alexa Fluor 568 (Lichtman and Conchello, 2005). In the same vein, mouse immunoglobulin isotype-specific secondary antibodies were used in all studies, which also optimized the signal-to-noise ratio (Manning et al., 2012). Parallel control studies were conducted to ensure both primary and secondary antibody fidelity (Lorincz and Nusser, 2008b). In all cases, primary antibody omission abolished immunoreactivity. Secondary antibody specificity evaluated via cross-reactivity showed no signal between all possible primary × secondary host and/or isotype combinations.

Confocal Microscopy

Image acquisition was performed using a laser-scanning confocal microscope (LSM 710, Carl Zeiss). Since sham vs. mTBI groups could be readily differentiated based on YFP+ profiles, we used DAPI visualized under epifluorescence to center the stage over the ROI. In this way, the investigator was blinded from the experimental/dependent variable channel, thus adhering to stereological principles including random sampling. Using a 10× objective (low-power) the field-of-view (FOV) was centered over the S1BF region along the dorsolateral edge of the hippocampus. We used continuous laser scanning to guide rotation of the FOV until it was orthogonal to the underlying SCWM. Images were acquired with optimal Nyquist sampling using Plan-Apochromat 10×/0.45 NA (XY = 0.41 μm/pixel; Z = 5.8 μm), 20×/0.8 NA (XY = 0.152 μm/pixel; Z = 0.94 μm), 40×/1.4 (XY = 0.094 μm/pixel; Z = 0.52 μm) and 63×/1.2 NA (XY = 0.088 μm/pixel) oil immersion objective lenses. All multichannel images were acquired using sequential scanning at the lowest possible laser power to avoid crosstalk (488 Argon, 561 DPSS and 633 HeNe). All images for quantitative analysis were acquired using identical laser settings per channel across samples. Gain and offset were adjusted for optimal signal range. The pinhole was set to 1.0 Airy unit for the red channel (i.e., ankG, NaV1.6 and GAD67). To maintain identical optical slice thickness with respect to the red channel, in multichannel *z*-stack images the green (YFP) and far-red (PV) the pinhole ranged from 0.8 to 1.2 Airy units.

Intact YFP+ Pyramidal Neuron Sampling

Within the 10× overview images we measured ever YFP+ pyramidal neuron that met our inclusion criteria. Specifically, intact neurons were defined by YFP+ axons that were continuous from the soma of origin to the SCWM interface. YFP+ that were transected during tissue processing were excluded in both sham and mTBI samples. Since AIS structure and composition vary even within a particular neuronal subtype (Kuba, 2012; King et al., 2014), we set *a priori* conditions to control for any potential confounds. Specifically, layer 5 is subdivided into layer 5a and 5b, which are populated by multiple subtypes of pyramidal neurons with different morphological and physiological properties, as well as projections to different anatomical regions of the brain (Chagnac-Amitai et al., 1990; Schubert et al., 2006; Hattox and Nelson, 2007). To control for potential confounding of layer 5 pyramidal neurons based on neocortical depth, for each AIS sample we also measured the distance from the axo-somatic vertex to where YFP+ profiles entered SCWM, indicated by the sharp change in trajectory. Additionally, we excluded pyramidal neurons with axons emerging from basal dendrites because of their unique intrinsic and synaptic properties (Thome et al., 2014; Hamada et al., 2016). Overall, the number of intact YFP+ pyramidal neurons meeting our inclusion criteria ranged from 5 to 14 per section. This data set met the recommended minimum of five measurements per animal to obtain a robust and unbiased estimates of variance using multilevel modeling described below (Walsh, 1947; Maas and Hox, 2004; Galbraith et al., 2010). Further, the Wilcoxon test showed sample sizes between sham and mTBI groups were similar for both ankG (sham: $n = 53$ AIS from 5 mice; mTBI: $n = 54$ AIS from 6 mice; $X^2 = 0.079$, $p = 0.7782$) and NaV1.6 (sham: $n = 54$ AIS from 5 mice; mTBI: $n = 44$ AIS from 6 mice; $X^2 = 3.36$, $p = 0.0666$) analyses of AIS structure. These samples sizes allowed us to detect a 1.5 μm (5%–10%) change in AIS end position with 80% power (G*Power; Franz Faul, Kiel University) based on mean ± SD sham ankG end position (25.5 ± 2.94 μm; $n = 50$ AIS from 3 mice) determined from pilot experiments. For perisomatic GABAergic bouton density, sample sizes between sham ($n = 48$ somas from 5 mice) and mTBI ($n = 50$ somas from 5 mice; one section lost during processing) groups were also similar ($X^2 = 0.1$, $p = 0.7518$; Wilcoxon test).

Quantification of AIS

To capture ankG and NaV1.6 fluorescent profiles along YFP+ intact pyramidal neurons, a 40× objective at 3× zoom (760 × 760 pixels) in *z*-stacks (mean 4.5 μm, range 2.7–5.3 μm). Because of the diffuse nature of YFP+ pathology following mTBI, these constrained images allowed tracing the YFP+ axon through and past the AIS region in a blinded fashion. Further, we set a limit of 10 optical slices to minimize error caused by tilted AIS orientation in the *z*-plane. AIS measurements were performed using a previously described method (Grubb and Burrone, 2010; Evans et al., 2013). Specifically, *z*-stacks were collapsed into a single maximum intensity projections that were imported into MATLAB software (MathWorks) for analyses using custom-written functions (Matthew Grubb and Thomas Watkins, King's College London, UK; freely available at www.mathworks.com/matlabcentral/fileexchange/28181-ais-quantification). While visualizing only the YFP channel, an axonal profile was traced starting at the edge of the soma, continuing distally along the axon, through and past the region of the AIS. Immunofluorescent profiles of ankG/NaV1.6 were then superimposed on traces of YFP+ axons. At each pixel along this profile, fluorescent intensity values were averaged over a 3 × 3 pixel square centered on the pixel of interest. Averaged profile values were then smoothed using a 40-point (∼5 mm) sliding mean and normalized between 1 (maximum smoothed fluorescence) and 0 (minimum smoothed fluorescence). With respect to the soma edge, delineated at the axo-somatic vertex, ankG and NaV1.6 proximal (start) and distal (end) positions were obtained at points where the profiles reached thresholds of 0.33 and 0.5 relative to maximum fluorescence, respectively. These optimal threshold values were determined empirically and varying ± 0.2 did not change the overall pattern of results.

Quantification of Perisomatic Bouton Density

The total number of GAD67+ and GAD67+/PV+ puncta were quantified along the perisomatic domain of YFP+ intact pyramidal neurons within layer 5 of S1BF. Single optical slices (0.9 μm thick) were captured using a 63× objective at 3× zoom (512 × 512 pixels, 45 μm × 45 μm; resolution = 0.088 μm/pixel) using sequential scanning and a single laser intensity for each channel for all samples. Confocal images were imported to Fiji (a distribution of ImageJ) then processed and analyzed using custom written macros for automated analyses. YFP images were converted into binary images to segment the pyramidal neuron profile, which was then dilated and eroded to generate a 2 μm thick band approximating the perimeter/perisomatic domain. Quantification of puncta within this band was performed using both gray scale and segmented/binary images. Specifically, perisomatic GAD67+ puncta in gray scale (8-bit) images were quantified using the "Find Maxima" function. To quantify perisomatic GAD67+/PV+ puncta, profiles in each channel were segmented from background subtracted 8-bit images by converting into binary using a minimum gray-value threshold. Varying the threshold ±10 gray-values did not change the overall pattern of results. GAD67+/PV+ colocalized populations were isolated using the "Image Calculator" function. The "Particle Analysis" function with appropriate size and shape exclusion filters was used to determine the total number of objects per unit area (FOV). GAD67+ (PV+) puncta within this band were quantified and normalized by dividing by the area of the band to determine perisomatic bouton density, summarized as puncta per 100 μm^2.

Computational Modeling

Simulations in Neuron v7.1 used a previously published realistic model of neocortical layer 5 pyramidal neuron AP initiation (Hallermann et al., 2012). The model was based on Neurolucida reconstructions using ion channel properties determined from experimental recordings. Simulations were executed using default setting with the exception of AIS ion channel densities and length modifications based on our experimental observations. Specifically, the default AIS length (63 μm) in this model was ~60% longer than our experimental measurements. To compare the effect of AIS length using our experimentally observed values (~24–26 μm), the peak NaV1.6 density at the distal AIS was increased proportionally from the default value of 7000–11,200 pS μm^{-2}. Importantly, this control NaV1.6 density remained within the realistic estimates reported by Hallermann et al. (2012). Default current-clamp parameters were used to evoke an AP within 5 ms of injection. Overall, simulations using our adjusted AIS parameters resulted in AP waveforms that were qualitatively similar to those produced using default settings and also our electrophysiological recordings. This allowed us to investigate the kinetics (i.e., acceleration; described below) of the AP at the AIS in isolation from the AP at the soma. Specifically, we compared the effect of changing AIS length using experimentally determined values (i.e., sham vs. mTBI) and NaV1.6 density on AP acceleration. Note, in these layer 5 pyramidal neuron simulations, AIS length was modulated at the distal position with respect to the soma of origin. Additionally, changing length or peak NaV1.6 density at the distal AIS did not change the distribution ratio of ion channels.

Electrophysiology

In addition to the above, a separate cohort of sham-injured ($n = 3$) and mTBI ($n = 4$) mice were anesthetized with isoflurane and decapitated for quick brain removal 2 days postinjury. The brains were immediately chilled in ice-cold oxygenated sucrose-modified artificial cerebral spinal fluid (aCSF) slicing solution (mM: 2.5 KCl, 10 $MgSO_4$, 0.5 $CaCl_2$, 1.25 NaH_2PO_4, 234 sucrose, 11 glucose and 26 $NaHCO_3$). Using a vibratome (VT 1200, Leica Microsystems) brains were coronally sectioned at 300 μm and then incubated for 30–45 min at 34°C in an oxygenated aCSF (mM: 126 NaCl, 3.5 KCl, 1 $MgSO_4$, 1.2 $CaCl_2$, 1.25 NaH_2PO_4, 10 glucose and 26 $NaHCO_3$). Thereafter, slices remained at room temperature until placed in the recording chamber maintained at 32 ± 0.5°C.

As previously described (Sun and Jacobs, 2016), whole-cell patch-clamp recordings were performed under infrared Dodt contrast microscopy (Zeiss AxioExaminer). A 60× water-immersion objective was used to visually identify YFP+ layer 5 pyramidal neurons of S1BF with axons descending from the soma into the white matter (intact) or ending with an axonal swelling (DAI), deep to the surface of the slice to avoid those transected by the vibratome. We have shown previously that these morphologies are easily identified in the living slice for YFP+ layer 5 pyramidal neurons (Greer et al., 2012). Consistent with our structural assessments, only these intact YFP+ pyramidal neurons were recorded in both sham and mTBI slices. Additionally, all layer 5 YFP+ samples had an apical dendrite, a characteristic morphological feature of pyramidal neurons. The slices were continuously perfused with aCSF solution saturated with 95% O_2 and 5% CO_2. Patch electrodes (final resistances, 2–4 MΩ) were pulled from borosilicate glass (World Precision Instruments) on a horizontal Flaming-Brown microelectrode puller (Model P-97, Sutter Instruments). The intracellular solution contained (in mM): 130 K-gluconate, 10 Hepes, 11 EGTA, 2.0 $MgCl_2$, 2.0 $CaCl_2$, 4 Na-ATP and 0.2 Na-GTP. Electrode capacitance was electronically compensated. Data were acquired and digitized at 200 kHz using a MultiClamp 700B amplifier and Digidata 1440A with pClamp software, respectively (Molecular Devices). Whole-cell patch-clamp was approached under voltage-clamp mode at −65 mV. After 2–5 min stabilization, APs were recorded in current-clamp mode to obtain intrinsic property measurements. Pipette Capacitance Neutralization was set at 9.6 pF, Bessel Filter at bypass, auto Bridge Balance, and Gain at one. APs were evoked with 10 depolarizing steps (30 ms) beginning with a 100 pA step, and increased by 10 pA every 5 s while neurons were maintained at −60 mV. Access resistance was continuously monitored and rechecked after each recording. If the series resistance increased by 20% at any time, the recording was terminated. Previously we showed that there was no significant difference between the results for naïve and sham animals (Greer et al., 2012). Despite this similarity, for added rigor the control group contained only age- and survival time-matched sham-injured animals. Additionally, passive membrane properties (mean ± standard deviation; SD) compared using a t test showed no statistical differences in capacitance (pF: sham = 196 ± 46.5, mTBI = 176 ± 28.4; $t_{25} = -1.35$, $p = 0.1882$), input resistance (MΩ: sham = 67 ± 21.5, mTBI = 79 ± 25.1; $t_{25} = 1.28$, $p = 0.2111$), access resistance (MΩ: sham = 9.2 ± 3.21, mTBI = 9.11 ± 3.06; $t_{25} = -0.07$, $p = 0.9409$), or resting membrane potential (mV: sham = −69.8 ± 3.03, mTBI = −70.7 ± 5.79; $t_{25} = -0.49$, $p = 0.6298$) between sham ($n = 13$ cells from 3 mice) and mTBI ($n = 14$ cells from 4 mice) groups.

In this report, we use a newly implemented protocol for intrinsic property analysis that allows us to measure the first AP on each sweep (5 sweeps per cell). To assess AP kinetics, we applied three successive seven-point boxcar filters to the membrane voltage, and then calculated the first and then second derivative, which yielded two peaks. Specifically, the first and second peak in the plot of the second derivative of the membrane voltage corresponded to AP acceleration at the AIS and soma, respectively (Khaliq and Raman, 2006; Meeks and Mennerick, 2007). All recorded cells from sham and mTBI slices resulted in two peaks, and their amplitudes were measured for each of five APs per cell. For statistical analyses, the first AP on each of the five sweeps was nested within each cell. There were two cells in sham slices where only four sweeps were recorded. In total, we recorded and analyzed 63 AP from sham and 70 AP from mTBI mice. The number of recorded cells per animal, (range = 2–6) was similar

($X^2 = 0.5283$, $p = 0.4673$) between sham ($n = 3$ mice) and mTBI ($n = 4$ mice). For statistical analysis using multilevel modeling described below, each neuron had and additional nested set of five APs.

Statistics

Statistical analysis of data sets was performed using JMP Pro version 12.2.0 (a distribution of SAS). Data sets were assessed for normality using quantile (QQ) plots and the Shapiro-Wilk test. For all analyses, the variance in data between sham and mTBI groups was not significantly different ($p > 0.05$, Brown-Forsythe test). Physiology data and loss of righting reflex were statistically analyzed using unpaired *t* tests. Statistical analyses (described below) tested for covariance of distance from SCWM with AIS measurements. If covariance was significant, AIS measurements were leveraged with respect to distance from SCWM. Non-leveraged vs. leveraged AIS measurements were statistically assessed for significant difference using the Wilcoxon signed-rank test. For this test, the statistical unit corresponded to the average difference (non-leveraged—leveraged) in AIS measurements per animal.

To determine statistically significant differences among intact YFP+ pyramidal neuron outcome variables (distance from SCWM, AIS structure, perisomatic bouton density and AIS function) between sham-injury and mTBI groups, we employed multilevel modeling (Nieuwenhuis et al., 2011; Button et al., 2013; Aarts et al., 2014). For statistical analysis, we constructed a multilevel model using an experimental condition at the animal level (sham-injury or mTBI), where the outcome variable (e.g., AIS length) consists of multiple measurements per animal (i.e., nested data). In other words, each animal had nested data consisting of a series of measurements. Because some variability is expected in the average outcome measure as a function of each animal, the data from each animal are not independent (Nieuwenhuis et al., 2011). Thus, failure to account for such dependent data can inflate the Type I error rate (α) above the standard nominal value of 0.05 (Snijders and Bosker, 1993). Multilevel modeling accounts for this within-animal dependence on the outcome measure (e.g., AIS length) and thus preserves the true Type I error rate for the statistical test (Walsh, 1947; Galbraith et al., 2010), which we have set to $\alpha = 0.05$.

Statistical analysis using multilevel modeling performs linear regressions in a sequential fashion (Aarts et al., 2014). In addition to accounting for intra-animal variability, this statistical model also allowed us to test whether distance from SCWM was a covariate of AIS length, and if there were any interactions with sham vs. mTBI groups. To conduct multilevel modeling, first an *F* test was used to determine if the multilevel model accounted for the variability in the data set. If the *F* test yielded $p < 0.05$, we inferred that the model fit the data and continued our analysis. We then evaluated the adjusted coefficient of determination (R^2), which describes how much of the variability in the data is accounted for in the multilevel model (e.g., the proportion of AIS length that is a function of mTBI and distance to SCWM). In predictive statistics, the R^2 can be used to assess the effect size of a multilevel linear regression model, where 0.01, 0.09 and 0.25 are defined as small, medium and large effects, respectively (Aarts et al., 2014). In next step, a two-tailed *t* test in linear regression terms was used to determine whether each specific parameter (e.g., sham vs. mTBI and distance to SCWM) had a significant effect on the outcome measure (e.g., AIS length), with the threshold for significance set at $\alpha < 0.05$ adjusted for multiple comparisons. When analyzing only two experimental groups (e.g., sham vs. mTBI), a generally accepted index for reporting a standardized effect size is Cohen's *d*, which equals the difference in the means of the two groups in units of SD. Cohen defined 0.2, 0.5 and 0.8 as small, medium and large effects, respectively (Cohen, 1988).

For ankG multilevel modeling, intact YFP+ pyramidal neuron summary statistics (*t* ratio, degrees of freedom, and *p*-value) and outcome measures (mean ± SEM) were calculated from nested data sets (e.g., $N = 53$ AIS total, 10–11 AIS nested per animal, $n = 5$ mice). To summarize multilevel modeling statistics, we report the number of animals per group (*n*) and total number of measurements per animal (*N*), the degrees of freedom (denoted as the subscript in the *t* ratio, and the *p*-value). All statistical data are summarized using mean ± SEM, unless otherwise noted. Descriptive data are summarized with mean and 95% confidence intervals (CI). All statistical tests were two-tailed and considered significantly different for $p < 0.05$.

RESULTS

Intraoperative physiology was normal and consistent with previous reports on mice under isoflurane anesthesia (Cesarovic et al., 2010; Ewald et al., 2011; Hånell et al., 2015b). Specifically, the arterial oxygen saturation (sham = 97.8 ± 0.1%; mTBI = 97.7 ± 0.2%), heart rate (sham = 513 ± 12 BPM; mTBI = 505 ± 14 BPM) and RPM (sham = 63 ± 6 RPM; mTBI = 74 ± 6 BRPM) were similar between sham ($n = 8$ mice) and mTBI ($n = 10$ mice) groups (SpO_2: $t_{12.8} = 0.73$, $p = 0.4770$; BPM: $t_{16.0} = 0.42$, $p = 0.6811$; RPM: $t_{15.4} = -1.23$, $p = 0.2251$; *t* test). Consistent with our previous reports (Greer et al., 2011; Hånell et al., 2015b), the loss of righting reflex duration in mTBI mice (4.7 ± 0.24 min; $n = 10$) was significantly greater ($t_{11.4} = 7.13$, $p < 0.0001$; *t* test) than shams (1.2 ± 0.42 min; $n = 8$). Additionally, mTBI mice for confocal (4.7 ± 0.39 min; $n = 6$) and electrophysiological (4.6 ± 0.25 min; $n = 4$) studies had similar loss of righting reflex ($t_{7.8} = -0.35$, $p = 0.7337$; *t* test). Importantly, signs of hypoxia/apnea were not observed during surgical preparation or postinjury. Overall, these physiological assessments did not show any evidence of confounding mechanisms that play a role in secondary insults.

Macroscopically, both sham and mTBI brain tissue appeared normal without evidence of surgically induced lesions (**Figures 1A–E**), as previously reported. Post-mTBI tissue sections revealed no macroscopic change (**Figure 2**) consistent with the mild and diffuse nature of cFPI. Importantly, the dorsal neocortex underneath the craniectomy site did not show evidence of focal contusion, cavitation, or overt subarachnoid hemorrhage induced by the fluid pressure wave (**Figure 2B**).

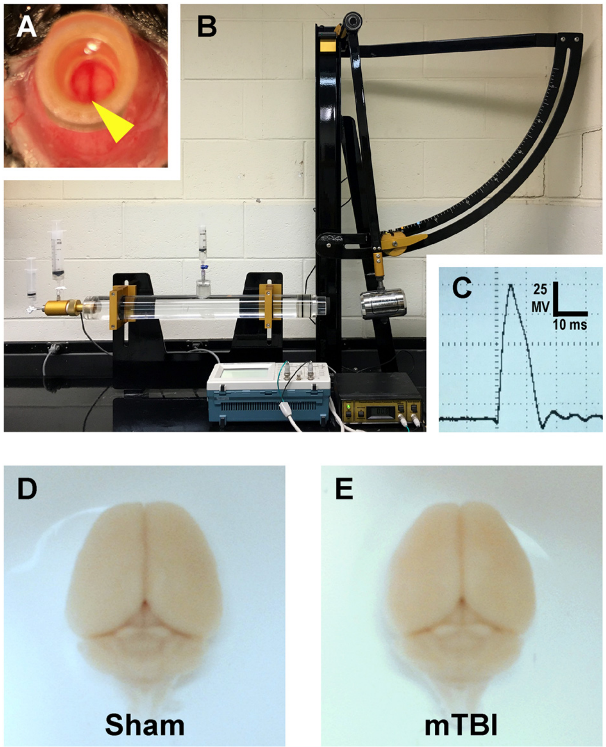

FIGURE 1 | Mouse model of mild traumatic brain injury (mTBI) via midline central fluid percussion injury (cFPI). **(A)** Dorsal view showing craniectomy site with the dura intact. The superior sagittal sinus (yellow arrowhead) can be seen through the saline-filled hub. **(B)** Fluid percussion injury device with the pendulum in the cocked position. Severity of injury is determined by arc height. After releasing the trigger the pendulum strikes a piston in a cylinder reservoir generating a fluid pressure wave. The mouse cranium is attached to the cylinder at the opposite end via the installed hub, forming a closed mechanical system. **(C)** A representative fluid pressure wave that is transmitted directly onto the intact dura. **(D,E)** Representative images of dissected brains perfused 2 days after cFPI-induced mTBI. Sham **(D)** and mTBI **(E)** brains show no evidence of surgically-induced damage. After cFPI, there is no evidence of mass lesions and/or contusion. There is no focal damage at the craniectomy site where the pressure wave entered the cranium.

Overall, the brain parenchyma was devoid of overt hemorrhage, the ventricular system maintained a regular contour, with no evidence of trauma-related ventricular enlargement. Taken together these data support our premise that cFPI in YFP-H mice is a reproducible model of mTBI.

YFP+ Pyramidal Neuron DAI

Consistent with previous work from our laboratory and others that utilized the YFP-H strain (Feng et al., 2000; Greer et al., 2011; Antón-Fernández et al., 2015; Hånell et al., 2015b), we observed YFP+ pyramidal neurons in sham (**Figures 3A,D**) and mTBI (**Figures 4A,D**) mice primarily within layer 5 neocortex (**Figure 2**). Following sham-injury, we did not observe any YFP+ axonal swellings or morphological irregularities indicative of axonal damage within neocortex or underlying SCWM (**Figure 2A**). Descending axons from YFP+ pyramidal neurons in shams demonstrated a continuous trail from their soma of origin to the SCWM interface. Following cFPI, all tissue sections processed for YFP visualization and parallel immunohistochemical analyses revealed a pattern of microscopic change consistent with that routinely described in rat and mouse cFPI models. Despite the overall preservation of brain parenchymal integrity typical of a mild diffuse TBI in both humans and rodents, the fluid pressure wave consistently evoked YFP+ axonal swellings indicating DAI. At 2 days post-mTBI, comparable to previous reports, we observed pathologic YFP+ axonal profiles in continuity with their somas of origin (**Figures 2B**, **4A**) and their detached axonal segments distributed throughout layer 5/6 of the dorsolateral neocortex corresponding to S1BF (**Figure 2B**). Underscoring the diffuse nature of mild cFPI, the distribution of YFP+ pyramidal neurons proximal and distal axonal swellings were interspersed among numerous YFP+ profiles showing no morphological evidence of either primary axonal injury or retrograde neuronal involvement. Similar to shams, we readily identified these non-DAI/intact YFP+ pyramidal neurons via tracing YFP+ axons continuously from the edge of soma of origin to the SCWM interface (**Figure 2C**). Importantly, we observed consistent YFP+ pyramidal neuron axonal injury within the same neocortical regions of all mTBI mice, indicating a generalized diffuse response to cFPI-induced mTBI in mice rather than an isolated focal event.

Intact YFP+ Pyramidal Neuron Responses

AIS Structural Plasticity

To estimate AIS position and length (**Figure 6**), we quantified immunofluorescent profiles of ankG, a key structural protein underpinning AIS function (Grubb and Burrone, 2010). Consistent with previous reports from our laboratory and others (Greer et al., 2013; Gutzmann et al., 2014; Clark et al., 2016), ankG labeling throughout the neocortex was restricted to the AIS and nodes of Ranvier (**Figure 3B**). Importantly, ankG labeling of intact YFP+ pyramidal neurons clearly delineated the AIS in sections from both sham and mTBI mice (**Figures 6B,E**). For ankG multilevel modeling, intact YFP+ pyramidal neuron summary of outcome measures (mean ± SEM) and statistics were calculated from nested data sets (sham: $N = 53$ AIS total, 10–11 AIS nested per animal, $n = 5$ mice; mTBI: $N = 54$ AIS total, 5–13 AIS nested per animal, $n = 6$ mice). The sampling distribution of intact YFP+ pyramidal neurons with respect to distance from the SCWM interface (**Figure 5**) was symmetrical between groups (sham = 372 ± 14 μm, mTBI = 368 ± 14 μm; $t_{8.0} = 0.18$, $p = 0.8585$). Within this same data set (**Figure 6**), the ankG start position with respect to soma of origin was similar between groups (sham = 2.1 ± 0.16 μm, mTBI = 2.2 ± 0.16 μm; $t_{6.41} = -0.50$, $p = 0.6342$). In contrast, we observed a statistically significant decrease by 6.8% (-1.8 ± 0.59) in ankG end position (sham = 26.6 ± 0.42 μm, mTBI = 24.8 ± 0.42 μm; $t_{7.4} = -3.08$, $p = 0.0167$). Overall, this resulted in ankG length significantly decreasing by 7.8% (-1.9 ± 0.58 μm) from the distal end (sham = 24.4 ± 0.41 μm, mTBI = 22.5 ± 0.41 μm; $t_{7.7} = -3.30$, $p = 0.0114$; $R^2 = 0.16$). Because layer 5 pyramidal neurons are heterogeneous (Chagnac-Amitai et al., 1990; Hattox and Nelson, 2007; Le Bé et al., 2007),

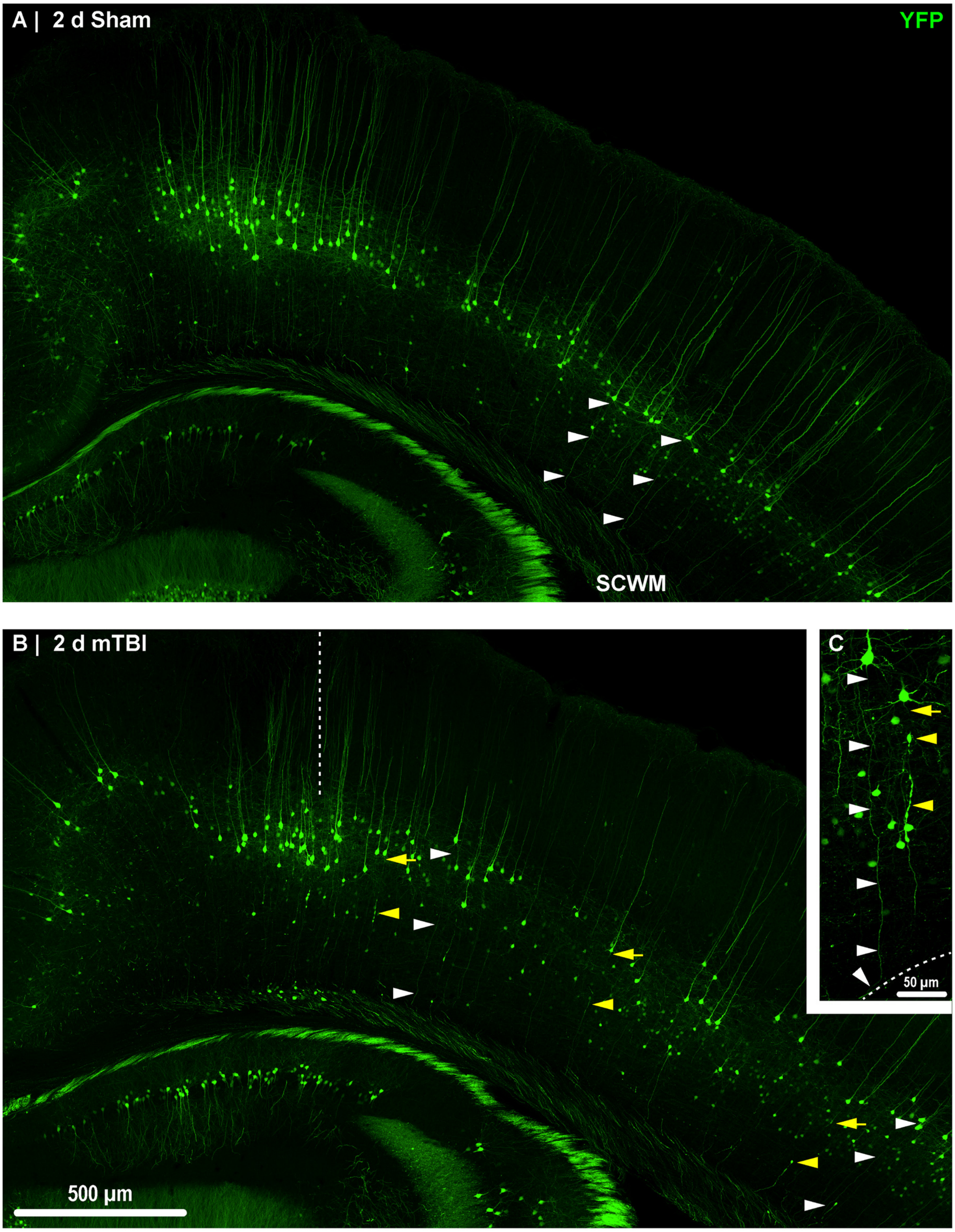

FIGURE 2 | Yellow fluorescent protein (YFP) expression in neocortical layer 5 pyramidal neurons. Representative images of sections from sham **(A)** and mTBI **(B)** brains shown in **Figure 1**. Thy1 driven YFP expression results in restricted labeling of a discrete subset of layer 5 pyramidal neurons. **(A–C)** The selective YFP expression allows identification of individual axons that be traced from their soma of origin to the subcortical white matter (SCWM; white arrowheads). **(B)** Two days after mTBI, evidence of diffuse axonal injury (DAI) indicated by YFP+ axonal swellings is seen dispersed across the dorsolateral neocortex (yellow arrowheads). The craniectomy boundary is depicted by the vertical dashed line. No evidence of focal injury is observed under the craniectomy site. **(C)** A representative intact YFP+ pyramidal neuron juxtaposed by an injured axon. The intact axonal profile can be continuously traced from the soma of origin to where it enters the SCWM (dashed line), indicated by the acute change in trajectory.

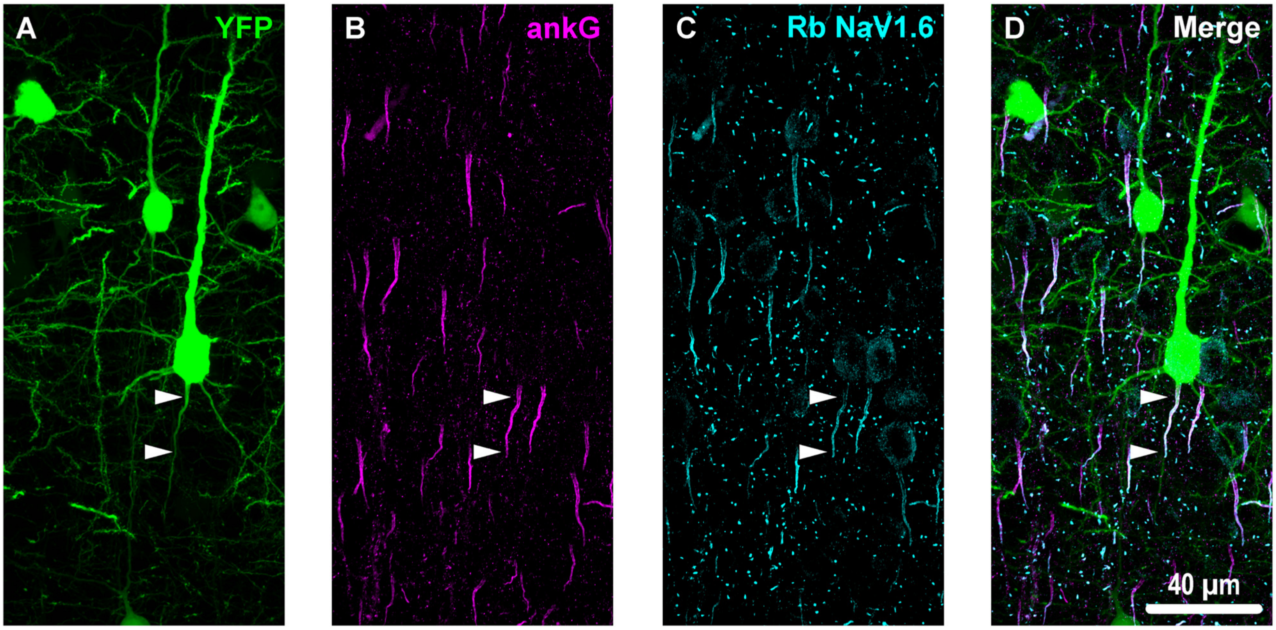

FIGURE 3 | Overview of ankyrin-G (ankG) and voltagegated sodium channels (NaV1.6) immunofluorescent profiles in YFP mice. **(A)** Neocortical layer 5 YFP+ pyramidal neurons (green). **(B)** AnkG immunoreactivity visualized using Alexa Fluor 568 (magenta) shows characteristic tapered morphology. **(C)** NaV1.6 immunolabeled with a polyclonal rabbit (Rb) antibody visualized using Alexa Fluor 633 (cyan) reveals shorter profiles corresponding to the distal axon initial segment (AIS). Punctate profiles indicate Nodes of Ranvier. **(D)** Composite image clearly demonstrating the utility of ankG as an AIS marker. The proximal axon of the YFP+ pyramidal neuron in the center of the field-of-view (FOV) colocalizes with ankG and NaV1.6, which is expressed at the distal AIS. Several ankG+ profiles highlight NaV1.6 expression at the distal AIS.

varying structurally and functionally with cortical depth (e.g., layer 5a vs. 5b), we controlled for this potential confound in analyzing plasticity (Jacob et al., 2012) by measuring the AIS distance from SCWM. Multilevel analysis ($N = 107$ AIS total) revealed that distance from SCWM is a significant covariate (d_{SCWM}) of both ankG end position ($t_{88.0} = 4.07$, $p < 0.0001$) and overall length ($t_{79.0} = 4.52$, $p < 0.0001$). Specifically, ankG end position ($d_{\mathrm{SCWM}} = 0.019 \pm 0.005$) and length ($d_{\mathrm{SCWM}} = 0.020 \pm 0.004$) are directly proportional to distance from SCWM. The equal slopes of the best-fit lines for ankG length as a function of distance from SCWM (**Figure 6I**) indicated that there was no interaction with experimental groups (end position: $t_{86.0} = -0.82$, $p = 0.3120$; length: $t_{80.3} = 0.69$, $p = 0.5512$). Consistent with the symmetrical sample distribution intact YFP+ pyramidal neurons in layer 5 S1BF (**Figure 5**), the statistical model yielded similar values after leveraging, with respect to distance from SCWM, ankG end position (sham = 26.6 ± 0.36 μm, mTBI = 24.9 ± 0.39 μm) and length (sham = 24.4 ± 0.33 μm, mTBI = 22.6 ± 0.35 μm). Additionally, the leveraged ankG length after mTBI was significantly shorter

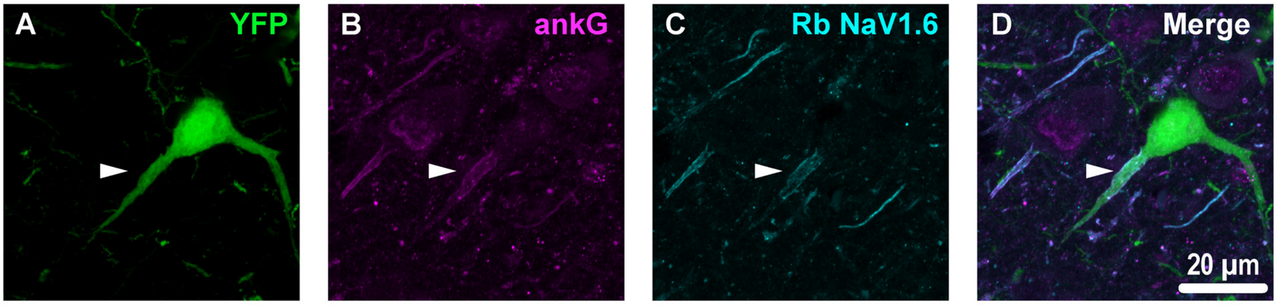

FIGURE 4 | YFP+ pyramidal neuron axonal injury attenuates ankG and NaV1.6 expression at the AIS. **(A–C)** Representative images of YFP **(A)** ankG **(B)** and NaV1.6 **(C)**. **(A)** Evidence of DAI occurring at the AIS of a YFP+ pyramidal neuron (green) is indicated by a severely swollen proximal segment (arrowhead). **(B,C)** AnkG (magenta) and NaV1.6 (cyan) expression persists, but is substantially attenuated with abnormal morphology after mTBI-induced AIS injury. **(D)** Composite image showing ankG and NaV1.6 within the swollen AIS of a YFP+ pyramidal neuron.

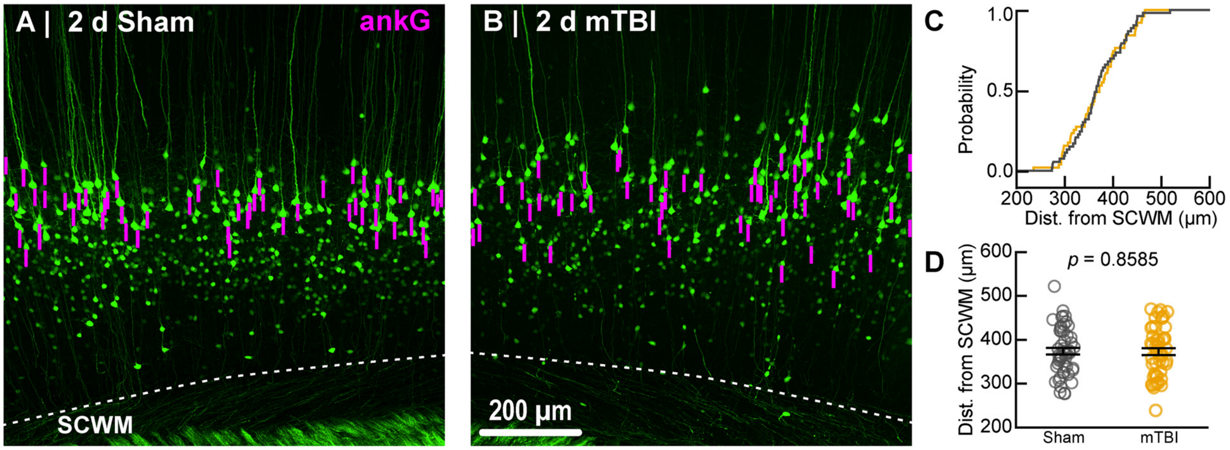

FIGURE 5 | Sampling distribution of intact YFP+ pyramidal neurons for ankG quantitative analysis. **(A,B)** Superimposed maximum intensity projections of 10× overview images for sham **(A)** and mTBI **(B)**. The intact YFP+ pyramidal neuron sampling distribution (magenta bars) is symmetric with respect to the SCWM. **(C)** Cumulative frequency distribution plot shows a high degree of overlap between sham (gray) and mTBI (gold). **(D)** Quantitative analysis confirmed no sampling difference. Statistics: multilevel analysis with animals as a random variable. Data summarized with means and standard error of the mean (SEM) error bars.

by 7.4% (−1.8 ± 0.48 µm) compared to shams ($t_{7.4} = -3.74$, $p = 0.0066$; $R^2 = 0.28$). Notably, accounting for this covariate resulted in 20% decrease in SEM (0.41–0.33) and a 75% increase in the R^2 (0.16–0.28). Hence, while this reduction in ankG length is relatively modest, multilevel modeling revealed that mTBI accounted for almost 30% of the variability between data sets, and the effect size was robust (Cohen's $d = 0.76$). Further, ankG was shortened from the distal AIS microdomain that contains the "trigger zone" for AP firing, where a highly dense distribution of NaV1.6 sets the threshold for AP initiation (Kole et al., 2008).

To estimate the distal AIS "trigger zone" position and length (**Figure 8**), we quantified immunofluorescent profiles of NaV1.6. Consistent with previous reports from other labs (Lorincz and Nusser, 2008a; King et al., 2014), NaV1.6 labeling throughout the neocortex was restricted to the distal AIS and nodes of Ranvier (**Figure 3C**). Importantly, NaV1.6 labeling of intact YFP+ pyramidal neurons clearly delineated the distal AIS in sections from both sham and mTBI mice (**Figures 8B,E**). For NaV1.6 multilevel modeling, intact YFP+ pyramidal neuron summary of outcome measures (mean ± SEM) and statistics were calculated from nested data sets (sham: $N = 54$ AIS total, 7–14 AIS nested per animal, $n = 5$ mice; mTBI: $N = 44$ AIS total, 5–9 AIS nested per animal, $n = 6$ mice). The sampling distribution of intact YFP+ pyramidal neurons with respect to distance from the SCWM interface (**Figure 7**) was not statistical different between groups (sham = 339 ± 16 µm, mTBI = 384 ± 15 µm; $t_{9.55} = 1.99$, $p = 0.0761$). Within this same data set (**Figure 8**), the NaV1.6 start position with respect to soma of origin was similar between groups (sham = 11.0 ± 0.28 µm, mTBI = 11.0 ± 0.32 µm; $t_{5.3} = 0.12$, $p = 0.8708$). Unlike our ankG findings at the distal AIS, we did not observe a statistically significant difference in NaV1.6 end position (sham = 26.0 ± 0.61 µm, mTBI = 27.0 ± 0.59 µm; $t_{9.7} = 1.20$, $p = 0.2876$) or overall length (sham = 15.0 ± 0.60 µm, mTBI = 16.0 ± 0.60 µm; $t_{9.9} = 1.24$, $p = 0.2448$).

In line with our ankG findings (**Figure 6I**), multilevel analysis also revealed that distance from SCWM is a significant covariate of both NaV1.6 end position ($t_{71.7} = 3.80$, $p = 0.0003$; $d_{\text{SCWM}} = 0.020 \pm 0.005$) and NaV1.6 length ($t_{59.9} = 3.38$, $p = 0.0013$; $d_{\text{SCWM}} = 0.021 \pm 0.006$; **Figure 8I**). Notably, the coefficient of distance from SCWM (d_{SCWM}) was remarkably similar between ankG and NaV1.6 for both end position and length (average = 0.02, 95% CI: 0.018–0.021; $n = 4$). This observations provided further evidence supporting that AIS length is directly proportional to distance from SCWM, wherein upper vs. lower pyramidal neurons have longer and shorter AIS, respectively. Specifically, the statistical model predicts AIS length from distal end increases ∼2 µm for every 100 µm from SCWM (**Figures 6I, 8I**). Considering layer 5 S1BF is ∼300 µm thick (**Figures 5, 7**), this corresponds to ∼6 µm difference in AIS length from the distal end between upper and lower pyramidal neuron populations. While the sampling distributions with respect to the distance from SCWM interface between sham and mTBI were not significantly different (as described above), in light of this covariate's magnitude, we compared the means of non-leveraged vs. leveraged with respect to distance from SCWM of NaV1.6 end position and length using the Wilcoxon signed-rank test. For sham data ($n = 5$ mice), including the distance from SCWM covariate in our multilevel model did result in a statistically significant difference between the means NaV1.6 end position (leveraged = 26.1 ± 0.52 µm; $X^2 = -2.5$, $p = 0.6250$) or length (leveraged = 15.4 ± 0.55 µm; $X^2 = -6.5$, $p = 0.1250$). In contrast, for mTBI data ($n = 6$ mice) the distance from SCWM covariate in the multilevel model yielded significantly decreased mean values for both NaV1.6 end position (leveraged = 26.2 ± 0.52 µm; $X^2 = 10.5$, $p = 0.0313$) and length (leveraged = 15.4 ± 0.56 µm; $X^2 = 10.5$, $p = 0.0313$). This difference in NaV1.6 end position (−0.70 ± 0.38) and length (−0.58 ± 0.42) from the distal AIS is consistent with our model's predicted effect of a −45 µm difference between sham

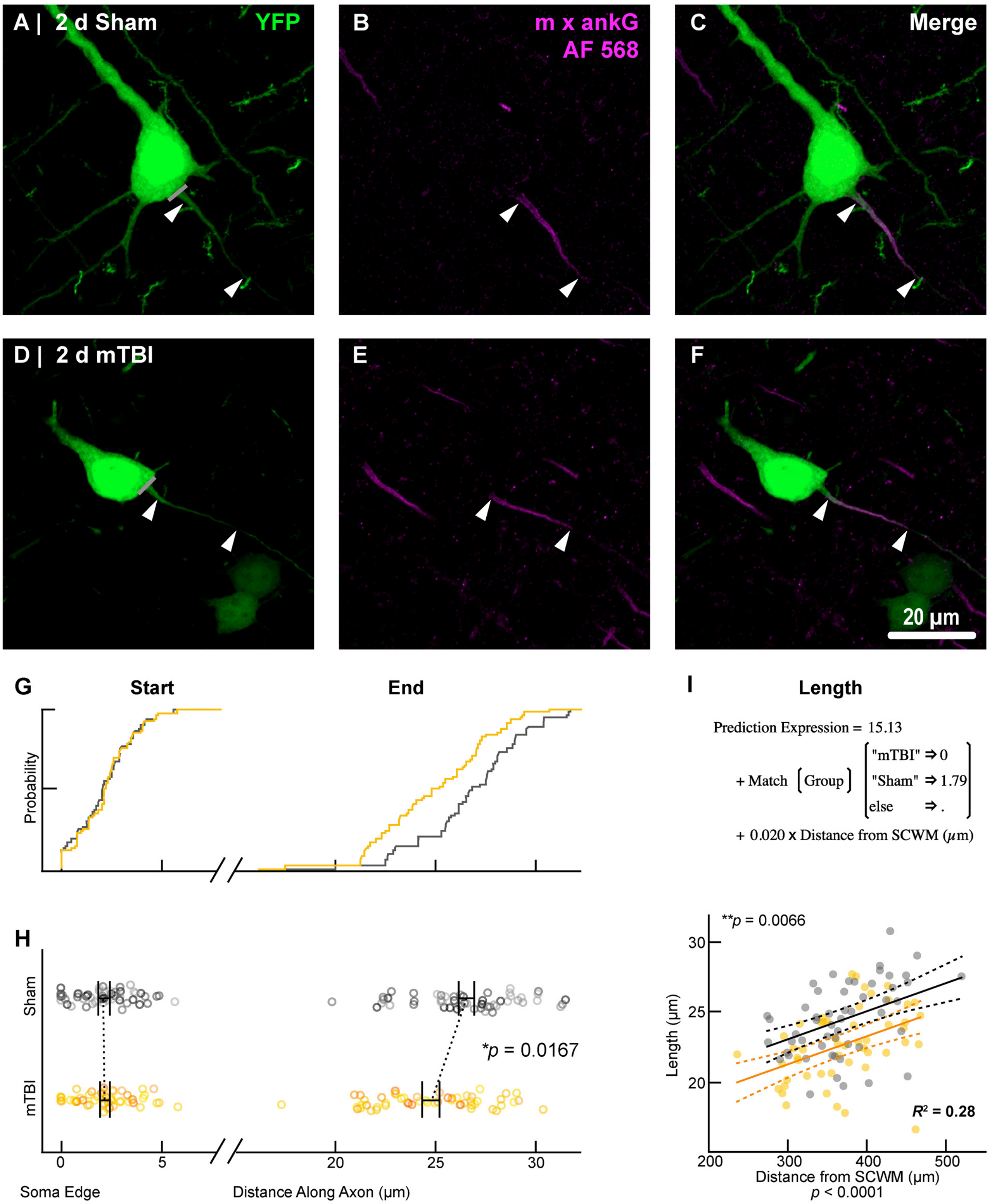

FIGURE 6 | AnkG length decreases from the distal AIS after 2 days post-mTBI. Representative images of sham **(A–C)** and mTBI **(D–F)** of YFP (**A,D**; green) and ankG (**B,E**; magenta). **(C,F)** Composite image showing YFP+ axon colocalization with ankG, demarcating the AIS. YFP traces were taken from the line drawn across the ado-somatic vertex **(A,D)**, through and past the region of the AIS **(C,F)**. **(G–I)** Quantitative analysis of ankG profiles of sham (gray) and mTBI (gold). **(G)** Cumulative frequency distribution plots showing overlap in start position but a proximal shift in mTBI end position. **(H)** Multilevel analysis of start and end positions with animals as a random variable depicted by different shades. Data summarized with means and SEM error bars. Note that there is no change in ankG start position; however, there was a significant decrease in the end position. This resulted in an overall decrease in length from the distal AIS. **(I)** Multilevel analysis of ankG length with animals as a random variable and distance from SCWM as a covariate. Plot of ankG length as a function of distance from SCWM (solid lines) with 95% confidence intervals (CI; dashed lines) for sham and mTBI. Note that distance from SCWM is a significant covariate of ankG length, but there is no interaction with experimental groups indicated seen as a parallel shift in lines.

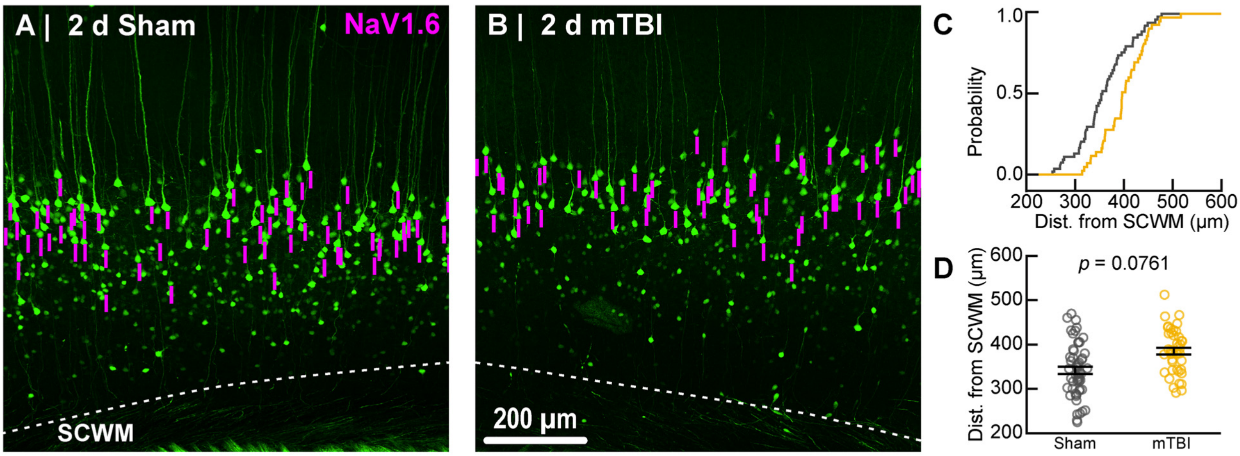

FIGURE 7 | Sampling distribution of intact YFP+ pyramidal neurons for NaV1.6 quantitative analysis. **(A,B)** Superimposed maximum intensity projections of 10× overview images for sham **(A)** and mTBI **(B)**. The intact YFP+ pyramidal neuron sampling distribution (magenta bars) with respect to the SCWM appeared slightly asymmetric, with mTBI having several samples located more superficially (upper right aspect). **(C)** Cumulative frequency distribution plot showing mTBI (gold) samples are shifted toward increased distance from SCWM compared to sham (gray). **(D)** Quantitative analysis confirmed revealed there was no statistically significant difference in sampling. Statistics: multilevel analysis with animals as a random variable. Data summarized with means and SEM error bars.

(339 μm) and mTBI (384 μm) mean distance from SCWM (e.g., 0.02 × −45 μm = −0.9 μm; **Figures 7C,D**).

Collectively, these data suggest disparate responses between ankG and NaV1.6 at the distal AIS 2 days after mTBI. Restructuring our multilevel model by changing the experimental condition to AIS component allowed us to directly assess for differences between ankG and NaV1.6 end position. As described above, we accounted for nested measurements per animal. Additionally, in this multilevel model we also accounted for the dependency resulting from sampling two sections per animal for single labeling of ankG and NaV1.6. To determine if there was a differential response at the distal AIS, we compared the leveraged means of ankG and NaV1.6 end positions in both sham and mTBI data sets. In shams (n = 5 mice), the leveraged end position for ankG (26.3 ± 0.55 μm; N = 53 AIS, 10–11 AIS nested per animal) and NaV1.6 (26.0 ± 0.55 μm; N = 54 AIS, 7–14 AIS nested per animal) were similar ($t_{8.2}$ = 0.47, p = 0.6522; N = 10 sections, 2 per animal). Conversely, after mTBI (n = 6 mice) the leveraged end position for ankG (25.0 ± 0.34 μm; N = 54 AIS, 5–13 AIS nested per animal, 54 AIS total) was less distal than NaV1.6 (26.5 ± 0.37 μm; N = 44 AIS, 5–9 AIS nested per animal). This difference of 5.6% (–1.48 ± 0.50) between ankG and NaV1.6 end positions was statistically significant ($t_{8.6}$ = −2.94, p = 0.0172; N = 12 sections, 2 per animal). Overall, the multilevel model accounted for a large proportion of the variability between data sets (R^2 = 0.23) and the effect size was substantial (Cohen's d = 0.61). Taken together, these data show that ankG structural plasticity is uncoupled from NaV1.6 at 2 days post-mTBI. Further, these data provide compelling evidence for S1BF layer 5 pyramidal neuron AIS length as a function of distance from the SCWM. Lastly, these findings reveal that AIS length both after mTBI and as a function of distance from the SCWM is modulated at the site of AP initiation that is regulated by NaV1.6.

Perisomatic GABAergic Bouton Density

In concert with intrinsic/postsynaptic AIS structural plasticity, we observed a loss of GABAergic inputs along the perisomatic domain of intact YFP+ pyramidal neurons in layer 5 S1BF, revealing evidence for extrinsic/presynaptic change 2 days after mTBI (**Figure 9**). Immunolabeling GAD67, the GABA-synthesizing enzyme enriched in PV+ presynaptic boutons (Fish et al., 2011) allowed us to conduct a high precision quantitative analysis of the major source of inhibitory input at the perisomatic domain, which strongly regulates AIS activity. We quantified perisomatic GABAergic bouton density of only intact YFP+ pyramidal neurons in S1BF using the same sampling method for AIS studies (**Figures 5**, **7**). For perisomatic GABAergic bouton density (puncta/100 μm^2) multilevel modeling, intact YFP+ pyramidal neuron summary of outcome measures (mean ± SEM) and statistics were calculated from nested data sets (sham: N = 48 somas total, 5–13 somas nested per animal, n = 5 mice; mTBI: N = 50 somas total, 5–14 somas nested per animal, n = 5 mice). Using two different quantitative methods, we observed a decrease in perisomatic GABAergic bouton density in both GAD67+ (**Figures 9B,F,J**) and GAD67+/PV+ (**Figures 9C,G,K,L**) immunoreactive profiles 2 days after mTBI. Specifically, the density of GAD67+ profiles in gray-scale images between sham (13.0 ± 0.57 puncta/100 μm^2) and mTBI (10.9 ± 0.57 puncta/100 μm^2) were significantly different; $t_{7.8}$ = −2.61, p = 0.0321). Similarly, the density of GAD67+/PV+ profiles in binary images between sham (12.0 ± 0.55 puncta/100 μm^2) and mTBI (8.7 ± 0.56 puncta/100 μm^2) were also significantly different; $t_{5.4}$ = −4.04, p = 0.0086). The magnitudes of change were comparable between gray and binary quantitative methods, with intact YFP+ pyramidal neuron perisomatic GABAergic bouton density decreasing by 16% and 24%, respectively. Additionally, the effect sizes were robust for both methods

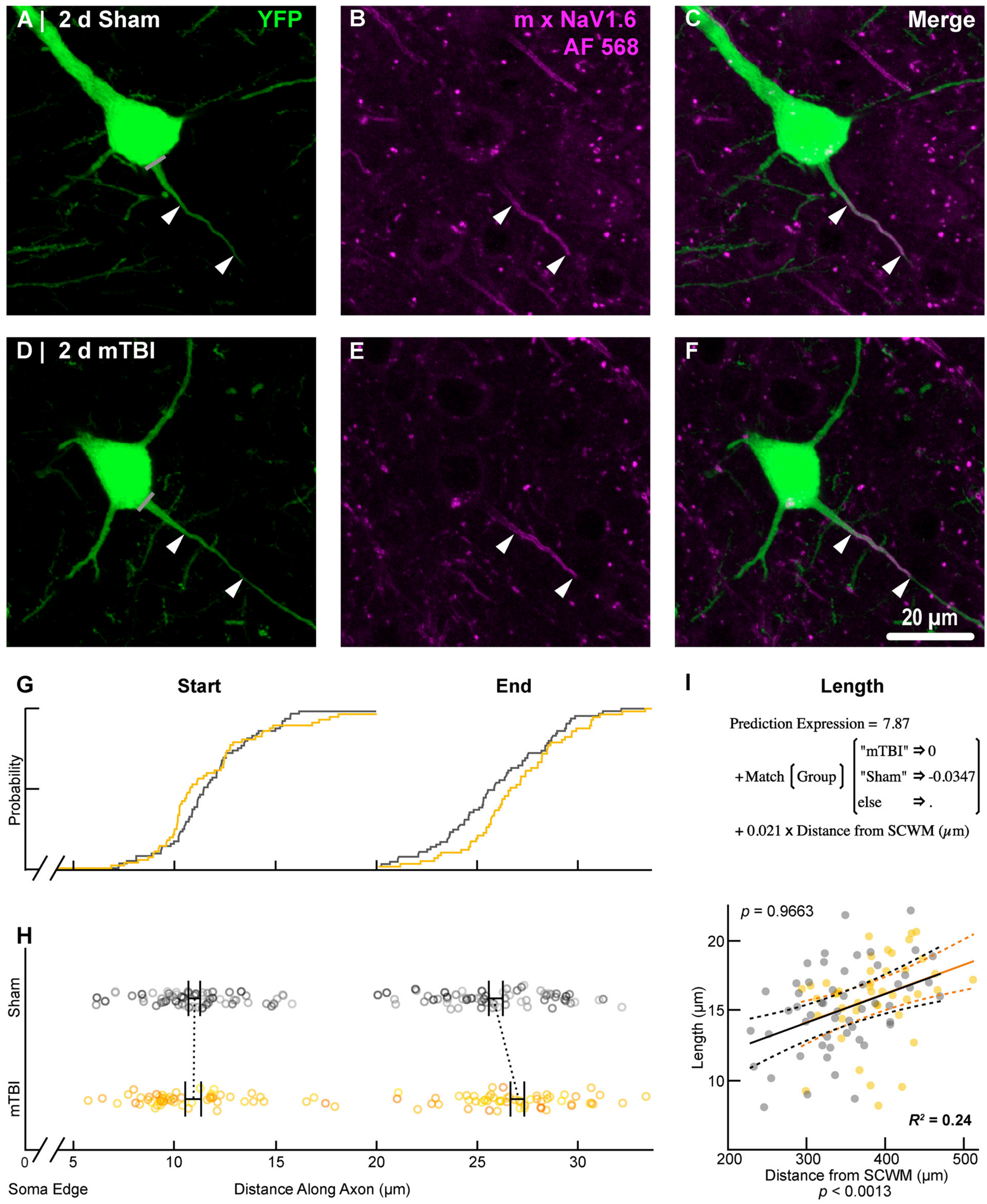

FIGURE 8 | NaV1.6 geometry does not change after mTBI. Representative images of sham **(A–C)** and mTBI **(D–F)** of YFP (**A,D**; green) and NaV1.6 (**B,E**; magenta). **(C,F)** Composite image showing YFP+ axon colocalization with NaV1.6, demarcating the distal AIS. **(G–I)** Quantitative analysis of NaV1.6 profiles of sham (gray) and mTBI (gold). **(G)** Cumulative frequency distribution plots showing overlap in start position but a distal shift in mTBI end position. **(H)** Multilevel analysis of start and end positions with animals as a random variable depicted by different shades. Data summarized with means and SEM error bars. Note that there was no change in NaV1.6 start or end position. **(I)** Multilevel analysis of NaV1.6 length with animals as a random variable and distance from SCWM as a covariate. Plot of NaV1.6 length as a function of distance from SCWM (solid lines) with 95% CI (dashed lines) for sham and mTBI. Distance from SCWM is a significant covariate of NaV1.6 length. This accounted for the overlap in sham and mTBI plots compared to the shift seen in the uncorrected distribution of the end position **(G)**.

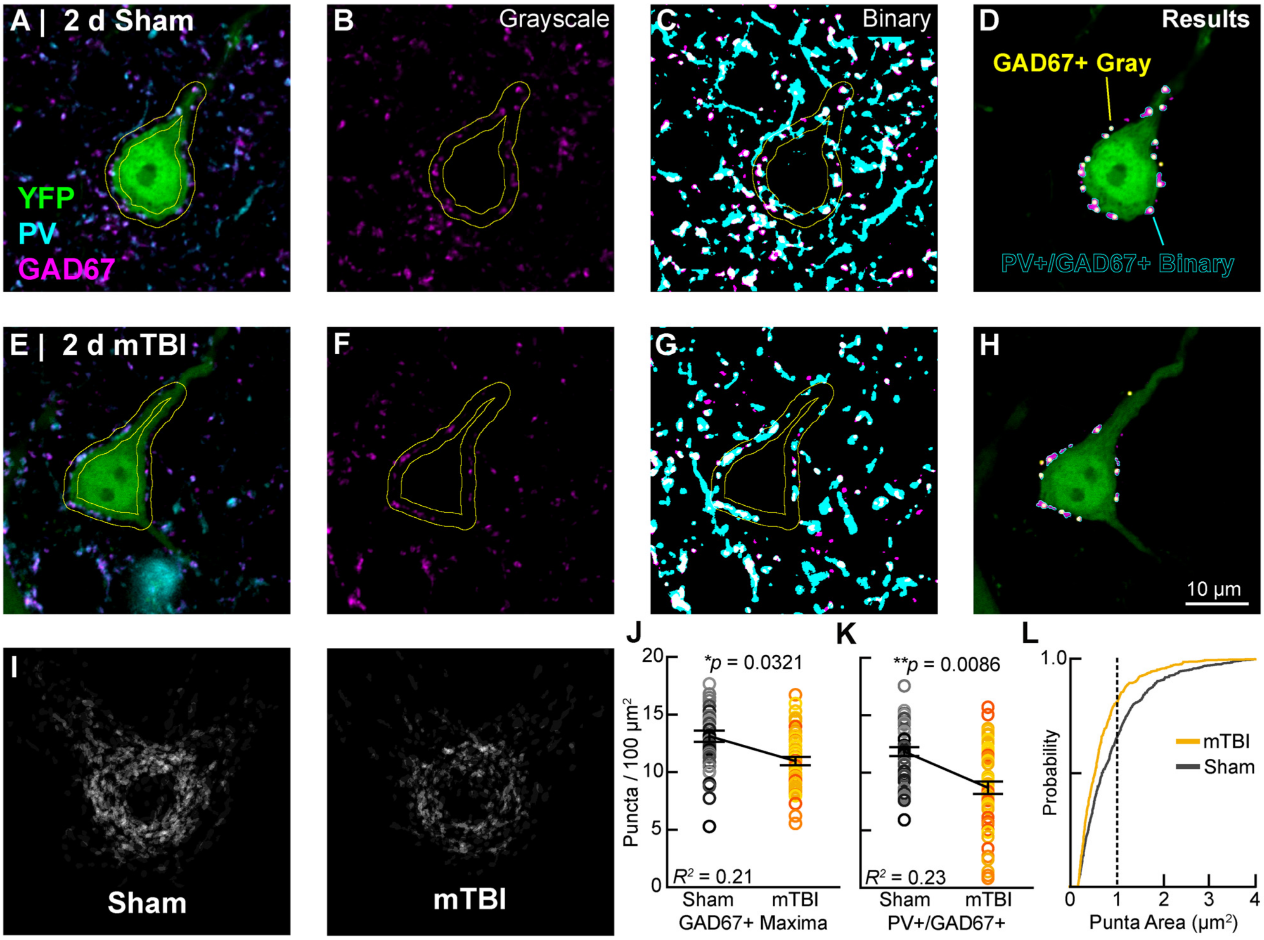

FIGURE 9 | Intact YFP+ pyramidal neuron perisomatic GABAergic bouton density decreases 2 days post-mTBI. Representative images of sham **(A–D)** and mTBI **(E–H)** glutamate decarboxylase-67 (GAD67+; **B,F**; magenta) and parvalbumin (PV+; **A,C,E,G**; cyan) punch along the perimeter of YFP+ pyramidal neurons (**A,E,D,H**; green). Perisomatic bouton density was quantified in 8-bit gray scale images of GAD67 expression **(B,F,J)** and also binary images of colocalized PV+/GAD67+ puncta **(C,G,I,K,L)**. **(D,H)** Outcome of automated quantification using gray scale and binary images was comparable. Perisomatic GAD67 expression (magenta) and result of gray scale analysis (yellow dots) largely overlapped with results of PV+/GAD67+ binary image analysis (cyan outlines). **(I)** A qualitative decrease in perisomatic GABAergic bouton density is seen in superimposed images of binary PV+/GAD67+ profiles. **(J,K)** Multilevel analysis with animals as a random variable depicted by different shades for sham (gray) and mTBI (gold/orange). Data summarized with means and SEM error bars. GAD67+ maxima in gray-scale images and PV+/GAD67 puncta in binary images were both significantly reduced in mTBI vs. sham. The absolute values as well as relative decrease were similar between gray-scale and binary image analyses. **(L)** Cumulative frequency distribution of PV+/GAD67+ puncta area. Vertical line at 1 μm^2 corresponds to average size of a GABAergic presynaptic bouton. This shift in the mTBI plot shows that PV+/GAD67+ puncta approximating the average area of a GABAergic bouton accounting for the majority of the loss.

(Cohen's *d*: gray-scale = 0.71; binary = 0.99). Lastly, analysis of the cumulative distribution plot of the size of PV+/GAD67+ puncta (segmented particles in binary images) revealed that the greatest decrease occurred in particles that were the average size (~1 μm^2) of GABAergic puncta (**Figure 9L**). Taken together, these data provide substantial evidence for diffuse presynaptic GABAergic terminal loss 2 days after mTBI.

AIS Functional Plasticity

Our findings of presynaptic input loss in concert with postsynaptic AIS remodeling have been associated with alterations of neuronal excitability in sensory circuits reported by others (Kuba et al., 2010, 2014). Appreciating the known intrinsic properties of the AIS and the mechanisms that modulate its structure and function (Bender and Trussell, 2012), we followed our morphological studies with electrophysiological assessments at 2 days post-mTBI. Specifically, we employed whole-cell patch-clamp analysis of intact YFP+ pyramidal neurons in layer 5 S1BF to compare intrinsic AIS functional properties between sham (*n* = 13 cells from 3 mice; 4–5 AP nested per cell, *N* = 63 AP total) and mTBI (*n* = 14 cells from 4 mice; 5 AP nested per cell, *N* = 70 AP total) groups using multilevel modeling. Similar to shams, current injection evoked an AP in all patched intact YFP+ pyramidal neurons after mTBI, consistent with the diffuse and subtle nature of mTBI pathophysiology. While AP waveforms were comparable between sham and mTBI (**Figures 10A,B**), AP decay tau significantly decreased by 79% after mTBI ($p = 0.0014$; **Table 1**). Additionally, we found that AP threshold was ~3 mV more depolarized after mTBI (-46.2 ± 1.0 mV) compared to shams (-49.6 ± 1.0 mV). This difference in AP threshold was statistical significant ($t_{25} = 2.41$, $p = 0.0236$; Cohen's $d = 0.95$), and consistent with altered AIS intrinsic function. While AP initiation occurs at the AIS, after spiking the signal travels both anterograde down the axon, and retrograde toward the soma. Therefore, AP recorded by patching the cell body reflects a combination of AP generation at the AIS and back-propagation in the soma (Hu et al., 2009). To further dissect intrinsic AIS function from patch-recordings at the cell body, we calculated the second derivative of membrane voltage (i.e., AP acceleration), which showed two peaks (**Figure 10C**). In the plot of the second derivative, the amplitude of the first and second peaks corresponded to AP acceleration at the AIS and soma, respectively (Khaliq and Raman, 2006; Meeks and Mennerick, 2007). Interestingly, multilevel modeling revealed AP acceleration is significantly reduced at the AIS ($t_{25} = -2.57$, $p = 0.0164$), but not the soma ($t_{25} = 0.58$, $p = 0.5701$; **Figures 10C,D**). Specifically, AP acceleration at the AIS decreased by 21% after mTBI (4104 ± 296 $\text{mV}/\mu\text{s}^2$) compared to shams (5203 ± 308 $\text{mV}/\mu\text{s}^2$), and the effect size was large (Cohen's $d = 1.01$). AP threshold in pyramidal neurons is set by NaV1.6 channels localized at the distal AIS (Kole et al., 2008). These data showing AP threshold depolarization and attenuation of AP acceleration specifically at the AIS are consistent with alteration of NaV1.6 membrane distribution after mTBI. Together, our morphological and electrophysiological studies provide significant evidence of intact YFP+ pyramidal neuron AIS structural and functional plasticity after mTBI.

Layer 5 Pyramidal Neuron Modeling

While AIS excitability varies with axial geometry such as length (Kuba et al., 2010), voltage-gated ion channel density is also a critical determinant of intrinsic AP properties (Kole et al., 2008). To investigate the functional consequences of AIS structural plasticity and explore the effect varying NaV1.6 density we used an anatomically and physiologically accurate computational model of a layer 5 pyramidal neuron (Hallermann et al., 2012). This computational model allowed us to probe AP dynamics specifically at the AIS. The AP waveforms in the model (**Figure 10E**) were qualitatively similar to those observed experimentally (**Figure 10B**). Comparing the effect of AIS length differences based on our experimental observations of ankG immunofluorescent profiles, we found that shortening the length by 7% resulted in a 19% decrease in the peak of the second derivative of membrane voltage, reflecting attenuated AP acceleration (**Figure 10F**). To help elucidate potential functional consequences of ankG and NaV1.6 uncoupling we evaluated the effect of a proportionate decrease in NaV density at the distal AIS. Without changing AIS length, a 7% decrease in NaV density at the distal AIS also attenuated AP acceleration by 10%. Thus, AP kinetics at the AIS depends on both geometry and density of functional components. Collectively, these morphological and

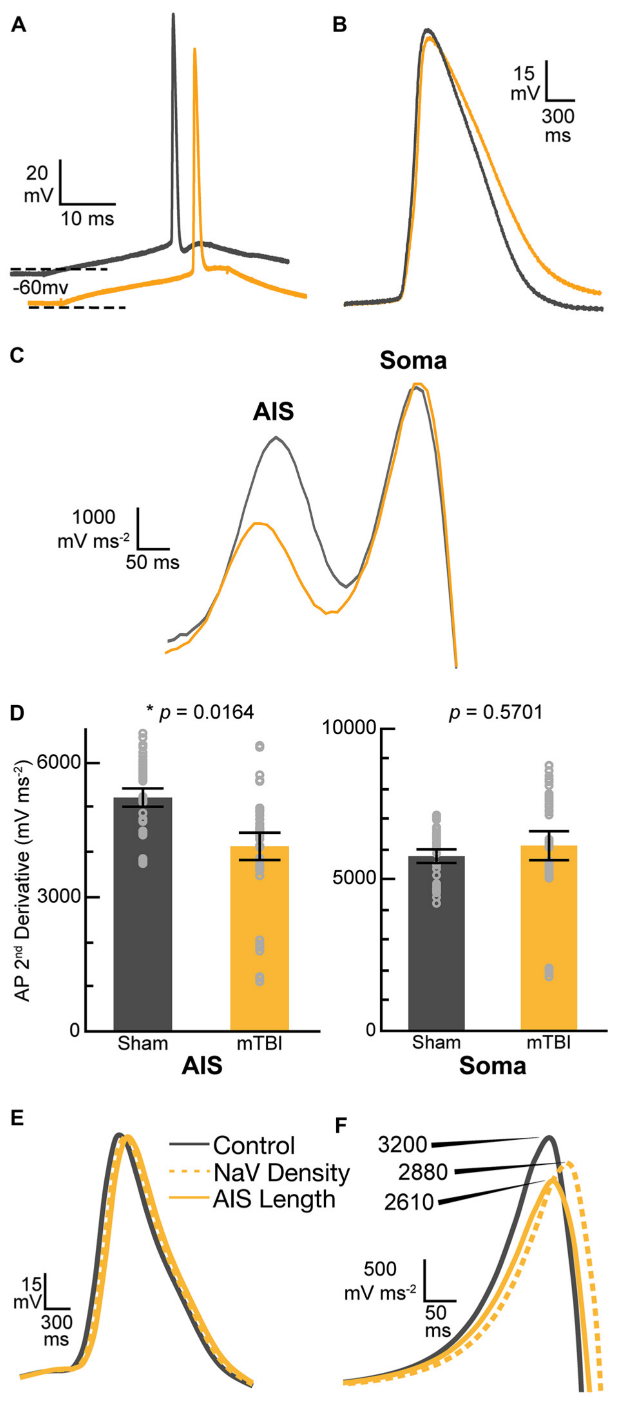

FIGURE 10 | Action potential (AP) acceleration at the AIS is reduced 2 days post-mTBI. **(A–D)** Whole-cell patch-clamp analysis of intact YFP+ pyramidal neurons of layer 5 primary somatosensory barrel field (S1BF) in sham (gray) and mTBI (gold) *ex vivo* live slices. **(A)** Representative traces of AP recorded at somas. The mTBI trace is offset for better comparison. Dashed lines indicate holding potential. **(B)** Enlarged traces from **(A)** showing AP waveform. Note slightly longer AP decay after mTBI. **(C)** Plot of second derivative of the membrane voltage. The first and second peak amplitudes were used to compare AP acceleration at the AIS and soma, respectively. **(D)** Multilevel analysis of the second derivative of membrane voltage (AP acceleration) with

(Continued)

FIGURE 10 | Continued
animals as a random variable and accounting for the five recorded AP nested within each cell. Data summarized with means and 95% CI error bars. The peak amplitude at the AIS was significantly reduced, reflecting attenuated AP acceleration. In contrast, there was no change in the AP acceleration at the soma. **(E,F)** Computational modeling of a layer 5 pyramidal neuron. Evoked AP waveforms in simulations **(E)** using experimentally observed AIS lengths were similar to AP recorded from intact YFP+ pyramidal neurons **(A)**. Overall, changing AIS length or NaV density at the distal AIS by 7% did not have an overt effect on AP waveform. **(F)** The plots of computationally derived second derivatives of membrane voltage were also comparable to experimental observations **(B)**. Modeling data showed that a 7% decrease in AIS length or NaV1.6 density at the distal AIS both decrease peak amplitude of the second derivative plot, consistent with attenuated AP acceleration.

computational findings suggest that even subtle AIS changes may alter AP spike dynamics among intact pyramidal neurons after mTBI.

DISCUSSION

This study provides compelling evidence of intact pyramidal neuron AIS structural and functional plasticity after clinically relevant mTBI in mice. Consistent with human mTBI, midline cFPI reproducibly evoked DAI without mass lesions, neocortical contusion, and/or overt cell death (Mittl et al., 1994; Saatman et al., 2008; Andriessen et al., 2010; Bigler and Maxwell, 2012; Yuh et al., 2013; Shultz et al., 2016). Exploiting restricted YFP expression in a discrete subset of layer 5 pyramidal neurons and an established AIS marker (ankG), we confirmed subcellular structural plasticity within the non-DAI/intact population. In this mTBI-mediated response, the loss of presynaptic GABAergic boutons surrounding the perisomatic domain of intact pyramidal neurons suggested compromised AIS inhibition mediated by PV+ interneuron input. Consistent with AIS structural change, patch-clamp recordings of intact YFP+ layer 5 pyramidal neurons revealed attenuated AP acceleration after mTBI. This finding was further supported by simulations using a realistic layer 5 pyramidal neuron model that showed even a subtle decrease in AIS length or NaV1.6 density attenuates AP acceleration. Taken together, these findings demonstrate significant structural and functional changes of both intrinsic and extrinsic/synaptic components that are major regulators of AIS activity. The conclusions of this study depart from current thought on mTBI, which has been based primarily on the role of structural disconnection of white matter tracts (Sharp and Ham, 2011; Sharp et al., 2014). Collectively, the novel subcellular and neurophysiologic substrates identified in this study significantly extend our knowledge of neocortical circuit dysfunction following mTBI.

cFPI: Clinical Relevance and Utility for Evaluating Neocortical Circuit Dysfunction

Several features of our cFPI model underscore its clinical relevance and utility for evaluating both DAI and intact neuronal populations in neocortical circuits after mTBI. We used loss of righting reflex in mice as a surrogate for loss of consciousness in humans to assess injury severity, which had a similar duration ranging 3–5 min (Shaw, 2002; Malec et al., 2007; Schrader et al., 2009). While this was our only behavioral assessment, we monitored arterial oxygen saturation, heart rate, RPM and core body temperature in all mice used for structural and functional studies. Specifically, all mice were in physiological homeostasis. Importantly, evaluating these parameters help distinguish our work from most other investigators who do not perform routine physiologic monitoring to exclude secondary insults, which could severely confound the assessment of network disruption via diffuse structural and functional changes.

Capitalizing on restricted neuronal labeling with YFP including the total axonal length, readily traceable within the neocortical gray, allowed the unequivocal identification of mTBI-induced DAI vs. non-DAI/intact populations in both fixed tissue sections and live slices. Specifically, we readily identified intact pyramidal neurons by following their YFP+ axons from the soma of origin to the SCWM interface. Previously, we reported that mTBI induces DAI primarily within the AIS of the YFP+ layer 5 pyramidal neurons (Greer et al., 2013). Additionally, in a former publication we showed that the most commonly used DAI marker (β-amyloid precursor protein) did not colocalize with YFP axons in either the SCWM or corpus callosum (Hånell et al., 2015b). Taken together, these findings strongly support the premise that virtually all YFP+ pyramidal neuron DAI occurs within the neocortical gray. Based on this premise, intact YFP+ pyramidal neurons vs. those undergoing DAI can be reliably identified by examining their axonal segments spanning neocortical layers 5/6 to the SCWM interface.

Pyramidal neurons are the major excitatory component in cortical networks (Fairen et al., 1984; DeFelipe and Fariñas, 1992; Somogyi et al., 1998). Previously we showed that intact YFP+ pyramidal neurons intrinsic and extrinsic/synaptic properties were altered post-mTBI and developed over time (Greer et al., 2012; Hånell et al., 2015a; Sun and Jacobs, 2016). Initially after mTBI, the intrinsic properties of intact

TABLE 1 | Intrinsic action potential (AP) properties of intact yellow fluorescent protein (YFP+) pyramidal neurons 2 days postinjury.

AP Property	Sham	mTBI	t_{25} ratio	*p*-value
Amplitude (mV)	108 ± 4.5	106 ± 4.4	–0.25	0.8039
Half-width (ms)	0.74 ± 0.040	0.81 ± 0.038	1.30	0.2048
Rise Tau (ms)	0.23 ± 0.115	0.44 ± 0.111	1.34	0.1933
Decay Tau (ms)	6.3 ± 1.03	1.2 ± 0.99	–3.6	0.0014

Data summarized as mean ± SEM. Statistics: multilevel analysis of group and animals with five AP nested in each cell. Sham n = 13 cells from three mice (63 AP, 2 missing) and mTBI n = 14 cells from four mice (70 AP total).

pyramidal neurons paralleled that found in the DAI population, suggesting that ion and/or neurotransmitter imbalance had an indiscriminant overriding effect on currents (Greer et al., 2012). However, by 2 days post-mTBI a functional divergence was identified wherein the intact YFP+ pyramidal neuron population showed distinct electrophysiological changes implicating AIS structural-functional alteration. These changes occurred in parallel with overall increased network excitability (Hånell et al., 2015a), implicating loss of inhibition (Isaacson and Scanziani, 2011; Yizhar et al., 2011; Lazarus et al., 2015). Collectively, these previous findings by our laboratory formed the basis of the current study focusing on the effect of mTBI on intrinsic structure and function of the AIS as well as the extrinsic/synaptic GABAergic inputs that control its output (Cobb et al., 1995; Pouille and Scanziani, 2001; Freund, 2003; Klausberger et al., 2003; Klausberger and Somogyi, 2008; Cardin et al., 2009; Atallah et al., 2012; Pouille et al., 2013; Lazarus et al., 2015; Wefelmeyer et al., 2015).

Building upon our previous studies in YFP-H mice, we succeeded in conducting a highly detailed analysis within this specific subset of neocortical layer 5 intact pyramidal neurons showing no evidence of DAI. This was a crucial component of our study since the AIS ion channel distribution differs across neuronal subtypes (Lorincz and Nusser, 2008a), and even within a neuronal subtype (Hu et al., 2009). Additionally, as seen shown in the current study, there is substantial variability in position and length. Further, because DAI affects only a small fraction of neurons within a pyramidal neuron population (Greer et al., 2011) that represent 80% of all neocortical neurons (DeFelipe and Fariñas, 1992), quantification of such heterogeneous population (Molnár and Cheung, 2006) remains an important confounder. Our previous reports underscore this issue, showing that the neocortical pyramidal neuron AIS has a predilection for DAI (Greer et al., 2013). In the current study we show DAI occurring within the AIS severely disrupts ankG and NaV1.6 expression (**Figure 4**). Hence, even a 5% burden of DAI (Greer et al., 2011) causing AIS disruption would substantially contribute to data variability.

Layer 5 Pyramidal Neuron AIS "Tuning"

To the best of our knowledge, this is the first study to account for these issues by examining only intact, Thy1-expressing, layer 5 pyramidal neurons. The important distinction in the current report is that we detected a decrease in AIS length within 2 days after cFPI-induced mTBI specifically within the layer 5 pyramidal neuron populations with no overt structural axonal abnormalities and/or evidence of DAI. For structural studies, we relied on immunofluorescent labeling of ankG and NaV1.6 as surrogate markers of the AIS and associated "trigger zone" at the distal end, respectively (Grubb et al., 2011; Kole and Stuart, 2012). An unexpected finding in the current study that followed from our *a priori* control parameters was that distance from SCWM was a significant covariate of AIS length (**Figure 6I**). Specifically, intact YFP+ pyramidal neurons AIS length from the distal end varied within the ~300 μm span of layer 5 neocortex. Importantly, this pattern was observed in both ankG and NaV1.6 assessments, which yielded virtually the same coefficient of 0.02 in each of the statistical models. This observed variance in AIS structure is consistent with known properties of layer 5 pyramidal neurons which are subdivided into layer 5a and 5b and populated by multiple subtypes characterized by different morphological and electrophysiological features (Chagnac-Amitai et al., 1990; Schubert et al., 2001; Hattox and Nelson, 2007). Additionally, the novel findings in this study are consistent with the "fine-tuning" of the AIS previously described in visual (Gutzmann et al., 2014), as well as auditory circuits (Kuba et al., 2010; Kuba, 2012). Specifically, Gutzmann et al. (2014) showed AIS length from the distal end varies between layer 2/3 and layer 5, representing functionally distinct regions within a neocortical column (Mountcastle, 1979; Somogyi et al., 1998; DeFelipe et al., 2003). Building on this previous work showing inter-laminar differences, in the current report we demonstrate intra-laminar AIS variability, consistent with the presence of layer 5 pyramidal neuron subpopulations (Molnár and Cheung, 2006). While AIS varying as a function of neocortical depth was observed in both 2 days sham-injury and mTBI mice, the lack of interaction between distance from SCWM and experimental groups supports that this finding reflects a novel AIS property with important basic science implications beyond the scope of our injury paradigm.

Uncoupling of ankG and NaV1.6 after mTBI

The current report highlights the importance of measuring both AIS proximal and distal positions with respect to soma of origin. Since structural remodeling can occur at the start and/or end of the AIS (Grubb and Burrone, 2010; Kuba et al., 2010; Evans et al., 2013, 2015), knowledge of AIS position with respect to soma of origin is an important metric. This issue becomes even more critical when factoring proximal and distal AIS subdomains are populated by different ion channel subtypes (Lorincz and Nusser, 2008a; Hu et al., 2009). A key morphological finding in this current study is that while there was no change in ankG position with respect to the soma of origin, the length significantly decreased from the distal end (**Figure 6H**). This finding adds to the repertoire of studies demonstrating AIS length modulation with altered neuronal activity (Evans et al., 2015), sensory circuit development (Kuba et al., 2010; Gutzmann et al., 2014), models of injury (Baalman et al., 2013; Hinman et al., 2013), and also congenital or acquired diseases (Kaphzan et al., 2011; Hamada and Kole, 2015; Clark et al., 2016).

Surprisingly, we did not observe parallel changes in NaV1.6 length at the distal AIS, the site of AP initiation (Stuart et al., 1997; Palmer and Stuart, 2006; Kole et al., 2008; Popovic et al., 2011). To our knowledge, this is the first report that demonstrates ankG remodeling uncoupled from changes in NaV1.6 geometric distribution. Hence, this observation raises the question whether other AIS components may stabilize NaV1.6 in the absence of ankG. For example, the cell adhesion molecule neurofascin-186, which is known to stabilize the AIS (Ratcliffe et al., 2001; Hedstrom et al., 2007; Zonta et al., 2011; Kriebel et al., 2012). Alternatively, a decrease in ankG length could elicit a subtle decrease NaV1.6 density (Hedstrom et al., 2008; Gasser et al., 2012) in the absence of length change. In such a case, a decrease in ankG length from the distal end resulting in NaV1.6 redistribution may be a potential mechanism underlying AIS functional changes discussed below. On the other hand, NaV1.6 activity and/or association with ankG may be modulated biochemically (Garrido et al., 2003; Bréchet et al., 2008; Hund et al., 2010; Evans et al., 2015). Notably, is the potential involvement of calcineurin, a phosphatase that has been implicated in both AIS plasticity (Evans et al., 2013, 2015) and mTBI axonal pathophysiology (Singleton et al., 2001; Marmarou and Povlishock, 2006; Reeves et al., 2007; Campbell et al., 2012). Ultimately, in addition to this studies limitation of a single time point, our morphological analyses were confined to ankG and NaV1.6. Thus, future studies are needed with more time points that target other AIS structural proteins as well as different voltage-gate ion channels modulating AP dynamics.

Evidence for AIS Functional Plasticity

Following our structural studies with electrophysiological assessments revealed further evidence for intact YFP+ pyramidal neuron AIS plasticity after mTBI. While AP waveform was not overtly different after mTBI, we did find a significant change in the decay tau. Interestingly, this suggested potential involvement of potassium channels within the AIS, which have been shown to redistribute after sensory deprivation (Kuba et al., 2015) and modulate AP waveform (Kole et al., 2007). Additionally, we observed that the AP threshold was more depolarized after mTBI. Since NaV1.6 channels set AP threshold (Kole et al., 2008), this provided indirect evidence for intrinsic AIS functional plasticity localized at the distal AIS. Notwithstanding the maintenance of NaV1.6 geometry after mTBI, patch-clamp recordings show AP acceleration is attenuated at the AIS but not the soma. Together, these observations lend further support to the supposition that subtler AIS ion channel redistribution and/or post-translation modification may be operant in the absence of morphological changes. Computer simulations using a realistic model of a layer 5 pyramidal neuron supported this premise. Specifically, decreasing either AIS length by experimentally observed values or NaV1.6 density by the same proportion also decreased AP acceleration, consistent with the data reported by Hallermann et al. (2012) in their characterization of this layer 5 pyramidal neuron model. All together, these data reflect slower NaV1.6 activation specifically at the AIS. Based on these collective findings, we now posit that at 2 days post-mTBI the AIS is in a state of flux, wherein the initial ankG structural remodeling precedes the NaV1.6 geometric redistribution that leads to length reduction.

Diffuse Loss of Perisomatic GABAergic Terminals

Neocortical balance of excitation-inhibition is regulated by PV+ interneurons that are highly interconnected with local pyramidal neurons (Gulyás et al., 1999; Pouille and Scanziani, 2001; Isaacson and Scanziani, 2011; Packer and Yuste, 2011; Hu et al., 2014; Scholl et al., 2015). The proximity of PV+ terminals to the AIS allows for strong inhibitory control over AIS output (Cobb et al., 1995; Klausberger et al., 2003; Freund and Katona, 2007; Atallah et al., 2012; Pouille et al., 2013; Lazarus et al., 2015; Wefelmeyer et al., 2015). Previously, it has been demonstrated that fulminant deafferentation of sensory input can induce AIS structural plasticity associated with altered neuronal excitability (Kuba et al., 2010). In light of the known features of AIS structure-function and that mTBI-induced abnormal network activity is associated with imbalanced excitation-inhibition, we also evaluated extrinsic/synaptic structural changes in concert with our AIS investigations. In the current study, quantitative analysis of layer 5 intact YFP+ pyramidal neuron perisomatic GAD67+ and PV+/GAD67+ puncta revealed a significant decrease in density. While determining the actual functional consequences of this structural finding is beyond the scope of the current study, this parallel observation to our AIS findings provides additional evidence that local neocortical disruption is a consistent feature of mTBI. In future studies, it would be important to determine if such loss of presynaptic GABAergic input elicits postsynaptic AIS shortening to decrease pyramidal neuron excitability to restore network homeostasis after mTBI.

While the mechanism underlying PV+ interneuron terminal loss was not critically addressed in the current study, recently we showed for the first time that locally projecting neocortical GABAergic interneurons undergo DAI (Vascak et al., 2017). Specifically, we showed that the majority of GABAergic DAI is represented by the PV+ interneuron subclass. Importantly, PV+ interneuron DAI manifested shortly after mTBI and occurred primarily in the perisomatic/AIS domain, prior to the initial branch point of their expansive axonal arbor. Since PV+ interneurons target hundreds of postsynaptic pyramidal neurons (Woodruff et al., 2010; Packer and Yuste, 2011; Taniguchi et al., 2013; Scholl et al., 2015; Takács et al., 2015), disconnection prior to the initial branch point results in widespread, diffuse inhibitory terminal loss. In our recent study, widespread PV+ axonal debris fields within 1 day post-mTBI indicated diffuse terminal degeneration. Consistent with PV+ interneuron DAI and anterograde deafferentation of postsynaptic target sites, in an earlier report from our laboratory we showed ultrastructural evidence of diffuse terminal degeneration along the perisomatic domain of healthy pyramidal neurons within layer 5 neocortex within 2 days post-mTBI (Singleton et al., 2002). Together, these findings suggest that the observed loss of PV+ terminals along the perisomatic domain of intact YFP+ pyramidal neurons is likely due to DAI-induced deafferentation of target postsynaptic sites.

CONCLUSION

The AIS is a highly complex and dynamic domain (Hallermann et al., 2012; King et al., 2014; Evans et al., 2015). Intrinsically linked structure-function relationships between scaffolding proteins and ion channels are a crucial for AIS activity (Zhou et al., 1998; Jenkins and Bennett, 2001; Yang et al., 2007). In this way, the neocortical pyramidal neuron AIS is a major determinant of network function and homeostatic plasticity (Grubb et al., 2011; Bender and Trussell, 2012; Kole and Stuart, 2012). This premise has been evaluated in several studies showing AIS disruption associated with multiple disease states involving an imbalance of network function (Kaphzan et al., 2011; Hinman et al., 2013; Hamada and Kole, 2015; Clark et al., 2016). The findings of this study broaden the cerebral landscape affected by mTBI, emphasizing the role of postsynaptic functional disruption of intact neurons. Based on the current data, we posit that AIS plasticity may constitute a compensatory response to mTBI. However, future studies are needed to determine whether AIS structural-functional plasticity is adaptive or maladaptive, which has important implications for restoring excitatory-inhibitory balance in neocortical circuits disrupted by mTBI.

AUTHOR CONTRIBUTIONS

MV, KMJ and JTP contributed to the design of the experiments. MV performed all surgeries and confocal imaging. JS collected all electrophysiological data. Both MV and MB performed statistical data analyses. MV, JS, KMJ and JTP contributed to writing of the manuscript.

FUNDING

This work was funded by National Institutes of Health (NIH) Grant NS077675.

ACKNOWLEDGMENTS

The authors thank Carol Davis, Susan Walker and Jesse Sims for their invaluable technical assistance, Scott Henderson and Frances White for sharing their expertise in confocal microscopy, Jeff Dupree, Anders Hanell, Audrey Lafrenaye, Vishal Patel and Chris Jurgens for their scientific insights.

REFERENCES

Aarts, E., Verhage, M., Veenvliet, J. V., Dolan, C. V., and van der Sluis, S. (2014). A solution to dependency: using multilevel analysis to accommodate nested data. *Nat. Neurosci.* 17, 491–496. doi: 10.1038/nn.3648

Alexander, M. P. (1995). Mild traumatic brain injury: pathophysiology, natural history, and clinical management. *Neurology* 45, 1253–1260. doi: 10.1212/WNL.45.7.1253

Andriessen, T. M. J. C., Jacobs, B., and Vos, P. E. (2010). Clinical characteristics and pathophysiological mechanisms of focal and diffuse traumatic brain injury. *J. Cell. Mol. Med.* 14, 2381–2392. doi: 10.1111/j.1582-4934.2010.01164.x

Antón-Fernández, A., Rubio-Garrido, P., DeFelipe, J., and Muñoz, A. (2015). Selective presence of a giant saccular organelle in the axon initial segment of a subpopulation of layer V pyramidal neurons. *Brain Struct. Funct.* 220, 869–884. doi: 10.1007/s00429-013-0689-1

Atallah, B. V., Bruns, W., Carandini, M., and Scanziani, M. (2012). Parvalbumin-expressing interneurons linearly transform cortical responses to visual stimuli. *Neuron* 73, 159–170. doi: 10.1016/j.neuron.2011.12.013

Baalman, K. L., Cotton, R. J., Rasband, S. N., and Rasband, M. N. (2013). Blast wave exposure impairs memory and decreases axon initial segment length. *J. Neurotrauma* 30, 741–751. doi: 10.1089/neu.2012.2478

Bashir, S., Vernet, M., Yoo, W.-K., Mizrahi, I., Theoret, H., and Pascual-Leone, A. (2012). Changes in cortical plasticity after mild traumatic brain injury. *Restor. Neurol. Neurosci.* 30, 277–282. doi: 10.3233/RNN-2012-110207

Bazarian, J. J., Zhong, J., Blyth, B., Zhu, T., Kavcic, V., and Peterson, D. (2007). Diffusion tensor imaging detects clinically important axonal damage after mild traumatic brain injury: a pilot study. *J. Neurotrauma* 24, 1447–1459. doi: 10.1089/neu.2007.0241

Bender, K. J., and Trussell, L. O. (2012). The physiology of the axon initial segment. *Annu. Rev. Neurosci.* 35, 249–265. doi: 10.1146/annurev-neuro-062111-150339

Bigler, E. D., and Maxwell, W. L. (2012). Neuropathology of mild traumatic brain injury: relationship to neuroimaging findings. *Brain Imaging Behav.* 6, 108–136. doi: 10.1007/s11682-011-9145-0

Bonnelle, V., Leech, R., Kinnunen, K. M., Ham, T. E., Beckmann, C. F., De Boissezon, X., et al. (2011). Default mode network connectivity predicts sustained attention deficits after traumatic brain injury. *J. Neurosci.* 31, 13442–13451. doi: 10.1523/JNEUROSCI.1163-11.2011

Borg, J., Holm, L., Cassidy, J. D., Peloso, P. M., Carroll, L. J., von Holst, H., et al. (2004). Diagnostic procedures in mild traumatic brain injury: results of the WHO collaborating centre task force on mild traumatic brain injury. *J. Rehabil. Med.* 36, 61–75. doi: 10.1080/16501960410023822

Bouix, S., Pasternak, O., Rathi, Y., Pelavin, P. E., Zafonte, R., and Shenton, M. E. (2013). Increased gray matter diffusion anisotropy in patients with persistent post-concussive symptoms following mild traumatic brain injury. *PLoS One* 8:e66205. doi: 10.1371/journal.pone.0066205

Bréchet, A., Fache, M. P., Brachet, A., Ferracci, G., Baude, A., Irondelle, M., et al. (2008). Protein kinase CK2 contributes to the organization of sodium channels in axonal membranes by regulating their interactions with ankyrin G. *J. Cell Biol.* 183, 1101–1114. doi: 10.1083/jcb.200805169

Buffington, S. A., and Rasband, M. N. (2011). The axon initial segment in nervous system disease and injury. *Eur. J. Neurosci.* 34, 1609–1619. doi: 10.1111/j.1460-9568.2011.07875.x

Büki, A., and Povlishock, J. T. (2006). All roads lead to disconnection?—Traumatic axonal injury revisited. *Acta Neurochir. (Wien)* 148, 181–193; discussion 193–194. doi: 10.1007/s00701-005-0674-4

Button, K. S., Ioannidis, J. P. A., Mokrysz, C., Nosek, B. A., Flint, J., Robinson, E. S. J., et al. (2013). Power failure: why small sample size undermines the reliability of neuroscience. *Nat. Rev. Neurosci.* 14, 365–376. doi: 10.1038/nrn3475

Campbell, J. N., Register, D., and Churn, S. B. (2012). Traumatic brain injury causes an FK506-sensitive loss and an overgrowth of dendritic spines in rat forebrain. *J. Neurotrauma* 29, 201–217. doi: 10.1089/neu.2011.1761

Cardin, J. A., Carlén, M., Meletis, K., Knoblich, U., Zhang, F., Deisseroth, K., et al. (2009). Driving fast-spiking cells induces γ rhythm and controls sensory responses. *Nature* 459, 663–667. doi: 10.1038/nature08002

Cassidy, J. D., Carroll, L. J., Peloso, P. M., Borg, J., von Holst, H., Holm, L., et al. (2004). Incidence, risk factors and prevention of mild traumatic brain injury: results of the WHO collaborating centre task force on mild traumatic brain injury. *J. Rehabil. Med.* 36, 28–60. doi: 10.1080/16501960410023732

CDC. (2003). *Report to Congress on Mild Traumatic Brain Injury in the United States: Steps to Prevent a Serious Public Health Problem.* Atlanta, GA: Centers for Disease Control and Prevention.

Cesarovic, N., Nicholls, F., Rettich, A., Kronen, P., Hässig, M., Jirkof, P., et al. (2010). Isoflurane and sevoflurane provide equally effective anaesthesia in laboratory mice. *Lab. Anim.* 44, 329–336. doi: 10.1258/la.2010.009085

Chagnac-Amitai, Y., Luhmann, H. J., and Prince, D. A. (1990). Burst generating and regular spiking layer 5 pyramidal neurons of rat neocortex have different morphological features. *J. Comp. Neurol.* 296, 598–613. doi: 10.1002/cne.902960407

Clark, K. C., Josephson, A., Benusa, S. D., Hartley, R. K., Baer, M., Thummala, S., et al. (2016). Compromised axon initial segment integrity in EAE is preceded by microglial reactivity and contact. *Glia* 64, 1190–1209. doi: 10.1002/glia.22991

Cobb, S. R., Buhl, E. H., Halasy, K., Paulsen, O., and Somogyi, P. (1995). Synchronization of neuronal activity in hippocampus by individual GABAergic interneurons. *Nature* 378, 75–78. doi: 10.1038/378075a0

Cohen, A. S., Pfister, B. J., Schwarzbach, E., Grady, M. S., Goforth, P. B., and Satin, L. S. (2007). Injury-induced alterations in CNS electrophysiology. *Prog. Brain Res.* 161, 143–169. doi: 10.1016/s0079-6123(06)61010-8

Cohen, J. (1988). *Statistical Power Analysis for the Behavioral Sciences.* Hillsdale, NJ: Erlbaum.

Coronado, V. G., Xu, L., Basavaraju, S. V., McGuire, L. C., Wald, M. M., Faul, M. D., et al. (2011). Surveillance for traumatic brain injury-related deaths—United States, 1997–2007. *MMWR Surveill. Summ.* 60, 1–32.

DeFelipe, J., Alonso-Nanclares, L., and Arellano, J. I. (2003). Microstructure of the neocortex: comparative aspects. *J. Neurocytol.* 31, 299–316. doi: 10.1023/A:1024130211265

DeFelipe, J., and Fariñas, I. (1992). The pyramidal neuron of the cerebral cortex: morphological and chemical characteristics of the synaptic inputs. *Prog. Neurobiol.* 39, 563–607. doi: 10.1016/0301-0082(92)90015-7

Dixon, C. E., Lyeth, B. G., Povlishock, J. T., Findling, R. L., Hamm, R. J., Marmarou, A., et al. (1987). A fluid percussion model of experimental brain injury in the rat. *J. Neurosurg.* 67, 110–119. doi: 10.3171/jns.1987.67.1.0110

Douglas, R. J., Koch, C., Mahowald, M., Martin, K. A., and Suarez, H. H. (1995). Recurrent excitation in neocortical circuits. *Science* 269, 981–985. doi: 10.1126/science.7638624

Evans, M. D., Dumitrescu, A. S., Kruijssen, D. L. H., Taylor, S. E., and Grubb, M. S. (2015). Rapid modulation of axon initial segment length influences repetitive spike firing. *Cell Rep.* 13, 1233–1245. doi: 10.1016/j.celrep.2015.09.066

Evans, M. D., Sammons, R. P., Lebron, S., Dumitrescu, A. S., Watkins, T. B. K., Uebele, V. N., et al. (2013). Calcineurin signaling mediates activity-dependent relocation of the axon initial segment. *J. Neurosci.* 33, 6950–6963. doi: 10.1523/JNEUROSCI.0277-13.2013

Ewald, A. J., Werb, Z., and Egeblad, M. (2011). Monitoring of vital signs for long-term survival of mice under anesthesia. *Cold Spring Harb. Protoc.* 2011:pdb.prot5563. doi: 10.1101/pdb.prot5563

Fairen, A., DeFelipe, J., and Regidor, J. (1984). "Nonpyramidal neurons: general account," in *Cellular Components of the Cerebral Cortex*, eds A. Peters and E. G. Jones (New York, NY: Plenum Press), 201–253.

Feng, G., Mellor, R. H., Bernstein, M., Keller-Peck, C., Nguyen, Q. T., Wallace, M., et al. (2000). Imaging neuronal subsets in transgenic mice expressing multiple spectral variants of GFP. *Neuron* 28, 41–51. doi: 10.1016/s0896-6273(00)00084-2

Fish, K. N., Sweet, R. A., and Lewis, D. A. (2011). Differential distribution of proteins regulating GABA synthesis and reuptake in axon boutons of subpopulations of cortical interneurons. *Cereb. Cortex* 21, 2450–2460. doi: 10.1093/cercor/bhr007

Freund, T. F. (2003). Interneuron Diversity series: rhythm and mood in perisomatic inhibition. *Trends Neurosci.* 26, 489–495. doi: 10.1016/s0166-2236(03)00227-3

Freund, T. F., and Katona, I. (2007). Perisomatic inhibition. *Neuron* 56, 33–42. doi: 10.1016/j.neuron.2007.09.012

Galbraith, S., Daniel, J. A., and Vissel, B. (2010). A study of clustered data and approaches to its analysis. *J. Neurosci.* 30, 10601–10608. doi: 10.1523/JNEUROSCI.0362-10.2010

Garrido, J. J., Giraud, P., Carlier, E., Fernandes, F., Moussif, A., Fache, M.-P., et al. (2003). A targeting motif involved in sodium channel clustering at the axonal initial segment. *Science* 300, 2091–2094. doi: 10.1126/science.1085167

Gasser, A., Ho, T. S.-Y., Cheng, X., Chang, K.-J., Waxman, S. G., Rasband, M. N., et al. (2012). An ankyrinG-binding motif is necessary and sufficient for targeting Nav1.6 sodium channels to axon initial segments and nodes of Ranvier. *J. Neurosci.* 32, 7232–7243. doi: 10.1523/JNEUROSCI.5434-11.2012

Greer, J. E., Hånell, A., McGinn, M. J., and Povlishock, J. T. (2013). Mild traumatic brain injury in the mouse induces axotomy primarily within the axon initial segment. *Acta Neuropathol.* 126, 59–74. doi: 10.1007/s00401-013-1119-4

Greer, J. E., McGinn, M. J., and Povlishock, J. T. (2011). Diffuse traumatic axonal injury in the mouse induces atrophy, c-Jun activation, and axonal outgrowth in the axotomized neuronal population. *J. Neurosci.* 31, 5089–5105. doi: 10.1523/JNEUROSCI.5103-10.2011

Greer, J. E., Povlishock, J. T., and Jacobs, K. M. (2012). Electrophysiological abnormalities in both axotomized and nonaxotomized pyramidal neurons following mild traumatic brain injury. *J. Neurosci.* 32, 6682–6687. doi: 10.1523/JNEUROSCI.0881-12.2012

Grimm, K., Lamont, L., Tranquilli, W., Greene, S., and Roberston, S. (2015). *Veterinary Anesthesia and Analgesia.* 5th Edn. Ames, IA: John Wiley and Sons.

Grubb, M. S., and Burrone, J. (2010). Activity-dependent relocation of the axon initial segment fine-tunes neuronal excitability. *Nature* 465, 1070–1074. doi: 10.1038/nature09160

Grubb, M. S., Shu, Y., Kuba, H., Rasband, M. N., Wimmer, V. C., and Bender, K. J. (2011). Short- and long-term plasticity at the axon initial segment. *J. Neurosci.* 31, 16049–16055. doi: 10.1523/JNEUROSCI.4064-11.2011

Gulyás, A. I., Megías, M., Emri, Z., and Freund, T. F. (1999). Total number and ratio of excitatory and inhibitory synapses converging onto single interneurons of different types in the CA1 area of the rat hippocampus. *J. Neurosci.* 19, 10082–10097.

Gutzmann, A., Ergül, N., Grossmann, R., Schultz, C., Wahle, P., and Engelhardt, M. (2014). A period of structural plasticity at the axon initial segment in developing visual cortex. *Front. Neuroanat.* 8:11. doi: 10.3389/fnana.2014.00011

Hallermann, S., de Kock, C. P. J., Stuart, G. J., and Kole, M. H. P. (2012). State and location dependence of action potential metabolic cost in cortical pyramidal neurons. *Nat. Neurosci.* 15, 1007–1014. doi: 10.1038/nn.3132

Hamada, M. S., Goethals, S., de Vries, S. I., Brette, R., and Kole, M. H. P. (2016). Covariation of axon initial segment location and dendritic tree normalizes the somatic action potential. *Proc. Natl. Acad. Sci. U S A* 113, 14841–14846. doi: 10.1073/pnas.1607548113

Hamada, M. S., and Kole, M. H. P. (2015). Myelin loss and axonal ion channel adaptations associated with gray matter neuronal hyperexcitability. *J. Neurosci.* 35, 7272–7286. doi: 10.1523/JNEUROSCI.4747-14.2015

Hånell, A., Greer, J. E., and Jacobs, K. M. (2015a). Increased network excitability due to altered synaptic inputs to neocortical layer V intact and axotomized pyramidal neurons after mild traumatic brain injury. *J. Neurotrauma* 32, 1590–1598. doi: 10.1089/neu.2014.3592

Hånell, A., Greer, J. E., McGinn, M. J., and Povlishock, J. T. (2015b). Traumatic brain injury-induced axonal phenotypes react differently to treatment. *Acta Neuropathol.* 129, 317–332. doi: 10.1007/s00401-014-1376-x

Hasenstaub, A., Shu, Y., Haider, B., Kraushaar, U., Duque, A., and McCormick, D. A. (2005). Inhibitory postsynaptic potentials carry synchronized frequency information in active cortical networks. *Neuron* 47, 423–435. doi: 10.1016/j.neuron.2005.06.016

Hattox, A. M., and Nelson, S. B. (2007). Layer V neurons in mouse cortex projecting to different targets have distinct physiological properties. *J. Neurophysiol.* 98, 3330–3340. doi: 10.1152/jn.00397.2007

Hedstrom, K. L., Ogawa, Y., and Rasband, M. N. (2008). AnkyrinG is required for maintenance of the axon initial segment and neuronal polarity. *J. Cell Biol.* 183, 635–640. doi: 10.1083/jcb.200806112

Hedstrom, K. L., Xu, X., Ogawa, Y., Frischknecht, R., Seidenbecher, C. I., Shrager, P., et al. (2007). Neurofascin assembles a specialized extracellular matrix at the axon initial segment. *J. Cell Biol.* 178, 875–886. doi: 10.1083/jcb.200705119

Hinman, J. D., Rasband, M. N., and Carmichael, S. T. (2013). Remodeling of the axon initial segment after focal cortical and white matter stroke. *Stroke* 44, 182–189. doi: 10.1161/STROKEAHA.112.668749

Hoge, C. W., McGurk, D., Thomas, J. L., Cox, A. L., Engel, C. C., and Castro, C. A. (2008). Mild traumatic brain injury in U.S. Soldiers returning from Iraq. *N. Engl. J. Med.* 358, 453–463. doi: 10.1056/NEJMoa072972

Hu, H., Gan, J., and Jonas, P. (2014). Interneurons. Fast-spiking, parvalbumin$^+$ GABAergic interneurons: from cellular design to microcircuit function. *Science* 345:1255263. doi: 10.1126/science.1255263

Hu, W., Tian, C., Li, T., Yang, M., Hou, H., and Shu, Y. (2009). Distinct contributions of $Na_v1.6$ and $Na_v1.2$ in action potential initiation and backpropagation. *Nat. Neurosci.* 12, 996–1002. doi: 10.1038/nn.2359

Huang, M.-X., Harrington, D. L., Robb Swan, A., Angeles Quinto, A., Nichols, S., Drake, A., et al. (2017). Resting-state magnetoencephalography reveals different patterns of aberrant functional connectivity in combat-related mild traumatic brain injury. *J. Neurotrauma* 34, 1412–1426. doi: 10.1089/neu.2016.4581

Hund, T. J., Koval, O. M., Li, J., Wright, P. J., Qian, L., Snyder, J. S., et al. (2010). A β_{IV}-spectrin/CaMKII signaling complex is essential for membrane excitability in mice. *J. Clin. Invest.* 120, 3508–3519. doi: 10.1172/JCI43621

Ilvesmäki, T., Luoto, T. M., Hakulinen, U., Brander, A., Ryymin, P., Eskola, H., et al. (2014). Acute mild traumatic brain injury is not associated with white matter change on diffusion tensor imaging. *Brain* 137, 1876–1882. doi: 10.1093/brain/awu095

Isaacson, J. S., and Scanziani, M. (2011). How inhibition shapes cortical activity. *Neuron* 72, 231–243. doi: 10.1016/j.neuron.2011.09.027

Jacob, V., Petreanu, L., Wright, N., Svoboda, K., and Fox, K. (2012). Regular spiking and intrinsic bursting pyramidal cells show orthogonal forms of experience-dependent plasticity in layer V of barrel cortex. *Neuron* 73, 391–404. doi: 10.1016/j.neuron.2011.11.034

Jenkins, S. M., and Bennett, V. (2001). Ankyrin-G coordinates assembly of the spectrin-based membrane skeleton, voltage-gated sodium channels, and L1 CAMs at Purkinje neuron initial segments. *J. Cell Biol.* 155, 739–746. doi: 10.1083/jcb.200109026

Jiao, Y., Sun, Z., Lee, T., Fusco, F. R., Kimble, T. D., Meade, C. A., et al. (1999). A simple and sensitive antigen retrieval method for free-floating and slide-mounted tissue sections. *J. Neurosci. Methods* 93, 149–162. doi: 10.1016/s0165-0270(99)00142-9

Johnson, V. E., Stewart, W., and Smith, D. H. (2013). Axonal pathology in traumatic brain injury. *Exp. Neurol.* 246, 35–43. doi: 10.1016/j.expneurol.2012.01.013

Kaphzan, H., Buffington, S. A., Jung, J. I., Rasband, M. N., and Klann, E. (2011). Alterations in intrinsic membrane properties and the axon initial segment in a mouse model of Angelman syndrome. *J. Neurosci.* 31, 17637–17648. doi: 10.1523/JNEUROSCI.4162-11.2011

Khaliq, Z. M., and Raman, I. M. (2006). Relative contributions of axonal and somatic Na channels to action potential initiation in cerebellar Purkinje neurons. *J. Neurosci.* 26, 1935–1944. doi: 10.1523/JNEUROSCI.4664-05.2006

King, A. N., Manning, C. F., and Trimmer, J. S. (2014). A unique ion channel clustering domain on the axon initial segment of mammalian neurons. *J. Comp. Neurol.* 522, 2594–2608. doi: 10.1002/cne.23551

Kinnunen, K. M., Greenwood, R., Powell, J. H., Leech, R., Hawkins, P. C., Bonnelle, V., et al. (2011). White matter damage and cognitive impairment after traumatic brain injury. *Brain* 134, 449–463. doi: 10.1093/brain/awq347

Klausberger, T., and Somogyi, P. (2008). Neuronal diversity and temporal dynamics: the unity of hippocampal circuit operations. *Science* 321, 53–57. doi: 10.1126/science.1149381

Klausberger, T., Magill, P. J., Márton, L. F., Roberts, J. D. B., Cobden, P. M., Buzsáki, G., et al. (2003). Brain-state- and cell-type-specific firing of hippocampal interneurons *in vivo*. *Nature* 421, 844–848. doi: 10.1038/nature01374

Kole, M. H. P., Ilschner, S. U., Kampa, B. M., Williams, S. R., Ruben, P. C., and Stuart, G. J. (2008). Action potential generation requires a high sodium channel density in the axon initial segment. *Nat. Neurosci.* 11, 178–186. doi: 10.1038/nn2040

Kole, M. H. P., Letzkus, J. J., and Stuart, G. J. (2007). Axon initial segment Kv1 channels control axonal action potential waveform and synaptic efficacy. *Neuron* 55, 633–647. doi: 10.1016/j.neuron.2007.07.031

Kole, M. H. P., and Stuart, G. J. (2012). Signal processing in the axon initial segment. *Neuron* 73, 235–247. doi: 10.1016/j.neuron.2012.01.007

Kriebel, M., Wuchter, J., Trinks, S., and Volkmer, H. (2012). Neurofascin: a switch between neuronal plasticity and stability. *Int. J. Biochem. Cell Biol.* 44, 694–697. doi: 10.1016/j.biocel.2012.01.012

Kuba, H. (2012). Structural tuning and plasticity of the axon initial segment in auditory neurons. *J. Physiol.* 590, 5571–5579. doi: 10.1113/jphysiol.2012.237305

Kuba, H., Adachi, R., and Ohmori, H. (2014). Activity-dependent and activity-independent development of the axon initial segment. *J. Neurosci.* 34, 3443–3453. doi: 10.1523/JNEUROSCI.4357-13.2014

Kuba, H., Oichi, Y., and Ohmori, H. (2010). Presynaptic activity regulates Na^+ channel distribution at the axon initial segment. *Nature* 465, 1075–1078. doi: 10.1038/nature09087

Kuba, H., Yamada, R., Ishiguro, G., and Adachi, R. (2015). Redistribution of Kv1 and Kv7 enhances neuronal excitability during structural axon initial segment plasticity. *Nat. Commun.* 6:8815. doi: 10.1038/ncomms9815

Langlois, J. A., Rutland-Brown, W., and Wald, M. M. (2006). The epidemiology and impact of traumatic brain injury: a brief overview. *J. Head Trauma Rehabil.* 21, 375–378. doi: 10.1097/00001199-200609000-00001

Lazarus, M. S., Krishnan, K., and Huang, Z. J. (2015). GAD67 deficiency in parvalbumin interneurons produces deficits in inhibitory transmission and network disinhibition in mouse prefrontal cortex. *Cereb. Cortex* 25, 1290–1296. doi: 10.1093/cercor/bht322

Le Bé, J.-V., Silberberg, G., Wang, Y., and Markram, H. (2007). Morphological, electrophysiological, and synaptic properties of corticocallosal pyramidal cells in the neonatal rat neocortex. *Cereb. Cortex* 17, 2204–2213. doi: 10.1093/cercor/bhl127

Lichtman, J. W., and Conchello, J.-A. (2005). Fluorescence microscopy. *Nat. Methods* 2, 910–919. doi: 10.1038/nmeth817

Ling, J. M., Klimaj, S., Toulouse, T., and Mayer, A. R. (2013). A prospective study of gray matter abnormalities in mild traumatic brain injury. *Neurology* 81, 2121–2127. doi: 10.1212/01.WNL.0000437302.36064.b1

Lorincz, A., and Nusser, Z. (2008a). Cell-type-dependent molecular composition of the axon initial segment. *J. Neurosci.* 28, 14329–14340. doi: 10.1523/JNEUROSCI.4833-08.2008

Lorincz, A., and Nusser, Z. (2008b). Specificity of immunoreactions: the importance of testing specificity in each method. *J. Neurosci.* 28, 9083–9086. doi: 10.1523/JNEUROSCI.2494-08.2008

Maas, C. J. M., and Hox, J. J. (2004). Robustness issues in multilevel regression analysis. *Stat. Neerl.* 58, 127–137. doi: 10.1046/j.0039-0402.2003.00252.x

Mac Donald, C. L., Johnson, A. M., Cooper, D., Nelson, E. C., Werner, N. J., Shimony, J. S., et al. (2011). Detection of blast-related traumatic brain injury in U.S. military personnel. *N. Engl. J. Med.* 364, 2091–2100. doi: 10.1056/NEJMoa1008069

Malec, J. F., Brown, A. W., Leibson, C. L., Flaada, J. T., Mandrekar, J. N., Diehl, N. N., et al. (2007). The mayo classification system for traumatic brain injury severity. *J. Neurotrauma* 24, 1417–1424. doi: 10.1089/neu.2006.0245

Manning, C. F., Bundros, A. M., and Trimmer, J. S. (2012). Benefits and pitfalls of secondary antibodies: why choosing the right secondary is of primary importance. *PLoS One* 7:e38313. doi: 10.1371/journal.pone.0038313

Mannix, R., Meehan, W. P. III, and Pascual-Leone, A. (2016). Sports-related concussions—media, science and policy. *Nat. Rev. Neurol.* 12, 486–490. doi: 10.1038/nrneurol.2016.99

Marmarou, C. R., and Povlishock, J. T. (2006). Administration of the immunophilin ligand FK506 differentially attenuates neurofilament compaction and impaired axonal transport in injured axons following diffuse traumatic brain injury. *Exp. Neurol.* 197, 353–362. doi: 10.1016/j.expneurol.2005.10.003

Mayer, A. R., Ling, J., Mannell, M. V., Gasparovic, C., Phillips, J. P., Doezema, D., et al. (2010). A prospective diffusion tensor imaging study in mild traumatic brain injury. *Neurology* 74, 643–650. doi: 10.1212/WNL.0b013e3181d0ccdd

Mayer, A. R., Mannell, M. V., Ling, J., Gasparovic, C., and Yeo, R. A. (2011). Functional connectivity in mild traumatic brain injury. *Hum. Brain Mapp.* 32, 1825–1835. doi: 10.1002/hbm.21151

Meeks, J. P., and Mennerick, S. (2007). Action potential initiation and propagation in CA3 pyramidal axons. *J. Neurophysiol.* 97, 3460–3472. doi: 10.1152/jn.01288.2006

Mesulam, M. M. (1990). Large-scale neurocognitive networks and distributed processing for attention, language, and memory. *Ann. Neurol.* 28, 597–613. doi: 10.1002/ana.410280502

Mittl, R. L., Grossman, R. I., Hiehle, J. F., Hurst, R. W., Kauder, D. R., Gennarelli, T. A., et al. (1994). Prevalence of MR evidence of diffuse axonal injury in patients with mild head injury and normal head CT findings. *Am. J. Neuroradiol.* 15, 1583–1589.

Molnár, Z., and Cheung, A. F. P. (2006). Towards the classification of subpopulations of layer V pyramidal projection neurons. *Neurosci. Res.* 55, 105–115. doi: 10.1016/j.neures.2006.02.008

Morehead, M., Bartus, R. T., Dean, R. L., Miotke, J. A., Murphy, S., Sall, J., et al. (1994). Histopathologic consequences of moderate concussion in an animal model: correlations with duration of unconsciousness. *J. Neurotrauma* 11, 657–667. doi: 10.1089/neu.1994.11.657

Mountcastle, V. (1979). "An organizing principle for cerebral function: the unit module and the distributed system," in *The Neurosciences, Fourth Study Program*, eds F. Schmidt and F. Worden (Cambridge, MA: MIT Press), 21–42.

Newcombe, V. F. J., Outtrim, J. G., Chatfield, D. A., Manktelow, A., Hutchinson, P. J., Coles, J. P., et al. (2011). Parcellating the neuroanatomical basis of impaired decision-making in traumatic brain injury. *Brain* 134, 759–768. doi: 10.1093/brain/awq388

Nieuwenhuis, S., Forstmann, B. U., and Wagenmakers, E.-J. (2011). Erroneous analyses of interactions in neuroscience: a problem of significance. *Nat. Neurosci.* 14, 1105–1107. doi: 10.1038/nn.2886

Packer, A. M., and Yuste, R. (2011). Dense, unspecific connectivity of neocortical parvalbumin-positive interneurons: a canonical microcircuit for inhibition? *J. Neurosci.* 31, 13260–13271. doi: 10.1523/JNEUROSCI.3131-11.2011

Palacios, E. M., Yuh, E. L., Chang, Y.-S., Yue, J. K., Schnyer, D. M., Okonkwo, D. O., et al. (2017). Resting-state functional connectivity alterations associated with six-month outcomes in mild traumatic brain injury. *J. Neurotrauma* 34, 1546–1557. doi: 10.1089/neu.2016.4752

Palmer, L. M., and Stuart, G. J. (2006). Site of action potential initiation in layer 5 pyramidal neurons. *J. Neurosci.* 26, 1854–1863. doi: 10.1523/JNEUROSCI.4812-05.2006

Popovic, M. A., Foust, A. J., McCormick, D. A., and Zecevic, D. (2011). The spatio-temporal characteristics of action potential initiation in layer 5 pyramidal neurons: a voltage imaging study. *J. Physiol.* 589, 4167–4187. doi: 10.1113/jphysiol.2011.209015

Pouille, F., and Scanziani, M. (2001). Enforcement of temporal fidelity in pyramidal cells by somatic feed-forward inhibition. *Science* 293, 1159–1163. doi: 10.1126/science.1060342

Pouille, F., Watkinson, O., Scanziani, M., and Trevelyan, A. J. (2013). The contribution of synaptic location to inhibitory gain control in pyramidal cells. *Physiol. Rep.* 1:e00067. doi: 10.1002/phy2.67

Povlishock, J. T., and Katz, D. I. (2005). Update of neuropathology and neurological recovery after traumatic brain injury. *J. Head Trauma Rehabil.* 20, 76–94. doi: 10.1097/00001199-200501000-00008

Raichle, M. E. (2010). Two views of brain function. *Trends Cogn. Sci.* 14, 180–190. doi: 10.1016/j.tics.2010.01.008

Ratcliffe, C. F., Westenbroek, R. E., Curtis, R., and Catterall, W. A. (2001). Sodium channel β-1 and β-3 subunits associate with neurofascin through their extracellular immunoglobulin-like domain. *J. Cell Biol.* 154, 427–434. doi: 10.1083/jcb.200102086

Reeves, T. M., Phillips, L. L., Lee, N. N., and Povlishock, J. T. (2007). Preferential neuroprotective effect of tacrolimus (FK506) on unmyelinated axons following traumatic brain injury. *Brain Res.* 1154, 225–236. doi: 10.1016/j.brainres.2007.04.002

Saatman, K. E., Duhaime, A.-C., Bullock, R., Maas, A. I. R., Valadka, A., and Manley, G. T. (2008). Classification of traumatic brain injury for targeted therapies. *J. Neurotrauma* 25, 719–738. doi: 10.1089/neu.2008.0586

Salmond, C. H., Menon, D. K., Chatfield, D. A., Williams, G. B., Pena, A., Sahakian, B. J., et al. (2006). Diffusion tensor imaging in chronic head injury survivors: correlations with learning and memory indices. *Neuroimage* 29, 117–124. doi: 10.1016/j.neuroimage.2005.07.012

Scholl, B., Pattadkal, J. J., Dilly, G. A., Priebe, N. J., and Zemelman, B. V. (2015). Local integration accounts for weak selectivity of mouse neocortical parvalbumin interneurons. *Neuron* 87, 424–436. doi: 10.1016/j.neuron.2015.06.030

Schrader, H., Mickeviciene, D., Gleizniene, R., Jakstiene, S., Surkiene, D., Stovner, L. J., et al. (2009). Magnetic resonance imaging after most common form of concussion. *BMC Med. Imaging* 9:11. doi: 10.1186/1471-2342-9-11

Schubert, D., Kötter, R., Luhmann, H. J., and Staiger, J. F. (2006). Morphology, electrophysiology and functional input connectivity of pyramidal neurons characterizes a genuine layer va in the primary somatosensory cortex. *Cereb. Cortex* 16, 223–236. doi: 10.1093/cercor/bhi100

Schubert, D., Staiger, J. F., Cho, N., Kötter, R., Zilles, K., and Luhmann, H. J. (2001). Layer-specific intracolumnar and transcolumnar functional connectivity of layer V pyramidal cells in rat barrel cortex. *J. Neurosci.* 21, 3580–3592.

Sharp, D. J., Beckmann, C. F., Greenwood, R., Kinnunen, K. M., Bonnelle, V., De Boissezon, X., et al. (2011). Default mode network functional and structural connectivity after traumatic brain injury. *Brain* 134, 2233–2247. doi: 10.1093/brain/awr175

Sharp, D. J., and Ham, T. E. (2011). Investigating white matter injury after mild traumatic brain injury. *Curr. Opin. Neurol.* 24, 558–563. doi: 10.1097/WCO.0b013e32834cd523

Sharp, D. J., Scott, G., and Leech, R. (2014). Network dysfunction after traumatic brain injury. *Nat. Rev. Neurol.* 10, 156–166. doi: 10.1038/nrneurol.2014.15

Shaw, N. A. (2002). The neurophysiology of concussion. *Prog. Neurobiol.* 67, 281–344. doi: 10.1016/s0301-0082(02)00018-7

Shultz, S. R., McDonald, S. J., Vonder Haar, C., Meconi, A., Vink, R., van Donkelaar, P., et al. (2016). The potential for animal models to provide insight into mild traumatic brain injury: translational challenges and strategies. *Neurosci. Biobehav. Rev.* doi: 10.1016/j.neubiorev.2016.09.014 [Epub ahead of print].

Singleton, R. H., Stone, J. R., Okonkwo, D. O., Pellicane, A. J., and Povlishock, J. T. (2001). The immunophilin ligand FK506 attenuates axonal injury in an impact-acceleration model of traumatic brain injury. *J. Neurotrauma* 18, 607–614. doi: 10.1089/089771501750291846

Singleton, R. H., Zhu, J., Stone, J. R., and Povlishock, J. T. (2002). Traumatically induced axotomy adjacent to the soma does not result in acute neuronal death. *J. Neurosci.* 22, 791–802.

Snijders, T. A. B., and Bosker, R. J. (1993). Standard errors and sample sizes for two-level research. *J. Educ. Stat.* 18, 237–259. doi: 10.3102/10769986018003237

Somogyi, P., Tamás, G., Lujan, R., and Buhl, E. H. (1998). Salient features of synaptic organisation in the cerebral cortex. *Brain Res. Rev.* 26, 113–135.

Sponheim, S. R., McGuire, K. A., Kang, S. S., Davenport, N. D., Aviyente, S., Bernat, E. M., et al. (2011). Evidence of disrupted functional connectivity in the brain after combat-related blast injury. *Neuroimage* 54, S21–S29. doi: 10.1016/j.neuroimage.2010.09.007

Stuart, G., Schiller, J., and Sakmann, B. (1997). Action potential initiation and propagation in rat neocortical pyramidal neurons. *J. Physiol.* 505, 617–632. doi: 10.1111/j.1469-7793.1997.617ba.x

Styrke, J., Stålnacke, B.-M., Sojka, P., and Björnstig, U. (2007). Traumatic brain injuries in a well-defined population: epidemiological aspects and severity. *J. Neurotrauma* 24, 1425–1436. doi: 10.1089/neu.2007.0266

Sun, J., and Jacobs, K. M. (2016). Knockout of cyclophilin-d provides partial amelioration of intrinsic and synaptic properties altered by mild traumatic brain injury. *Front. Syst. Neurosci.* 10:63. doi: 10.3389/fnsys.2016.00063

Takács, V. T., Szonyi, A., Freund, T. F., Nyiri, G., and Gulyás, A. I. (2015). Quantitative ultrastructural analysis of basket and axo-axonic cell terminals in the mouse hippocampus. *Brain Struct. Funct.* 220, 919–940. doi: 10.1007/s00429-013-0692-6

Taniguchi, H., Lu, J., and Huang, Z. J. (2013). The spatial and temporal origin of chandelier cells in mouse neocortex. *Science* 339, 70–74. doi: 10.1126/science.1227622

Thome, C., Kelly, T., Yanez, A., Schultz, C., Engelhardt, M., Cambridge, S. B., et al. (2014). Axon-carrying dendrites convey privileged synaptic input in hippocampal neurons. *Neuron* 83, 1418–1430. doi: 10.1016/j.neuron.2014.08.013

Thurman, D. J., Alverson, C., Dunn, K. A., Guerrero, J., and Sniezek, J. E. (1999). Traumatic brain injury in the united states: a public health perspective. *J. Head Trauma Rehabil.* 14, 602–615. doi: 10.1097/00001199-199912000-00009

Tremblay, S., de Beaumont, L., Lassonde, M., and Théoret, H. (2011). Evidence for the specificity of intracortical inhibitory dysfunction in asymptomatic concussed athletes. *J. Neurotrauma* 28, 493–502. doi: 10.1089/neu.2010.1615

Varela, F., Lachaux, J. P., Rodriguez, E., and Martinerie, J. (2001). The brainweb: phase synchronization and large-scale integration. *Nat. Rev. Neurosci.* 2, 229–239. doi: 10.1038/35067550

Vascak, M., Jin, X., Jacobs, K. M., and Povlishock, J. T. (2017). Mild traumatic brain injury induces structural and functional disconnection of local neocortical inhibitory networks via parvalbumin interneuron diffuse axonal injury. *Cereb. Cortex* 4, 1–20. doi: 10.1093/cercor/bhx058

Wäljas, M., Lange, R. T., Hakulinen, U., Huhtala, H., Dastidar, P., Hartikainen, K., et al. (2014). Biopsychosocial outcome after uncomplicated mild traumatic brain injury. *J. Neurotrauma* 31, 108–124. doi: 10.1089/neu.2013.2941

Walsh, J. E. (1947). Concerning the effect of intraclass correlation on certain significance tests. *Ann. Math. Stat.* 18, 88–96. doi: 10.1214/aoms/1177730495

Wefelmeyer, W., Cattaert, D., and Burrone, J. (2015). Activity-dependent mismatch between axo-axonic synapses and the axon initial segment controls neuronal output. *Proc. Natl. Acad. Sci. U S A* 112, 9757–9762. doi: 10.1073/pnas.1502902112

Wolf, J. A., and Koch, P. F. (2016). Disruption of network synchrony and cognitive dysfunction after traumatic brain injury. *Front. Syst. Neurosci.* 10:43. doi: 10.3389/fnsys.2016.00043

Woodruff, A. R., Anderson, S. A., and Yuste, R. (2010). The enigmatic function of chandelier cells. *Front. Neurosci.* 4:201. doi: 10.3389/fnins.2010.00201

Yang, Y., Ogawa, Y., Hedstrom, K. L., and Rasband, M. N. (2007). βIV spectrin is recruited to axon initial segments and nodes of Ranvier by ankyrinG. *J. Cell Biol.* 176, 509–519. doi: 10.1083/jcb.200610128

Yizhar, O., Fenno, L. E., Prigge, M., Schneider, F., Davidson, T. J., O'Shea, D. J., et al. (2011). Neocortical excitation/inhibition balance in information processing and social dysfunction. *Nature* 477, 171–178. doi: 10.1038/nature10360

Yuh, E. L., Mukherjee, P., Lingsma, H. F., Yue, J. K., Ferguson, A. R., Gordon, W. A., et al. (2013). Magnetic resonance imaging improves 3-month outcome prediction in mild traumatic brain injury. *Ann. Neurol.* 73, 224–235. doi: 10.1002/ana.23783

Zhang, K., Johnson, B., Pennell, D., Ray, W., Sebastianelli, W., and Slobounov, S. (2010). Are functional deficits in concussed individuals consistent with white matter structural alterations: combined FMRI and DTI study. *Exp. Brain Res.* 204, 57–70. doi: 10.1007/s00221-010-2294-3

Zhang, D., and Raichle, M. E. (2010). Disease and the brain's dark energy. *Nat. Rev. Neurol.* 6, 15–28. doi: 10.1038/nrneurol.2009.198

Zhou, D., Lambert, S., Malen, P. L., Carpenter, S., Boland, L. M., and Bennett, V. (1998). Ankyrin$_G$ is required for clustering of voltage-gated Na channels at axon initial segments and for normal action potential firing. *J. Cell Biol.* 143, 1295–1304. doi: 10.1083/jcb.143.5.1295

Zonta, B., Desmazieres, A., Rinaldi, A., Tait, S., Sherman, D. L., Nolan, M. F., et al. (2011). A critical role for Neurofascin in regulating action potential initiation through maintenance of the axon initial segment. *Neuron* 69, 945–956. doi: 10.1016/j.neuron.2011.02.021

Conflict of Interest Statement: The authors declare that the research was conducted in the absence of any commercial or financial relationships that could be construed as a potential conflict of interest.

frontiers
in Cellular Neuroscience

MINI REVIEW
published: 22 December 2016
doi: 10.3389/fncel.2016.00293

Early Degeneration of Both Dopaminergic and Serotonergic Axons – A Common Mechanism in Parkinson's Disease

Janina Grosch, Jürgen Winkler and Zacharias Kohl*

Department of Molecular Neurology, Friedrich-Alexander University Erlangen-Nürnberg, Erlangen, Germany

Motor symptoms in Parkinson's disease (PD) are tightly linked to the degeneration of substantia nigra dopaminergic neurons and their projections into the striatum. Moreover, a broad range of non-motor symptoms like anxiety and depression frequently occur in PD, most likely related to the loss of serotonergic neurons and their projections into corresponding target regions. Strikingly, nigral dopaminergic neurons and raphe serotonergic neurons are severely affected in PD showing characteristic hallmarks of PD neuropathology, in particular alpha-synuclein containing Lewy bodies and Lewy neurites. So far, the initial events underlying neurodegenerative processes in PD are not well understood. Several observations, however, indicate that neurites and synapses of diseased neurons may be the first subcellular compartments compromised by alpha-synuclein associated pathology. In particular axonal pathology and deficits in axonal transport may be leading to the onset of synucleinopathies such as PD. This review will highlight current findings derived from imaging and neuropathological studies in PD patients, as well as cellular and animal PD models, which define the initial underlying structural and molecular events within dopaminergic and serotonergic circuits leading to the 'dying back' degeneration of axonal projections in PD.

Keywords: Parkinson's disease, axon degeneration, dying back, synaptic loss, dopamine, 5-HT

Edited by:
Maren Engelhardt,
Heidelberg University, Germany

Reviewed by:
Mohamed Jaber,
University of Poitiers, France
Daniella Rylander Ottosson,
Lund University, Sweden

****Correspondence:***
Zacharias Kohl
zacharias.kohl@uk-erlangen.de

Received: *31 October 2016*
Accepted: *08 December 2016*
Published: *22 December 2016*

Citation:
Grosch J, Winkler J and Kohl Z (2016) Early Degeneration of Both Dopaminergic and Serotonergic Axons – A Common Mechanism in Parkinson's Disease. Front. Cell. Neurosci. 10:293. doi: 10.3389/fncel.2016.00293

INTRODUCTION

Parkinson's disease (PD) represents the second most common neurodegenerative disorder, affecting up to ten million people worldwide (de Lau and Breteler, 2006), with a predicted increase of more than twofold by 2030 (Dorsey et al., 2007). PD patients show progressive motor symptoms such as bradykinesia, rigidity, and resting tremor. Moreover, PD is accompanied by a broad range of non-motor symptoms (NMS), including cognitive deficits, autonomic dysfunctions, and mood disorders (Marras and Chaudhuri, 2016). While the etiology of PD still remains unclear, the aggregation of the presynaptic protein alpha-synuclein, either within Lewy bodies or Lewy neurites of susceptible neurons is of ultimate diagnostic value (Dickson et al., 2009). The other major neuropathological hallmark of PD is the degeneration and subsequent loss of dopaminergic neurons in the substantia nigra (SN) leading to prototypic motor deficits (Greffard et al., 2006). Interestingly, Lewy pathology was also described in numerous other neuronal subpopulations in distinct brain regions, most likely occurring even prior to dopaminergic SN neurons, e.g., in the medulla oblongata, olfactory bulb, and pontine tegmentum (Braak et al., 2003). These findings are paralleled by deficits of several neurotransmitter systems including serotonergic, noradrenergic, cholinergic, GABAergic, and glutamatergic signaling (reviewed in Brichta et al., 2013). PD pathology in these non-dopaminergic systems, in particular serotonergic neurotransmission, may be related to NMS like anhedonia, anxiety and depression, affecting up to 50% of PD patients and having a strong impact on patients' quality of life (Gallagher and Schrag, 2012; Duncan et al., 2014; Bugalho et al., 2016).

Several studies imply that dysfunction of different neurotransmitter systems occur even prior to the presence of Lewy pathology and the consequent neuronal loss [e.g., reviewed in (Burke and O'Malley, 2013)]. This led to the overall hypothesis, that the main pathophysiological process is related to a "dying back" of axons prior to the loss of neuronal perikarya (Hornykiewicz, 1998; Cheng et al., 2010). This review will discuss recent findings of clinical and neuropathological studies, as well as molecular mechanisms from cellular and animal models supporting the concept of an early axonal pathology in PD.

LOSS OF DOPAMINERGIC NEURONS AND THEIR PROJECTIONS IN PD

The involvement of the nigrostriatal dopaminergic system in PD was noted as early as neuropathological studies detected the loss of melanin-containing dopaminergic neurons in the SN of affected patients (Pakkenberg and Brody, 1965; Hirsch et al., 1988). The extent of neuronal loss in the SN by the time of clinical diagnosis was subject of several subsequent studies: While many reviews repeatedly state that first motor symptoms appear after 50% of SN dopaminergic neurons are lost (Lang and Lozano, 1998; Nandhagopal et al., 2008), comprehensive clinico-neuropathological studies used regression analysis to more precisely determine the loss of dopaminergic neurons at the time of symptom onset. Fearnley and Lees (1991) estimated the percentage of lost pigmented SN neurons at symptom onset by 31%. Subsequent stereological analyses provided similar results extrapolating the number of remaining pigmented SN neurons to the time of motor symptom onset to about 70% (Ma et al., 1997; Greffard et al., 2006). In summary, neuropathological-clinical correlations suggest that initial motor signs in PD occur as early as around 30% of total SN neurons are lost.

In contrast, the loss of dopaminergic striatal nerve terminals at motor symptoms onset is rather difficult to determine: An early neurochemical study focused on caudate dopamine levels in *post-mortem* tissue in two different cohorts (about 60 years vs. 73 years of age), and allowed an extrapolation to the time of symptom onset ranging from 68 to 82% of dopamine reduction (Riederer and Wuketich, 1976). To circumvent the concerns about *post-mortem* delay, another study utilized measurement of vesicular monoamine transporter (VMAT2) binding with tritiated alpha-dihydrotetrabenazine ([^{3}H]TBZOH) in *post-mortem* caudate from PD patients with different disease duration (Scherman et al., 1989). Here, the regression analysis indicated a loss of 49% of binding sites by the time of motor symptom onset. In general, the loss of dopamine terminals is higher in the putamen compared to the caudate (Kish et al., 1988), allowing the assumption that the loss of binding in the putamen ranges even higher than 50% by the time of onset of motor symptoms. Recently, Kordower et al. (2013) described in detail the integrity of nigrostriatal dopaminergic connectivity using tyrosine hydroxylase (TH) and dopamine transporter (DAT) as markers for dopaminergic function: In PD, dopaminergic fiber density in the dorsal putamen was rapidly and severely decreased leading to a virtually complete neuritic loss at 4 years after the clinical diagnosis compared to controls. In contrast, TH$^+$ SN neurons were less severely affected from the earliest time points on, with a minor loss over time, resulting in a residual population of dopaminergic neurons even decades after diagnosis (Kordower et al., 2013). In another study, this group detected an early loss of kinesin protein (anterograde transport motor protein) in the putamen of PD patients (H&Y stage 1 and 2), representing axonal loss, while reductions of typical cytoplasmic proteins like dynein light chain Tctex 3 as well as TH protein levels in the SN were only observed at later PD stages (Chu et al., 2012). Taken together, these observations support the hypothesis of an early axonal degeneration involving transport deficits in PD.

IMPAIRED NIGROSTRIATAL DOPAMINERGIC PROJECTIONS *IN VIVO*

While there are concerns about the significance of neuro-pathological and -chemical measures due to *post-mortem* delay, several *in vivo* studies investigated axonal or synaptic loss by using radioligand imaging (reviewed recently by Politis, 2014), in particular measuring DAT and VMAT2 (**Table 1**). Again, particularly those studies performing regression analysis to the onset of motor symptoms are relevant: the proportion of lost striatal and putaminal dopaminergic terminals was estimated up to 56% (Schwartz et al., 2004). Using [^{123}I]beta-CIT SPECT to label presynaptic DAT an early study described a loss of dopaminergic terminals contralateral to the unaffected side by 39–51% in the striatum and 51–64% in the putamen (Tissingh et al., 1998). In a larger study using two different PET markers, for DAT and VMAT2, the loss of putaminal dopaminergic innervation was between 51 and 71% for both tracers (Lee et al., 2000). More recent work using these established PET markers suggests that younger PD patients are able to compensate over several years the progressive dysfunction of the dopaminergic system before the first motor symptoms are recognized (de la Fuente-Fernandez et al., 2011).

At present, neuro-pathological and -imaging findings suggest that at the onset of motor symptoms in PD the loss of striatal or putaminal dopaminergic projections largely exceeds that of dopaminergic SN neurons, again supporting the hypothesis of a "dying back" of axons to their dopaminergic perikarya in PD (Cheng et al., 2010; Chu et al., 2012; Burke and O'Malley, 2013).

LOSS OF SEROTONERGIC NEURONS AND THEIR PROJECTIONS IN PD

Serotonergic neurotransmission is widely distributed in the brain and mediated by serotonergic neurons in

TABLE 1 | Parkinson's disease (PD) imaging studies of dopaminergic and serotonergic deficits.

Modality	Method	Ligand	*N*	Region	Marker loss (%)	Type of analysis	Reference
Dopamine imaging							
DAT binding	SPECT	[^{123}I]- IPT	6	Striatum	43	Regression to time of symptom onset	Schwartz et al., 2004
				Putamen	56		
	SPECT	[^{123}I]- β-CIT	8 (H&Y I)	Striatum	39–51	H&Y I (ipsi- vs. contralateral)	Tissingh et al., 1998
				Putamen	51–64		
	PET	[^{11}C]- MP	13 (H&Y I)	Putamen	56–71	H&Y I (ipsi- vs. contralateral)	Lee et al., 2000
VMAT2 binding	PET	[^{11}C]- DTBZ	13 (H&Y I)	Putamen	51–62	H&Y I (ipsi- vs. contralateral)	Lee et al., 2000
	PET	[^{11}C]- DTBZ	78 (H&Y I-II)	Putamen	71 (younger) 34 (older)	Regression to time of symptom onset; younger vs. older age of onset	de la Fuente-Fernandez et al., 2011
Serotonin imaging							
SERT binding	PET	[^{11}C]McN5652	13	Caudate	50	H&Y I-IV vs. controls	Kerenyi et al., 2003
				Putamen	35		
	PET	[^{11}C]- DASB	9	Caudate	30	H&Y II-III vs. controls	Guttman et al., 2007
				Putamen	26		
				Midbrain	29		
				Orbitofrontal cortex	22		
	PET	[^{11}C]- DASB	5	Forebrain regions	40–50	H&Y I-II,5 vs. controls	Albin et al., 2008
				Caudal brain stem regions	∼20		
	PET	[^{11}C]- DASB	30	Caudate	28	H&Y I-II vs. controls	Politis et al., 2010
				Thalamus	17		
				Anterior cingulate cortex	32		
				+ Putamen	33	H&Y II-III vs. controls	
				+ Prefrontal cortex	40		
				+ Raphe nuclei	19/22	H&Y III-IV vs. controls	
				+ Amygdala	25		
	PET	[^{11}C]- DASB	30	Ventral striatum Anterior cingulate cortex Caudate (R) Orbitofrontal cortex (R)	Significant loss	Apathetic vs. non-apathetic drug naïve early PD	Maillet et al., 2016

IPT, N-(3-iodopropen-2-yl)-2beta-carboxymethoxy-3beta-(4-chlorophenyl)-tropane; β-CIT, beta-carbomethoxy-3 beta-(4-iodophenyltropane); MP, methylphenidate; DTBZ, dihydrotetrabenazine; McN5652, (l,2,3,5,6,10βhexahydro6[4(methylthio) phenyl] pyrrolo[2,1-a]isoquinoline); DASB, 3-amino-4-(2-dimethylaminomethyl-phenylsufanyl-)benzonitrile.

the raphe nuclei (RN). Clusters of rostral RN neurons mainly project to the forebrain innervating basal ganglia, amygdala, hippocampus, hypothalamus, and several cortical regions (Parent et al., 2011; Wallman et al., 2011). Important functions are linked to the serotonergic system including motor function, as well as cognition and mood: Dysfunction of serotonin (5-hydroxytryptamine, 5-HT) neurotransmission contributes to resting tremor and levodopa-induced dyskinesias (Doder et al., 2003; Rylander et al., 2010; Politis et al., 2014) as well as to typical NMS of PD, in particular apathy, anxiety, anhedonia, and depression (Pavese et al., 2010; Ballanger et al., 2012).

Neuropathological analyses demonstrated an early involvement of serotonergic neurons in PD (Halliday et al., 1990; Paulus and Jellinger, 1991), associated with the presence of Lewy pathology within the RN at an early disease stage (Braak et al., 2003; Seidel et al., 2015). In detail, work by Halliday et al. (1990) described a loss of serotonergic neurons in the median RN of PD patients by 56%. Intriguingly, serotonergic cell loss was correlated with depression in PD, revealing an increased cell loss in the RN of depressed PD patients (Paulus and Jellinger, 1991). Typical NMS, possibly related to the serotonergic system like anxiety or depression, are often present before the onset of motor symptoms (Weintraub et al., 2015). Moreover, serotonin depletion was observed in several target regions of the RN including basal ganglia, hypothalamus, hippocampus, and prefrontal cortex (Fahn et al., 1971; Shannak et al., 1994). In addition, levels of serotonin transporter (SERT) immunoreactivity, protein levels of tryptophan hydroxylase, 5-HT and its metabolites were reduced in the caudate nucleus compared to the putamen in *post-mortem* tissue from PD patients (Kish et al., 2008).

IN VIVO STUDIES ADDRESSING THE SEROTONERGIC SYSTEM IN PD

Specific radioligands for the serotonergic system allowed new insights in PD related alterations *in vivo* (**Table 1**): Besides selective radiotracers for 5-HT receptors, particularly the highly selective detection of SERT using [^{11}C]-DASB PET enabled tracing of serotonergic terminals in the brain. Early studies detected a reduced SERT binding in the caudate nucleus and the putamen of PD patients (Kerenyi et al., 2003; Guttman et al., 2007). A follow-up study stratified for disease duration and without history of depression, described in detail an early loss of serotonergic terminals in the caudate nucleus, thalamus, hypothalamus, and anterior cingulum, followed by further deficits in putamen, insula, posterior cingulum, and prefrontal cortex in PD (Politis et al., 2010). Interestingly, the loss of SERT binding in the caudal and rostral RN occurred in advanced disease stages only, which points to an earlier affection of serotonergic projections compared to serotonergic neurons. This notion was supported by another [^{11}C]-DASB-PET study showing reduced forebrain, but preserved brain stem SERT binding in PD patients (Albin et al., 2008). Interestingly, a recent PET study in PD patients without signs of apathy mainly showed dopaminergic denervation, while serotonergic innervation remained preserved. In contrast, PD patients with apathy exhibited additional serotonergic loss within the right caudate, insula, orbitofrontal cortex, and cingulum without prominent dopaminergic deficits (Maillet et al., 2016). Despite these new insights into the dysfunction of the serotonergic system in PD, a temporal dissociation of the loss of serotonergic terminals in the forebrain and the number of RN neurons has not been well established, although these imaging studies point to an early degeneration of serotonergic nerve terminals.

AXONAL DEGENERATION IN MURINE PD MODELS

In order to get a more precise insight into the temporal pattern of degenerative events, several animal as well as cellular models are relevant:

Numerous transgenic animal models for PD have been generated, mostly carrying mutations in genes associated with monogenic PD such as alpha-synuclein, leucine rich repeat kinase 2 (LRRK2), Parkin, PTEN-induced putative kinase 1 (PINK1), and protein deglycase DJ-1 (reviewed by Lee et al., 2012). Longitudinal studies provide important information about the temporal progression of neurodegenerative events within the dopaminergic system (**Figure 1**).

Chung et al. (2009) injected adeno-associated virus (AAV) 2 encoding for human A53T alpha-synuclein into the SN of rats. After 4 weeks, dopaminergic axons within the striatum were dystrophic and swollen, and levels of dynein, mediating retrograde axonal transport, were significantly decreased. Eight weeks after AAV injection, several microtubule based motor proteins required for anterograde transport were reduced in the striatum. Since these findings were not observed in the SN, an initial impairment of dopaminergic axons is implied. BAC alpha-synuclein transgenic mice, expressing human alpha-synuclein had a reduced striatal dopamine release without a loss of dopaminergic SN neurons at 3 months of age (Janezic et al., 2013). In contrast, the number of dopaminergic SN neurons was significantly reduced in aged (18-month-old) mice accompanied by a motor phenotype. This temporal pattern of structural and functional measures indicated an early axonal phenotype prior to the loss of SN perikarya. Using another BAC alpha-synuclein construct, an increased DAT level in whole brain lysates without reduction of dopaminergic SN neurons was observed in 24-month-old mice (Yamakado et al., 2012). BAC transgenic rats overexpressing full-length human alpha-synuclein show a severe motor impairment at 12 months of age with severe striatal dopamine depletion. Importantly, TH^{+} striatal fibers and TH^{+} SN neurons were reduced in 18-month-old rat, but not in 3-month-old rat (Nuber et al., 2013).

While there was already some evidence for the onset of PD pathology within projection areas of dopaminergic neurons, recent animal studies revealed a similar temporal pattern of events within the serotonergic system of murine PD models (**Figure 1**).

Aforementioned BAC transgenic rats (published by Nuber et al., 2013) additionally display severe impairment of hippocampal neurogenesis, a feature strongly associated with early behavioral phenotypes like depression and anxiety at 4 months of age, even prior to the onset of a motor phenotype (Kohl et al., 2016). Impaired hippocampal neurogenesis was accompanied by a profoundly reduced serotonergic innervation of the hippocampal dentate gyrus (DG; Kohl et al., 2016). Furthermore, 5-HT receptor expression was altered and 5-HT levels were significantly reduced in the hippocampal DG and CA3 region of transgenic animals, strongly indicating an early dysfunction of serotonergic terminals. The number of serotonergic neurons in the RN, however, remained unaltered. This temporal pattern of structural changes and the functional phenotype in the BAC transgenic rat model demonstrates that an early axonal phenotype preceding the loss of perikarya is also present in the serotonergic system in PD. Further evidence for an early axonal phenotype within the serotonergic system derives from the A53T alpha-synuclein mouse model (A53T mice) of PD. At 52 weeks of age, human synuclein was expressed in serotonergic RN neurons and their projections within the hippocampal formation (Deusser et al., 2015). While the number of serotonergic neurons was preserved in A53T mice, the density of serotonergic fibers within the dorsal DG was severely reduced. Furthermore, viral injections allowing the overexpression of alpha-synuclein selectively in serotonergic neurons resulted in a progressive degeneration of serotonergic axon terminals in the hippocampus, while the number of serotonergic RN neurons remained unaltered (Wan et al., 2016). Mutations in PINK1 are linked to monogenic forms of PD, as well. PINK1 deficient mice showed no motor phenotypes, but olfactory deficits at 19 months of age (Glasl et al., 2012). Olfactory dysfunction is a very common NMS in PD. Interestingly, serotonergic innervation was significantly diminished in the glomerular layer of the olfactory bulb, while again there was no reduction in the

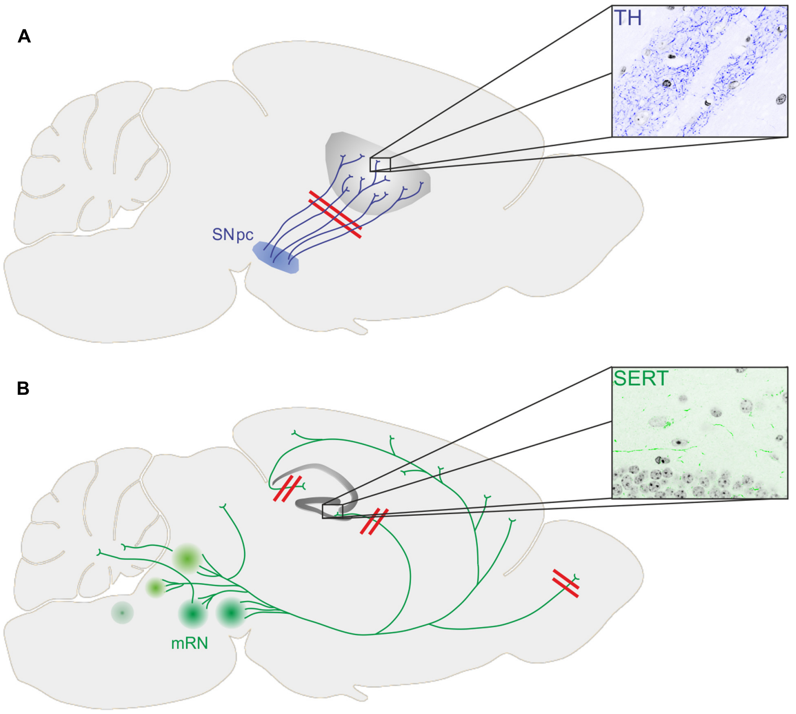

FIGURE 1 | (A) Loss of dopaminergic terminals (stained for tyrosine hydroxylase, TH) in the striatum precedes loss of substantia nigra pars compacta (SNpc) dopaminergic neurons in transgenic mouse models of PD. **(B)** While the number of serotonergic neurons within the medium raphe nuclei (mRN) was not changed in different transgenic mouse models of PD, the innervation of the hippocampal formation (stained for serotonin transporter, SERT) and the glomerular layer of the olfactory bulb was diminished together with depressive symptoms and impaired olfaction, respectively.

numbers of serotonergic RN neurons. This study also strongly indicates an early loss of serotonergic terminals in a second target region besides the hippocampal formation associated with NMS in PD.

Besides transgenic PD models acute neurotoxic models using toxins such as 1-methyl-4-phenyl-1,2,3,6-tetrahydropyridine (MPTP) or 6-hydroxydopamine (6-OHDA) specifically target dopaminergic SN neurons (reviewed by Blandini and Armentero, 2012). 6-OHDA is commonly injected directly into the striatum or the medial forebrain bundle, thereby directly damaging dopaminergic terminals. Few studies applied unilateral intranigral injections and revealed a severe loss of TH^+ neurons associated with a severe reduction of dopaminergic fibers (Moses et al., 2008; Grealish et al., 2010). For systemic application of MPTP which specifically diminishes dopaminergic neurons a severe loss of TH^+ striatal fibers was observed, but the temporal pattern of these events was not analyzed in detail. One day after MPTP treatment Serra et al. detected a 60% reduction of striatal dopaminergic fibers without significant increase in apoptotic TUNEL positive cells within the SN (Serra et al., 2002).

NEURITE DEGENERATION IN HUMAN STEM CELL MODELS OF PD

The opportunity to model PD by reprogramming patient derived cells into induced pluripotent stem cells (iPSC) and differentiating them into neurons recently advanced the availability of human cellular models of PD. Human dopaminergic neurons of sporadic and LRRK2 PD patients (carrying the *G2019S* mutation) showed markedly less neurites per dopaminergic neuron and shorter neurites in both patient cohorts after 75 days of neuronal differentiation. The number of caspase3 positive cells, however, was also significantly increased in patient derived neurons pointing toward higher rates of cell death in these cultures. The neuritic phenotype appeared rather simultaneously to the degeneration of the dopaminergic neurons in this iPSC derived PD model. Using another approach to generate dopaminergic neurons from LRRK2 patient derived iPSC carrying the identical G2019S mutation, Borgs et al. (2016) detected a different phenotype. LRRK2 patient derived neurons that were generated from neural progenitor cells using small molecules showed a reduced total neurite length and increased neurite branching while the number of TH positive neurons was not altered after 35 days of differentiation.

CONCLUDING REMARKS/ PERSPECTIVES

Enormous progress in imaging techniques, a large variety of animal models and the availability of PD patient iPSC derived neurons helped to significantly improve our knowledge of the temporal pattern of pathomechanisms underlying PD. Given the early appearance of NMS in PD and their tremendous impact on the patients' quality of life it is important to compare the timeline of pathogenic events within the serotonergic system with those more soundly explored in the dopaminergic system. One important recent milestone in PD research represents the appreciation that the onset of the disease may take place at the synaptic site and within the axonal compartment. Another milestone in PD research is the focus on other neurotransmitter systems besides dopamine, since especially early phenotypes of PD are strongly associated with e.g., alterations of the serotonergic system. One possible mechanism underlying axonal degeneration in PD may be the impairment of axonal transport due to protein aggregation, cytoskeleton instability, or motor protein dysregulation (Lee et al., 2006; Esteves et al., 2010; Volpicelli-Daley et al., 2014). Whether protein aggregation within the axon, motor protein dysfunction, or disturbance of motor protein binding to microtubules initiates the impairment of axonal transport remains to be elucidated. Another initial mechanism may be the reorganization of the synapse including altered availability of neurotransmitter receptors and transporters. Focusing on the mechanisms of axonal degeneration both in the dopaminergic and the serotonergic system or potentially even inducing axonal regeneration may be a very promising strategy to intervene at a very early stage with disease progression.

FUNDING

This work is supported by the Bavarian State Ministry of Education, Science, and the Arts (ForIPS grant).

AUTHOR CONTRIBUTIONS

JG, JW and ZK wrote the manuscript and designed figures/tables.

REFERENCES

Albin, R. L., Koeppe, R. A., Bohnen, N. I., Wernette, K., Kilbourn, M. A., and Frey, K. A. (2008). Spared caudal brainstem SERT binding in early Parkinson's disease. *J. Cereb. Blood Flow Metab.* 28, 441–444. doi: 10.1038/sj.jcbfm.9600599

Ballanger, B., Poisson, A., Broussolle, E., and Thobois, S. (2012). Functional imaging of non-motor signs in Parkinson's disease. *J. Neurol. Sci.* 315, 9–14. doi: 10.1016/j.jns.2011.11.008

Blandini, F., and Armentero, M. T. (2012). Animal models of Parkinson's disease. *FEBS J.* 279, 1156–1166. doi: 10.1111/j.1742-4658.2012.08491.x

Borgs, L., Peyre, E., Alix, P., Hanon, K., Grobarczyk, B., Godin, J. D., et al. (2016). Dopaminergic neurons differentiating from LRRK2 G2019S induced pluripotent stem cells show early neuritic branching defects. *Sci. Rep.* 6, 33377. doi: 10.1038/srep33377

Braak, H., Del Tredici, K., Rub, U., de Vos, R. A., Jansen Steur, E. N., and Braak, E. (2003). Staging of brain pathology related to sporadic Parkinson's disease. *Neurobiol. Aging* 24, 197–211. doi: 10.1016/S0197-4580(02)00065-9

Brichta, L., Greengard, P., and Flajolet, M. (2013). Advances in the pharmacological treatment of Parkinson's disease: targeting neurotransmitter systems. *Trends Neurosci.* 36, 543–554. doi: 10.1016/j.tins.2013.06.003

Bugalho, P., Lampreia, T., Miguel, R., Mendonca, M. D., Caetano, A., and Barbosa, R. (2016). Non-Motor symptoms in Portuguese Parkinson's Disease patients: correlation and impact on quality of life and activities of daily living. *Sci. Rep.* 6, 32267. doi: 10.1038/srep32267

Burke, R. E., and O'Malley, K. (2013). Axon degeneration in Parkinson's disease. *Exp. Neurol.* 246, 72–83. doi: 10.1016/j.expneurol.2012.01.011

Cheng, H. C., Ulane, C. M., and Burke, R. E. (2010). Clinical progression in Parkinson disease and the neurobiology of axons. *Ann. Neurol.* 67, 715–725. doi: 10.1002/ana.21995

Chu, Y., Morfini, G. A., Langhamer, L. B., He, Y., Brady, S. T., and Kordower, J. H. (2012). Alterations in axonal transport motor proteins in sporadic and experimental Parkinson's disease. *Brain* 135, 2058–2073. doi: 10.1093/brain/aws133

Chung, C. Y., Koprich, J. B., Siddiqi, H., and Isacson, O. (2009). Dynamic changes in presynaptic and axonal transport proteins combined with striatal neuroinflammation precede dopaminergic neuronal loss in a rat model of AAV alpha-synucleinopathy. *J. Neurosci.* 29, 3365–3373. doi: 10.1523/JNEUROSCI.5427-08.2009

de la Fuente-Fernandez, R., Schulzer, M., Kuramoto, L., Ramachandiran, N., Au, W. L., Mak, E., et al. (2011). Age-specific progression of nigrostriatal dysfunction in Parkinson's disease. *Ann. Neurol.* 69, 803–810. doi: 10.1002/ana.22284

de Lau, L. M., and Breteler, M. M. (2006). Epidemiology of Parkinson's disease. *Lancet Neurol.* 5, 525–535. doi: 10.1016/S1474-4422(06)70471-9

Deusser, J., Schmidt, S., Ettle, B., Plotz, S., Huber, S., Muller, C. P., et al. (2015). Serotonergic dysfunction in the A53T alpha-synuclein mouse model of Parkinson's disease. *J. Neurochem.* 135, 589–597. doi: 10.1111/jnc.13253

Dickson, D. W., Fujishiro, H., Orr, C., DelleDonne, A., Josephs, K. A., Frigerio, R., et al. (2009). Neuropathology of non-motor features of Parkinson disease. *Parkinsonism Relat. Disord.* 15(Suppl. 3), S1–S5. doi: 10.1016/S1353-8020(09)70769-2

Doder, M., Rabiner, E. A., Turjanski, N., Lees, A. J., Brooks, D. J., and 11C-Way 100635 Pet study. (2003). Tremor in Parkinson's disease and serotonergic dysfunction: an 11C-WAY 100635 PET study. *Neurology* 60, 601–605. doi: 10.1212/01.WNL.0000031424.51127.2B

Dorsey, E. R., Constantinescu, R., Thompson, J. P., Biglan, K. M., Holloway, R. G., Kieburtz, K., et al. (2007). Projected number of people with Parkinson disease in the most populous nations, 2005 through 2030. *Neurology* 68, 384–386. doi: 10.1212/01.wnl.0000247740.47667.03

Duncan, G. W., Khoo, T. K., Yarnall, A. J., O'Brien, J. T., Coleman, S. Y., Brooks, D. J., et al. (2014). Health-related quality of life in early Parkinson's disease: the impact of nonmotor symptoms. *Mov. Disord.* 29, 195–202. doi: 10.1002/mds.25664

Esteves, A. R., Arduino, D. M., Swerdlow, R. H., Oliveira, C. R., and Cardoso, S. M. (2010). Microtubule depolymerization potentiates alpha-synuclein oligomerization. *Front. Aging Neurosci.* 1:5. doi: 10.3389/neuro.24.005.2009

Fahn, S., Libsch, L. R., and Cutler, R. W. (1971). Monoamines in the human neostriatum: topographic distribution in normals and in Parkinson's disease and their role in akinesia, rigidity, chorea, and tremor. *J. Neurol. Sci.* 14, 427–455. doi: 10.1016/0022-510X(71)90178-X

Fearnley, J. M., and Lees, A. J. (1991). Ageing and Parkinson's disease: substantia nigra regional selectivity. *Brain* 114(Pt 5), 2283–2301. doi: 10.1093/brain/114.5.2283

Gallagher, D. A., and Schrag, A. (2012). Psychosis, apathy, depression and anxiety in Parkinson's disease. *Neurobiol. Dis.* 46, 581–589. doi: 10.1016/j.nbd.2011.12.041

Glasl, L., Kloos, K., Giesert, F., Roethig, A., Di Benedetto, B., Kühn, R., et al. (2012). Pink1-deficiency in mice impairs gait, olfaction and serotonergic innervation of the olfactory bulb. *Exp. Neurol.* 235, 214–227. doi: 10.1016/j.expneurol.2012.01.002

Grealish, S., Mattsson, B., Draxler, P., and Bjorklund, A. (2010). Characterisation of behavioural and neurodegenerative changes induced by intranigral 6-hydroxydopamine lesions in a mouse model of Parkinson's disease. *Eur. J. Neurosci.* 31, 2266–2278. doi: 10.1111/j.1460-9568.2010.07265.x

Greffard, S., Verny, M., Bonnet, A. M., Beinis, J. Y., Gallinari, C., Meaume, S., et al. (2006). Motor score of the Unified Parkinson Disease Rating Scale as a good predictor of Lewy body-associated neuronal loss in the substantia nigra. *Arch. Neurol.* 63, 584–588. doi: 10.1001/archneur.63.4.584

Guttman, M., Boileau, I., Warsh, J., Saint-Cyr, J. A., Ginovart, N., McCluskey, T., et al. (2007). Brain serotonin transporter binding in non-depressed patients with Parkinson's disease. *Eur. J. Neurol.* 14, 523–528. doi: 10.1111/j.1468-1331.2007.01727.x

Halliday, G. M., Blumbergs, P. C., Cotton, R. G., Blessing, W. W., and Geffen, L. B. (1990). Loss of brainstem serotonin- and substance P-containing neurons in Parkinson's disease. *Brain Res.* 510, 104–107. doi: 10.1016/0006-8993(90)90733-R

Hirsch, E., Graybiel, A. M., and Agid, Y. A. (1988). Melanized dopaminergic neurons are differentially susceptible to degeneration in Parkinson's disease. *Nature* 334, 345–348. doi: 10.1038/334345a0

Hornykiewicz, O. (1998). Biochemical aspects of Parkinson's disease. *Neurology* 51, S2–S9. doi: 10.1212/WNL.51.2_Suppl_2.S2

Janezic, S., Threlfell, S., Dodson, P. D., Dowie, M. J., Taylor, T. N., Potgieter, D., et al. (2013). Deficits in dopaminergic transmission precede neuron loss and dysfunction in a new Parkinson model. *Proc. Natl. Acad. Sci. U.S.A.* 110, E4016–E4025. doi: 10.1073/pnas.1309143110

Kerenyi, L., Ricaurte, G. A., Schretlen, D. J., McCann, U., Varga, J., Mathews, W. B., et al. (2003). Positron emission tomography of striatal serotonin transporters in Parkinson disease. *Arch. Neurol.* 60, 1223–1229. doi: 10.1001/archneur.60.9.1223

Kish, S. J., Shannak, K., and Hornykiewicz, O. (1988). Uneven pattern of dopamine loss in the striatum of patients with idiopathic Parkinson's disease. Pathophysiologic and clinical implications. *N. Engl. J. Med.* 318, 876–880. doi: 10.1056/NEJM198804073181402

Kish, S. J., Tong, J., Hornykiewicz, O., Rajput, A., Chang, L. J., Guttman, M., et al. (2008). Preferential loss of serotonin markers in caudate versus putamen in Parkinson's disease. *Brain* 131, 120–131.

Kohl, Z., Ben Abdallah, N., Vogelgsang, J., Tischer, L., Deusser, J., Amato, D., et al. (2016). Severely impaired hippocampal neurogenesis associates with an early serotonergic deficit in a BAC alpha-synuclein transgenic rat model of Parkinson's disease. *Neurobiol. Dis.* 85, 206–217. doi: 10.1016/j.nbd.2015.10.021

Kordower, J. H., Olanow, C. W., Dodiya, H. B., Chu, Y., Beach, T. G., Adler, C. H., et al. (2013). Disease duration and the integrity of the nigrostriatal system in Parkinson's disease. *Brain* 136, 2419–2431. doi: 10.1093/brain/awt192

Lang, A. E., and Lozano, A. M. (1998). Parkinson's disease. Second of two parts. *N. Engl. J. Med.* 339, 1130–1143. doi: 10.1056/NEJM199810153391607

Lee, C. S., Samii, A., Sossi, V., Ruth, T. J., Schulzer, M., Holden, J. E., et al. (2000). In vivo positron emission tomographic evidence for compensatory changes in presynaptic dopaminergic nerve terminals in Parkinson's disease. *Ann. Neurol.* 47, 493–503. doi: 10.1002/1531-8249(200004)47:4<493::AID-ANA13>3.0.CO;2-4

Lee, H. J., Khoshaghideh, F., Lee, S., and Lee, S. J. (2006). Impairment of microtubule-dependent trafficking by overexpression of alpha-synuclein. *Eur. J. Neurosci.* 24, 3153–3162. doi: 10.1111/j.1460-9568.2006.05210.x

Lee, Y., Dawson, V. L., and Dawson, T. M. (2012). Animal models of Parkinson's disease: vertebrate genetics. *Cold Spring Harb. Perspect. Med.* 2, a009324. doi: 10.1101/cshperspect.a009324

Ma, S. Y., Roytta, M., Rinne, J. O., Collan, Y., and Rinne, U. K. (1997). Correlation between neuromorphometry in the substantia nigra and clinical features in Parkinson's disease using disector counts. *J. Neurol. Sci.* 151, 83–87. doi: 10.1016/S0022-510X(97)00100-7

Maillet, A., Krack, P., Lhommée, E., Météreau, E., Klinger, H., Favre, E., et al. (2016). The prominent role of serotonergic degeneration in apathy, anxiety and depression in de novo Parkinson's disease. *Brain* 139, 2486–2502. doi: 10.1093/brain/aww162

Marras, C., and Chaudhuri, K. R. (2016). Nonmotor features of Parkinson's disease subtypes. *Mov. Disord.* 31, 1095–1102. doi: 10.1002/mds.26510

Moses, D., Drago, J., Teper, Y., Gantois, I., Finkelstein, D. I., and Horne, M. K. (2008). Fetal striatum- and ventral mesencephalon-derived expanded neurospheres rescue dopaminergic neurons in vitro and the nigro-striatal system in vivo. *Neuroscience* 154, 606–620. doi: 10.1016/j.neuroscience.2008.03.058

Nandhagopal, R., McKeown, M. J., and Stoessl, A. J. (2008). Functional imaging in Parkinson disease. *Neurology* 70, 1478–1488. doi: 10.1212/01.wnl.0000310432.92489.90

Nuber, S., Harmuth, F., Kohl, Z., Adame, A., Trejo, M., Schönig, K., et al. (2013). A progressive dopaminergic phenotype associated with neurotoxic conversion of alpha-synuclein in BAC-transgenic rats. *Brain* 136, 412–432. doi: 10.1093/brain/aws358

Pakkenberg, H., and Brody, H. (1965). The number of nerve cells in the substantia nigra in paralysis agitans. *Acta Neuropathol.* 5, 320–324. doi: 10.1007/BF00686528

Parent, M., Wallman, M. J., Gagnon, D., and Parent, A. (2011). Serotonin innervation of basal ganglia in monkeys and humans. *J. Chem. Neuroanat.* 41, 256–265. doi: 10.1016/j.jchemneu.2011.04.005

Paulus, W., and Jellinger, K. (1991). The neuropathologic basis of different clinical subgroups of Parkinson's disease. *J. Neuropathol. Exp. Neurol.* 50, 743–755. doi: 10.1097/00005072-199111000-00006

Pavese, N., Metta, V., Bose, S. K., Chaudhuri, K. R., and Brooks, D. J. (2010). Fatigue in Parkinson's disease is linked to striatal and limbic serotonergic dysfunction. *Brain* 133, 3434–3443. doi: 10.1093/brain/awq268

Politis, M. (2014). Neuroimaging in Parkinson disease: from research setting to clinical practice. *Nat. Rev. Neurol.* 10, 708–722. doi: 10.1038/nrneurol.2014.205

Politis, M., Wu, K., Loane, C., Brooks, D. J., Kiferle, L., Turkheimer, F. E., et al. (2014). Serotonergic mechanisms responsible for levodopa-induced dyskinesias in Parkinson's disease patients. *J. Clin. Invest.* 124, 1340–1349. doi: 10.1172/JCI71640

Politis, M., Wu, K., Loane, C., Kiferle, L., Molloy, S., Brooks, D. J., et al. (2010). Staging of serotonergic dysfunction in Parkinson's disease: an in vivo 11C-DASB PET study. *Neurobiol. Dis.* 40, 216–221. doi: 10.1016/j.nbd.2010.05.028

Riederer, P., and Wuketich, S. (1976). Time course of nigrostriatal degeneration in parkinson's disease. A detailed study of influential factors in human brain amine analysis. *J. Neural Transm.* 38, 277–301. doi: 10.1007/BF01249445

Rylander, D., Parent, M., O'Sullivan, S. S., Dovero, S., Lees, A. J., Bezard, E., et al. (2010). Maladaptive plasticity of serotonin axon terminals in levodopa-induced dyskinesia. *Ann. Neurol.* 68, 619–628. doi: 10.1002/ana.22097

Scherman, D., Desnos, C., Darchen, F., Pollak, P., Javoy-Agid, F., and Agid, Y. (1989). Striatal dopamine deficiency in Parkinson's disease: role of aging. *Ann. Neurol.* 26, 551–557. doi: 10.1002/ana.410260409

Schwartz, M., Groshar, D., Inzelberg, R., and Hocherman, S. (2004). Dopamine-transporter imaging and visuo-motor testing in essential tremor, practical possibilities for detection of early stage Parkinson's disease. *Parkinsonism Relat. Disord.* 10, 385–389. doi: 10.1016/j.parkreldis.2004.03.004

Seidel, K., Mahlke, J., Siswanto, S., Krüger, R., Heinsen, H., Auburger, G., et al. (2015). The brainstem pathologies of Parkinson's disease and dementia with Lewy bodies. *Brain Pathol.* 25, 121–135. doi: 10.1111/bpa.12168

Serra, P. A., Sciola, L., Delogu, M. R., Spano, A., Monaco, G., Miele, E., et al. (2002). The neurotoxin 1-methyl-4-phenyl-1,2,3,6-tetrahydropyridine induces apoptosis in mouse nigrostriatal glia. Relevance to nigral neuronal death and striatal neurochemical changes. *J. Biol. Chem.* 277, 34451–34461. doi: 10.1074/jbc.M202099200

Shannak, K., Rajput, A., Rozdilsky, B., Kish, S., Gilbert, J., and Hornykiewicz, O. (1994). Noradrenaline, dopamine and serotonin levels and metabolism in the human hypothalamus: observations in Parkinson's disease and normal subjects. *Brain Res.* 639, 33–41. doi: 10.1016/0006-8993(94)91761-2

Tissingh, G., Booij, J., Bergmans, P., Winogrodzka, A., Janssen, A. G., van Royen, E. A., et al. (1998). Iodine-123-N-omega-fluoropropyl-2beta-carbomethoxy-3beta-(4-iod ophenyl)tropane SPECT in healthy controls and early-stage, drug-naive Parkinson's disease. *J. Nucl. Med.* 39, 1143–1148.

Volpicelli-Daley, L. A., Gamble, K. L., Schultheiss, C. E., Riddle, D. M., West, A. B., and Lee, V. M. (2014). Formation of alpha-synuclein Lewy neurite-like aggregates in axons impedes the transport of distinct endosomes. *Mol. Biol. Cell* 25, 4010–4023. doi: 10.1091/mbc.E14-02-0741

Wallman, M. J., Gagnon, D., and Parent, M. (2011). Serotonin innervation of human basal ganglia. *Eur. J. Neurosci.* 33, 1519–1532. doi: 10.1111/j.1460-9568.2011.07621.x

Wan, O. W., Shin, E., Mattsson, B., Caudal, D., Svenningsson, P., and Bjorklund, A. (2016). alpha-Synuclein induced toxicity in brain stem serotonin neurons mediated by an AAV vector driven by the tryptophan hydroxylase promoter. *Sci. Rep.* 6, 26285. doi: 10.1038/srep26285

Weintraub, D., Simuni, T., Caspell-Garcia, C., Coffey, C., Lasch, S., Siderowf, A., et al. (2015). Cognitive performance and neuropsychiatric symptoms in early, untreated Parkinson's disease. *Mov. Disord.* 30, 919–927. doi: 10.1002/mds.26170

Yamakado, H., Moriwaki, Y., Yamasaki, N., Miyakawa, T., Kurisu, J., Uemura, K., et al. (2012). alpha-Synuclein BAC transgenic mice as a model for Parkinson's disease manifested decreased anxiety-like behavior and hyperlocomotion. *Neurosci. Res.* 73, 173–177. doi: 10.1016/j.neures.2012.03.010

Conflict of Interest Statement: The authors declare that the research was conducted in the absence of any commercial or financial relationships that could be construed as a potential conflict of interest.

frontiers
in Cellular Neuroscience

ORIGINAL RESEARCH
published: 19 October 2016
doi: 10.3389/fncel.2016.00241

Mdivi-1 Inhibits Astrocyte Activation and Astroglial Scar Formation and Enhances Axonal Regeneration after Spinal Cord Injury in Rats

Gang Li[1], **Yang Cao**[1], **Feifei Shen**[2], **Yangsong Wang**[1], **Liangjie Bai**[3], **Weidong Guo**[1], **Yunlong Bi**[1], **Gang Lv**[1]* **and Zhongkai Fan**[1]*

[1] Department of Orthopaedics, The First Affiliated Hospital, Jinzhou Medical University, Jinzhou, China, [2] Department of Pathology, College of Basic Medical Sciences, China Medical University, Shenyang, China, [3] Department of Orthopaedics, The First Affiliated Hospital, China Medical University, Shenyang, China

After spinal cord injury (SCI), astrocytes become hypertrophic, and proliferative, forming a dense network of astroglial processes at the site of the lesion. This constitutes a physical and biochemical barrier to axonal regeneration. Mitochondrial fission regulates cell cycle progression; inhibiting the cell cycle of astrocytes can reduce expression levels of axon growth-inhibitory molecules as well as astroglial scar formation after SCI. We therefore investigated how an inhibitor of mitochondrial fission, Mdivi-1, would affect astrocyte proliferation, astroglial scar formation, and axonal regeneration following SCI in rats. Western blot and immunofluorescent double-labeling showed that Mdivi-1 markedly reduced the expression of the astrocyte marker glial fibrillary acidic protein (GFAP), and a cell proliferation marker, proliferating cell nuclear antigen, in astrocytes 3 days after SCI. Moreover, Mdivi-1 decreased the expression of GFAP and neurocan, a chondroitin sulfate proteoglycan. Notably, immunofluorescent labeling and Nissl staining showed that Mdivi-1 elevated the production of growth-associated protein-43 and increased neuronal survival at 4 weeks after SCI. Finally, hematoxylin-eosin staining, and behavioral evaluation of motor function indicated that Mdivi-1 also reduced cavity formation and improved motor function 4 weeks after SCI. Our results confirm that Mdivi-1 promotes motor function after SCI, and indicate that inhibiting mitochondrial fission using Mdivi-1 can inhibit astrocyte activation and astroglial scar formation and contribute to axonal regeneration after SCI in rats.

Keywords: spinal cord injury, mitochondrial division inhibitor-1, astrocytes, astroglial scar, axonal regeneration

Edited by:
Maren Engelhardt,
Heidelberg University, Germany

Reviewed by:
Xiaojing J. Gao,
Stanford University, USA
Yu-Feng Wang,
Harbin Medical University, China

***Correspondence:**
Gang Lv
lvgang_lnyxy@126.com
Zhongkai Fan
fanzk_ln@163.com

Received: *23 June 2016*
Accepted: *30 September 2016*
Published: *19 October 2016*

Citation:
Li G, Cao Y, Shen F, Wang Y, Bai L, Guo W, Bi Y, Lv G and Fan Z (2016) Mdivi-1 Inhibits Astrocyte Activation and Astroglial Scar Formation and Enhances Axonal Regeneration after Spinal Cord Injury in Rats. Front. Cell. Neurosci. 10:241. doi: 10.3389/fncel.2016.00241

INTRODUCTION

Spinal cord injury (SCI) is a global medical problem. It often leads to very limited regeneration of damaged axons and subsequent permanent functional impairment, the exact mechanisms of which remain to be elucidated (Silver and Miller, 2004; Tuszynski and Steward, 2012). The lack of spontaneous anatomical and functional repair is due not merely to an intrinsic inability of the neuron to regenerate its injured axon, but also to the presence of an inhospitable local environment in the lesion site constituting a physical and biochemical barrier—the so-called glial scar—composed essentially of reactive astrocytes (Silver and Miller, 2004). Astrocytes are the major cell type in the spinal cord and provide a variety of critical supportive functions that establish and maintain neuronal homeostasis (Tian et al., 2006). However, after SCI, they become hypertrophic and proliferative, and form a physical barrier at the site of injury, which significantly impedes axonal regeneration (Lin et al., 2014). In addition, chondroitin sulfate proteoglycans (CSPGs) form a biochemical barrier which also plays a crucial part in regeneration failure (Yiu and He, 2006; Gervasi et al., 2008; Jefferson et al., 2011). Therefore, inhibition of astrocyte activation, astroglial scar formation and CSPG production would create a favorable environment for axonal regeneration.

Astrocytes undergo cell division following SCI. Therefore, a possible approach for promoting axonal regeneration after SCI would be by inhibiting the division of cells that contribute to glial scar formation or by reducing production and secretion of inhibitory molecules (Karimi-Abdolrezaee and Billakanti, 2012). Mitochondria are organelles that are essential for a diverse range of important cellular functions, including cell metabolism, growth, differentiation, survival, and programmed cell death (DiMauro and Schon, 2008; Green and Van Houten, 2011). Recently, mitochondria were demonstrated to undergo frequent fission, and fusion (Cao et al., 2013), which are integrated with cell cycle progression (Mitra et al., 2009; Qian et al., 2012). Dynamin-related protein 1 (Drp1)-mediated mitochondrial fission is required for the proper progression of the cell cycle phases following G1/S transition. Thus, inhibition of mitochondrial division might be an important way to inhibit cell mitosis. However, it is unclear whether this would inhibit astrocyte activation and astroglial scar formation after SCI.

Mitochondrial division inhibitor 1 (Mdivi-1) is the most effective pharmacological inhibitor of mitochondrial division (Tanaka and Youle, 2008). It can cross the blood—brain barrier, and its half-life is about 12 h (Cui et al., 2016). Notably, Mdivi-1 exerts a protective effect in SCI (Li G. et al., 2015), spinal cord ischemia—reperfusion injury (Liu et al., 2015), acute cerebral ischemic injury (Cui et al., 2016), and seizures (Xie et al., 2013), and can also inhibit the proliferation, invasion and metastasis of breast cancer (Zhao et al., 2013) and ovarian cancer (Wang et al., 2015). However, the physiological and pathological roles of Mdivi-1 in astrocyte proliferation and astroglial scar formation after SCI are not yet known. Therefore, in the present study, we investigate the effects of Mdivi-1 on astrocyte proliferation, neurocan production, astroglial scar formation, and axonal regeneration after SCI in rats.

MATERIALS AND METHODS

Animals and Experimental Design

Adult female Sprague—Dawley rats, weighing 250–300 g, were provided by the Experiment Animal Center of Jinzhou Medical University. All experimental procedures were approved by the Institutional Animal Care and Use Committee of Jinzhou Medical University. Rats were randomly divided into three groups: SCI (Li G. et al., 2015), SCI + Mdivi-1 (Park et al., 2011), and sham (T9–11 laminectomy only). In the Mdivi-1 group, the rats were injected with Mdivi-1 (25 mg/kg i.p.; Sigma-Aldrich, St. Louis, MO) immediately after SCI and every 24 h thereafter for 3 or 9 days (Lin et al., 2014; Cui et al., 2016). Rats in the sham and SCI groups received an equivalent volume of dimethyl sulfoxide. Each group was then equally and randomly divided into three subgroups for the following experiments: (A) motor function test; (B) Western blot; and (C) histology (double immunofluorescent labeling, hematoxylin-eosin staining, and Nissl staining). The rats in all groups were sacrificed 3 days or 4 weeks after injury or laminectomy.

SCI Model Establishment

Rats were anesthetized using pentobarbital sodium (40 mg/kg, i.p.). The weight-drop model of SCI was established as described previously (Li G. et al., 2015). In brief, the skin and muscle overlying the spinal column were incised and a laminectomy was performed at T9–11, leaving the dura intact. A 20 g weight was then dropped onto the exposed T10 region of the spinal cord from a height of 25.0 mm. Postoperatively, all animals received an injection of 0.9% normal saline (30 ml/kg) to prevent postoperative dehydration. Rats were housed individually in cages under a 12 h light/dark cycle, with free access to food and water, and underwent assisted urination three times per day after SCI throughout the study.

Motor Function Evaluation

The motor function of rats in each group was evaluated using the Basso, Beattie, and Bresnahan (BBB) scale at 3 days and 4 weeks after SCI, as described previously (Li G. et al., 2015). The experiments were performed six independent times.

Western Blot

Spinal cords were removed 3 days or 4 weeks after SCI. The protein lysates were fractioned on 6 or 10% SDS-polyacrylamide gels, and then transferred to 0.45 μm polyvinylidene fluoride membranes. The membranes were blocked with 0.1% bovine serum albumin for 1 h, then incubated overnight at 4°C with primary antibodies against glial fibrillary acidic protein GFAP (ab7260, 1:2000), neurocan (ab31979, 1:300), proliferating cell nuclear antigen (PCNA; ab29, 1:1000), growth-associated protein-43 (GAP-43; ab16053, 1:1000) (all from Abcam, USA), and β-actin (C4; sc-47778, 1:1000; Santa Cruz Biotechnology, Inc., USA). The membranes were then incubated with the corresponding second antibody: goat anti-rabbit or anti-mouse IgG-HRP (sc-2004 or sc-2005; 1:2000; Santa Cruz Biotechnology) at room temperature for 1 h. The remaining steps were performed as described in our previous study (Li G. et al., 2015), and the protein bands were analyzed using NIH Image J software. Grayscale values of bands corresponding to GFAP, PCNA, neurocan, and GAP-43 were normalized to that of β-actin to determine expression levels of the proteins of interest. The experiments were performed six independent times.

Immunofluorescent Double Labeling

At 3 days and 4 weeks after surgery, the injured spinal cords from rats in all groups were fixed in 4% paraformaldehyde, immersed in 30% sucrose, embedded in compound 4583, and then sectioned on a freezing microtome as described previously (Li G. et al., 2015). Serial 5-μm-thick transverse

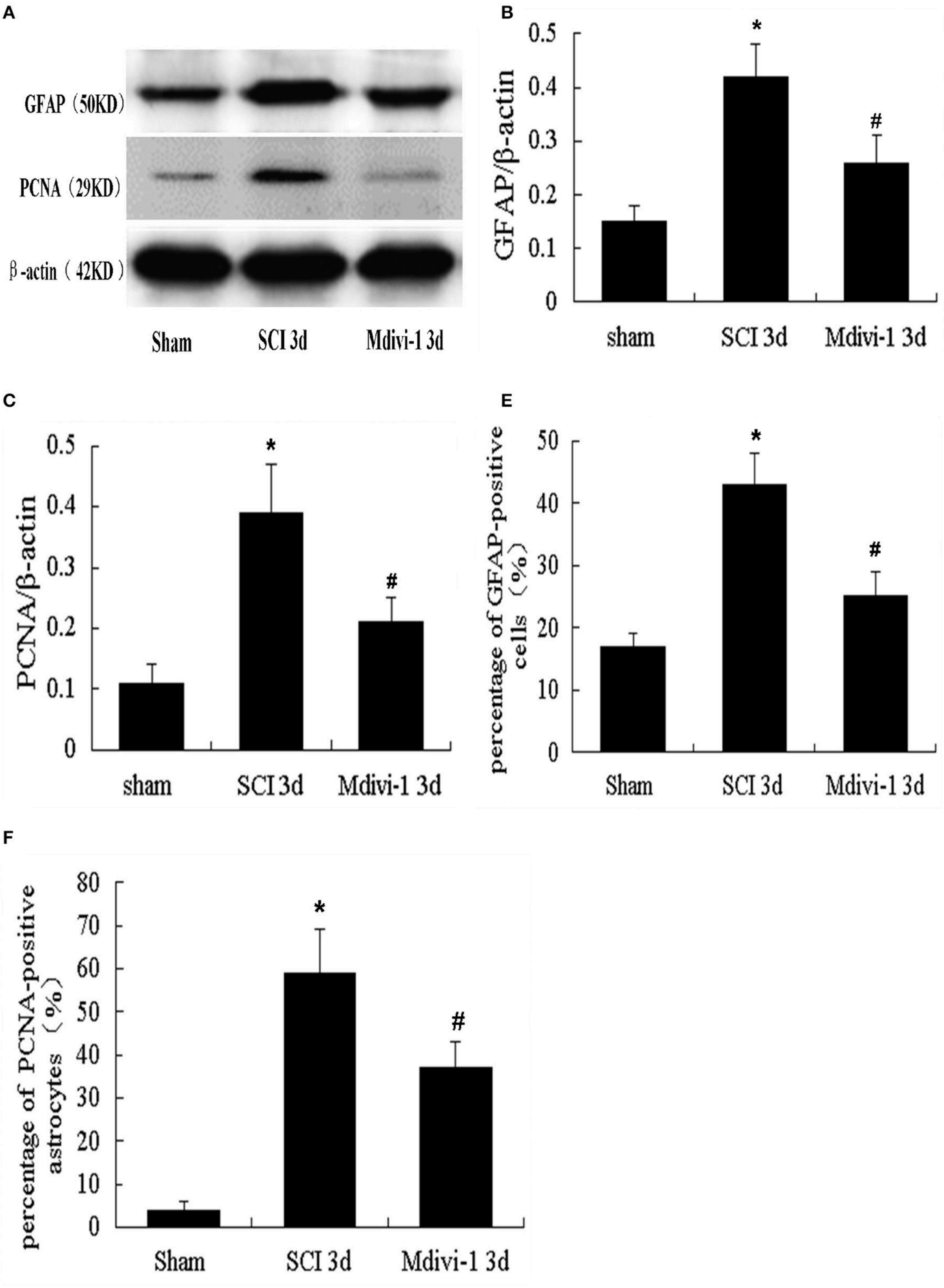

FIGURE 1 | Continued

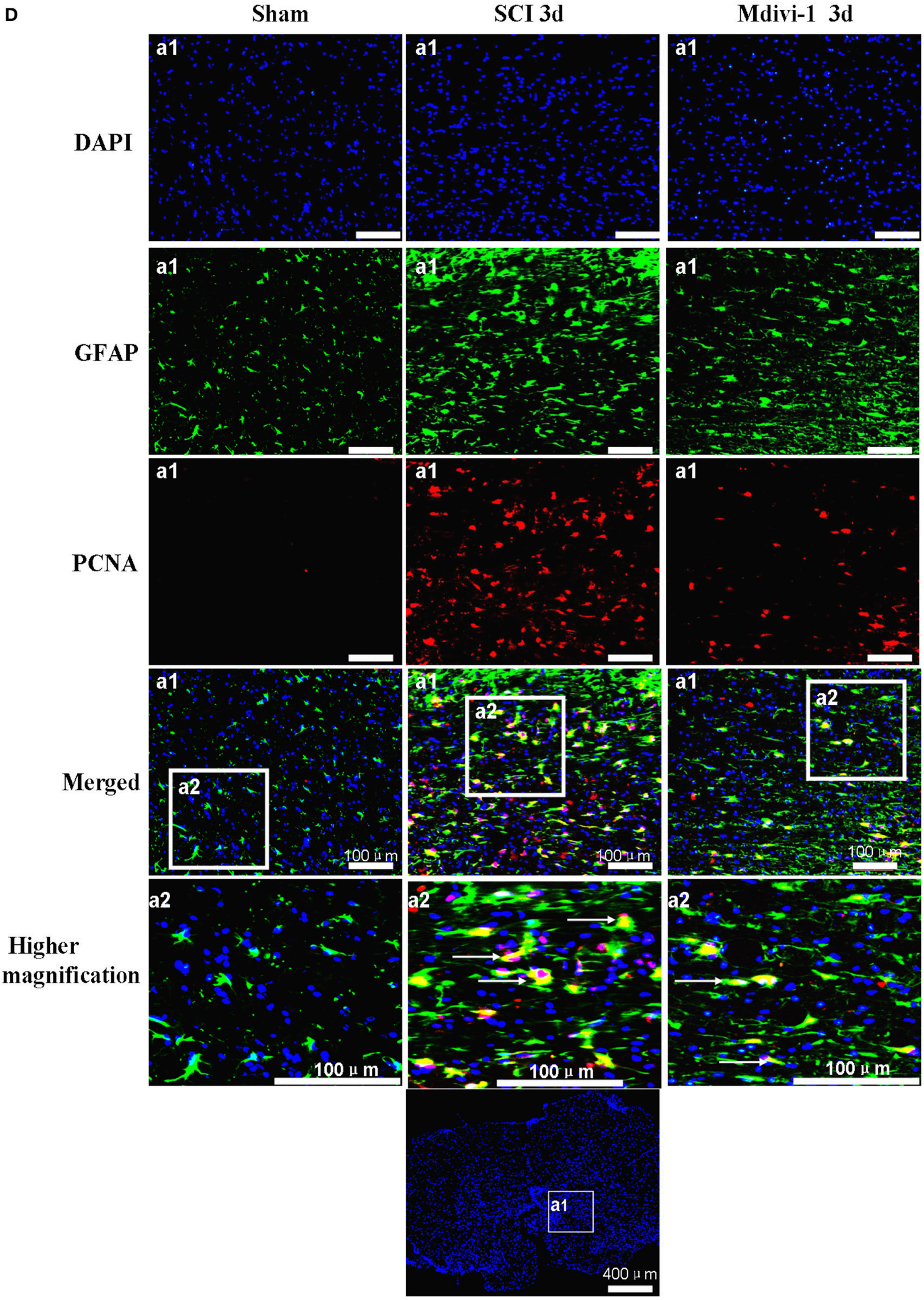

FIGURE 1 | Mdivi-1 increases the expressions of GFAP and PCNA in astrocytes at 3 days after SCI. (A–C) Western blot analysis and quantitative analysis of GFAP **(A,B)** and PCNA **(A,C)** ($n = 6$, respectively). **(D–F)** PCNA/GFAP/DAPI triple labeling and quantitative analysis of GFAP **(D,E)** and PCNA **(D,F)** in astrocytes ($n = 6$, respectively). White arrows indicate proliferative astrocytes. The expression of PCNA and GFAP, and the number of GFAP-positive cells and PCNA-positive astrocytes, were greater in the SCI group than in the sham group. PCNA and GFAP expression, and the number of GFAP-positive cells and PCNA-positive astrocytes were lower in the Mdivi-1 group than in the SCI group. $^{*}P < 0.01$ vs. Sham. $^{\#}P < 0.01$ vs. SCI.

frozen sections from the epicenter of the SCI were used for immunofluorescent double labeling and hematoxylin-eosin staining. After permeabilizing the cells and blocking non-specific binding sites, these spinal cord tissue sections were incubated with the following primary antibodies diluted in 5% normal goat serum (005-000-121, Jackson): anti-GFAP (ab7260, 1:500), anti-neurocan (ab31979, 1:50), anti-PCNA (ab29, 1:200), anti-GAP-43 (ab16053, 1:200) (all from Abcam, USA), and anti-NeuN (MAB377X, 1:50; Millipore, USA) in a humidified chamber overnight at 4°C. Tissue sections were incubated with the secondary antibodies Alexa Fluor 488 goat anti-rabbit IgG (H+L; A-11034, 1:250; Thermo Fisher Scientific, USA) and Alexa Fluor 594 goat anti-mouse IgG (H+L; A-11005, 1:250; Thermo Fisher Scientific) for 1 h at room temperature in the dark. After immunostaining, the sections were incubated with 1 μg/ml 4′,6-diamidino-2-phenylindole (DAPI) for 5 min in the dark to mark the nuclei. Negative control sections were incubated with phosphate-buffered saline in place of the primary antibody. The sections were visualized under a fluorescent microscope (Leica DMI4000B, Germany) connected to an Olympus Magnafire digital camera (Olympus Corp., Melville, NY, USA). Each fluorescent color was photographed under the same fluorescence microscopy settings. To avoid counting the same cell in more than one section, we counted every 11th section (100 μm apart). Immunopositive cells (those showing red or green fluorescence) were counted using the counting function in Photoshop CS3, and expressed as a percentage of the total number of cells (those showing blue fluorescence) (Li G. et al., 2015). Mean fluorescence intensity was used to quantify neurocan and GAP-43 expression, measured using Image J. Mean fluorescence intensity = Integrated Density/Area (Tian et al., 2006). The experiments were performed six independent times.

Nissl Staining

The 5 μm transverse frozen sections were dried and then soaked overnight in a 1:1 mixture of alcohol and chloroform in the dark at 22 ± 1°C. The following day, the sections were rehydrated, and stained in 0.1% cresyl violet solution (Sigma, St. Louis, MO, USA) for 5 min. Differentiation, dehydration, and rinsing was performed as described previously (Li H.-T. et al., 2015). The sections were then mounted with Permount (Beyotime Institute of Biotechnology, Shanghai, China) and observed under a light microscope (Olympus) equipped with a CCD camera (Leica DMI4000B, Germany). Surviving neurons were counted using Photoshop CS3. The experiments were performed six independent times.

Hematoxylin-Eosin Staining

To measure the cavity area of spinal cord tissue in each group after SCI, animals in all groups were sacrificed 4 weeks after injury. Spinal cord tissue was cut into frozen sagittal sections of 5 μm thickness. Spinal cord tissue was prepared, cut into frozen sagittal sections of 5 μm thickness, and stained with hematoxylin-eosin, as described previously (Tian et al., 2006) and examined with a light microscope (Olympus) equipped with a CCD camera (Leica DMI4000B). The maximum area of the cavity in the sagittal sections including the damage epicenter was measured in Photoshop CS3, using the area analysis function. The experiments were performed six independent times.

Statistical Analysis

All data are expressed as mean ± standard deviation (SD), and were analyzed using one-way analysis of variance (ANOVA) with the least significant difference (LSD) *post hoc* test. SPSS version 19.0 was used for all analysis. $P < 0.05$ was considered statistically significant.

RESULTS

Mdivi-1 Inhibits Astroglial Proliferation at 3 Days after SCI

Astrocytes upregulate the expression of GFAP, a widely recognized astrocyte marker, and form a physical barrier at the site of injury that impedes axonal regeneration (Lin et al., 2014). PCNA is known to be a reliable marker of proliferating cells (Tian et al., 2006). We used western blots to investigate astroglial proliferation after Mdivi-1 treatment. GFAP and PCNA expression were significantly greater in the SCI group (0.42 ± 0.08 and 0.40 ± 0.06, respectively) than in the sham group (0.15 ± 0.05 and 0.11 ± 0.03), indicating that astroglial proliferation was induced after SCI ($P < 0.01$) (**Figures 1A–C**). In the Mdivi-1 group (0.26 ± 0.06 and 0.21 ± 0.06), GFAP and PCNA expression were lower than in the SCI group which suggests that Mdivi-1 inhibits astroglial proliferation ($P < 0.01$).

Double immunofluorescence labeling of PCNA/GFAP was performed to confirm astrocyte proliferation, in combination with the nuclear marker DAPI. Thus, proliferative astrocytes were visible as PCNA/GFAP/DAPI-positive cells, showing red dots (PCNA) in a green cells (GFAP) with a blue nucleus (DAPI). Not all GFAP-positive cells were positive for PCNA, and some GFAP-negative cells were positive for PCNA (**Figures 1D–F**). There were more GFAP-positive cells and PCNA-positive astrocytes in the SCI group (0.43 ± 0.06 and 0.59 ± 0.11, respectively) than in the sham group (0.17 ± 0.03 and 0.04 ± 0.02). However, there were fewer GFAP-positive cells and PCNA-positive astrocytes in the Mdivi-1 group (0.25 ± 0.05 and 0.36 ± 0.05) than in the SCI group ($P < 0.01$). These findings indicate that inhibition of mitochondrial division by Mdivi-1 can inhibit astroglial proliferation after SCI.

Mdivi-1 Decreases the Expressions of GFAP and Neurocan at 4 Weeks after SCI

Neurocan is a CSPG produced mainly by astrocytes (Jones et al., 2003; Silver and Miller, 2004). We used Western blots to investigate neurocan expression after SCI with or without Mdivi-1 treatment. GFAP and neurocan expression in the SCI group (0.72 ± 0.12 and 0.62 ± 0.10, respectively) were significantly greater than in the sham group (0.15 ± 0.04 and 0.21 ± 0.04; $P < 0.01$). However, expression of GFAP and neurocan in the Mdivi-1 group (0.33 ± 0.05 and 0.40 ± 0.08, respectively) was lower than in the SCI group. This suggests that Mdivi-1 inhibits

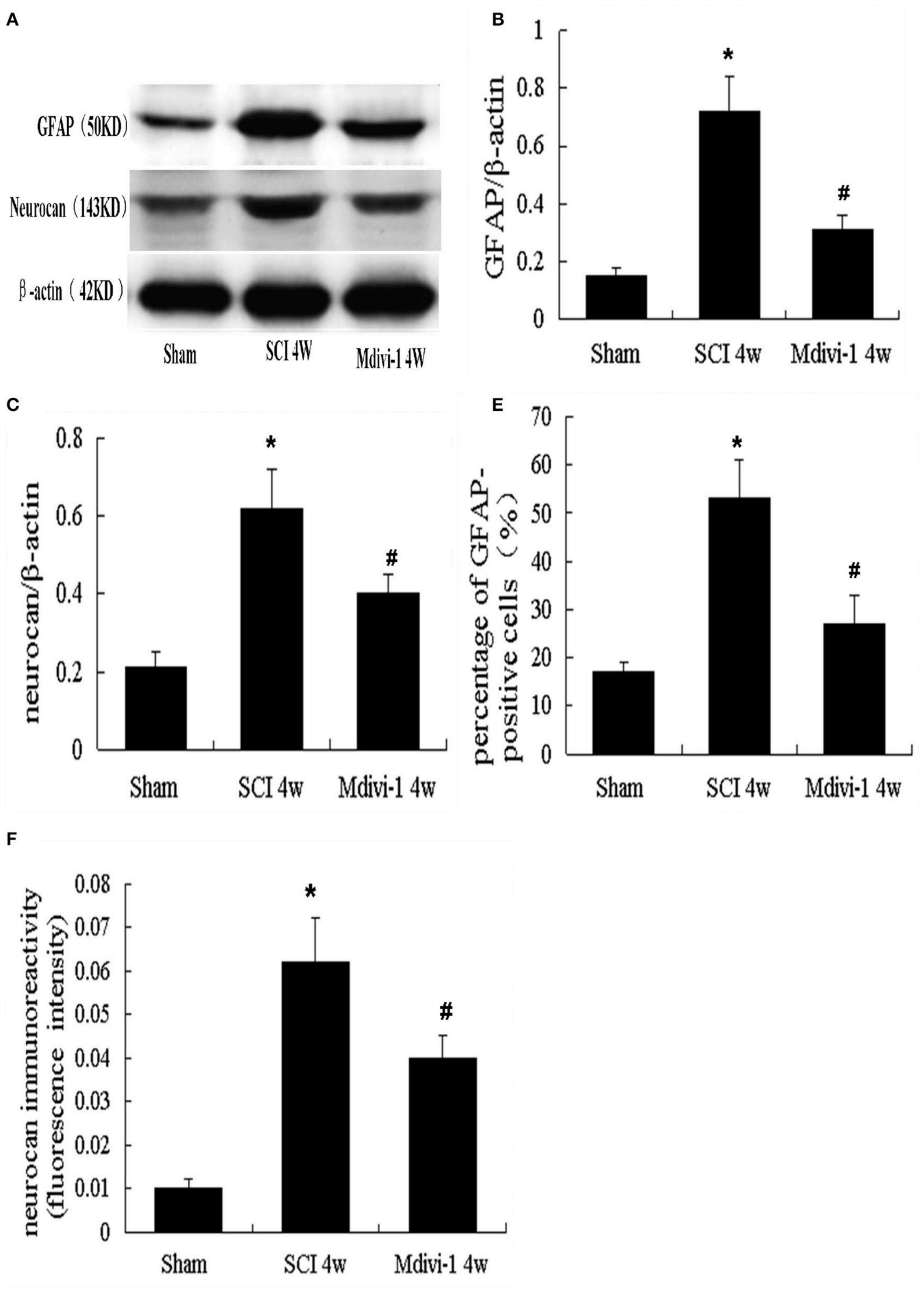

FIGURE 2 | Continued

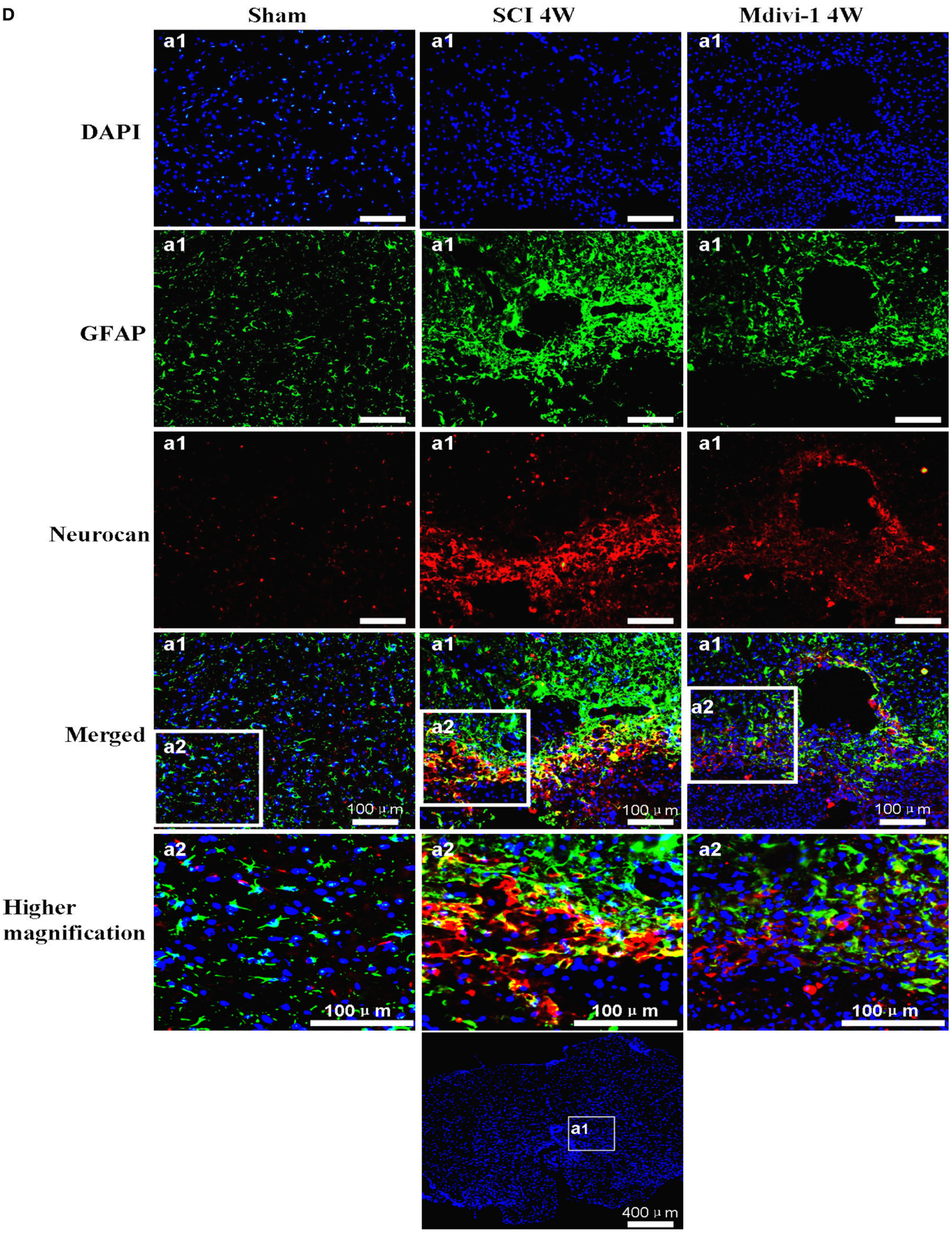

FIGURE 2 | Mdivi-1 decreases the expressions of GFAP and neurocan at 4 weeks after SCI. (A–C) Western blot analysis and quantitative analysis of GFAP **(A,B)** and neurocan **(A,C)** ($n = 6$, respectively). **(D–F)** Neurocan/GFAP/DAPI triple labeling and quantitative analysis of GFAP **(D,E)** and neurocan **(D,F)** in astrocytes ($n = 6$, respectively). Compared with the sham group, the expression of GFAP and neurocan, number of GFAP-positive cells, and mean fluorescence intensity of neurocan were elevated after SCI. GFAP, neurocan expression, number of GFAP-positive cells, and mean fluorescence intensity of neurocan were lower in the Mdivi-1 group than in the SCI group. $^{*}P < 0.01$ vs. Sham. $^{\#}P < 0.01$ vs. SCI.

neurocan production after SCI ($P < 0.01$), which might reduce the biochemical barrier to axonal regeneration (**Figures 2A–C**).

Double immunofluorescence labeling for neurocan and GFAP was performed to further characterize the production and secretion of neurocan in astrocytes after SCI with or without Mdivi-1 treatment. Triple-positive neurocan/GFAP/DAPI-positive cells were observed. Neurocan (red dots) was distributed mainly in the extracellular matrix and cytoplasm of astrocytes (green); nuclei appeared blue. Expression of GFAP and neurocan was lower in the SCI group (0.54 ± 0.10 and 0.064 ± 0.012, respectively) than in the sham group (0.17 ± 0.02 and 0.011 ± 0.003; $P < 0.01$). Furthermore, in the Mdivi-1 group, the number of GFAP-positive cells and mean fluorescence intensity of neurocan (0.26 ± 0.08 and 0.040 ± 0.007, respectively) were lower than in the SCI group ($P < 0.01$). These findings indicate that astrocyte proliferation and neurocan expression and secretion were inhibited by Mdivi-1 after SCI (**Figures 2D–F**).

Mdivi-1 Increases the Expressions of GAP-43 at 4 Weeks after SCI

GAP-43 is a cytoplasmic and membrane-associated protein located mainly in neuronal growth cones and upregulated within growing neurites (Benowitz and Routtenberg, 1997; Irwin and Madsen, 1997). Western blots were used to investigate GAP-43 expression after SCI with or without Mdivi-1 treatment. Compared with the sham group (0.20 ± 0.06), the expression of GAP-43 was significantly greater after SCI (0.50 ± 0.09; $P < 0.01$). Moreover, GAP-43 expression was greater in the Mdivi-1 group (0.75 ± 0.15) than in the SCI group ($P < 0.01$), which suggests that Mdivi-1 enhances axonal regeneration after SCI (**Figures 3A,B**).

Immunofluorescent staining of GAP-43 was performed to further identify it in neurons after Mdivi-1 treatment. Higher magnification indicated that the GAP-43/NeuN/DAPI triple-labeled neurons had green, punctate GAP-43 dots in red neurons with a blue nucleus. The percentage of neurons and mean fluorescence intensity of GAP-43 were calculated. Not all neurons were positive for GAP-43 (**Figure 3C**). In the SCI group, the percentage of neurons (3.6 ± 0.7) was lower than in the sham group (8.6 ± 1.1), whereas the mean fluorescence intensity of GAP-43 was greater (0.022 ± 0.005) than in the sham group (0.009 ± 0.003; $P < 0.01$). Compared with the SCI group, the percentage of neurons and GAP-43 expression were both higher in the Mdivi-1 group (5.7 ± 0.9 and 0.049 ± 0.009; $P < 0.01$). These findings provide evidence that axonal regeneration and neuronal survival were enhanced by Mdivi-1 after SCI (**Figures 3C–E**).

Mdivi-1 Decreases the Number of Surviving Neurons at 4 Weeks after SCI

To determine the effects of Mdivi-1 on spinal cord tissue, Nissl staining was used to illustrate the injured areas in the different groups. The surviving neurons in the sections were subsequently

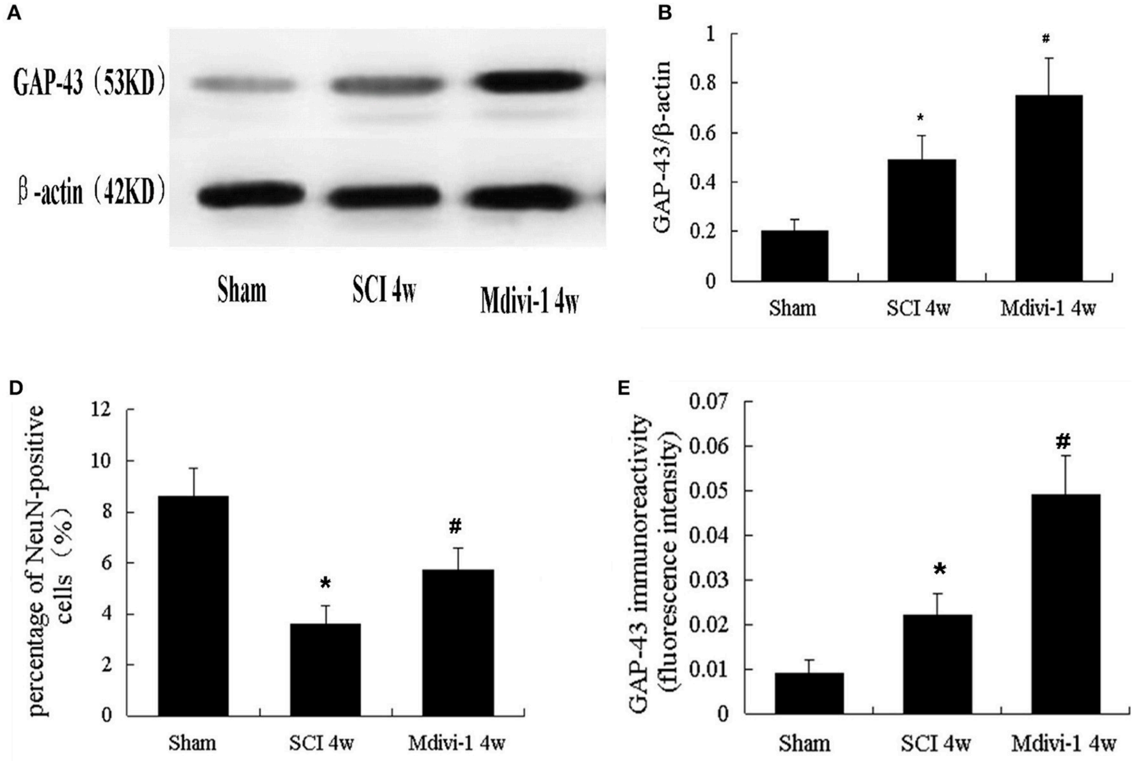

FIGURE 3 | Continued

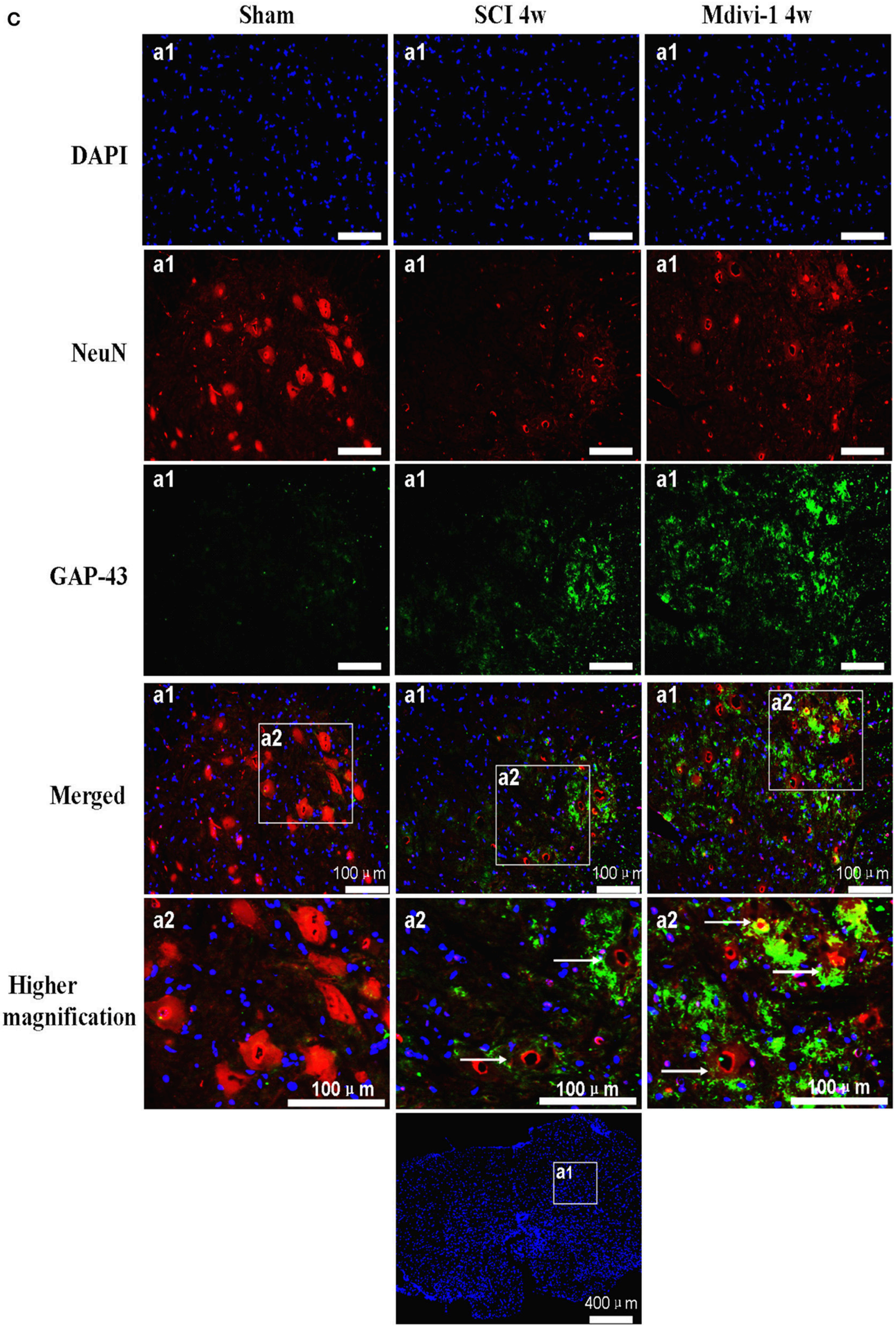

FIGURE 3 | Mdivi-1 increases the expressions of GAP-43 at 4 weeks after SCI. (A,B) Western blot analysis **(A)** and quantitative analysis of GAP-43 **(B)** ($n = 6$, respectively). **(C–E)** Cells triple-labeled for GAP-43/NeuN/DAPI and quantification of NeuN **(C,D)** and GAP-43 **(C,E)**. White arrows: neurons indicate GAP-43. Expression of GAP-43 was greater in the SCI group than in the sham group, and the percentage of neurons was lower. Compared with the SCI group, Mdivi-1 can increase GAP-43 expression and the percentage of surviving neurons. $^{*}P < 0.01$ vs. sham. $^{\#}P < 0.01$ vs. SCI.

examined at a higher magnification. The number of surviving neurons was lower in the SCI group than in the sham group ($P < 0.01$); however, the number of surviving neurons was greater in the Mdivi-1 group than in the SCI group ($P < 0.01$). These results demonstrate the significant protective effect of Mdivi-1 (**Figure 4**).

Mdivi-1 Decreases the Cavity Formation at 4 Weeks after SCI

The size of the cavity in the spinal cord can reflect astroglial scar formation after SCI (Tian et al., 2006). Compared with the sham group (0.20 ± 0.10 mm^2), the cavity area was significantly greater after SCI (4.5 ± 0.8 mm^2, $P < 0.01$). Compared with the SCI group, the cavity area was smaller in the Mdivi-1 group (2.9 ± 0.6 mm^2, $P < 0.01$), which suggests that Mdivi-1 inhibits astroglial scar formation after SCI (**Figure 5**).

Mdivi-1 Improves the Hindlimb Motor Function at 3 Days and 4 Weeks after SCI

The BBB locomotor rating scores were assessed at 3 days and 4 weeks after SCI. Compared with the sham group (3 days, 20.6 ± 0.6; 4 weeks, 20.6 ± 0.6), the BBB scores were significantly lower after SCI (2.0 ± 0.8 and 9.3 ± 1.1, respectively; $P < 0.01$). Compared with the SCI group, the BBB scores were significantly greater in the Mdivi-1 group at 3 days and 4 weeks (4.0 ± 0.8 and 13 ± 1.3, respectively; $P < 0.01$). These findings support the neuroprotective effect of Mdivi-1 (**Figure 6**).

DISCUSSION

Astrocytes are the most abundant glial cells in the central nervous system (CNS). In chronic SCI, they become hypertrophic and proliferative (Wilhelmsson et al., 2006), upregulate the production of inhibitory CSPG (Bradbury et al., 2002; Su et al.,

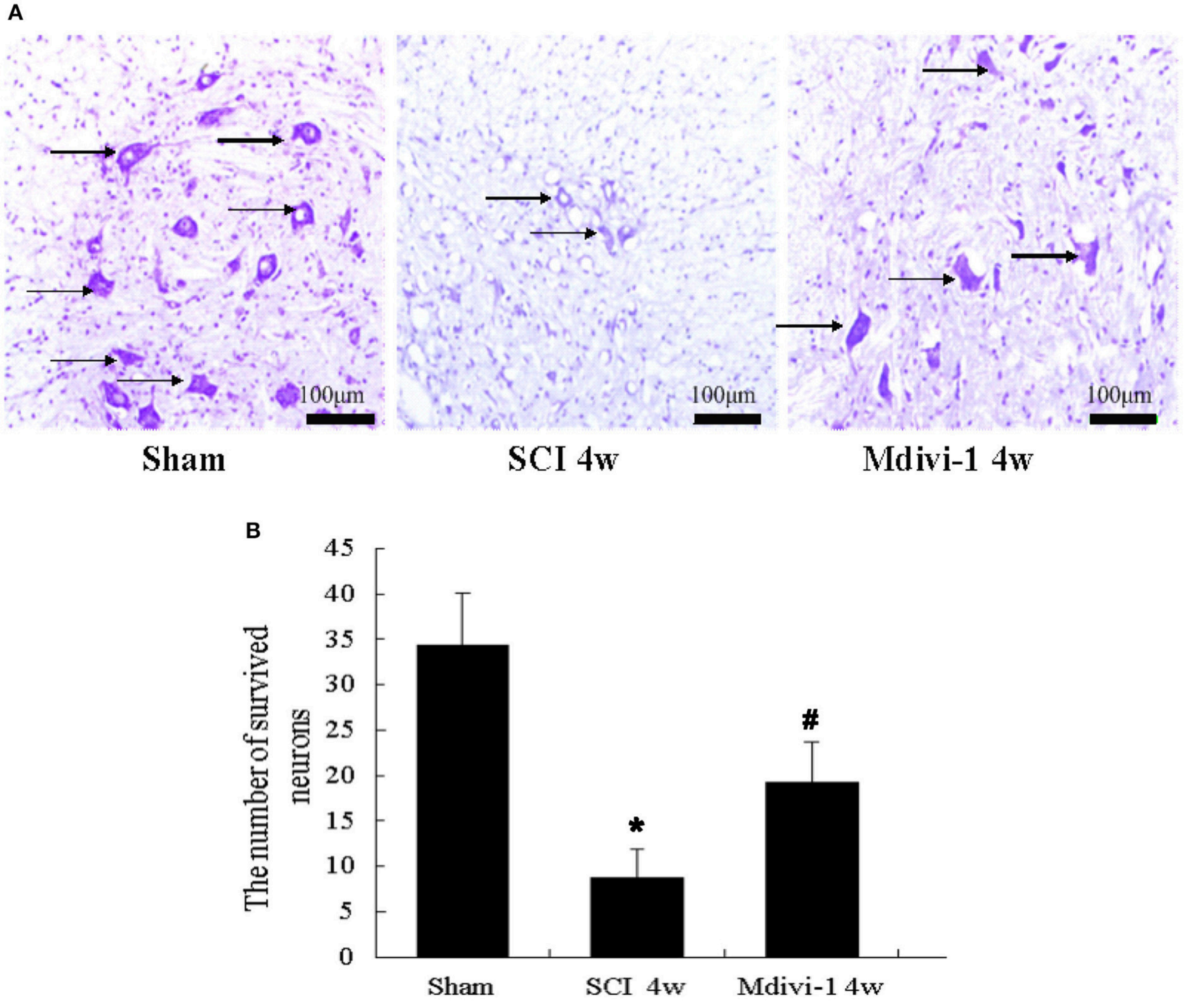

FIGURE 4 | Mdivi-1 decreases the number of surviving neurons at 4 weeks after SCI. (A) Histological assessments of spinal cord tissue. Black arrows: surviving neurons. **(B)** Quantification of surviving neurons. The number of surviving neurons was lower in the SCI group than in the sham group. Compared with the SCI group, the number of surviving neurons was lower in the Mdivi-1 group. $^*P < 0.01$ vs. sham. $^\#P < 0.01$ vs. SCI.

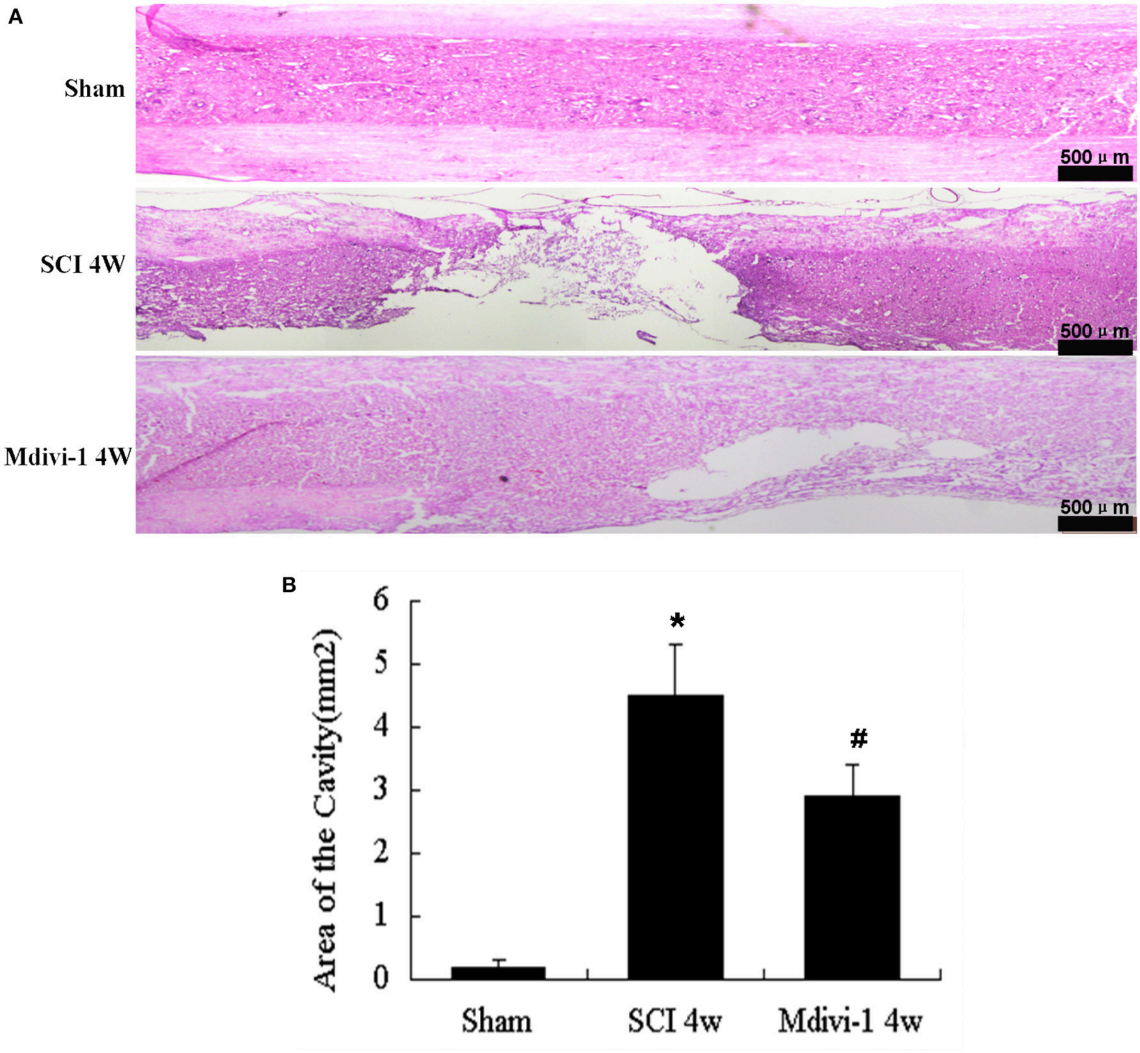

FIGURE 5 | Mdivi-1 decreases the cavity formation at 4 weeks after SCI. (A) Representative hematoxylin-eosin staining micrographs show cavity formation in each group after SCI. **(B)** Quantification of cavity area shows that Mdivi-1-treated animals had significantly smaller spinal cord cavities compared than those in the SCI group. $^{*}P < 0.01$ vs. Sham. $^{\#}P < 0.01$ vs. SCI.

2011), and eventually contribute to the formation of an astroglial scar that might hinder axonal regeneration in chronic SCI (Lin et al., 2014). Finding effective ways to inhibit glial scar formation and enhance axon regeneration is essential after SCI. To our knowledge, this study is the first study to confirm that Mdivi-1 inhibits astrocyte activation and astroglial scar formation, and contributes to axonal regeneration as well as recovery of motor function after SCI in rats.

Cell cycle regulation is a relatively new research direction in nerve repair therapy (Zhu et al., 2007). Restarting of the cell cycle plays a key role in astroglial activation and proliferation after SCI (Byrnes et al., 2007; Zhu et al., 2007; Lin et al., 2014). Administration of olomoucine, flavopiridol, and MEK can decrease neuronal cell death and inhibit glial proliferation after SCI. These agents reduce axon growth-inhibitory molecule expression and astroglial scar formation at the site of injury by inhibiting the cell cycle *in vivo* (Tian et al., 2006; Byrnes et al., 2007; Li et al., 2011; Wu et al., 2011; Lin et al., 2014). Moreover, cell cycle inhibition protects against traumatic brain injury by reducing glial proliferation and scar formation in rats (Di Giovanni et al., 2005). Results from an astrocyte scratch-wound model showed that scratch damage can significantly promote the proliferation of cultured astrocytes and increase the number of 5-bromo-deoxyuridine-positive cells *in vitro* (Yang et al., 2009). Cyclins and PCNA expression increased significantly after SCI (Tian et al., 2006), suggesting that astrocytes proliferate and then form a dense glial scar in the damaged area, thus preventing normal reconstruction of axons and functional recovery after SCI *in vivo*. Previous studies found that PCNA expression peaked 3 days after SCI (Tian et al., 2006), and that changes in glial scars and motor function reached a plateau in rats at 4 weeks after SCI (Hu et al., 2010; Li et al., 2011). So we chose 3 days and

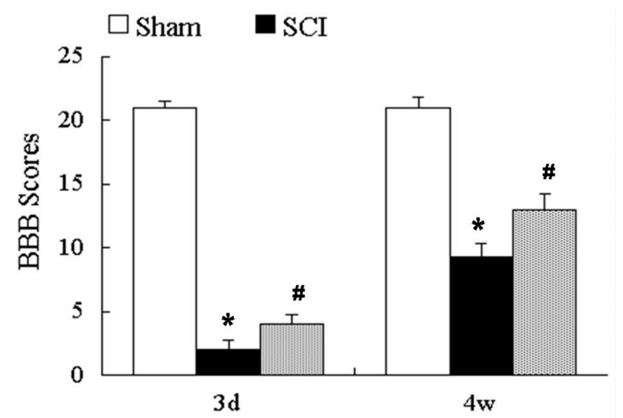

FIGURE 6 | Mdivi-1 improves the hindlimb motor function at 3 days and 4 weeks after SCI. BBB scores showed that Mdivi-1 reduced hindlimb motor dysfunction at 3 days and 4 weeks after SCI. $^*P < 0.01$ vs. Sham. $^\#P < 0.01$ vs. SCI.

4 weeks after SCI as our evaluation points. Western blot and immunofluorescence double labeling showed that the expression of PCNA increased significantly at 3 days after SCI in rats, which is consistent with previous studies (Tian et al., 2006). Notably, Mdivi-1 significantly inhibited the expression of PCNA at 3 days after SCI in rats, suggesting that inhibiting mitochondrial division after SCI can inhibit the cell cycle progression of astrocytes, and supporting previous studies (Mitra et al., 2009; Qian et al., 2012). Surprisingly, we also found some PCNA-immunoreactivity in GFAP-negative cells that might be microglia or endothelial cells, which further supports previous studies (Krum and Khaibullina, 2003; Tian et al., 2007).

Following SCI, astrocytes are activated and show hypertrophy of the cell body, abnormal proliferation, and upregulation of GFAP (Tang et al., 2003; Bramanti et al., 2010). They rapidly secrete a variety of inhibitory proteins, especially CSPGs, and ultimately form the glial scar tissue in the SCI lesion, which is the physical and biochemical barrier of repair, and is not conducive to the growth or regeneration of axons (Tang et al., 2003; Yuan and He, 2013). In addition to an increase in astrocyte number at the lesion site in response to SCI injury, GFAP production, a feature of astrogliosis, also increases, and its production can reflect the changes in number or activation degree of astrocytes (Jones et al., 2003). Our present Western blot and immunofluorescence studies show that astrocytes undergo changes in morphology and GFAP expression at 3 days and 4 weeks after SCI, which supports previous studies (Yang et al., 2009; Bramanti et al., 2010). Importantly, Mdivi-1 significantly inhibited the expression of GFAP and astrocyte performance after SCI, suggesting that inhibition of mitochondrial division can inhibit astroglial proliferation and hypertrophy after SCI.

CSPGs are extracellular matrix molecules that are widely expressed throughout the developing and adult CNS (Bradbury et al., 2002). *In vitro* studies demonstrate their potential to restrict neurite outgrowth, and it is believed that CSPGs also inhibit axonal regeneration after CNS injury *in vivo* (Yuan and He, 2013). After SCI, members of the CSPG family, including neurocan, brevican, versican and NG2, are upregulated, and might have important roles in limiting axonal regeneration (Jones et al., 2003; Tang et al., 2003). Previous studies have reported that neurocan, secreted by reactive astrocytes, increases within 2 days in injured spinal cord, peaks at 2 weeks, and remains persistently elevated for 4 weeks after SCI (Bradbury et al., 2002; Jones et al., 2003). Our Western blot and immunofluorescence results showed that neurocan expression was significantly increased 4 weeks after SCI, whereas Mdivi-1 inhibited the expression of neurocan significantly. This indicates that inhibition of mitochondrial fission may inhibit astrocyte proliferation, then inhibit the expression, and secretion of neurocan, and finally inhibit the formation of biochemical barriers after SCI. Moreover, results of the hematoxylin-eosin stain show that Mdivi-1 significantly reduces cavity formation after SCI, suggesting that inhibition of mitochondrial fission can also inhibit the formation of the physical glial barrier after SCI. These results support previous studies (Byrnes et al., 2007; Zhu et al., 2007; DiMauro and Schon, 2008; Lin et al., 2014) and contribute to our understanding of the relationship between mitochondrial fission and astroglial proliferation after SCI.

Our previous results indicate that Mdivi-1 plays a role in reducing apoptosis by inhibiting the translocation of dynamin-related protein 1 (Drp1) and Bax to the mitochondria (Li G. et al., 2015). At the same time, Liu et al. (2015) reported that Mdivi-1 may be an effective therapeutic agent for spinal cord ischemia–reperfusion injury via activation of large-conductance Ca^{2+}-activated K$^+$ channels as well as reduction of oxidative stress, mitochondrial dysfunction and neuronal apoptosis. To further confirm the protective effect of Mdivi-1 *in vivo*, we investigated the survival of neurons directly by immunofluorescence staining and Nissl staining. Spinal cord neurons were marked by NeuN (the neuronal marker). The percentage of neurons via immunofluorescence staining and the number of surviving neurons via Nissl staining decreased significantly at 4 weeks after SCI and increased in the Mdivi-1 group, which supports our previous study. In the present study, we found that Mdivi-1 can inhibit astroglial proliferation and increase the number of surviving neurons, but the relationship between these two results needs further study. In addition, the upregulation of GAP-43 is considered a useful marker of neurite growth or sprouting after SCI (Benowitz and Routtenberg, 1997; Irwin and Madsen, 1997). Notably, in this study, we found that SCI alone led to a limited upregulation of GAP-43 expression. Moreover, the Mdivi-1-treated group had a significantly higher expression of GAP-43 at 4 weeks after SCI, which may be related to the promotion of neuronal survival. However, we cannot rule out the possibility that the increase in GAP-43 by Mdivi-1 is related to the inhibition of astroglial scar formation (Lin et al., 2014). We also found that Mdivi-1 significantly mitigated functional deficits as assessed by the measures of the BBB scale. Our data indicated that Mdivi-1 administration has a protective effect after SCI, which supports previous studies (Li G. et al., 2015; Liu et al., 2015).

In cancer growth, mitochondria grow continuously throughout the cell cycle, and the organization of the mitochondrial network is sophisticatedly controlled across the different phases of the cell cycle (Qian et al., 2013). At the G1/S border, mitochondria form a single, giant tubular network, which is associated with increased energy production in order to prepare for the initiation of the highly energy consuming process—DNA synthesis (Mitra et al., 2009). In addition, such mitochondrial hyperfusion also facilitates the mixing of mitochondrial contents such as mtDNA between adjacent mitochondria, to maintain a homogenous mitochondrial network within the cell, thus ensuring proper inheritance following cellular division. The formation of a highly connected mitochondrial network at G1/S border is transient. During the subsequent S, G2 and M phases, the hyperfused mitochondrial network is then disassembled and becomes increasingly fragmented (Qian et al., 2013). Notably, mitochondrial fission disorders can lead to sustained mitochondrial hyperfusion beyond the G1/S border, which further inhibits mitosis and ultimately cell proliferation (Qian et al., 2012). Our results indicate that Mdivi-1 inhibits astrocyte activation after SCI. However, whether the effects of Mdivi-1 on the astroglial phenotype result from the inhibition of mitochondrial fission in astrocytes directly, or indirectly via Mdivi's protective effect against neuronal apoptosis, warrants further investigation. We will examine the detailed mechanism of Drp1-mediated mitochondrial fission during astroglial division using gene knockout and transfection technology, and confirm whether Mdivi-1 can inhibit mitochondrial fission in astroglia in the astrocyte scratch-wound model.

In summary, this is the first study to demonstrate that Mdivi-1 inhibits astrocyte activation and astroglial scar formation, and contributes to the axonal regeneration after SCI in rats. This indicates that regulation of mitochondrial dynamics maybe an effective therapeutic target for SCI. However, as the effect of Mdivi-1 is not cell specific, we cannot rule out the possibility that neuroprotection by Mdivi-1 is associated with the inhibition of other proliferating cells, such as microglia and endothelial cells, in the spinal cord after SCI. Further research is needed to clarify these issues.

AUTHOR CONTRIBUTIONS

GLv and ZF designed and supervised the project. GLi, FS, YW, LB, WG, and YB performed research; YC analyzed data and GLi wrote the article.

ACKNOWLEDGMENTS

This research was supported by the National Natural Science Foundation of China (Grant No. 81272074, 81501659), Program for Liaoning Excellent Talents in University (Grant No. 2014091), and Natural Science Foundation of Liaoning Province (Grant No. 201602277).

REFERENCES

Benowitz, L. I., and Routtenberg, A. (1997). GAP-43: an intrinsic determinant of neuronal development and plasticity. *Trends Neurosci.* 20, 84–91.

Bradbury, E. J., Moon, L. D., Popat, R. J., King, V. R., Bennett, G. S., Patel, P. N., et al. (2002). Chondroitinase ABC promotes functional recovery after spinal cord injury. *Nature* 416, 636–640. doi: 10.1038/416636a

Bramanti, V., Tomassoni, D., Avitabile, M., Amenta, F., and Avola, R. (2010). Biomarkers of glial cell proliferation and differentiation in culture. *Front. Biosci. (Schol. Ed).* 2, 558–570. doi: 10.2741/85

Byrnes, K. R., Stoica, B. A., Fricke, S., Di Giovanni, S., and Faden, A. I. (2007). Cell cycle activation contributes to post-mitotic cell death and secondary damage after spinal cord injury. *Brain* 130, 2977–2992. doi: 10.1093/brain/awm179

Cao, Y., Lv, G., Wang, Y. S., Fan, Z. K., Bi, Y. L., Zhao, L., et al. (2013). Mitochondrial fusion and fission after spinal sacord injury in rats. *Brain Res.* 1522, 59–66. doi: 10.1016/j.brainres.2013.05.033

Cui, M., Ding, H., Chen, F., Zhao, Y., Yang, Q., and Dong, Q. (2016). Mdivi-1 protects against ischemic brain injury via elevating extracellular adenosine in a cAMP/CREB-CD39-dependent manner. *Mol. Neurobiol.* 53, 240–253. doi: 10.1007/s12035-014-9002-4

Di Giovanni, S., Movsesyan, V., Ahmed, F., Cernak, I., Schinelli, S., Stoica, B., et al. (2005). Cell cycle inhibition provides neuroprotection and reduces glial proliferation and scar formation after traumatic brain injury. *Proc. Natl. Acad. Sci. U.S.A.* 102, 8333–8338. doi: 10.1073/pnas.0500989102

DiMauro, S., and Schon, E. A. (2008). Mitochondrial disorders in the nervous system. *Annu. Rev. Neurosci.* 31, 91–123. doi: 10.1146/annurev.neuro.30.051606.094302

Gervasi, N. M., Kwok, J. C., and Fawcett, J. W. (2008). Role of extracellular factors in axon regeneration in the CNS: implications for therapy. *Regen. Med.* 3, 907–923. doi: 10.2217/17460751.3.6.907

Green, D. R., and Van Houten, B. (2011). SnapShot: mitochondrial quality control. *Cell* 147:e1. doi: 10.1016/j.cell.2011.10.036

Hu, R., Zhou, J., Luo, C., Lin, J., Wang, X., Li, X., et al. (2010). Glial scar and neuroregeneration: histological, functional, and magnetic resonance imaging analysis in chronic spinal cord injury. *J. Neurosurg. Spine* 13, 169–180. doi: 10.3171/2010.3.SPINE09190

Irwin, N., and Madsen, J. R. (1997). Molecular biology of axonal outgrowth. 1. Growth cones and GAP-43. *Pediatr. Neurosurg.* 27, 113–120. doi: 10.1159/000121247

Jefferson, S. C., Tester, N. J., and Howland, D. R. (2011). Chondroitinase ABC promotes recovery of adaptive limb movements and enhances axonal growth caudal to a spinal hemisection. *J. Neurosci.* 31, 5710–5720. doi: 10.1523/JNEUROSCI.4459-10.2011

Jones, L. L., Margolis, R. U., and Tuszynski, M. H. (2003). The chondroitin sulfate proteoglycans neurocan, brevican, phosphacan, and versican are differentially regulated following spinal cord injury. *Exp. Neurol.* 182, 399–411. doi: 10.1016/S0014-4886(03)00087-6

Karimi-Abdolrezaee, S., and Billakanti, R. (2012). Reactive astrogliosis after spinal cord injury-beneficial and detrimental effects. *Mol. Neurobiol.* 46, 251–264. doi: 10.1007/s12035-012-8287-4

Krum, J. M., and Khaibullina, A. (2003). Inhibition of endogenous VEGF impedes revascularization and astroglial proliferation: roles for VEGF in brain repair. *Exp. Neurol.* 181, 241–257. doi: 10.1016/S0014-4886(03)00039-6

Li, G., Jia, Z., Cao, Y., Wang, Y., Li, H., Zhang, Z., et al. (2015). Mitochondrial division inhibitor 1 ameliorates mitochondrial injury, apoptosis, and motor dysfunction after acute spinal cord injury in rats. *Neurochem. Res.* 40, 1379–1392. doi: 10.1007/s11064-015-1604-3

Li, H.-T., Zhao, X.-Z., Zhang, X.-R., Li, G., Jia, Z.-Q., Sun, P., et al. (2015). Exendin-4 enhances motor function recovery via promotion of autophagy and inhibition of neuronal apoptosis after spinal cord injury in rats. *Mol. Neurobiol.* 53, 4073–4082. doi: 10.1007/s12035-015-9327-7

Li, Z. W., Tang, R. H., Zhang, J. P., Tang, Z. P., Qu, W. S., Zhu, W. H., et al. (2011). Inhibiting epidermal growth factor receptor attenuates reactive astrogliosis and improves functional outcome after spinal cord injury in rats. *Neurochem. Int.* 58, 812–819. doi: 10.1016/j.neuint.2011.03.007

Lin, B., Xu, Y., Zhang, B., He, Y., Yan, Y., and He, M. C. (2014). MEK inhibition reduces glial scar formation and promotes the recovery of sensorimotor function in rats following spinal cord injury. *Exp. Ther. Med.* 7, 66–72. doi: 10.3892/etm.2013.1371

Liu, J. M., Yi, Z., Liu, S. Z., Chang, J. H., Dang, X. B., Li, Q. Y., et al. (2015). The mitochondrial division inhibitor mdivi-1 attenuates spinal cord ischemia-reperfusion injury both *in vitro* and *in vivo*: involvement of BK channels. *Brain Res.* 1619, 155–165. doi: 10.1016/j.brainres.2015.03.033

Mitra, K., Wunder, C., Roysam, B., Lin, G., and Lippincott-Schwartz, J. (2009). A hyperfused mitochondrial state achieved at G1-S regulates cyclin E buildup and entry into S phase. *Proc. Natl. Acad. Sci. U.S.A.* 106, 11960–11965. doi: 10.1073/pnas.0904875106

Park, S. W., Kim, K. Y., Lindsey, J. D., Dai, Y., Heo, H., Nguyen, D. H., et al. (2011). A selective inhibitor of drp1, mdivi-1, increases retinal ganglion cell survival in acute ischemic mouse retina. *Invest. Ophthalmol. Vis. Sci.* 52, 2837–2843. doi: 10.1167/iovs.09-5010

Qian, W., Choi, S., Gibson, G. A., Watkins, S. C., Bakkenist, C. J., and Van Houten, B. (2012). Mitochondrial hyperfusion induced by loss of the fission protein Drp1 causes ATM-dependent G2/M arrest and aneuploidy through DNA replication stress. *J. Cell Sci.* 125, 5745–5757. doi: 10.1242/jcs.109769

Qian, W., Wang, J., and Van Houten, B. (2013). The role of dynamin-related protein 1 in cancer growth: a promising therapeutic target? *Expert Opin. Ther. Targets* 17, 997–1001. doi: 10.1517/14728222.2013.823160

Silver, J., and Miller, J. H. (2004). Regeneration beyond the glial scar. *Nat. Rev. Neurosci.* 5, 146–156. doi: 10.1038/nrn1326

Su, Z., Yuan, Y., Chen, J., Zhu, Y., Qiu, Y., Zhu, F., et al. (2011). Reactive astrocytes inhibit the survival and differentiation of oligodendrocyte precursor cells by secreted TNF-α. *J. Neurotrauma* 28, 1089–1100. doi: 10.1089/neu.2010.1597

Tanaka, A., and Youle, R. J. (2008). A chemical inhibitor of DRP1 uncouples mitochondrial fission and apoptosis. *Mol. Cell* 29, 409–410. doi: 10.1016/j.molcel.2008.02.005

Tang, X., Davies, J. E., and Davies, S. J. (2003). Changes in distribution, cell associations, and protein expression levels of NG2, neurocan, phosphacan, brevican, versican V2, and tenascin-C during acute to chronic maturation of spinal cord scar tissue. *J. Neurosci. Res.* 71, 427–444. doi: 10.1002/jnr.10523

Tian, D. S., Xie, M. J., Yu, Z. Y., Zhang, Q., Wang, Y. H., Chen, B., et al. (2007). Cell cycle inhibition attenuates microglia induced inflammatory response and alleviates neuronal cell death after spinal cord injury in rats. *Brain Res.* 1135, 177–185. doi: 10.1016/j.brainres.2006.11.085

Tian, D. S., Yu, Z. Y., Xie, M. J., Bu, B. T., Witte, O. W., and Wang, W. (2006). Suppression of astroglial scar formation and enhanced axonal regeneration associated with functional recovery in a spinal cordinjury rat model by the cell cycle inhibitor olomoucine. *J. Neurosci. Res.* 84, 1053–1063. doi: 10.1002/jnr.20999

Tuszynski, M. H., and Steward, O. (2012). Concepts and methods for the study of axonal regeneration in the CNS. *Neuron* 74, 777–791. doi: 10.1016/j.neuron.2012.05.006

Wang, J., Hansen, K., Edwards, R., Van Houten, B., and Qian, W. (2015). Mitochondrial division inhibitor 1 (mdivi-1) enhances death receptor-mediated apoptosis in human ovarian cancer cells. *Biochem. Biophys. Res. Commun.* 456, 7–12. doi: 10.1016/j.bbrc.2014.11.010

Wilhelmsson, U., Bushong, E. A., Price, D. L., Smarr, B. L., Phung, V., Terada, M., et al. (2006). Redefining the concept of reactive astrocytes as cells that remain within their unique domains upon reaction to injury. *Proc. Natl. Acad. Sci. U.S.A.* 103, 17513–17518. doi: 10.1073/pnas.0602841103

Wu, J., Stoica, B. A., and Faden, A. I. (2011). Cell cycle activation and spinal cord injury. *Neurotherapeutics* 8, 221–228. doi: 10.1007/s13311-011-0028-2

Xie, N., Wang, C., Lian, Y., Zhang, H., Wu, C., and Zhang, Q. (2013). A selective inhibitor of Drp1, mdivi-1, protects against cell death of hippocampal neurons in pilocarpine-induced seizures in rats. *Neurosci. Lett.* 545, 64–68. doi: 10.1016/j.neulet.2013.04.026

Yang, H., Cheng, X. P., Li, J. W., Yao, Q., and Ju, G. (2009). De-differentiation response of cultured astrocytes to injury induced by scratch or conditioned culture medium of scratch-insulted astrocytes. *Cell. Mol. Neurobiol.* 29, 455–473. doi: 10.1007/s10571-008-9337-3

Yiu, G., and He, Z. (2006). Glial inhibition of CNS axon regeneration. *Nat. Rev. Neurosci.* 7, 617–627. doi: 10.1038/nrn1956

Yuan, Y. M., and He, C. (2013). The glial scar in spinal cord injury and repair. *Neurosci. Bull.* 29, 421–435. doi: 10.1007/s12264-013-1358-3

Zhao, J., Zhang, J., Yu, M., Xie, Y., Huang, Y., Wolff, D. W., et al. (2013). Mitochondrial dynamics regulates migration and invasion of breast cancer cells. *Oncogene* 32, 4814–4824. doi: 10.1038/onc.2012.494

Zhu, Z., Zhang, Q., Yu, Z., Zhang, L., Tian, D., Zhu, S., et al. (2007). Inhibiting cell cycle progression reduces reactive astrogliosis initiated by scratch injury *in vitro* and by cerebral ischemia *in vivo*. *Glia* 55, 546–558. doi: 10.1002/glia.20476

Conflict of Interest Statement: The authors declare that the research was conducted in the absence of any commercial or financial relationships that could be construed as a potential conflict of interest.

frontiers
in Cellular Neuroscience

REVIEW
published: 11 January 2018
doi: 10.3389/fncel.2017.00430

Biomaterial-Supported Cell Transplantation Treatments for Spinal Cord Injury: Challenges and Perspectives

Shengwen Liu[1, 2], **Thomas Schackel**[1], **Norbert Weidner**[1] **and Radhika Puttagunta**[1]*

[1] *Spinal Cord Injury Center, Heidelberg University Hospital, Heidelberg, Germany,* [2] *Department of Neurosurgery, Tongji Hospital, Tongji Medical College, Huazhong University of Science and Technology, Wuhan, China*

Spinal cord injury (SCI), resulting in para- and tetraplegia caused by the partial or complete disruption of descending motor and ascending sensory neurons, represents a complex neurological condition that remains incurable. Following SCI, numerous obstacles comprising of the loss of neural tissue (neurons, astrocytes, and oligodendrocytes), formation of a cavity, inflammation, loss of neuronal circuitry and function must be overcome. Given the multifaceted primary and secondary injury events that occur with SCI treatment options are likely to require combinatorial therapies. While several methods have been explored, only the intersection of two, cell transplantation and biomaterial implantation, will be addressed in detail here. Owing to the constant advance of cell culture technologies, cell-based transplantation has come to the forefront of SCI treatment in order to replace/protect damaged tissue and provide physical as well as trophic support for axonal regrowth. Biomaterial scaffolds provide cells with a protected environment from the surrounding lesion, in addition to bridging extensive damage and providing physical and directional support for axonal regrowth. Moreover, in this combinatorial approach cell transplantation improves scaffold integration and therefore regenerative growth potential. Here, we review the advances in combinatorial therapies of Schwann cells (SCs), astrocytes, olfactory ensheathing cells (OECs), mesenchymal stem cells, as well as neural stem and progenitor cells (NSPCs) with various biomaterial scaffolds.

Keywords: cell transplantation, biomaterial scaffolds, spinal cord injury, axonal regeneration, combinatorial therapy

Edited by:
Vann Bennett,
Howard Hughes Medical Institute (HHMI), United States

Reviewed by:
Gregory W. J. Hawryluk,
University of Utah, United States
Florence Evelyne Perrin,
Université de Montpellier, France

****Correspondence:***
Radhika Puttagunta
radhika.puttagunta@med.uni-heidelberg.de

Received: *21 August 2017*
Accepted: *20 December 2017*
Published: *11 January 2018*

Citation:
Liu S, Schackel T, Weidner N and Puttagunta R (2018) Biomaterial-Supported Cell Transplantation Treatments for Spinal Cord Injury: Challenges and Perspectives.
Front. Cell. Neurosci. 11:430.
doi: 10.3389/fncel.2017.00430

INTRODUCTION

Traumatic spinal cord injury (SCI) results in the disruption of neuronal circuitry leading to the partial or complete loss of motor control, autonomic function and sensory input. Paraplegic or tetraplegic patients must also contend with chronic consequences ranging from spasticity, neuropathic pain, bladder and bowel dysfunction, pressure ulcers, respiratory and cardiovascular complications which significantly decreases quality of life. World-wide SCI has an annual incidence ranging from 20 to 30 patients per million people (Lee et al., 2014; Singh et al., 2014; Jain et al., 2015; Jazayeri et al., 2015). However, to date there is no effective SCI therapy that can entirely restore neurological deficits. Such therapies must address various complex obstacles that develop after SCI, in particular, cyst formation, neural cell death, a growth-inhibitory microenvironment, scar formation, demyelination, and the disruption of the blood supply (Silva et al., 2014). Although, any treatment option that allows a patient to partially regain lost neuronal circuitry, whether it be motor, sensory or autonomic, will prove to be invaluably beneficial.

In previous decades, a myriad of experimental studies have been conducted to develop potential treatment options for SCI patients. Many studies showed a certain degree of morphological changes partially accompanied by behavioral improvements in various animal models (Fouad et al., 2005; Blesch and Tuszynski, 2009; Franz et al., 2012; McCall et al., 2012; Zhao et al., 2013; Danilov and Steward, 2015; Gomes-Osman et al., 2016; Kadoya et al., 2016). Amongst these studies, cell-based transplantation has been considered as a promising therapeutic strategy due to: (1) direct replacement of the damaged neural tissue, (2) neuroprotective properties for spared neuronal connections, and (3) providing a permissive and supportive cellular growth substrate for axonal regrowth and/or plasticity (Ohta et al., 2004; Feron et al., 2005; Granger et al., 2014; Kanno et al., 2015). Obstacles for cell-based transplantation therapy remain to be the low survival rates of the grafted cells after transplantation into the injured spinal cord, retention of grafted cell at the lesion site without migration, filling the lesion cavity that has formed as well as directional guidance of axonal growth (Pearse and Barakat, 2006; Pearse et al., 2007; Parr et al., 2008; Takahashi et al., 2011). Although a huge effort has been made to modify delivery mechanisms and surgical techniques, success has been modest and relatively inconsistent. In addition to the beneficial effects stated above, some drawbacks of cell transplantation must also be stated and further explored, including tumorgenic formation (Matsuda et al., 2009; Fu et al., 2012; Liu et al., 2013), maladaptive plasticity such as pain hypersensibility (Hofstetter et al., 2005; Macias et al., 2006; Davies et al., 2008), non-beneficial differentiation or dedifferentiation (Hill et al., 2004; Lepore et al., 2004), increased immunoreactivity to transplanted cells (Swanger et al., 2005), complications arising from surgical delivery (Takahashi et al., 2011) and deficits due to immunosuppression (Antonic et al., 2013). Nonetheless, some candidate cell types have already been investigated in clinical trials in SCI patients such as autologous (cells from the same individual) Schwann cells (SCs) (Anderson et al., 2017), olfactory ensheathing cells (OECs) (Mackay-Sim et al., 2008; Tabakow et al., 2013), bone-marrow mesenchymal stem cells (BMSCs) (Park et al., 2005; Kumar et al., 2009; Karamouzian et al., 2012; Mendonca et al., 2014; Oraee-Yazdani et al., 2016) and different neural stem and progenitor cells (NSPCs) (Shin et al., 2015).

Biomaterials have been combined with various cell types to address the issues of cell viability, cell retention at the lesion site, supportive physical matrix, filling of the lesion cavity as well as mediating directed growth (Atala, 2000; Madigan et al., 2009; Cao et al., 2011; Luo et al., 2016; Ogle et al., 2016). Numerous studies have proven diverse biomaterials to be appropriate delivery vehicles for cells as well as bioactive molecules and drugs in different injury and disease models in the central nervous system (CNS) (Krishna et al., 2013; Führmann et al., 2017).

FUNCTION OF CELL-SEEDED BIOMATERIALS IN EXPERIMENTAL SCI MODELS

Biomaterial scaffolds can fulfill multiple functions for SCI transplantation approaches: (1) specific three-dimensional microarchitectures can be designed with small "chambers" or aligned channels/fibers suited for cell seeding and axonal growth in a directed linear pattern facilitating substantial axonal growth across the lesion for establishment of synaptic connections (Gros et al., 2010; Gunther et al., 2015a; Onuma-Ukegawa et al., 2015); (2) serves as a physical matrix for cell adhesion and thereby enhancing survival and retention of grafted cells at the lesion site (Hurtado et al., 2006; Olson et al., 2009; Bozkurt et al., 2010; Park et al., 2012) and affect host cell migration (e.g., SCs and astrocytes) (Suzuki et al., 2015); (3) influence the behavior of grafted cells and differentiation (Mekhail et al., 2015); and (4) control the release of encapsulated bio-active molecules (Mothe et al., 2013).

Biomaterials can be fabricated from natural or synthetic polymers and subdivided into three major forms: solid scaffolds, hydrogels and micro-/nanoparticles (Boisserand et al., 2016). Various types of biomaterials have been explored in tissue engineering for SCI repair (**Table 1**). Crosslinking of hydrogels typically increases the overall long-term stability of biomaterials, however this also increases the stiffness and the balance between stiffness and stability is a delicate one for cell adhesion, migration and neuroregenerative work (Khaing et al., 2011; Seyedhassantehrani et al., 2016). Additionally, surface modification with extracellular matrix (ECM) components, e.g., laminin and fibronectin, or synthetic peptides represents another way to improve cell adhesion and survival by generating a less hostile molecular microenvironment within the biomaterial (Miller et al., 2001; Chen et al., 2009). Injectable *in situ* polymerizing hydrogels help to deliver cells and factors directly into a lesion site with less invasive surgical interventions, forming a homogenous three-dimensional matrix mimicking natural ECM microstructure to modulate cell fate (Bidarra et al., 2014; Führmann et al., 2016). Importantly, biomaterials can effectively fill a cystic cavity and bridge the lesion dramatically reducing the number of cells required for transplantation. This is particularly appealing for clinical use since the availability of autologous cells from patients is limited.

The potential of biomaterial application alone in SCI treatment has been explored in numerous pre-clinical studies and now even clinical trials (Carballo-Molina and Velasco, 2015; Siebert et al., 2015; Theodore et al., 2016; Xiao et al., 2016). Fibroglial scarring around the graft is a prominent phenomenom after biomaterial scaffold implantation. Typically, only sparse axons re-enter the caudal host spinal cord, while most are confined within the scar surrounding the implants (Suzuki et al., 2002; Grulova et al., 2015; Gunther et al., 2015b; Pawar et al., 2015a; **Figure 1**). To overcome this barrier without interference with its beneficial roles, targeting inhibitory molecules is one possible solution. For instance, delivery of Chondroitin sulfate proteoglycan (CSPG) cleaving enzyme chondroitinase ABC

TABLE 1 | Biomaterials of different origins used for animal SCI experimentation.

Origin	Biomaterials
Natural	Agarose
	Alginate
	Chitosan
	Collagen
	Fibrin
	Fibronectin
	Gellan gum
	Hyaluronan
	Hyaluronic acid
Synthetic	Calcium sulfate cement
	Oligo[poly(ethylene glycol) fumarate] (OPF)
	Poly(ethylene glycol) (PEG)
	Poly-b-hydroxybutyrate (PHB)
	Poly(2-hydroxyethylmethacrylate) (PHEMA)
	Poly(D, L-lactic acid) (PLA)
	Poly(lactide-co-glycolide) (PLG)
	Poly(lactic-co-glycolic acid) (PLGA)

(ChABC) rostral and caudal to the graft was able to facilitate axonal growth through and beyond the scar (Fouad et al., 2005). Alternatively, cell injections into the host parenchyma around the biomaterial implantation site provide a continous permissive cellular substrate spanning the lesion cavity and biomaterial bridge (tissue bridging) (Ramon-Cueto et al., 1998; Fouad et al., 2005; Deumens et al., 2006a; Liu et al., 2017).

In this review, we assess combinatorial strategies of biomaterial-supported cell transplantation to reconstruct lost host tissue physically, cellularly and chemically after SCI. This includes the integration of biomaterials into the host tissue, bridging the host-graft interface, limiting the effect of the surrounding scar formation which may prevent axonal growth into and through the injury site as well as increasing cell survival to provide the axons with physical, directional guidance and trophic support to regenerate toward disconnected targets (Geller and Fawcett, 2002; Tetzlaff et al., 2011; Kim et al., 2014; Assuncao-Silva et al., 2015; Wu et al., 2015; Lin et al., 2016). Candidate cell populations that enhance biomaterial integration into host tissue such as SCs, astrocytes, OECs, mesenchymal stem cells as well as NSPCs (Tetzlaff et al., 2011; Wu et al., 2015; Badner et al., 2017) will be discussed here.

The delivery method of biomaterials and cells into a SCI has been undertaken by several different techniques which we will group into categories here for reference throughout the review (**Figure 2**). Category I, transplantation matrix, is when cells and biomaterials are mixed together *in vitro* and allowed to form a matrix prior to implantation. This technique has been widely used as a delivery system to confine the transplanted cells to the injury site and will not be covered extensively in this review. Category II, pre-seeded scaffold, is when a pre-fabricated biomaterial is seeded with cells prior to implantation. This technique is primarily used for solid scaffolds with a pre-determined shape. Category III, injection and *in situ* gelling, is when self-assembling biomaterials are injected along with cells into the injury site to assemble a seeded scaffold *in vivo*. This technique has become popular to fill irregular lesion cavities that form after SCI. Category IV, facilitated biomaterial implantation, is when a biomaterial is implanted and cells are injected surrounding the biomaterial. This technique has been used to increase the integration of the scaffold into the host tissue, to increase axonal bridging.

CELLULAR CANDIDATES

Schwann Cells

In the peripheral nervous system, SCs are vital for regenerative growth following an axonal injury by providing trophic and physical support as well as remyelination (Rath et al., 1995; Triolo et al., 2006). SCs secrete ECM components (Tabesh et al., 2009) and neurotrophic factors such as brain-derived neurotrophic factor (BDNF), neurotrophin-3 (NT-3), nerve growth factor (NGF) (Dey et al., 2013; Godinho et al., 2013) and glial cell-derived neurotrophic factor (GDNF) (Iannotti et al., 2004). Therefore, transplantation of SCs after SCI has been widely studied and numerous results demonstrate that SCs can support survival and maintenance of spared neural tissue, bridge lesion cavities, promote re-growth of both motor and sensory axons into the lesion after engraftment and remyelinate CNS axons (Xu et al., 1997; Weidner et al., 1999; Marcol et al., 2015). Unfortunately, SCs form a distinct divide between themselves and CNS tissue both *in vitro* and *in vivo* (Ghirnikar and Eng, 1994; Lakatos et al., 2000). A reformation of the glial limitans and increased production of growth inhibitory CSPG (Plant et al., 2001) likely restrict the regenerative effect of SCs on descending motor neuronal tracts (Vroemen et al., 2007; Kanno et al., 2014).

Xu and colleagues conducted a series of studies demonstrating that naïve SCs or SCs overexpressing neurotropic factors embedded in a semi-permeable single channel composed of polyacrylonitrile and polyvinylchloride copolymers (PAN/PVC) (Category II) in T8 hemisection and transection rat SCI models enhanced the growth of propriospinal and some supraspinal axons into the lesion (Xu et al., 1995a,b, 1997, 1999). However, most often axons did not exit the lesion site on the caudal side likely due to the formation of the glial limitans restricting the SC migration and further beneficial effects. In addition, in a rat C4 2–3 mm hemisection model, biodegradable tubular poly-β-hydroxybutyrate (PHB) scaffolds filled with SCs (Category II) were able to support the survival of the SCs by promoting attachment as well as facilitating raphespinal and sensory axonal growth within the conduit; similar to previous observations, no rubrospinal or corticospinal tract (CST) re-growth was observed (Novikova et al., 2008).

To address the lack of re-innervation of the uninjured host parenchyma caudal to the biomaterial bridge by regenerating axons one aspect is to limit the formation of the glial limitans and reactive astrogliosis. One method that at least extended growth of descending axons (serotonergic) back out of a 2 mm alginate-based anisotropic capillary hydrogel in a C4 unilateral hemisection was the injection of SCs caudal to the SC-seeded hydrogel with the additional caudal viral expression of BDNF (Liu et al., 2017) (Category II and IV). Further work needs to be done to elucidate if this moved the glial limitans further down the

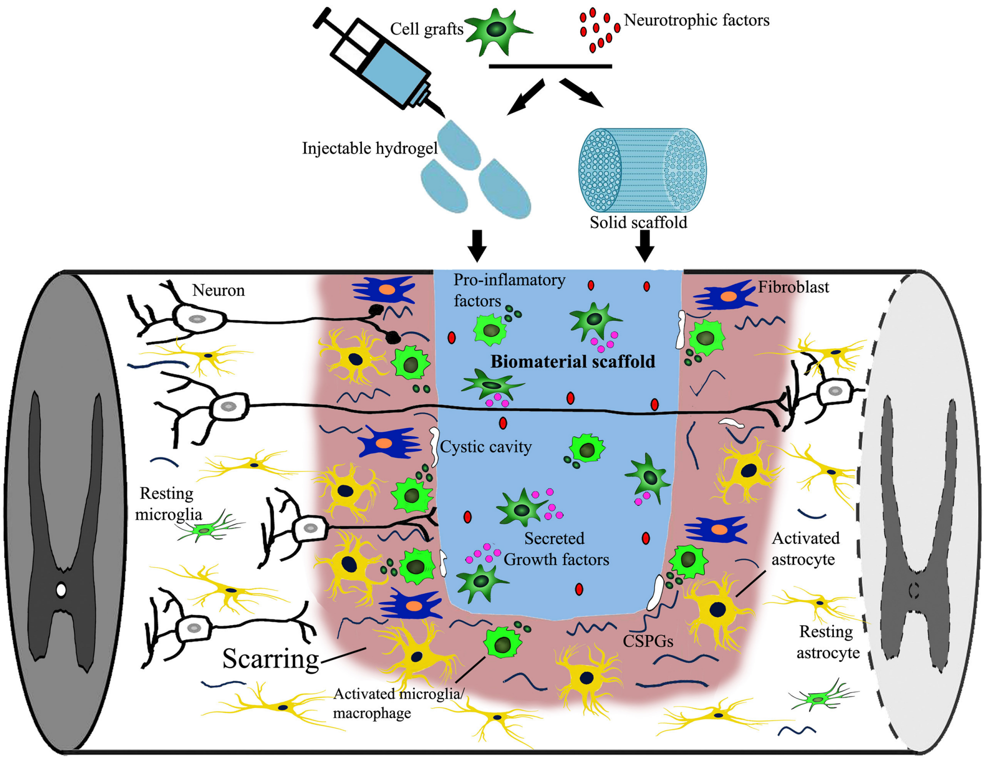

FIGURE 1 | Targets of combined biomaterial-supported cell transplantation following SCI. SCI induced neural damage leads to severed connections, tissue loss and the appearance of a cystic cavity. Combined biomaterials and cell transplantation can be used to fill the lesion cavity to provide physical support and bridge the distance that regrowing axons must traverse. Cell transplantation as well as newly introduced neurotrophic factors may provide trophic support (secreted growth factors) supporting axonal growth. An immune reaction, consisting of activated microglia, macrophages, fibroblasts and astrocytes, is elicited following injury to close off and prevent the spread of damage as well as re-establish the blood-spinal-barrier, possibly obstructing axonal regrowth. Additionally, neural injury leads to the release of growth inhibitory components [myelin debris, inflammatory cytokines, and chondroitin sulfate proteoglycans (CSPG)] that can be down regulated by either cell transplantation or the release of biomolecules into the lesion site.

cord to the host spinal injection site of SCs or if growth past the grafted SCs is possible. It was found in a 4 mm rat T8 complete transection that the unique combination of SC in fluid Matrigel in a PAN/PVC single channel scaffold, with OEC grafting in host parenchyma surrounding the lesion (Category II, III, and IV) and the delivery of ChABC led to functional improvement (BBB motor recovery score; up to 6 at 9 weeks vs. 2 with no treatment) (Fouad et al., 2005). Although this did not correlate to increased serotonergic fiber number caudal to the injury site but to SC myelinated fibers in the lesion site. Another approach to limit reactive astrogliosis (reduction of GFAP upregulation and CSPG expression) as well as further the intermingling of SCs and astrocytes within the graft and host tissue was the genetic modification of SCs to overexpress GDNF in a single PAN/PVC channel in a 3 mm T9-T10 hemisection rat model which led to enhanced SC remyelination of regenerating axons that were also aligned with protruding astrocytic extensions (Category II) (Deng et al., 2011). Additionally, SC grafting without neurotrophic factor delivery in a full T8 transection with fluid Matrigel (Category III) vs. pre-gelled Matrigel (Category I) in a PAN/PVC single channel (combined with Category II) showed greater growth of virally traced brainstem-derived (vestibular, noradrenergic, serotonergic, and reticular nuclei) axons into and up to the caudal interface where they are believed to have formed synaptic junctions with the help of newly formed supportive astrocytic protrusions (Williams et al., 2015). This significantly correlated to increased motor recovery as scored by BBB. It was proposed that fluid Matrigel led to better bridging of the host-graft interface and limited meningeal cell infiltration restricting the re-establishment of the glial limitans.

SC transplantation alone has been found to be beneficial, however the combination of SCs with biomaterials and other components provided substantial enhanced axonal regrowth and thereby functional improvement by eliciting better host-graft integration (**Table 2**). This includes the migration of SCs into the host parenchyma as well as astrocytic protrusions into the graft, the reduction of the glial limitans and reactive astrogliosis.

Astrocytes/Glial-Restricted Progenitors/Glial-Restricted Progenitor-Derived Astrocytes

Making up the majority of the glia cells in the CNS, astrocytes fulfill essential homeostatic and supportive functions such as

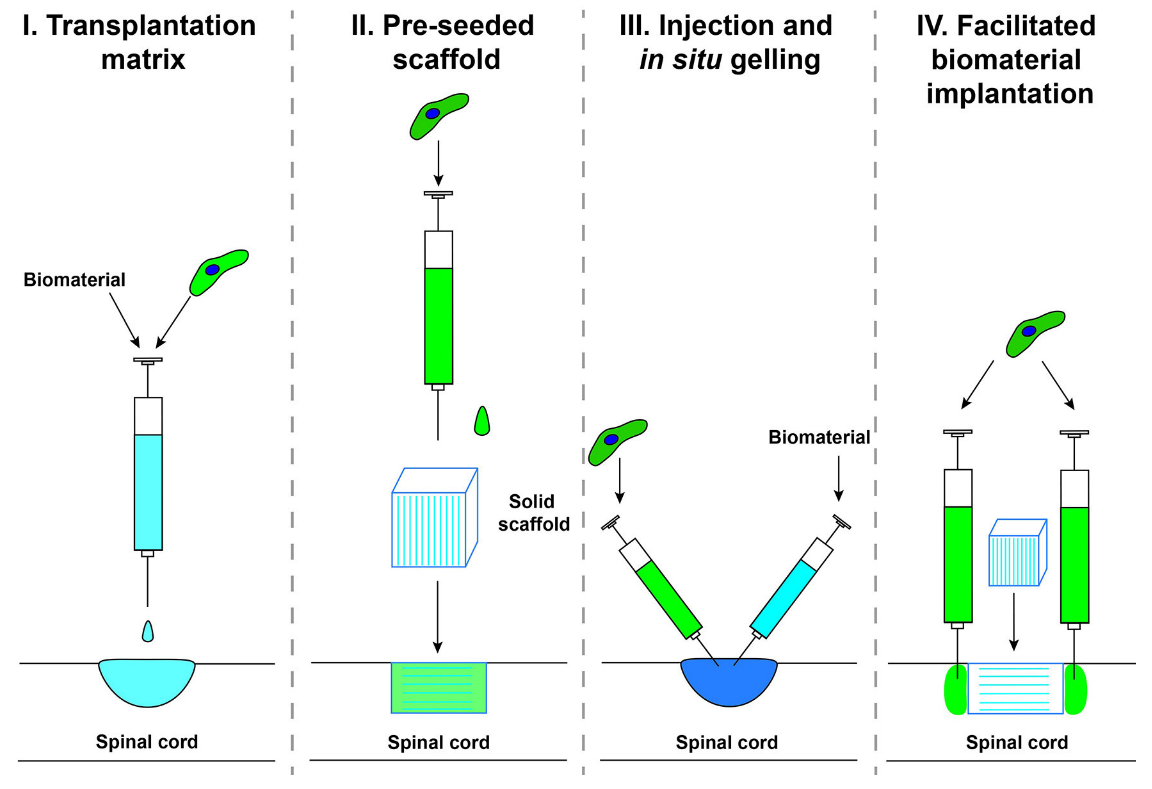

FIGURE 2 | Delivery methods for biomaterials combined with cell transplantation.

providing an organized physical matrix as well as producing neurotrophic factors for axonal remodeling and plasticity (Powell and Geller, 1999; Kimelberg and Nedergaard, 2010; Lukovic et al., 2015). In response to SCI, a dense network of reactive astrocytes physically restricts the lesion site by preventing the spread of neuroinflammation and necrosis immediately after injury (Faulkner et al., 2004; Sofroniew and Vinters, 2010; Anderson et al., 2016), although its persistence in the chronic phase may pose a physical and chemical barrier for re-growing axons (Smith-Thomas et al., 1994; Afshari et al., 2009; Sofroniew, 2009; Hellal et al., 2011; Cregg et al., 2014). Nonetheless, reactive astrogliosis is an essential part of the regenerative process as complete genetic ablation of reactive astrogliosis resulted in insufficient axonal regrowth (Faulkner et al., 2004; Anderson et al., 2016; Hara et al., 2017). Furthermore, networks of intermingled astrocytic protrusions serve as physical guidance structures for growing axons around spinal lesion sites (Silver et al., 1982; Fouad et al., 2005; Williams et al., 2015). Given these beneficial effects, astrocytes have been explored for restoration of spinal tissue integrity to mediate functional recovery (Chu et al., 2014). In line with the role of astrocytes in axonal guidance (Silver et al., 1982) and synapse formation (Baldwin and Eroglu, 2017; Liddelow and Barres, 2017) during development, it has been shown that immature (embryonic or neonatal) astrocytes provide greater regenerative bridging potential than mature astrocytes in the injured brain in both mice and rats (Smith and Silver, 1988; Smith and Miller, 1991; Filous et al., 2010). In a rat C3 fasciculus gracilis aspiration model, either oriented fetal E14 rat spinal cord tissue or astrocytes derived from E14 rat spinal cord were grafted (Bernstein and Goldberg, 1991). Over a 90 day period, the E14 derived astrocytes showed a significant increase in errors when crossing a horizontal ladder in comparison to the controls (aspiration-only), while the E14 rat spinal cord tissue graft showed a significant decrease in errors when crossing the ladder. This was found to be due to the astrocytic migration to the nucleus gracilis, where they protected neurons from denervation, increasing neuronal survival and networks only from astrocytes migrating out of the E14 spinal tissue but not from the E14 derived spinal cord astrocytes. Moreover, GFP labeled adult rat cortical astrocytes injected caudally (T11) 1 week after a T7-T8 full transection showed survival, integration and long distance migration to the lesion site and beyond 6 weeks post-transplantation (Pencalet et al., 2006).

Astrocytes are extremely heterogeneous and an adaptive cell population that vary morphologically and functionally, with phenotypes shifting with maturity, location, environmental cues and disease/injury-context (Zhang and Barres, 2010; Khakh and Sofroniew, 2015). For this reason, pre-cursors of the astrocytic and oligodendrocytic lineages (glial-restricted pre-cursors; GRPs) have been differentiated into homogenous subpopulations of astrocytes, GRP-derived astrocytes (GDA) differentiated with bone morphogenic protein 4 (BMP4, GDA^{BMP4}) or with ciliary

TABLE 2 | Schwann Cell-seeded biomaterial SCI studies.

SCI model	Biomaterial	Cell type	Outcome	References
Rat T8 transection	5 mm PAN/PVC and Matrigel (Category II)	Adult rat SC + BDNF and NT-3 infusion	Increased axonal growth up to biomaterial with NTFs	Xu et al., 1995a
Rat T8 transection	10 mm PAN/PVC and Matrigel (Category II)	Adult rat SC	Increased myelination of propriospinal and sensory axons within the scaffold but not exiting	Xu et al., 1995b
Rat T8 transection	8 mm PAN/PVC and Matrigel (Category II)	Adult rat SC	Increased myelination of propriospinal and sensory axons within the scaffold but not exiting	Xu et al., 1997
Rat T8 hemisection	5 mm PAN/PVC and Matrigel (Category II)	Adult rat SC	Increased myelination of propriospinal and sensory axons within the scaffold with some exiting	Xu et al., 1999
Rat C4 hemisection	2–3 mm PHB (Category II)	Adult rat SC	Some raphespinal and sensory axonal growth within the scaffold	Novikova et al., 2008
Rat C4 unilateral hemisection	2 mm alginate-based anisotropic capillary hydrogel (Category II and IV)	Adult rat GFP-SC	Serotonergic growth through and caudal to the biomaterial up to the 1 mm SC injection site	Liu et al., 2017
Rat T8 transection	4 mm PAN/PVC and fluid or pre-gelled Matrigel (Category I, II, III and IV)	Adult rat SC and OEC surrounding the lesion + ChABC	Increased SC myelination within the scaffold with increased BBB scores	Fouad et al., 2005
Rat T9-T10 hemisection	3 mm PAN/PVC (Categroy II)	Adult rat SC expressing GDNF	Enhanced SC remyelination of regenerating axons aligned with protruding astrocytic extensions	Deng et al., 2011
Rat T8 transection	4 mm PAN/PVC and fluid or pre-gelled Matrigel (Category I, II, and III)	Adult rat SC	Greater growth of virally traced brainstem-derived axons into and up to the caudal interface, formed synaptic junctions with the help of newly formed supportive astrocytic protrusions	Williams et al., 2015

neurotrophic factor (CNTF, GDA^{CNTF}). Firstly it should be noted, that after a T10 contusion in rats, transplantation of E13.5-derived GRPs alone retain their differentiation potential along the glial lineage, decrease reactive astrogliosis and CSPG expression levels as well as decrease axonal dieback of CST fibers from the lesion site and exhibit axonal growth cones (Hill et al., 2004). Injection of rat or human-derived GRPs or GDA^{CNTF} or GDA^{BMP4} into a rat C4/C5 dorsal column SCI model equally supported regeneration of ascending sensory tracts into the lesion site but not out (Haas et al., 2012; Haas and Fischer, 2013). Similarly, in a T10 moderate contusion in athymic rats human GRP and GDA^{BMP4} produced astrocytes at the lesion site that migrated out of the lesion and led to decreased cystic cavitation and reactive astrogliosis as well as increased sprouting. However, this did not lead to any significant changes in thermal and mechanical sensitivity or motor recovery (GridWalk) compared to controls (Jin et al., 2011). Several studies have been undertaken with GDA^{BMP4} showing increased growth of ascending sensory neurons of the dorsal columns into and through the lesion site, increased preservation of rubrospinal tracts and decreased misstep rates on the GridWalk (Davies et al., 2006; Fan et al., 2013; Wu et al., 2013), whereas GDA^{CNTF} has not shown any functional benefit or axonal regeneration but has led to allodynia as well as thermal and mechanical hyperalgesia (Davies et al., 2008, 2011).

Given that previous work with astrocytic grafting shows a lack of regenerative potential, astrocytes, themselves may be better suited as living scaffolds, linearly guiding axons in and out of biomaterials. Comparison of cultured astrocytes on either anisotropic poly(L-lactic acid) (PLLA) fibers or isotropic PLLA films revealed linear orientation of astrocytes to the anisotropic substrate, which provided a guidance matrix for the cultured astrocytes and dorsal root ganglia (DRG) neurons (Zuidema et al., 2015). When tethered self-aligning collagen gels aligned both the biomaterial with astrocytes this lead to significant increased growth of adult rat DRG in the aligned portions compared to the unaligned portions (East et al., 2010). Furthermore, alginate-based anisotropic capillary hydrogels lead to linear migration of astrocytes along capillary channels that are supportive of axonal outgrowth from neonatal rat entorhinal cortex and spinal cord slice cultures (Pawar et al., 2015b). Early studies already demonstrated that the implantation of fetal (E16 or E18) spinal cord astrocyte-seeded Millipore pennants (Category II) into a L5 dorsal root fiber crush model promoted substantial axonal growth into spinal gray matter tracts (Kliot et al., 1990). Additionally, implantation of neonatal rat cortical astrocytes situated in a Gelfoam matrix (Category II) or transplantation of astrocytes alone into a rat L3 dorsal lateral hemisection reduced host astrogliosis, scar formation and slightly increased density of neurofilament (NF) positive fibers when compared to controls (transplantation of Hanks buffered saline or implantation of empty Gelfoam) (Wang et al., 1995). While it is unclear which method has a greater beneficial effect, it was noted that the Gelfoam delayed the migration of the astrocytes from the lesion site and that cell-seeded Gelfoam appeared to be better integrated into the lesion site than Gelfoam alone. Fast blue labeled neonatal (P3) neocortical astrocytes embedded for retention in a collagen gel (modified Category I/II) were implanted into a 2 mm spanning T8 dorsal hemisection leading to increased neurofilament positive regenerating fibers within the implant, aligned along processes of the labeled astrocytes (Joosten et al., 2004). However, a minimal growth of biotinylated dextran amine (BDA) labeled CST fibers into the rostral edge of the gel scaffold was observed, although did not exit the lesion site. Limited improvements were observed in fine motor movements with the BBB subscore and Catwalk, analyzing hindlimb stride length and swing duration parameters, but not in the overall locomotor BBB score or Gridwalk analysis, when compared to collagen gel implantation alone. These changes may be due to the other fiber tracts not labeled in this study such as serotonergic fibers. To increase continuous tissue integrity across a large lesion site, Hoechst labeled P1 neonatal rat astrocytes were aligned on PLA/PLA-b-PEO matrices and implanted into a 2 mm T11/T12 dorsal hemisection with injection of astrocytes 1 mm both rostral and caudal of the lesion site (Category II and IV) (Deumens et al., 2006b). An increased BDA-labeled CST was observed up to the lesion site with astrocytes than controls (empty lesion site with media injected into the host parenchyma), however growth into the biomaterial was not observed likely due to the lack of astrocyte survival within the matrix. Naturally, no functional benefits were observed by the BBB locomotor score or stride length performed by Catwalk gait analysis.

Grafting of astrocytes, GRPs and GDAs into SCI lesions has shown their ability to reduce reactive astrogliosis, support neuronal survival and a minimal amount of axonal growth into but rarely beyond the lesion site. However, the regenerative potential of astrocytic grafting alone appears to be limited possibly due to their extensive migration away from the lesion. The combination of astrocytes with biomaterials delays their migration from the lesion site and enhances the host integration of the biomaterial by supplying directed growth of the axons along aligned astrocytes into the biomaterial. What remains to be examined is the use of GRPs or GDA^{BMP4}, both of which had greater axonal support potential alone than neonatal astrocytes, in combination with biomaterials to not only enhance biomaterial integration through tissue continuity across the lesion but also possibly increase axonal growth. For combinatorial work with astrocytes (**Table 3**) likely other factors such as neurotrophic factors will need to be utilized to increase axonal regrowth beyond the lesion site.

Olfactory Ensheathing Cells

Acquired from the olfactory bulb and mucosa, OECs represent an intermediary glial cell type between SCs and astrocytes (Granger et al., 2014). OECs express both the astrocytic marker GFAP (glial fibrillary acidic protein) and the SC marker p75-NTR (p75-neurotrophic factor receptor), however microarray profiling puts OECs in closer genetic proximity to SCs (Vincent et al., 2005). Similar to SCs, OECs have been shown to remyelinate injured axons (Li et al., 1997) and produce neurotrophic factors (Sasaki et al., 2006), although unlike SCs, OECs intermingle with host astrocytes to form supportive physical pathways presenting a growth inducing cellular and molecular substrate (Lakatos et al., 2000; Li et al., 2005). A review of OEC transplantation studies following SCI listed 41 studies showing beneficial effects, ranging from axonal regrowth, tissue sparring, angiogenesis, migration and remyelination, yet 13 studies showed no effects (Franssen et al., 2007). Several studies directly compared the transplantation of OECs or SCs and consistently observed benefits from SCs in axonal regeneration rather than OECs (Takami et al., 2002; Pearse et al., 2007). Furthermore, various OEC extraction protocols have led to varying purity which likely contributes to the observed high variability of effects of OECs in SCI studies (Ramon-Cueto and Nieto-Sampedro, 1992; Vincent et al., 2003; Rizek and Kawaja, 2006; Novikova et al., 2011).

In an attempt to further bridge nerve injuries, biomaterials have been combined with OECs to support axonal growth. OECs show a higher compatibility in terms of attachment and proliferation as well as nerve outgrowth on different biomaterials such as PLGA (Li et al., 2010), collagen (Wang et al., 2006), alginate and Matrigel scaffolds (Novikova et al., 2006) when combined with components of the ECM in a peripheral nerve injury model or *in vitro*. In rats a 2 mm long T11/T12 dorsal hemisection was filled with aligned OEC/ONF (olfactory nerve fibroblasts) -poly(D,L)-lactide biomatrix bridges (Category II) accompanied by Hoescht-labeled OEC/ONF injections surrounding the lesion site (1 mm rostral and caudal, Category IV), which led to migration of these cells up to the biomatrix but not within nor did the cells seeded within the biomatrix survive well, possibly due to the degradation of the biomatrix (Deumens et al., 2006a). All the same, this cell-seeded biomaterial implantation led to increased axonal growth into the lesion site than biomaterial alone, excluding CST growth, coupled with minimally increased gait parameters of stride length and swing speed (CatWalk) but no increased locomotor recovery (BBB). While the cause of this improvement was not specifically examined it was hypothesized to be due to other descending or ascending axonal tracts than the CST or the formation of new intraspinal relays. The use of OEC-seeded collagen-based multi-channel 3D matrices (Category II) in a 2 mm spanning T13 unilateral hemisection in rats showed no improvement on motor function (CatWalk) or alleviation of allodynia (von Frey hair filament test), furthermore axonal regrowth or scaffold integration was not examined (Deumens et al., 2013). Most recently, it was found that OEC-seeded PLGA scaffolds (Category II) in a 2 mm T9/T10 complete transection rat SCI model increased motor recovery (BBB score of 9 vs. 6 of controls and more successful crossings of an inclined plane) which correlated with increased axonal preservation and decreased astrogliosis reflecting neuroprotection as the underlying mechanism (Wang et al., 2017). As previously mentioned, the combination of OEC injection surrounding a PAN/PVC SC-seeded Matrigel implant in a full thoracic transection led to long distance growth both of ascending and descending axonal tracts into and through the lesion site (Ramon-Cueto et al., 1998; Fouad et al., 2005).

These studies (**Table 4**) show that OEC when injected surrounding the biomaterial help with growth of axons up to the lesion site, however they do not appear to migrate out from

TABLE 3 | Astrocyte-seeded biomaterial SCI studies.

SCI model	Biomaterial	Cell type	Outcome	References
Rat L5 dorsal root fiber crush model	Millipore pennants (Category II)	Rat fetal (E16 or E18) spinal cord astrocytes	Promoted substantial axonal growth into spinal gray matter tracts	Kliot et al., 1990
Rat L3 dorsal lateral hemisection	Gelfoam matrix (Category II)	Neonatal rat cortical astrocytes	Reduced host astrogliosis, scar formation, and slightly increased density NF	Wang et al., 1995
Rat T8 dorsal hemisection	2 mm Collagen gel (modified Category I/II)	Neonatal rat (P3) neocortical astrocytes	Increased NF within biomaterial aligned along astrocytes, minimal CST growth into rostral end without exiting biomaterial, improvements in BBB sub-score and Catwalk stride length and swing duration	Joosten et al., 2004
Rat T11/T12 dorsal hemisection	2 mm PLA/PLA-b-PEO matrices (Category II and IV)	P1 neonatal rat astrocytes, 1 mm rostrocaudal injections	Increased CST growth up to the lesion site, poor astrocyte survival within matrix	Deumens et al., 2006b

or into the biomaterial to increase tissue continuity, decrease cavitation surrounding the biomaterial or survive well when seeded in a biomaterial (this may have been due to biomaterial integrity, which should be re-examined), therefore currently at this time, OECs alone may not be the best candidate for combination with biomaterials.

Bone Marrow Mesenchymal Stem Cells

BMSCs are a widely used cell type for transplantation studies that can be easily isolated from a bone marrow aspiration and extensively expanded in culture, which makes autologous transplantation possible (Mendonca et al., 2014). BMSCs not only differentiate into a variety of mesodermal lines but also have been described to differentiate into microglia, oligodendrocytes and macrophages when transplanted into the spinal cord (Corti et al., 2002; Cizkova et al., 2006). However, the phenomenon of transdifferentation into neural cells has been challenged (Lu et al., 2004) and is likely not relevant for beneficial effects observed after SCI transplantation. More importantly for use in SCI, BMSCs can fill the lesion cavity and produce ECM components, thereby providing structural support for growing axons (Kim et al., 2013; Volpato et al., 2013). Furthermore, BMSCs display anti-inflammatory properties by producing immunoregulatory cytokines (interleukins and transforming growth factor-β) (Bartholomew et al., 2002; Noh et al., 2016) and interactions with host immune cells (Deans and Moseley, 2000; Zhang et al., 2016). In this context, transplantation of BMSCs diminished reactive astrogliosis and microglial activation (Abrams et al., 2009; Ruff et al., 2012). In addition to cytokines, BMSCs secrete permissive growth factors (Chen et al., 2002; Ohta et al., 2004; Kim et al., 2013; Ritfeld et al., 2015), although at relatively low levels. To enhance the role of BMSC paracrine secretion on axonal regeneration, genetically modified BMSCs have been used in various studies to deliver neurotrophic factors (Gong et al., 2015; Ritfeld et al., 2015; Zhu et al., 2015; Brock et al., 2016) in experimental SCI models. Although MSCs have been shown in a meta-analysis of relevant pre-clinical studies to increase the BBB score of thoracic SCI rats on average by 3.9 points the relevance of this increase has to be treated with caution due to the lack of a baseline from which locomotor activity is assessed (Oliveri et al., 2014).

While biomaterials fill the lesion site, they still require tissue continuity to allow for axonal growth into them. To this end, BMSC-seeded in porous but undirected 2-hydroxyethyl methacrylate (HEMA) or 2-hydroxypropyl methacrylamide (HPMA) scaffolds (Category II) implanted in a unilateral hemisection increased neurofilament positive axonal growth into the hydrogels (Sykova et al., 2006). Additionally, growth permissive BDNF expressing BMSCs were seeded into multi-component fiber bundled agarose scaffolds (Category II) after a 2 mm long T3 complete transection which led to increased growth of both descending (raphespinal and reticulospinal tracts) as well as ascending sensory fibers into the lesion site, far greater than GFP expressing BMSC-seeded biomaterials (Gao et al., 2013). To confirm this observation, BMSCs expressing BDNF seeded in a 2 mm alginate-based anisotropic capillary hydrogel (Category II) in a rat C5 unilateral hemisection enhanced directed axonal regrowth in comparison to hydrogels seeded with BMSCs alone (Gunther et al., 2015a,b). Both studies observed a significant increase of BDNF-driven axonal growth into and through the biomaterial but not exiting it nor did either study examine behavioral outcomes. By co-culture with NT3 overexpressing SCs in a 3D gelatin sponge scaffold, genetically modified BMSCs overexpressing Neurotrophic Receptor Tyrosine Kinase 3 (TrkC) differentiated into cells exhibiting neuronal features (neurofilament and post-synaptic density 95) (Category II), which were implanted into a rat 2 mm-wide T9-T10 transection SCI (Zeng et al., 2015). This treatment led to enhanced axonal growth throughout the biomaterial, synaptic association of these cells with mostly serotonergic neurons and some CST axons (electron microscopy), the upregulation of c-Fos in the grafted as well as host lumbar spinal cord cells in response to motor cortex stimulation and the improvement of locomotor function (BBB score of 8 for the cell-seeded biomaterial vs. 3 for biomaterial alone). The biomaterial alone vs. control SCI alone was not significantly different in axonal growth or functional parameters examined.

Overall, an added value of the combinatorial therapy with BMSCs and biomaterials is observable (**Table 5**) over biomaterials alone by increased ingrowth into scaffolds (Gao et al., 2013; Zeng et al., 2015), however it appears to not be

TABLE 4 | OEC-seeded biomaterial SCI studies.

SCI model	Biomaterial	Cell type	Outcome	References
Rat T11/T12 dorsal hemisection	2 mm poly(D,L)-lactide biomatrix (Category II and IV)	OEC/ONF within and 1 mm rostrocaudal injections	Migration of cells up to but not within biomatrix, poor cell survival within biomatrix, increased axonal growth excluding CST, increased stride length and swing speed	Deumens et al., 2006a
Rat T13 unilateral hemisection	2 mm collagen-based multi-channel 3D matrices (Category II)	OEC	No improvement in CatWalk gait analysis or alleviation of allodynia	Deumens et al., 2013
Rat T9/T10 complete transection	2 mm PLGA scaffolds (Category II)	OEC	Increased BBB score and crossing of inclined plane, increased axonal preservation, decreased astrogliosis	Wang et al., 2017

sufficient enough growth for functionally relevant improvements alone without being coupled with other therapies such as neurotrophin overexpression or co-culture with other cell types.

Neural Stem and Progenitor Cells

NSPCs can be generated from embryonic, fetal or adult CNS tissues and bear the unique feature of extensive self-renewal *in vivo* as well as differentiation into any desired neural cell type (Iwanami et al., 2005). NSPCs represent a promising and powerful tool to replace damaged tissue and bridge the lesion cavity by providing a cellular matrix, tissue replacement through targeted differentiation, neuroprotection and trophic support, (Assinck et al., 2017; Vismara et al., 2017). More recently, fetal spinal cell grafting after SCI is performed with growth factor trophic support and a fibrin matrix (Category I) to enhance cell survival and retention of the cells at the lesion site (Lu et al., 2012; Kadoya et al., 2016; Robinson and Lu, 2017). This encouraged the most extensive neuronal growth from NSPCs observed in a SCI (T3 full transection, CST and right quadrant lesions or C4 CST lesion) with resulting functional improvement in either hindlimb function (BBB score 6.5 vs. 1.5 BBB score for the lesion-only controls at 6 weeks post-grafting) or forelimb function (the staircase task with increased level reached and pellets eaten in the graft vs. lesion alone) or increased electrophysiology between grafted cells and CSTs through the creation of functional neuronal relays. Generally in the absence of growth factors and matrices, neural restricted progenitors (NRPs) and GRPs survive acute SCI grafting better than do multipotent neuroepithelial (NEP) stem cells, however delayed grafting of the fetal or embryonic NSPCs does allow for better survival and filling of the lesion site (Theele et al., 1996; Lepore et al., 2004; Iwanami et al., 2005; Lu et al., 2012, 2014a). It was found in mouse C4-CST lesions that grafted GRPs with NRPs or NPCs alone had surviving neurons and glia that filled the lesion site and supported CST regenerative growth, however grafted GRPs alone failed to do so (Kadoya et al., 2016). Moreover, it was found that adult NSPCs are incapable of filling the lesion cyst after transplantation into the injured spinal cord (Vroemen et al., 2003; Sandner et al., 2013). Another study has found that transplantation of NSPCs that differentiate primarily into astrocytes in response to SCI leads to the development of thermal and mechanical allodynia (Macias et al., 2006). Astrocytes do support axonal growth, however the type of growth they support may be determined by their dysregulation by the surrounding injury environment hence the development of astrocytic-dependent pain (Falnikar et al., 2015). Protection from direct contact with the lesion environment may provide NSPC-derived astrocytes with a different outcome (Cao et al., 2002).

Following SCI, the overall aim of seeding NSPCs into biomaterial scaffolds is to increase CNS regeneration by (1) improving the survival and potential differentiation of grafted NPSCs into mature cells to preserve tissue integrity by serving as a supportive matrix and (2) decreasing the host response to the biomaterial implantation by reducing inflammation and fibroglial scarring (Reeves and Keirstead, 2012; Bellenchi et al., 2013; Matsui et al., 2014). NSPCs derived from the subventricular zone (SVZ) of adult rats were incorporated into a PDGF-A-conjugated hyaluronan and methyl cellulose-based hydrogel blend (HAMC) (modified Category III/IV) and grafted 9 days post-clip T2 compression injury 1 mm rostral and 1 mm caudal to the injury site (Mothe et al., 2013). Even though cell survival was increased 1 week post-grafting, hardly any cells survived after 8 weeks when transplanted alone or in combination with the hydrogel. Nevertheless, sparing of host oligodendrocytes and neurons was enhanced, positively affecting functional outcomes for fine motor (horizontal ladder) changes but not gross motor skills (BBB). Murine NSCs (clone C17.2) were either seeded on a 4 mm oriented porous PLGA scaffold (Category II) or transplanted alone in comparison to naïve PLGA scaffolds or no treatment controls in a rat T9/T10 lateral hemisection model (Teng et al., 2002). To avoid additional neuroprotective effects no immunosuppression was used (Guo et al., 2001). Implanted scaffolds increased cell survival over transplanted cells alone. The greatest tissue preservation (white matter sparing) was served by the cell-seeded scaffolds followed by the scaffold alone, cells alone and finally the no treatment group. In addition to increased NF positive axonal growth within the lesion site, the scaffolds with or without cells had increased sensorimotor cortex traced BDA fibers both rostral and caudal to the lesion site co-labeled with growth-associated protein 43 kDa (GAP-43, an axonal regenerating marker) rostral to the lesion site, which was not observed in the cell transplantation or no treatment control groups. Both tissue preservation and regenerating fibers are thought to contribute to the increased motor recovery seen in the cell-seeded scaffold group (BBB score 11 vs. BBB score

TABLE 5 | BMSC-seeded biomaterial SCI studies.

SCI model	Biomaterial	Cell type	Outcome	References
Rat unilateral hemisection	2-hydroxyethyl methacrylate (HEMA) or 2-hydroxypropyl methacrylamide (HPMA) scaffolds (Category II)	BMSC	Increased neurofilament positive axonal growth	Sykova et al., 2006
Rat T3 transection	2 mm multi-component fiber bundled agarose scaffolds (Category II)	BMSC-BDNF and BMSC-GFP	Increased growth of raphespinal, reticulospinal tracts and sensory fibers into but not exiting scaffold	Gao et al., 2013
Rat C5 unilateral hemisection	2 mm alginate-based anisotropic capillary hydrogel (Category II)	BMSC-BDNF and BMSC-GFP	Enhanced directed axonal regrowth into but not exiting hydrogels	Gunther et al., 2015a,b
Rat T9-T10 transection	2 mm 3D gelatin sponge scaffold (Category II)	co-culture SC-NT-3 and BMSC-TrkC	Enhanced axonal growth throughout the biomaterial, synaptic association of these cells with serotonergic neurons and some CST axons, upregulation of c-Fos in the grafted as well as host lumbar spinal cord cells and improvement of BBB score	Zeng et al., 2015

8 for scaffold alone, and BBB score ∼6 for cells alone or no treatment controls at 70 days). Implanted in a rat 2 mm full T8/T9 transection, PLGA scaffolds (with 7 longitudinal channels, each with a diameter of 660 μm) were seeded with rat E14.5 NSCs (telencephalon/diencephalon) or adult rat SCs suspended in Matrigel (Category II) or no cells (Olson et al., 2009). Even though seeded PGLA scaffolds increased axonal fibers throughout the scaffold after 4 weeks it did not lead to increased motor recovery in such a severe lesion (BBB score ∼1). An oriented PLGA scaffold filled with a macroporous 4-arm poly(ethylene glycol) (PEG) hydrogel and coated with Poly(L-lysine) (PLL) was seeded with endothelial cells and NSPCs (from the SVZ zone of P1 GFP rats) in a rat T9-T10 lateral hemisection (Category II) (Rauch et al., 2009). This yielded a several fold increase in functional blood vessels over groups with either cell type seeded alone, biomaterial alone or lesion alone, recreating the blood spinal barrier. At 8 weeks post-injury, this also led to differentiation of the seeded NSPCs as well as increased NF staining at the host/graft interface and lesion epicenter coupled with GAP-43 staining of regenerating axons not colocalizing with GFP transplanted cells but with host axons. In another study, 10 mm long laminin-coated chitosan channels were seeded with either adult brain or spinal NSPCs (Category II) in a T8 transection rat model which led to long-term survival (14 weeks), differentiation (astrocytes and oligodendrocytes), decreased cyst formation and increased tissue bridge formation compared to empty scaffold or no scaffold (Nomura et al., 2008). Not surprisingly given the lesion size, no change in functional improvement occurred nor did any BDA labeled CST axons enter the channel. Implantation of adult neurosphere NSPC-seeded un-coated chitosan channels (Category II) 3 weeks post-T8 clip compression SCI in rats revealed a 5-fold increase in cell survival compared to NSPC grafting alone, however no tissue bridging or functional change was observed at 9 weeks (BBB scores ranging between 9 and 11) (Bozkurt et al., 2010). Non-proliferating NSPCs differentiated ∼50% into oligodendrocytes, with very few differentiating into astrocytes or neurons, and ∼50% remaining undifferentiated in the NSPC-seeded chitosan channels. NSPC grafting alone had greater number of oligodendrocytes and fewer undifferentiated cells, however overall cell survival was less than those seeded in channels.

To further improve these beneficial effects, either neurotrophic factors were overexpressed or bioactive molecules were conjugated into scaffold backbones. In an oriented macroporous PLGA scaffold seeded with rat P1-P3 hippocampal NSCs infected with NT-3 or TrkC (co-culture), naïve NSCs or unseeded PLGA were implanted into a 2 mm T10 full transection (Category II) (Du et al., 2011). Immunohistology and electron microscopy (EM) confirm differentiation into mature neurons (MAP2) forming synapases (PSD95) in the co-culture-seeded biomaterial group. This treatment also specifically led to the preservation of neurons in the sensorimotor cortex, red nucleus (descending tracts) and Clarke's nuclei (ascending tracts) as well as a significant increase in NF positive staining rostral and caudal to the scaffold and in the epicenter. Moreover, at 8 weeks post-injury this increased the motor recovery from 1.5 BBB score in the PLGA unseeded group to 3.5 in the NSC + PLGA group and 8.5 in the co-culture NT-3/TrkC-NSC + PLGA group. A similar study published at the same time in a T10 full transection implanted 2 mm Gelfoam scaffolds seeded with co-cultured NT-3-SC and TrkC-NSC (Category II) compared to Gelfoam alone, with NSC, with LacZ-SC + LacZ-NSC, with NT-3-SC + NSCs (Wang et al., 2011). The combination of NT-3-SC + TrkC-NSC seeded Gelfoam led to increased motor improvements (BBB 7.6 vs. NSC Gelfoam 1.6 and SCI alone 0.5, 60 days after injury) along with increased cortical somatosensory evoked potentials and cortical motor evoked potentials. This treatment also led to increased neuronal differentiation (MAP2), increased cell survival of internal pyramidal layer, red nuclei (descending tracts) and Clarke's nucleus (ascending tracts), increased SC myelination (EM) and synapse formation (EM and pre/post-synapse markers). While it needs to be further examined, the study indicates synapse formation at the epicenter of the lesion between transplanted NSCs and regenerating host axons leading to the enhanced functional recovery. A human immortalized NSC line (F3) was seeded with the addition of NT-3 expression in poly(ε-caprolactone) (PCL) scaffolds (Category II) in rat lateral T7-T8 hemisection which led to increased differentiation in neurons and oligodendrocytes, white matter sparing, regenerative markers (GAP-43 and synaptotagmin) by ELISA and Western blot analysis caudal to the lesion, than the F3-PCL group (Hwang et al., 2011). This correlated with increased motor recovery (BBB score up to 15 for the F3-NT-3-PCL, 13 for the F3-PCL, 11 for PCL and 10 for lesion alone as well as significantly less errors on a GridWalk at 4 and 7 weeks, errors decreasing with each additional treatment). Moreover, the addition of Chondroitinase ABC reduced CSPGs and increased motor recovery of the F3-NT-3-PCL group, including motor evoked potentials. Another study was conducted using rat neonatal NPCs (telencephalons) embedded into a 4 mm porous collagen and collagen-cetuximab scaffolds conjugated with a neutralizing antibody of epidermal growth factor receptor (EGFR, to block downstream inhibitory Nogo receptor signaling) (Koprivica et al., 2005), reducing the microglial inflammatory response (Qu et al., 2012) and reactive astrogliosis (Li et al., 2011) as well as increasing neuronal over astrocytic differentiation (Ayuso-Sacido et al., 2010) in a rat T13-L2 lateral hemisection (Category II) (Li et al., 2013). Here, neuronal differentiation was increased, whereas astrocytic differentiation was decreased and modest functional improvement was observed (BBB score 6 from 2 of empty collagen scaffold control and increased angle on inclined plane between seeded scaffolds vs. empty scaffolds).

In move toward clinical application both canine and African green monkey models of SCI (a 5 mm T11 lateral hemisection and a 10 mm T9/T10 lateral hemisection, respectively) have been developed to test the use of coated and uncoated PLGA scaffolds seeded with human NSC lines expressing NT-3 or not (Kim et al., 2010; Pritchard et al., 2010). While these studies found grafting to be feasible more work needs to be done to understand the efficacy of the treatments.

The combination of biomaterial scaffolds with NSPCs (**Table 6**) clearly has an enhanced effect on cell survival and to a lesser extent on differentiation as well as decreased cyst formation and increased tissue preservation. Many studies observed increased tissue bridging and regenerating axonal growth, however this was not always coupled with increased functional improvement. Importantly, with the addition of other factors, such as growth factors and biomolecules within the biomaterial, there was a greater increase in axonal growth into the scaffold, along with mature neuronal synapse formation with host neurons and supposed neuronal relays leading to functional improvements. Here, the combination of biomaterials with NSPCs (and other treatments) demonstrates a greater effect than NSPC transplantation alone after a SCI. Interestingly, this effect appears to be greater than the combination of biomaterials with other cell types.

It should be noted that while not covered in this review that both the embryonic stem (ES) cells and induced pluripotent stem cells (iPSCs) are viable cellular candidates for biomaterial-supported cell transplantation. Both ES cells and iPSCs are capable of becoming any cell type and with this ability comes the potential for undifferentiated proliferation and tumorigenesis (Assuncao-Silva et al., 2015), which may be further enhanced by combination with a biomaterial. While ethical concerns constrict the use of ES cells and find benefit in the iPSCs which can be made autologously from a patient's skin sample, there still remains the concern of viral expression to induce pluripotency as well as the time frame it takes from collection of the patient sample until the iPSC or differentiated iPSC is produced. In addition, neuronal differentiation of iPSCs is more complicated than ES cells (Hu et al., 2010). In comparison to the work done with NSPCs and biomaterials in animal models, work done combining ES cells or iPSCs with biomaterials is more limited at this time (Hatami et al., 2009; Lu et al., 2014b; McCreedy et al., 2014).

CHALLENGES FACING CELL-SEEDED BIOMATERIAL STRATEGIES

More single application treatments (SCs, OECs, BMSCs, biomaterial scaffolds) are slowly making their way into clinical trials (Mackay-Sim et al., 2008; Kumar et al., 2009; Karamouzian et al., 2012; Tabakow et al., 2013; Amr et al., 2014; Mendonca et al., 2014; Theodore et al., 2016; Xiao et al., 2016; Anderson et al., 2017), however combinatory treatments are still primarily pre-clinical. Currently the field of cell-seeded biomaterials is in its infancy and targeting proof of concept experiments. If an experimental combination moves from *in vitro* to *in vivo* and shows substantial axonal regeneration linked to functional recovery then we can start addressing questions of clinical relevance. For example, many of the studies presented here were drastic hemisection or full transection injury models vs. the human relevant contusion/compression models (Devivo et al., 2002). In addition, many are thoracic lesions vs. the more common cervical lesions observed in SCI patients (Singh et al., 2014). In this thread, most studies work on acute or subacute SCI, as chronic SCI is time consuming and challenging for a treatment that has not already shown some promise in the acute phase. However, patients recruited for such clinical trials would likely be stable chronic patients who are no longer spontaneously recovering following the reduction of inflammation or other secondary damage, thus the obstacles faced in their lesion microenvironment would be different from that of the acute or subacute phase and must be taken into consideration.

In regards to cell transplantation in humans, autologous cells would be ideal, otherwise allogenic samples from other individuals may require long-term immunosuppression which will create other obstacles that need to be overcome. For some autologous cell types, longer periods of culturing are required to improve purity, quantity or differentiation which make immediate transplantation impossible in sub-acute SCI where much of the current preclinical work has been conducted (Mertens et al., 2016; Vismara et al., 2017).

Great progress has been made in both the fields of tissue engineering (cell purification procedures, autologous cell culture, culture methods increasing viability and genetic modifications) as well as biomaterial sciences (stability, combatibility, purity, self-assembling scaffolds, consistent capillary scaffolds, and biomolecule delivery), creating solutions (linear directed growth, increased viability, increased tissue stablity, decreased immune

TABLE 6 | NSPC-seeded biomaterial SCI studies.

SCI model	Biomaterial	Cell type	Outcome	References
Rat T3 transection	Fibrin matrix (Category I)	Rat E14 fetal spinal cells with cocktail of growth factors	Neuronal differentiation and growth of NSPCs, extensive axonal growth (serotonergic) into the matrix creating neuronal relays, increased BBB score and electrophysiology	Lu et al., 2012
Rat bilateral CST and right quadrant lesions	Fibrin matrix (Category I)	Rat E14 fetal spinal cells with cocktail of growth factors	Neuronal differentiation and growth of NSPCs, extensive CST growth into the matrix creating neuronal relays, the staircase task with increased level reached and pellets eaten	Kadoya et al., 2016
Rat T2 clip compression	PDGF-A-conjugated HAMC (modified Category III/IV)	Adult rat SVZ-derived NSPCs	Enhanced sparing of host oligodendrocytes and neurons, increased fine motor (horizontal ladder) changes but not gross motor skills (BBB)	Mothe et al., 2013
Rat T9/T10 lateral hemisection	4 mm oriented porous PLGA scaffold (Category II)	Murine NSCs (clone C17.2)	Increased cell survival, tissue preservation, increased NF axonal growth within lesion site, increased sensorimotor cortex traced BDA fibers rostral and caudal to graft coupled with GAP-43, increased BBB	Teng et al., 2002
Rat T8/T9 transection	2 mm PLGA scaffolds (with 7 longitudinal channels, each with a diameter of 660 μm) and Matrigel (Category II)	Rat E14.5 NSCs (telencephalon/diencephalon) or adult rat SCs	Increased axonal fibers throughout scaffold but no change in BBB score	Olson et al., 2009
Rat T9-T10 lateral hemisection	Oriented PLGA scaffold with macroporous 4-arm PEG hydrogel coated with PLL (Category II)	Endothelial cells and NSPCs (from the SVZ zone of P1 GFP rats)	Increase in functional blood vessels, differentiation of NSPCs, increased NF staining at host/graft interface and epicenter and regenerating axons	Rauch et al., 2009
Rat T8 transection	10 mm laminin-coated chitosan channels (Category II)	Adult rat brain or spinal NSPCs	14 week survival, differentiation (astrocytes and oligodendrocytes), decreased cyst formation and increased tissue bridge formation, no CST growth into scaffold nor functional improvement.	Nomura et al., 2008
Rat T8 clip compression	Un-coated chitosan channels (Category II)	Adult rat neurosphere NSPC	5-fold increase in cell survival but no tissue bridging or functional change at 9 weeks	Bozkurt et al., 2010
Rat T10 transection	2 mm oriented macroporous PLGA scaffold (Category II)	Rat P1-P3 hippocampal NSC-NT-3/NSC-TrkC (co-culture), naïve NSCs	Differentiation into mature neurons with synapse formation, preservation of neurons in the sensorimotor cortex, red nucleus and Clarke's nuclei, increased NF rostrocaudal and epicenter staining, increased BBB score	Du et al., 2011
Rat T10 transection	2 mm Gelfoam scaffolds (Category II)	Co-cultured NT-3-SC and TrkC-NSC, naïve NSCs	Increased BBB score, increased cortical somatosensory evoked potentials and cortical motor evoked potentials, increased neuronal differentiation, increased cell survival of internal pyramidal layer, red nuclei and Clarke's nucleus, increased SC myelination and synapse formation	Wang et al., 2011
Rat lateral T7-T8 hemisection	NT-3 expression PCL scaffolds (Category II)	Human immortalized NSC line (F3) + ChABCase	Differentiation into neurons and oligodendrocytes, white matter sparing, regenerative markers (GAP-43 and synaptotagmin), increased BBB score and MEP, decreased errors on the GridWalk	Hwang et al., 2011
Rat T13-L2 lateral hemisection	4 mm porous collagen scaffold conjugated with neutralizing antibody of EGFR (Category II)	Neonatal NPCs	Increased neuronal differentiation, increased in BBB score and angle on inclined plane	Li et al., 2013

reactions) that were non-existent previously, allowing for new multifaceted approaches. Given these advances it may be of importance to revisit many combinations that were presented here but not performed under ideal conditions. For example, cell survival on some scaffolds was poor, likely due to the degradation of the scaffold during the study. Such work can now be repeated with more stable scaffolds and with additional coating of the scaffold with extracellular matrix proteins to increase survival and attachement (Hou et al., 2005; Tian et al., 2005). In addition, experiments comparing the combination of a single biomaterial with various cell types in a given SCI model would be beneficial in contrasting the effectiveness of each combinatorial therapy. For example, PGLA scaffolds seeded with NSPCs or SCs (Category II) were compared to empty scaffolds in a 2 mm full transection T8-T9 model, clearly showing that cell-seeded scaffolds increased axonal regeneration over empty control scaffolds and while not significant SC-seeded scaffolds trended to greater axonal regrowth than NSPC-seeded scaffolds (Olson et al., 2009). The current use of transgenic lines provides easy visual tracking of grafted cells allowing for a better understanding of cell survival, cell migration, differentiation, tissue bridging, synaptic connections and neuronal relays forming. For future studies it is of great importance that relevant functional assays be performed in combination with histological work along with proper controls showing the observed improvement can be directly linked to the observed host-graft integration or axonal regeneration, for example through a re-transection or ablation study.

PERSPECTIVES OF CELL-SEEDED BIOMATERIAL STRATEGIES

The combination of cell transplantation and biomaterial scaffold implantation provides a promising tissue engineering strategy for SCI treatment that addresses the replacement of lost neural tissue and the support of axonal regeneration to achieve functional recovery. The poor survival rate of cells transplanted into the harsh post-SCI environment challenges their ability to fill and bridge the spinal lesion cavity or even provide physical and/or trophic support for axonal regrowth. In this context, biomaterial scaffolds provide a physical matrix for cell attachment, proliferation and differentiation that is protected from the harsh lesion microenvironment (Novikova et al., 2006; Führmann et al., 2017). In addition in such combinatorial approaches, the grafted cells aid scaffold integration into the host spinal environment by forming tissue bridges enticing axonal growth into and through the scaffold, recreating the lost neural tissue. While it is difficult to compare different SCI lesion models and severities, species, cell types and biomaterial scaffolds used, many studies indicate that cell-seeded biomaterial scaffolds lead to greater axonal regrowth and sometimes better functional outcomes than biomaterial scaffolds alone (Wang et al., 1995, 2011, 2017; Teng et al., 2002; Joosten et al., 2004; Deumens et al., 2006a; Nomura et al., 2008; Olson et al., 2009; Rauch et al., 2009; Du et al., 2011; Hwang et al., 2011; Gao et al., 2013; Li et al., 2013; Zeng et al., 2015). Additionaly, from a few studies presented here there is a strong indication that biomaterial-supported cell transplantation is greater than cell transplantation alone (Teng et al., 2002; Rauch et al., 2009; Bozkurt et al., 2010), unfortunately this is not a direct comparison that is often performed. Biomaterial-supported cell transplantation reduces tissue loss, inflammation and reactive astrogliosis, increases tissue integrity and bridging of the lesion site which has led to increased axonal growth across the lesion as well as increased functional improvements. Combining various cell types and growth factors to increase tissue bridging and integration of the biomaterial along with increased support of axonal regeneration not only into the biomaterial but also re-entry and long distance growth into the host parenchyma would likely substanstially promote functional improvements. Taken together thus far the work in biomaterial-supported cell transplantation strongly encourages a path forward toward combinatorial treatment of SCI.

AUTHOR CONTRIBUTIONS

SL, TS, and RP: Researched, wrote, and edited the manuscript. NW: Edited the manuscript and provided expert feedback.

FUNDING

Supported by a grant from the Deutsche Forschungsgemeinschaft (BL414/3-1) (awarded to NW).

REFERENCES

Abrams, M. B., Dominguez, C., Pernold, K., Regera, R., Wiesenfeld-Hallin, Z., Olson, L., et al. (2009). Multipotent mesenchymal stromal cells attenuate chronic inflammation and injury-induced sensitivity to mechanical stimuli in experimental spinal cord injury. *Restor. Neurol. Neurosci.* 27, 307–321. doi: 10.3233/RNN-2009-0480

Afshari, F. T., Kappagantula, S., and Fawcett, J. W. (2009). Extrinsic and intrinsic factors controlling axonal regeneration after spinal cord injury. *Expert Rev. Mol. Med.* 11:e37. doi: 10.1017/S1462399409001288

Amr, S. M., Gouda, A., Koptan, W. T., Galal, A. A., Abdel-Fattah, D. S., Rashed, L. A., et al. (2014). Bridging defects in chronic spinal cord injury using peripheral nerve grafts combined with a chitosan- laminin scaffold and enhancing regeneration through them by co-transplantation with bone-marrow-derived mesenchymal stem cells: case series of 14 patients. *J. Spinal Cord Med.* 37, 54–71. doi: 10.1179/2045772312Y.0000000069

Anderson, K. D., Guest, J. D., Dietrich, W. D., Bunge, M. B., Curiel, R., Dididze, M., et al. (2017). Safety of autologous human Schwann cell transplantation in subacute thoracic spinal cord injury. *J. Neurotrauma* 34, 2950–2963. doi: 10.1089/neu.2016.4895

Anderson, M. A., Burda, J. E., Ren, Y., Ao, Y., O'shea, T. M., Kawaguchi, R., et al. (2016). Astrocyte scar formation aids central nervous system axon regeneration. *Nature* 532, 195–200. doi: 10.1038/nature17623

Antonic, A., Sena, E. S., Lees, J. S., Wills, T. E., Skeers, P., Batchelor, P. E., et al. (2013). Stem cell transplantation in traumatic spinal cord injury: a systematic review and meta-analysis of animal studies. *PLoS Biol.* 11:e1001738. doi: 10.1371/journal.pbio.1001738

Assinck, P., Duncan, G. J., Hilton, B. J., Plemel, J. R., and Tetzlaff, W. (2017). Cell transplantation therapy for spinal cord injury. *Nat. Neurosci.* 20, 637–647. doi: 10.1038/nn.4541

Assuncao-Silva, R. C., Gomes, E. D., Sousa, N., Silva, N. A., and Salgado, A. J. (2015). Hydrogels and cell based therapies in spinal cord injury regeneration. *Stem Cells Int.* 2015:948040. doi: 10.1155/2015/948040

Atala, A. (2000). Tissue engineering of artificial organs. *J. Endourol.* 14, 49–57. doi: 10.1089/end.2000.14.49

Ayuso-Sacido, A., Moliterno, J. A., Kratovac, S., Kapoor, G. S., O'rourke, D. M., Holland, E. C., et al. (2010). Activated EGFR signaling increases proliferation, survival, and migration and blocks neuronal differentiation in post-natal neural stem cells. *J. Neurooncol.* 97, 323–337. doi: 10.1007/s11060-009-0035-x

Badner, A., Siddiqui, A. M., and Fehlings, M. G. (2017). Spinal cord injuries: how could cell therapy help? *Expert Opin. Biol. Ther.* 17, 529–541. doi: 10.1080/14712598.2017.1308481

Baldwin, K. T., and Eroglu, C. (2017). Molecular mechanisms of astrocyte-induced synaptogenesis. *Curr. Opin. Neurobiol.* 45, 113–120. doi: 10.1016/j.conb.2017.05.006

Bartholomew, A., Sturgeon, C., Siatskas, M., Ferrer, K., McIntosh, K., Patil, S., et al. (2002). Mesenchymal stem cells suppress lymphocyte proliferation *in vitro* and prolong skin graft survival *in vivo*. *Exp. Hematol.* 30, 42–48. doi: 10.1016/S0301-472X(01)00769-X

Bellenchi, G. C., Volpicelli, F., Piscopo, V., Perrone-Capano, C., and Di Porzio, U. (2013). Adult neural stem cells: an endogenous tool to repair brain injury? *J. Neurochem.* 124, 159–167. doi: 10.1111/jnc.12084

Bernstein, J. J., and Goldberg, W. J. (1991). Grafted fetal astrocyte migration can prevent host neuronal atrophy: comparison of astrocytes from cultures and whole piece donors. *Restor. Neurol. Neurosci.* 2, 261–270.

Bidarra, S. J., Barrias, C. C., and Granja, P. L. (2014). Injectable alginate hydrogels for cell delivery in tissue engineering. *Acta Biomater.* 10, 1646–1662. doi: 10.1016/j.actbio.2013.12.006

Blesch, A., and Tuszynski, M. H. (2009). Spinal cord injury: plasticity, regeneration and the challenge of translational drug development. *Trends Neurosci.* 32, 41–47. doi: 10.1016/j.tins.2008.09.008

Boisserand, L. S., Kodama, T., Papassin, J., Auzely, R., Moisan, A., Rome, C., et al. (2016). Biomaterial applications in cell-based therapy in experimental stroke. *Stem Cells Int.* 2016:6810562. doi: 10.1155/2016/6810562

Bozkurt, G., Mothe, A. J., Zahir, T., Kim, H., Shoichet, M. S., and Tator, C. H. (2010). Chitosan channels containing spinal cord-derived stem/progenitor cells for repair of subacute spinal cord injury in the rat. *Neurosurgery* 67, 1733–1744. doi: 10.1227/NEU.0b013e3181f9af35

Brock, J. H., Graham, L., Staufenberg, E., Collyer, E., Koffler, J., and Tuszynski, M. H. (2016). Bone marrow stromal cell intraspinal transplants fail to improve motor outcomes in a severe model of spinal cord injury. *J. Neurotrauma* 33, 1103–1114. doi: 10.1089/neu.2015.4009

Cao, J., Sun, C., Zhao, H., Xiao, Z., Chen, B., Gao, J., et al. (2011). The use of laminin modified linear ordered collagen scaffolds loaded with laminin-binding ciliary neurotrophic factor for sciatic nerve regeneration in rats. *Biomaterials* 32, 3939–3948. doi: 10.1016/j.biomaterials.2011.02.020

Cao, Q. L., Howard, R. M., Dennison, J. B., and Whittemore, S. R. (2002). Differentiation of engrafted neuronal-restricted precursor cells is inhibited in the traumatically injured spinal cord. *Exp. Neurol.* 177, 349–359. doi: 10.1006/exnr.2002.7981

Carballo-Molina, O. A., and Velasco, I. (2015). Hydrogels as scaffolds and delivery systems to enhance axonal regeneration after injuries. *Front. Cell. Neurosci.* 9:13. doi: 10.3389/fncel.2015.00013

Chen, B. K., Knight, A. M., De Ruiter, G. C. W., Spinner, R. J., Yaszemski, M. J., Currier, B. L., et al. (2009). Axon regeneration through scaffold into distal spinal cord after transection. *J. Neurotrauma* 26, 1759–1771. doi: 10.1089/neu.2008.0610

Chen, X. G., Katakowski, M., Li, Y., Lu, D. Y., Wang, L., Zhang, L. J., et al. (2002). Human bone marrow stromal cell cultures conditioned by traumatic brain tissue extracts: growth factor production. *J. Neurosci. Res.* 69, 687–691. doi: 10.1002/jnr.10334

Chu, T., Zhou, H., Li, F., Wang, T., Lu, L., and Feng, S. (2014). Astrocyte transplantation for spinal cord injury: current status and perspective. *Brain Res. Bull.* 107, 18–30. doi: 10.1016/j.brainresbull.2014.05.003

Cizkova, D., Rosocha, J., Vanicky, I., Jergova, S., and Cizek, M. (2006). Transplants of human mesenchymal stem cells improve functional recovery after spinal cord injury in the rat. *Cell. Mol. Neurobiol.* 26, 1167–1180. doi: 10.1007/s10571-006-9093-1

Corti, S., Locatelli, F., Donadoni, C., Strazzer, S., Salani, S., Del Bo, R., et al. (2002). Neuroectodermal and microglial differentiation of bone marrow cells in the mouse spinal cord and sensory ganglia. *J. Neurosci. Res.* 70, 721–733. doi: 10.1002/jnr.10455

Cregg, J. M., Depaul, M. A., Filous, A. R., Lang, B. T., Tran, A., and Silver, J. (2014). Functional regeneration beyond the glial scar. *Exp. Neurol.* 253, 197–207. doi: 10.1016/j.expneurol.2013.12.024

Danilov, C. A., and Steward, O. (2015). Conditional genetic deletion of PTEN after a spinal cord injury enhances regenerative growth of CST axons and motor function recovery in mice. *Exp. Neurol.* 266, 147–160. doi: 10.1016/j.expneurol.2015.02.012

Davies, J. E., Huang, C., Proschel, C., Noble, M., Mayer-Proschel, M., and Davies, S. J. (2006). Astrocytes derived from glial-restricted precursors promote spinal cord repair. *J. Biol.* 5:7. doi: 10.1186/jbiol35

Davies, J. E., Proschel, C., Zhang, N., Noble, M., Mayer-Proschel, M., and Davies, S. J. (2008). Transplanted astrocytes derived from BMP- or CNTF-treated glial-restricted precursors have opposite effects on recovery and allodynia after spinal cord injury. *J. Biol.* 7:24. doi: 10.1186/jbiol85

Davies, S. J., Shih, C. H., Noble, M., Mayer-Proschel, M., Davies, J. E., and Proschel, C. (2011). Transplantation of specific human astrocytes promotes functional recovery after spinal cord injury. *PLoS ONE* 6:e17328. doi: 10.1371/journal.pone.0017328

Deans, R. J., and Moseley, A. B. (2000). Mesenchymal stem cells: biology and potential clinical uses. *Exp. Hematol.* 28, 875–884. doi: 10.1016/S0301-472X(00)00482-3

Deng, L. X., Hu, J. G., Liu, N. K., Wang, X. F., Smith, G. M., Wen, X. J., et al. (2011). GDNF modifies reactive astrogliosis allowing robust axonal regeneration through Schwann cell-seeded guidance channels after spinal cord injury. *Exp. Neurol.* 229, 238–250. doi: 10.1016/j.expneurol.2011.02.001

Deumens, R., Koopmans, G. C., Honig, W. M., Hamers, F. P., Maquet, V., Jerome, R., et al. (2006a). Olfactory ensheathing cells, olfactory nerve fibroblasts and biomatrices to promote long-distance axon regrowth and functional recovery in the dorsally hemisected adult rat spinal cord. *Exp. Neurol.* 200, 89–103. doi: 10.1016/j.expneurol.2006.01.030

Deumens, R., Koopmans, G. C., Honig, W. M., Maquet, V., Jerome, R., Steinbusch, H. W., et al. (2006b). Limitations in transplantation of astroglia-biomatrix bridges to stimulate corticospinal axon regrowth across large spinal lesion gaps. *Neurosci. Lett.* 400, 208–212. doi: 10.1016/j.neulet.2006.02.050

Deumens, R., Van Gorp, S. F., Bozkurt, A., Beckmann, C., Fuhrmann, T., Montzka, K., et al. (2013). Motor outcome and allodynia are largely unaffected by novel olfactory ensheathing cell grafts to repair low-thoracic lesion gaps in the adult rat spinal cord. *Behav. Brain Res.* 237, 185–189. doi: 10.1016/j.bbr.2012.09.036

Devivo, M. J., Go, B. K., and Jackson, A. B. (2002). Overview of the national spinal cord injury statistical center database. *J. Spinal Cord Med.* 25, 335–338. doi: 10.1080/10790268.2002.11753637

Dey, I., Midha, N., Singh, G., Forsyth, A., Walsh, S. K., Singh, B., et al. (2013). Diabetic Schwann cells suffer from nerve growth factor and neurotrophin-3 underproduction and poor associability with axons. *Glia* 61, 1990–1999. doi: 10.1002/glia.22570

Du, B. L., Xiong, Y., Zeng, C. G., He, L. M., Zhang, W., Quan, D. P., et al. (2011). Transplantation of artificial neural construct partly improved spinal tissue repair and functional recovery in rats with spinal cord transection. *Brain Res.* 1400, 87–98. doi: 10.1016/j.brainres.2011.05.019

East, E., De Oliveira, D. B., Golding, J. P., and Phillips, J. B. (2010). Alignment of astrocytes increases neuronal growth in three-dimensional collagen gels and is maintained following plastic compression to form a spinal cord repair conduit. *Tissue Eng. Part A* 16, 3173–3184. doi: 10.1089/ten.tea.2010.0017

Falnikar, A., Li, K., and Lepore, A. C. (2015). Therapeutically targeting astrocytes with stem and progenitor cell transplantation following traumatic spinal cord injury. *Brain Res.* 1619, 91–103. doi: 10.1016/j.brainres.2014.09.037

Fan, C., Zheng, Y., Cheng, X., Qi, X., Bu, P., Luo, X., et al. (2013). Transplantation of D15A-expressing glial-restricted-precursor-derived astrocytes improves anatomical and locomotor recovery after spinal cord injury. *Int. J. Biol. Sci.* 9, 78–93. doi: 10.7150/ijbs.5626

Faulkner, J. R., Herrmann, J. E., Woo, M. J., Tansey, K. E., Doan, N. B., and Sofroniew, M. V. (2004). Reactive astrocytes protect tissue and preserve function after spinal cord injury. *J. Neurosci.* 24, 2143–2155. doi: 10.1523/JNEUROSCI.3547-03.2004

Feron, F., Perry, C., Cochrane, J., Licina, P., Nowitzke, A., Urquhart, S., et al. (2005). Autologous olfactory ensheathing cell transplantation in human spinal cord injury. *Brain* 128, 2951–2960. doi: 10.1093/brain/awh657

Filous, A. R., Miller, J. H., Coulson-Thomas, Y. M., Horn, K. P., Alilain, W. J., and Silver, J. (2010). Immature astrocytes promote CNS axonal regeneration when combined with chondroitinase ABC. *Dev. Neurobiol.* 70, 826–841. doi: 10.1002/dneu.20820

Fouad, K., Schnell, L., Bunge, M. B., Schwab, M. E., Liebscher, T., and Pearse, D. D. (2005). Combining Schwann cell bridges and olfactory-ensheathing glia grafts with chondroitinase promotes locomotor recovery after complete transection of the spinal cord. *J. Neurosci.* 25, 1169–1178. doi: 10.1523/JNEUROSCI.3562-04.2005

Franssen, E. H., De Bree, F. M., and Verhaagen, J. (2007). Olfactory ensheathing glia: their contribution to primary olfactory nervous system regeneration and their regenerative potential following transplantation into the injured spinal cord. *Brain Res. Rev.* 56, 236–258. doi: 10.1016/j.brainresrev.2007.07.013

Franz, S., Weidner, N., and Blesch, A. (2012). Gene therapy approaches to enhancing plasticity and regeneration after spinal cord injury. *Exp. Neurol.* 235, 62–69. doi: 10.1016/j.expneurol.2011.01.015

Fu, W., Wang, S. J., Zhou, G. D., Liu, W., Cao, Y., and Zhang, W. J. (2012). Residual undifferentiated cells during differentiation of induced pluripotent stem cells *in vitro* and *in vivo*. *Stem Cells Dev.* 21, 521–529. doi: 10.1089/scd.2011.0131

Führmann, T., Anandakumaran, P. N., and Shoichet, M. S. (2017). Combinatorial therapies after spinal cord injury: how can biomaterials help? *Adv. Healthc. Mater.* 6:1601130. doi: 10.1002/adhm.201601130

Führmann, T., Tam, R. Y., Ballarin, B., Coles, B., Elliott Donaghue, I., Van Der Kooy, D., et al. (2016). Injectable hydrogel promotes early survival of induced pluripotent stem cell-derived oligodendrocytes and attenuates longterm teratoma formation in a spinal cord injury model. *Biomaterials* 83, 23–36. doi: 10.1016/j.biomaterials.2015.12.032

Gao, M. Y., Lu, P., Bednark, B., Lynam, D., Conner, J. M., Sakamoto, J., et al. (2013). Templated agarose scaffolds for the support of motor axon regeneration into sites of complete spinal cord transection. *Biomaterials* 34, 1529–1536. doi: 10.1016/j.biomaterials.2012.10.070

Geller, H. M., and Fawcett, J. W. (2002). Building a bridge: engineering spinal cord repair. *Exp. Neurol.* 174, 125–136. doi: 10.1006/exnr.2002.7865

Ghirnikar, R. S., and Eng, L. F. (1994). Astrocyte-Schwann cell interactions in culture. *Glia* 11, 367–377. doi: 10.1002/glia.440110409

Godinho, M. J., Teh, L., Pollett, M. A., Goodman, D., Hodgetts, S. I., Sweetman, I., et al. (2013). Immunohistochemical, ultrastructural and functional analysis of axonal regeneration through peripheral nerve grafts containing Schwann cells expressing BDNF, CNTF or NT3. *PLoS ONE* 8:e69987. doi: 10.1371/journal.pone.0069987

Gomes-Osman, J., Cortes, M., Guest, J., and Pascual-Leone, A. (2016). A systematic review of experimental strategies aimed at improving motor function after acute and chronic spinal cord injury. *J. Neurotrauma* 33, 425–438. doi: 10.1089/neu.2014.3812

Gong, Y., Wang, H. F., and Xia, H. J. (2015). Stable transfection into rat bone marrow mesenchymal stem cells by lentivirus-mediated NT-3. *Mol. Med. Rep.* 11, 367–373. doi: 10.3892/mmr.2014.2727

Granger, N., Franklin, R. J., and Jeffery, N. D. (2014). Cell therapy for spinal cord injuries: what is really going on? *Neuroscientist* 20, 623–638. doi: 10.1177/1073858413514635

Gros, T., Sakamoto, J. S., Blesch, A., Havton, L. A., and Tuszynski, M. H. (2010). Regeneration of long-tract axons through sites of spinal cord injury using templated agarose scaffolds. *Biomaterials* 31, 6719–6729. doi: 10.1016/j.biomaterials.2010.04.035

Grulova, I., Slovinska, L., Blasko, J., Devaux, S., Wisztorski, M., Salzet, M., et al. (2015). Delivery of alginate scaffold releasing two trophic factors for spinal cord injury repair. *Sci. Rep.* 5:13702. doi: 10.1038/srep13702

Gunther, M. I., Gunther, M., Schneiders, M., Rupp, R., and Blesch, A. (2015a). AngleJ: a new tool for the automated measurement of neurite growth orientation in tissue sections. *J. Neurosci. Methods* 251, 143–150. doi: 10.1016/j.jneumeth.2015.05.021

Gunther, M. I., Weidner, N., Muller, R., and Blesch, A. (2015b). Cell-seeded alginate hydrogel scaffolds promote directed linear axonal regeneration in the injured rat spinal cord. *Acta Biomater.* 27, 140–150. doi: 10.1016/j.actbio.2015.09.001

Guo, X., Dillman, J. F. III., Dawson, V. L., and Dawson, T. M. (2001). Neuroimmunophilins: novel neuroprotective and neuroregenerative targets. *Ann. Neurol.* 50, 6–16. doi: 10.1002/ana.1030

Haas, C., and Fischer, I. (2013). Human astrocytes derived from glial restricted progenitors support regeneration of the injured spinal cord. *J. Neurotrauma* 30, 1035–1052. doi: 10.1089/neu.2013.2915

Haas, C., Neuhuber, B., Yamagami, T., Rao, M., and Fischer, I. (2012). Phenotypic analysis of astrocytes derived from glial restricted precursors and their impact on axon regeneration. *Exp. Neurol.* 233, 717–732. doi: 10.1016/j.expneurol.2011.11.002

Hara, M., Kobayakawa, K., Ohkawa, Y., Kumamaru, H., Yokota, K., Saito, T., et al. (2017). Interaction of reactive astrocytes with type I collagen induces astrocytic scar formation through the integrin-N-cadherin pathway after spinal cord injury. *Nat. Med.* 23, 818–828. doi: 10.1038/nm.4354

Hatami, M., Mehrjardi, N. Z., Kiani, S., Hemmesi, K., Azizi, H., Shahverdi, A., et al. (2009). Human embryonic stem cell-derived neural precursor transplants in collagen scaffolds promote recovery in injured rat spinal cord. *Cytotherapy* 11, 618–630. doi: 10.1080/14653240903005802

Hellal, F., Hurtado, A., Ruschel, J., Flynn, K. C., Laskowski, C. J., Umlauf, M., et al. (2011). Microtubule stabilization reduces scarring and causes axon regeneration after spinal cord injury. *Science* 331, 928–931. doi: 10.1126/science.1201148

Hill, C. E., Proschel, C., Noble, M., Mayer-Proschel, M., Gensel, J. C., Beattie, M. S., et al. (2004). Acute transplantation of glial-restricted precursor cells into spinal cord contusion injuries: survival, differentiation, and effects on lesion environment and axonal regeneration. *Exp. Neurol.* 190, 289–310. doi: 10.1016/j.expneurol.2004.05.043

Hofstetter, C. P., Holmstrom, N. A., Lilja, J. A., Schweinhardt, P., Hao, J., Spenger, C., et al. (2005). Allodynia limits the usefulness of intraspinal neural stem cell grafts; directed differentiation improves outcome. *Nat. Neurosci.* 8, 346–353. doi: 10.1038/nn1405

Hou, S., Xu, Q., Tian, W., Cui, F., Cai, Q., Ma, J., et al. (2005). The repair of brain lesion by implantation of hyaluronic acid hydrogels modified with laminin. *J. Neurosci. Methods* 148, 60–70. doi: 10.1016/j.jneumeth.2005.04.016

Hu, B. Y., Weick, J. P., Yu, J., Ma, L. X., Zhang, X. Q., Thomson, J. A., et al. (2010). Neural differentiation of human induced pluripotent stem cells follows developmental principles but with variable potency. *Proc. Natl. Acad. Sci. U.S.A.* 107, 4335–4340. doi: 10.1073/pnas.0910012107

Hurtado, A., Moon, L. D. F., Maquet, V., Blits, B., Jerome, R., and Oudega, M. (2006). Poly (D,L-lactic acid) macroporous guidance scaffolds seeded with Schwann cells genetically modified to secrete a bi-functional neurotrophin implanted in the completely transected adult rat thoracic spinal cord. *Biomaterials* 27, 430–442. doi: 10.1016/j.biomaterials.2005.07.014

Hwang, D. H., Kim, H. M., Kang, Y. M., Joo, I. S., Cho, C. S., Yoon, B. W., et al. (2011). Combination of multifaceted strategies to maximize the therapeutic benefits of neural stem cell transplantation for spinal cord repair. *Cell Transplant.* 20, 1361–1379. doi: 10.3727/096368910X557155

Iannotti, C., Ping Zhang, Y., Shields, C. B., Han, Y., Burke, D. A., and Xu, X. M. (2004). A neuroprotective role of glial cell line-derived neurotrophic factor following moderate spinal cord contusion injury. *Exp. Neurol.* 189, 317–332. doi: 10.1016/j.expneurol.2004.05.033

Iwanami, A., Kaneko, S., Nakamura, M., Kanemura, Y., Mori, H., Kobayashi, S., et al. (2005). Transplantation of human neural stem cells for spinal cord injury in primates. *J. Neurosci. Res.* 80, 182–190. doi: 10.1002/jnr.20436

Jain, N. B., Ayers, G. D., Peterson, E. N., Harris, M. B., Morse, L., O'connor, K. C., et al. (2015). Traumatic spinal cord injury in the United States, 1993-2012. *J. Am. Med. Assoc.* 313, 2236–2243. doi: 10.1001/jama.2015.6250

Jazayeri, S. B., Beygi, S., Shokraneh, F., Hagen, E. M., and Rahimi-Movaghar, V. (2015). Incidence of traumatic spinal cord injury worldwide: a systematic review. *Eur. Spine J.* 24, 905–918. doi: 10.1007/s00586-014-3424-6

Jin, Y., Neuhuber, B., Singh, A., Bouyer, J., Lepore, A., Bonner, J., et al. (2011). Transplantation of human glial restricted progenitors and derived astrocytes into a contusion model of spinal cord injury. *J. Neurotrauma* 28, 579–594. doi: 10.1089/neu.2010.1626

Joosten, E. A., Veldhuis, W. B., and Hamers, F. P. (2004). Collagen containing neonatal astrocytes stimulates regrowth of injured fibers and promotes modest locomotor recovery after spinal cord injury. *J. Neurosci. Res.* 77, 127–142. doi: 10.1002/jnr.20088

Kadoya, K., Lu, P., Nguyen, K., Lee-Kubli, C., Kumamaru, H., Yao, L., et al. (2016). Spinal cord reconstitution with homologous neural grafts enables robust corticospinal regeneration. *Nat. Med.* 22, 479–487. doi: 10.1038/nm.4066

Kanno, H., Pearse, D. D., Ozawa, H., Itoi, E., and Bunge, M. B. (2015). Schwann cell transplantation for spinal cord injury repair: its significant therapeutic potential and prospectus. *Rev. Neurosci.* 26, 121–128. doi: 10.1515/revneuro-2014-0068

Kanno, H., Pressman, Y., Moody, A., Berg, R., Muir, E. M., Rogers, J. H., et al. (2014). Combination of engineered Schwann cell grafts to secrete neurotrophin and chondroitinase promotes axonal regeneration and locomotion after spinal cord injury. *J. Neurosci.* 34, 1838–1855. doi: 10.1523/JNEUROSCI.2661-13.2014

Karamouzian, S., Nematollahi-Mahani, S. N., Nakhaee, N., and Eskandary, H. (2012). Clinical safety and primary efficacy of bone marrow mesenchymal cell transplantation in subacute spinal cord injured patients. *Clin. Neurol. Neurosurg.* 114, 935–939. doi: 10.1016/j.clineuro.2012.02.003

Khaing, Z. Z., Milman, B. D., Vanscoy, J. E., Seidlits, S. K., Grill, R. J., and Schmidt, C. E. (2011). High molecular weight hyaluronic acid limits astrocyte activation and scar formation after spinal cord injury. *J. Neural Eng.* 8:046033. doi: 10.1088/1741-2560/8/4/046033

Khakh, B. S., and Sofroniew, M. V. (2015). Diversity of astrocyte functions and phenotypes in neural circuits. *Nat. Neurosci.* 18, 942–952. doi: 10.1038/nn.4043

Kim, B. G., Kang, Y. M., Phi, J. H., Kim, Y. H., Hwang, D. H., Choi, J. Y., et al. (2010). Implantation of polymer scaffolds seeded with neural stem cells in a canine spinal cord injury model. *Cytotherapy* 12, 841–845. doi: 10.3109/14653249.2010.501784

Kim, J. W., Ha, K. Y., Molon, J. N., and Kim, Y. H. (2013). Bone marrow-derived mesenchymal stem cell transplantation for chronic spinal cord injury in rats comparative study between intralesional and intravenous transplantation. *Spine* 38, E1065–E1074. doi: 10.1097/BRS.0b013e31829839fa

Kim, M., Park, S. R., and Choi, B. H. (2014). Biomaterial scaffolds used for the regeneration of spinal cord injury (SCI). *Histol. Histopathol.* 29, 1395–1408. doi: 10.14670/HH-29.1395

Kimelberg, H. K., and Nedergaard, M. (2010). Functions of astrocytes and their potential as therapeutic targets. *Neurotherapeutics* 7, 338–353. doi: 10.1016/j.nurt.2010.07.006

Kliot, M., Smith, G. M., Siegal, J. D., and Silver, J. (1990). Astrocyte-polymer implants promote regeneration of dorsal root fibers into the adult mammalian spinal cord. *Exp. Neurol.* 109, 57–69. doi: 10.1016/S0014-4886(05)80008-1

Koprivica, V., Cho, K. S., Park, J. B., Yiu, G., Atwal, J., Gore, B., et al. (2005). EGFR activation mediates inhibition of axon regeneration by myelin and chondroitin sulfate proteoglycans. *Science* 310, 106–110. doi: 10.1126/science.1115462

Krishna, V., Konakondla, S., Nicholas, J., Varma, A., Kindy, M., and Wen, X. (2013). Biomaterial-based interventions for neuronal regeneration and functional recovery in rodent model of spinal cord injury: a systematic review. *J. Spinal Cord Med.* 36, 174–190. doi: 10.1179/2045772313Y.0000000095

Kumar, A. A., Kumar, S. R., Narayanan, R., Arul, K., and Baskaran, M. (2009). Autologous bone marrow derived mononuclear cell therapy for spinal cord injury: a phase I/II clinical safety and primary efficacy data. *Exp. Clin. Transplant.* 7, 241–248.

Lakatos, A., Franklin, R. J. M., and Barnett, S. C. (2000). Olfactory ensheathing cells and Schwann cells differ in their *in vitro* interactions with astrocytes. *Glia* 32, 214–225. doi: 10.1002/1098-1136(200012)32:3<214::AID-GLIA20>3.0.CO;2-7

Lee, B. B., Cripps, R. A., Fitzharris, M., and Wing, P. C. (2014). The global map for traumatic spinal cord injury epidemiology: update 2011, global incidence rate. *Spinal Cord* 52, 110–116. doi: 10.1038/sc.2012.158

Lepore, A. C., Han, S. S., Tyler-Polsz, C. J., Cai, J., Rao, M. S., and Fischer, I. (2004). Differential fate of multipotent and lineage-restricted neural precursors following transplantation into the adult CNS. *Neuron Glia Biol.* 1, 113–126. doi: 10.1017/S1740925X04000213

Li, B. C., Jiao, S. S., Xu, C., You, H., and Chen, J. M. (2010). PLGA conduit seeded with olfactory ensheathing cells for bridging sciatic nerve defect of rats. *J. Biomed. Mater. Res. A* 94, 769–780. doi: 10.1002/jbm.a.32727

Li, X., Xiao, Z., Han, J., Chen, L., Xiao, H., Ma, F., et al. (2013). Promotion of neuronal differentiation of neural progenitor cells by using EGFR antibody functionalized collagen scaffolds for spinal cord injury repair. *Biomaterials* 34, 5107–5116. doi: 10.1016/j.biomaterials.2013.03.062

Li, Y., Field, P. M., and Raisman, G. (1997). Repair of adult rat corticospinal tract by transplants of olfactory ensheathing cells. *Science* 277, 2000–2002. doi: 10.1126/science.277.5334.2000

Li, Y., Li, D., and Raisman, G. (2005). Interaction of olfactory ensheathing cells with astrocytes may be the key to repair of tract injuries in the spinal cord: the "pathway hypothesis". *J. Neurocytol.* 34, 343–351. doi: 10.1007/s11068-005-8361-1

Li, Z. W., Tang, R. H., Zhang, J. P., Tang, Z. P., Qu, W. S., Zhu, W. H., et al. (2011). Inhibiting epidermal growth factor receptor attenuates reactive astrogliosis and improves functional outcome after spinal cord injury in rats. *Neurochem. Int.* 58, 812–819. doi: 10.1016/j.neuint.2011.03.007

Liddelow, S. A., and Barres, B. A. (2017). Reactive astrocytes: production, function, and therapeutic potential. *Immunity* 46, 957–967. doi: 10.1016/j.immuni.2017.06.006

Lin, X. Y., Lai, B. Q., Zeng, X., Che, M. T., Ling, E. A., Wu, W., et al. (2016). Cell transplantation and neuroengineering approach for spinal cord injury treatment: a summary of current laboratory findings and review of literature. *Cell Transplant.* 25, 1425–1438. doi: 10.3727/096368916X690836

Liu, S., Sandner, B., Schackel, T., Nicholson, L., Chtarto, A., Tenenbaum, L., et al. (2017). Regulated viral BDNF delivery in combination with Schwann cells promotes axonal regeneration through capillary alginate hydrogels after spinal cord injury. *Acta Biomater*. 60, 167–180. doi: 10.1016/j.actbio.2017.07.024

Liu, Z., Tang, Y., Lu, S., Zhou, J., Du, Z., Duan, C., et al. (2013). The tumourigenicity of iPS cells and their differentiated derivates. *J. Cell. Mol. Med.* 17, 782–791. doi: 10.1111/jcmm.12062

Lu, P., Blesch, A., and Tuszynski, M. H. (2004). Induction of bone marrow stromal cells to neurons: differentiation, transdifferentiation, or artifact? *J. Neurosci. Res.* 77, 174–191. doi: 10.1002/jnr.20148

Lu, P., Graham, L., Wang, Y., Wu, D., and Tuszynski, M. (2014a). Promotion of survival and differentiation of neural stem cells with fibrin and growth factor cocktails after severe spinal cord injury. *J. Vis. Exp.* e50641. doi: 10.3791/50641

Lu, P., Wang, Y., Graham, L., McHale, K., Gao, M., Wu, D., et al. (2012). Long-distance growth and connectivity of neural stem cells after severe spinal cord injury. *Cell* 150, 1264–1273. doi: 10.1016/j.cell.2012.08.020

Lu, P., Woodruff, G., Wang, Y., Graham, L., Hunt, M., Wu, D., et al. (2014b). Long-distance axonal growth from human induced pluripotent stem cells after spinal cord injury. *Neuron* 83, 789–796. doi: 10.1016/j.neuron.2014.07.014

Lukovic, D., Stojkovic, M., Moreno-Manzano, V., Jendelova, P., Sykova, E., Bhattacharya, S. S., et al. (2015). Concise review: reactive astrocytes and stem cells in spinal cord injury: good guys or bad guys? *Stem Cells* 33, 1036–1041. doi: 10.1002/stem.1959

Luo, Z., Yang, Y., Deng, Y., Sun, Y., Yang, H., and Wei, S. (2016). Peptide-incorporated 3D porous alginate scaffolds with enhanced osteogenesis for bone tissue engineering. *Colloids Surf. B Biointerfaces* 143, 243–251. doi: 10.1016/j.colsurfb.2016.03.047

Macias, M. Y., Syring, M. B., Pizzi, M. A., Crowe, M. J., Alexanian, A. R., and Kurpad, S. N. (2006). Pain with no gain: allodynia following neural stem cell transplantation in spinal cord injury. *Exp. Neurol.* 201, 335–348. doi: 10.1016/j.expneurol.2006.04.035

Mackay-Sim, A., Feron, F., Cochrane, J., Bassingthwaighte, L., Bayliss, C., Davies, W., et al. (2008). Autologous olfactory ensheathing cell transplantation in human paraplegia: a 3-year clinical trial. *Brain* 131, 2376–2386. doi: 10.1093/brain/awn173

Madigan, N. N., McMahon, S., O'brien, T., Yaszemski, M. J., and Windebank, A. J. (2009). Current tissue engineering and novel therapeutic approaches to axonal regeneration following spinal cord injury using polymer scaffolds. *Respir. Physiol. Neurobiol.* 169, 183–199. doi: 10.1016/j.resp.2009.08.015

Marcol, W., Slusarczyk, W., Larysz-Brysz, M., Francuz, T., Jedrzejowska-Szypulka, H., Labuzek, K., et al. (2015). Grafted activated Schwann cells support survival of injured rat spinal cord white matter. *World Neurosurg.* 84, 511–519. doi: 10.1016/j.wneu.2015.04.027

Matsuda, R., Yoshikawa, M., Kimura, H., Ouji, Y., Nakase, H., Nishimura, F., et al. (2009). Cotransplantation of mouse embryonic stem cells and bone marrow stromal cells following spinal cord injury suppresses tumor development. *Cell Transplant.* 18, 39–54. doi: 10.3727/096368909788237122

Matsui, T., Akamatsu, W., Nakamura, M., and Okano, H. (2014). Regeneration of the damaged central nervous system through reprogramming technology: basic concepts and potential application for cell replacement therapy. *Exp. Neurol.* 260, 12–18. doi: 10.1016/j.expneurol.2012.09.016

McCall, J., Weidner, N., and Blesch, A. (2012). Neurotrophic factors in combinatorial approaches for spinal cord regeneration. *Cell Tissue Res.* 349, 27–37. doi: 10.1007/s00441-012-1388-6

McCreedy, D. A., Wilems, T. S., Xu, H., Butts, J. C., Brown, C. R., Smith, A. W., et al. (2014). Survival, differentiation, and migration of high-purity mouse embryonic stem cell-derived progenitor motor neurons in fibrin scaffolds after sub-acute spinal cord injury. *Biomater. Sci.* 2, 1672–1682. doi: 10.1039/C4BM00106K

Mekhail, M., Almazan, G., and Tabrizian, M. (2015). Purine-crosslinked injectable chitosan sponges promote oligodendrocyte progenitor cells' attachment and differentiation. *Biomater. Sci.* 3, 279–287. doi: 10.1039/C4BM00215F

Mendonca, M. V. P., Larocca, T. F., Souza, B. S. D., Villarreal, C. F., Silva, L. F. M., Matos, A. C., et al. (2014). Safety and neurological assessments after autologous transplantation of bone marrow mesenchymal stem cells in subjects with chronic spinal cord injury. *Stem Cell Res. Ther.* 5:126. doi: 10.1186/scrt516

Mertens, J., Marchetto, M. C., Bardy, C., and Gage, F. H. (2016). Evaluating cell reprogramming, differentiation and conversion technologies in neuroscience. *Nat. Rev. Neurosci.* 17, 424–437. doi: 10.1038/nrn.2016.46

Miller, C., Shanks, H., Witt, A., Rutkowski, G., and Mallapragada, S. (2001). Oriented Schwann cell growth on micropatterned biodegradable polymer substrates. *Biomaterials* 22, 1263–1269. doi: 10.1016/S0142-9612(00)00278-7

Mothe, A. J., Tam, R. Y., Zahir, T., Tator, C. H., and Shoichet, M. S. (2013). Repair of the injured spinal cord by transplantation of neural stem cells in a hyaluronan-based hydrogel. *Biomaterials* 34, 3775–3783. doi: 10.1016/j.biomaterials.2013.02.002

Noh, M. Y., Lim, S. M., Oh, K. W., Cho, K. A., Park, J., Kim, K. S., et al. (2016). Mesenchymal stem cells modulate the functional properties of microglia via TGF-beta secretion. *Stem Cells Transl. Med.* 5, 1538–1549. doi: 10.5966/sctm.2015-0217

Nomura, H., Zahir, T., Kim, H., Katayama, Y., Kulbatski, I., Morshead, C. M., et al. (2008). Extramedullary chitosan channels promote survival of transplanted neural stem and progenitor cells and create a tissue bridge after complete spinal cord transection. *Tissue Eng. Part A* 14, 649–665. doi: 10.1089/tea.2007.0180

Novikova, L. N., Lobov, S., Wiberg, M., and Novikov, L. N. (2011). Efficacy of olfactory ensheathing cells to support regeneration after spinal cord injury is influenced by method of culture preparation. *Exp. Neurol.* 229, 132–142. doi: 10.1016/j.expneurol.2010.09.021

Novikova, L. N., Mosahebi, A., Wiberg, M., Terenghi, G., Kellerth, J. O., and Novikov, L. N. (2006). Alginate hydrogel and matrigel as potential cell carriers for neurotransplantation. *J. Biomed. Mater. Res. A* 77, 242–252. doi: 10.1002/jbm.a.30603

Novikova, L. N., Pettersson, J., Brohlin, M., Wiberg, M., and Novikov, L. N. (2008). Biodegradable poly-beta-hydroxybutyrate scaffold seeded with Schwann cells to promote spinal cord repair. *Biomaterials* 29, 1198–1206. doi: 10.1016/j.biomaterials.2007.11.033

Ogle, B. M., Bursac, N., Domian, I., Huang, N. F., Menasche, P., Murry, C. E., et al. (2016). Distilling complexity to advance cardiac tissue engineering. *Sci. Transl. Med.* 8:342ps313. doi: 10.1126/scitranslmed.aad2304

Ohta, M., Suzuki, Y., Noda, T., Ejiri, Y., Dezawa, M., Kataoka, K., et al. (2004). Bone marrow stromal cells infused into the cerebrospinal fluid promote functional recovery of the injured rat spinal cord with reduced cavity formation. *Exp. Neurol.* 187, 266–278. doi: 10.1016/j.expneurol.2004.01.021

Oliveri, R. S., Bello, S., and Biering-Sorensen, F. (2014). Mesenchymal stem cells improve locomotor recovery in traumatic spinal cord injury: systematic review with meta-analyses of rat models. *Neurobiol. Dis.* 62, 338–353. doi: 10.1016/j.nbd.2013.10.014

Olson, H. E., Rooney, G. E., Gross, L., Nesbitt, J. J., Galvin, K. E., Knight, A., et al. (2009). Neural stem cell- and Schwann cell-loaded biodegradable polymer scaffolds support axonal regeneration in the transected spinal cord. *Tissue Eng. Part A* 15, 1797–1805. doi: 10.1089/ten.tea.2008.0364

Onuma-Ukegawa, M., Bhatt, K., Hirai, T., Kaburagi, H., Sotome, S., Wakabayashi, Y., et al. (2015). Bone marrow stromal cells combined with a honeycomb collagen sponge facilitate neurite elongation *in vitro* and neural restoration in the hemisected rat spinal cord. *Cell Transplant.* 24, 1283–1297. doi: 10.3727/096368914X682134

Oraee-Yazdani, S., Hafizi, M., Atashi, A., Ashrafi, F., Seddighi, A. S., Hashemi, S. M., et al. (2016). Co-transplantation of autologous bone marrow mesenchymal stem cells and Schwann cells through cerebral spinal fluid for the treatment of patients with chronic spinal cord injury: safety and possible outcome. *Spinal Cord* 54, 102–109. doi: 10.1038/sc.2015.142

Park, H. C., Shim, Y. S., Ha, Y., Yoon, S. H., Park, S. R., Choi, B. H., et al. (2005). Treatment of complete spinal cord injury patients by autologous bone marrow cell transplantation and administration of granulocyte-macrophage colony stimulating factor. *Tissue Eng.* 11, 913–922. doi: 10.1089/ten.2005.11.913

Park, S. S., Lee, Y. J., Lee, S. H., Lee, D., Choi, K., Kim, W. H., et al. (2012). Functional recovery after spinal cord injury in dogs treated with a combination of Matrigel and neural-induced adipose-derived mesenchymal Stem cells. *Cytotherapy* 14, 584–597. doi: 10.3109/14653249.2012.658913

Parr, A. M., Kulbatski, I., Zahir, T., Wang, X., Yue, C., Keating, A., et al. (2008). Transplanted adult spinal cord-derived neural stem/progenitor cells promote early functional recovery after rat spinal cord injury. *Neuroscience* 155, 760–770. doi: 10.1016/j.neuroscience.2008.05.042

Pawar, K., Cummings, B. J., Thomas, A., Shea, L. D., Levine, A., Pfaff, S., et al. (2015a). Biomaterial bridges enable regeneration and re-entry of corticospinal tract axons into the caudal spinal cord after SCI: association with recovery of forelimb function. *Biomaterials* 65, 1–12. doi: 10.1016/j.biomaterials.2015.05.032

Pawar, K., Prang, P., Muller, R., Caioni, M., Bogdahn, U., Kunz, W., et al. (2015b). Intrinsic and extrinsic determinants of central nervous system axon outgrowth into alginate-based anisotropic hydrogels. *Acta Biomater.* 27, 131–139. doi: 10.1016/j.actbio.2015.08.032

Pearse, D. D., and Barakat, D. J. (2006). Cellular repair strategies for spinal cord injury. *Expert Opin. Biol. Ther.* 6, 639–652. doi: 10.1517/14712598.6.7.639

Pearse, D. D., Sanchez, A. R., Pereira, F. C., Andrade, C. M., Puzis, R., Pressman, Y., et al. (2007). Transplantation of Schwann cells and/or olfactory ensheathing glia into the contused spinal cord: survival, migration, axon association, and functional recovery. *Glia* 55, 976–1000. doi: 10.1002/glia.20490

Pencalet, P., Serguera, C., Corti, O., Privat, A., Mallet, J., and Gimenez Y Ribotta, M. (2006). Integration of genetically modified adult astrocytes into the lesioned rat spinal cord. *J. Neurosci. Res.* 83, 61–67. doi: 10.1002/jnr.20697

Plant, G. W., Bates, M. L., and Bunge, M. B. (2001). Inhibitory proteoglycan immunoreactivity is higher at the caudal than the rostral Schwann cell graft-transected spinal cord interface. *Mol. Cell. Neurosci.* 17, 471–487. doi: 10.1006/mcne.2000.0948

Powell, E. M., and Geller, H. M. (1999). Dissection of astrocyte-mediated cues in neuronal guidance and process extension. *Glia* 26, 73–83.

Pritchard, C. D., Slotkin, J. R., Yu, D., Dai, H., Lawrence, M. S., Bronson, R. T., et al. (2010). Establishing a model spinal cord injury in the African green monkey for the preclinical evaluation of biodegradable polymer scaffolds seeded with human neural stem cells. *J. Neurosci. Methods* 188, 258–269. doi: 10.1016/j.jneumeth.2010.02.019

Qu, W. S., Tian, D. S., Guo, Z. B., Fang, J., Zhang, Q., Yu, Z. Y., et al. (2012). Inhibition of EGFR/MAPK signaling reduces microglial inflammatory response and the associated secondary damage in rats after spinal cord injury. *J. Neuroinflammation* 9:178. doi: 10.1186/1742-2094-9-178

Ramon-Cueto, A., and Nieto-Sampedro, M. (1992). Glial cells from adult rat olfactory bulb: immunocytochemical properties of pure cultures of ensheathing cells. *Neuroscience* 47, 213–220. doi: 10.1016/0306-4522(92)90134-N

Ramon-Cueto, A., Plant, G. W., Avila, J., and Bunge, M. B. (1998). Long-distance axonal regeneration in the transected adult rat spinal cord is promoted by olfactory ensheathing glia transplants. *J. Neurosci.* 18, 3803–3815.

Rath, E. M., Kelly, D., Bouldin, T. W., and Popko, B. (1995). Impaired peripheral nerve regeneration in a mutant strain of mice (Enr) with a Schwann cell defect. *J. Neurosci.* 15, 7226–7237.

Rauch, M. F., Hynes, S. R., Bertram, J., Redmond, A., Robinson, R., Williams, C., et al. (2009). Engineering angiogenesis following spinal cord injury: a coculture of neural progenitor and endothelial cells in a degradable polymer implant leads to an increase in vessel density and formation of the blood-spinal cord barrier. *Eur. J. Neurosci.* 29, 132–145. doi: 10.1111/j.1460-9568.2008.06567.x

Reeves, A., and Keirstead, H. S. (2012). Stem cell based strategies for spinal cord injury repair. *Adv. Exp. Med. Biol.* 760, 16–24. doi: 10.1007/978-1-4614-4090-1_2

Ritfeld, G. J., Patel, A., Chou, A., Novosat, T. L., Castillo, D. G., Roos, R., et al. (2015). The role of brain-derived neurotrophic factor in bone marrow stromal cell-mediated spinal cord repair. *Cell Transplant.* 24, 2209–2220. doi: 10.3727/096368915X686201

Rizek, P. N., and Kawaja, M. D. (2006). Cultures of rat olfactory ensheathing cells are contaminated with Schwann cells. *Neuroreport* 17, 459–462. doi: 10.1097/01.wnr.0000209000.32857.1b

Robinson, J., and Lu, P. (2017). Optimization of trophic support for neural stem cell grafts in sites of spinal cord injury. *Exp. Neurol.* 291, 87–97. doi: 10.1016/j.expneurol.2017.02.007

Ruff, C. A., Wilcox, J. T., and Fehlings, M. G. (2012). Cell-based transplantation strategies to promote plasticity following spinal cord injury. *Exp. Neurol.* 235, 78–90. doi: 10.1016/j.expneurol.2011.02.010

Sandner, B., Rivera, F. J., Caioni, M., Nicholson, L., Eckstein, V., Bogdahn, U., et al. (2013). Bone morphogenetic proteins prevent bone marrow stromal cell-mediated oligodendroglial differentiation of transplanted adult neural progenitor cells in the injured spinal cord. *Stem Cell Res.* 11, 758–771. doi: 10.1016/j.scr.2013.05.003

Sasaki, M., Hains, B. C., Lankford, K. L., Waxman, S. G., and Kocsis, J. D. (2006). Protection of corticospinal tract neurons after dorsal spinal cord transection and engraftment of olfactory ensheathing cells. *Glia* 53, 352–359. doi: 10.1002/glia.20285

Seyedhassantehrani, N., Li, Y., and Yao, L. (2016). Dynamic behaviors of astrocytes in chemically modified fibrin and collagen hydrogels. *Integr. Biol.* 8, 624–634. doi: 10.1039/C6IB00003G

Shin, J. C., Kim, K. N., Yoo, J., Kim, I. S., Yun, S., Lee, H., et al. (2015). Clinical trial of human fetal brain-derived neural stem/progenitor cell transplantation in patients with traumatic cervical spinal cord injury. *Neural Plast.* 2015:630932. doi: 10.1155/2015/630932

Siebert, J. R., Eade, A. M., and Osterhout, D. J. (2015). Biomaterial approaches to enhancing neurorestoration after spinal cord injury: strategies for overcoming inherent biological obstacles. *Biomed Res. Int.* 2015:752572. doi: 10.1155/2015/752572

Silva, N. A., Sousa, N., Reis, R. L., and Salgado, A. J. (2014). From basics to clinical: a comprehensive review on spinal cord injury. *Prog. Neurobiol.* 114, 25–57. doi: 10.1016/j.pneurobio.2013.11.002

Silver, J., Lorenz, S. E., Wahlsten, D., and Coughlin, J. (1982). Axonal guidance during development of the great cerebral commissures: descriptive and experimental studies, *in vivo*, on the role of preformed glial pathways. *J. Comp. Neurol.* 210, 10–29. doi: 10.1002/cne.902100103

Singh, A., Tetreault, L., Kalsi-Ryan, S., Nouri, A., and Fehlings, M. G. (2014). Global prevalence and incidence of traumatic spinal cord injury. *Clin. Epidemiol.* 6, 309–331. doi: 10.2147/CLEP.S68889

Smith, G. M., and Miller, R. H. (1991). Immature type-1 astrocytes suppress glial scar formation, are motile and interact with blood vessels. *Brain Res.* 543, 111–122. doi: 10.1016/0006-8993(91)91054-5

Smith, G. M., and Silver, J. (1988). Transplantation of immature and mature astrocytes and their effect on scar formation in the lesioned central nervous system. *Prog. Brain Res.* 78, 353–361. doi: 10.1016/S0079-6123(08)60304-0

Smith-Thomas, L. C., Fok-Seang, J., Stevens, J., Du, J. S., Muir, E., Faissner, A., et al. (1994). An inhibitor of neurite outgrowth produced by astrocytes. *J. Cell Sci.* 107(Pt 6), 1687–1695.

Sofroniew, M. V. (2009). Molecular dissection of reactive astrogliosis and glial scar formation. *Trends Neurosci.* 32, 638–647. doi: 10.1016/j.tins.2009.08.002

Sofroniew, M. V., and Vinters, H. V. (2010). Astrocytes: biology and pathology. *Acta Neuropathol.* 119, 7–35. doi: 10.1007/s00401-009-0619-8

Suzuki, H., Kanchiku, T., Imajo, Y., Yoshida, Y., Nishida, N., Gondo, T., et al. (2015). Artificial collagen-filament scaffold promotes axon regeneration and long tract reconstruction in a rat model of spinal cord transection. *Med. Mol. Morphol.* 48, 214–224. doi: 10.1007/s00795-015-0104-5

Suzuki, Y., Kitaura, M., Wu, S. F., Kataoka, K., Suzuki, K., Endo, K., et al. (2002). Electrophysiological and horseradish peroxidase-tracing studies of nerve regeneration through alginate-filled gap in adult rat spinal cord. *Neurosci. Lett.* 318, 121–124. doi: 10.1016/S0304-3940(01)02359-X

Swanger, S. A., Neuhuber, B., Himes, B. T., Bakshi, A., and Fischer, I. (2005). Analysis of allogeneic and syngeneic bone marrow stromal cell graft survival in the spinal cord. *Cell Transplant.* 14, 775–786. doi: 10.3727/000000005783982594

Sykova, E., Jendelova, P., Urdzikova, L., Lesny, P., and Hejcl, A. (2006). Bone marrow stem cells and polymer hydrogels–two strategies for spinal cord injury repair. *Cell Mol. Neurobiol.* 26, 1113–1129. doi: 10.1007/s10571-006-9007-2

Tabakow, P., Jarmundowicz, W., Czapiga, B., Fortuna, W., Miedzybrodzki, R., Czyz, M., et al. (2013). Transplantation of autologous olfactory ensheathing cells in complete human spinal cord injury. *Cell Transplant.* 22, 1591–1612. doi: 10.3727/096368912X663532

Tabesh, H., Amoabediny, G., Nik, N. S., Heydari, M., Yosefifard, M., Siadat, S. O. R., et al. (2009). The role of biodegradable engineered scaffolds seeded with Schwann cells for spinal cord regeneration. *Neurochem. Int.* 54, 73–83. doi: 10.1016/j.neuint.2008.11.002

Takahashi, Y., Tsuji, O., Kumagai, G., Hara, C. M., Okano, H. J., Miyawaki, A., et al. (2011). Comparative study of methods for administering neural stem/progenitor cells to treat spinal cord injury in mice. *Cell Transplant.* 20, 727–739. doi: 10.3727/096368910X536554

Takami, T., Oudega, M., Bates, M. L., Wood, P. M., Kleitman, N., and Bunge, M. B. (2002). Schwann cell but not olfactory ensheathing glia transplants improve hindlimb locomotor performance in the moderately contused adult rat thoracic spinal cord. *J. Neurosci.* 22, 6670–6681.

Teng, Y. D., Lavik, E. B., Qu, X., Park, K. I., Ourednik, J., Zurakowski, D., et al. (2002). Functional recovery following traumatic spinal cord injury mediated by a unique polymer scaffold seeded with neural stem cells. *Proc. Natl. Acad. Sci. U.S.A.* 99, 3024–3029. doi: 10.1073/pnas.052678899

Tetzlaff, W., Okon, E. B., Karimi-Abdolrezaee, S., Hill, C. E., Sparling, J. S., Plemel, J. R., et al. (2011). A systematic review of cellular transplantation therapies for spinal cord injury. *J. Neurotrauma* 28, 1611–1682. doi: 10.1089/neu.2009.1177

Theele, D. P., Schrimsher, G. W., and Reier, P. J. (1996). Comparison of the growth and fate of fetal spinal iso- and allografts in the adult rat injured spinal cord. *Exp. Neurol.* 142, 128–143. doi: 10.1006/exnr.1996.0184

Theodore, N., Kim, K. D., Hsieh, P. C., Ray, W. Z., Barry, M., Layer, R., et al. (2016). 178 High abbreviated injury scale grade conversion rate following neuro-spinal scaffold implantation in acute thoracic complete abbreviated injury scale a spinal cord injury: potential mechanisms. *Neurosurgery* 63(Suppl. 1):171. doi: 10.1227/01.neu.0000489747.92587.18

Tian, W. M., Hou, S. P., Ma, J., Zhang, C. L., Xu, Q. Y., Lee, I. S., et al. (2005). Hyaluronic acid-poly-D-lysine-based three-dimensional hydrogel for traumatic brain injury. *Tissue Eng.* 11, 513–525. doi: 10.1089/ten.2005.11.513

Triolo, D., Dina, G., Lorenzetti, I., Malaguti, M., Morana, P., Del Carro, U., et al. (2006). Loss of glial fibrillary acidic protein (GFAP) impairs Schwann cell proliferation and delays nerve regeneration after damage. *J. Cell Sci.* 119, 3981–3993. doi: 10.1242/jcs.03168

Vincent, A. J., Taylor, J. M., Choi-Lundberg, D. L., West, A. K., and Chuah, M. I. (2005). Genetic expression profile of olfactory ensheathing cells is distinct from that of Schwann cells and astrocytes. *Glia* 51, 132–147. doi: 10.1002/glia.20195

Vincent, A. J., West, A. K., and Chuah, M. I. (2003). Morphological plasticity of olfactory ensheathing cells is regulated by cAMP and endothelin-1. *Glia* 41, 393–403. doi: 10.1002/glia.10171

Vismara, I., Papa, S., Rossi, F., Forloni, G., and Veglianese, P. (2017). Current options for cell therapy in spinal cord injury. *Trends Mol. Med.* 23, 831–849. doi: 10.1016/j.molmed.2017.07.005

Volpato, F. Z., Fuhrmann, T., Migliaresi, C., Hutmacher, D. W., and Dalton, P. D. (2013). Using extracellular matrix for regenerative medicine in the spinal cord. *Biomaterials* 34, 4945–4955. doi: 10.1016/j.biomaterials.2013.03.057

Vroemen, M., Aigner, L., Winkler, J., and Weidner, N. (2003). Adult neural progenitor cell grafts survive after acute spinal cord injury and integrate along axonal pathways. *Eur. J. Neurosci.* 18, 743–751. doi: 10.1046/j.1460-9568.2003.02804.x

Vroemen, M., Caioni, M., Bogdahn, U., and Weidner, N. (2007). Failure of Schwann cells as supporting cells for adult neural progenitor cell grafts in the acutely injured spinal cord. *Cell Tissue Res.* 327, 1–13. doi: 10.1007/s00441-006-0252-y

Wang, B., Zhao, Y., Lin, H., Chen, B., Zhang, J., Zhang, J., et al. (2006). Phenotypical analysis of adult rat olfactory ensheathing cells on 3-D collagen scaffolds. *Neurosci. Lett.* 401, 65–70. doi: 10.1016/j.neulet.2006.02.085

Wang, C., Sun, C., Hu, Z., Huo, X., Yang, Y., Liu, X., et al. (2017). Improved neural regeneration with olfactory ensheathing cell inoculated PLGA scaffolds in spinal cord injury adult rats. *Neurosignals.* 25, 1–14. doi: 10.1159/000471828

Wang, J. J., Chuah, M. I., Yew, D. T., Leung, P. C., and Tsang, D. S. (1995). Effects of astrocyte implantation into the hemisected adult rat spinal cord. *Neuroscience* 65, 973–981. doi: 10.1016/0306-4522(94)00519-B

Wang, J. M., Zeng, Y. S., Wu, J. L., Li, Y., and Teng, Y. D. (2011). Cograft of neural stem cells and Schwann cells overexpressing TrkC and neurotrophin-3 respectively after rat spinal cord transection. *Biomaterials* 32, 7454–7468. doi: 10.1016/j.biomaterials.2011.06.036

Weidner, N., Blesch, A., Grill, R. J., and Tuszynski, M. H. (1999). Nerve growth factor-hypersecreting Schwann cell grafts augment and guide spinal cord axonal growth and remyelinate central nervous system axons in a phenotypically appropriate manner that correlates with expression of L1. *J. Comp. Neurol.* 413, 495–506.

Williams, R. R., Henao, M., Pearse, D. D., and Bunge, M. B. (2015). Permissive Schwann cell graft/spinal cord interfaces for axon regeneration. *Cell Transplant.* 24, 115–131. doi: 10.3727/096368913X674657

Wu, L., Li, J., Chen, L., Zhang, H., Yuan, L., and Davies, S. J. (2013). Combined transplantation of GDAs(BMP) and hr-decorin in spinal cord contusion repair. *Neural. Regen. Res.* 8, 2236–2248. doi: 10.3969/j.issn.1673-5374.2013.24.003

Wu, M. C., Yuan, H., Li, K. J., and Qiu, D. L. (2015). Cellular transplantation-based evolving treatment options in spinal cord injury. *Cell Biochem. Biophys.* 71, 1–8. doi: 10.1007/s12013-014-0174-3

Xiao, Z., Tang, F., Tang, J., Yang, H., Zhao, Y., Chen, B., et al. (2016). One-year clinical study of NeuroRegen scaffold implantation following scar resection in complete chronic spinal cord injury patients. *Sci. China Life Sci.* 59, 647–655. doi: 10.1007/s11427-016-5080-z

Xu, X. M., Chen, A., Guenard, V., Kleitman, N., and Bunge, M. B. (1997). Bridging Schwann cell transplants promote axonal regeneration from both the rostral and caudal stumps of transected adult rat spinal cord. *J. Neurocytol.* 26, 1–16. doi: 10.1023/A:1018557923309

Xu, X. M., Guenard, V., Kleitman, N., Aebischer, P., and Bunge, M. B. (1995a). A combination of BDNF and NT-3 promotes supraspinal axonal regeneration into Schwann cell grafts in adult rat thoracic spinal cord. *Exp. Neurol.* 134, 261–272. doi: 10.1006/exnr.1995.1056

Xu, X. M., Guenard, V., Kleitman, N., and Bunge, M. B. (1995b). Axonal regeneration into Schwann cell-seeded guidance channels grafted into transected adult-rat spinal-cord. *J. Comp. Neurol.* 351, 145–160. doi: 10.1002/cne.903510113

Xu, X. M., Zhang, S. X., Li, H., Aebischer, P., and Bunge, M. B. (1999). Regrowth of axons into the distal spinal cord through a Schwann-cell-seeded mini-channel implanted into hemisected adult rat spinal cord. *Eur. J. Neurosci.* 11, 1723–1740. doi: 10.1046/j.1460-9568.1999.00591.x

Zeng, X., Qiu, X. C., Ma, Y. H., Duan, J. J., Chen, Y. F., Gu, H. Y., et al. (2015). Integration of donor mesenchymal stem cell-derived neuron-like cells into host neural network after rat spinal cord transection. *Biomaterials* 53, 184–201. doi: 10.1016/j.biomaterials.2015.02.073

Zhang, L. L., Zhang, H. T., Cai, Y. Q., Han, Y. J., Yao, F., Yuan, Z. H., et al. (2016). Anti-inflammatory effect of mesenchymal stromal cell transplantation and quercetin treatment in a rat model of experimental cerebral ischemia. *Cell. Mol. Neurobiol.* 36, 1023–1034. doi: 10.1007/s10571-015-0291-6

Zhang, Y., and Barres, B. A. (2010). Astrocyte heterogeneity: an underappreciated topic in neurobiology. *Curr. Opin. Neurobiol.* 20, 588–594. doi: 10.1016/j.conb.2010.06.005

Zhao, R. R., Andrews, M. R., Wang, D., Warren, P., Gullo, M., Schnell, L., et al. (2013). Combination treatment with anti-Nogo-A and chondroitinase ABC is more effective than single treatments at enhancing functional recovery after spinal cord injury. *Eur. J. Neurosci.* 38, 2946–2961. doi: 10.1111/ejn.12276

Zhu, T. Q., Yu, D. H., Feng, J. X., Wu, X. J., Xiang, L., Gao, H. Y., et al. (2015). GDNF and NT-3 induce progenitor bone mesenchymal stem cell differentiation into neurons in fetal gut culture medium. *Cell. Mol. Neurobiol.* 35, 255–264. doi: 10.1007/s10571-014-0120-3

Zuidema, J. M., Desmond, G. P., Rivet, C. J., Kearns, K. R., Thompson, D. M., and Gilbert, R. J. (2015). Nebulized solvent ablation of aligned PLLA fibers for the study of neurite response to anisotropic-to-isotropic fiber/film transition (AFFT) boundaries in astrocyte-neuron co-cultures. *Biomaterials* 46, 82–94. doi: 10.1016/j.biomaterials.2014.12.046

Conflict of Interest Statement: The authors declare that the research was conducted in the absence of any commercial or financial relationships that could be construed as a potential conflict of interest.